

Published in Journals: Alloys, Applied Sciences,
Coatings, Materials and Metals

Topic Reprint

Numerical Modelling on Metallic Materials

Edited by
Shuwen Wen, Yongle Sun and Xin Chen

mdpi.com/topics



Numerical Modelling on Metallic Materials

Numerical Modelling on Metallic Materials

Topic Editors

Shuwen Wen

Yongle Sun

Xin Chen



Basel • Beijing • Wuhan • Barcelona • Belgrade • Novi Sad • Cluj • Manchester

Topic Editors

Shuwen Wen
AMRC Castings
University of Sheffield
Sheffield
UK

Yongle Sun
Welding and Additive
Manufacturing Centre
Faculty of Engineering and
Applied Sciences
Cranfield University
Cranfield
UK

Xin Chen
Welding and Additive
Manufacturing Centre
Faculty of Engineering and
Applied Sciences
Cranfield University
Cranfield
UK

Editorial Office

MDPI AG
Grosspeteranlage 5
4052 Basel, Switzerland

This is a reprint of the Topic, published open access by the journals *Alloys* (ISSN 2674-063X), *Applied Sciences* (ISSN 2076-3417), *Coatings* (ISSN 2079-6412), *Materials* (ISSN 1996-1944) and *Metals* (ISSN 2075-4701), freely accessible at: <https://www.mdpi.com/topics/modelling-metallic>.

For citation purposes, cite each article independently as indicated on the article page online and as indicated below:

Lastname, A.A.; Lastname, B.B. Article Title. <i>Journal Name</i> Year , Volume Number, Page Range.
--

ISBN 978-3-7258-3881-3 (Hbk)

ISBN 978-3-7258-3882-0 (PDF)

<https://doi.org/10.3390/books978-3-7258-3882-0>

© 2025 by the authors. Articles in this book are Open Access and distributed under the Creative Commons Attribution (CC BY) license. The book as a whole is distributed by MDPI under the terms and conditions of the Creative Commons Attribution-NonCommercial-NoDerivs (CC BY-NC-ND) license (<https://creativecommons.org/licenses/by-nc-nd/4.0/>).

Contents

Shuwen Wen, Yongle Sun and Xin Chen

Numerical Modelling on Metallic Materials

Reprinted from: *Metals* **2025**, 15, 423, <https://doi.org/10.3390/met15040423> 1

Semyon T. Baidak and Alexey V. Lukoyanov

Common Topological Features in Band Structure of RNiSb and RSb Compounds for R = Tb, Dy, Ho

Reprinted from: *Materials* **2023**, 16, 242, <https://doi.org/10.3390/ma16010242> 5

Guojin Xiang, Xu Luo, Tianxu Cao, Ankang Zhang and Hui Yu

Atomic Diffusion and Crystal Structure Evolution at the Fe-Ti Interface: Molecular Dynamics Simulations

Reprinted from: *Materials* **2022**, 15, 6302, <https://doi.org/10.3390/ma15186302> 16

Hongyu Zheng, Jingwen Sun, Na Guo and Mingjie Wang

Atomic Research on the Diffusion Behavior, Mechanical Properties and Fracture Mechanism of Fe/Cu Solid–Liquid Interface

Reprinted from: *Coatings* **2022**, 12, 1299, <https://doi.org/10.3390/coatings12091299> 28

Bo Lv, Chen Chen, Fucheng Zhang, Gennady M. Poletaev and Roman Y. Rakitin

Potentials for Describing Interatomic Interactions in γ Fe-Mn-C-N System

Reprinted from: *Metals* **2022**, 12, 982, <https://doi.org/10.3390/met12060982> 43

Simbarashe Fashu, Binting Huang and Nan Wang

Modification of Precipitate Coarsening Kinetics by Intragranular Nanoparticles—A Phase Field Study

Reprinted from: *Metals* **2022**, 12, 892, <https://doi.org/10.3390/met12060892> 51

Theerawat Kumnorkaew, Junhe Lian, Vitoon Uthaisangsuk and Wolfgang Bleck

Kinetic Model of Isothermal Bainitic Transformation of Low Carbon Steels under Ausforming Conditions

Reprinted from: *Alloys* **2022**, 1, 93–115, <https://doi.org/10.3390/alloys1010007> 67

Xuan Chen, Boya Wu, Jiayuan Li, Xiaoxiao Zhang, Pengpeng Zuo, Xiaochun Wu and Junwan Li

Microstructural Evolution in Large-Section Plastic Mould Steel during Multi-Directional Forging

Reprinted from: *Metals* **2022**, 12, 1175, <https://doi.org/10.3390/met12071175> 90

Radosław Ciepielewski and Danuta Miedzińska

A Study of Aluminum Honeycomb Structures under Dynamic Loading, with Consideration Given to the Effects of Air Leakage

Reprinted from: *Materials* **2023**, 16, 2211, <https://doi.org/10.3390/ma16062211> 108

Yanhua Zhao, Chuanbin Du, Peifu Wang, Wei Meng and Changming Li

The Mechanism of In-Situ Laser Polishing and Its Effect on the Surface Quality of Nickel-Based Alloy Fabricated by Selective Laser Melting

Reprinted from: *Metals* **2022**, 12, 778, <https://doi.org/10.3390/met12050778> 127

Abdulnaser M. Alshoaibi

Fatigue Crack Growth Analysis under Constant Amplitude Loading Using Finite Element Method

Reprinted from: *Materials* **2022**, 15, 2937, <https://doi.org/10.3390/ma15082937> 148

Wenliang Ma, Zihan Sun, Han Wu, Leige Xu, Yong Zeng, Yanxing Wang and Guangyin Huang Buckling Analysis of Thin-Walled Circular Shells under Local Axial Compression using Vector Form Intrinsic Finite Element Method Reprinted from: <i>Metals</i> 2023 , 13, 564, https://doi.org/10.3390/met13030564	162
Ricardo Daniel Lopez-Garcia, Israel Medina-Juárez and Araceli Maldonado-Reyes Effect of Quenching Parameters on Distortion Phenomena in AISI 4340 Steel Reprinted from: <i>Metals</i> 2022 , 12, 759, https://doi.org/10.3390/met12050759	182
Yongli Peng, Zhengyi Kong, Ba Huu Dinh, Huu-Hue Nguyen, Truong-Son Cao, George Papazafeiropoulos and Quang-Viet Vu Web Bend-Buckling of Steel Plate Girders Reinforced by Two Longitudinal Stiffeners with Various Cross-Section Shapes Reprinted from: <i>Metals</i> 2023 , 13, 323, https://doi.org/10.3390/met13020323	203
Zhenwei Huang and Xinlu Yu Numerical Simulation Study of Expanding Fracture of 45 Steel Cylindrical Shell under Different Detonation Pressure Reprinted from: <i>Materials</i> 2022 , 15, 3980, https://doi.org/10.3390/ma15113980	221
Tongzheng He and Yuyong Chen Influence of Mold Design on Shrinkage Porosity of Ti-6Al-4V Alloy Ingots Reprinted from: <i>Metals</i> 2022 , 12, 2122, https://doi.org/10.3390/met12122122	237
Myung-Sung Kim, Hee-Tae Kim, Young-Hwan Choi, Jeong-Hyeon Kim, Seul-Kee Kim and Jae-Myung Lee A New Computational Method for Predicting Ductile Failure of 304L Stainless Steel Reprinted from: <i>Metals</i> 2022 , 12, 1309, https://doi.org/10.3390/met12081309	252
Leonie Wallat, Patrick Altschuh, Martin Reder, Britta Nestler and Frank Poehler Computational Design and Characterisation of Gyroid Structures with Different Gradient Functions for Porosity Adjustment Reprinted from: <i>Materials</i> 2022 , 15, 3730, https://doi.org/10.3390/ma15103730	271
Ming Liu, Peng Yan, Pengbo Liu, Jinwei Qiao and Zhi Yang An Improved Particle-Swarm-Optimization Algorithm for a Prediction Model of Steel Slab Temperature Reprinted from: <i>Applied Sciences</i> 2022 , 12, 11550, https://doi.org/10.3390/app122211550	284
Tianze Zhao, Yanze Gao, Rui Shi, Zhuo Li and Qingfeng Shi Structure of Randomly Distributed Nanochain Aggregates on Silicon Substrates: Modeling and Optical Absorption Characteristics Reprinted from: <i>Materials</i> 2022 , 15, 4778, https://doi.org/10.3390/ma15144778	301
Yao Chen, Yonghong Gao, Chuanxiang Guo, Yanping Guo, Zhijun Guo, Yingbin Liu and Tiansheng Liu Effect of the Addition of Steel Fibers on the Bonding Interface and Tensile Properties of Explosion-Welded 2A12 Aluminum Alloy and SS-304 Steel Reprinted from: <i>Materials</i> 2023 , 16, 116, https://doi.org/10.3390/ma16010116	317

Numerical Modelling on Metallic Materials

Shuwen Wen ^{1,*}, Yongle Sun ² and Xin Chen ²

¹ AMRC Castings, University of Sheffield, Advanced Manufacturing Park, Brunel Way, Rotherham S60 5WG, UK

² Welding and Additive Manufacturing Centre, Faculty of Engineering and Applied Sciences, Cranfield University, Cranfield MK43 0AL, UK; yongle.sun@cranfield.ac.uk (Y.S.); x.chen1@cranfield.ac.uk (X.C.)

* Correspondence: shuwen.wen@amrc.co.uk

1. Introduction

Numerical modelling of metallic materials has emerged as a pivotal research area in modern materials science and engineering [1]. With the advancement of computational power and the development of sophisticated modelling techniques, numerical simulation has become an indispensable tool for studying the microstructural evolution, enhancing process understanding and optimisation, and predicting the mechanical properties of metallic materials [2–9]. By employing accurate mathematical models and efficient computational methods, researchers can simulate the complex behaviours of real-world materials in a virtual environment. This approach not only reduces experimental costs and boosts research efficiency, but also uncovers physical phenomena that are challenging to observe directly through experiments [10–15].

This Topic is dedicated to the “Numerical Modelling on Metallic Materials” and presents a curated collection of twenty cutting-edge research papers in the field. These studies span multiple scales, from microstructural evolution to macroscopic mechanical behaviour, and explore the response of various metallic materials under diverse processing and service conditions. At the microscopic level, numerical modelling is applied extensively to explore phase transformations, diffusion behaviours, and microstructural evolution in metallic materials. At the mesoscopic and macroscopic levels, numerical simulations are employed to predict the mechanical properties and failure mechanisms of metallic materials, offering insights into performance and durability. The studies featured in this collection highlight the vital role of advanced modelling techniques, including finite element analysis (FEA), molecular dynamics simulations (MDS), computational fluid dynamics (CFD), discrete element method (DEM), and phase-field (PF) and other modelling techniques, in optimising engineering designs, predicting material performance, and improving manufacturing processes.

Additionally, this Topic also showcases emerging numerical modelling approaches, such as topology optimisation and the applications of various other optimisation algorithms, in metallic material simulations. These innovative approaches, when combined with traditional physical modelling techniques, extend the capabilities of numerical modelling to encompass intelligent computation and multi-scale analysis. Such advancements pave the way for more efficient and effective strategies for the design and optimisation of future materials.

2. Outline of This Topic

This Topic includes twenty technical papers contributed by the authors working in the field and is organised into three main sections, each offering a comprehensive exploration



Received: 26 March 2025

Accepted: 7 April 2025

Published: 9 April 2025

Citation: Wen, S.; Sun, Y.; Chen, X.

Numerical Modelling on Metallic Materials. *Metals* **2025**, *15*, 423.

<https://doi.org/10.3390/met15040423>

Copyright: © 2025 by the authors.

Licensee MDPI, Basel, Switzerland.

This article is an open access article distributed under the terms and

conditions of the Creative Commons Attribution (CC BY) license

(<https://creativecommons.org/licenses/by/4.0/>).

of numerical modelling applications in metallic materials. The three sections comprise atomic-scale and microstructural evolution modelling, meso- and macro-scale mechanical behaviour simulations, and emerging computational techniques and advanced applications in metallic materials research. These contributions are summarised and listed below.

2.1. Atomic-Scale and Microstructural Evolution Modelling

Baidak, S.T. et al. (contribution 1) analysed the electronic band structures of intermetallic compounds and their topological characteristics using an ab initio method. Xiang, G., et al. (contribution 2) investigated the diffusion of atoms and crystal structure evolution at the Fe-Ti interface through MDS. Zheng, H., et al. (contribution 3) employed MDS to examine how different orientations, temperatures, and strain rates influence the diffusion behaviour and mechanical properties of the Fe/Cu solid-liquid interface. Lv, B., et al. (contribution 4) developed computational interatomic potentials for accurately modelling the behaviours of multi-component metallic systems. Fashu, S., et al. (contribution 5) explored the impact of intragranular nanoparticles on precipitate-coarsening behaviours in metallic alloys based on PF modelling. Kumnorkaew, T., et al. (contribution 6) presented a kinetic model for predicting bainitic transformation kinetics in low-carbon steels under different thermomechanical treatments. Chen, X., et al. (contribution 7) investigated how multi-directional forging (MDF) at 1150 °C affects the microstructure of SDP1 steel and compared it to traditional forging methods.

2.2. Meso- and Macro-Scale Mechanical Behaviour Simulations

Ciepielewski, R., et al. (contribution 8) investigated the energy-absorbing properties of aluminium honeycomb structures, particularly focusing on the impact of entrapped air within the cells during dynamic loading conditions. Zhao, Y., et al. (contribution 9) developed a model combining CFD with DEM and investigated the mechanism of laser polishing and its influence on the surface finish of additively manufactured nickel alloys. Alshoaibi, A.M., et al. (contribution 10) applied FEA to predict fatigue crack growth behaviours under cyclic loading conditions. Ma, W., et al. (contribution 11) modelled the buckling and post-buckling behaviours of thin-walled structures under axial loads. Lopez-Garcia, R.D., et al. (contribution 12) studied how quenching parameters influence distortion and residual stresses in high-strength steel components. Peng, Y., et al. (contribution 13) examined the effectiveness of different stiffener geometries in enhancing the stability of steel girders. Huang, Z., et al. (contribution 14) simulated fracture expansion behaviours in steel cylindrical shells subjected to explosive loads. In addition, He, T., et al. (contribution 15) analysed the effects of mould design on shrinkage porosity in titanium alloy casting.

2.3. Emerging Computational Techniques and Advanced Applications

Kim, M.S., et al. (contribution 16) introduced a novel constitutive model to predict ductile fracture initiation and progression. Wallat, L., et al. (contribution 17) explored computational methods for designing gyroid-based porous structures with tuneable mechanical properties. Liu, M., et al. (contribution 18) enhanced the accuracy of temperature prediction for steel slabs in industrial heating processes using an optimised particle swarm algorithm. Zhao, T., et al. (contribution 19) modelled and analysed the optical properties of nanochain aggregates on silicon surfaces. Chen, Y., et al. (contribution 20) used smooth particle hydrodynamic simulation to examine how steel fibre reinforcement enhances the tensile and bonding properties of explosion-welded aluminium-steel composites.

3. Concluding Remarks

This Topic is intended for researchers, engineers, and graduate students engaged in metallic materials research. Through these research papers, readers will gain valu-

able insights into the latest advancements in numerical modelling, explore cutting-edge computational techniques, and discover diverse applications of numerical modelling and simulation in materials science and engineering. This Topic serves as a comprehensive reference for both academic research and industrial practice, advancing the field of metallic materials.

Funding: This research received no external funding.

Conflicts of Interest: The authors declare no conflicts of interest.

List of Contributions

1. Baidak, S.T.; Lukoyanov, A.V. Common topological features in band structure of RNiSb and RSb compounds for R= Tb, Dy, Ho. *Materials* **2023**, *16*, 242. <https://doi.org/10.3390/ma16010242>.
2. Xiang, G.; Luo, X.; Cao, T.; Zhang, A.; Yu, H. Atomic diffusion and crystal structure evolution at the Fe-Ti interface: molecular dynamics simulations. *Materials* **2022**, *15*, 6302. <https://doi.org/10.3390/ma15186302>.
3. Zheng, H.; Sun, J.; Guo, N.; Wang, M. Atomic Research on the Diffusion Behavior, Mechanical Properties and Fracture Mechanism of Fe/Cu Solid–Liquid Interface. *Coatings* **2022**, *12*, 1299. <https://doi.org/10.3390/coatings12091299>.
4. Lv, B.; Chen, C.; Zhang, F.; Poletaev, G.M.; Rakitin, R.Y. Potentials for describing interatomic interactions in γ Fe-Mn-CN system. *Metals* **2022**, *12*, 982. <https://doi.org/10.3390/met12060982>.
5. Fashu, S.; Huang, B.; Wang, N. Modification of Precipitate Coarsening Kinetics by Intragranular Nanoparticles—A Phase Field Study. *Metals* **2022**, *12*, 892. <https://doi.org/10.3390/met12060892>.
6. Kumnorkaew, T.; Lian, J.; Uthaisangasuk, V.; Bleck, W. Kinetic model of isothermal bainitic transformation of low carbon steels under ausforming conditions. *Alloys* **2022**, *1*, 93–115. <https://doi.org/10.3390/alloys1010007>.
7. Chen, X.; Wu, B.; Li, J.; Zhang, X.; Zuo, P.; Wu, X.; Li, J. Microstructural Evolution in Large-Section Plastic Mould Steel during Multi-Directional Forging. *Metals* **2022**, *12*, 1175. <https://doi.org/10.3390/met12071175>.
8. Ciepielewski, R.; Miedzińska, D. A Study of Aluminum Honeycomb Structures under Dynamic Loading, with Consideration Given to the Effects of Air Leakage. *Materials* **2023**, *16*, 2211. <https://doi.org/10.3390/ma16062211>.
9. Zhao, Y.; Du, C.; Wang, P.; Meng, W.; Li, C. The mechanism of in-situ laser polishing and its effect on the surface quality of nickel-based alloy fabricated by selective laser melting. *Metals* **2022**, *12*, 778. <https://doi.org/10.3390/met12050778>.
10. Alshoaibi, A.M. Fatigue crack growth analysis under constant amplitude loading using finite element method. *Materials* **2022**, *15*, 2937. <https://doi.org/10.3390/ma15082937>.
11. Ma, W.; Sun, Z.; Wu, H.; Xu, L.; Zeng, Y.; Wang, Y.; Huang, G. Buckling Analysis of Thin-Walled Circular Shells under Local Axial Compression using Vector Form Intrinsic Finite Element Method. *Metals* **2023**, *13*, 564. <https://doi.org/10.3390/met13030564>.
12. Lopez-Garcia, R.D.; Medina-Juárez, I.; Maldonado-Reyes, A. Effect of quenching parameters on distortion phenomena in AISI 4340 steel. *Metals* **2022**, *12*, 759. <https://doi.org/10.3390/met12050759>.
13. Peng, Y.; Kong, Z.; Dinh, B.H.; Nguyen, H.H.; Cao, T.S.; Papazafeiropoulos, G.; Vu, Q.V. Web Bend-Buckling of Steel Plate Girders Reinforced by Two Longitudinal Stiffeners with Various Cross-Section Shapes. *Metals* **2023**, *13*, 323. <https://doi.org/10.3390/met13020323>.
14. Huang, Z.; Yu, X. Numerical simulation study of expanding fracture of 45 steel cylindrical shell under different detonation pressure. *Materials* **2022**, *15*, 3980. <https://doi.org/10.3390/ma15133980>.
15. He, T.; Chen, Y. Influence of Mold Design on Shrinkage Porosity of Ti-6Al-4V Alloy Ingots. *Metals* **2022**, *12*, 2122. <https://doi.org/10.3390/met12122122>.
16. Kim, M.S.; Kim, H.T.; Choi, Y.H.; Kim, J.H.; Kim, S.K.; Lee, J.M. A new computational method for predicting ductile failure of 304L stainless steel. *Metals* **2022**, *12*, 1309. <https://doi.org/10.3390/met12081309>.

17. Wallat, L.; Altschuh, P.; Reder, M.; Nestler, B.; Poehler, F. Computational design and characterisation of gyroid structures with different gradient functions for porosity adjustment. *Materials* **2022**, *15*, 3730. <https://doi.org/10.3390/ma15103730>.
18. Liu, M.; Yan, P.; Liu, P.; Qiao, J.; Yang, Z. An improved particle-swarm-optimization algorithm for a prediction model of steel slab temperature. *Appl. Sci.* **2022**, *12*, 11550. <https://doi.org/10.3390/app122211550>.
19. Zhao, T.; Gao, Y.; Shi, R.; Li, Z.; Shi, Q. Structure of Randomly Distributed Nanochain Aggregates on Silicon Substrates: Modeling and Optical Absorption Characteristics. *Materials* **2022**, *15*, 4778. <https://doi.org/10.3390/ma15144778>.
20. Chen, Y.; Gao, Y.; Guo, C.; Guo, Y.; Guo, Z.; Liu, Y.; Liu, T. Effect of the Addition of Steel Fibers on the Bonding Interface and Tensile Properties of Explosion-Welded 2A12 Aluminum Alloy and SS-304 Steel. *Materials* **2023**, *16*, 116. <https://doi.org/10.3390/ma16010116>.

References

1. Rappaz, M.; Bellet, M.; Deville, M.O.; Snyder, R. *Numerical Modeling in Materials Science and Engineering*; Springer: Berlin, Germany, 2003; Volume 20.
2. Liu, H.; Xu, X.; Zhang, J.; Liu, Z.; He, Y.; Zhao, W.; Liu, Z. The state of the art for numerical simulations of the effect of the microstructure and its evolution in the metal-cutting processes. *Int. J. Mach. Tools Manuf.* **2022**, *177*, 103890. [CrossRef]
3. DebRoy, T.; Mukherjee, T.; Wei, H.L.; Elmer, J.W.; Milewski, J.O. Metallurgy, mechanistic models and machine learning in metal printing. *Nat. Rev. Mater.* **2021**, *6*, 48–68. [CrossRef]
4. Bandyopadhyay, A.; Traxel, K.D. Invited review article: Metal-additive manufacturing—Modeling strategies for application-optimized designs. *Addit. Manuf.* **2018**, *22*, 758–774. [CrossRef] [PubMed]
5. Klingenberg, W.; Singh, U.P. Further observations and review of numerical simulations of sheet metal punching. *Int. J. Adv. Manuf. Technol.* **2006**, *30*, 638–644. [CrossRef]
6. Dal, M.; Fabbro, R. An overview of the state of art in laser welding simulation. *Opt. Laser Technol.* **2016**, *78*, 2–14. [CrossRef]
7. Thomas, B.G. Review on modeling and simulation of continuous casting. *Steel Res. Int.* **2018**, *89*, 1700312. [CrossRef]
8. Sun, Y.; Li, Q.M. Dynamic compressive behaviour of cellular materials: A review of phenomenon, mechanism and modelling. *Int. J. Impact Eng.* **2018**, *112*, 74–115. [CrossRef]
9. Zhang, Z.; Wang, Y.; Ge, P.; Wu, T. A review on modelling and simulation of laser additive manufacturing: Heat transfer, microstructure evolutions and mechanical properties. *Coatings* **2022**, *12*, 1277. [CrossRef]
10. Kiran, A.; Hodek, J.; Vavřík, J.; Urbánek, M.; Džugan, J. Numerical simulation development and computational optimization for directed energy deposition additive manufacturing process. *Materials* **2020**, *13*, 2666. [CrossRef]
11. Chen, X.; Wang, C.; Ding, J.; Bridgeman, P.; Williams, S. A three-dimensional wire-feeding model for heat and metal transfer, fluid flow, and bead shape in wire plasma arc additive manufacturing. *J. Manuf. Process.* **2022**, *83*, 300–312. [CrossRef]
12. Gu, H.; Li, L. Computational fluid dynamic simulation of gravity and pressure effects in laser metal deposition for potential additive manufacturing in space. *Int. J. Heat Mass Transf.* **2019**, *140*, 51–65. [CrossRef]
13. Taghizadeh, M.; Zhu, Z.H. A comprehensive review on metal laser additive manufacturing in space: Modeling and perspectives. *Acta Astronaut.* **2024**, *222*, 403–421. [CrossRef]
14. Zhou, N.; Lv, D.C.; Zhang, H.L.; McAllister, D.; Zhang, F.; Mills, M.J.; Wang, Y. Computer simulation of phase transformation and plastic deformation in IN718 superalloy: Microstructural evolution during precipitation. *Acta Mater.* **2014**, *65*, 270–286. [CrossRef]
15. Zepeda-Ruiz, L.A.; Stukowski, A.; Oppelstrup, T.; Bulatov, V.V. Probing the limits of metal plasticity with molecular dynamics simulations. *Nature* **2017**, *550*, 492–495. [CrossRef] [PubMed]

Disclaimer/Publisher’s Note: The statements, opinions and data contained in all publications are solely those of the individual author(s) and contributor(s) and not of MDPI and/or the editor(s). MDPI and/or the editor(s) disclaim responsibility for any injury to people or property resulting from any ideas, methods, instructions or products referred to in the content.

Article

Common Topological Features in Band Structure of RNiSb and RSb Compounds for R = Tb, Dy, Ho

Semyon T. Baidak ^{1,2} and Alexey V. Lukoyanov ^{1,2,*}

¹ Institute of Physics and Technology, Ural Federal University Named after the First President of Russia B.N. Yeltsin, 620002 Ekaterinburg, Russia

² M.N. Mikheev Institute of Metal Physics of Ural Branch of Russian Academy of Sciences, 620108 Ekaterinburg, Russia

* Correspondence: lukoyanov@imp.uran.ru; Tel.: +7-3433783886

Abstract: The electronic and band structures of ternary RNiSb and binary RSb compounds for R = Tb, Dy, Ho, have been investigated using an ab initio method accounting for strong electron correlations in the 4f shell of the rare-earth metals. These ternary compounds are found to be semiconductors with the indirect gap of 0.21, 0.21, and 0.26 eV for Tb, Dy, and Ho(NiSb), respectively. In contrast, in all binary RSb compounds, bands near the Fermi energy at the Γ and X points are shifted relatively to RNiSb and form hole and electron pockets, so the energy gap is closed in RSb. The band structure typical for semimetals is formed in all RSb compounds for R = Tb, Dy, Ho. For the first time, we identify similar features near the Fermi level in the considered binary semimetals, namely, the presence of the hole and electron pockets in the vicinity of the Γ and X points, the nonsymmetric electron pocket along Γ -X-W direction and hole pockets along the L- Γ -X direction, which were previously found experimentally in the other compound of this series GdSb. The magnetic moment of all considered compounds is fully determined by magnetic moments of the rare earth elements, the calculated effective magnetic moments of these ions have values close to the experimental values for all ternary compounds.

Keywords: electronic structure; topologic structure; alloys; intermetallics; first principles calculations

Citation: Baidak, S.T.; Lukoyanov, A.V. Common Topological Features in Band Structure of RNiSb and RSb Compounds for R = Tb, Dy, Ho. *Materials* **2023**, *16*, 242. <https://doi.org/10.3390/ma16010242>

Academic Editors: Shuwen Wen, Yongle Sun, Xin Chen and Luca Spiridigliozzi

Received: 16 November 2022

Revised: 7 December 2022

Accepted: 23 December 2022

Published: 27 December 2022



Copyright: © 2022 by the authors. Licensee MDPI, Basel, Switzerland. This article is an open access article distributed under the terms and conditions of the Creative Commons Attribution (CC BY) license (<https://creativecommons.org/licenses/by/4.0/>).

1. Introduction

The RTX is a family of compounds, where R is a rare earth element, T designates a transition metal, and X is a s/p element. These types of compounds have been known for their unusual electronic and magnetic properties, such as heavy fermion behavior [1,2], magnetic superconductivity [3,4], the presence of Weyl fermions [5], magnetocaloric effect [6–8], large magnetoresistance and negative temperature coefficient of resistivity [9,10], and more. Another outstanding characteristic of many RNiSb compounds is giant magnetoresistance [11,12] found in half-Heusler structure [13]. Such ternary materials with remarkable thermoelectric properties can be used for thermoelectric power generation and for conversion of waste heat in electricity with high efficiency [14]. High values of ZT, which is thermoelectric figure of merit, were observed in TmNiSb and Sn-doped ErNiSb with the value of 0.25 for TmNiSb at 700 K [15] and even higher value of 0.29 at 669 K for ErNiSb [16] and other compounds of this series [15,17–19].

Magnetic susceptibility measurements for RNiSb compounds have also been conducted and experiments show that most of the compounds exhibit Curie-Weiss behavior where magnetism is dominated by the magnetic moments of rare earth elements [20]. Theoretical electronic structure calculations for GdNiSb [21], as well as for the close GdNiGe compound [22], indeed show that the dominant contribution to the total magnetic moment is due to R while the contribution of Ni and Sb (Ge) is negligible. There is also a close binary compound GdSb that is found to have a pair of Weyl fermions, the presence of which can lead to chiral anomaly-induced negative longitudinal magnetoresistance under external

magnetic field [23]. High-resolution angle-resolved photoemission spectroscopy (ARPES) measurements for DySb and HoSb were conducted and revealed at least two concentric hole pockets at the Γ point and two intersecting electron pockets at the X point [24], similar features were found in the band structure of LuSb calculated within GGA not accounting for electron correlations reported in [24]. Binary compound DySb was found to have extremely large positive magnetoresistance from experimental results with the suggested non-trivial band topology from DFT calculations with an inversion point seated about 0.34 eV below the Fermi level [25]. A recent experimental study of the binary compound HoSb also found extremely large magnetoresistance, the close interplay between conduction electrons and magnetism was suggested [26].

The ternary Tb/Ho/DyNiSb intermetallics, which are studied in this work, are half-Heusler compounds and crystallize in the cubic MgAgAs-type structure. This structure may be regarded as NaCl-type structure, where the rare earth and Sb atoms take the positions of the Na and Cl atoms, while the Ni atoms occupy one half of the tetrahedral voids formed by the Sb atoms [13]. It has also been shown that compounds in question exhibit large negative magnetoresistance at low temperatures which is caused by the reduction of spin disorder scattering due to the alignment of the moments under a magnetic field [11,12]. The ternary DyNiSb compound is found to be a narrow-gap intrinsic p-type semiconductor with the experimental value of the energy gap of 0.130–0.171 eV [9], 0.089–0.130 eV [15], for HoNiSb it is estimated as 0.08–0.11 eV [9].

In this study, we consider in detail the band (and electronic) structure, as well as magnetic properties, of the RSb and RNiSb compounds for R = Tb, Dy, Ho, in order to identify common topological features of the band structure, electronic structure and magnetic properties.

2. Materials and Methods

The ternary Tb/Dy/HoNiSb compounds have MgAgAs-type half-Heusler structure (space group F-43m, number 216) [13] with the lattice parameters: $a = b = c = 6.304$ Å for TbNiSb, $a = b = c = 6.298$ Å for DyNiSb and $a = b = c = 6.262$ Å for the HoNiSb compound [20] with following atomic positions Tb/Dy/Ho in $4a$ (0, 0, 0), Ni in $4c$ ($1/4$, $1/4$, $1/4$) and Sb in $4b$ ($1/2$, $1/2$, $1/2$). Binary RSb compounds have similar cubic crystal structure with the same atomic positions of rare earth element and Sb atoms with the following lattice parameters: $a = b = c = 6.170$ Å for TbSb, $a = b = c = 6.150$ Å for DySb and $a = b = c = 6.130$ Å for the HoSb compound [27].

The crystal structure of Tb/Dy/HoNiSb is plotted in Vesta [28] in Figure 1. The unit cell of RNiSb contains 1 rare-earth atom, 1 nickel atom and 1 antimony atom. The Sb atom has an environment of four Ni atoms in the form of a tetrahedron.

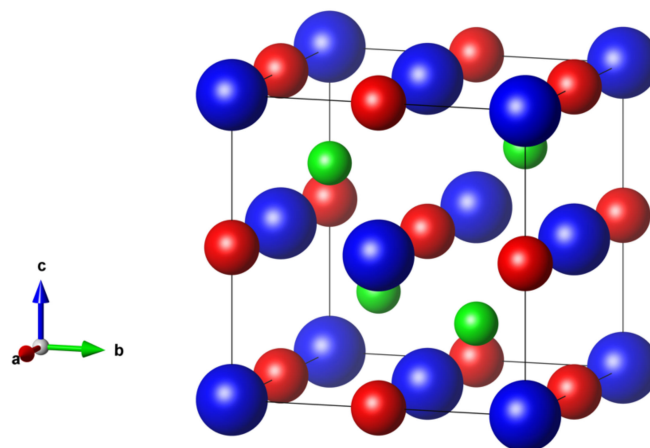


Figure 1. Crystal structure of RNiSb compounds. R atoms are shown in blue, Ni—in green, Sb—in red.

Electronic structure calculations were conducted in the Quantum Espresso package [29,30] using GGA+U version of LSDA+U method. Such method is widely used to take into account strong electron correlations between electrons of 4f shells in ions of rare earth elements. Parameters in GGA+U method have following values: Hund's exchange parameter $J = 0.7$ eV for all three considered elements and direct Coulomb interaction U is equal to 5.4 eV for Tb, 5.8 eV for Dy and 5.9 eV for Ho [2,31]. In this work we assume that magnetic moments of rare earth elements have ferromagnetic ordering. The exchange correlation potential was employed in generalized gradient approximation (GGA) of Perdew-Burke-Ernzerhof (PBE) [32]. The calculations used the standard ultrasoft potentials from the pseudopotential library of Quantum ESPRESSO for Ni and Sb [33], projected augmented wave method (PAW) scalar-relativistic potentials for rare-earth elements from work [34]. Wave functions were expanded in plane waves, Blochl's tetrahedron method was employed for Brillouin-zone integration on a $12 \times 12 \times 12$ k-point mesh, interactions between ions and valence electrons were taken into account within the framework of the method of plane augmented waves.

3. Results

3.1. TbNiSb and TbSb Intermetallic Compounds

In Figure 2, the total and partial densities of electronic states of the TbNiSb and TbSb intermetallic compounds are given for two opposite spin directions. Two intense peaks in the total density of states for the majority spin direction of the TbNiSb (TbSb) compound in Figure 2a are formed by the 4f states of Tb at following energies: -7.2 (-7.8) eV and -6.1 (-6.6) eV below the valence band. Another two noticeable intense peaks in Figure 2a for the minority spin projection are found in the conduction band at energies 2.9 (2.3) eV and 3.3 (2.7) eV. One can see that valence band in TbNiSb compound is mostly formed by non-spin-polarized Ni 3d states Figure 2b with some contribution from Tb-5d and Sb-5p states. In binary TbSb compound the biggest contribution to the valence band is due to Sb-5p states Figure 2c. For both compounds and both spin projections Tb-5d states lay in the conduction band mostly unoccupied Figure 2b. The other electronic states are not shown in this figure due to their negligible contribution.

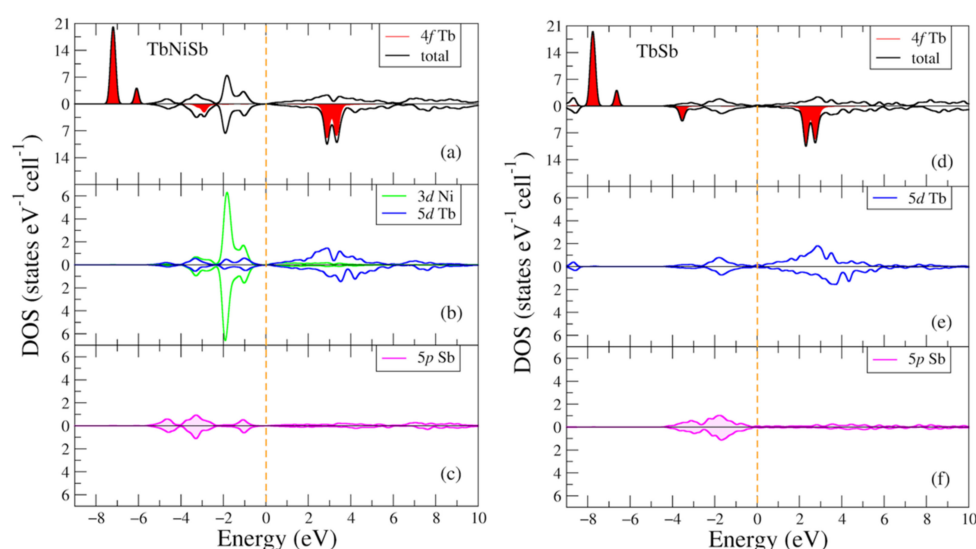


Figure 2. Densities of electronic states from DFT+U for (a–c) TbNiSb; (d–f) TbSb. (a,d) Total and partial Tb-4f densities of states; (b,e) Partial density of states for Tb-5d (Ni-3d); (c,f) Partial density of states for Sb-5p. The plot is shifted relatively to the Fermi energy shown at zero as a vertical line.

The band structure for the majority and minority spin projections of TbNiSb is shown in Figure 3. One can see the energy gap of 0.43 eV in the majority spin projection in Figure 3a and energy gap of 0.21 eV for the other spin projection in Figure 3b. Point Γ

is the highest point in the valence band and the lowest point in the conduction band is X, so the compound is a semiconductor with an indirect gap. There are localized bands at the energies of eV -7.2 eV and -6.1 eV in Figure 3a and at the energies of (2.9; 3.3) eV in Figure 3b which correspond to intense peaks at the same energies in the density of states Figure 2a. There is also the presence of the occupied states near the Γ point at the Fermi level.

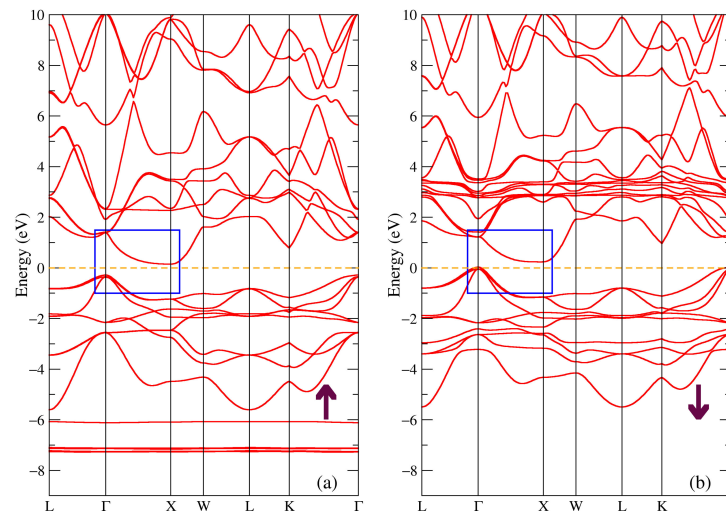


Figure 3. Band structure of TbNiSb: (a) majority and (b) minority spin projections. The blue rectangle points out the bands involved in the band gap formation.

The band structure for the majority and minority spin projections of TbSb is shown in Figure 4. The bands near the Fermi energy at the Γ and X points are shifted relatively to the band structure of TbNiSb shown in Figure 3 and here they form hole and electron pockets (see the blue rectangle in Figure 4), so there is no energy gap for both spin projections. Such a band structure is typical for a semimetal. There is also a presence of similar to Figure 3 localized bands from 4f states of Tb at pretty much the same energies, only a few tenths of eV lower, one can find narrow intense peaks at these energies in the total density of states in Figure 2d.

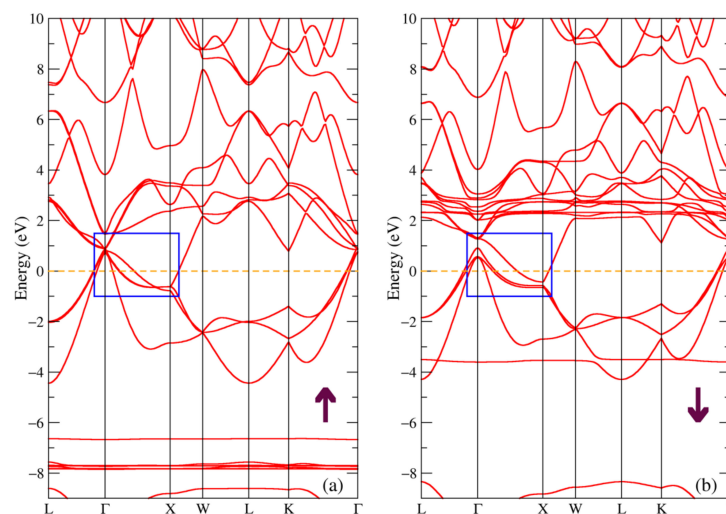


Figure 4. Band structure of TbSb: (a) majority and (b) minority spin projections. The blue rectangle points out the bands involved in the formation of pockets, see in the text.

3.2. DyNiSb and DySb Intermetallic Compounds

In Figure 5, the total and partial densities of electronic states of the DyNiSb and DySb intermetallic compounds are given for two opposite spin directions. In Figure 5a,d one can find similar to Figure 2a,d narrow intense peaks which manifest 4f states of rare earth metals. For the DyNiSb (DySb) compound and the majority spin projection such peaks are found at following energies: -7.8 (-8.3) eV and -6.6 (-7.3 , -6.9) eV below the valence band. For the minority spin projection intense peaks are found at 2.4 (1.7) eV and 3.0 (2.2) eV. There is also a noticeable peak at -4.1 (4.6) eV contrary to Figure 2a,d for the minority spin projection for both DyNiSb and DySb in the bottom part of the valence band. The densities of Ni-3d, Dy-5d, and Sb-5p states in Figure 5 exhibit the behavior identical to those plotted in Figure 2.

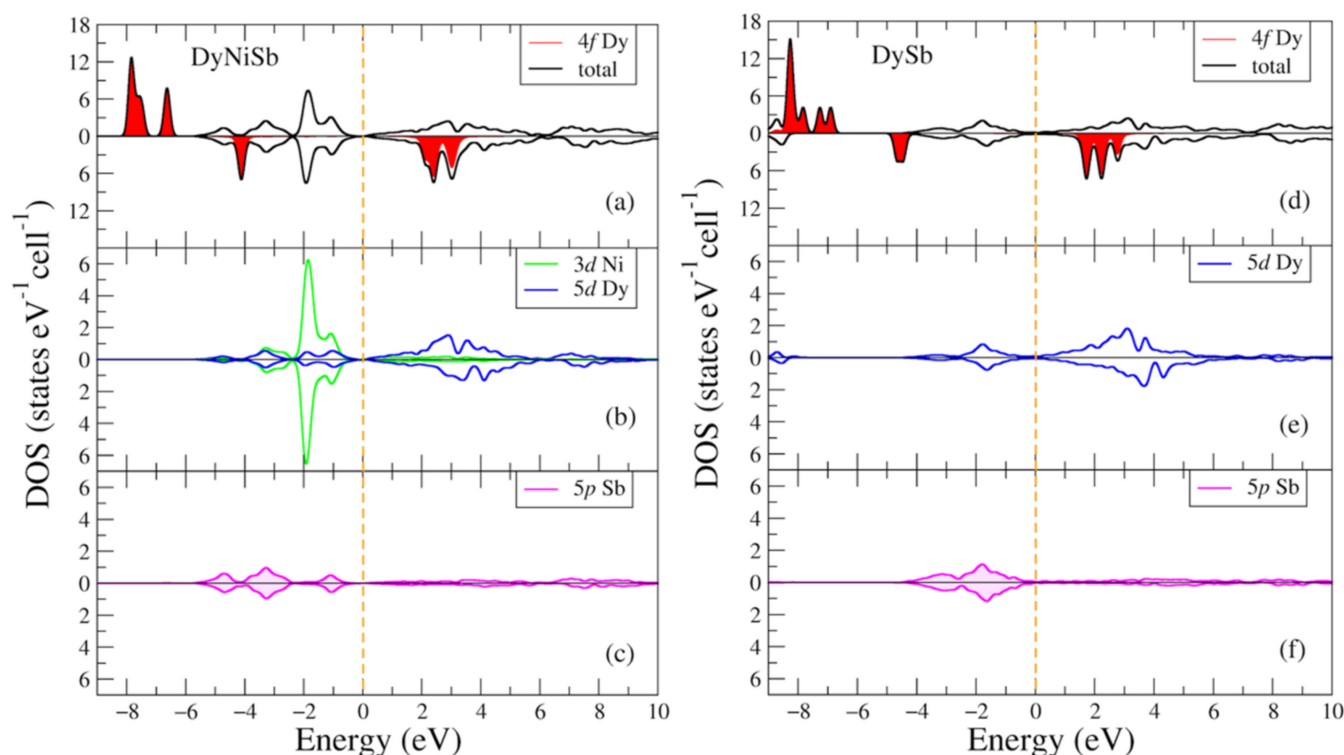


Figure 5. Densities of electronic states from DFT+U for (a–c) DyNiSb; (d–f) DySb. (a,d) Total and partial Dy-4f densities of states; (b,e) partial density of states for Dy-5d (Ni-3d); (c,f) partial density of states for Sb-5p. The plot is shifted relatively to the Fermi energy shown at zero as a vertical dashed line.

The band structure for the majority and minority spin projections of DyNiSb compound is shown in Figure 6. The electronic states near the Fermi energy are mostly dominated by the Ni-3d and Dy-5d states, so the band structure near this level looks similar to the one in Figure 3 with the main difference being the value of the energy gap (see the blue rectangle in Figure 6). Thus, we conclude that the ternary DyNiSb compound is a semiconductor with an indirect gap of 0.39 eV for the majority spin projection and of 0.21 eV for the minority spin projection. It is in a good agreement with the experimental value of the energy gap of 0.130 – 0.171 eV [9], 0.089 – 0.130 eV [15] for DyNiSb. The localized bands from the 4f states of dysprosium similarly to previous Tb-compounds in Figures 3 and 4 produce intense peaks at the same energies in the density of states in Figure 5a.

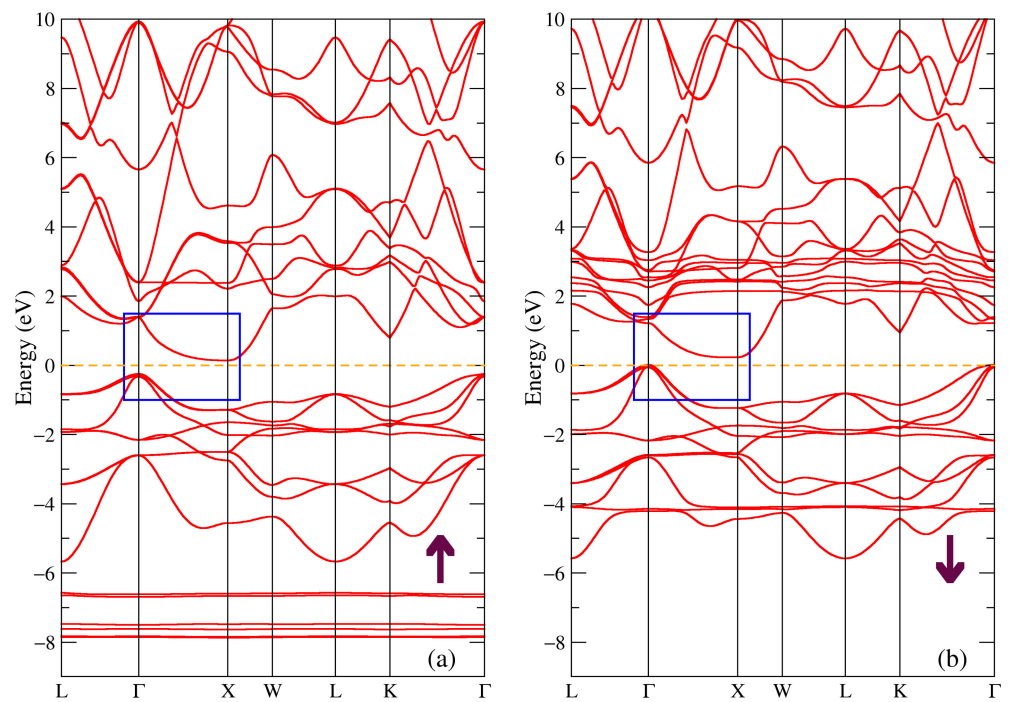


Figure 6. Band structure of DyNiSb: (a) majority and (b) minority spin projections. The blue rectangle points out the bands involved in the band gap formation.

The band structure for DySb is shown in Figure 7. One can see that this picture is resembling Figure 4 where the band structure for the TbSb compound is shown, since the largest contribution to the states near the Fermi level is due to the Sb 5p and Dy 5d electronic states. The calculated band structure is similar to the one proposed for DySb in [25]. From Figure 7 and the blue rectangle pointing out the bands near the Fermi level, one can conclude that DySb is a semimetal with the hole and electron pockets in the band structure around Γ and X points in the Brillouin zone.

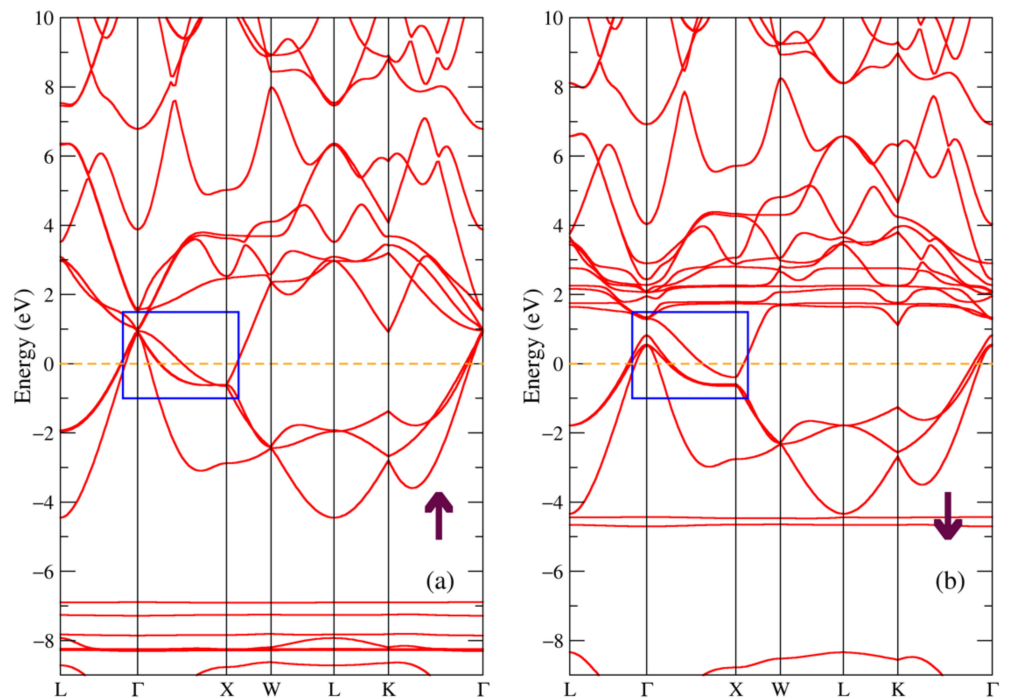


Figure 7. Band structure of DySb: (a) majority and (b) minority spin projections.

3.3. HoNiSb and HoSb Intermetallic Compounds

In Figure 8, the total and partial densities of electronic states of the HoNiSb and HoSb intermetallic compounds are given for two opposite spin directions. Densities of states for both compounds look similar to ones in Figures 2 and 5 with the main difference being due to the holmium 4f shell. The positions of the intense peaks for this shell in the energy spectrum Figure 8a,d are following: -7.9 (-8.4) eV and -6.7 (-7.4) eV below the valence band for the majority spin projection and 2.0 , 2.8 (1.7) eV for the minority spin projection. There is also another Ho-4f intense peak for the minority spin direction at -4.8 eV at the lower part of the valence band for the HoNiSb compound in Figure 8a, such as a peak which seems to be isolated from the Ho-5d and Sb-5p states in the binary HoSb compound at -5.5 eV (Figure 8d), it is not similar to that in the previous compounds.

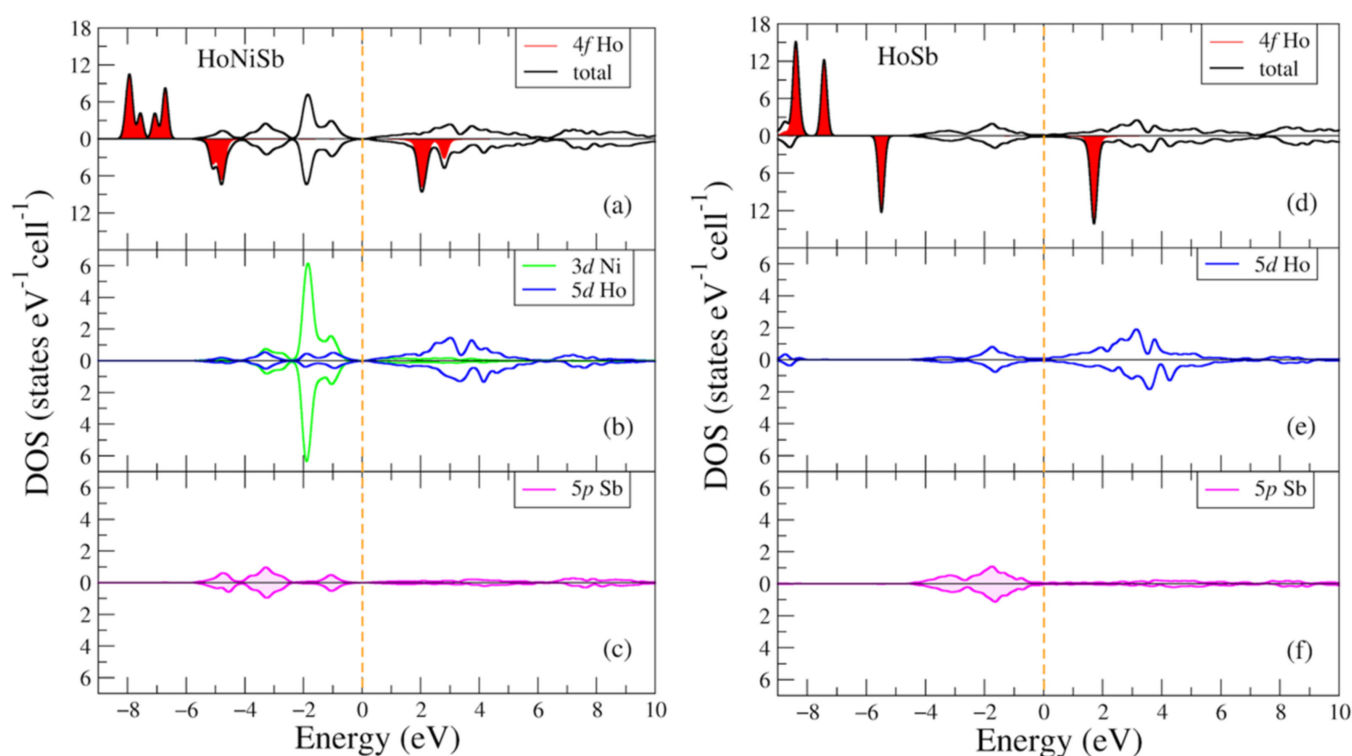


Figure 8. Densities of electronic states from DFT+U for (a–c) HoNiSb; (d–f) HoSb per cell. (a,d) Total and partial Ho-4f densities of states; (b,e) partial density of states for Ho-5d (Ni-3d); (c,f) partial density of states for Sb-5p. The plot is shifted relatively to the Fermi energy shown at zero as a vertical dashed line.

The band structure for the majority and minority spin projections of HoNiSb compound is shown in Figure 9. Once again, we can see that ternary HoNiSb compound is a semiconductor with an indirect gap in the band structure resembling that of TbNiSb and DyNiSb in Figures 3 and 6, respectively. The value for the energy gap is 0.37 eV for the majority spin projection and 0.26 eV for the minority spin projection. It is in a good agreement with the experimental value of the energy gap of 0.08 – 0.11 eV [9] for HoNiSb. Worth mentioning that the localized bands above the Fermi level from the 4f states of holmium are closest to the Fermi energy for HoNiSb in Figure 9b among all three ternary compounds.

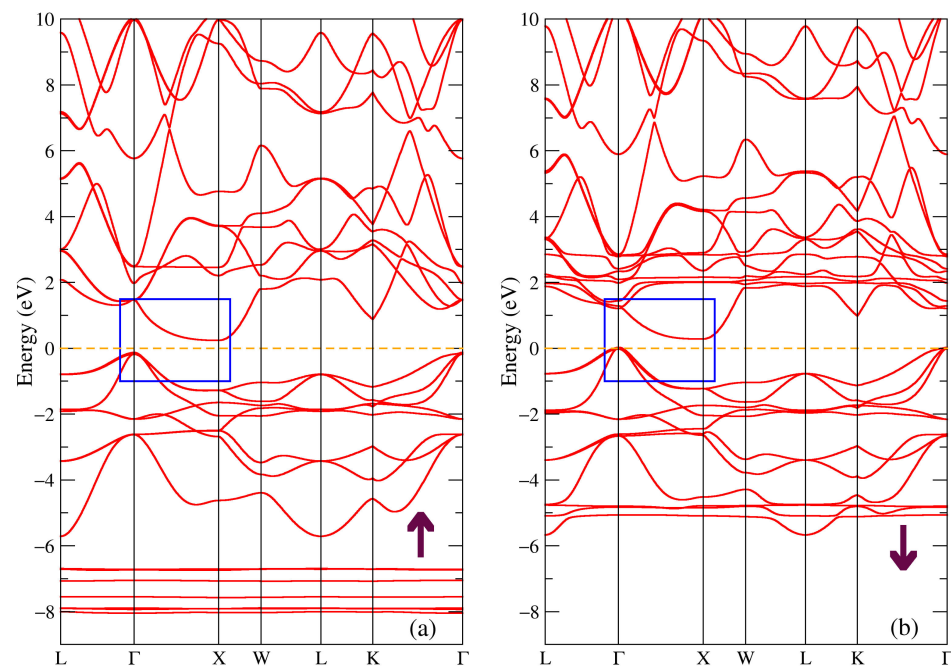


Figure 9. Band structure of HoNiSb: (a) majority and (b) minority spin projections. The blue rectangle points out the bands involved in the band gap formation.

The band structure for the majority and minority spin projections of the HoSb compound is shown in Figure 10. There is a noticeable flat band from the Ho-4f states in the minority spin projection Figure 10b only 1.8 eV above the Fermi level which is closest of all compounds. We can also see another localized band below the valence band in the minority spin projection which was discussed earlier. In the band structure near the Fermi level several bands are touching at X, see the blue rectangle in Figure 10. It is clearly seen that the binary HoSb compound is a semimetal with the band structure near the Fermi level very similar to that of the TbSb and DySb compounds shown in Figures 4 and 7.

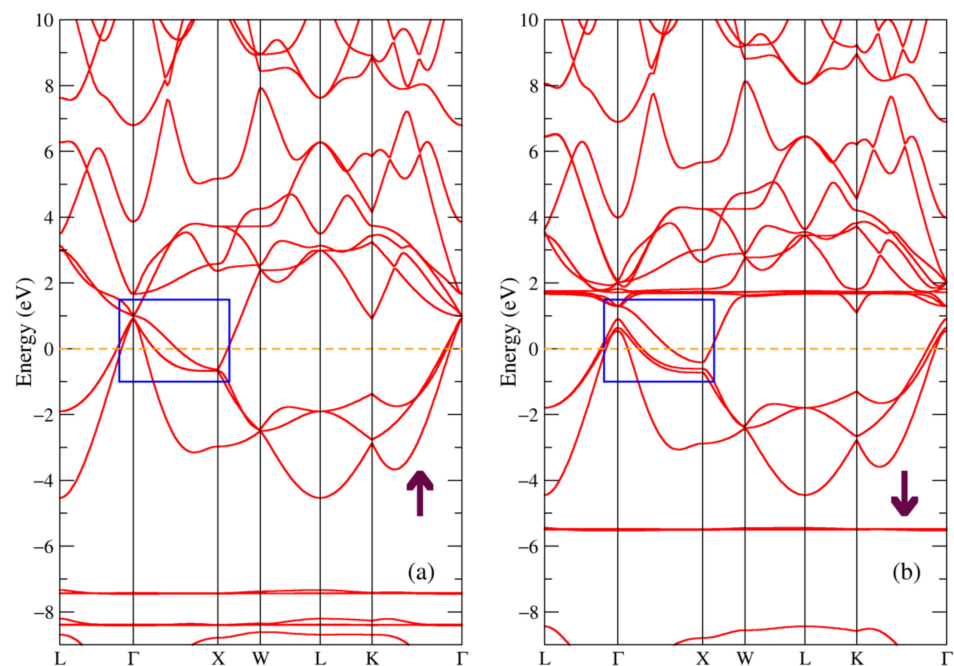


Figure 10. Band structure of HoSb: (a) majority and (b) minority spin projections.

3.4. Magnetic Moments

In addition to the densities of states and band structures, the values of the magnetic moments of compounds were calculated within the framework of GGA+U. Magnetic moments of the nickel and stibium ions in the compounds are found to be negligible so we can consider it zero. Then all of the magnetic properties of considered RNiSb and RSb compounds are determined by those of rare earth elements [20]. The spin moments of rare earth ions, which are mostly defined by the 4f electronic states [22], as calculated in the present work, have following values: $5.92 \mu_B$ for the Tb ions in both TbSb and TbNiSb compounds, $4.92 \mu_B$ for Dy in DySb and DyNiSb compounds and $3.94 \mu_B$ for the Ho ions in HoSb and HoNiSb. These values are close to the ones for the corresponding R^{3+} ions, but do not exactly coincide, see [20]. We can get the values of orbital momentum as for R^{3+} ions, $L = 3, 5$, and 6 for Tb, Dy, and Ho, respectively. Now, we are able to calculate the effective magnetic moments, and the results are $9.64 \mu_B$ for TbSb and TbNiSb, $10.56 \mu_B$ for DySb and DyNiSb, $10.55 \mu_B$ for HoSb and HoNiSb vs. the experimental values reported as $10.2(4) \mu_B$ for TbNiSb, $10.6(4) \mu_B$ for DyNiSb, $10.7(4) \mu_B$ for HoNiSb [20], $10.8 \mu_B$ for HoSb [26].

4. Conclusions

In this work, we investigated the electronic and band structures of three ternary compounds Tb,Dy,Ho(NiSb) and three binary compounds Tb,Dy,Ho(Sb). Calculations were carried out in the framework of the GGA+U method and revealed that these ternary compounds are semiconductors with an indirect gap and the binary compounds are semimetals. The Tb,Dy,Ho(NiSb) semiconductors have the following values of the energy gap: 0.43, 0.39, and 0.37 eV for the majority spin projection and 0.21, 0.21, and 0.26 eV for the minority spin projection, respectively, which are in a good agreement with the published experimental values. From the band structure, we identify similar to each other topological features near the Fermi level in the Tb,Dy,Ho(Sb) binary semimetals, these are the hole and electron pockets in the vicinity of Γ and X points, the non-symmetric electron pocket along Γ -X-W direction and hole pockets along the L- Γ -X direction. It is emphasized that the corresponding band structures can be found experimentally in the other compound of this series GdSb. It was also shown that the magnetic moment of all considered compounds is fully determined by magnetic moments of rare earth elements, the calculated effective magnetic moments of such ions have values close to experimental values.

Author Contributions: Conceptualization, methodology, software, investigation, writing—review and editing, S.T.B. and A.V.L.; project administration, supervision, A.V.L. All authors have read and agreed to the published version of the manuscript.

Funding: This research was supported by Russian Science Foundation (project No. 22-42-02021) for the electronic structure calculations in Sections 3.1 and 3.2, the magnetic values (Sections 3.3 and 3.4) were calculated within the state assignment of Ministry of Science and Higher Education of the Russian Federation (theme “Electron” No. 122021000039-4).

Institutional Review Board Statement: Not applicable.

Informed Consent Statement: Not applicable.

Data Availability Statement: The data presented in this study are available on request from the corresponding author.

Conflicts of Interest: The authors declare no conflict of interest. The funders had no role in the design of the study; in the collection, analyses, or interpretation of data; in the writing of the manuscript, or in the decision to publish the results.

References

1. Hundley, M.F.; Thompson, J.D.; Canfield, P.C.; Fisk, Z. Electronic transport properties of the semimetallic heavy fermion YbBiPt. *Phys. Rev. B* **1997**, *56*, 8098–8102. [CrossRef]
2. Gupta, S.; Suresh, K.G.; Nigam, A.K.; Lukoyanov, A.V. Magnetism in RRhGe (R = Tb, Dy, Er, Tm): An experimental and theoretical study. *J. Alloys Compd.* **2015**, *640*, 56–63. [CrossRef]

3. Nakajima, Y.; Hu, R.; Kirshenbaum, K.; Hughes, A.; Syers, P.; Wang, X.; Wang, K.; Wang, R.; Saha, S.R.; Pratt, D.; et al. Topological RPDBi half-Heusler semimetals: A new family of noncentrosymmetric magnetic superconductors. *Sci. Adv.* **2015**, *1*, e1500242. [CrossRef] [PubMed]
4. Pavlosiuk, O.; Kaczorowski, D.; Fabreges, X.; Gukasov, A.; Wisniewski, P. Antiferromagnetism and superconductivity in the half-Heusler semimetal HoPdBi. *Sci. Rep.* **2016**, *6*, 18797. [CrossRef] [PubMed]
5. Hirschberger, M.; Kushwaha, S.; Wang, Z.; Gibson, Q.; Liang, S.; Belvin, C.A.; Bernevig, B.A.; Cava, R.J.; Ong, N.P. The chiral anomaly and thermopower of Weyl fermions in the half-Heusler GdPtBi. *Nat. Mater.* **2016**, *15*, 1161–1165. [CrossRef]
6. Gupta, S.; Suresh, K.G.; Nigam, A.K.; Knyazev, Y.V.; Kuz'min, Y.I.; Lukoyanov, A.V. The magnetic, electronic and optical properties of HoRhGe. *J. Phys. D Appl. Phys.* **2014**, *47*, 365002. [CrossRef]
7. Singh, N.K.; Suresh, K.G.; Nirmala, R.; Nigam, A.K.; Malik, S.K. Correlation between magnetism and magnetocaloric effect in the intermetallic compound DyNiAl. *J. Appl. Phys.* **2006**, *99*, 08K904. [CrossRef]
8. Singh, N.K.; Suresh, K.G.; Nirmala, R.; Nigam, A.K.; Malik, S.K. Effect of magnetic polarons on the magnetic, magnetocaloric, and magnetoresistance properties of the intermetallic compound HoNiAl. *J. Appl. Phys.* **2007**, *101*, 093904. [CrossRef]
9. Ciesielski, K.; Synoradzki, K.; Wolanska, I.; Stachowiak, P.; Kepinski, L.; Jezowski, A.; Tolinski, T.; Kaczorowski, D. High-temperature power factor of half-Heusler phases RENiSb (RE = Sc, Dy, Ho, Er, Tm, Lu). *J. Alloys Compd.* **2020**, *816*, 152596. [CrossRef]
10. Gnida, D.; Ciesielski, K.; Kaczorowski, D. Origin of the negative temperature coefficient of resistivity in the half-Heusler antimonides LuNiSb and YPdSb. *Phys. Rev. B* **2021**, *103*, 174206. [CrossRef]
11. Pierre, J.; Karla, I. Giant magnetoresistance in RENiSb semiconductors (RE = Tb, Dy, Ho). *J. Magn. Magn. Mater.* **2000**, *217*, 74–82. [CrossRef]
12. Pierre, J.; Karla, I.; Kaczmarzka, K. Giant magnetoresistance in Heusler-type rare earth and 3d semiconductors. *Physica B Condens. Matter.* **1999**, *259–261*, 845–846. [CrossRef]
13. Pecharskii, V.K.; Pankevich, Y.V.; Bodak, O.I. Crystal structures of the compounds RNiSb with various rare earth elements. *Sov. Phys. Crystallogr.* **1983**, *28*, 97–98.
14. Zhu, H.; He, R.; Mao, J.; Zhu, Q.; Li, C.; Sun, J.; Ren, W.; Wang, Y.; Liu, Z.; Tang, Z.; et al. Discovery of ZrCoBi based half Heuslers with high thermoelectric conversion efficiency. *Nat. Commun.* **2018**, *9*, 2497. [CrossRef]
15. Ciesielski, K.; Synoradzki, K.; Veremchuk, I.; Skokowski, P.; Szymański, D.; Grin, Y.; Kaczorowski, D. Thermoelectric Performance of the Half-Heusler Phases RNiSb (R=Sc,Dy,Er,Tm,Lu): High Mobility Ratio between Majority and Minority Charge Carriers. *Phys. Rev. Appl.* **2020**, *14*, 054046. [CrossRef]
16. Kawano, K.; Kurosaki, K. Effect of Sn doping on the thermoelectric properties of ErNiSb-based *p*-type half-Heusler compound. *Appl. Phys. Lett.* **2007**, *91*, 062115. [CrossRef]
17. Ciesielski, K.; Wolańska, I.; Synoradzki, K.; Szymański, D.; Kaczorowski, D. Mobility Ratio as a Probe for Guiding Discovery of Thermoelectric Materials: The Case of Half-Heusler Phase ScNiSb_{1-x}TeX. *Phys. Rev. Appl.* **2021**, *15*, 044046. [CrossRef]
18. Jia, X.; Deng, Y.; Bao, X.; Yao, H.; Li, S.; Li, Z.; Chen, C.; Wang, X.; Mao, J.; Cao, F.; et al. Unsupervised machine learning for discovery of promising half-Heusler thermoelectric materials. *Npj Comput. Mater.* **2022**, *8*, 34. [CrossRef]
19. Satyam, J.K.; Saini, S.M. Role of R-f states on electronic structure and thermoelectric performance of RNiSb (R = Gd, Er and Lu) half Heusler compounds: Narrow gap thermoelectric materials. *Appl. Phys. A* **2021**, *127*, 828. [CrossRef]
20. Hartjes, K.; Jeitschko, W. Crystal structures and magnetic properties of the lanthanoid nickel antimonides LnNiSb (Ln = LaNd, Sm, GdTm, Lu). *J. Alloys Compd.* **1995**, *226*, 81–86. [CrossRef]
21. Sahariya, J.; Kumar, P.; Bhamu, K.C.; Soni, A. Electronic structure of Gd based transition metal antimonides GdTsb (T = Ni, Pt). *AIP Conf. Proc.* **2018**, *1953*, 110010. [CrossRef]
22. Baglasov, E.D.; Lukoyanov, A.V. Electronic structure of intermetallic antiferromagnet GdNiGe. *Symmetry* **2019**, *11*, 737. [CrossRef]
23. Li, Z.; Xu, D.-D.; Ning, S.-Y.; Su, H.; Iitaka, T.; Tohyama, T.; Zhang, J.-X. Predicted Weyl fermions in magnetic GdBi and GdSb. *Int. J. Mod. Phys. B* **2017**, *31*, 1750217. [CrossRef]
24. Wu, Y.; Lee, Y.; Kong, T.; Mou, D.; Jiang, R.; Huang, L.; Bud'ko, S.L.; Canfield, P.C.; Kaminski, A. Electronic structure of RSb (R = Y, Ce, Gd, Dy, Ho, Tm, Lu) studied by angle-resolved photoemission spectroscopy. *Phys. Rev. B* **2017**, *96*, 035134. [CrossRef]
25. Liang, D.D.; Wang, Y.J.; Xi, C.Y.; Zhen, W.L.; Yang, J.; Pi, L.; Zhu, W.K.; Zhang, C.J. Extreme magnetoresistance and Shubnikov-de Haas oscillations in ferromagnetic DySb. *APL Mater.* **2018**, *6*, 086105. [CrossRef]
26. Xia, Z.-L.; Tang, F.; Xu, C.-Q.; Cong, S.; Zhao, W.; Zhang, L.; Han, Z.-D.; Qian, B.; Jiang, X.-F.; Ke, X.; et al. Influence of magnetization anisotropy on angular magnetoresistance in the antiferromagnetic topological semimetal HoSb. *Phys. Rev. B* **2022**, *106*, 115137. [CrossRef]
27. Abdusalyamova, M.N.; Shokirov, H.S.; Rakhmatov, O.I. Investigation of the rare earth monoantimonides. *J. Less Common Metals* **1990**, *166*, 221–227. [CrossRef]
28. Momma, K.; Izumi, F. VESTA 3 for three-dimensional visualization of crystal, volumetric and morphology data. *J. Appl. Crystallogr.* **2011**, *44*, 1272–1276. [CrossRef]
29. Giannozzi, P.; Baroni, S.; Bonini, N.; Calandra, M.; Car, R.; Cavazzoni, C.; Ceresoli, D.; Chiarotti, G.L.; Cococcioni, M.; Dabo, I.; et al. Quantum ESPRESSO: A modular and open-source software project for Quantum simulations of materials. *J. Phys. Condens. Matter* **2009**, *21*, 395502. [CrossRef]

30. Giannozzi, P.; Andreussi, O.; Brumme, T.; Bunau, O.; Buongiorno Nardelli, M.; Calandra, M.; Car, R.; Cavazzoni, C.; Ceresoli, D.; Cococcioni, M.; et al. Advanced capabilities for materials modelling with Quantum ESPRESSO. *J. Phys. Condens. Matter* **2017**, *29*, 465901. [CrossRef]
31. Knyazev, Y.V.; Lukoyanov, A.V.; Kuz'min, Y.I.; Kuchin, A.G. Electronic structure and optical spectroscopy studies of HoNi₅ and ErNi₅ compounds doped with Cu. *Phys. Status Solidi B* **2012**, *249*, 824–828. [CrossRef]
32. Perdew, J.P.; Burke, J.P.; Ernzerhof, M. Generalized gradient approximation made simple. *Phys. Rev. Lett.* **1996**, *77*, 3865–3868. [CrossRef]
33. Quantum ESPRESSO. Available online: <https://www.quantum-espresso.org/pseudopotentials> (accessed on 7 December 2022).
34. Topsakal, M.; Wentzcovitch, R. Accurate projected augmented wave (PAW) datasets for rare-earth elements (RE = La–Lu). *Comput. Mater. Sci.* **2014**, *95*, 263–270. [CrossRef]

Disclaimer/Publisher's Note: The statements, opinions and data contained in all publications are solely those of the individual author(s) and contributor(s) and not of MDPI and/or the editor(s). MDPI and/or the editor(s) disclaim responsibility for any injury to people or property resulting from any ideas, methods, instructions or products referred to in the content.

Article

Atomic Diffusion and Crystal Structure Evolution at the Fe-Ti Interface: Molecular Dynamics Simulations

Guojin Xiang ^{1,2}, Xu Luo ², Tianxu Cao ¹, Ankang Zhang ¹ and Hui Yu ^{1,*}

¹ School of Mechanical Engineering, Yanshan University, Qinhuangdao 066000, China

² Pangang Group Research Institute Co., Ltd., Panzhihua 617000, China

* Correspondence: yuhui@ysu.edu.cn; Tel.: +86-137-8035-0181

Abstract: The diffusion bonding method is one of the most essential manufacturing technologies for Ti-steel composite plates. In this paper, the atomic diffusion behavior at the Fe-Ti interface during the bonding process of Ti-steel composite plates is studied using classical diffusion theory and molecular dynamics (MD) simulation. Henceforth, the diffusion mechanism of Fe and Ti atoms at the bonding interface is obtained at the atomic scale. The results show that Fe and Ti atoms diffused deeply into each other during the diffusion process. This behavior consequently increased the thickness of the diffusion layer. Moreover, the diffusion quantity of Fe atoms to the Ti side was much greater than that of Ti atoms to the Fe side. Large plastic deformation and shear strain occurred at the diffusion interface during diffusion. The crystal structure of the diffusion zone was damaged and defects were generated, which was beneficial to the diffusion behavior of the interface atoms. As the diffusion time and temperature increased, the shear strain of the atoms at the interface also increased. Furthermore, there is a relationship between the mutual diffusion coefficient and the temperature. Subsequently, after the diffusion temperature was raised, the mutual diffusion coefficient and atomic disorder (Fe atom and Ti atom) increased accordingly.

Keywords: diffusion bonding; molecular dynamics; diffusion mechanism; shear strain; diffusion coefficient

Citation: Xiang, G.; Luo, X.; Cao, T.; Zhang, A.; Yu, H. Atomic Diffusion and Crystal Structure Evolution at the Fe-Ti Interface: Molecular Dynamics Simulations. *Materials* **2022**, *15*, 6302. <https://doi.org/10.3390/ma15186302>

Academic Editors: Shuwen Wen, Yongle Sun and Xin Chen

Received: 9 August 2022

Accepted: 7 September 2022

Published: 11 September 2022

Publisher's Note: MDPI stays neutral with regard to jurisdictional claims in published maps and institutional affiliations.



Copyright: © 2022 by the authors. Licensee MDPI, Basel, Switzerland. This article is an open access article distributed under the terms and conditions of the Creative Commons Attribution (CC BY) license (<https://creativecommons.org/licenses/by/4.0/>).

1. Introduction

The Ti-steel composite plate is a kind of composite metal plate that applies heating, pressure, or two types of combination procedures to create strong metallurgical bonding at the interface between the titanium plate and steel plate. In some circumstances, the combination of titanium and steel produces components with both strong corrosion resistance and the price advantages of titanium and steel, thus, effectively utilizing the complementary advantages of titanium and steel in performance and economy. Researchers have conducted a lot of research work to solve the problem of insufficient bonding strength of the composite plates, which is caused by bonding interface defects in Ti-steel composite plates. According to a large number of studies, the intermediate compounds formed on the composite interface are the primary motivation for the interface bonding limitation of the composite plate, which leads to the formation of interface defects. The more kinds of interfacial compounds, the greater the influence on interfacial bonding strength [1,2].

Jiang et al. [3] performed heat treatment on the Ti-steel composite plate produced by the explosive composite method. It was observed that the major compound generated at the composite interface at 850 °C was TiC. At 950 °C, the main products were Fe₂Ti, FeTi, and a trace of TiC. Momono et al. [4] investigated the influence of C element mass fraction on Ti-steel diffusion welding performance. When the steel with 0.01 % C element was heated at temperatures over 900 °C, FeTi and Fe₂Ti compounds were formed at the composite interface, reducing composite strength. TiC, FeTi, and Fe₂Ti compounds were produced at the composite interface in the steel with a 0.19 % mass fraction of C when the temperature exceeded 900 °C and the composite strength dropped. The grain orientation of titanium has

a great influence on the interfacial reaction behavior of titanium and steel. When the basal plane of a titanium cell is parallel to the Fe/Ti interface, it has a strong inhibitory impact on the diffusion of C atoms and the TiC layer is thin, according to Li et al. [5] The TiC layer is thicker when the titanium cell base surface is perpendicular to the titanium/steel interface. This is owing to the anisotropy of the gap carbon atom transport in titanium cells.

Molecular dynamics (MD) is a powerful approach for simulating molecular systems using Newtonian mechanics. It can explain some macroscopic properties of matter and conduct an experiment at the micro level, which is significant for revealing the development of atomic-scale structures. Nowadays, MD simulation has become an effective tool for studying the interface diffusion bonding process.

Firstly, Leo Miglio et al. [6] investigated the mathematical simulation of Si diffusion in TiS_2 compounds and discovered that the diffusion of Si in this compound was mostly owing to its low formation energy. Since then, numerous researchers have investigated the diffusion phenomena by MD simulation. Chen et al. [7] simulated the formation process of the Cu-Ag diffusion bond using the MD method and discovered that the thickness of the interface area is mainly dictated by stress. In the process of diffusion bonding, the interface region is transformed into an amorphous form. However, it often transitions from an amorphous to a crystal structure when it cooled to room temperature. Chen et al. [8] used MD simulation to investigate atomic diffusion during explosive welding of $\text{Ni}_{50}\text{Ti}_{50}\text{-Cu}$ (at. %). The geometric similarity of concentration distribution curves at different points during diffusion was applied to compute the distribution of atomic concentration at any time throughout the explosive welding process and the simulation results are virtually identical to the experimental results. Similarly, Xiu et al. [9] applied MD to simulate W/Cu diffusion bonding. The atomic diffusion behavior of W and Cu atoms was investigated in their study and the diffusion coefficient and radial distribution function (RDF) were also calculated. The diffusion mechanism of the W/Cu diffusion bond is as follows: when the temperature and diffusion time rise, the thickness of the diffusion layer and atomic disorder increase as W and Cu atoms propagate along the crystal defect surface. Solid-state wetness (SSW) happens not only at the micron scale but also at the nanoscale, according to research by M. Samsonov et al. [10], who simulated the spread of solid copper (Cu) and gold (Au) nanoparticles over the same metal (100) surface. The temperature effect is stronger than the pressure effect during diffusion, according to research by Zhang et al. [11], which looked at the effects of temperature, pressure, and surface roughness on the diffusion welding of stainless steel and pure Ni. By simulating self-diffusion along the screw dislocation core in the metals aluminum, nickel, copper, and silver, Soltani et al. [12] simulated the effect of screw dislocation on boosting self-diffusion for each metal mentioned above. In a nanostructured Cu/Ag system, Béjaud et al. [13] investigated the interaction between interface and deformation twins and precisely analyzed the effects of misfit dislocation on twin nucleation and thickening in a face-centered cubic structure. Yang et al. [14] investigated the diffusion behavior of Al and Cu atoms in ultrasonic welding using MD modeling. Their findings revealed that asymmetric diffusion occurred at the Al/Cu interface during the ultrasonic welding (UW) process. Simultaneously, the recovery of disordered Al blocks at low temperatures was observed and the thickness of the diffusion layer increased as welding time increased. Because of the significant trapping effect of the grain boundaries in nanocrystalline Fe, Zhou et al.'s study [15] on the dependency of the hydrogen diffusion coefficient on grain size revealed that smaller grain sizes correspond to reduced hydrogen diffusion coefficients. The effects of temperature and pressure on atomic interdiffusion along the direction perpendicular to the Cu/Al solid-liquid interface were revealed by Mao et al. [16] and found that while the thickness of the diffusion layer exhibits a parabolic connection with diffusion time, the Cu atoms' depth of diffusion exhibits a linear relationship with system temperatures. Using the MD approach, Chen et al. [17] investigated the influence of temperature on the diffusion rate and mechanical characteristics of the nano-scale TiAl/Ti₃Al interface. The elastic modulus, yield strength, and flow stress all reduced as the temperature increased from 1273 K to 1473 K. Wang et al. [18] investigated

the atomic diffusion behavior of the Mo/Au interface using classical diffusion theory and MD simulation and the mutual diffusion coefficient and radial distribution function of Mo and Au atoms were obtained. In a recycled asphalt mixture, Zhan et al. [19] described the behavior of new asphalt and aged asphalt diffusion, which revealed that the diffusion direction was mostly from virgin asphalt to aged asphalt and that the diffusion efficiency improved with temperature. Zurhelle et al. [20] studied the oxygen atoms' diffusion characteristics in platinum atoms with extended defects and their results demonstrated that platinum vacancies prevent oxygen atom diffusion across the platinum lattice by trapping oxygen atoms. Amorphization of Cu atoms during diffusion was noted in this study by Zhang et al. [21], who simulated the diffusion process and atomic structure of the interface between metallic glass Cu₅₀Zr₅₀ and crystalline Cu.

In this paper, MD simulation was used to study the atomic diffusion behavior and crystal structure evolution at the Fe-Ti interface in the diffusion bonding process of the Ti-steel composite plates and classical diffusion theory. The diffusion process of Fe-Ti interface was characterized through the calculation of profiles for atomic trajectory, atomic concentration distribution, diffusion layer thickness, atomic shear strain, radial distribution function (RDF), mean square displacement (MSD), and diffusion coefficient. The relationship between the calculation profiles and diffusion temperature was also presented, which will benefit our understanding of the atomic diffusion mechanism in the Fe-Ti interface.

2. Simulation Method

2.1. Potential Function

Potential function describes the interaction of atoms or molecules, also known as a force field. The correctness of the potential function has a significant impact on the dependability of MD simulation results. Daw and Baskes [22] developed the embedded atom method (EAM) based on density functional theory and effective medium theory in 1983. It could solve the inadequacies in the two-body potential model that are incompatible with particle interaction in metal systems. Furthermore, in order to implement the EAM potential to covalent bond materials, the non-spherical symmetric distribution of electrons should be considered. Baskes et al. [23] developed a modified embedded atom method (MEAM). The potential function of MEAM is represented as follows:

$$E = \sum_i \{F_i(\vec{\rho}_i) + \frac{1}{2} \sum_{i \neq j} S_{ij} \phi_{ij}(R_{ij})\} \quad (1)$$

$$F_i(\vec{\rho}) = A_i E_i^0 \vec{\rho}_i \ln \vec{\rho}_i \quad (2)$$

where E is the total energy in the system; F_i is the embedding function for an atom i embedded in a background electron density ρ_i ; and S_{ij} and $\phi_{ij}(R_{ij})$ are the screening function and the pair interaction between atoms i and j separated by a distance R_{ij} ; E_i^0 is the binding energy of atom i ; and A_i is the structure parameter.

The embedded atomic method (MEAM) interatomic potential of the Fe-Ti-C binary alloy system was developed by Kim et al. [24]. The MEAM potentials were validated in the literature by Prasanthi et al. [25]. At an equilibrium distance of 2.879 Å, they calculated that the cohesive energy for the Fe-Ti system was 4.360 eV, which was quite compatible with MEAM potentials. As well, the calculated bulk moduli of Fe (153 GPa) and Ti (110 GPa) were in good agreement with the experimentally measured values of 166 GPa for "Armco Iron" and 108 GPa for Ti [26,27].

In addition, by examining the overall structural consistency of atoms in the system before and after the relaxation process, it is demonstrated that utilizing this potential function for relaxation yields a relatively stable starting model, which is adequate for the simulation system.

2.2. Simulation Model

The lattice type of Fe and Ti at home temperature is a body-centered cubic and hexagonal close-packed structure, respectively. The lattice constants of Fe and Ti are 0.286 nm and 0.295 nm, respectively. Where the size of Fe is $90 \text{ \AA} \times 90 \text{ \AA} \times 50 \text{ \AA}$ and the size of Ti is $90 \text{ \AA} \times 90 \text{ \AA} \times 50 \text{ \AA}$, as depicted in Figure 1. Among them, the blue atoms are Fe atoms and the yellow atoms are Ti atoms. The total numbers of the Fe and Ti atoms in the model were 33,597 and 22,971, respectively. There is an initial gap of 2 \AA between the Fe and Ti samples, which aims to reduce the strong interaction force between the two atoms at the interface, causing the samples to fit better.

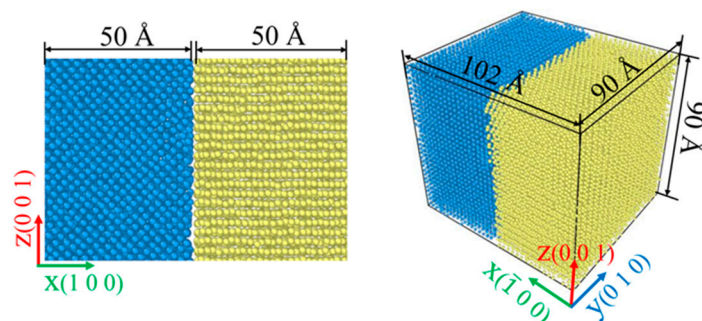


Figure 1. Simulation model.

The large-scale atomic molecular massively parallel simulator (LAMMPS) program is used in this paper [28]. To begin with, the two models are completely relaxed by the normal pressure and temperature (NPT) ensemble with a goal temperature at the time of 500 ps to reach a rather stable state. Then, they are merged in the y-z surface and the periodic boundary conditions in the y and z directions are applied, while the shrinking boundary conditions are applied in the x-direction. The ensemble is set to NVT (N: number of particles; V: volume; T: temperature) and the Nosé–Hoover method is used to maintain a constant system temperature of 1123 K and no external pressure is applied to the whole system. The timestep is 0.001 ps and the initial velocity of atoms follows the Maxwell distribution.

3. Result and Discussion

3.1. Interface Diffusion Behavior

Figure 2 shows the atomic diffusion behavior of the Fe/Ti diffusion interface at the temperature $T = 1123 \text{ K}$, (a) 0.001 ns; (b) 0.5 ns; (c) 1.5 ns; (d) 2 ns. The diffusion area between Fe and Ti is defined as the region between the farthest diffused Fe atom (i.e., the Fe atom with the largest x coordinate) and the farthest diffused Ti atom (i.e., the Ti atom with the smallest x coordinate). A distinct interface was produced at the time of $t = 0.001 \text{ ns}$ and $t = 0.5 \text{ ns}$, as shown in Figure 2a,b, in which a tiny quantity of Fe atoms diffused into the Ti layer and a few Ti atoms diffused into the Fe layers. As the diffusion time increased to $t = 1.5 \text{ ns}$ and $t = 2 \text{ ns}$, more Fe atoms diffused into the other side and the diffusion area became thicker, as shown in Figure 2c,d. Additionally, the interface between the Fe layer and Ti layer began to diminish as the diffusion time increased. This phenomenon can be explained as follows: binding energy was produced as the Fe layer contacted with the Ti layer, which enhanced the interaction and movement between Fe and Ti atoms. Figure 3 illustrates the atomic concentration distribution at different diffusion times. As the time increased from $t = 0.001 \text{ ns}$ to $t = 1.5 \text{ ns}$, the thickness of the diffusion area increased from 4.47 \AA to 11.22 \AA . While the diffusion area just increased to 1.32 \AA as the time rose from $t = 1.5 \text{ ns}$ to $t = 2 \text{ ns}$, as shown in Figure 3a,d, whereas the number of Fe atoms (or Ti atoms) entering the titanium lattice (or Fe lattice) is still increasing as the time increases from $t = 1.5 \text{ ns}$ to $t = 2 \text{ ns}$, as shown in Figure 3c,d. This result indicates that when the diffusion time is sufficient, the thickness of the diffusion area will no longer increase, but atoms will always enter the diffusion region.

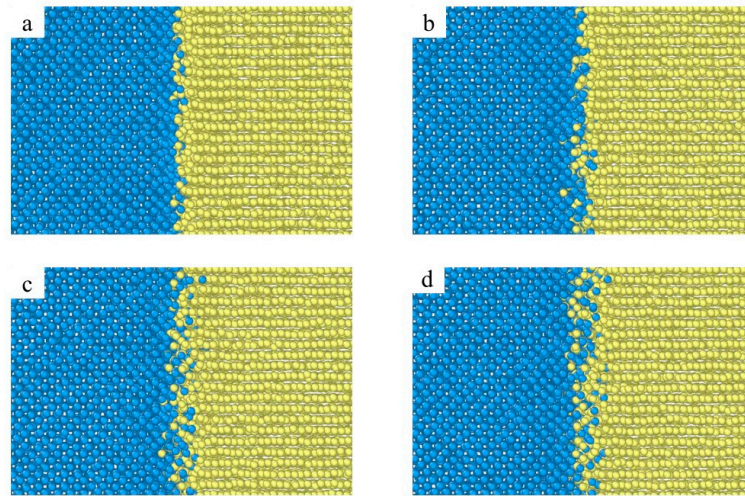


Figure 2. Atomic diffusion behavior of Fe/Ti diffusion interface at the temperature $T = 1123$ K ((a) 0.001 ns; (b) 0.5 ns; (c) 1.5 ns; (d) 2 ns).

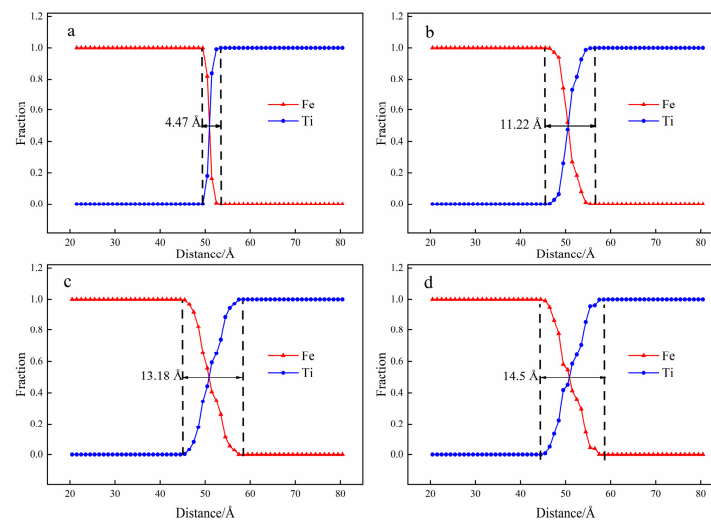


Figure 3. Atomic concentration distribution at the temperature $T = 1123$ K ((a) 0.001 ns; (b) 0.5 ns; (c) 1.5 ns; (d) 2 ns).

Figure 4 shows the atomic diffusion behavior of the Fe/Ti diffusion interface at different temperatures and the atom diffusion behavior is temperature dependent. The number of diffusion atoms rises with the increase in diffusion temperature. At a temperature of 973 K, a few Fe atoms diffuse into the Ti layer and nearly no Ti atoms diffuse into the Fe layer, as shown in Figure 3a. A growing number of atoms diffuse into the other side as the diffusion temperature increases and the diffusion area becomes thicker, as shown in Figure 3b,d. Furthermore, the overall number of Ti atoms that diffused and the diffusion depth are significantly smaller than those of Fe atoms in the titanium lattice, indicating asymmetric diffusion.

The atomic concentration distribution curves at different temperatures are depicted in Figure 5. The thickness of the diffusion and the number of atoms in the diffusion region increase with the rise in the diffusion temperature. The thickness of the diffusion zone increases from 9.5 Å to 10 Å as the diffusion temperature increases from 973 K to 1023 K. Similarly, when the diffusion temperature is 1073 K and 1123 K, the thickness of the diffusion zone increases to 11.41 Å and 14.5 Å, respectively. Further, the higher the temperature, the more pronounced the effect. All in all, diffusion temperature plays an effective role in promoting interface diffusion between Fe and Ti layers.

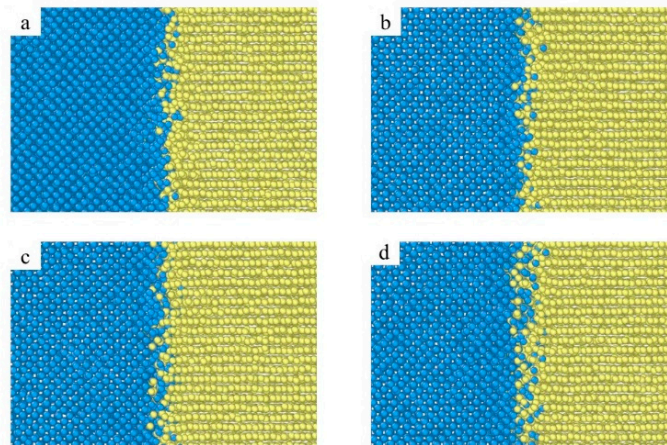


Figure 4. Atomic diffusion behavior of Fe/Ti diffusion interface at the time $t = 2$ ns ((a) 973 K; (b) 1023 K; (c) 1073 K; (d) 1123 K).

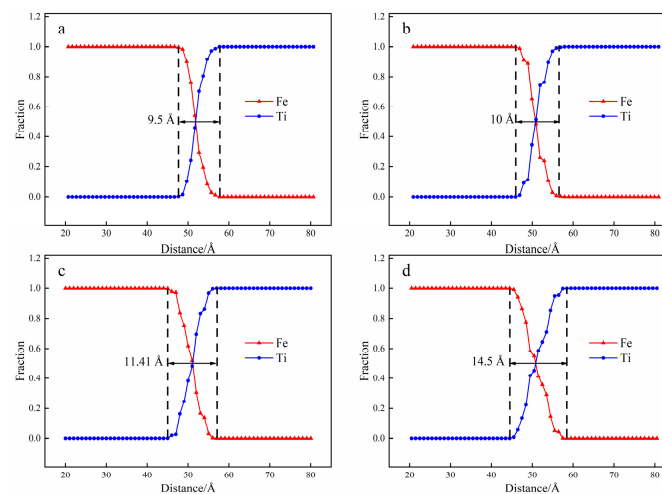


Figure 5. Atomic concentration distribution at the time $t = 2$ ns ((a) 973 K; (b) 1023 K; (c) 1073 K; (d) 1123 K).

The number of diffused atoms was counted by the means of the “selection” function in the open visualization tool (OVITO) [29]. Figure 6 shows the number of diffused atoms of Fe and Ti after each specific time and temperature and the number of diffusion atoms increases with the increase in temperature and diffusion time and the curve gradually becomes gentle over time, which showed a linear relationship with the diffusion time after $t = 0.5$ ns. In addition, the number of diffused Fe atoms is always greater than that of Ti atoms, which is consistent with the previous analysis results.

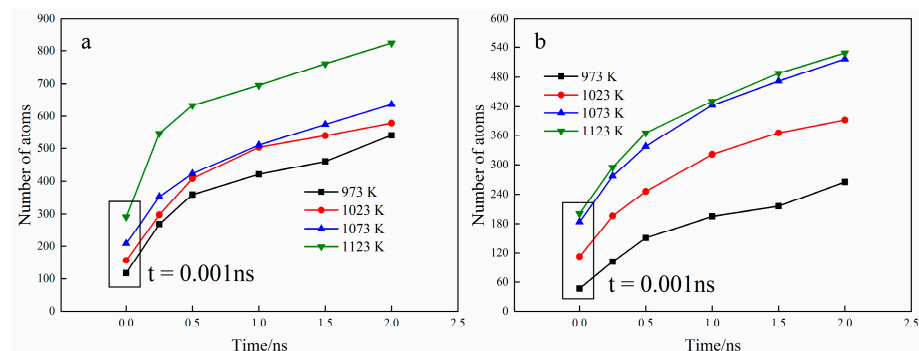


Figure 6. Number of diffused atoms with specific time and temperature ((a) Fe atoms; (b) Ti atoms).

3.2. Crystal Structure Analysis

Figure 7 depicts the shear strain distribution at different diffusion times and a narrow shear plastic deformation zone was observed at the bonding interface. At the time of $t = 0.001$ ns, a limited number of atoms are influenced by the plastic deformation and the value of the shear strain is negligible, as depicted in Figure 7a. Furthermore, from $t = 0.001$ ns to $t = 2$ ns, the shear strain gradually increases and the plastic deformation band spreads to both sides, as shown in Figure 7a–d, indicating the deformation of the interface area during interface bonding. As a result, a large number of Fe and Ti atoms migrate from the original equilibrium position to a new position on both sides of the adjacent interface, so that the vacancies appear near the binding interface and the vacancy concentration increases continuously. Since the activation energy of high-density diffusion is much lower than that of lattice diffusion, the vacancy can be considered as the best place for large-scale diffusion of dissimilar atoms, so mutual diffusion between Fe and Ti atoms occurs when the vacancy on the iron side (or Ti side) reaches a new equilibrium. It can also be found in Figure 8 that temperature has a significant effect on the atomic shear strain in the diffusion area. The atomic shear strain in the diffusion zone rises with the increase in temperature and the effect range expands with the increase in diffusion zone thickness.

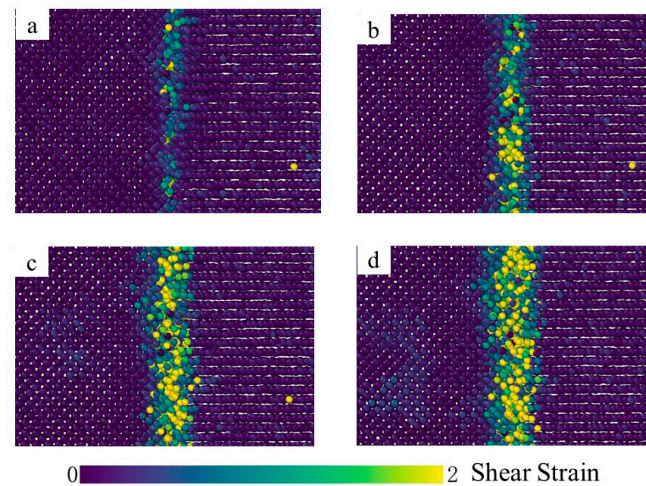


Figure 7. Shear strain distribution at the temperature $T = 1123$ K ((a) 0.001 ns; (b) 0.5 ns; (c) 1.5 ns; (d) 2 ns).

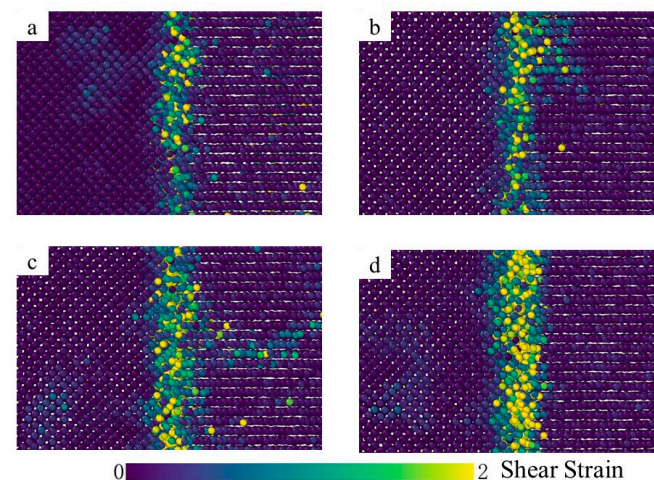


Figure 8. Shear strain at the time $t = 2$ ns ((a) 973 K; (b) 1023 K; (c) 1073 K; (d) 1123 K).

Radial distribution function (RDF) is an effective method for describing system structure, which can characterize the disorder degree of the structure [30]. The RDF refers to the

probability of finding another atom at a distance r from one atom, which can be used to represent information, such as the relationship between atoms and the interaction intensity, so as to study the atomic structure.

Figures 9 and 10 show the RDF curves ($g(r)$) of Fe and Ti atoms at different diffusion times and diffusion temperatures, respectively. At different diffusion times and temperatures, the RDF curves of Fe and Ti atoms are essentially the same. There is only one main peak, representing the binding strength between the first nearest neighbor atoms of the central atom. Its sharp shape indicates that the number density of atoms in this radius range is much higher than the average density and the binding strength between the central atom and the nearest neighbor atom is also relatively large. As presented in Figure 9a, the main peak of $g(r_{\text{Fe-Fe}})$ (the RDF curve of the Fe-Fe atom) appears at $r = 2.55 \text{ \AA}$, suggesting that the nearest atoms of Fe atoms appear at $r = 2.55 \text{ \AA}$ and the bond length of Fe-Fe can be obtained at 2.55 \AA . Furthermore, Figure 9b depicts that the nearest atom of Ti atom could be found at $r = 2.93 \text{ \AA}$ and the Ti-Ti bond length can be gained at 2.93 \AA . Similarly, the bond length of Fe-Ti can be calculated at 2.65 \AA , as shown in Figure 9c, which is consistent with the previous simulation results [31]. Furthermore, it could be found that the value of $r(\text{Fe-Ti})$ (the bond length of Fe-Ti) is between $r(\text{Fe-Fe})$ and $r(\text{Ti-Ti})$ and this problem is caused by the electronic interaction between metals [32]. In addition, the RDF curve in Figure 9a,b has another peak at $r > 2.55 \text{ \AA}$ and 2.93 \AA , except for the first main peak, which indicates that the Fe and Ti crystal structures are ordered.

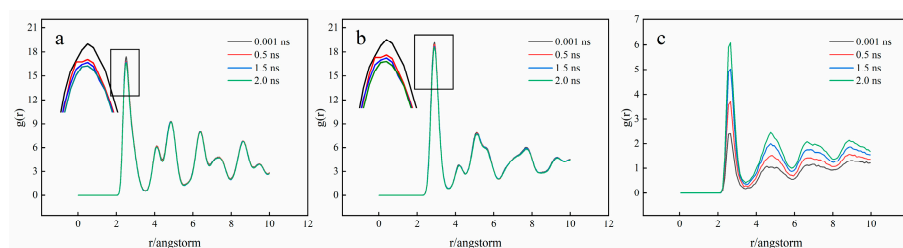


Figure 9. RDF curves of Fe and Ti atoms at $T = 1123 \text{ K}$ ((a) Fe-Fe; (b) Ti-Ti; (c) Fe-Ti).

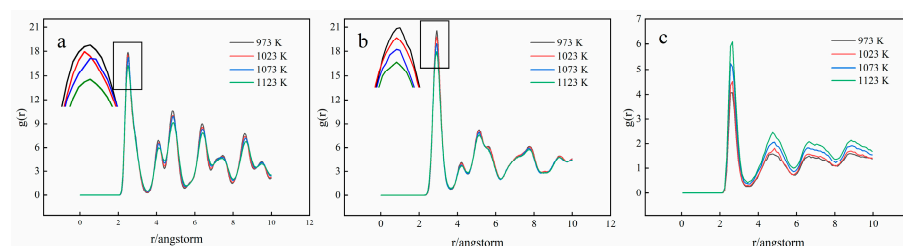


Figure 10. RDF curves of Fe and Ti atoms at $t = 2 \text{ ns}$ ((a) Fe-Fe; (b) Ti-Ti; (c) Fe-Ti).

The peak values of $g(r_{\text{Fe-Fe}})$ and $g(r_{\text{Ti-Ti}})$ are much larger than that of $g(r_{\text{Fe-Ti}})$, because the bonding strength of Fe-Fe and Ti-Ti is greater than that of Fe-Ti. With the increase in diffusion time, the peak strength of $g(r_{\text{Fe-Fe}})$ and $g(r_{\text{Ti-Ti}})$ decreases, whereas the peak strength of $g(r_{\text{Fe-Ti}})$ increases. It can be explained as follows: during the diffusion process, the atoms in the crystal migrate, resulting in the crystal structure becoming disordered and the bonding strength between the same atoms decreasing. While the bonding reaction between different atoms occurs, the Fe atoms and Ti atoms combine with each other, resulting in an increase in bonding strength. In addition, raising the temperature will also result in $g(r_{\text{Fe-Fe}})$ and $g(r_{\text{Ti-Ti}})$ peak decreases and $g(r_{\text{Fe-Ti}})$ peak increases. It indicates that the increase in temperature will accelerate the disorder of crystal structure at the interface and the mutual diffusion of atoms at the interface.

3.3. Diffusion Coefficient Analysis

The Einstein method has been used to investigate the atom diffusion behavior at the interface. Firstly, the mean square displacement (MSD) of the atom was calculated.

Through the relationship between the MSD curves and the diffusion coefficient, the diffusion coefficient D of the particle can be obtained, in which the MSD can be calculated as [33]:

$$MSD = \frac{1}{N} \sum_{i=1}^N \langle |r_i(t) - r_i(0)|^2 \rangle \quad (3)$$

where N is the number of atoms; $r_i(t)$ and $r_i(0)$ are displacement vectors of i atom at zero and t moment, respectively; the calculated symbol $\langle \rangle$ is temporal correlation.

When the running time tends to be infinite:

$$\lim_{t \rightarrow \infty} MSD = c + 2dDt \quad (4)$$

where d is the dimension of the system; D is the diffusion coefficient; c is constant. The mean square displacement is listed as a function of time and the slope of the curve is $2dDt$. The system discussed in this paper is three-dimensional, so the diffusion coefficient can be expressed as [9]:

$$D = \frac{1}{6} \lim_{t \rightarrow \infty} \left(\frac{d}{dt} \langle |r_i(t) - r_i(0)|^2 \rangle \right) \quad (5)$$

The temperature was discovered to be a key factor influencing the diffusion rate in the preceding investigation. The general expression of diffusion coefficient can be established by Arrhenius relation [33]:

$$D = D_0 \exp\left(-\frac{Q}{RT}\right), \quad (6)$$

where D is the diffusion coefficient; D_0 is diffusion factor; Q is the diffusion activation energy; R is the gas constant, $R = 8.314 \text{ J/(mol K)}$.

Taking the logarithm of Equation (6), the relationship between D and T could be expressed as:

$$\ln D = \ln D_0 - \frac{Q}{RT}, \quad (7)$$

The MSD curves of the Fe and Ti atoms were obtained by the MD simulations, illustrated in Figure 11. The diffusion of Fe atoms is relatively stable, while the movement of Ti atoms is relatively intense at the beginning of diffusion and then gradually tends to be stable. Furthermore, the MSD of Fe and Ti atoms gradually increases as temperature rises.

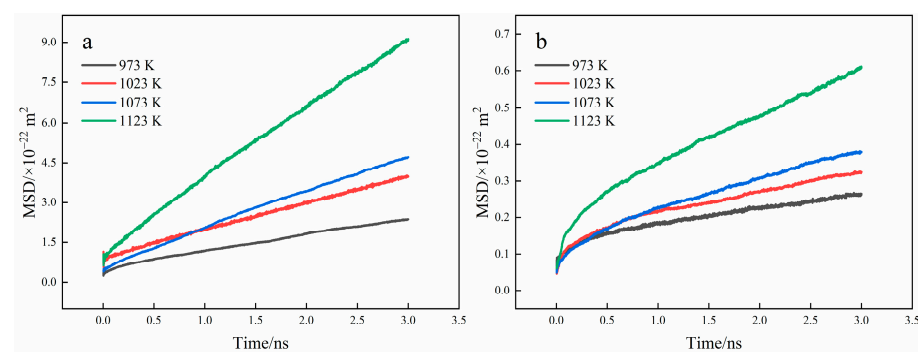


Figure 11. MSD curves of Fe and Ti atoms at different temperature ((a) Fe atoms; (b) Ti atoms).

The diffusion coefficients of Fe and Ti atoms at the interface with different temperatures are calculated according to the MSD curves and Equation (5). It can be found from Figure 12 that the diffusion coefficient is exponentially related to the diffusion temperature, which is consistent with the results of Equation (6) and Equation (7). The D -value of Fe atoms is higher than that of Ti atoms and the D -value of Fe atoms and Ti atoms increases with the rise in temperature. When the diffusion temperature is 973 K, the diffusion coefficients of Fe and Ti atoms are $9.57 \times 10^{-15} \text{ m}^2/\text{s}$ and $8.12 \times 10^{-16} \text{ m}^2/\text{s}$, respectively. In addition, when the diffusion temperature is less than 1073 K, the diffusion coefficients of Fe and Ti atoms are

small and the atoms are in the low-speed diffusion stage. When the diffusion temperature is greater than 1073 K, the diffusion coefficient of Fe atoms and Ti atoms increases obviously and the atoms are in the rapid diffusion stage. As the diffusion temperature reaches 1123 K, the diffusion coefficients of iron and titanium atoms reach $4.45 \times 10^{-14} \text{ m}^2/\text{s}$ and $2.43 \times 10^{-15} \text{ m}^2/\text{s}$, respectively. As a result, atomic diffusion behavior occurs mostly at high temperatures, whereas there are no discernible diffusion phenomena at low temperatures. This is because atoms at low temperatures cannot get sufficient energy to break the potential barrier, yet atoms at high temperatures can obtain sufficient kinetic energy.

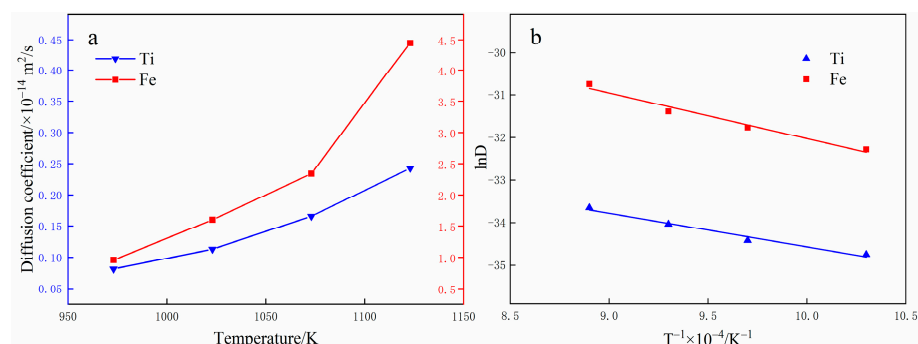


Figure 12. Relationship between diffusion coefficient and temperature.

4. Conclusions

The atomic diffusion behavior of the Fe-Ti composite interface at different times and temperature was simulated by using MD simulation. The following conclusions can be obtained:

1. As diffusion time and temperature rise, the boundary between the Fe and Ti layer dissolves, the thickness of the diffusion layer grows, and the diffusion amount of Fe atoms to the Ti layer exceeds that of Ti atoms to the Fe layers.
2. During the diffusion process, the diffusion boundary experienced significant plastic deformation and shear strain. The structure of the diffusion area was disrupted and flaws were formed, which enhanced atom diffusion at the interface. The shear strain of atoms at the contact rose as diffusion time and temperature increased.
3. There is only one primary peak in the RDF curves of Ti and Fe atoms. Both short- and long-range order may be seen in the crystal structure. As the diffusion time and temperature increase, the peak intensity decreases and the order of the crystal structure is destroyed during diffusion.
4. The MSD curves were extracted and utilized to calculate Ti and Fe atom's diffusion coefficients and the diffusion rate of Fe atoms is greater than that of Ti atoms.
5. As the diffusion temperature rises, the diffusion coefficients and the thickness of the diffusion area in the interaction area increase and there is a linear relationship between the logarithm of the diffusion coefficient

Author Contributions: Conceptualization, X.L. and H.Y.; methodology, G.X. and T.C.; software, G.X. and X.L.; validation, A.Z.; formal analysis, G.X.; investigation, G.X.; resources, T.C.; data curation, G.X.; writing—original draft preparation, G.X.; writing—review and editing, T.C.; visualization, A.Z.; supervision, H.Y.; project administration, H.Y.; funding acquisition, H.Y. All authors have read and agreed to the published version of the manuscript.

Funding: This research was funded by the Natural Science Foundation of Hebei Province, grant number E2021203237 and the Central Government Guides Local Science and Technology Development Fund Projects, grant number 216Z1002G.

Institutional Review Board Statement: Not applicable.

Informed Consent Statement: Not applicable.

Data Availability Statement: Not applicable.

Conflicts of Interest: The authors declare no conflict of interest.

References

1. Luo, Z.; Wang, G.; Xie, G.; Wang, L.; Zhao, K. Effect of niobium interlayer on microstructure and properties of vacuum rolling composite Ti-stainless steel plate. *J. Nonferrous Met. China* **2013**, *23*, 3335–3340.
2. Yadegari, M.; Ebrahimi, A.R.; Karami, A. Effect of Heat Treatment on Interface Microstructure and Bond Strength in Explosively Welded Ti/304L Stainless Steel Clad. *Mater. Sci. Technol.* **2013**, *29*, 69–75. [CrossRef]
3. Jiang, H.; Yan, X.; Liu, J.; Zeng, S.; Duan, X. Diffusion behavior and mathematical model of titanium-steel explosive composite plate during heat treatment. *Rare Met. Mater. Eng.* **2015**, *44*, 972–976.
4. Momono, T.; Enjo, T.; Ikeuchi, K. Effect of Carbon Content on the Diffusion Bonding of Iron and Steel to Titanium. *ISIJ Int.* **1990**, *30*, 978–984. [CrossRef]
5. Li, B.; Chen, Z.; He, W.; Zhou, T.; Wang, Y.; Peng, L.; Li, J.; Liu, Q. Effect of titanium grain orientation on the growth of compounds at diffusion bonded titanium/steel interfaces. *Mater. Charact.* **2019**, *148*, 243–251. [CrossRef]
6. Miglio, L.; Iannuzzi, M.; Raiteri, P.; Celino, M. Silicon diffusion in competitive TiSi₂ phases by molecular dynamics simulations. *Microelectron. Eng.* **2001**, *55*, 83–92. [CrossRef]
7. Chen, S.D.; Soh, A.K.; Ke, F.J. Molecular dynamics modeling of diffusion bonding. *Scr. Mater.* **2005**, *52*, 1135–1140. [CrossRef]
8. Chen, S.Y.; Wu, Z.W.; Liu, K.X. Atomic diffusion across Ni50Ti50—Cu explosive welding interface: Diffusion layer thickness and atomic concentration distribution. *Chin. Phys. B* **2014**, *23*, 066802. [CrossRef]
9. Xiu, L.; Wu, J.F. Atomic diffusion behavior in W/Cu diffusion bonding process. *J. Fusion Energy* **2015**, *34*, 769–773. [CrossRef]
10. Samsonov, V.M.; Bembel, A.G.; Popov, I.V.; Vasilyev, S.A.; Talyzin, I.V. Solid-state wetting at the nanoscale: Molecular dynamics and surface diffusion approach. *Surf. Innov.* **2017**, *5*, 161–169. [CrossRef]
11. Zhang, Y.; Jiang, S. Atomistic investigation on diffusion welding between stainless steel and pure Ni based on molecular dynamics simulation. *Mater.* **2018**, *11*, 1957. [CrossRef] [PubMed]
12. Soltani, S.; Abdolrahim, N.; Sepehrband, P. Molecular dynamics study of self-diffusion in the core of a screw dislocation in face centered cubic crystals. *Scr. Mater.* **2017**, *133*, 101–104. [CrossRef]
13. Béjaud, R.; Durinck, J.; Brochard, S. Twin-interface interactions in nanostructured Cu/Ag: Molecular dynamics study. *Acta Mater.* **2018**, *144*, 314–324. [CrossRef]
14. Yang, J.; Zhang, J.; Qiao, J. Molecular dynamics simulations of atomic diffusion during the Al–Cu ultrasonic welding process. *Mater.* **2019**, *12*, 2306. [CrossRef]
15. Zhou, X.; Zhu, J.; Wu, H. Molecular dynamics studies of the grain-size dependent hydrogen diffusion coefficient of nanogained Fe. *Int. J. Hydrogen Energy* **2021**, *46*, 5842–5851. [CrossRef]
16. Mao, A.; Zhang, J.; Yao, S.; Wang, A.; Wang, W.; Li, Y.; Qiao, C.; Xie, J.; Jia, Y. The diffusion behaviors at the Cu–Al solid-liquid interface: A molecular dynamics study. *Results Phys.* **2020**, *16*, 102998. [CrossRef]
17. Chen, J.; Chen, W.; Wang, C. Modeling and investigation for atomic diffusion and mechanical properties of TiAl/Ti₃Al interface: Temperature effect. *Appl. Phys. A* **2020**, *126*, 1–9. [CrossRef]
18. Wang, K.; Bai, H.; Hu, W.; Wu, S.; Wang, H.; Fan, H. Investigation of atomic diffusion behavior of Mo/Au interface. *Mater. Chem. Phys.* **2021**, *257*, 123839. [CrossRef]
19. Zhan, Y.; Wu, H.; Song, W.; Zhu, L. Molecular Dynamics Study of the Diffusion between Virgin and Aged Asphalt Binder. *Coat* **2022**, *12*, 403. [CrossRef]
20. Zurhelle, A.F.; Stehling, W.; Waser, R.; De Souza, R.A.; Menzel, S. Oxygen Diffusion in Platinum Electrodes: A Molecular Dynamics Study of the Role of Extended Defects. *Adv. Mater. Interfaces* **2022**, *9*, 2101257. [CrossRef]
21. Zhang, W.; Huang, J.; Yu, X.; Liu, G.; Fan, D. Atomic-level diffusion at the amorphous Zr₅₀Cu₅₀/crystalline Cu interface: A molecular dynamics study. *J. Adv. Join. Processes* **2022**, *6*, 100120. [CrossRef]
22. Daw, M.S.; Baskes, M.I. Embedded-atom method: Derivation and application to impurities, surfaces, and other defects in metals. *Phys. Rev. B* **1984**, *29*, 6443. [CrossRef]
23. Baskes, M.I. Modified embedded-atom potentials for cubic materials and impurities. *Phys. Rev. B* **1992**, *46*, 2727. [CrossRef] [PubMed]
24. Kim, H.K.; Jung, W.S.; Lee, B.J. Modified embedded-atom method interatomic potentials for the Fe–Ti–C and Fe–Ti–N ternary systems. *Acta Mater.* **2009**, *57*, 3140–3147. [CrossRef]
25. Prasanthi, T.N.; Sudha, C.; Saroja, S. Molecular Dynamics Simulation of Diffusion of Fe in HCP Ti Lattice. *Trans. Indian Inst. Met.* **2018**, *71*, 1951–1955. [CrossRef]
26. Ledbetter, H.M.; Reed, R.P. Elastic properties of metals and alloys, I. Iron, nickel, and iron-nickel alloys. *J. Phys. Chem. Ref. Data* **1973**, *2*, 531–618. [CrossRef]
27. Song, Y.; Yang, R.; Li, D.; Guo, Z. A first-principles study of the theoretical strength and bulk modulus of hcp metals. *Philos. Mag. A* **2001**, *81*, 321–330. [CrossRef]
28. Plimpton, S. Fast parallel algorithms for short-range molecular dynamics. *J. Comput. Phys.* **1995**, *117*, 1–19. [CrossRef]

29. Stukowski, A. Visualization and analysis of atomistic simulation data with OVITO—the Open Visualization Tool. *Model. Simul. Mater. Sci. Eng.* **2009**, *18*, 015012. [CrossRef]
30. Terban, M.W.; Billinge, S.J.L. Structural analysis of molecular materials using the pair distribution function. *Chem. Rev.* **2021**, *122*, 1208–1272. [CrossRef]
31. Sa, I.; Lee, B.J. Modified embedded-atom method interatomic potentials for the Fe-Nb and Fe-Ti binary systems. *Scr. Mater.* **2008**, *59*, 595–598. [CrossRef]
32. Trong, D.N.; Long, V.C.; Țălu, Ș. Effects of Number of Atoms and Doping Concentration on the Structure, Phase Transition, and Crystallization Process of Fe_{1-x}–yNixCoy Alloy: A Molecular Dynamic Study. *Appl. Sci.* **2022**, *12*, 8473. [CrossRef]
33. Yuan, J.; Yu, A.; Zou, P.; Zhao, S.; Li, Y.; Wu, Q. Molecular dynamics simulation of hot pressing diffusion behavior between diamond and titanium. *Rare Met. Mater. Eng.* **2022**, *51*, 159–165.

Article

Atomic Research on the Diffusion Behavior, Mechanical Properties and Fracture Mechanism of Fe/Cu Solid–Liquid Interface

Hongyu Zheng *, Jingwen Sun, Na Guo and Mingjie Wang *

School of Intelligent Manufacturing, Huanghuai University, Zhumadian 463000, China

* Correspondence: 20191887@huanghuai.edu.cn (H.Z.); 15513882577@163.com (M.W.)

Abstract: A molecular dynamics simulation was applied to investigate the diffusion behavior and mechanical properties of a Fe/Cu solid–liquid interface with different orientations, temperatures, and strain rates. The results show that the displacement distance of Fe atoms' diffusion into the Cu matrix was obviously larger than that of Cu atoms' diffusion into the Fe matrix at any diffusion temperature and diffusion time. Moreover, the diffusion coefficient and diffusion distance both increase with temperature and time, and reach the highest value when the temperature and diffusion time are 1523 K and 3 ns, respectively. Additionally, the diffusion coefficients of the Fe atoms are arranged in the following order: Fe (100) < Fe (110) < Fe (111). The diffusion coefficients of the Cu atoms are arranged in the following order: Cu (110) > Cu (111) > Cu (100), when temperature and time are 1523 K and 3 ns, respectively. The yield strength and fracture strain of the bimetallic interface is positively correlated with the strain rate, but negatively correlated with the tensile temperature. Moreover, the yield strength of the three orientations can be arranged as follows: Fe (110)/Cu (110) > Fe (100)/Cu (100) > Fe (111)/Cu (111), and the yield strength and fracture strain of Fe (110)/Cu (110) diffusion interface are 12.1 GPa and 21% when the strain rate was 1×10^9 /s and the tensile temperature was 300 K. The number of stacking faults and dislocations of the diffused Fe/Cu interface decreased significantly in comparison to the undiffused Fe/Cu interface, even in the length of Stair-rod dislocation and Shockley dislocation. All these results lead to a decrease in the tensile yield strength after interface diffusion.

Keywords: diffusion behavior and mechanical properties; Fe/Cu solid–liquid interface; molecular dynamics; orientation; temperature and strain rate

Citation: Zheng, H.; Sun, J.; Guo, N.; Wang, M. Atomic Research on the Diffusion Behavior, Mechanical Properties and Fracture Mechanism of Fe/Cu Solid–Liquid Interface. *Coatings* **2022**, *12*, 1299. <https://doi.org/10.3390/coatings12091299>

Academic Editor: Gianni Barucca

Received: 13 August 2022

Accepted: 1 September 2022

Published: 4 September 2022

Publisher's Note: MDPI stays neutral with regard to jurisdictional claims in published maps and institutional affiliations.



Copyright: © 2022 by the authors. Licensee MDPI, Basel, Switzerland. This article is an open access article distributed under the terms and conditions of the Creative Commons Attribution (CC BY) license (<https://creativecommons.org/licenses/by/4.0/>).

1. Introduction

Over the last few years, high-strength and highly wear resistant bimetallic materials have been attracted worldwide attention and demonstrated important application prospects in aerospace, ships, automobiles, and other fields due to their excellent dual performance structure and the comprehensive high-strength and high wear resistance properties [1–5]. The steel–copper bimetallic materials are one of the typical representatives, combining the advantages of both steel (high strength and stiffness) and copper (high wear resistance), and have been used to fabricate military aerospace rotors [6]. Additionally, for steel–copper bimetallic materials with a high bonding strength, the relationship between the diffusion mechanism, the diffusion distance, and the tensile stress-strain of the interface atoms play a more important role in determining the bonding strength and the diffusion coefficient of the bimetallic interface [7,8]. However, the pivotal technique of steel–copper bimetallic materials, the interfacial diffusion and interface enhancement mechanism of steel–copper bimetallic materials, has hardly been published and investigated.

Up to now, atomic calculations have been demonstrated to be an effective method to comprehensively investigate the solid–liquid interface, as it is difficult to carry out an experimental investigation at high temperature [9–11]. According to the relevant reports,

several theoretical investigations of solid–liquid interfaces and multi-layer interfaces have been proposed, such as the Cu/Pb interface [12,13], Al/Cu interface [14,15], Ni/Al multi-layer [16], Al/Al₂O₃ interface [17], and Fe/Li interface [18]. Especially, Mao et al. [19] studied the diffusion behavior of the Cu/Al solid–liquid interface using the molecular dynamic (MD) method, and found that the influence of temperature and pressure on the diffusion behavior of Cu/Al solid–liquid interface is greater than that of time, and all of these results depend on the formation of θ -Al₂Cu. S. Raman et al. [20] investigated the thermodynamic and kinetic properties of Fe/Mn solid–liquid interface utilizing MD simulations, and successfully revealed that the average value of solid–liquid interfacial free energy and anisotropy parameters remain constant with fluctuating temperature and the variation in diffusion speed is higher than that of the bulk liquid diffusion coefficient with increasing temperature. Moreover, a number of researchers have explored some incurable factors associated with the mechanical properties of solid–liquid interface, such as stress–strain curves and microstructure evolution in the course of the tensile process [21–23]. Su et al. [24] investigated the tensile behavior of Ti/Ni multilayered films and predicted the tensile process, stress–strain curve, and other tensile behaviors through MD simulations. Liu et al. [25] simulated the diffusion process of the Al/Cu interface, analyzed the tensile behavior, and improved the mechanical properties of the Al/Cu solid–liquid interface after diffusion solidification and cooling. All these mechanical property investigations of the solid–liquid interface have been studied by quite a few scholars, but there has been no systematic analysis of the Fe/Cu solid–liquid interface.

In this paper, we aimed to propose a theoretical framework based on the diffusion behavior and mechanical properties of Fe/Cu solid–liquid interface using MD simulation. In detail, we analyzed the diffusion coefficient, the diffusion distance, the atomic concentration distribution, and the diffusion mechanism of Fe/Cu solid–liquid interfaces at different temperatures and diffusion times. Meanwhile, the mechanical properties, i.e., tensile stress–strain curve, influence of tensile orientation, strain rate, and tensile temperature of the Fe/Cu solid–liquid interface, are also investigated. Although the diffusion and bonding characteristics of steel–copper bimetallic interfaces cannot be directly characterized in time scale and space scale in this study, our calculations provide a theoretical guidance for the production and manufacture of high-performance Fe/Cu bimetallic materials.

2. Simulation Methodology

All MD simulations are calculated using the Large-scale Atomic/Molecular Massively Parallel Simulator (LAMMPS) [26] with a time step of 1.0 fs. Additionally, an embedded atomic method (EAM) potential developed by Byeong-Joo Lee et al. [27] was used for modeling the atomic interaction between FCC Fe atoms and FCC Cu atoms near the interface, which has been employed in exploring diffusion properties, mechanical properties [28], and magnetic properties [29–31] of the Fe–Cu alloys. An open visualization tool (OVITO) [32] was used to observe diffusion behavior and the deformation process. Moreover, periodic boundary conditions were applied in three transverse (x, y, and z) directions. The initial velocity of atoms was assumed to accord with Maxwell–Boltzmann random distribution. Additionally, the Verlet integration algorithm was introduced to solve the Newtonian equation of motion integration.

In this study, three surface orientations ((100), (110), and (111)) of the γ -Fe/Cu interface were used to calculate the diffusion behavior and mechanical properties of Fe/Cu bimetallic materials. An additional advantage of using a case study approach is that our simulation models are based on our steel–copper bimetallic casting experiment at high temperature [33,34]. The modeling consists of FCC Fe bulk and FCC Cu bulk, and the initialization configurations of a cross-section are shown in Figure 1. As seen in Figure 1, the initial Fe/Cu interface model consisted of two parts: an upper Cu block containing 6400 atoms with the size of $10a_{\text{Cu}} \times 5a_{\text{Cu}} \times 30a_{\text{Cu}}$ and a lower Fe block with the same number of atoms and the size of $10a_{\text{Fe}} \times 5a_{\text{Fe}} \times 30a_{\text{Fe}}$ (the lattice constant of the a_{Cu} and a_{Fe} atoms are 0.36147 and 0.36457 nm respectively). To perform the solid–liquid interface

calculations, five different temperatures—1323, 1373, 1423, 1473, and 1523 K—were selected according to the melting point of Cu and Fe. Additionally, the overall diffusion process was relaxed at 300 K under a constant pressure-temperature (NPT) ensemble for 100 ps, and then relaxed at the target diffusion temperature under a constant pressure-temperature (NPT) ensemble for 1000 ps. Finally, the system was quickly cooled to 300 K, shown in Figure 1.

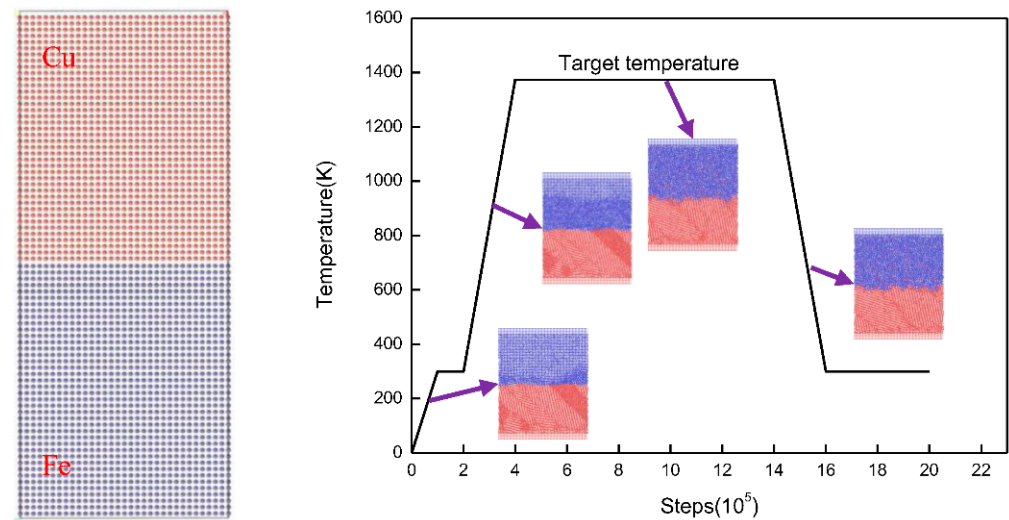


Figure 1. Atomic configuration of Fe/Cu interface model and the temperature–time relationship of the diffusion process.

According to [35], the mean square displacement (MSD) of the solid–liquid interface can be approximately calculated in such a complicated system. Thus, the MSD of Cu and Fe was calculated first to forecast the diffusion coefficient. The MSD can be defined by the following equation [36]:

$$\text{MSD} = \langle r^2(t) \rangle = \langle |r_i(t) - r_i(0)|^2 \rangle$$

where $r_i(t)$ is the position vector of atom i at time t , which represents the average ensemble of the atoms in the simulated time. Accordingly, the diffusion coefficient is defined by the following equation [37]:

$$D = \lim_{t \rightarrow \infty} \frac{1}{2Nt} \langle |r(t) - r(0)|^2 \rangle$$

where D is the diffusion coefficient, N denotes the dimension of the simulated system, and $N = 3$ for the simulation of blocks.

3. Result and Discussion

3.1. Diffusion Behavior

Temperature and diffusion time, as the two main factors determining the Fe/Cu interface, were considered first in our simulation. Thus, the snapshots of the cross-section diffusion process of Fe bulk and Cu bulk at different temperatures and times are distinctively illustrated in Figure 2. By comparing the four snapshots under the same temperature with the diffusion time elevated, the portion of atoms diffusing across the initial Fe/Cu interface can be seen to increase gradually and the diffusion depth of the Fe atoms diffusing into the Cu bulk is deeper, while that of Cu atoms diffusing into the Fe bulk is shorter. From these snapshots, it can be seen that only a small amount of Fe atoms cross through the initial interface, while much less Cu atoms cross the interface at 0.5 ns. After 3.0 ns, the diffusion distance of Cu atoms and Fe atoms both increase, the percentage of Fe atoms that diffuse across the interface increases to 1.5% from 0.3% at 0.5 ns, and the percentage of Cu atoms increases to 0.3% from 0.05% at 0.5 ns. These asymmetrical diffusion phenomena

have similarly appeared in Al/Cu [38], Mo/Ti [39], and Fe/W [40] interfaces. Likewise, by comparing five different temperatures at the same diffusion time, one can see that only a few Fe atoms diffuse into the Cu bulk at 1323 K, the interfacial structure is relatively smooth, and the degree of atomic confusion is lower. However, when temperature is increased, the portion of Fe and Cu atoms that cross initial interface increases and the diffusion distance of Fe atoms diffusing into the Cu bulk is also deeper than that of the Cu atoms diffusing into the Fe bulk at every temperature. Meanwhile, when the temperature is increased to 1523 K from 1323 K with a 50 K temperature interval, the percentages of the number of Fe atoms diffusing into the Cu bulk are 0.1%, 0.13%, 0.15%, 0.17%, and 0.2%, while that of the Cu atoms diffusing into Fe bulk are 0.03%, 0.035%, 0.05%, 0.08%, and 0.1%. Therefore, the influence of time on the diffusion distance is greater than that of temperature.

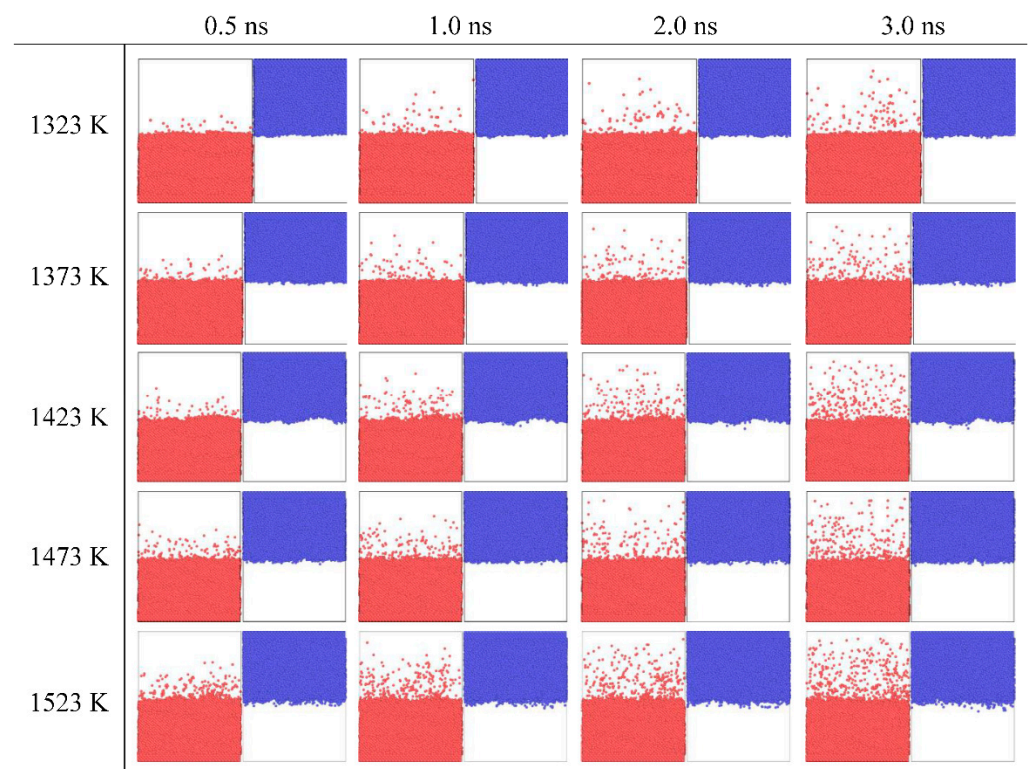


Figure 2. Snapshots of Fe atoms and Cu atoms under different diffusion times and temperatures. Red is Fe, blue is Cu.

Figure 3 illustrates the snapshots of the planar views of the equilibrium diffusion Fe/Cu interface at different temperature after 3 ns, respectively. As shown in Figure 3, when the temperature is increased, the Cu bulk presents an obvious liquid amorphous structure due to the disordered arrangement of atoms, while the Fe bulk maintains a solid crystalline structure. Furthermore, after the Cu atoms diffuse into the Fe lattice, the Cu atoms show an ordered state and occupy the lattice position of the Fe bulk, while the majority of the Fe atoms are located in the vacancies of the Cu lattice after diffusing into the inner Cu lattice. Thus, the Cu atoms gradually form agglomerations due to the increasing number of Fe atoms occupying more and more vacant positions in Cu bulk, explaining why the diffusion distance of Fe atoms diffusing into the Cu bulk is deeper than that of the Cu atoms diffusing into the Fe bulk.

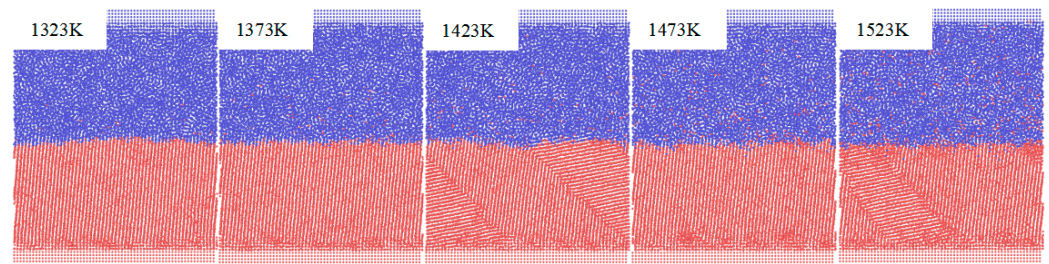


Figure 3. Atomic structure of Fe/Cu interface at different temperatures.

To deeply understand the non-uniform diffusion phenomena of the three Fe/Cu interface models, the MSDs of the Fe surface and the Cu surface in different directions at 1523 K were determined. As shown in Figure 4, the MSD curves of the Cu atoms in all orientations increase linearly, while the MSD curves of Fe atoms in different orientations areas fluctuate upward, which is consistent with the liquid and solid diffusion characteristics of the Cu and Fe matrixes. For the MSD curves of Fe atoms and Cu atoms in different directions, the MSD value of the diffusion of Cu atoms along the y-axis is higher than that along the x-axis and z-axis, indicating that Cu atoms mainly diffuse along the y-axis. The diffusion of Fe atoms on Fe (100) and Fe (111) surfaces is mainly along the x-axis, while on Fe (110) surfaces, the diffusion of Fe atoms is mainly along the y-axis. It can be seen that the degree of diffusion of the Fe/Cu interface in the diffusion process along the perpendicular direction is lower than that along the parallel direction of the interface.

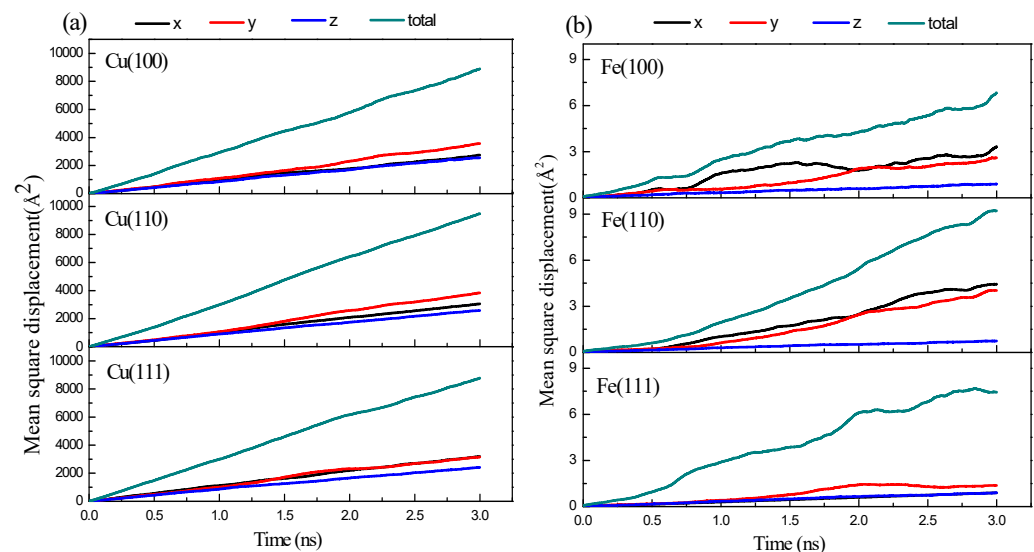


Figure 4. The mean square displacement curves of Fe/Cu interface at 1523 K with different orientation: (a) Cu (100), Cu (110), and Cu (111); (b) Fe (100), Fe (110), and Fe (111).

Table 1 shows the atomic diffusion coefficients of different surfaces and directions, and it can be seen that the diffusion coefficients of the Cu slabs in the z-axis direction can be ordered as (110) < (111) < (100), and the diffusion coefficients of Fe atoms in the z-axis direction can be ordered as (111) < (100) < (110). For all the Cu slabs, the diffusion coefficient of Cu atoms along y-axis is greater than that along the x-axis and z-axis, which can be ranked as follows: $z < x < y$, indicating that the blocking effect of Fe matrix on Cu atoms reduces the movement of Cu atoms along z-axis. However, for all the Fe slabs, the diffusion coefficient of Fe atoms along the z-axis is also smaller than other directions, which indicates that the transverse movement is greater than the axial movement during the diffusion process of Fe/Cu interface, and the Fe (110)/Cu (110) interface displays the best diffusion effect for the Fe atoms diffusing into the Cu matrix.

Table 1. Diffusion coefficient of atoms under different surface and orientation.

Diffusion Direction	Cu (100)	Cu (110)	Cu (111)	Fe (100)	Fe (110)	Fe (111)
D_x (10^{-11} m ² /s)	409.5	523.6	528.6	0.803	0.296	0.745
D_y (10^{-11} m ² /s)	605.7	735.2	626.6	0.456	0.575	0.813
D_z (10^{-11} m ² /s)	431.1	421.8	389.3	0.126	0.159	0.117
D_{total} (10^{-11} m ² /s)	491.7	549.6	512.6	0.353	0.464	0.554

In the in-depth investigation of the specific diffusion information of the Fe (110)/Cu (110) interface, the mean square displacement (MSD) of Cu atoms and Fe atoms along z-direction were calculated as shown in Figure 5. Additionally, the diffusion coefficient and the concentration distributions along the z-direction of Fe and Cu atoms was calculated to characterize the atomic diffusion at the Fe (100)/Cu (100) interface with temperature increase, as shown in Figure 5. One can see that all the MSD curves of the Cu atoms and Fe atoms are not only increased with increasing diffusion time at different temperatures, but also increased with increasing temperature due to the higher kinetic energy of atomic diffusion. Additionally, as shown in Figure 5a, the MSD curves of the Cu atoms present as straightly increasing trends as the diffusion time is incremented, but that of the Fe atoms does not maintain a straight line, as shown in Figure 5b. This is possibly due to the fact that the solid Fe matrix exhibits obvious volume instability when the ambient temperature approaches the melting point. From Figure 5c, it can be seen that the diffusion coefficient of Fe and Cu atoms exhibits a significantly increasing trend with increasing temperature, this is possibly due to an increase in the internal energy of the system. The diffusion coefficient of Cu atoms is far smaller than that of Fe atoms, seen in Figure 5c, but the diffusion depth of Fe atoms the diffuse into the Cu area is much extensive than that of Cu atoms, as seen in Figure 5d. This phenomenon concurs with the above results (see the snapshots in Figure 1), and is possibly due to the lower melting point of Cu than that of Fe. In contrast, the interface migrates to the Fe sides during the diffusion process. As shown in Figure 5d, the moving distance of the red dotted line is greater than that of the black dotted line. Thus, the interface migration may appear in these Fe/Cu interface models.

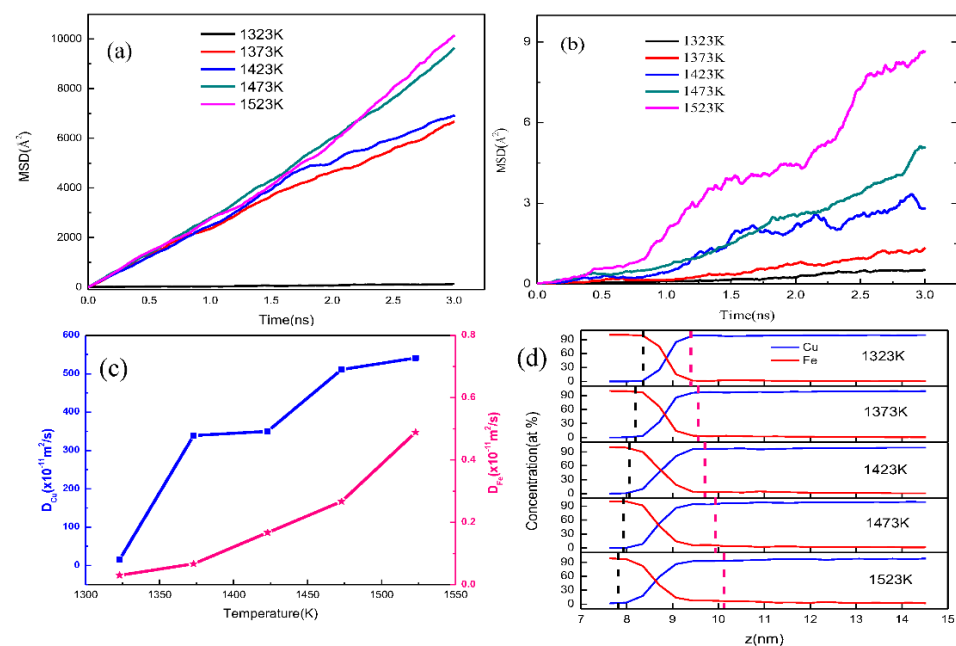


Figure 5. The diffusion behavior of atoms and the diffusion distance of Fe (110)/Cu (110) interface under different temperatures. (a) MSD curves of Cu atoms under different temperatures; (b) MSD curves of Fe atoms under different temperatures; (c) diffusion coefficient of Fe and Cu atoms; (d) atomic concentration of Fe and Cu atoms.

To clearly observe the phenomenon of interface migration, we compared the snapshots of the diffusion Fe/Cu interface at the initial simulation time and the final simulation time, as shown in Figure 6. Compared with Figure 6a,b, the Cu atoms become disordered in comparison to the initial model. The Fe atoms keep the original crystal structure, yet only a few Cu atoms replaced the position of Fe atoms, which elucidates the results of the concentration distributions. Furthermore, the red dashed line in Figure 6 migrates to the Fe side after the diffusion of Fe/Cu bimetallic material, indicating that Cu atoms are difficult to diffuse into the Fe matrix, regardless of displacement diffusion and gap diffusion. Hence, it has been demonstrated that the interface migration is authentically consistent in these Fe/Cu diffusion interface systems.

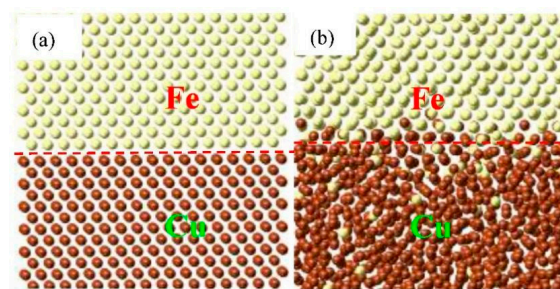


Figure 6. Atomic snapshots concerning Kirkendall effect of the Fe/Cu bimetallic interface. (a) Initial atomic structures; (b) the final atomic structures after the diffusion at 1523 K.

To deeply understand the inner diffusion mechanism of the Fe/Cu interface, the transition state search (TSS) tool was calculated to find the minimum energy and saddle points of the diffusion process. Figure 7 shows the diffusion energy barrier of five diffusion paths and the schematic diagram of the possible atomic diffusion paths near the interface boundary of the Fe and Cu atoms. Comparing five diffusion energy barriers in Figure 7, we can find that the diffusion of Cu and Fe atoms is mainly dominated by first-nearest-neighbor diffusion, and the diffusion activation energy of Fe atoms in the Cu matrix is greater than that of Cu atoms in the Fe matrix, indicating that the diffusion of Fe atoms in Cu matrix is easier than that of Cu atoms in Fe matrix.

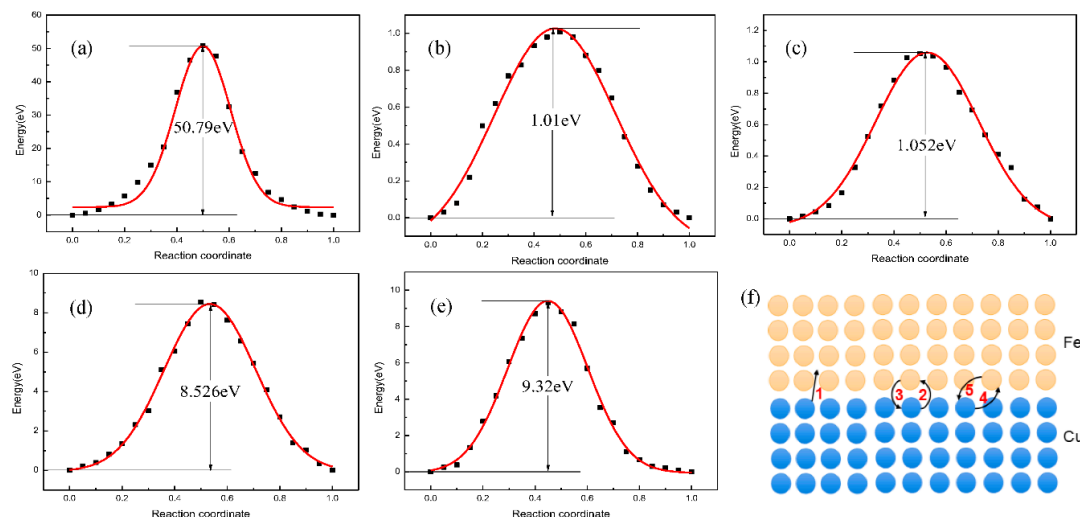


Figure 7. Atomic snapshots concerning Kirkendall effect of the Fe/Cu bimetallic interface. (a) the diffusion energy of the interstitial diffusion path of Cu atom; (b) the diffusion energy of the first nearest neighbor diffusion path of Cu atom; (c) the diffusion energy of the first nearest neighbor diffusion path of Fe atom; (d) the diffusion energy of the second nearest neighbor diffusion path of Cu atom; (e) the diffusion energy of the second nearest neighbor diffusion path of Cu atom; (f) schematic diagram of diffusion mechanism of Fe/Cu diffusion interface.

3.2. Mechanical Properties

3.2.1. Strain Rate and Orientation Effect

The strain rate's dependence of the stress–strain relationships of the Fe (100)/Cu (100) interface, the Fe (110)/Cu (110) interface, and the Fe (111)/Cu (111) interface under uniaxial tension are shown in Figure 8. As shown in Figure 8a, the strain–stress curves of the Fe (100)/Cu (100) interface are almost linear at the initial stage of uniaxial tension, which indicates that the Fe (100)/Cu (100) interface undergoes elastic deformation. After that, the stress decreases slowly with the increase in strain when the tension reaches ultimate strength, indicating that the Fe (100)/Cu (100) interface presented a plastic deformation ability and ductile fracture characteristics. From Figure 8b,c, one can see that the strain–stress curves are almost increasing linearly at the early stage in all the strain rates, which indicates that the Young's modulus is less sensitive to the strain rate. However, with the application of increasing strain, the curves present apparent ups and downs at the end of elastic deformation, which indicates that fracture occurred. Additionally, all the strain–stress curves decrease suddenly at the stress peak point at different strain rates, and no obvious plastic deformation can be observed. These results imply that the brittle fracture of the Fe (100)/Cu (100) interface and the Fe (111)/Cu (111) interface occurred at all simulated strain rates. Meanwhile, the yield strength and fracture strain both increase with the increasing strain rates, and the yield strength of three orientations can be arranged in the following order: Fe (111)/Cu (111) > Fe (110)/Cu (110) > Fe (100)/Cu (100), which reaches a remarkable agreement with the diffusion behavior of the three models.

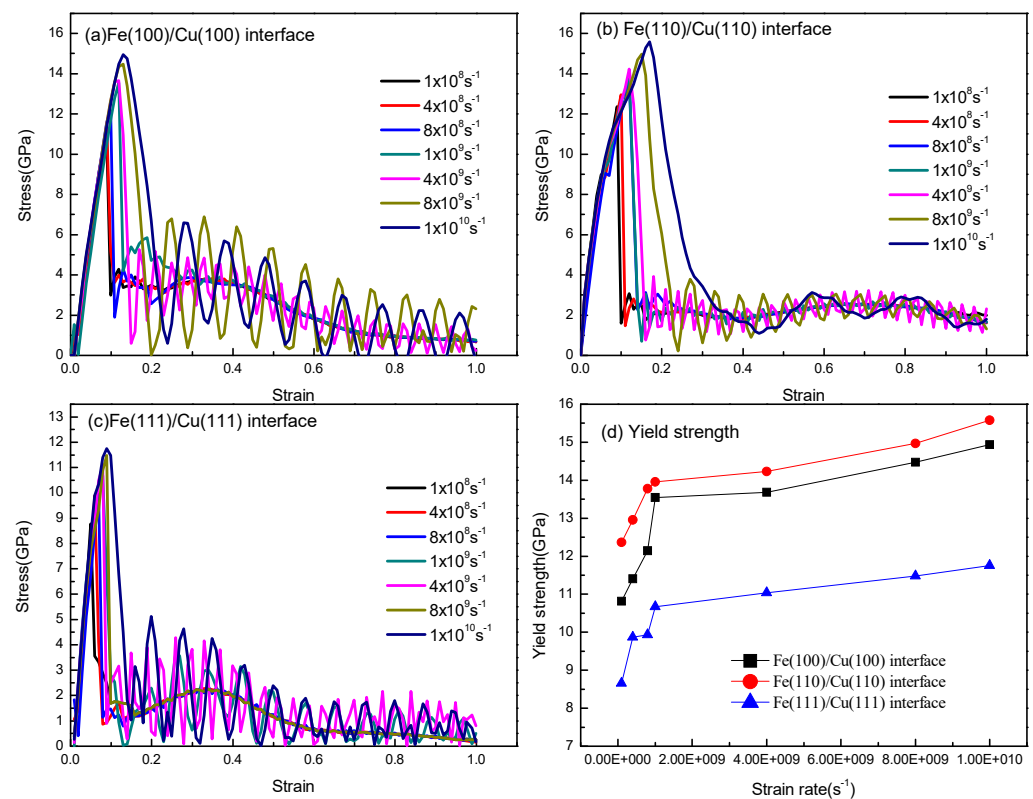


Figure 8. Stress–strain curves of (a) Fe (100)/Cu (100) interface at different strain rates from $1 \times 10^8/\text{s}$ to $1 \times 10^{10}/\text{s}$; (b) Fe (110)/Cu (110) interface at different strain rates from $1 \times 10^8/\text{s}$ to $1 \times 10^{10}/\text{s}$; (c) Fe (111)/Cu (111) interface at different strain rates from $1 \times 10^8/\text{s}$ to $1 \times 10^{10}/\text{s}$; (d) the yield strength of three different interface models under different strain rates.

Referring to Figure 8a–c, the yield strength and fracture strain curves with different strain rates are described in Figure 8d. As shown in Figure 8d, the yield strength and fracture strain are particularly susceptible to strain rate when the strain stress is less than

$1 \times 10^9 \text{ s}^{-1}$. Nevertheless, when the strain rate exceeds $1 \times 10^9 \text{ s}^{-1}$, the tensile strength still increases slowly with the growth of strain rate, this is possibly due to the fact that the reinforcement effect is not statistically significant. Furthermore, the brittle fracture behavior of the three Fe/Cu interface models at a high strain rate is similar to that of single-crystal titanium [41].

All the atomic visualizations of the Fe/Cu interface are described using the Open Visualization Tool (OVITO), and all the inner structure of Fe/Cu bimetallic materials is characterized to observe the defect's behavior from HCP environments with common neighbor analysis (CNA) [42]. Additionally, the centrosymmetric parameter (CSP) and dislocation extraction algorithm (DXA) [43] analysis are powerful modules that were used to analyze the dislocation motion and defects of the Fe/Cu interface. To clearly describe the fracture mechanism of the Fe (100)/Cu (100) interface, the Fe (110)/Cu (110) interface and the Fe (111)/Cu (111) interface, the atomic snapshots (rendered by CNA, CSP, and DXA results) of the three interface models under uniaxial loading at different strain are described and shown in Figures 9–11.

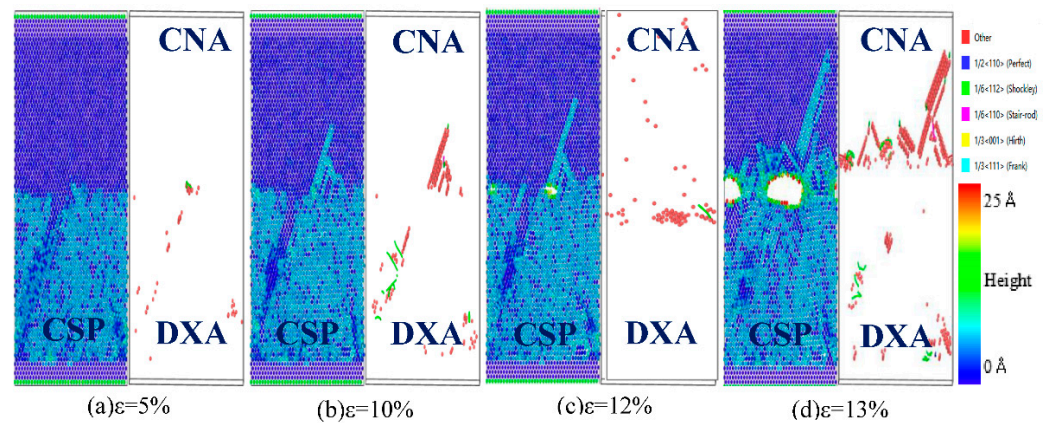


Figure 9. Atomic CSP, CNA, and DXA analysis of the Fe (100)/Cu (100) undiffused interface during z-axis tensile process.

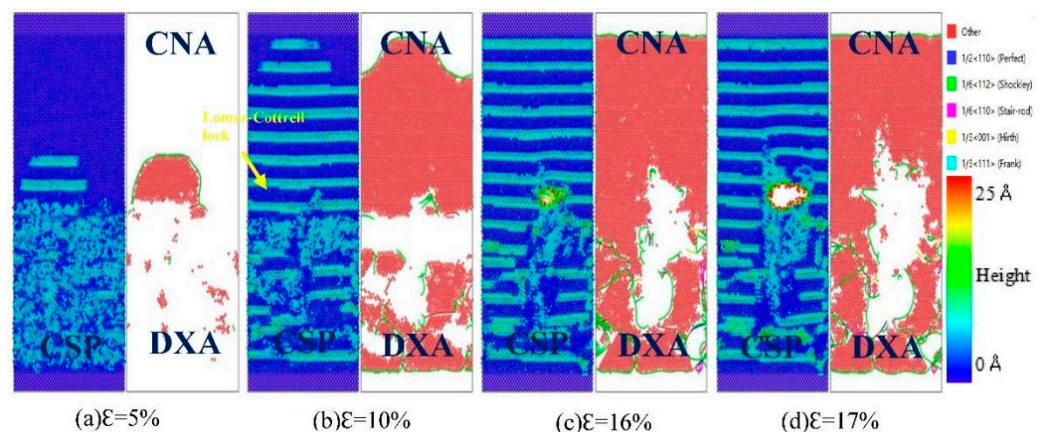


Figure 10. Atomic CSP, can, and DXA analysis of the Fe (110)/Cu (110) undiffused interface during z-axis tensile process.

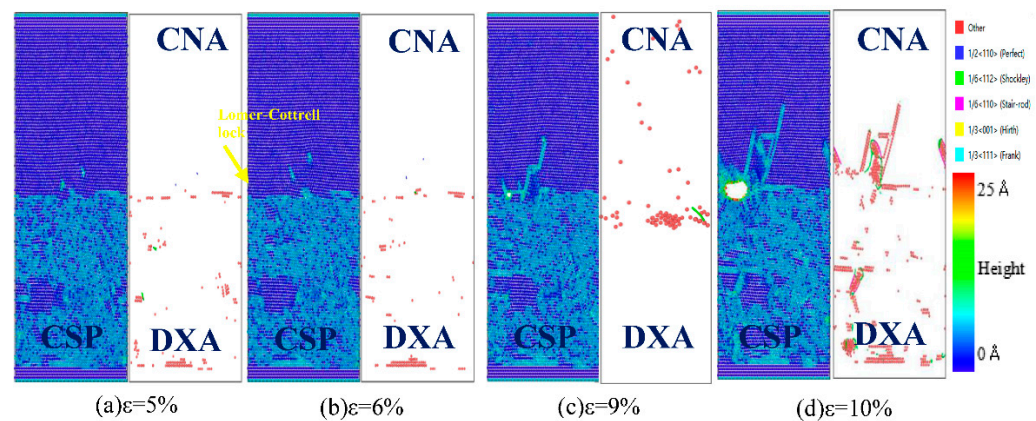


Figure 11. Atomic CSP, can, and DXA analysis of the Fe (111)/Cu (111) undiffused interface during z-axis tensile process.

From the CSP analysis in Figure 9, the atoms of the Fe (100)/Cu (100) interface are arranged neatly and represent an elastic deformation process on both sides of the interface at the beginning of the tension, and the interface structure hardly changes when the strain is lower than 5%. With gradually increasing stress, the Fe (100)/Cu (100) interface emits surface angular dislocations to the Cu side when the strain reaches 10%. Then, micropores are formed at the surface's angular dislocations when the strain reaches 12%. With continuous increase in strain, the interface gradually expands into a microcrack along the micropore, which results in a sudden drop of the interface stress value, and brittle fracture occurs. In addition, according to the CNA and DXA analysis, the stacking faults on the Cu side increase gradually with the progression of the Fe (100)/Cu (100) interface tension, and the evolution of the $1/6 \langle 112 \rangle$ Shockley dislocations occupied a dominant position during the dislocation movement in the tensile process. Additionally, the number of Shockley dislocations near the interface increases sharply when a large number of cracks appear at the interface, while the number of Shockley dislocations is less before the fracture, indicating that brittle fracture begins at the strain of 13% in the Fe (100)/Cu (100) interface.

From Figure 10, it can be seen that a large number of stacking faults appear on both sides of the interface during the tensile fracture of Fe (110)/Cu (110) interface. Firstly, according to the CSP analysis, the steady stacking fault forms on the Cu side when the strain is 5%, but a large number of stacking faults appear on both sides of the Fe/Cu interface and surface angle dislocations are emitted to the Cu side when the strain increases to 10%. These results cause the development of micropores and cracks, resulting in interface fracture. Similarly, through integrated DXA analysis and CNA analysis, we can observe that a large number of stacking faults appear in the tensile process of Fe (110)/Cu (110) interface, and more $1/6 \langle 112 \rangle$ Shockley dislocations appear near the interface. These phenomena hinder the progress of z-axis loading tensile, but improve the maximum stress value of the Fe (110)/Cu (110) interface.

In Figure 11, it can be seen that the Fe (111)/Cu (111) interface starts to emit Lomer–Cottrell lock to the Cu side when the strain reaches 6%, expands into micropores when the strain is 9%, and then expands into a microcrack when the strain is 10%. Comparing the tensile process with the two above interface models, one can see that there are fewer interlayer faults and Shockley dislocations at the Fe (111)/Cu (111) interface in the tensile process, resulting in lower yield strength and lower interface bonding strength of the Fe (111)/Cu (111) interface. To summarize, the yield strengths of the three orientation's interface models can be ranked as follows: Fe (110)/Cu (110) > Fe (100)/Cu (100) > Fe (111)/Cu (111). In addition, the Fe/Cu bimetallic interface shows brittle fracture characteristics in the tensile process, and the Fe (110)/Cu (110) interface shows a certain fracture toughness compared with the other two interface models.

3.2.2. Temperature Effect

To systematically study the influence of z-axis tensile temperature on the mechanical properties of Fe/Cu interface, the diffused Fe (110)/Cu (110) interface (the diffusion temperature is 1523 K, and the time is 3 ns) and undiffused Fe (110)/Cu (110) interface models were selected to carry out the z-axis tensile test at different temperatures (50, 100, 200, 300, 400, and 500 K). The stress–strain tensile results are shown in Figure 12; all these strain–stress curves show a linear and sharp increasing trend when the strain value is less than 10%, consistent with the characteristics of elastic deformation. Additionally, the slope of the stress–strain curve decreases with the increase in temperature, which indicates that the elastic modulus of the Fe/Cu interface decreases with the increase in temperature. Moreover, the Fe/Cu interface tension enters the plastic deformation stage after the yield strength, and the dislocation and the slip phenomenon are more prominent, and the tensile stress drops sharply and then changes slowly, indicating that brittle fracture occurs in the Fe (110)/Cu (110) interface before and after diffusion at all temperatures. Additionally, the maximum yield stress of the undiffused Fe (110)/Cu (110) interface at 50 and 500 K are 15.8 and 13.9 GPa, respectively, and the corresponding strain values are 18.9% and 16.1%, respectively. However, for the diffused Fe (110)/Cu (110) interface, the maximum yield stress values are 13.4 and 10.4 GPa, respectively, and the corresponding strain values are 11.9% and 10.7%, respectively. Moreover, the yield strength of the Fe (110)/Cu (110) interface is lower after interfacial diffusion, which is caused by the weakening of the inter-atomic bonding energy caused by the bimetal interface reconstruction after diffusion. When temperature increases from 50 to 100 K, the yield strength of the Fe (110)/Cu (110) interface decreases from 13.5 to 13.3 GPa respectively. However, when the temperature is raised from 400 to 500 K, the yield strength decreases from 11.2 to 10.3 GPa. Thus, the decreasing rates were 1.5% and 8.0%, respectively, indicating that the tensile Fe (110)/Cu (110) interface is more sensitive to temperature changes.

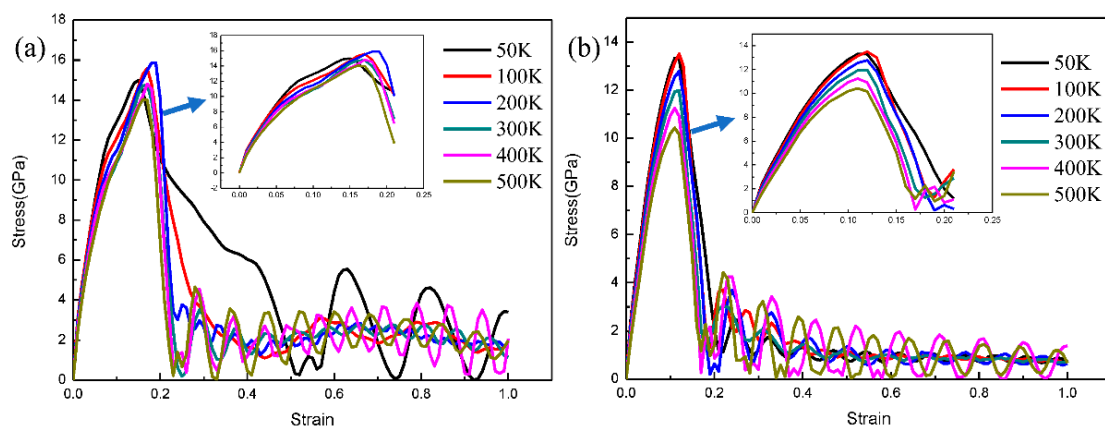


Figure 12. Strain–stress curves of z-axis tensile of Fe (111)/Cu (111) interface before and after diffusion under different temperature. (a) z-axis tensile stress–strain curve before diffusion; (b) z-axis tensile stress–strain curve after diffusion.

Thus, the atomic oscillation amplitude of Fe/Cu bimetallic interface is small when the tensile temperature is 50 K, resulting in a stable structure and a higher bonding strength. However, due to the increase in movement speed of atoms at the Fe/Cu bimetallic interface and the interaction force between atoms decreases when the tensile temperature is 500 K, a reduction in the energy required for dislocation, nucleation and emission, and lattice deformation occurred easily under the same load.

To reveal the fracture mechanism of the Fe (110)/Cu (110) interface at different working temperatures, the undiffused Fe (110)/Cu (110) interface at 300 and 500 K were selected to analyze the changes and atomic defects of the interface structure, and the results are shown in Figures 10 and 13 respectively. By comparing Figures 10 and 13, it can be found

that a large number of stacking faults also appear at the undiffused Fe (110)/Cu (110) interface at 500 K, which indicates that the main factor affecting stacking faults is the orientation relationship instead of tensile temperature. Additionally, the undiffused Fe (110)/Cu (110) interface emits a plane angular dislocation at the Cu side, and then evolves into a micropore when the strain is 10% and the stacking faults in the interface tensile process gradually decrease with the increase in temperature. This is possibly due to the higher tensile temperature, resulting in disordered structure arrangement and interface amorphization [44], which hinder the extended motion of dislocation and reduce the yield strength of the interface model. Although the number and length of dislocations increase or decrease, the types of the dislocations are all Shockley dislocations. Moreover, the fracture strain of the undiffused Fe (110)/Cu (110) interface decreases gradually with the gradual increase in temperature, possibly due to the early occurrence of interface fracture with the gradual increase in stress and the obstruction of dislocation propagation.

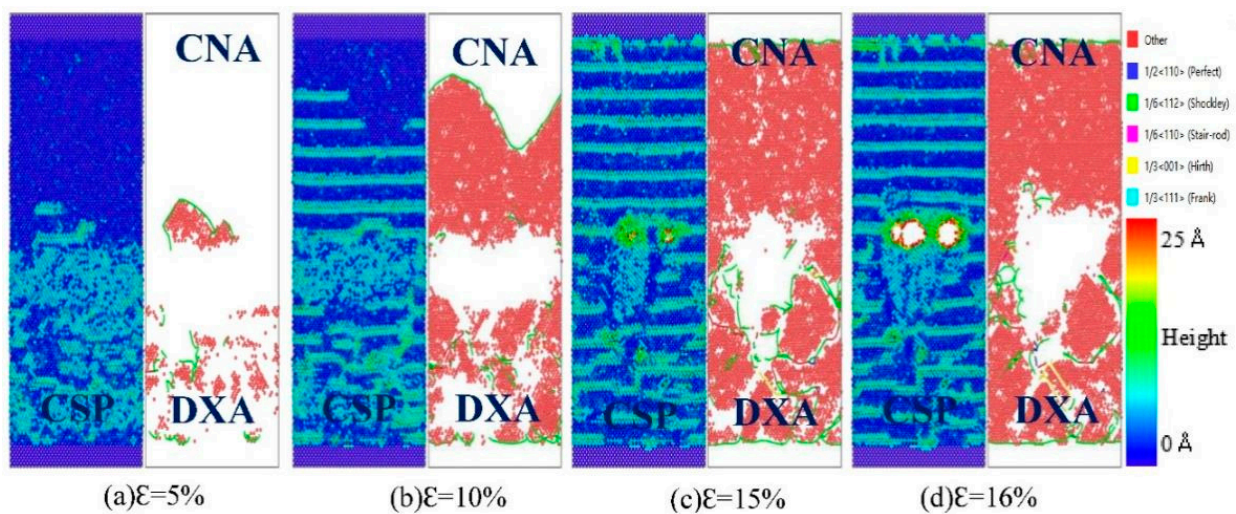


Figure 13. Atomic CSP, CNA, and DXA analysis of the Fe (110)/Cu (110) undiffused interface under z-axis tensile process at 500 K.

Figures 14 and 15 show the interface structure and atomic defect analysis during the tensile process of the diffused Fe (110)/Cu (110) interface at 300 and 500 K, respectively. From Figure 14, one can see that the micropores and microcrack at the diffused Fe (110)/Cu (110) interface appeared far from the interface on the Cu side, indicating that the bonding strength of the diffused Fe (110)/Cu (110) interface is greater than that of the Cu matrix. Similarly, the amorphization near the interface increase with increase in temperature, resulting in the reduction of interface stacking faults and the yield strength. From Figure 15, compared with the tension at 300 K, the fracture strain of the diffused Fe (110)/Cu (110) interface decreases from 20% to 19%, but the dislocation types are mainly $1/6 \langle 112 \rangle$ Shockley dislocation at both 300 and 500 K. In summary, temperature will not change the dislocation and defect types of the Fe (110)/Cu (110) interface model under a certain temperature range, but will reduce or improve the yield strength and fracture strain of bimetallic interface by hindering or promoting the growth of dislocation.

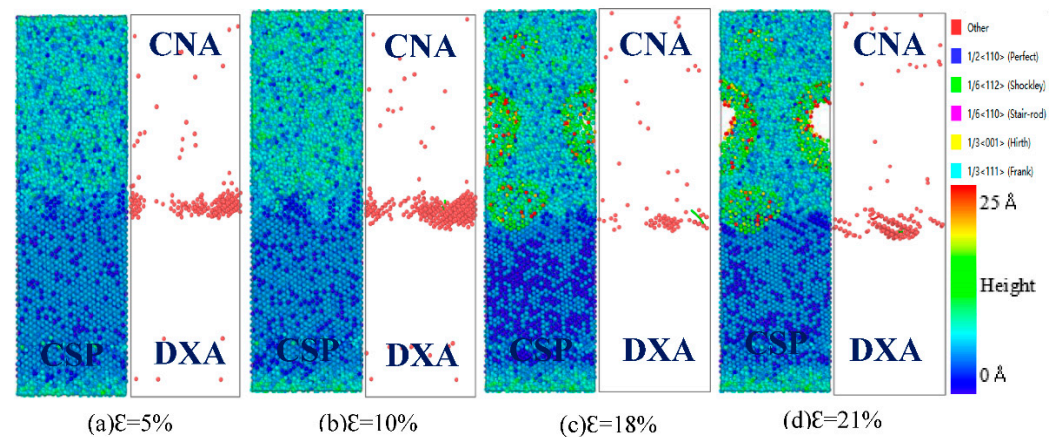


Figure 14. Atomic CSP, CNA, and DXA analysis of the Fe (110)/Cu (110) diffused interface under z-axis tensile process at 300 K.

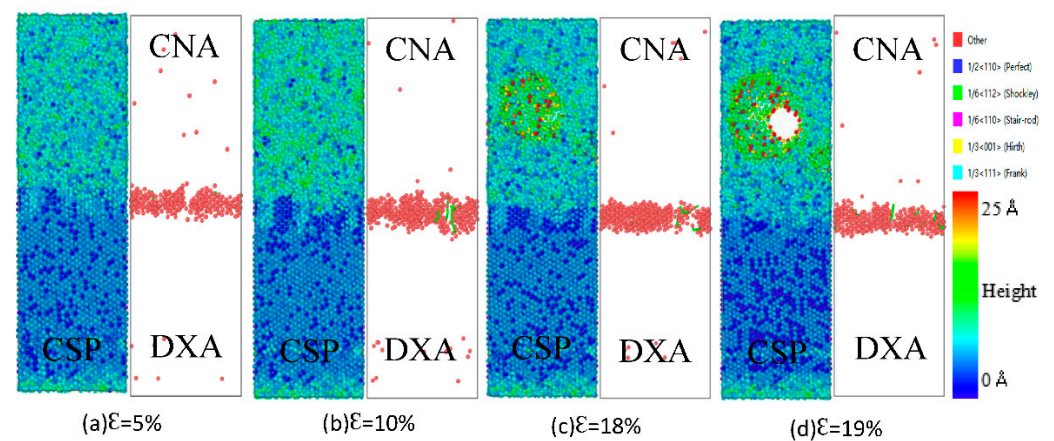


Figure 15. Atomic CSP, CNA, and DXA analysis of the Fe (110)/Cu (110) diffused interface under z-axis tensile process at 500 K.

4. Conclusions

In this research, the diffusion behavior, mechanical properties, and fracture mechanism of Fe/Cu solid–liquid interfaces were calculated by using a molecular dynamics simulation. The main conclusions obtained are as follows:

- (1) Regarding the diffusion phenomenon of the Fe/Cu interface, it was observed that the diffusion distance increases with the increase in diffusion temperature and diffusion time. In addition, the diffusion distance of the Cu atoms diffusing into the Fe matrix is obviously less than that of the Fe atoms diffusing into the Cu matrix. The diffusion coefficient and the diffusion distance reach their maximums when the solid–liquid temperature is 1523 K, and the diffusion time is 3 ns.
- (2) The diffusion coefficients of the Fe atoms when the temperature and time is 1523 K and 3 ns, respectively, are arranged in the following order: Fe (100) < Fe (110) < Fe (111). The diffusion coefficients of the Cu atoms are arranged in the following order: Cu (110) > Cu (111) > Cu (100).
- (3) The yield strength and fracture strain of Fe/Cu bimetallic interface increase with the increase in strain rate and gradually decrease with the increase in tensile temperature. The yield strength of the three orientations can be ranked in the following order: Fe (110)/Cu (110) > Fe (100)/Cu (100) > Fe (111)/Cu (111). The Fe/Cu bimetallic interface shows brittle fracture characteristics during the tensile process, and the Fe (110)/Cu (110) interface shows a certain fracture toughness compared with the other two interface models.

- (4) The yield strength of undiffused Fe/Cu bimetallic interface is higher than that of the diffused Fe/Cu interface. The number and length of $1/6\langle 112 \rangle$ Shockley dislocations in the tensile process of the Fe/Cu bimetallic interface decreased after diffusion and the bonding performance of the Fe/Cu bimetallic interface is also reduced. In the undiffused Fe (110)/Cu (110) interface, bimetallic interface fractures occur along the interface, while in the diffused Fe (110)/Cu (110) interface, these occur on the Cu side, away from the interface.

Author Contributions: H.Z.: conceptualization, methodology, software; J.S.: visualization, investigation and supervision; N.G.: investigation; M.W.: investigation, writing, reviewing, and editing. All authors have read and agreed to the published version of the manuscript.

Funding: This research was funded by the Natural Science Foundation of Henan Province, China, under Grant No.: 212300410205.

Institutional Review Board Statement: Not applicable.

Informed Consent Statement: Not applicable.

Data Availability Statement: Some or all data, models, or code generated or used during the study are proprietary or confidential in nature and may only be provided with restrictions.

Conflicts of Interest: The authors declare no conflict of interest. The founders had no role in the design of the study; in the collection, analyses, or interpretation of the data; in the writing of the manuscript, or in the decision to publish the results.

References

- Lozhkomoev, A.S.; Lerner, M.I.; Pervikov, A.V.; Kazantsev, S.O.; Fomenko, A.N. Development of Fe/Cu and Fe/Ag Bimetallic nanoparticles for promising biodegradable materials with antimicrobial effect. *Nanotechnol. Russ.* **2018**, *13*, 18–25. [CrossRef]
- Kaczmar, J.W.; Pietrzak, K.; Wlosinski, W. The production and application of metal matrix composite materials. *J. Mater. Process. Technol.* **2000**, *106*, 58–67. [CrossRef]
- Ghosh, M.; Chatterjee, S. Effect of interface microstructure on the bond strength of the diffusion welded joints between titanium and stainless steel. *Mater. Charact.* **2006**, *54*, 327–337. [CrossRef]
- Hai, C.B.; Zhang, H.P.; Du, L.Y.; Wang, D.X.; Xing, D.J.; Zhang, M.Z. Nickel/iron based bimetallic MOF-derived nickel ferrite materials for triethylamine sensing. *Cryst. Eng. Comm.* **2020**, *22*, 1286–1293. [CrossRef]
- Cheng, J.; Zhao, J.H.; Zhang, J.Y.; Guo, Y.; He, K.; Wen, F.L. Microstructure and mechanical properties of galvanized-45 steel/AZ91D bimetallic material by liquid-solid compound casting. *Materials* **2019**, *12*, 1651. [CrossRef]
- Chen, Y.; Wang, Y. Calculating method for the leakage between slipper and swashplate in spherical swashplate type axial piston pump with conical cylinder. *Adv. Mater. Res.* **2013**, *753–755*, 2736–2741. [CrossRef]
- Li, Y.; Gao, J.; Xu, N.; Li, P.; Gong, M.; Tong, W. Fabrication of a high chromium cast iron/low carbon steel bimetal: Diffusion behavior and bonding strength. *J. Mater. Eng. Perform.* **2019**, *28*, 6904–6911. [CrossRef]
- Tan, C.; Zhou, K.; Ma, W.; Min, L. Interfacial characteristic and mechanical performance of maraging steel-copper functional bimetal produced by selective laser melting based hybrid manufacture. *Mater. Des.* **2018**, *155*, 77–85. [CrossRef]
- Guo, Y.; Donatas, S.; Yoshiaki, K.; Hiroki, M.; Liu, X. A molecular dynamics study on the effect of surfactant adsorption on heat transfer at a solid-liquid interface. *Int. J. Heat Mass Transf.* **2019**, *135*, 115–123. [CrossRef]
- Debenedetti, P.G.; Chen, M.; Vella, J.R.; Furstenberg, S.; Carter, E.A.; Stillinger, F.H.; Panagiotopoulos, A.Z. Characterization of the liquid-solid Mo (110) interface from classical molecular dynamics for plasma-facing applications. *Nucl. Fusion* **2017**, *57*, 11. [CrossRef]
- Jesse, L.; Kern, P.R.; Barry, B.B.L. Characterization of the Al-Ga solid-liquid interface using classical and ab initio molecular dynamics simulation. *Phys. Rev. Mater.* **2020**, *4*, 043604. [CrossRef]
- Hoyt, J.J. Molecular dynamics study of equilibrium concentration profiles and the gradient energy coefficient in Cu-Pb nanodroplets. *Phys. Rev. B. Condens. Matter Mater. Phys.* **2007**, *76*, 094102. [CrossRef]
- Palafox-Hernandez, J.P.; Laird, B.B. Orientation dependence of heterogeneous nucleation at the Cu-Pb solid-liquid interface. *J. Chem. Phys.* **2016**, *145*, 211914. [CrossRef] [PubMed]
- Tanaka, Y.; Kajihara, M.; Watanabe, Y. Growth behavior of compound layers during reactive diffusion between solid Cu and liquid Al. *Mater. Sci. Eng. A* **2007**, *445–446*, 355–363. [CrossRef]
- Tanaka, Y.; Kajihara, M. Numerical analysis for migration of interface between liquid and solid phases during reactive diffusion in the binary Cu-Al system. *Mater. Sci. Eng. A* **2007**, *459*, 101–110. [CrossRef]
- Scott, W.N.; Rice, B.M. A molecular dynamics study of the role of relative melting temperatures in reactive Ni/Al nanolaminates. *J. Phys. Condens. Matter* **2011**, *23*, 5701. [CrossRef]

17. Yan, R.; Sun, W.; Ma, S.; Jing, T.; Dong, H. The orientation dependence of liquid ordering at α - Al_2O_3 /Al solid-liquid interfaces: A molecular dynamics study. *Comput. Mater. Sci.* **2020**, *174*, 109489. [CrossRef]
18. Gan, X.; Xiao, S.; Deng, H.; Sun, X.; Li, X.; Hu, W. Atomistic simulations of the Fe(001)-Li solid-liquid interface. *Fusion Eng. Des.* **2014**, *89*, 2894–2901. [CrossRef]
19. Mao, A.; Zhang, J.; Yao, S.; Wang, A.; Wang, W.; Li, Y.; Qiao, C.; Xie, J.; Jia, Y. The diffusion behaviors at the Cu-Al solid-liquid interface: A molecular dynamics study. *Results Phys.* **2020**, *16*, 102998. [CrossRef]
20. Raman, S.; Hoyt, J.J.; Saidi, P.; Asta, M. Molecular dynamics study of the thermodynamic and kinetic properties of the solid-liquid interface in FeMn. *Comput. Mater. Sci.* **2020**, *182*, 109773. [CrossRef]
21. Liu, L.; Deng, D.; Su, M.; An, M.; Wang, R. Strain rate and temperature effects on tensile behavior of Ti/Al multilayered nanowire: A molecular dynamics study. *Superlattices Microstruct.* **2019**, *135*, 106272. [CrossRef]
22. Nishida, S.; Surblys, D.; Yamaguchi, Y.; Kuroda, K.; Kagawa, M.; Nakajima, T.; Fujimura, H. Molecular dynamics analysis of multiphase interfaces based on in situ extraction of the pressure distribution of a liquid droplet on a solid surface. *J. Chem. Phys.* **2014**, *140*, 074707. [CrossRef] [PubMed]
23. Yan, R.; Sun, W.; Ma, S.; Davidchack, R.L.; Di Pasquale, N.; Hai, Q.; Jing, T.; Dong, H. Structural and mechanical properties of homogeneous solid-liquid interface of Al modelled with COMB3 potential. *Comput. Mater. Sci.* **2018**, *155*, 136–143. [CrossRef]
24. Su, M.; Deng, Q.; An, M.; Liu, L.; Ma, C. Molecular dynamics study of the tensile behaviors of Ti(0 0 0 1) / Ni(1 1 1) multilayered nanowires. *Comput. Mater. Sci.* **2019**, *158*, 149–158. [CrossRef]
25. Liu, H.; Ke, F.; Pan, H.; Zhou, M. Molecular dynamics simulation of the diffusion bonding and tensile behavior of a Cu-Al interface. *Acta Phys. Sin.* **2008**, *56*, 407–412. [CrossRef]
26. Plimpton, S. Fast parallel algorithms for short-range molecular dynamics. *J. Comput. Phys.* **1995**, *117*, 1–19. [CrossRef]
27. Lee, B.J.; Wirth, B.D.; Shim, J.H.; Kwon, J.; Kwon, S.C.; Hong, J.H. Modified embedded-atom method interatomic potential for the Fe-Cu alloy system and cascade simulations on pure Fe and Fe-Cu alloys. *Phys. Rev. Ser. B* **2005**, *71*, 4205. [CrossRef]
28. Guo, Q.; Greer, J.R. Compressive properties of interface-containing Cu-Fe nano-pillars. *Scr. Mater.* **2017**, *66*, 272–275. [CrossRef]
29. Lee, S.G.; Chung, Y.C. Atomic investigation of Fe-Cu magnetic thin films by molecular dynamics simulation. *Jpn. J. Appl. Phys.* **2007**, *46*, 6309–6311. [CrossRef]
30. Lee, S.G.; Chung, Y.C. The early stage of deposition process for Fe-Cu magnetic multilayer systems: Molecular dynamics simulation. *J. Phys. D Appl. Phys.* **2009**, *42*, 135305–135309. [CrossRef]
31. Lee, S.G.; Chung, Y.C. Molecular-dynamics investigation of the surface characteristics of Fe-Cu magnetic thin-film layers. *J. Vac. Sci. Technol. A Vac. Surf. Film.* **2008**, *26*, 1392–1396. [CrossRef]
32. Stukowski, A. Visualization and analysis of atomistic simulation data with OVITO-the open visualization tool. *Model. Simul. Mater. Sci. Eng.* **2010**, *18*, 015012. [CrossRef]
33. Zhang, G.; Kang, Y.; Wang, M.; Xu, H.; Jia, H. Atomic diffusion behavior and diffusion mechanism in Fe-Cu bimetal casting process studied by molecular dynamics simulation and experiment. *Mater. Res. Express* **2020**, *7*, 096519. [CrossRef]
34. Wang, M.; Zhang, G.; Xu, H. Atomistic simulations and experimental investigations of the diffusion behavior of steel/ZCuPb20Sn5 bimetals. *Coatings* **2020**, *10*, 549. [CrossRef]
35. Meis, C.; Fleche, J.L. Study of the solubility limit of oxygen vacancies in TiO_{2-x} using molecular dynamics. *Solid State Ion.* **1997**, *1*, 333–335. [CrossRef]
36. Trong, D.N.; Long, V.C.; Tălu, S. Molecular dynamics simulation of bulk Cu material under various factors. *Appl. Sci.* **2022**, *12*, 4437. [CrossRef]
37. Quoc, T.T.; Long, V.C.; Tălu, S.; Trong, D.N. Molecular dynamics study on the crystallization process of cubic Cu-Au alloy. *Appl. Sci.* **2022**, *12*, 946. [CrossRef]
38. Li, C.; Li, D.; Tao, X.; Chen, H.; Ouyang, Y. Molecular dynamics simulation of diffusion bonding of Al-Cu interface. *Model. Simul. Mater. Sci. Eng.* **2014**, *22*, 1. [CrossRef]
39. Luo, M.; Liang, L.; Lang, L.; Xiao, S.; Hu, W.; Deng, H. Molecular dynamics simulations of the characteristics of Mo/Ti interfaces. *Comput. Mater. Sci.* **2018**, *141*, 293–301. [CrossRef]
40. Wei, J.; Xu, C.; Li, P.; Deng, H.; Xiao, S.; Hu, W. Molecular dynamics simulations of the diffusion characteristics on the Fe-W interfaces system. *Fusion Eng. Des.* **2020**, *159*, 111850. [CrossRef]
41. Chang, L.; Zhou, C.; Liu, H.; Li, J.; He, X. Orientation and strain rate dependent tensile behavior of single crystal titanium nanowires by molecular dynamics simulations. *J. Mater. Sci. Technol.* **2018**, *34*, 864–877. [CrossRef]
42. Honeycutt, J.D.; Andersen, H.C. Molecular dynamics study of melting and freezing of small Lennard-Jones clusters. *J. Phys. Chem.* **1987**, *91*, 4950–4963. [CrossRef]
43. Tukowski, A.; Albe, K. Extracting dislocations and non-dislocation crystal defects from atomistic simulation data. *Model. Simul. Mater. Sci. Eng.* **2010**, *18*, 025016. [CrossRef]
44. Wang, J.; Shi, J.; Lu, Y.; Jin, G.; Wang, J.; Jiang, Y.; Zhou, Q. Deformation evolution of Cu/Ta nanoscale multilayer during nanoindentation by a molecular dynamics study. *Surf. Coat. Technol.* **2022**, *441*, 128562. [CrossRef]

Potentials for Describing Interatomic Interactions in γ Fe-Mn-C-N System

Bo Lv ¹, Chen Chen ^{2,3,*}, Fucheng Zhang ^{2,3}, Gennady M. Poletaev ⁴ and Roman Y. Rakitin ⁵

¹ College of Environmental and Chemical Engineering, Yanshan University, Qinhuangdao 066004, China; lvbo@ysu.edu.cn

² State Key Laboratory of Metastable Materials Science and Technology, Yanshan University, Qinhuangdao 066004, China; zfc@ysu.edu.cn

³ National Engineering Research Center for Equipment and Technology of Cold Strip Rolling, Yanshan University, Qinhuangdao 066004, China

⁴ Information Technologies Faculty, Altai State Technical University, Lenin Str. 46, 656038 Barnaul, Russia; gmpoletaev@mail.ru

⁵ College of ASU, Altai State University, Lenin Str. 61, 656049 Barnaul, Russia; movehell@gmail.com

* Correspondence: chenchen@ysu.edu.cn

Abstract: Potentials for describing interatomic interactions in a γ Fe-Mn-C-N multicomponent system, modified Hadfield steel, where face-centered cubic (f.c.c.) iron is the main component, are proposed. To describe the Fe-Fe interactions in austenite, it is proposed to use Lau EAM potential. For all other interactions, Morse potentials are proposed, the parameters of which were found from various experimental characteristics: in particular, the energy of dissolution and migration of an impurity in an f.c.c. iron crystal, the radius of atoms, their electronegativity, mutual binding energy, etc. The found potentials are intended for modeling the atomic structures and processes occurring at the atomic level in Hadfield steel using relatively large computational cells by the molecular dynamics method.

Keywords: molecular dynamics; interatomic potential; Hadfield steel; potential parameters; impurity

Citation: Lv, B.; Chen, C.; Zhang, F.; Poletaev, G.M.; Rakitin, R.Y.

Potentials for Describing Interatomic Interactions in γ Fe-Mn-C-N System. *Metals* **2022**, *12*, 982. <https://doi.org/10.3390/met12060982>

Academic Editors: Shuwen Wen, Yongle Sun and Xin Chen

Received: 28 April 2022

Accepted: 2 June 2022

Published: 7 June 2022

Publisher's Note: MDPI stays neutral with regard to jurisdictional claims in published maps and institutional affiliations.



Copyright: © 2022 by the authors. Licensee MDPI, Basel, Switzerland. This article is an open access article distributed under the terms and conditions of the Creative Commons Attribution (CC BY) license (<https://creativecommons.org/licenses/by/4.0/>).

1. Introduction

Despite the interest in Hadfield steel and a long history of research on its unique properties, mainly associated with its excellent work hardening ability [1–3], there are very few works devoted to the modeling of its atomic structures and the processes occurring in it under deformation conditions at the atomic level. At the same time, computer modeling can help answer a number of questions regarding the mechanisms and regularities of the deformation behavior of this steel, which relates to the peculiarities of the interaction of dislocations with twins and grain boundaries.

The present work is devoted to the search for potentials for describing interatomic interactions in Hadfield steel for their subsequent application in molecular dynamics simulation. Hadfield steel is a multicomponent system and, in addition to classical iron, manganese, and carbon, it may contain some other alloying elements [1,3]. To describe interatomic interactions even in the three-component system, it is necessary, at least, to specify six potentials (or pair components for many-body potentials) to describe the interactions of different pairs of atoms in a given system: Fe-Fe, Fe-Mn, Mn-Mn, Fe-C, Mn-C, C-C. Unfortunately, there are very few works, within the framework of one approach, where potentials are proposed simultaneously for several of these bonds.

Lee et al., developed modified EAM potentials that take into account two coordination spheres and anisotropy of electron clouds (2N MEAM potentials). Despite the physical validity, the Lee potentials [4–7] have two disadvantages. Firstly, these potentials are relatively very cumbersome. They include at least 11 parameters and additional calculations of the mutual orientation of atoms, which is used to calculate the screening functions of

electron clouds. This significantly slows down the calculation of a computer experiment and is critical for models that include a large number of atoms. Secondly, while strictly taking into account many factors that affect interatomic interactions, the 2N MEAM Lee potentials take into account the interaction of atoms no further than only the 2nd coordination sphere. This is not enough according to our previous work [8]. There are only six atoms in the second coordination sphere of an f.c.c. lattice, at a distance of $\sqrt{3}/2a$, where a is the lattice parameter. There are 24 atoms in the third sphere at a distance of $\sqrt{2}a$, i.e., only $0.19a$ beyond the 2nd coordination sphere. According to the calculations previously made [8], the third coordination sphere contributes about 20% to the calculation of atomic energy depending on the metals, and the second even less, about 15%. Xie et al. [9] proposed a set of Morse pair potentials for describing all the desired interactions, except for the Fe-Mn bond. However, they are not suitable for modeling interactions in Hadfield steel, since they were selected not for steels, but for Mn_7C_3 and Fe_7C_3 carbides. For example, when using one potential for the Fe-Fe bond [9], it was not possible to obtain satisfactory results for the basic characteristics of f.c.c. iron. In the present paper, we propose a set of Morse potentials to describe all interactions in the four-component $\gamma\text{Fe-Mn-C-N}$ system.

2. Choice of Potential for Describing Interatomic Interactions in F.C.C. Iron

In view of the foregoing, we decided to independently select the potentials for the $\gamma\text{Fe-Mn-C}$ system, which must satisfy two important criteria: (1) not be mathematically cumbersome, so that relatively large computational cells can be simulated (including 10^5 – 10^6 atoms); (2) satisfactorily describe the known experimental characteristics of the $\gamma\text{Fe-Mn-C}$ system. The potential for describing the Fe-Fe bond is a main potential in the $\gamma\text{Fe-Mn-C}$ system. As a basis, it was decided to take one of the known and tested EAM potentials that well describe the properties of austenite. Most of the known potentials for iron were created to describe its body-centered cubic (b.c.c.) modification, and in the majority of cases, the f.c.c. phase is considered as secondary. As a result, not all known potentials describe austenite well. For this reason, we abandoned the well-known EAM potential of Ackland and Mendelev [10–12].

Of all the potentials that we have examined, the potentials for Fe-Fe and Fe-C bonds in austenite proposed by Lau et al. [13] are best suited for our purposes. These are classic EAM potentials, where the energy of the i -th atom is calculated as the sum of the pair and multiparticle components:

$$E_{\alpha,i} = -A_{\alpha} \sqrt{\sum_{j \neq i} \rho_{\beta\alpha}(r_{ij})} + \frac{1}{2} \sum_{j \neq i} \phi_{\beta\alpha}(r_{ij})$$

$$\rho_{\beta\alpha}(r_{ij}) = t_1(r - r_{c,\rho})^2 + t_2(r - r_{c,\rho})^3, \quad r \leq r_{c,\rho}$$

$$\phi_{\beta\alpha}(r_{ij}) = (r - r_{c,\phi})^2(k_1 + k_2r + k_3r^2), \quad r \leq r_{c,\phi}$$
(1)

The potential for the Fe-Fe bond in the article of Lau et al. [13] is a modified potential from the work of Rosato [14]. We drew attention to this potential primarily because it was tested to describe the structural, energy, and elastic characteristics of austenite [15]. The obtained values are in satisfactory agreement with the experiment: the lattice parameter at 0 K is 3.573 Å, the sublimation energy (per atom) is 4.228 eV, and the bulk modulus is 156.7 GPa. In addition, good agreement with the reference value of thermal expansion coefficient of $16 \cdot 10^{-6} \text{ K}^{-1}$ was obtained.

3. Fe-C, C-C, Fe-Mn, Mn-Mn, and Mn-C Bonds in the Crystal Lattice of F.C.C. Iron

An adjustment was necessary for the Fe-C bond, since such values as the energy of carbon dissolution in f.c.c. iron; the difference between energies of carbon impurity in octahedral and tetrahedral voids of the lattice; the migration energy of a carbon atom in f.c.c. iron; and the binding energy with a vacancy were unsatisfactorily described by potentials proposed by Lau et al. [13]. It was decided for all the other five bonds to build pair Morse potentials that would satisfactorily describe the known characteristics. The Morse potential

is a pair potential, but it is often used in molecular dynamics calculations, including the description of interatomic interactions in metals. Pair potentials are often used by various researchers to describe interatomic interactions in metal-impurity systems [9,16–23]. The procedure for calculating forces using many-body and pair potentials in a computer program is fundamentally different, and therefore, the latter (with the same methods of optimizing the computer code) always wins in the speed of calculating forces in the model. The Morse potential determines the interaction energy of a pair of atoms located at a distance r from each other:

$$\varphi(r) = D\beta e^{-\alpha r}(\beta e^{-\alpha r} - 2) \quad (2)$$

where α , β , D are the potential parameters.

When determining the parameters of the Morse potential for the Fe-C bond, we relied on the already known potentials from [13,24], only slightly correcting them to obtain good agreement with the experimental data and first-principle calculations on the energy of carbon dissolution in f.c.c. iron (E_{sol}); the difference between the energies of carbon impurity in octahedral and tetrahedral voids of the lattice (ΔE_{OT}); the migration energy of a carbon atom in f.c.c. iron (E_m); and the binding energy with a vacancy (E_{bv}). These energy characteristics are listed in Table 1. In addition, the radius of the Fe and C atoms was also taken into account. As can be seen, the potentials proposed here simultaneously well describe the considered energy characteristics of the carbon impurity in austenite, even better than the known EAM potentials for this system [13,24].

Table 1. Energy characteristics of carbon impurity in f.c.c. iron.

Energy Characteristics	Our Model	Experiments or FP-Calc.	Potentials from [24]	Potentials from [13]
E_{sol} (eV/atom)	0.38	0.25–0.48 [25,26] (experiment, FP-calc.)	1.01	0.78
ΔE_{OT} (eV)	1.36	1.48 [27] (FP-calc.)	1.03	1.12
E_m (eV)	1.20	1.40–1.53 [4,28,29] (experiment)	0.33	0.86
E_{bv} (eV)	0.41	0.37–0.41 [30] (experiment)	0.50	0.54

To describe the interaction between carbon atoms in an austenite lattice, we transformed the potentials [16,24] into Morse potentials. The justification given in these works seemed quite reasonable. When searching for parameters for the Mn-Mn bond, we focused on the radius of Mn atoms, the sublimation energy, and the bulk modulus of metallic Mn [31]. The equilibrium distance for the Fe-Mn bond was calculated as the sum of the radii of Fe and Mn atoms [31], the elastic modulus, as the mean of the modules for Fe and Mn. The depth of the potential, i.e., the parameter D in Formula (2), was determined by the value of the mixing energy of Mn in f.c.c. Fe, where it was calculated by first principles (ab initio) method [32]. For a concentration of 13 wt.% Mn, the mixing energy of Mn in Fe was -0.0182 eV/atom [32]. A minus sign indicates that mixing is energetically favorable, and a relatively small value refers that the tendency to order the atomic structure of the alloy is very weak. The parameter D was selected so that this value was exactly obtained.

The last of the six necessary potentials, for the Mn-C bond, was chosen, taking into account the potentials proposed in [5,7,9], the radii of the Mn and C atoms [31], as well as the binding energy between Mn and C atoms in f.c.c. Fe. The potential parameters were selected in such a way as to accurately reproduce the binding energy of Mn and C atoms experimentally obtained in a f.c.c. Fe lattice, 0.35 eV [33]. This energy seems very large and comparable with the binding energy of a carbon atom with a vacancy in iron. However, if we pay attention to the difference in electronegativities of Mn and C atoms

compared to Fe and C, 1.00 and 0.72, respectively [31], such a strong bond becomes clear, which is comparable in strength, probably, to an Al-C bond, for which the difference in electronegativities is close to the Mn-C bond and amounts to 0.94 [31].

When calculating the binding energy of a C atom with an Mn atom in a f.c.c. lattice of Fe, the carbon atom was introduced into the octahedral interstitial closest to the Mn atom, as shown in Figure 1. It is known that impurity atoms of light elements (such as C, N, O, etc.) occupy octahedral voids in f.c.c., h.c.p., and b.c.c. lattices of metals [20,34].

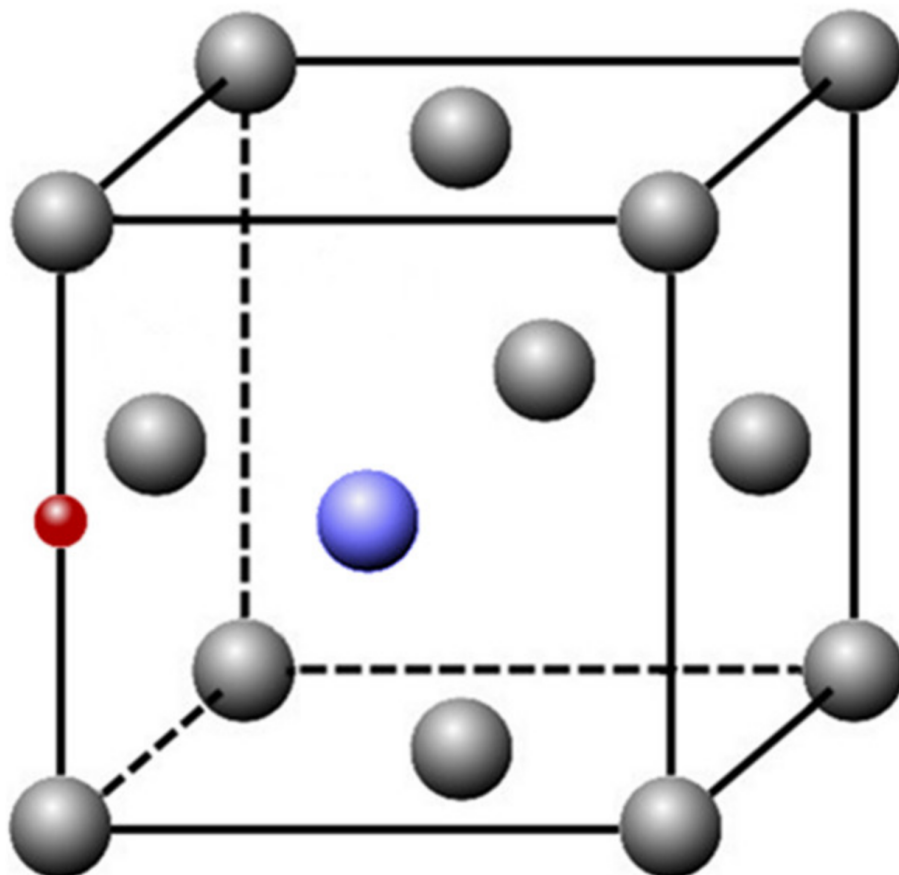


Figure 1. The positions of Mn (blue) and C (red) atoms in a f.c.c. Fe lattice (gray atoms). (The positions of the atoms are shown without taking into account structural relaxation).

4. Interatomic Potentials for Describing Nitrogen Impurity in Hadfield Steel

Nitrogen impurity is not a classic component of Hadfield steel. At the same time, it is sometimes considered as an additional alloying element that stabilizes austenite and increases strength [1]. The radius of N atom is slightly less than that of C atom: 0.71 and 0.77 Å, respectively [34]. The difference between the electronegativities of iron and nitrogen is 1.21, while for iron and carbon, it is 0.72 [31]. The high difference between the electronegativity means a strong interatomic bond, and its character is close to the covalent type.

The dissolution energy of nitrogen in f.c.c. iron is an important characteristic by which the depth of the interatomic potential can be determined. Unfortunately, there is a very large run-off of this value in the literature: -0.13 eV [35], -0.27 eV [36], and -0.53 eV [37]. Another important energy characteristic is the activation energy of migration of an impurity atom in the metal lattice. Based on the analysis of data on the migration energy of C and N impurity atoms in α -Fe and γ -Fe [6,28,29,38,39], we took a benchmark value of migration energy of nitrogen impurity in the f.c.c. iron lattice of 1.29 eV. Therefore, we were guided by the radius of iron and nitrogen atoms, the energy of dissolution, the energy of migration, and the assumed depth of the potential found from the empirical dependencies [20]. Table 2

shows the data by which we were guided when selecting the potentials and the values obtained in our work.

Table 2. Some energy characteristics of nitrogen impurity in f.c.c. iron.

Energy Characteristics	Our Model	Experiment or FP-Calc.
E_{sol} (eV/atom)	−0.13	−0.13 [35] (experiment) −0.27 [36] (ab initio calculations) −0.53 [37] (thermodynamic evaluation)
E_m (eV)	1.29	1.29 [6,28,29,38,39]
E_{bv} (eV)	0.45	—

Mn atoms have a high binding energy with N atoms and a large difference in electronegativities compared to iron atoms, which causes a high effect of Mn impurity on the solubility of nitrogen in iron [40]. When searching for the potential parameters for the Mn-N bond in f.c.c. iron, we took into account the radius of Mn and N atoms, empirical regularities [20], and the data on the solubility of Mn and N in iron [40]. To describe the interactions of nitrogen atoms with each other in metals, the considerations and pair potentials proposed by Vashishta et al. [17] and San et al. [19] were taken as a basis. According to these potentials, impurity atoms, such as nitrogen and oxygen, repel each other in the crystal lattice of metals. To describe the N-N and O-O bonds in metals, the parameters of the Morse potentials were calculated [20]. The radius of atoms and their electronegativity were also taken into account to determine the parameters of the C-N potential. The binding energy of C and N atoms in the metal lattice was calculated using Lorentz–Berthelot mixing rules [41], taking into account the ratio of the C-C bond energies in the metal and graphene, as well as the C-N bond in the organic molecule.

5. Potential Parameters

Table 3 shows the obtained parameters of Morse potentials. Figure 2 illustrates graphs of the found potentials. Table 3 also contains the parameters for the Fe-Fe bond, found from the values of the γ -Fe lattice parameter, sublimation energy, and bulk modulus obtained using the potential from [13]. The Morse potential for the Fe-Fe bond is a simpler analogue of the EAM potential [13] and similarly well describes the above characteristics, including thermal expansion. It can be used in models with a large number of atoms and in lengthy computer experiments requiring large resources. All Morse potentials were found for a cutoff radius of 4.7 Å, i.e., taking into account the three coordination spheres in f.c.c. Fe.

Table 3. Parameters of Morse potentials for the considered interactions.

Bond	α (Å ^{−1})	β	D (eV)
Fe-Fe	1.285	35.878	0.433
Fe-C	1.82	41	0.41
C-C	1.97	50	0.65
Mn-Mn	1.321	39.792	0.373
Mn-Fe	1.306	38.030	0.413
Mn-C	1.87	43	0.777
Fe-N	1.788	34.046	0.579
Mn-N	1.812	36.482	0.940
C-N	2.140	58.323	0.230
N-N	1.556	700	0.001

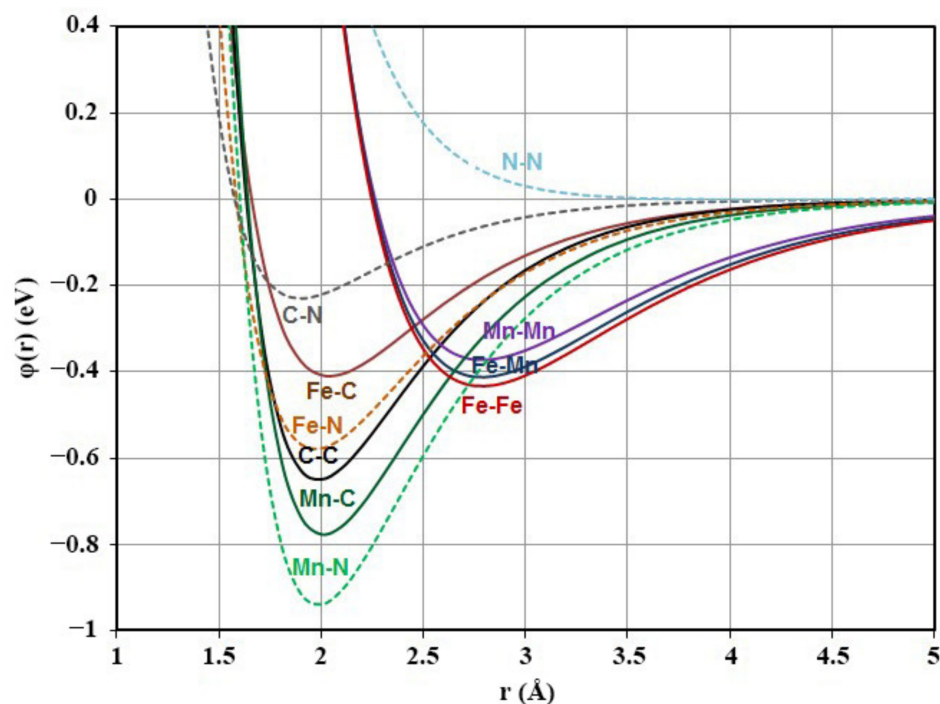


Figure 2. Morse potentials for bonds in the γ Fe-Mn-C-N system (the potentials describing interactions with a nitrogen impurity are shown by a dotted line).

For the Fe-Fe and Mn-Mn bonds, the classical method by Girifalco and Weiser [42] was used to determine the potential parameters from the crystal lattice parameter, bulk modulus, and sublimation energy, so these characteristics are reproduced quite accurately. For other bonds describing the interaction of C, Mn, and N impurities with atoms of the γ -Fe lattice and with each other, the potential parameters were chosen in such a way as to reproduce, as best as possible, above-mentioned experimental characteristics: in particular, the energy of dissolution and the energy of migration of an impurity in an f.c.c. iron crystal, the radius of atoms, their electronegativity, mutual binding energy, etc.

It should be borne in mind that in complex multicomponent systems such as γ Fe-Mn-C-N, the bonds of impurity atoms depend on the mutual arrangement of neighboring atoms of different types in the austenite lattice space. However, strict consideration of this in our case, when the system consists of four components, will lead to a significant complication in calculations. It will be not allowed to perform molecular dynamics simulations using relatively large computational cells.

6. Conclusions

Potentials for describing interatomic interactions in a γ Fe-Mn-C-N multicomponent system, modified Hadfield steel, where f.c.c. iron is the main component, are proposed. To describe the Fe-Fe interactions in austenite, it is proposed to use Lau EAM potential, which reproduces well the structural, energy, and elastic characteristics of austenite. For all other nine interactions, Morse potentials are proposed, the parameters of which were found from various experimental characteristics: in particular, the energy of dissolution and the energy of migration of an impurity in a f.c.c. iron crystal, the radius of atoms, their electronegativity, mutual binding energy, etc. The found potentials are intended for modeling the atomic structure and processes occurring at the atomic level in Hadfield steel using relatively large computational cells by the molecular dynamics method.

Author Contributions: Resources, B.L. and F.Z.; data curation, G.M.P. and R.Y.R.; writing—original draft preparation, B.L.; writing—review and editing, C.C. and G.M.P.; supervision, F.Z.; funding acquisition, B.L. All authors have read and agreed to the published version of the manuscript.

Funding: The authors gratefully acknowledge the National Natural Science Foundation of China (Nos. 52171049, 51831008 and U1810207), the Key Research & Development Program of Hebei Province (No. 19211018D).

Institutional Review Board Statement: Not applicable.

Informed Consent Statement: Not applicable.

Data Availability Statement: No new data were created or analyzed in this study. Data sharing is not applicable to this article.

Conflicts of Interest: The authors declare no conflict of interest.

References

- Chen, C.; Zhang, F.; Wang, F.; Liu, H.; Yu, B. Effect of N+Cr alloying on the microstructures and tensile properties of Hadfield steel. *Mater. Sci. Eng. A* **2016**, *679*, 95–103. [CrossRef]
- Zhang, F.C.; Lv, B.; Wang, T.S.; Zheng, C.L.; Zhang, M.; Luo, H.H.; Liu, H.; Xu, A.Y. Explosion hardening of Hadfield steel crossing. *Mater. Sci. Technol.* **2010**, *26*, 223–229. [CrossRef]
- Chen, C.; Lv, B.; Ma, H.; Sun, D.; Zhang, F. Wear behavior and the corresponding work hardening characteristics of Hadfield steel. *Tribol. Int.* **2018**, *121*, 389–399. [CrossRef]
- Lee, B.J.; Baskes, M.I.; Kim, H.; Cho, Y.K. Second nearest-neighbor modified embedded atom method potentials for B.C.C. transition metals. *Phys. Rev. B* **2001**, *64*, 184102. [CrossRef]
- Lee, B.-J.; Lee, J.W. A modified embedded atom method interatomic potential for carbon. *Calphad* **2005**, *29*, 7–16. [CrossRef]
- Lee, B.-J. A modified embedded-atom method interatomic potential for the Fe–C system. *Acta Mater.* **2006**, *54*, 701–711. [CrossRef]
- Kim, Y.-M.; Shin, Y.-H.; Lee, B.-J. Modified embedded-atom method interatomic potentials for pure Mn and the Fe–Mn system. *Acta Mater.* **2009**, *57*, 474–482. [CrossRef]
- Poletaev, G.M.; Starostenkov, M.D.; Zorya, I.V. Morse potentials for F.C.C. metals taking into account the interaction of the five coordination spheres. *Fundam. Probl. Sovrem. Materialoved.* **2017**, *14*, 70–75.
- Xie, J.-Y.; Chen, N.-X.; Shen, J.; Teng, L.; Seetharaman, S. Atomistic study on the structure and thermodynamic properties of Cr₇C₃, Mn₇C₃, Fe₇C₃. *Acta Mater.* **2005**, *53*, 2727–2732. [CrossRef]
- Numakura, H.; Yotsui, G.; Koiwa, M. Calculation of the strength of Snoek relaxation in dilute ternary B.C.C. alloys. *Acta Met. Mater.* **1995**, *43*, 705–714. [CrossRef]
- Mendelev, M.I.; Han, S.; Srolovitz, D.J.; Ackland, G.J.; Sun, D.Y.; Asta, M. Development of new interatomic potentials appropriate for crystalline and liquid iron. *Philos. Mag.* **2003**, *83*, 3977–3994. [CrossRef]
- Ackland, G.J.; Mendelev, M.I.; Srolovitz, D.J.; Han, S.; Barashev, A.V. Development of an interatomic potential for phosphorus impurities in α -iron. *J. Phys. Condens. Matter.* **2004**, *16*, S2629. [CrossRef]
- Lau, T.T.; Först, C.J.; Lin, X.; Gale, J.D.; Yip, S.; van Vliet, K.J. Many-Body Potential for Point Defect Clusters in Fe–C Alloys. *Phys. Rev. Lett.* **2007**, *98*, 215501. [CrossRef] [PubMed]
- Rosato, V. Comparative behavior of carbon in B.C.C. and F.C.C. iron. *Acta Met.* **1989**, *37*, 2759–2763. [CrossRef]
- Oila, A.; Bull, S.J. Atomistic simulation of Fe–C austenite. *Comp. Mater. Sci.* **2009**, *45*, 235–239. [CrossRef]
- Ruda, M.; Farkas, D.; Abriata, J. Interatomic potentials for carbon interstitials in metals and intermetallics. *Scr. Mater.* **2002**, *46*, 349–355. [CrossRef]
- Vashishta, P.; Kalia, R.K.; Nakano, A.; Rino, J.P. Interaction potentials for alumina and molecular dynamics simulations of amorphous and liquid alumina. *J. Appl. Phys.* **2008**, *103*, 083504. [CrossRef]
- Liu, S.; Shi, S.; Huang, H.; Woo, C. Interatomic potentials and atomistic calculations of some metal hydride systems. *J. Alloy. Compd.* **2001**, *330–332*, 64–69. [CrossRef]
- San Miguel, M.A.; Sanz, J.F. Molecular-dynamics simulations of liquid aluminum oxide. *Physical Review B* **1998**, *58*, 2369–2371. [CrossRef]
- Poletaev, G.M.; Zorya, I.V.; Rakitin, R.Y.; Iliina, M.A. Interatomic potentials for describing impurity atoms of light elements in F.C.C. metals. *Mater. Phys. Mech.* **2019**, *42*, 380–388.
- Poletaev, G.M.; Starostenkov, M.D.; Dmitriev, S.V. Interatomic potentials in the systems Pd–H and Ni–H. *Mater. Phys. Mech.* **2016**, *27*, 53–59.
- Poletaev, G.M.; Zorya, I.V. Effect of Light Element Impurities on the Edge Dislocation Glide in Nickel and Silver: Molecular Dynamics Simulation. *J. Exp. Theor. Phys.* **2020**, *131*, 432–436. [CrossRef]
- Poletaev, G.M.; Zorya, I.V. Influence of light impurities on the crystal-melt interface velocity in Ni and Ag. Molecular dynamics simulation. *Tech. Phys. Lett.* **2020**, *46*, 575–578. [CrossRef]
- Ruda, M.; Farkas, D.; Garcia, G. Atomistic simulations in the Fe–C system. *Comput. Mater. Sci.* **2009**, *45*, 550–560. [CrossRef]
- Gustafson, P. A thermodynamic evaluation of the Fe–C System. *Scand. J. Metall.* **1985**, *14*, 259–267.
- Ridnyi, Y.M.; Mirzoev, A.A.; Mirzaev, D.A. Ab initio simulation of dissolution energy and carbon activity in F.C.C. Fe. *Phys. Solid State* **2017**, *59*, 1279–1284. [CrossRef]

27. Jiang, D.E.; Carter, E.A. Carbon dissolution and diffusion in ferrite and austenite from first principles. *Phys. Rev. B* **2003**, *67*, 214103. [CrossRef]
28. Askill, J. *Tracer Diffusion Data for Metals, Alloys and Simple Oxides*; Springer: Berlin/Heidelberg, Germany, 1970.
29. Brandes, E.A.; Brook, G.B. *Smithells Metals Reference Book*; Butterworth-Heinemann: Oxford, UK, 1992.
30. Slane, J.; Wolverton, C.; Gibala, R. Carbon–vacancy interactions in austenitic alloys. *Mater. Sci. Eng. A* **2003**, *370*, 67–72. [CrossRef]
31. Lide, D.R. (Ed.) *CRC Handbook of Chemistry and Physics (Internet Version 2005)*; CRC Press: Boca Raton, FL, USA, 2005.
32. Mirzoev, A.A.; Yalalov, M.M.; Mirzaev, D.A. Energy of mixing and magnetic state of components of Fe-Mn alloys: A first-principles calculation for the ground state. *Phys. Met. Met.* **2006**, *101*, 341–348. [CrossRef]
33. Massardier, V.; Merlin, J.; Le Patézour, E.; Soler, M. Mn-C interaction in Fe-C-Mn steels: Study by thermoelectric power and internal friction. *Met. Mater. Trans. A* **2005**, *36*, 1745–1755. [CrossRef]
34. Goldschmidt, H.J. *Interstitial Alloys*; Butterworths: London, UK, 1967.
35. Mogutnov, B.M.; Tomilin, I.A.; Shvartsman, L.A. *Thermodynamics of Iron Alloys*; Metallurgiya: Moscow, Russia, 1984. (In Russian)
36. Ridniy, Y.M.; Mirzoev, A.A.; Mirzaev, D.A. Ab initio modeling the energy of dissolution of nitrogen in F.C.C. lattice of iron. *Vestn. SUSU. Seriya Metall.* **2014**, *14*, 59–63. (In Russian)
37. Frisk, K. A Thermodynamic evaluation of the Cr-N, Fe-N, Mo-N and Cr-Mo-N systems. *CALPHAD* **1991**, *15*, 79–106. [CrossRef]
38. Rochana, P.; Lee, K.; Wilcox, J. Nitrogen adsorption, dissociation, and subsurface diffusion on the vanadium (110) surface: A DFT study for the nitrogen-selective catalytic membrane application. *J. Phys. Chem. C* **2014**, *118*, 4238–4249. [CrossRef]
39. Domain, C.; Becquart, C.S.; Foct, J. Ab initio study of foreign interstitial atom (C, N) interactions with intrinsic point defects in α -Fe. *Phys. Rev. B* **2004**, *69*, 144112. [CrossRef]
40. You, Z.; Paek, M.-K.; Jung, I.-H. Critical Evaluation and Optimization of the Fe-N, Mn-N and Fe-Mn-N Systems. *J. Phase Equilibria Diffus.* **2018**, *39*, 650–677. [CrossRef]
41. Yin, X.; Opara, A.; Du, H.; Miller, J.D. Molecular dynamics simulations of metal-cyanide complexes: Fundamental considerations in gold hydrometallurgy. *Hydrometallurgy* **2011**, *106*, 64–70. [CrossRef]
42. Girifalco, L.A.; Weiser, V.G. Application of the Morse potential function to cubic metals. *Phys. Rev.* **1959**, *114*, 687–790. [CrossRef]

Article

Modification of Precipitate Coarsening Kinetics by Intragranular Nanoparticles—A Phase Field Study

Simbarashe Fashu ¹, Bintong Huang ^{1,2} and Nan Wang ^{1,2,3,*}¹ Guangdong Technion-Israel Institute of Technology, #241 Daxue Rd, Shantou 515063, China; sfashu04@gmail.com (S.F.); huang.bintong@gtiit.edu.cn (B.H.)² Technion-Israel Institute of Technology, Technion City, Haifa 32000, Israel³ Guangdong Provincial Key Laboratory of Materials and Technologies for Energy Conversion, Guangdong Technion-Israel Institute of Technology, Shantou 515063, China

* Correspondence: nan.wang@gtiit.edu.cn; Tel.: +86-0752-88077177

Abstract: Precipitate coarsening is a major mechanism responsible for the degradation in mechanical properties of many precipitation-hardened alloys at high temperatures. With recent developments in processing of nanocomposite materials, a substantial volume fraction of inert second phase ceramic nanoparticles can be introduced into the grain interiors of polycrystalline materials. These intragranular nanoparticles can have synergistic effects of impeding dislocation motion and interacting with coarsening precipitates to modify the coarsening rate. In this work, the precipitate coarsening behavior of an alloy in the presence of intragranular inert nanoparticles was studied using the phase field method. Two key measurements of coarsening kinetics, precipitate size distribution and coarsening rate, were found to be affected by the volume fraction and the size of nanoparticles. Two novel mechanisms related to geometric constraints imposed by inter-nanoparticle distance and the blockage of solute diffusion path by nanoparticle–matrix interfaces were proposed to explain the observed changes in precipitate coarsening kinetics. The simulation results in general suggest that the use of small nanoparticles with large number density is effective in slowing down the coarsening kinetics.

Citation: Fashu, S.; Huang, B.; Wang, N. Modification of Precipitate

Coarsening Kinetics by Intragranular Nanoparticles—A Phase Field Study.

Metals **2022**, *12*, 892. <https://doi.org/10.3390/met12060892>

Academic Editors: Shuwen Wen, Yongle Sun, Xin Chen and John D. Clayton

Received: 12 April 2022

Accepted: 12 May 2022

Published: 24 May 2022

Publisher's Note: MDPI stays neutral with regard to jurisdictional claims in published maps and institutional affiliations.



Copyright: © 2022 by the authors. Licensee MDPI, Basel, Switzerland. This article is an open access article distributed under the terms and conditions of the Creative Commons Attribution (CC BY) license (<https://creativecommons.org/licenses/by/4.0/>).

Keywords: precipitates; coarsening; nanoparticles; phase field modeling; high temperature strength

1. Introduction

High performance alloys, including Al, Ni, and Co-based superalloys are strengthened by the heat treatment process to produce nano-sized, hard, and coherent precipitates through hindering of both dislocation movement and grain growth. However, at elevated temperatures, rapid increase in diffusion rate accelerates precipitate coarsening rate and results in the loss of mechanical strength. Precipitate coarsening refers to growth of larger particles at the expense of smaller shrinking particles in the matrix. Coarsening occurs when finely dispersed nanoprecipitates change their sizes, shapes, and distribution due to microstructural evolution driven by reduction in interfacial energy [1]. The kinetics of precipitate coarsening influence the strength of alloys such that this area continues to attract the interests of many researchers. Techniques like solute segregation at precipitate interfaces in Al alloys [2–6], formation of stacking fault ribbons in Ni alloys [7–9], introduction of slow diffusing elements in superalloys [10–14], and application of external compressive stresses [15,16] were proposed as measures to retard the precipitate coarsening process. The mechanisms responsible for precipitate coarsening resistance are thermodynamic and kinetic in nature and involve interfacial energy reduction, solute drag against precipitate growth, development of strain fields around growing precipitates, slowing down of solute diffusion [17], etc. Through proper incorporation of these effects during processing, the precipitate coarsening behavior can be forced to deviate significantly from the normal coarsening, described by the classical Lifshitz–Slyozov–Wagner (LSW) theory [18].

The practice of dispersing fine ceramic nanoparticles like titanium carbon nitride (TiCN), alumina (Al_2O_3), zirconia (ZrO_2), and yttria (Y_2O_3) for the synergistic purposes of retarding solidification coarsening [19–21] and pinning grain growth [22–27] at elevated service temperatures is now established. During solidification, the introduced mobile second-phase particles migrate and form assemblies around the established nuclei and retard dendritic growth through combined pushing and drag effects. Retarded grain growth causes many nuclei to form in the melt, thereby refining the microstructure. Due to slow solidification velocities found in conventional casting processes, the majority of the nanoparticles are incorporated along grain boundaries (due to particle pushing) and become intergranular particles in the final microstructure, and only a few are engulfed by the moving solidification front to become intragranular in the final microstructure. However, with small sized nanoparticles and high cooling rates such as those encountered in laser additive manufacturing, it is possible for a large volume fraction of nanoparticles to be engulfed into the grains owing to fast moving solidification fronts which are larger than the critical velocity required for engulfment [28]. This technique was recently applied to produce an aluminum metal containing a high content of uniformly dispersed TiCN nanoparticles of a volume fraction of 35% using selective laser melting method [28]. Ceramic nanoparticles can also be introduced in grain interiors during grain growth and recrystallization [29], and the presence of second-phase inert particles in grain interiors during recrystallization was also predicted using 3D simulations [27]. Several studies have suggested that the engulfed nanoparticles inside the grains are more effective in strengthening the alloy through interaction with dislocations [19,20] when compared with those segregated on the grain boundaries. It should be noted that in the presence of nano-ceramic particles of lower thermal conductivity like Al_2O_3 , SiO_2 , SiC, and ZrO_2 , it was observed [19,20] that during solidification cooling process the temperature of the particles is higher than that of the melt, and nucleation does not occur on the particles surface.

Many researchers to date have focused on the influence of nanoparticles on grain growth control, however at high temperatures, both grain growth and precipitate coarsening control are of considerable importance. The strengthening mechanism in conventionally solidified aluminum alloy containing 0.2–0.3 vol% of small sized coherent Al_3Sc precipitates and 30 vol% incoherent grain boundary Al_2O_3 ceramic particles (300 nm) was comprehensively studied by Karnesky et al. [26]. The results demonstrated synergistic strengthening due to dislocation pinning at the departure side of Al_2O_3 particles and back strain effects imposed on dislocations by the Al_3Sc precipitates due to lattice mismatch, but the coarsening kinetics of precipitates was not affected by the presence of intergranular ceramic particles. Although the presence of nanoparticles in grain interiors has been experimentally confirmed, according to our knowledge, their influence on precipitate coarsening kinetics has not yet been comprehensively studied. Since detailed experimental study of the influence of grain interior nanoparticles is not available, our present work begins by attempting to provide some insights, and this will guide future work.

The phase field method is a powerful continuum modelling method now extensively employed to simulate microstructural evolutions through characterizing phases using a set of conserved and non-conserved order parameters [30]. It has been used to model complex interface evolutions in a wide variety of materials by describing interfaces using smooth order parameters [30–33]. The coarsening kinetics of precipitates has been studied using the phase field method in many previous works [17,34–36], and the validity of the method has been established through experimental comparisons [17,37]. In this work, the effect of inert nanoparticles on precipitate coarsening kinetics is studied by extending the coarsening model [34] to include inert second-phase particles.

The article is arranged as follows: after the introduction section, the phase field model used in our simulations is formulated in the next section, then simulation results for the influence of various nanoparticle volume fractions and sizes on the coarsening kinetics are presented, together with discussions on potential mechanisms related to these results. This is then followed by conclusions.

2. Phase Field Model

In comparison with macroscopic models relying on thermodynamic equilibrium calculations, the phase field model consists of kinetic equations capable of predicting realistic mesoscale morphological and microstructural evolution rather than merely relying on final states, which is the case in macroscopic models. The phase field method was initially developed for simulating solidification microstructures [33] and solid-state phase transformation processes [30,31].

Coarsening of precipitates is satisfactorily explained by the Lifshitz–Slyozov–Wagner (LSW) theory in which large particles grow at the expense of small particles driven by interfacial energy reduction. In the classic LSW theory, the precipitate coarsening process occurs as the result of solute diffusion and the Gibbs–Thomson effect. The phase field method captures these two fundamental mechanisms by incorporating solute diffusions using the Cahn–Hilliard type generalized diffusion equation and the Gibbs–Thomson effect using an order parameter equation for precipitate–matrix interface evolution. Validity of the original phase field model from which the current work was developed has been previously verified by comparing experimental results with simulation results [35,38].

The phase field model used in this work is an extension of the previous coarsening model for binary alloys [34]. The free energy functional of the system is expressed using the following volume integral:

$$F = \int \left[f_0(C, \eta_i) + \frac{k_c}{2} (\nabla C)^2 + \sum_{i=1}^4 \frac{k_\eta}{2} (\nabla \eta_i)^2 \right] dv, \quad (1)$$

where $C(r)$ is the concentration field which is equal to the equilibrium concentration C_α in the host matrix, and, in the precipitate phase, it is set to the equilibrium concentration of the precipitate phase C_β , v is the system volume, η_i is the phase field parameter for tracking precipitate surface evolution of the grain with i th lattice orientation, and k_c and k_η are constant coefficients. The local term $f_0(C, \eta_i)$ is

$$f_0 = H \left[f_1(C) + \sum_{i=1}^4 f_2(C, \eta_i) + \sum_{i=1}^4 \sum_{j \neq i} f_3(\eta_i, \eta_j) + \phi \sum_{i=1}^4 (\eta_{nano})^2 (\eta_i)^2 \right] \quad (2)$$

where,

$$f_1(C) = -\frac{A}{2} (C - C_m)^2 + \frac{B}{4} (C - C_m)^4 + \frac{D_\alpha}{4} (C - C_\alpha)^4 + \frac{D_\beta}{4} (C - C_\beta)^4 \quad (3)$$

$$f_2(C, \eta_i) = -\frac{\gamma}{2} (C - C_\alpha)^2 (\eta_i)^2 + \frac{\delta}{4} (\eta_i)^4 \quad (4)$$

$$f_3(\eta_i, \eta_j) = \frac{\varepsilon_{ij}}{2} (\eta_i)^2 (\eta_j)^2 \quad (5)$$

The terms $C_m = \left(\frac{C_\alpha + C_\beta}{2} \right)$, A , B , D_α , D_β describe the concentration dependence of the thermodynamic free energy, γ and δ are used to describe the interfacial energy of precipitate matrix interfaces, η_{nano} is the nanoparticle phase field parameter, η_j is the phase field parameter for tracking precipitate surface evolution of the grain with j th lattice orientation, and ε_{ij} describes the interfacial energy between precipitates with different lattice orientations [34]. H is a dimensional constant with the unit of energy per volume which was introduced to quantify the total free energy of the system. The inert nanoparticles were introduced into the model through the phase field parameter, η_{nano} , which is equal to 1 inside the nanoparticle and 0 outside. The interfacial energy between nanoparticles and precipitates was incorporated in the model through the term $\phi \sum_{i=1}^4 (\eta_{nano})^2 (\eta_i)^2$, with ϕ being the interaction parameter term. This nanoparticle–precipitate interfacial term has the same form as the precipitate interfacial term $f_3(\eta_i, \eta_j)$ and the inert nanoparticle was treated

as a non-evolving precipitate phase, as will be seen in the evolution equations below. The free energy functional above does not include the elastic energy associated with coherent interfaces and transformation induced volume change. Evolutions of the concentration and precipitate surfaces were studied using the standard variational dynamics for conserved (Equation (6)) and non-conserved (Equation (7)) fields:

$$\frac{\partial C(r, t)}{\partial t} = \nabla \cdot \left[M_C \nabla \left(\frac{\delta F}{\delta C} \right) \right], \quad (6)$$

$$\frac{\partial \eta_i(r, t)}{\partial t} = -L_i \frac{\delta F}{\delta \eta_i}, \quad i = 1, 2, 3, 4, \quad (7)$$

where, L_i and M_C are kinetic coefficients, t is the time, and F is the free energy functional which is given in Equation (1). Since there is no solute diffusion inside inert nanoparticles, the concentration kinetic coefficient was chosen to be $M_C = Mg(\eta_{nano})$ where $g(\eta_{nano}) = (1 - (\eta_{nano}^3) * (6\eta_{nano}^2 - 15\eta_{nano} + 10))$, M is the solute mobility in the matrix (the solute mobility in the precipitate is assumed to be the same as in the matrix) such that the mobility M_C vanishes inside the nanoparticle and varies smoothly between either the nanoparticle–precipitate or nanoparticle–matrix interface. For simplicity, the kinetic coefficients of all the phase field parameters were set to be the same, i.e., $L_i = L$. One may notice that there are only four phase field parameters for precipitate surfaces appearing in the formulation. This choice is solely made for improving computational efficiency. It is acceptable when the precipitate volume fraction is low, but, at high precipitate volume fraction, unphysical precipitate coalescence may occur, since, by using only four phase field parameters, all the precipitates are assumed to have only 8 possible different lattice orientations ($\eta = \pm 1$). It was found from simulation tests that using 4 phase field parameters maintained the simulation efficiency while avoiding significant coalescence problems at the moderate precipitate volume fraction in our simulations.

Numerical implementation of the model was based on non-dimensionalized forms of Equations (8) and (9) as follows:

$$\frac{\partial C(r^*, t^*)}{\partial t^*} = \nabla^* \cdot \left[M^* g(\eta_{nano}) \nabla^* \left(\frac{\partial f_0^*}{\partial C} - k_c^* (\nabla^*)^2 C \right) \right] \quad (8)$$

$$\frac{\partial \eta_i(r^*, t^*)}{\partial t^*} = - \left(\frac{\partial f_0^*}{\partial \eta_i} - k_\eta^* (\nabla^*)^2 \eta_i \right) \quad (9)$$

where, dimensionless time $t^* = LtH$, particle radius $r^* = \frac{r}{l}$, $k_\eta^* = \frac{k_\eta}{(l^2H)}$, $k_c^* = \frac{k_c}{(l^2H)}$, $f^* = \frac{f}{H}$, $\nabla^* = l\nabla$ and the relative kinetic coefficient $M^* = \frac{M}{Ll^2}$. Here, $l = \sqrt{k_\eta/H}$ is the interface width. The mobility M is related to solute diffusivity D [39] and the choice of L does not significantly affect the coarsening result [31].

A single grain in the illustrated microstructure in Figure 1 was set to be the study domain where the coarsening of existing precipitates occurs. Since the purpose of the current study was to explore the general precipitate coarsening behavior in the presence of inert nanoparticles, only 2-dimensional (2D) simulations were performed, but it can be easily extended to 3 dimensions (3D). The nanoparticle volume fraction in this 2D case was equivalent to the area fraction such that in this article these two terms are used interchangeably. A square simulation box with a grid size of 1000×1000 and spatial discretization of $\frac{h}{l} = 1$ was used. The simulation time step was set to be $dt^* = 0.002$. The following model parameters $C_\alpha = 0.05$, $C_\beta = 0.95$, $C_m = 0.5$, $A = 2.0$, $B = 9.8$, $\gamma = 2.5$, $D_\alpha = D_\beta = 2.5$, $\delta = 1.0$, $\varepsilon_{ij} = 3.0$, $k_i^* = k_c^* = 3.0$ were adapted from ref. [34]. For simplicity, the kinetic coefficient M^* was set to have the same value equal to 1 in both the matrix and the precipitate. It has been shown that selecting M^* within the range of 1 to 100 does not significantly affect the numerical result [39]. Initially, a large number of small nuclei with concentration of $C = 0.95$ were randomly seeded into the system following an approach introduced by Simmons et al. [40]. The initial matrix concentration was set to be 0.22

which was enough for the precipitate volume fraction to reach about 20%. This precipitate volume fraction was small such that it was possible to vary the volume fraction of the inert nanoparticles within a large range. No further nucleation events were considered except those given as the initial nuclei. Equations (6) and (7) were solved numerically using center difference spatial discretization and forward Euler time integration. Periodic boundary conditions were applied to all the simulations. To properly capture the coarsening statistics, a simulation setup was repeated three times and coarsening statistics were averaged over the three simulations. For convenience, the volume fraction, equivalent average radii and particle size distributions of precipitates were post-processed from raw data with the aid of Image J software.

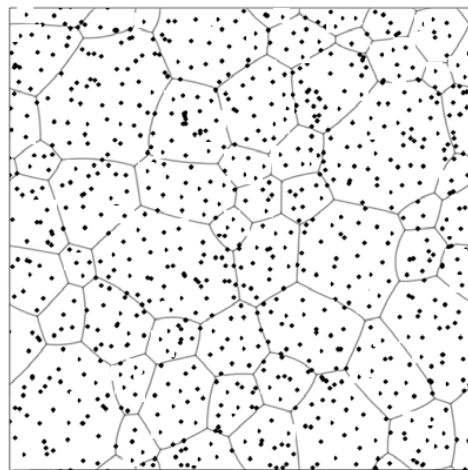


Figure 1. A schematic microstructure showing grains with randomly dispersed nanoparticles in both grain interiors and grain boundaries. Solid lines are grain boundaries, and dark dots are nanoparticles.

3. Results and Discussion

3.1. Coarsening Behavior in Absence of Nanoparticles

To evaluate the model, the precipitate coarsening process without inert nanoparticles was simulated first. Figure 2 shows the coarsening behavior of precipitates in the absence of nanoparticles at aging times of $t^* = 2000$, 12,000 and 24,000. The red particles are precipitates and the blue regions are the matrix phase. The spherical precipitate shape is the result of the simplified model formulation where surface energy anisotropy and elastic energy are both ignored [34]. The precipitate number declines from more than 300 at a time step of $t^* = 2000$ to less than 100 at a time step of $t^* = 24,000$, whilst the average precipitate size increases. Here, coarsening is mainly controlled by inter-precipitate diffusion through the matrix phase driven by free energy differences between small and large precipitates due to the curvature effect, and this results in simultaneous shrinkage and growth of precipitates. The coarsening kinetics was studied by plotting the cube of the average precipitate radius versus aging time according to the power law (i.e., $\bar{R}^n \propto t$) whilst fixing the value of the exponent n to 3. The precipitate radius is obtained from the relation $Radius = \sqrt{A/\pi}$ where A is the precipitate area. We adopted the cubic growth law, since it is the standard exponent from the LSW theory and was reported by many researchers in literature. Such an approach makes it easy to compare our results with previous simulation and experimental results. Besides a brief introduction in Section 2, detailed background of the LSW theory can be found elsewhere [1,18,41]. The plot of the cube of average precipitate size (\bar{R}^3) with coarsening time step (t) is given in Figure 3a. In the absence of nanoparticles, the cube of the particle size evolves linearly with time following the power growth law with the coarsening exponent of $n = 3$. The coarsening behavior satisfies the classical LSW theory [18] and this verifies that the process is controlled by bulk matrix diffusion. The variation of the precipitate area fraction with aging time step in absence of nanoparticles is shown in Figure 3b; it is evident that with time step, the area fraction rapidly decreases

before reaching a steady state. The sluggish behavior observed in the transient stage before the steady state condition is due to the seeding method used to introduce precipitates in the system. Figure 3c show the changes in a number of precipitates during coarsening and reflects that the numbers are continuously decreasing due to simultaneous growth and shrinkage of precipitates.

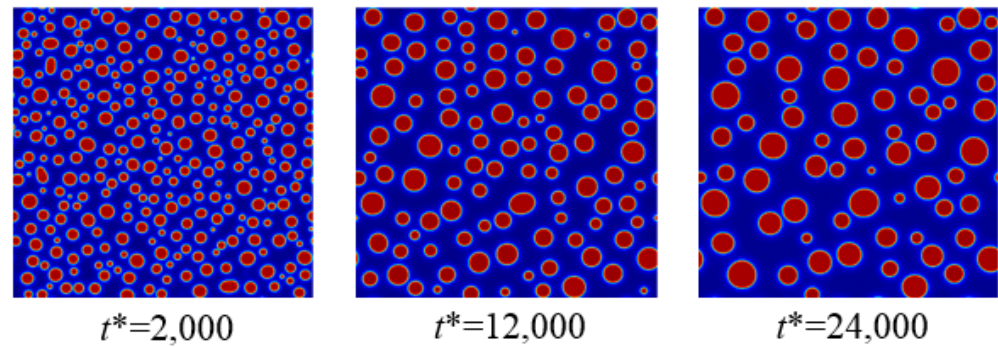


Figure 2. Simulation snapshots of the precipitate evolution in absence of nanoparticles at different times. The precipitates are colored red, and the matrix is in dark blue.

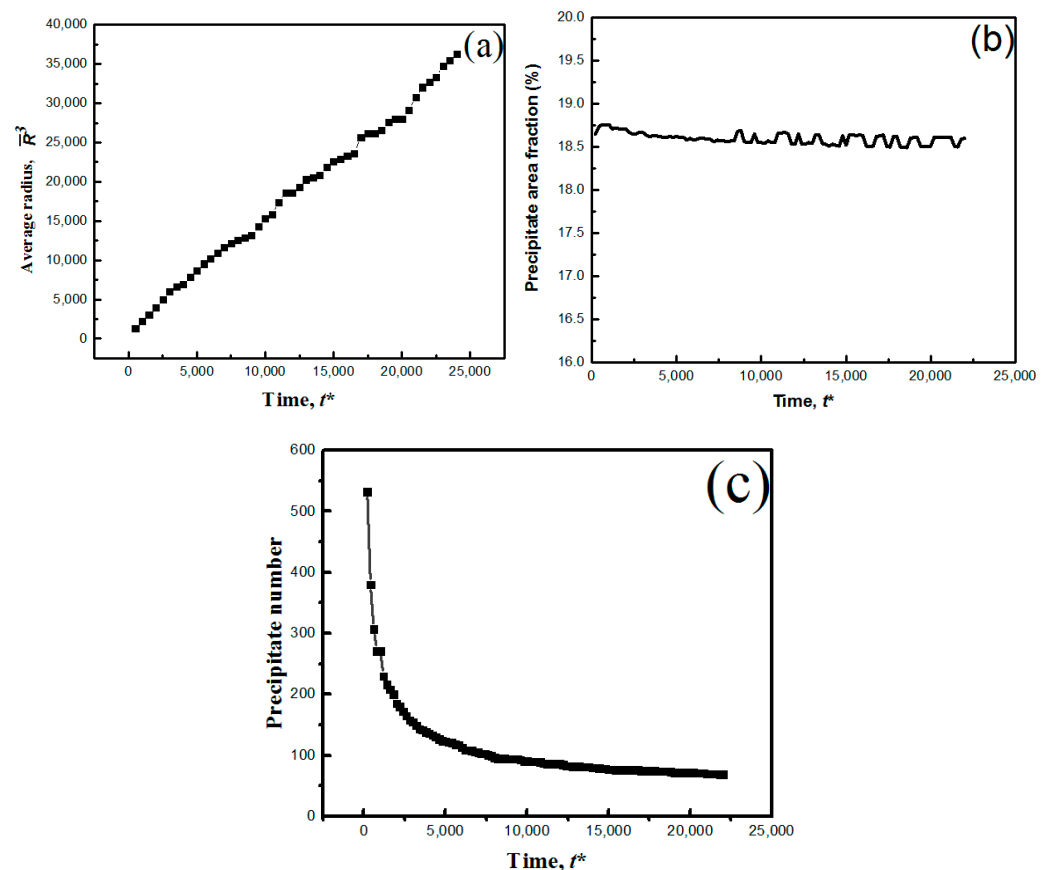


Figure 3. (a) Plots of the cube of the average precipitate radius with time in absence of nanoparticles, (b) the change in precipitate area fraction with time in absence of nanoparticles, and (c) the change of precipitate numbers with time in absence of nanoparticles in the system.

The LSW theory shows that regardless of the system initial particle size distribution, the particle size distribution (PSD) will always converge towards self-similarity with time [42]. The self-similarity can be examined by either calculating the structural function to verify dynamical scaling [36] or through analyzing the PSD shape that changes with time step. In this work, the latter was used to verify the self-similarity of our system. The normalized PSD shapes with fitted curves for precipitate coarsening at selected time

steps in absence of nanoparticles are shown in Figure 4a–d. Data for plotting histograms was extracted from coarsening results using Image J software before plotting histograms Microsoft Excel. The peak frequency of the PSD gradually decreases and shifts to the right with time due to coarsening and this is consistent with normal coarsening behavior [36]. The figure also shows that the size distribution range becomes broader with an increase in time, as expected in a normal coarsening process. Observations show that the PSD did not significantly change in shape with time step and this indicates that, for the time steps considered, a scaling behavior during coarsening has already been reached.

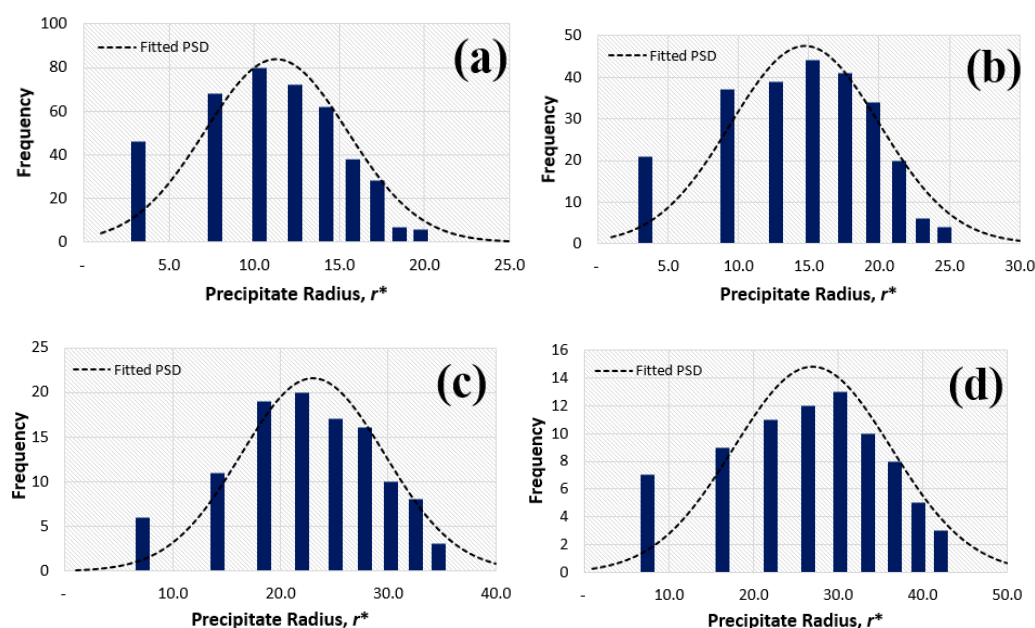


Figure 4. Histograms of the PSD in absence of nanoparticles at different times t^* of: (a) 1000, (b) 2500, (c) 10,000, and (d) 20,000.

To validate the model, our simulation results for precipitate coarsening in absence of nanoparticles were compared with results by Wu et al. [43], Wang et al. [44], and those from Zhu et al. [36] for coarsening of binary Ni Al alloys. The PSD shapes and curves of \bar{R}^3 vs t from our simulation results (Figures 3a and 4a–c) are similar with those from these previous results, i.e., they both obey the linear cube growth law and have similar unimodal skewed PSD shapes. Quantitative comparisons are necessary in the future to further clarify this aspect.

3.2. Coarsening Behavior in Presence of Nanoparticles

To understand the effect of nanoparticles on the precipitate coarsening process, inert nanoparticle phases with volume fractions of 10%, 20%, and 30% were introduced into the domain. A previous study on grain boundary pinning [24] showed that the size distribution of nanoparticles is not important in controlling grain growth. Thus, for a given nanoparticle volume fraction, mono-sized spherical nanoparticles with three radii sizes, r^* , of 10, 20 and 30 were used. All the nanoparticles were randomly distributed in the system. It should be noted that introduction of nanoparticles reduced the total solute content within the matrix, and, therefore, the volume fraction of the precipitate phase in the coarsening stage is also reduced.

Figure 5a–c shows the evolution of the precipitates with different nanoparticle volume fractions at a fixed nanoparticle size of $r^* = 20$. The relationships of the cube of the average precipitate size with the coarsening time under different volume fractions of nanoparticles, including zero volume fraction, are merged for comparison and plotted in Figure 6a. At a given time, the average precipitate size decreases with increasing nanoparticle volume fractions. Similar simulations with different nanoparticle sizes are also shown in Figure 6b,c.

In general, the average precipitate size curves deviate from the linear cubic growth law and become more nonlinear at higher volume fractions of nanoparticles. This behavior is expected, since low nanoparticle volume fraction systems are closer to the classic LSW coarsening theory, and one should expect a larger deviation of the average precipitate size from the LSW theory as more nanoparticles are added into the system. One may also notice that, at the same nanoparticle volume fraction, the deviation from linear LSW coarsening rate is more significant for smaller nanoparticles. This particle size effect will be discussed in a later section.

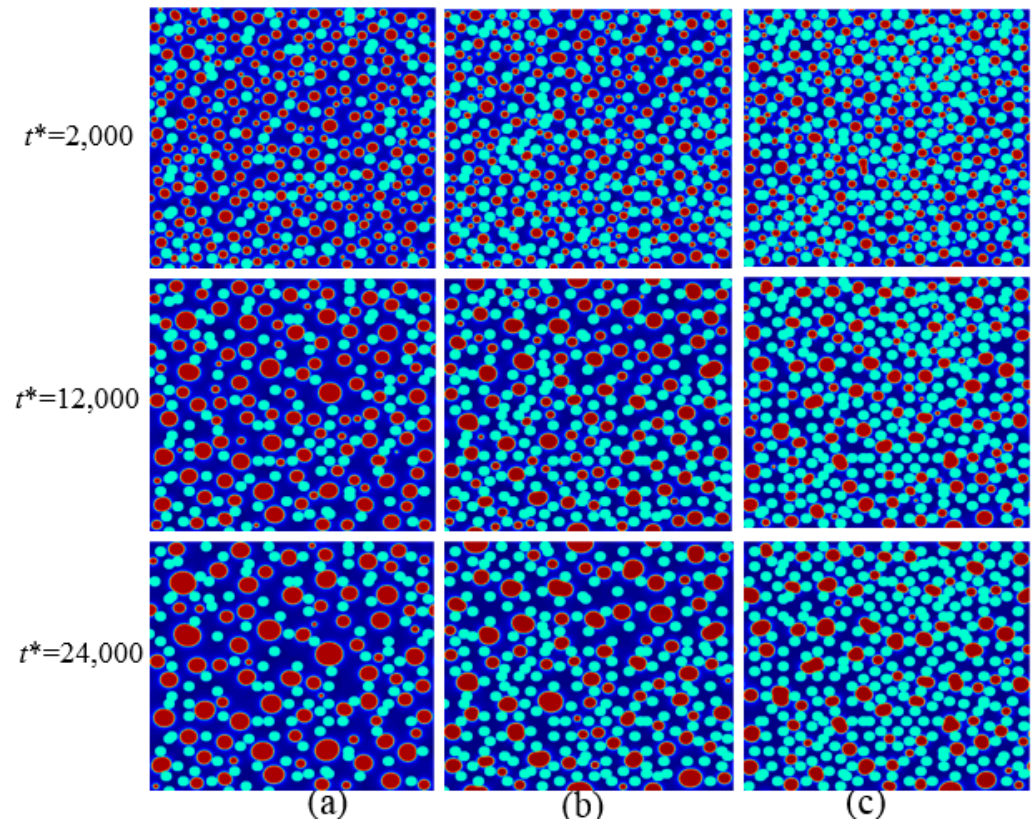


Figure 5. Simulation snapshots of the system at different times are shown in vertical columns. Particle size, r^* , is fixed to 20. Volume fractions of nanoparticles are: (a) 10%, (b) 20%, and (c) 30%. The nanoparticles are shown in light blue, precipitates are colored red, and the matrix is in dark blue.

Figure 6 also shows that, at a given time, the gradients of the curves are non-constant and gradually decrease with an increase in nanoparticle volume fraction, and this signifies the slowing down of the coarsening rate. The local slopes of the curves are the coarsening rate constants which indicate the kinetic and thermodynamic changes in terms of the diffusion coefficient, interfacial energy, and molar volume according to the coarsening rate constant relationship given below [37].

$$k = \frac{8}{9} D \frac{C_e \gamma_s V_m^2 f(\phi)}{RT} \quad (10)$$

where, V_m is the molar volume of the precipitates, D is the bulk diffusion of solutes in the matrix, C_e is the equilibrium solute concentration of the matrix, γ_s is the interfacial energy of the precipitate–matrix interface, R is the particle radius, T is the temperature, and $f(\phi)$ is the ratio of the coarsening rate with finite precipitate volume fraction to the coarsening rate with zero volume fraction. After examining the precipitate shrinkage and growth behavior in detail, it was found that the decelerated coarsening behavior experienced in this study is not attributed to inverse coarsening like the one experienced in the previous study [45], but

the behavior is in agreement with results obtained by Ryu et al. [46] for regular coarsening deceleration.

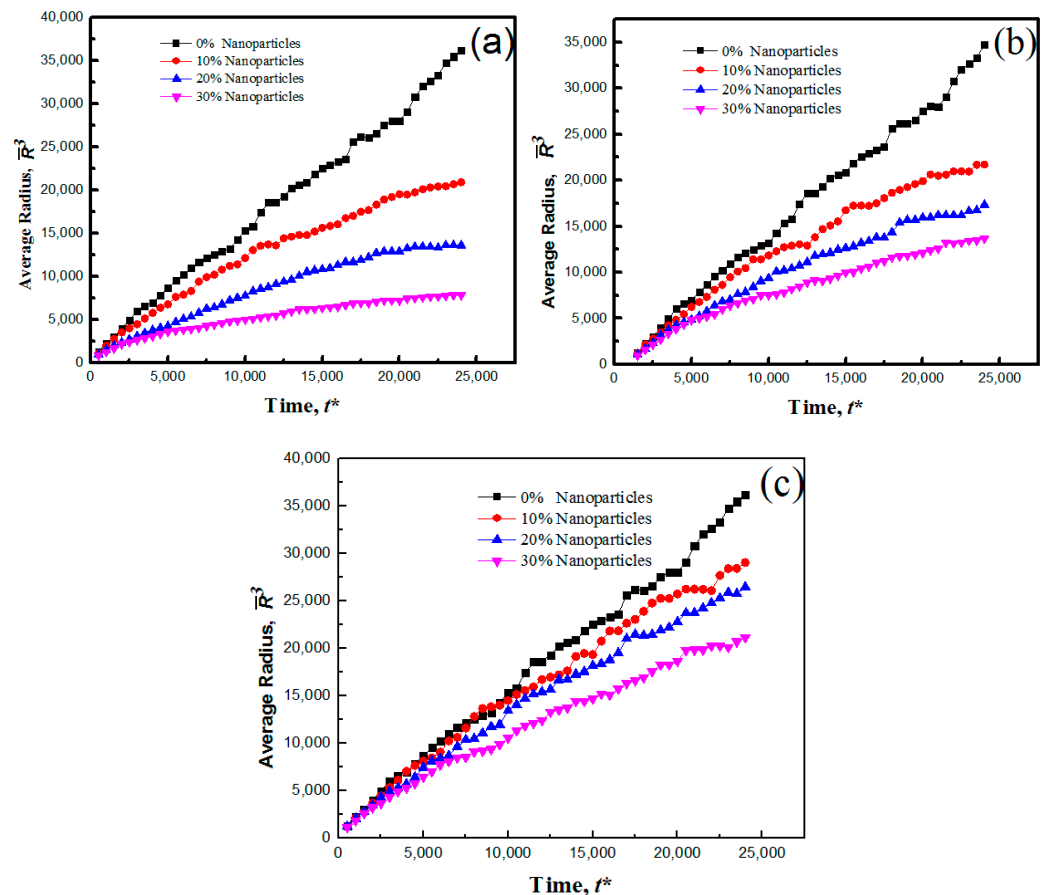


Figure 6. Plots of the cube of the average precipitate radius versus time. Nanoparticle area fractions are labeled in the figures. Nanoparticle sizes are: (a) 10, (b) 20 and (c) 30.

The PSD at different times in presence of nanoparticles of radius size $r^* = 10$ with different volume fractions in the system are given in Figures 7–9. The graphs show that with an increase in the system nanoparticle area fraction, the particle size distributions change and significant differences from the non-nanoparticles PSD in Figure 4 can be identified. Firstly, with an increase in volume fraction of nanoparticles, the PSD shapes become more disordered and peak positions do not significantly move to the right. This signifies much departure from the regular PSD observed in the absence of nanoparticles. Secondly, the rate of increase of the broadness of the precipitate size ranges becomes slower at higher volume fractions of precipitates (Figure 9) when compared to that in the absence of nanoparticles (Figure 4). After examining the coarsening simulation results carefully, it is found that, at high nanoparticle volume fraction, the shapes of the precipitates become irregular due to contact with nanoparticles. As seen in the high volume fraction PSD in Figure 9, the precipitate size range becomes narrow, and such PSD shapes are quite similar to those obtained for decelerated coarsening in the presence of stresses [15]. Figures 7–9 show that in the presence of nanoparticles in the system, the PSD shapes are constantly changing with time and are not self-similar according to the classic LSW theory. This behavior can be understood by identifying another precipitate size-limiting mechanism, which is the distance between randomly distributed inert nanoparticles. As shown in Figure 5, when the precipitates are in contact with nanoparticles, further growth of precipitates is constrained by the surrounding nanoparticles. Since the nanoparticles are randomly distributed in the matrix, the size distribution of the inter-particle space where the precipitates can grow is also random, with the average inter-particle space being inversely proportional to the number of

nanoparticles. The particle size distribution, particularly in the late stages of coarsening, is the combined result of the classic coarsening kinetics that pushes the distribution towards the standard LSW PSD shapes and the geometric constraint imposed by inter-particle distance which leads to random size distribution. Thus, with less size constraints at low nanoparticle volume fraction, the system will relax towards the standard PSD given by the LSW theory, and with strong size constraints at high nanoparticle volume fractions, precipitates will form a PSD that centers around the average inter-particle distance.

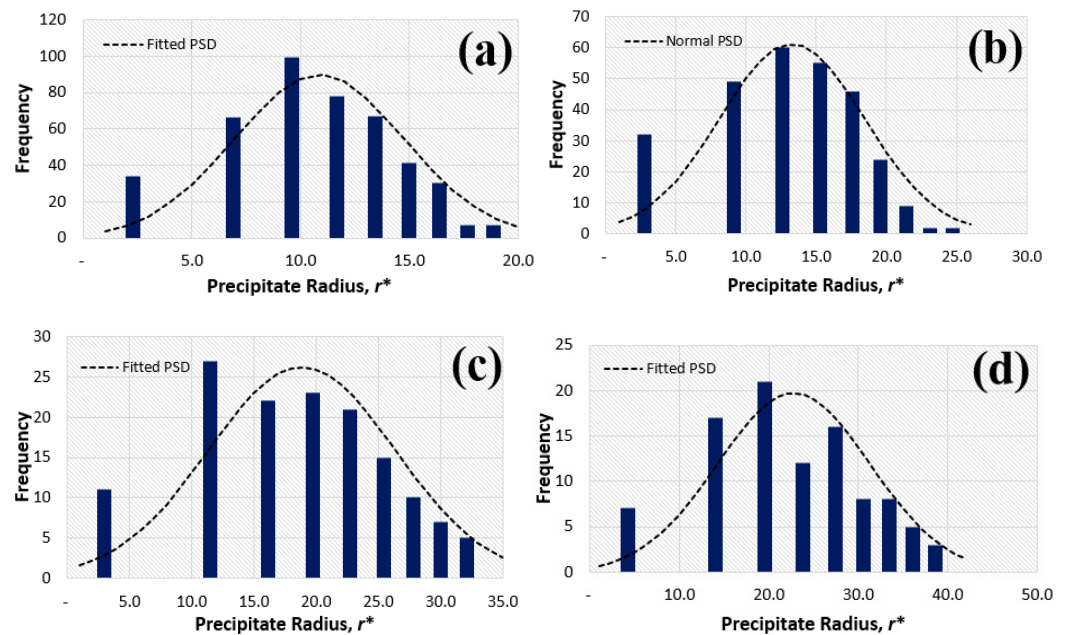


Figure 7. Histograms of the PSD in presence of 10% nanoparticles of size 10 at different times t^* of: (a) 1000, (b) 2500, (c) 10,000, and (d) 20,000.

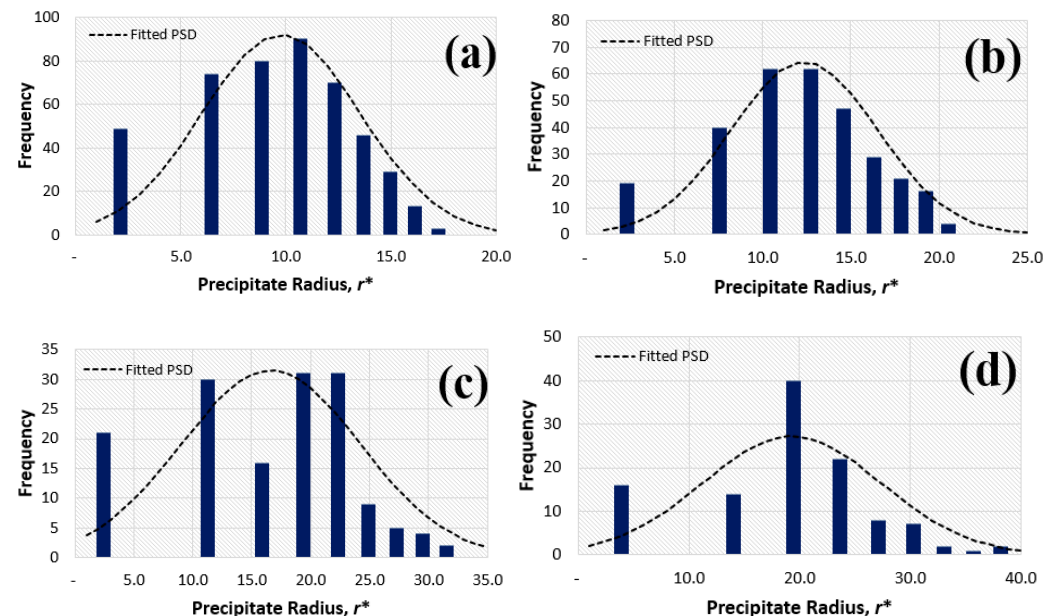


Figure 8. Histograms of the PSD in presence of 20% nanoparticles of size 10 at different times t^* of: (a) 1000, (b) 2500, (c) 10,000, and (d) 20,000.

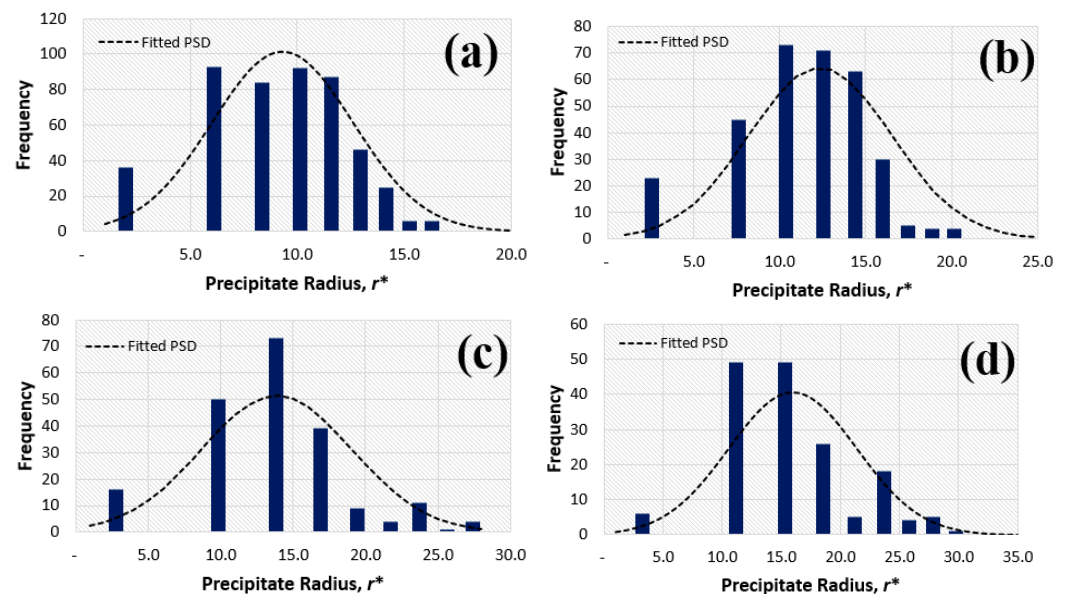


Figure 9. Histograms of the PSD in presence of 30% nanoparticles of size 10 at different times t^* of: (a) 1000, (b) 2500, (c) 10,000, and (d) 20,000.

To investigate the effect of nanoparticle sizes on the precipitate coarsening rate, the nanoparticle volume fractions were fixed and the nanoparticle sizes were varied. Figure 10a–c shows the evolution of precipitates with time steps for nanoparticles of a fixed volume fraction of 30% and different sizes, r^* , of 10, 20, and 30. In the presence of small sized nanoparticles, the late stage precipitate shape changes from circular to irregular, whilst for large nanoparticles the changes are insignificant. Figure 11a–c shows the plots of the cube of average precipitate radius with time for nanoparticles with fixed volume fractions and different particle sizes. It is shown that small-sized nanoparticles are more effective in suppressing precipitate coarsening when compared to large ones. The results show that, for the same volume fraction, the precipitate sizes and gradients of the curves decreases with a decrease in the nanoparticle size. The smallest precipitate sizes are obtained in the presence of a high volume fraction of nanoparticles of the smallest size, as shown in Figure 11c. On the contrary, a small area fraction of large nanoparticles, like those shown in Figure 11a, only slightly affects the precipitate' coarsening rate. At the same volume fraction, small nanoparticles possess larger overall surface area. Since the coarsening process involves the transportation of solute atoms from small precipitates to large precipitates through diffusion, the large amount of particle–matrix interfaces produced by small nanoparticles block more solute transportation path and, therefore, effectively slows down the coarsening process.

The effect of nanoparticle sizes on PSD are shown in Figures 9, 12 and 13 for nanoparticles with 30% volume fraction and size radii, R^* , of 10, 20, and 30. The figures show that with a decrease in the nanoparticle size, the PSD shapes become more random due to the inter-particle distance constraints from the increasing nanoparticle number density. With larger nanoparticle size, like in Figure 13, the PSD shape is close to the one in absence of nanoparticles since the inter-particle distance is also large. A similar behavior was observed in NiAl and Fe–Cr alloys, where it was shown that the coarsening rate can be decelerated by solute segregation, stresses and strains [10,47].

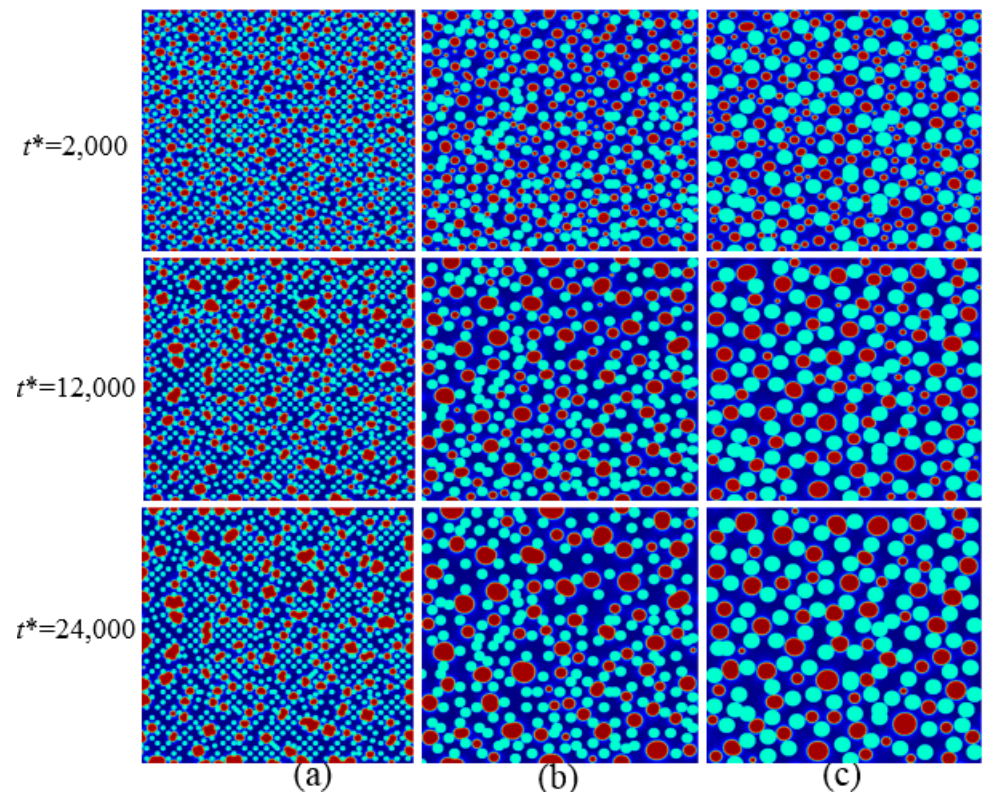


Figure 10. Simulation snapshots of the system at different times are shown in vertical columns. Particle volume fraction is set to 30%. Particle sizes are: (a) 10, (b) 20, and (c) 30. The same coloring scheme in Figure 5 is used.

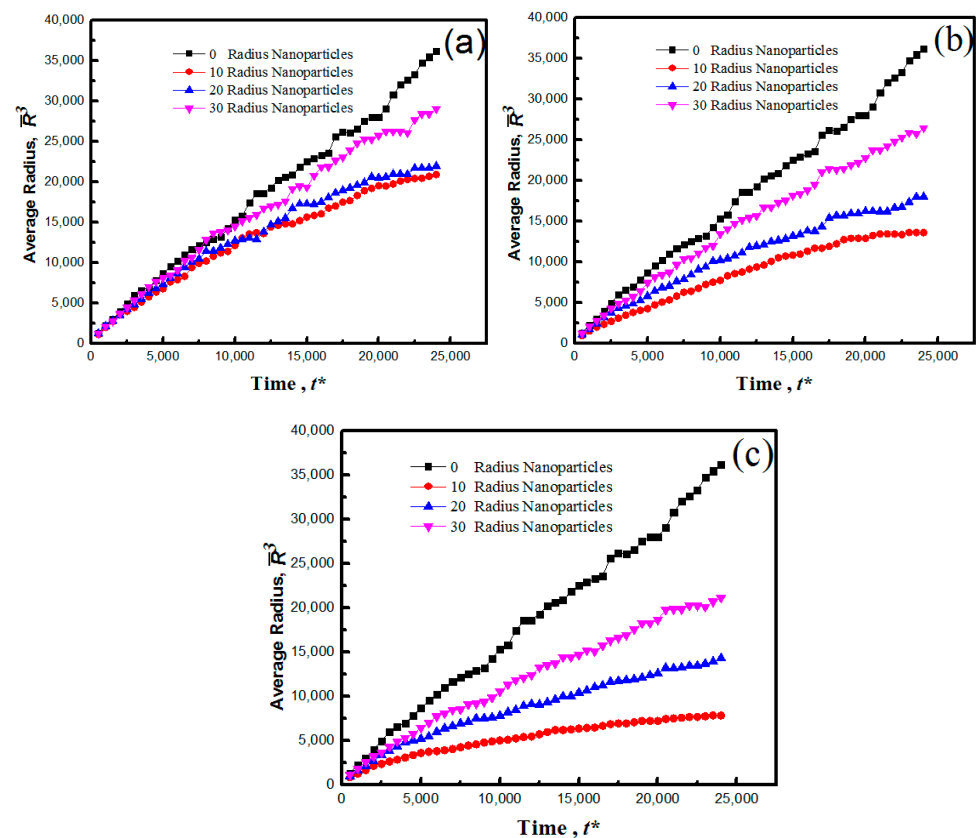


Figure 11. Plots of the cube of the average precipitate radius with time for different nanoparticles area fractions of: (a) 10%, (b) 20%, and (c) 30%. Particle sizes are labeled in the figures.

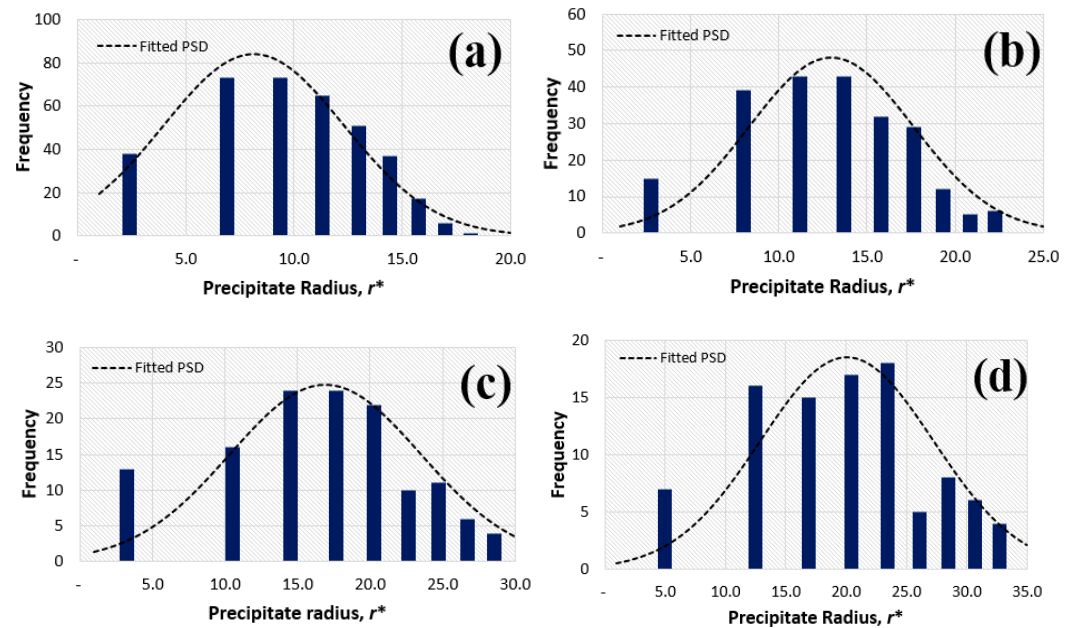


Figure 12. Histograms of the PSD in presence of 30% nanoparticles of size 20 at different times, t^* , of: (a) 1000, (b) 2500, (c) 10,000 and (d) 20,000.

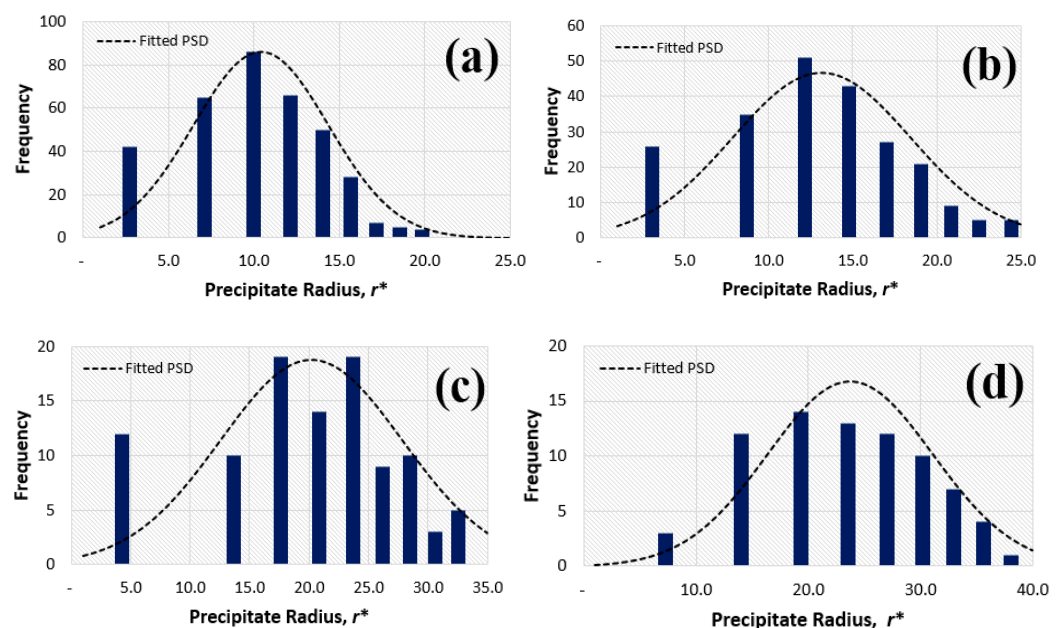


Figure 13. Histograms of the PSD in presence of 30% nanoparticles of size 30 at different times, t^* , of: (a) 1000, (b) 2500, (c) 10,000 and (d) 20,000.

4. Conclusions

The effects of intra-granular nanoparticles on early-stage coarsening behavior of precipitates were studied computationally by generalizing a previously proved phase field model for precipitate coarsening. Inert nanoparticles of various sizes and volume fractions were incorporated in the matrix phase using a non-evolving order parameter. It is found that both the precipitate size distribution and the coarsening rate may be affected by the presence and characteristics of nanoparticles. Two distinct mechanisms for these nanoparticle effects are proposed. The new length scale related to the inter-nanoparticle distance introduced by incorporating random nanoparticles may change the standard LSW precipitate size distribution by geometrically constraining the precipitate size, and the reduction of available diffusion paths due to the blockage of nanoparticle–matrix interfaces

can significantly slow down the coarsening process. As the first systematic computational study of the effects of nanoparticles on the precipitate coarsening process, this work sheds light on potential approaches to control the coarsening process and further improve the mechanical properties of nanoparticle-reinforced metal matrix composites.

The simulation results in general suggests that the use of smaller nanoparticles with large number density is effective in slowing down of the coarsening kinetics. However, since the current work was performed in 2D only, the diffusion path blockage mechanism that leads to this conclusion may become less significant in 3D due to an increasing transport path. Computationally intensive 3D simulations need to be carried out in the future in order to confirm the result. In addition, other potential contributing factors like the precipitate-matrix misfit stress and surface diffusion along the particle-matrix interface should be included when generalizing the results to real materials.

Author Contributions: Conceptualization and study design, N.W.; Model development, simulations, manuscript writing, S.F.; Data interpretation, data collection and manuscript revision, B.H. All authors have read and agreed to the published version of the manuscript.

Funding: This research received no external funding.

Data Availability Statement: Not applicable.

Acknowledgments: The authors acknowledge the computer time support from the High Performance Computing Center of Guangdong Technion—Israel Institute of Technology.

Conflicts of Interest: The authors of this manuscript declare that there is no any conflict of interest in this paper.

References

- Baldan, A. Review Progress in Ostwald ripening theories and their applications to the γ' -precipitates in nickel-base superalloys Part II Nickel-base superalloys. *J. Mater. Sci.* **2002**, *37*, 2379–2405. [CrossRef]
- Yang, C.; Cao, L.; Gao, Y.; Cheng, P.; Zhang, P.; Kuang, J.; Zhang, J.; Liu, G.; Sun, J. Nanostructural Sc-based hierarchy to improve the creep resistance of Al–Cu alloys. *Mater. Des.* **2020**, *186*, 108309. [CrossRef]
- Shower, P.; Morris, J.; DShin Radhakrishnan, B.; Poplawsky, J.; Shyam, A. Mechanisms for stabilizing θ' (Al₂Cu) precipitates at elevated temperatures investigated with Phase Field modeling. *Materialia* **2019**, *6*, 100335. [CrossRef]
- Devaraj, A.; Wang, W.; Vemuri, R.; Kovarik, L.; Jiang, X.; Bowden, M.; Trelewicz, J.R.; Mathaudhu, S.; Rohatgi, A. Grain boundary segregation and intermetallic precipitation in coarsening resistant nanocrystalline aluminum alloys. *Acta Mater.* **2019**, *165*, 698–708. [CrossRef]
- Gao, Y.H.; Guan, P.F.; Su, R.; Chen, H.W.; Yang, C.; He, C.; Cao, L.F.; Song, H.; Zhang, J.Y.; Zhang, X.F.; et al. Segregation-sandwiched stable interface suffocates nanoprecipitate coarsening to elevate creep resistance. *Mater. Res. Lett.* **2020**, *8*, 446–453. [CrossRef]
- Gao, Y.H.; Yang, C.; Zhang, J.Y.; Cao, L.F.; Liu, G.; Sun, J.; Ma, E. Stabilizing nanoprecipitates in Al–Cu alloys for creep resistance at 300 °C. *Mater. Res. Lett.* **2019**, *7*, 18–25. [CrossRef]
- Smith, T.M.; Good, B.S.; Gabb, T.P.; Esser, B.D.; Egan, A.J.; Evans, L.J.; McComb, D.W.; Mills, M.J. Effect of stacking fault segregation and local phase transformations on creep strength in Ni-base superalloys. *Acta Mater.* **2019**, *172*, 55–65. [CrossRef]
- Bian, H.; Xu, X.; Li, Y.; Koizumi, Y.; Wang, Z.; Chen, M.; Yamanaka, K.; Chiba, A. Regulating the coarsening of the γ' phase in superalloys. *NPG Asia Mater.* **2015**, *7*, e212. [CrossRef]
- Feng, L.; Rao, Y.; Ghazisaeidi, M.; Mills, M.J.; Wang, Y. Quantitative prediction of Suzuki segregation at stacking faults of the γ' phase in Ni-base superalloys. *Acta Mater.* **2020**, *200*, 223–235. [CrossRef]
- Mushongera, L.T.; Fleck, M.; Kundin, J.; Wang, Y.; Emmerich, H. Effect of Re on directional γ' -coarsening in commercial single crystal Ni-base superalloys: A phase field study. *Acta Mater.* **2015**, *93*, 60–72. [CrossRef]
- Wang, W.Z.; Jin, T.; Liu, J.L.; Sun, X.F.; Guan, H.R.; Hu, Z.Q. Role of Re and Co on microstructures and γ' coarsening in single crystal superalloys. *Mater. Sci. Eng. A* **2008**, *479*, 148–156. [CrossRef]
- Lu, F.; Antonov, S.; Lu, S.; Zhang, J.; Li, L.; Wang, D.; Zhang, J.; Feng, Q. Unveiling the Re effect on long-term coarsening behaviors of γ' precipitates in Ni-based single crystal superalloys. *Acta Mater.* **2022**, *233*, 117979. [CrossRef]
- Pyczak, F.; Devrient, B.; Neuner, F.C.; Mughrabi, H. The influence of different alloying elements on the development of the γ/γ' microstructure of nickel-base superalloys during high-temperature annealing and deformation. *Acta Mater.* **2005**, *53*, 3879–3891. [CrossRef]
- Chen, Y.; Slater, T.J.; Bai, M.; Mitchell, R.; Ciuca, O.; Preuss, M.; Haigh, S.J. An investigation of diffusion-mediated cyclic coarsening and reversal coarsening in an advanced Ni-based superalloy. *Acta Mater.* **2016**, *110*, 295–305. [CrossRef]

15. Prikhodko, S.V.; Ardell, A.J. Coarsening of γ' in Ni–Al alloys aged under uniaxial compression: I. Early-stage kinetics. *Acta Mater.* **2003**, *51*, 5001–5012. [CrossRef]
16. Ardell, A.J.; Prikhodko, S.V. Coarsening of γ' in Ni–Al alloys aged under uniaxial compression: II. Diffusion under stress and retardation of coarsening kinetics. *Acta Mater.* **2003**, *51*, 5013–5019.
17. Kundin, J.; Mushongera, L.; Goehler, T.; Emmerich, H. Phase-field modeling of the γ' -coarsening behavior in Ni-based superalloys. *Acta Mater.* **2012**, *60*, 3758–3772. [CrossRef]
18. Voorhees, P.W. The theory of Ostwald ripening. *J. Stat. Phys.* **1985**, *38*, 231–252. [CrossRef]
19. Chen, L.Y.; Xu, J.Q.; Li, X.C. Controlling phase growth during solidification by nanoparticles. *Mater. Res. Lett.* **2015**, *3*, 43–49. [CrossRef]
20. Wang, K.; Jiang, H.Y.; Jia, Y.W.; Zhou, H.; Wang, Q.D.; Ye, B.; Ding, W.J. Nanoparticle-inhibited growth of primary aluminum in Al–10Si alloys. *Acta Mater.* **2016**, *103*, 252–263. [CrossRef]
21. Chen, L.Y.; Xu, J.Q.; Choi, H.; Konishi, H.; Jin, S.; Li, X.C. Rapid control of phase growth by nanoparticles. *Nat. Commun.* **2014**, *5*, 3879. [CrossRef] [PubMed]
22. Vanherpe, L.; Moelans, N.; Blanpain, B.; Vandewalle, S. Pinning effect of spheroid second-phase particles on grain growth studied by three-dimensional phase-field simulations. *Comput. Mater. Sci.* **2010**, *49*, 340–350. [CrossRef]
23. Chakrabarti, T.; Manna, S. Zener pinning through coherent precipitate: A phase-field study. *Comput. Mater. Sci.* **2018**, *154*, 84–90. [CrossRef]
24. Chang, K.; Feng, W.; Chen, L.Q. Effect of second-phase particle morphology on grain growth kinetics. *Acta Mater.* **2009**, *57*, 5229–5236. [CrossRef]
25. Moelans, N.; Blanpain, B.; Wollants, P. Phase field simulations of grain growth in two-dimensional systems containing finely dispersed second-phase particles. *Acta Mater.* **2006**, *54*, 1175–1184. [CrossRef]
26. Karnesky, R.A.; Meng, L.; Dunand, D.C. Strengthening mechanisms in aluminum containing coherent Al₃Sc precipitates and incoherent Al₂O₃ dispersoids. *Acta Mater.* **2007**, *55*, 1299–1308. [CrossRef]
27. Moelans, N.; Blanpain, B.; Wollants, P. Pinning effect of second-phase particles on grain growth in polycrystalline films studied by 3-D phase field simulations. *Acta Mater.* **2007**, *55*, 2173–2182. [CrossRef]
28. Lin, T.C.; Cao, C.; Sokoluk, M.; Jiang, L.; Wang, X.; Schoenung, J.M.; Lavernia, E.J.; Li, X. Aluminum with dispersed nanoparticles by laser additive manufacturing. *Nat. Commun.* **2019**, *10*, 4124. [CrossRef]
29. Suwa, Y.; Saito, Y.; Onodera, H. Phase field simulation of grain growth in three dimensional system containing finely dispersed second-phase particles. *Scr. Mater.* **2006**, *55*, 407–410. [CrossRef]
30. DeWitt, S.; Thornton, K. Phase field modeling of microstructural evolution. *Comput. Mater. Syst. Des.* **2018**, pp. 67–87. Available online: https://link.springer.com/chapter/10.1007/978-3-319-68280-8_4 (accessed on 30 March 2022).
31. Moelans, N.; Blanpain, B.; Wollants, P. An introduction to phase-field modeling of microstructure evolution. *Calphad* **2008**, *32*, 268–294. [CrossRef]
32. Bellemans, I.; Moelans, N.; Verbeken, K. Phase-field modelling in extractive metallurgy. *Crit. Rev. Solid State Mater. Sci.* **2018**, *43*, 417–454. [CrossRef]
33. Boettinger, W.J.; Warren, J.A.; Beckermann, C.; Karma, A. Phase-field simulation of solidification. *Annu. Rev. Mater. Res.* **2002**, *32*, 163–194. [CrossRef]
34. Fan, D.; Chen, S.P.; Chen, L.Q.; Voorhees, P.W. Phase-field simulation of 2-D Ostwald ripening in the high volume fraction regime. *Acta Mater.* **2002**, *50*, 1895–1907. [CrossRef]
35. Vaithyanathan, V. Phase-Field Simulations of Coherent Precipitate Morphologies and Coarsening Kinetics. Ph.D. Thesis, The Pennsylvania State University, Centre County, PA, USA, 2002.
36. Zhu, J.Z.; Wang, T.; Ardell, A.J.; Zhou, S.H.; Liu, Z.K.; Chen, L.Q. Three-dimensional phase-field simulations of coarsening kinetics of γ' particles in binary Ni–Al alloys. *Acta Mater.* **2004**, *52*, 2837–2845. [CrossRef]
37. Li, X.; Saunders, N.; Miodownik, A.P. The coarsening kinetics of γ' particles in nickel-based alloys. *Metall. Mater. Trans. A* **2002**, *33*, 3367–3373. [CrossRef]
38. Ardell, A.J.; Nicholson, R.B. The coarsening of γ' in Ni–Al alloys. *J. Phys. Chem. Solids* **1966**, *27*, 1793–1794. [CrossRef]
39. Vaithyanathan, V.; Wolverson, C.; Chen, L.Q. Multiscale modeling of precipitate microstructure evolution. *Phys. Rev. Lett.* **2002**, *88*, 125503. [CrossRef]
40. Simmons, J.P.; Shen, C.; Wang, Y. Phase field modeling of simultaneous nucleation and growth by explicitly incorporating nucleation events. *Scr. Mater.* **2000**, *43*, 935–942. [CrossRef]
41. Marqusee, J.A.; Ross, J. Theory of Ostwald ripening: Competitive growth and its dependence on volume fraction. *J. Chem. Phys.* **1984**, *80*, 536–543. [CrossRef]
42. Sun, Y.; Andrews, W.B.; Thornton, K.; Voorhees, P.W. Self-similarity and the dynamics of coarsening in materials. *Sci. Rep.* **2018**, *8*, 17940. [CrossRef]
43. Wu, X.; Li, Y.; Huang, M.; Liu, W.; Hou, Z. Precipitation kinetics of ordered γ' phase and microstructure evolution in a NiAl alloy. *Mater. Chem. Phys.* **2016**, *182*, 125–132. [CrossRef]
44. Wang, T.; Sheng, G.; Liu, Z.K.; Chen, L.Q. Coarsening kinetics of γ' precipitates in the Ni–Al–Mo system. *Acta Mater.* **2008**, *56*, 5544–5551. [CrossRef]

45. Miyazaki, T.; Koyama, T. Stability bifurcation against coarsening in elastically constrained many-particle systems. *Mater. Sci. Eng. A* **1993**, *169*, 159–165. [CrossRef]
46. Ryu, H.J.; Hong, S.H.; Weber, J.; Tundermann, J.H. Effect of elastic interaction energy on coarsening of γ' precipitates in a mechanically alloyed ODS Ni-base superalloy. *J. Mater. Sci.* **1999**, *34*, 329–336. [CrossRef]
47. Zhu, L.; Li, Y.; Shi, S.; Yan, Z.; Chen, J.; Maqbool, S. Morphology and kinetics evolution of nanoscale phase in Fe–Cr alloys under external strain. *Nanomaterials* **2019**, *9*, 294. [CrossRef] [PubMed]



Article

Kinetic Model of Isothermal Bainitic Transformation of Low Carbon Steels under Ausforming Conditions

Theerawat Kumnorkaew ^{1,*}, Junhe Lian ², Vitoon Uthaisangsuk ³ and Wolfgang Bleck ¹¹ Steel Institute, RWTH Aachen University, 52072 Aachen, Germany; bleck@iehk.rwth-aachen.de² Department of Mechanical Engineering, Aalto University, 02150 Espoo, Finland; junhe.lian@aalto.fi³ Center for Lightweight Materials, Design and Manufacturing, Department of Mechanical Engineering, King Mongkut's University of Technology Thonburi, Bangkok 10140, Thailand; vitoon.uth@kmutt.ac.th

* Correspondence: theerawat.kumnorkaew@iehk.rwth-aachen.de

Abstract: Carbide-free bainitic steels show attractive mechanical properties but are difficult to process because of the sluggish phase transformation kinetics. A macroscopic model based on the classical nucleation theory in conjunction with the modified Koistinen–Marburger relationship is proposed in this study to simulate the kinetics of incomplete bainitic and martensitic phase transformations with and without austenite deformation. A 0.26C-1Si-1.5Mn-1Cr-1Ni-0.003B-0.03Ti steel and a 0.18C-1Si-2.5Mn-0.2Cr-0.2Ni-0.02B-0.03Ti steel were investigated with different levels of ausforming. The concept of ausforming is expected to accelerate the onset of the bainitic transformation and to enhance the thermodynamic stability of austenite by increased dislocation density. The phase transformation kinetics of both steels is quantitatively analyzed in the study by dilatometry and X-ray diffraction so that the carbon concentration in the retained austenite and bainitic ferrite, as well as their volume fractions, is determined. A critical comparison of the numerical and experimental data demonstrates that the isothermal kinetics of bainite formation and the variation of driving energy can be satisfactorily described by the developed model. This model captures the incompleteness of the bainite phase transformation and the carbon enrichment in the austenite well. A fitting parameter can be used to elucidate the initial energy barrier caused by the ausforming. An increase in austenite stability can be described by the nucleation reaction and the thermodynamic energies associated with the change of dislocation density. The proposed model provides an in-depth understanding of the effect of ausforming on the transformation kinetics under different low-carbon steels and is a potential tool for the future design of heat treatment processes and alloys.

Citation: Kumnorkaew, T.; Lian, J.; Uthaisangsuk, V.; Bleck, W. Kinetic Model of Isothermal Bainitic Transformation of Low Carbon Steels under Ausforming Conditions. *Alloys* **2022**, *1*, 93–115. <https://doi.org/10.3390/alloys1010007>

Academic Editors: Damien Fabregue, Shuwen Wen, Yongle Sun and Xin Chen

Received: 15 May 2022

Accepted: 8 June 2022

Published: 13 June 2022

Publisher's Note: MDPI stays neutral with regard to jurisdictional claims in published maps and institutional affiliations.



Copyright: © 2022 by the authors. Licensee MDPI, Basel, Switzerland. This article is an open access article distributed under the terms and conditions of the Creative Commons Attribution (CC BY) license (<https://creativecommons.org/licenses/by/4.0/>).

Keywords: bainitic steels; phase transformation; ausforming; carbon enrichment; activation energy; dislocation density

1. Introduction

Controlling the thermodynamic stability of austenite has been a challenging issue in the development of carbide-free bainitic (CFB) steels when considering carbon as an essential element for a bainitic transformation at low temperatures. With an addition of 1.5%wt.%Si, the decomposition of austenite occurs when supersaturated carbon from bainitic ferrite is rejected into adjacent austenitic regions and becomes robustly available for stabilization during the bainitic transformation instead of forming cementite (Fe₃C) [1–4]. The increased stability of the neighboring austenite via the enrichment of carbon thus leads to an incompleteness of the transformation that leaves two different features of the retained austenite (RA) as the secondary phase, namely film-like RA and blocky-type RA. These features of RA can be characterized by their stabilities in accordance with chemical contributions that can be statistically estimated by atom probe tomography (APT) [5,6]. The carbon-rich, thin-film RA is always more stable compared to the other type [7–10]. In light of the thermodynamic stability, Garcia Mateo et al. [11] reported that the blocky

RA could also be present in various granular morphologies, depending on the carbon concentration. The morphologies with low carbon content, particularly in the central zone, are prone to decompose further into fresh martensite (FM) during ambient cooling. Even though the formation of FM is beneficial in some applications that require material with high hardness, strength, and wear resistance (e.g., railway material and agricultural parts, etc.), the existence of such a hard phase is usually an impairment when the transformation-induced plasticity (TRIP) effect is desired [3]. Therefore, the recent progress in bainitic forging steel development is aimed at refining the microstructures by means of replacing the large granular blocky RA with nano-structured film-like RA. For instance, Caballero et al. and Garcia-Mateo et al. [12,13] exploited the T_0 concept as a thermodynamic limit of CFB transformation to design advanced carbon CFB steels with an ultra-fine structure (RA thickness < 100 nm). They achieved prominent steel properties, including strength and elongation of about 2.2–2.5 GPa and 20–30%, respectively. However, the concept is successful only in high- and medium-carbon steels (0.4–1.0 wt.%C), whereby transformation at very low temperatures above the martensite start temperature is necessary. Despite the attempt to take low-carbon steels (<0.2% C) into account, higher Gibbs free energy, associated with the insufficient C enrichment in austenite affected by the lower bulk density of C, has promoted the thermal instability of the austenite during the cooling process after isothermal holding.

Yao et al. [14] proposed an alloying modification strategy and considered a chemical Gibbs free energy change of the FCC to BCC transformation. An addition of 1.5%Ni encourages the austenite stability by means of enlarging the austenitic phase region so that an increase in the free energy difference retards the kinetics of the bainitic transformation and induces a reduction in the bainitic ferrite (BF) plate thickness. However, although the energy reduction due to another supplement of 1.5%Cr favors the bainitic transformation, a formation of iron carbide (Fe_3C) consequently deteriorates the thermal stability of the austenite. Herein, the stability of austenite likely depends on the free energy difference between the parent and the child phases. As a consequence, both Cr and Ni alloyed in nearly equivalent compositions, which causes another reduction in the driving energy by ~400 J/mol; thus, this is expected to enhance the thermal stability of austenite and stimulate bainitic transformation simultaneously. Hence, the enhanced stabilization of austenite is feasible by adjusting an appropriate amount of Cr and Ni addition in the concerned steel. Changle et al. [15] stated that steels alloyed with Mn content over 2.2 wt.% provide an excellent hardenability and a lower bainitic start temperature (B_s), which in turn yields an 18% volume fraction of retained austenite with a reduction in BF laths. Mn as a solid solution element is evidently effective in raising the free energy of ferrite and reducing that of austenite, causing a delay of austenite decomposition to bainite at low temperatures. Nevertheless, if the Mn content in bainitic steel exceeds its limitation and segregation occurs at the prior austenite grain boundaries, it may lead to an increase in transformation temperature and undesired brittleness.

Ausforming is one of the thermomechanical treatment processes, in which the structure of austenite is refined at its metastable temperature prior to phase transformation. The deformation plays an important part in accelerating the bainitic transformation due to increased bainitic nucleation sites, whereas raised dislocation density encourages the thermal stability of austenite. The process parameters of ausforming, such as deformation temperature, strain, and strain rate, are also reported as being the essential controlling parameters of the kinetics of isothermal bainitic transformation [16]. A sophisticated result showed that the stability of austenite is not improved when a severe ausforming strain of 50% is applied, because of a high BF volume fraction. It is noticed that such a result is confirmed in a few works concerning low-carbon steels [17,18]. Although these qualitative conclusions can be applied to optimize the microstructure of CFB steels, a reliable physical-based model for correlating the alloying composition with processing parameters is still required because the variations of both the alloy design and the process parameters are very high. Several models have been developed for describing phase transformation of alloys,

but one proposed by Bhadeshia and his co-workers has been widely employed [19,20]. Their model is based on a displacive approach, by which bainite growth without diffusion of any alloying elements is considered. In this approach, bainite formation is assumed to begin at prior nucleation sites on austenite grain boundaries and to successively form by autocatalytic nucleation at the newly formed sheaves. Consequently, the transformation of bainite is a nucleation-controlled process. The prior austenite grain size and the maximum driving energy are essential factors controlling the nucleation kinetics of bainitic transformation. Later, Magee [21] revealed that the number of nucleation sites as a function of prior austenite grain size should also be considered and can be determined by the driving energy difference. It is increased with a rise in undercooling. Van Bohemann formulated this concept to estimate the number of potential embryos for martensitic nucleation [22]. However, these displacive models use empirical constants by which the activation energy is only represented a net energy used to activate the transformation. In the model of isothermal martensitic transformation proposed by Ghosh and Olsen [23], an energy barrier consistent with the critical driving energy needed for the nucleation should be incorporated by the sum of the strain energy, the defect-size-dependent interfacial energy, and the composition-dependent interfacial work [24]. They also introduced a model that takes autocatalytic factors into account as material constants. The effectiveness of the γ/α interface boundaries and the thickness of the bainitic plate play a significant role in the overall transformation kinetics. Meng et al. [25] reported that morphological features also affect internal stresses by the autocatalytic nucleation of martensite. A stress field, which disperses outside a transformed martensite plate, is potentially capable of triggering unstable martensite embryos to become stable nuclei and then grow up. Zou et al. [26] studied the effects of prior deformation and undercooling on the isothermal bainitic transformation. They found that the pre-deformation provides a mechanical driving force, which further enhances the nucleation rate of bainite transformation, in addition to stresses internally generated by the dislocation density when new bainite plates are formed. Moreover, the difference in the activation energies between grain boundary nucleation and autocatalytic nucleation is proposed by Ravi et al. [27]. The autocatalytic nucleation, which is considered to have a dynamic nature, has been controlled by the degree of carbon enrichment in austenite during the transformation. Nevertheless, an empirical constant, which involves the autocatalytic term, remains undefined with any physical significance.

From the previous studies, it can be concluded that a more precise model of the bainitic transformation, especially for an ausforming process of low-carbon steels, is still to be developed. Thus, in this work, a unified physically based model is derived to thoroughly elucidate the isothermal bainitic transformation, while taking into consideration varying ausforming strain and alloy modifications. The model is derived from the theoretical basis of the displacive transformation concerning a modified T_0 concept and the empirical Koistinen–Marburger (KM) equation. The activation energy, nucleation activity, and carbon enrichment variations caused by the process contributions are also correlated with the kinetics of isothermal bainitic transformation. By means of the model, the thermal stability of austenite can be appropriately adjusted with an optimal design of the processing parameters of the ausforming and alloy modification of low-carbon CFB steels.

2. Materials and Methods

2.1. As-Received Materials

Two as-received low-carbon steels of different compositions were chosen. The steels are identified as MC1.5Mn1NiCr and LC2.5Mn0.2NiCr steels. The chemical compositions of both steels are represented in Table 1. Manganese as the former austenite element was added to increase the stability of the retained austenite and properly elevate the hardenability of the steels. Silicon was alloyed in the amount of 1 wt.% for retarding and suppressing the formation of cementite in the bainitic structure so that retained austenite as a secondary phase was promoted. The addition of boron was to provide a shift of the diffusion-controlled ferrite/pearlite transformation to a longer time. A precipitation of

boron nitride in solid solution was suppressed by alloying titanium of about 0.03 wt.%, whereas the interaction of nitrogen and titanium in the form of titanium nitride (TiN) could be formed. The steels were individually melted in a laboratory-scale vacuum arc furnace and cast into a square ingot with a dimension of $140 \times 140 \times 525$ mm. Afterwards, the ingots were homogenized at 1250°C for 2 h, then hot-forged into square billets with a dimension of $60 \times 60 \times 1000$ mm at a finishing temperature of 950°C . The billets were slowly cooled down to room temperature. Finally, the homogenized billets were cut parallel to the forged direction to manufacture cylindrical specimens of 10 ± 0.1 mm height and 5 ± 0.1 mm diameter.

Table 1. Chemical composition of the investigated steels in wt.%.

Steel	Fe	C	Si	Mn	Cr	Ni	B	Ti
MC1.5Mn1NiCr	Bal.	0.26	1.07	1.46	0.99	0.98	0.0031	0.027
LC2.5Mn0.2NiCr	Bal.	0.18	0.97	2.50	0.20	0.21	0.0018	0.033

2.2. Experiment

The cylindrical specimens were subjected to three different heat treatment conditions. These heat treatments are distinguished between quenching and isothermal tempering, with and without austenite deformation, as follows: direct quenching (DQ), pure isothermal tempering (PIT), and ausforming followed by isothermal tempering (AIT). All heat-treating experiments were conducted on a Bähr DIL805A/D dilatometer. The machine was additionally equipped with an optical module for cross-sectional measurement, which enabled a precise investigation of the phase transformations by monitoring changes in the length of the specimen in the longitudinal and radial directions. A Pt/Pt–10 Rh thermocouple (type S) was spot-welded at the central edge of the specimens so that the temperature signal was accurately gathered from the machine. The experiments were conducted within a vacuum chamber where the specimens were located in the middle between two quartz rods inside an induction coil. A cooling gas, e.g., helium, was directly fed into the chamber through a pressure control valve. The desired temperature could be achieved by balancing the heating coil and the cooling gas. A deformation module was also installed for uniaxial compression tests. As a result, the relative volume strains were determined by considering the profile variations of the specimens in the radial and longitudinal directions, as follows [28,29].

$$\Delta V/V_0 = (1 + \varepsilon_L)(1 + \varepsilon_R)^2 - 1 \quad (1)$$

where ΔV represents the volume change of specimen, V_0 is the initial volume, ε_L is the longitudinal strain, and ε_R is the radial strain of the specimen.

For all the experiments, the specimens were first heated to the austenitizing temperature at 950°C , at the rate of 18°C/s , and soaked for 5 min for homogenization. The PIT specimens were subsequently cooled to 400°C at a cooling rate of 50°C/s and isothermally treated for 1 h before cooling to room temperatures at 20°C/s . The AIT specimens were cooled after homogenization to a deformation temperature of 650°C at the same rate and held for 10 s. The specimens were subsequently deformed with an ausforming strain of either of 0.15 (AIT0.15) or 0.35 (AIT0.35), at a rate of 1 s^{-1} , and cooled to the isothermal temperature within the same period, as was conducted for the PIT samples. To examine changes in the martensite start (M_s) temperature, a specimen of each material was directly quenched from the austenitizing temperature. It was defined as the DQ specimen, and the volumetric expansion result was set as a reference. The M_s locus of the DQ specimens was captured from the first deviation of the dilation curve during cooling, whereas that of the AIT specimens was traced in the same manner specifically during the secondary stage of cooling after isothermal tempering. In the case of the DQ specimens, the volumetric transformations of the martensite were calculated by using a total volumetric expansion with respect to the relative tangent of the dilatation curve as a reference, bearing in mind

that in this research the M_s temperature was also empirically estimated, using the following equation [30,31].

$$M_s = 539 - 423x_C - 30.4x_{Mn} - 7.5x_{Si} + 30x_{Al} \quad (2)$$

where x_C , x_{Mn} , x_{Si} , and x_{Al} are the carbon, manganese, silicon, and aluminum contents in wt.%, respectively. The specimens for evaluating the prior austenite grain (PAG) were directly quenched from the ausforming stage to room temperature.

2.3. Characterization

In the beginning, the specimens were ground and polished with abrasive papers (grids no. 600, 1200, 2400, and 4000) and 0.1 μm diamond paste, respectively. For the PAG observation, they were chemically etched using 4 g of sodium dodecylbenzene sulfonic acid in 100 mL of aqueous saturated picric acid diluted in 100 mL of distilled water in a water bath. The optimized temperature and time for etching were 60 °C and 30 s, respectively. After etching, the average grain size of PAG (d_γ) was measured on a light optical microscope (LOM) and calculated by using the linear intercept method based on the ASTM112-12 standard [32]. The same preparation techniques were applied to the specimens for phase quantification by X-ray diffraction (XRD) measurement, except for the solution etching. Hence, after the polishing step, all the specimens were further electro-polished by means of a TenuPol-5 single-jet electro-polishing device. An A2 electrolyte was employed at room temperature with a voltage of 32 V and a flow rate of 15 mm/s. The XRD machine was operated using a filtered $\text{CrK}\alpha$ radiator at 40 kV and 30 mA, under the collection range between 60° and 165°, at a step width of 0.08° and a counting time of 2 s. The phase fractions of face-centered cubic (FCC) RA and body-centered cubic (BCC) bainitic ferrite or/and martensite were analyzed by the Rietveld's refinement method, using MAUD software. The carbon concentration of the retained austenite (x_C in wt.%) was estimated from its lattice parameter (a_γ), as given in Equation (3) [33]. The parameters x_{Ni} , x_{Cr} , x_N , x_{Co} , x_{Cu} , x_{Nb} , x_{Mo} , x_{Ti} , x_V , and x_W are the nickel, chromium, nitrogen, cobalt, copper, niobium, titanium, vanadium, and tungsten contents in wt.%, respectively.

$$a_\gamma(\text{\AA}) = 3.5780 + 0.0330x_C + 0.00095x_{Mn} - 0.0002x_{Ni} + 0.0006x_{Cr} + 0.0056x_{Al} + 0.0220x_N + 0.0004x_{Co} + 0.0015x_{Cu} + 0.0051x_{Nb} + 0.0031x_{Mo} + 0.0039x_{Ti} + 0.0018x_V + 0.0018x_W \quad (3)$$

Apart from phase quantification, the Rietveld method, which involves the Fourier analysis of the broadened peaks, was used to evaluate the microstructure parameters, such as the effective crystallite size and the average microstrain within the crystal [34]. Considering the plastically deformed materials, the Popa model was used to deconvolute the size and strain effect in the deformed crystals in accordance with the anisotropic size-strain broadening [35]. The peak shifting, broadening, and asymmetry experienced by the line profiles because of the accumulation of irradiation defects were analyzed using the Warren model [36]. The dislocation density due to the crystallite size contribution (ρ_C) was defined as the length of dislocation line per unit volume of crystal and could then be estimated using the Williamson and Smallman relation [37].

$$\rho_C = 3/D^2 \quad (4)$$

where D is the average crystal size. On the other hand, the dislocation density due to the contribution of the microstrain (ρ_S) was evaluated by the following relation.

$$\rho_S = k \frac{\langle \varepsilon_1^2 \rangle}{b^2} \quad (5)$$

where k is a material constant ($k = 0.9$ for cubic crystal), ε_1 is the microstrain within the crystal domain, and b is the Burger vector. Likewise, the average dislocation density (ρ) could be estimated from the relationship given as follows.

$$\rho = \sqrt{\rho_C \rho_S} \quad (6)$$

In order to determine the dislocation density for the bainitic transformation range, only the PIT, AIT0.15, and AIT0.35 specimens were taken into consideration. The dislocation density value of the PIT specimen was used as a reference and further compared with that of each AIT specimen so that the dislocation density influenced by the ausforming strain was calculated.

3. Transformation Models

3.1. Transformation Models

According to the thermodynamic principle of bainitic transformation [3,38,39], it has been suggested that if bainite forms under the displacive approach, the transformation can occur when the criteria of $\Delta G_m < \Delta G_N$ and $\Delta G^{\gamma \rightarrow \alpha} < -G_{SB}$ are satisfied. The first criterion is defined for the nucleation process, and the latter is for displacive growth. ΔG_m represents the maximum driving force available for the para-equilibrium nucleation. ΔG_N is the universal nucleation function, which was experimentally determined by Ali and Bhadeshia [40]. $\Delta G^{\gamma \rightarrow \alpha}$ is associated with a stored energy difference between austenite and bainite, and G_{SB} is a stored energy of bainite, which is usually considered to be 400 J/mol. A further suggestion is that ΔG_m and $\Delta G^{\gamma \rightarrow \alpha}$ are dependent on the chemical compositions of steel and undercooling [3]. The temperatures at which $\Delta G_m = \Delta G_N$ and $\Delta G^{\gamma \rightarrow \alpha} = -G_{SB}$ are called the T_h and T'_0 temperatures, respectively. Hence, it is understood that bainitic transformation can only occur when the transformation temperature is below both temperatures. In any silicon-rich steels in which the formation of cementite is most likely impossible, the concept of T'_0 can be used to indicate the incompleteness phenomena of bainitic transformation. This is with respect to carbon, which is only enriched into the adjacent austenite, instead of forming cementite, during the decomposition of austenite into bainite. The temperature is thus defined as a locus where the enrichment process of carbon ceases [10,41]. For steels subjected to ausforming, a prior austenite grain is subdivided into several sub-grains by plastic deformation such that it gives a greater defects per unit volume in an austenite grain, as shown in Figure 1a. The sub-grain boundaries acting as additional defects give rise to more nucleation sites which will then facilitate the bainitic transformation. Therefore, the deformation leads to an increase in austenite free energy and enables more carbon enrichment in austenite at the beginning stage of the transformation. However, on the other hand, the dislocations generated by the growth process will arrest the transformation as it reduces the austenite free energy, as presented in Figure 1b.

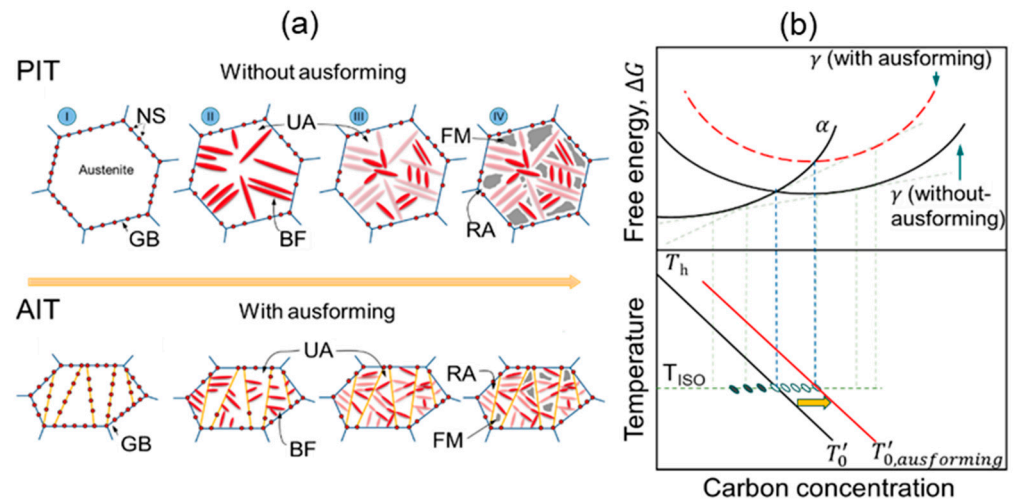


Figure 1. (a) Graphical illustrations of the isothermal decomposition of austenite into bainite for PIT and AIT specimens, and (b) schematic diagram showing relationships of Gibbs free energy, temperature, and composition of steels under various heat treatments. NS, GB, UA, BF, and FM stand for nucleation site, grain boundary, untransformed austenite, bainitic ferrite, and fresh martensite, respectively.

3.1.1. Nucleation Rate Model

By the displacive approach, the kinetics of the bainitic transformation is controlled by a nucleation rate reaction. Firstly, sub-units of bainitic ferrite (BF) are formed by activated nucleation at the interfaces of the austenite grain boundary (γ/γ interface) and the subsequent autocatalytic nucleation on the pre-existing platelets surrounding the UA (γ/α interface) [27]. The former process incorporates prior austenite grain, while the latter is essential for the growth of BF sheaves, which might arise spontaneously at the tip of previously formed sub-units due to elastic and plastic strain generations within the surrounding austenite [42]. According to this hypothesis, the processes have successively continued to form bainitic sheaves until their evolutions were arrested by the mechanical stabilization of austenite. Therefore, the development of these nucleation mechanisms can be expressed as follows.

$$\left(\frac{dN}{dt}\right)_t = \left(\frac{dN}{dt}\right)_{GB} + \left(\frac{dN}{dt}\right)_{AN} \quad (7)$$

where (dN/dt) is the total nucleation rate per unit volume, $(dN/dt)_{GB}$ and $(dN/dt)_{AN}$ are the nucleation rate per unit volume arising at the austenite grain boundaries and that caused by the autocatalytic nucleation, respectively. Considering the individual nucleation rate reaction, the density of the potential nucleation sites and the activation energy play a vital role in describing the principle of the nucleation kinetics, which is expressed by Equation (8).

$$\left(\frac{dN}{dt}\right)_i = \frac{k_B T}{h} N_i \exp\left(\frac{Q_i^*}{RT}\right) \quad (8)$$

where the subscript i represents either a nucleation process at the grain boundary (GB) or the successive nucleation by autocatalytic reaction (AN). k_B is the Boltzmann's constant, T is the isothermal transformation temperature, h is the Plank's constant, N_i is the number of potential nucleation sites at the very beginning stage, R is the gas constant, and Q_i^* is the activation energy required for the individual nucleation process. With respect to the original Koistinen–Marburger (KM) equation [43], Van Bohemann and Seitma indicated that the nucleation density is associated with the net driving energy and undercooling [22]. The driving energy is associated with thermodynamic activation, and it thus requires two atomic processes to trigger the reaction. On the one hand, the dissociation of certain

dislocation defects may partially facilitate sites for BF embryos. On the other hand, the enrichment of carbon into the surrounding austenite matrix allows a necessarily available driving force for the nucleation.

3.1.2. Activation Energy

As the activation energy accounts for the thermodynamic requirements of the nucleation processes, any energies stored within the parent phase can be presumed to be the parts of the energy barrier necessary for the isothermal transformation. As reported by Olsen and Cohen [44], the activation energy can be determined independently with the free energy sum, as expressed by Equation (9).

$$Q_i^* = Q_0^* + K_1 \Delta G_i \quad (9)$$

where Q_0^* is considered to be the activation energy when the nucleation process is absent, given here as a fitting parameter. However, Q_0^* can be also used to estimate the existing energy required for the phase transformation when no chemical energy is involved and only the effects of undercooling and ausforming are occupied; K_1 is a fitting parameter in the model; and ΔG_i is the total molar driving force of the associated event of nucleation.

In the present study, the extra stored energy due to the deformation of austenite is formulated based on the assumption that no dynamic recrystallization occurred. Thereby, the deformation likely introduces only two energy portions to the austenite, namely the grain boundary and the change of dislocation energy. The variation of these energies depends on two factors. Firstly, the deformation elongates the austenite grains and enhances the grain boundary areas. Secondly, the deformation increases the disorder of the grain structure, which leads to an increase in the grain boundary energy per unit area ($\sigma_{\gamma/\gamma}$), roughly 10% [45,46]. Note that it is not significantly increased if the deformation stress is relatively small. However, the total driving energy required for the grain boundary nucleation is not included the effect of an increase in the number of nucleation sites because it is already involved in the initial activation energy term. The total molar driving force can thus be represented by Equation (10).

$$\Delta G_{GB} = \Delta G_{ch} + \Delta G_{\gamma/\gamma} \quad (10)$$

where ΔG_{ch} is the difference in thermodynamic Gibbs free energy between the austenite and the bainite, determined by using the MUCG83 database [47], and $\Delta G_{\gamma/\gamma}$ is the semi-coherent interfacial energy of the γ/γ interfaces required to overcome its barrier, which can be expressed as the following relationship.

$$\Delta G_{\gamma/\gamma} = 2V_{mol} \frac{\sigma_{\gamma/\gamma}}{nd} \quad (11)$$

V_{mol} is the molar volume of austenite, $\sigma_{\gamma/\gamma}$ is the semi-coherent interfacial energy at the γ/γ interfaces, n is the number of FCC cubic planes along the nucleus thickness, and d is the spacing between the cubic planes, which equals 2.5×10^{-10} m for the FCC planes [44].

Considering the spontaneous association of the nucleation events, the driving force is related to the elastic and plastic stresses generated in the adjacent austenite. In addition to the chemical driving energy change owing to the variations of carbon in BF, the stored energy associated with the stress field can also provide a particular strain accompanying the stress-energy in the surrounding austenite, due to the dislocation barrier that significantly affects the bainitic transformation. Consequently, the semi-coherent interfacial energy between austenite and bainite (γ/α interfaces), established by Dong et al. [45], is a straightforward representation of the subsequent stage of the transformation. Therefore, the total

driving energy required for the iterative dynamic nature of the autocatalytic nucleation is represented by Equation (12).

$$\Delta G_{AN} = \Delta G_{chA} + \Delta G_{\gamma/\alpha} + G_{dislo} \quad (12)$$

Parameter ΔG_{chA} is the chemical free energy change depending on the degree of carbon enrichment in the austenite. $\Delta G_{\gamma/\alpha}$ is the semi-coherent interfacial energy between the austenite and bainite (γ/α interfaces). G_{dislo} is the dislocation interaction energy because of the bainitic stress field. The carbon rejected from BF during the transformation is thus specified by the chemical driving energy reduction, while the interfacial energy at the γ/α interfaces is neglected afterwards because its influence is negligible compared to the other factors [44]. Rees and Bhadeshia [20] suggested that the decrease in total energy change is caused by a mechanically induced stabilization surrounding the enrichment zone. Thus, the chemical energy change is then determined as shown in Equation (13).

$$\Delta G_{chA} = \Delta G_{chAi} \left(1 - d_s \times \left(\bar{w} + f_\alpha \frac{(\bar{w} - w_\alpha)}{(1 - f_\alpha)} \right) \right) \quad (13)$$

ΔG_{chAi} is the initial free energy change at the beginning of the transformation or grain boundary nucleation. d_s is a constant considered as a fitting parameter in the model. \bar{w} is the average carbon concentration of steel in wt.%. f_α is the fraction of bainite formed during the transformation. w_α denotes the fraction of carbon entrapped in the bainite, either in solid solution or in a form of iron carbide, depending on the condition of the applied heat treatment and the ability of the carbon enrichment in the austenite due to the alloy addition. For the interaction energy of the bainitic stress field mentioned above, it can be given as follows.

$$G_{dislo} \approx -\frac{3E^\gamma}{2(1+\nu)} (\epsilon_{22}^{tr})^2 \quad (14)$$

where ϵ_{22}^{tr} represents the internal elastic strain state resulting from the local strain incompatibility between the bainite and austenite, E^γ is the elastic modulus of austenite, and ν is the Poisson's ratio of austenitic steel (0.27). From Equation (9)–(14), the formation of the total energy difference required for activating the transformation at each iteration can be determined as follows.

$$\Delta Q^* = Q_{GB}^* - Q_{AN}^* \quad (15)$$

It is noted that the physical basis of such autocatalytic factors has been not adequately given in the current reported literature. Hence, the proposed model provides more details describing the particular net free energy changes caused by the elemental partitioning, particularly when the effect of ausforming is considered.

3.1.3. Potential Nucleation Site Density

In this model, the number density of the potential nucleation sites is estimated based on the original concept of Magee for athermal martensitic transformation [21]. It is reported to be linearly dependent on the undercooling temperature. In this regard, Van Bohemann and Seitsma [48] validated the increase in undercooling with a reduction in the M_s temperature due to carbon content. The higher density of nucleation sites results from the driving energy, which is increased when decreasing the transformation temperature of martensite. This concept is later reformulated to be applicable to an isothermal transformation and is given by the following expression.

$$N_0 = \varnothing(G_N(T_h) - G_N(T_{iso})) = \xi \Gamma (T_h - T_{iso}) \quad (16)$$

By analogy with the work of Magee on martensite nucleation, ξ is equal to $\alpha/(V_\alpha \Gamma)$. α is a material constant, and Γ is determined by the slope of $d(\Delta G_m)/dT$, which is approximately constant in the temperature range of martensitic/bainitic transformation. V_α represents the average volume of the bainite sub-unit [20,22]. T_h is the highest temperature

at which the displacive transformation occurs. Because of the experimental investigations, the number density of the pre-existing defects can be calculated by Equation (17).

$$N_i = \frac{m}{V_\alpha} (T_h - T_{iso}) \quad (17)$$

m is the proportionality constant between the number density of the bainite nucleation sites and the degree of undercooling. In the case of martensite formation, m and α are assumed to be identical and are used as material parameters. Their values are between 0.01 and 0.07 K⁻¹ and depend slightly on the chemical composition [21,43]. A fundamental difference between the nucleation of martensite and bainite is that the density of the pre-existing defects for martensite nucleation is governed by the prior austenitic grain size, whereas the bainitic nucleation is also controlled by the structural interfaces, namely the γ/γ and γ/α interfaces. According to Van Bohemann and Seitma's report [22], m can be replaced by b_{GB} and b_{AN} with consideration of the effects of the γ/γ and γ/α interfaces, respectively. The density of the available γ/γ interfaces is dependent on the volume fraction of the remaining available austenite and the austenite grain size. The b_{GB} parameter is thus given as follows.

$$b_{GB} = \frac{Z\delta}{d_\gamma} m f_\gamma \quad (18)$$

The proportional relationship of $Z\delta/d_\gamma$ is defined as the austenite grain boundary area per unit volume, in which δ and d_γ denote the effective thickness of the prior austenitic grain boundary and the austenitic grain size, respectively. f_γ represents the fraction of the UA. In addition, when the effective thickness of the austenitic grain boundary is considered as the atomic layers of a grain in the grain boundary region, a few of the outermost atomic layers in each grain can be presumed to participate in the nucleation process. Hereby, it is suggested that an austenitic grain size is composed of two atomic layers in each grain. With regard to the autocatalytic parameter represented by b_{AN} , it is controlled by the remaining available austenitic phase fraction, at which the α/γ interfaces are formed while the bainitic transformation progresses. The parameter can therefore be given by the following equation.

$$b_{AN} = \frac{Z\delta}{d_\gamma} m f_\gamma f_\alpha \quad (19)$$

where f_α represents the volume fraction of BF. In summary, the size of the BF sub-units has an inverse relationship with the density of the nucleation sites and the remaining available austenite grains.

3.1.4. Austenitic Phase Fraction as a Function of Carbon Enrichment

As shown in Equations (17) and (18), the variations of f_γ and f_α are the critical factors when estimating the density of the nucleation sites. It is kinetically changed during the formation of BF due to the carbon enrichment in the austenite. If the stored energy of bainite caused by shear transformation is involved, the process should be completely terminated at the T'_0 locus where the free energies of austenite and bainite are identical, as presented in Section 3.1. By this concept, the conservation of mass balance in the bainite and austenite can be applied, and the variation of carbon concentration in the austenite associated with the locus can be given as follows.

$$w_\gamma = \bar{w} + f_\alpha \frac{(\bar{w} - w_\alpha)}{(1 - f_\alpha)} \quad (20)$$

\bar{w} represents the bulk carbon concentration of steel, and w_α is the composition of carbon in a BF sub-unit. Ravi et al. [27] used the same concept to determine the bainitic

transformation temperature and found that the temperature linearly reduces with the increased carbon content in austenite, as provided in Equation (21).

$$T_h = T_{h\bar{x}} - C_1 \frac{(\bar{w} - f_\alpha w_\alpha)}{(1 - f_\alpha)} \quad (21)$$

where $T_{h\bar{x}}$ is the T_h temperature at the beginning of the transformation and is determined using thermodynamic calculation software called MUCG83 [47], and C_1 is a proportional constant relating T_h and the carbon concentration.

Moreover, the total fraction of UA, f_γ , is estimated by considering the T'_0 locus as being determined for the carbon enrichment. In this regard, a certain amount of austenite may not participate in the bainitic reaction and yields the incomplete phenomenon. It is assumed that the unavailable austenite certainly contains no potential nucleation site due to its stability. This fraction is thus subtracted while calculating the overall nucleation rate. Using the principles of the incomplete reaction phenomenon, f_γ and T'_0 can be expressed as follows.

$$f_\gamma = (1 - f_\alpha) \frac{(T'_0 - T_{iso})}{(T'_{0\bar{x}} - T_{iso})} \quad (22)$$

$$T'_0 = T'_{0\bar{x}} - C_2 f_\alpha \frac{(\bar{w} - w_\alpha)}{(1 - f_\alpha)} \quad (23)$$

where $T'_{0\bar{x}}$ is the T'_0 temperature at the beginning of the transformation, and C_2 is a proportional constant relating to T'_0 and the carbon concentration. Note that the influences of ausforming on the free energy change of austenite are not incorporated here due to the complexity of the implementation.

3.1.5. Bainitic Transformation Model

From Equations (7) to (23), the overall nucleation kinetics of the isothermal bainitic transformation can be summarized by the following equation.

$$\left(\frac{dN}{dt}\right)_t = \left(\frac{k_B T}{h} \frac{Z\delta}{d_\gamma} \frac{m}{V_\alpha} (1 - f_\alpha) \frac{(T'_0 - T_{iso})}{(T'_{0\bar{x}} - T_{iso})} (T_h - T_{iso}) \left\{ \exp\left(-\frac{Q_{GB}^*}{RT}\right) \right\} \{1 - \lambda f_\alpha\}\right) \quad (24)$$

The variable λ in this equation is represented by $\exp(\Delta Q^*/RT)$ as an autocatalytic factor. It plays an important role in the kinetics of bainitic transformation and mainly relies on the activation energy difference of the nucleation process. Thus, the autocatalytic function termed by $\{1 - \lambda f_\alpha\}$ can be given as the β parameter, which is similar to that defined in the literature [20,49]. As discussed earlier, the parameters w_α , d_s , ΔQ^* , and K_1 are given as the fitting parameters in this model, from which their physical significances can be defined.

In order to estimate the volume fraction of BF, it can be presumed that BF sheaves are formed by stacking sub-unit layers on the iterative sites of the nucleation and are therefore dependent on the number of nucleated sites. Nonetheless, the volume of a BF sub-unit examined by Matsuda and Bhadeshia [19] is not a constant value, it changes depending on the transformation temperature, which is given as follows.

$$V_\alpha = \left(2 \times 10^{-17}\right) \times \left(\frac{T_{iso} - 528}{150}\right)^3 \quad (25)$$

where V_α represents the average volume of a BF sub-unit in m^3 . Consequently, the kinetics of the isothermal bainitic transformation can be calculated by means of a numerical integration of the associated nucleation rates. The product of the integration is given by the following equation.

$$f_\alpha = \int \frac{dN}{dt} V_\alpha dt \quad (26)$$

3.2. Martensitic Transformation

As reported in a previous study [16], the UA after isothermally formed BF is not thermodynamically stable. It can be transformed to FM during ambient cooling because of the low carbon content. Therefore, only the overall kinetics equation for predicting all existing phases in the steel may not be satisfactory. To incorporate the course of martensitic transformation, the conventional KM equation [21,43,50] was modified based on Lee's equation [51] and further developed according to the fact that martensite does not directly transform from a fully austenite. The certain area of the untransformed product of austenite can be expressed as follows.

$$f_{\text{FM}} = (f_{\text{UA}}) - e^{-\alpha_{\text{FM}}(M_{\text{s,UA}} - T_{\text{RM}})^n} \quad (27)$$

f_{UA} is the phase fraction of UA and is equivalent to $1 - f_{\alpha}$. α_{FM} is a material parameter, which is calculated from the data reported for low-carbon steels with a high concentration of silicon and chromium [51], as given in Equation (28); $M_{\text{s,UA}}$ is a martensite start temperature after the isothermal tempering, indicated as being equal to M_{S}' ; and T_{RM} is room temperature. Moreover, n is also a material constant that depends on the chemical composition, as shown in Equation (29). Finally, the empirical equation of martensitic transformation can be written by Equation (30), where f_{RA} and f_{FM} are the volume fraction of the retained austenite and martensite after cooling, respectively.

$$\alpha_{\text{FM}}(K^{-1}) = 0.0231 - 0.0105x_{\text{C}} + 0.0074x_{\text{Cr}} - 0.0017x_{\text{Ni}} - 0.0193x_{\text{Mo}} \quad (28)$$

$$n = 1.4304 - 1.1836x_{\text{C}} + 0.7527x_{\text{Cr}}^2 - 0.739x_{\text{Si}} - 0.0258x_{\text{Ni}} + 0.3108x_{\text{Mo}} \quad (29)$$

$$f_{\text{UA}} = f_{\text{RA}} + f_{\text{FM}} \quad (30)$$

4. Results and Discussion

4.1. Experimentally Determined Phase Fractions

In our previous studies [16,52], no carbide precipitation was found in the examined steels with minimized alloys of around 1 wt.%Si. Therefore, the final microstructures of steel should comprise BF and RA ($\alpha + \gamma$), unless the enrichment of carbon in the UA after the bainitic transformation is thermodynamically unstable. In this circumstance, the UA can be partially decomposed to FM (α'), and the heterogeneous microstructure composed of $\alpha + \gamma + \alpha'$ consequently appears. Under thermodynamic equilibrium, the average carbon concentration in the microstructure components of steel could be expressed by $w_{\alpha}f_{\alpha} + w_{\gamma, \text{RA}}f_{\gamma, \text{RA}} + w_{\alpha'}f_{\alpha'} = \bar{w}$, where the quantity of w_{α} , $w_{\gamma, \text{RA}}$, and $w_{\alpha'}$ represents the carbon distribution in BF, RA, and FM, respectively, and \bar{w} is the bulk carbon content of the steels. Figure 2a illustrates the results of the XRD measurements of MC1.5Mn1NiCr steel with and without ausforming. Only the phases belonging to the body-centered and face-centered structures were quantified. The bainitic, ferritic, and martensitic phases that possessed the BCC structure were displayed all together on the same crystallographic planes. The RA whose peaks appeared at the (111), (200), (220) planes was apparently observed, especially in the case of the PIT and AIT specimens, whereas the identical peaks of BF and FM exposed at the (110), (200), and (211) planes were not distinguishable. Thus, the volumetric strain response in the DQ and PIT specimens were exploited together with the volumetric fraction of the BCC obtained by the XRD measurement so that the volumetric fractions of all the constituents could be quantified rationally. Figure 2b shows that the M_{S} temperature could be determined at the point where the cooling curve started to deviate from its tangent. A vertically measured distance between the tangent and the cooling curve at the final cooling temperature of the DQ results was given as the reference and accounted for the maximum volumetric expansion of the martensitic transformation. By comparing the reference value with the volumetric expansions for the AIT specimen using

the lever rule, the martensitic phase fraction of the AIT specimen could be estimated by Equation (31).

$$f_{\alpha'}(\text{AIT}) = \frac{f_{\alpha'}(\text{DQ, XRD}) \times \alpha'(\text{AIT, DIL})}{\alpha'(\text{DQ, DIL})} \quad (31)$$

where $f_{\alpha'}(\text{DQ, XRD})$ represents the volume fraction of martensite acquired from the XRD measurement, and $\alpha'(\text{AIT, DIL})$ and $\alpha'(\text{DQ, DIL})$ are the volumetric strains obtained from the dilatation curves of the AIT and DQ specimens during cooling, respectively. As aforementioned, the total phase fraction of BF was further evaluated from the curve for the change in volume strain at the time where the BF transformation was terminated (distance AB, shown in Figure 3). With help of Equation (30), the amount of UA in the AIT specimen was calculated from the summation of the RA fraction quantified by the XRD analysis and the FM fraction from Equation (31). Subsequently, the distance BC, with regard to the UA volume fraction, was obtained by referring the distance AC to the volume fraction of all the phases. Finally, the proportionality of the dilatation locus was applied to determine the kinetics evolution of the bainitic phase transformation.

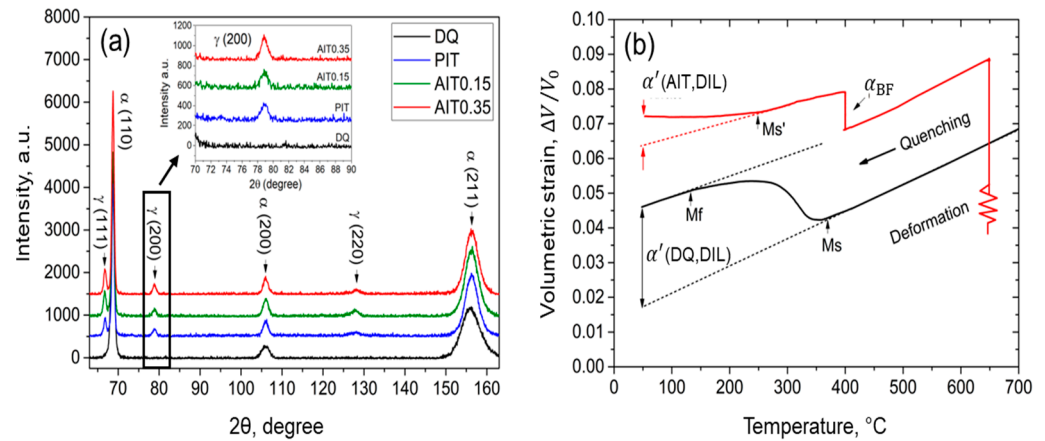


Figure 2. (a) Phase quantifications of examined steels using XRD measurement and (b) volumetric strain of DQ and AIT specimens after cooling from austenitizing and deformation stage.

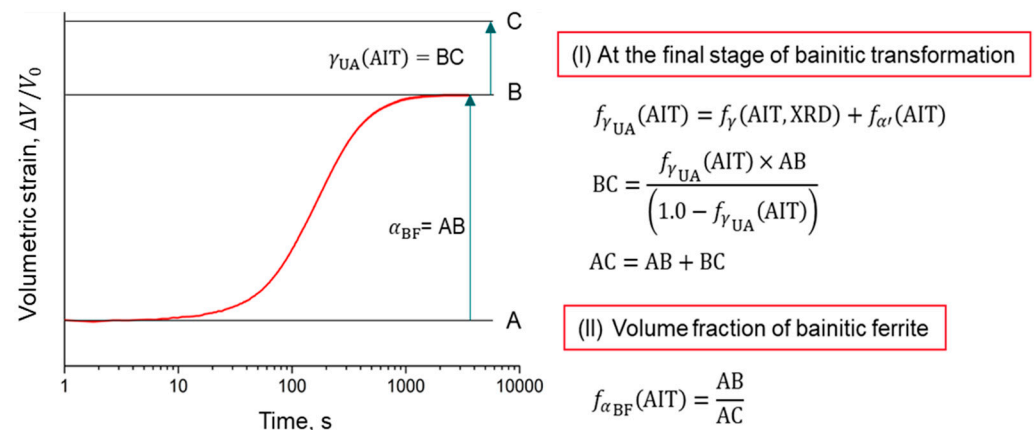


Figure 3. Determination of the volume fraction of bainitic ferrite during tempering at 400 °C.

From the calculations, as shown, the percentage of the developed phases, the amount of carbon enrichment in the austenite in wt.% ($w_{\gamma,RA}$), the martensite start temperature ($M_{s,exp}$) of the steels subjected to the DQ, PIT, and the AIT heat treatments were gathered, as listed in Table 2. It is noteworthy that the prior deformation and its degree have played the primary role in enhancing the stability of austenite and have resulted in a decrease in the BF fraction. However, the stabilized austenite in MC1.5Mn1NiCr steel, which had a higher carbon content and low alloyed Cr and Ni contents, was not always sustained

along the AIT process, especially when some UA decomposed into FM during cooling. The ausforming strains caused extreme deterioration of the thermodynamic stability of austenite, leading to a greater formation of FM with a slight reduction in the RA fraction. It seems that ausforming only influenced the FM formation, whereas the variation of RA was negligible.

Table 2. Volume phase fraction determined by means of quantitative analysis of XRD measurement combined with the dilatometry results.

Material/Condition	Volume Fraction, %			$w_{\gamma,RA}(=x_C)$ Equation (3)
	RA	BF	FM	
MC1.5Mn1NiCr/DQ	-	-	100	-
MC1.5Mn1NiCr/PIT	15.6 ± 3.3	77.4 ± 4.2	7.0 ± 2.8	0.78
MC1.5Mn1NiCr/AIT0.15	14.6 ± 5.1	62.0 ± 6.7	23.4 ± 6.3	0.68
MC1.5Mn1NiCr/AIT0.35	13.5 ± 5.8	47.9 ± 4.5	38.6 ± 3.4	0.56
LC2.5Mn0.2NiCr/DQ	1.2 ± 0.8	-	98.5 ± 2.8	0.04
LC2.5Mn0.2NiCr/PIT	8.5 ± 2.5	83.6 ± 4.6	7.9 ± 3.9	0.45
LC2.5Mn0.2NiCr/AIT0.15	11.3 ± 3.7	77.6 ± 3.4	11.1 ± 4.5	0.51
LC2.5Mn0.2NiCr/AIT0.35	16.9 ± 3.5	74.3 ± 4.9	8.8 ± 4.1	0.89

Meanwhile, it is somewhat surprising that increasing the ausforming strain in the LC2.5Mn0.2NiCr specimens undergoing AIT treatment was quite effective for suppressing the phase transformation. The enrichment of the dislocation density within the plastically deformed austenite had not only accumulated while ausforming, but remained propagating during the BF formation, resulting in the suppression of the formation of FM, with the leaving of more UA as a residual product. It is also noted that the degree of carbon enrichment in austenite during bainitic transformation was directly subjected to UA stability. It was resisted once the structural stability of UA was improved. The carbon concentrations listed in the table represent the overall carbon contents in RA, which take both the products of carbon enrichment and the partitioning processes into account. Therefore, the $w_{\gamma,RA}$ values should be evaluated further to quantify the exact value at individual stages of the transformations.

4.2. Modelling Results

4.2.1. M_s Temperature

The kinetics parameters and the theoretical start temperatures of martensite determined using the modified KM equation for both MC1.5Mn1NiCr and LC2.5Mn0.2NiCr steels under PIT and AIT conditions are presented in Table 3. Note that the parameters, α_{FM} and n , were dependent on the alloying composition and were not affected by the heat treatment conditions. The calculated values of α_{FM} and n for the MC1.5Mn1NiCr steel were 0.0205 and 0.96, respectively, whereas those for the LC2.5Mn0.2NiCr steel were 0.0243 and 1.06, respectively. The discrepancies between the experimental and the calculated values were highly acceptable. Clearly, the martensitic start temperature significantly depended on the heat treatment conditions and the material. For both steels, the M_s temperatures were decreased markedly with the application of ausforming. In the case of MC1.5Mn1NiCr steel, increasing the ausforming strain caused a slightly higher M_s value. The increased strain deteriorated the stability of the austenite and subsequently led to a higher fraction of FM. In contrast, the stability of the austenite in the LC2.5Mn0.2NiCr steel seemed to be effectively promoted by the enhancing of the ausforming strain in accordance with the lowered transformation temperature of the martensite. It implies that the chemical composition was of importance for adjusting the austenite stability of steel, particularly when carbon as an austenite former element was only the most important factor in controlling the bainitic transformation at low temperature.

Table 3. Determined kinetics parameters using the modified KM equation for the examined MC1.5Mn1NiCr and LC2.5Mn0.2NiCr steels under PIT and AIT conditions.

Material/Condition	α_{FM}, K^{-1}	$n, -$	$M_{s,exp}, C$	$M_{s,cal}, C$
MC1.5Mn1NiCr/DQ	0.0205	0.96	354 ± 5.1	344
MC1.5Mn1NiCr/PIT	0.0205	0.96	347 ± 4.7	332
MC1.5Mn1NiCr/AIT0.15	0.0205	0.96	260 ± 7.1	255
MC1.5Mn1NiCr/AIT0.35	0.0205	0.96	265 ± 6.3	260
LC2.5Mn0.2NiCr/DQ	0.0243	1.06	388 ± 2.4	380
LC2.5Mn0.2NiCr/PIT	0.0243	1.06	351 ± 4.2	345
LC2.5Mn0.2NiCr/AIT0.15	0.0243	1.06	270 ± 3.6	263
LC2.5Mn0.2NiCr/AIT0.35	0.0243	1.06	192 ± 5.8	184

4.2.2. Model Parameters

The input parameters and the critical temperatures calculated by Bhadeshia's program (see Section 3.1.4) are represented in Table 4. It has been seen that the PAGs are decreased by the ausforming treatments and by adding either carbon or other austenite stabilizer elements due to the reduction in the driving energy for grain growth. It is suggested in [45] that the condition of the parent phase controls the driving energy for lower-temperature phase transformation. In general, the energy stored for the nucleation reaction increases with rising the number of nucleation sites and can be considerably dependent on the chemical compositions, undercooling, and prior deformation. If austenite is plastically deformed and more defects are generated as nucleation sites, the primary driving energy of the phase transformation is most probably controlled by nucleation sites increased rather than the other factors. Furthermore, the locus of $T_{h,\bar{x}}$ is hereby broadened as $T'_{0,\bar{x}}$ is suppressed. However, changes in the critical temperature were observed only as a result of the chemical contributions and the undercooling, regardless of the ausforming effect.

Table 4. Parameters used for the transformation models.

Parameter	MC1.5Mn1NiCr			LC2.5Mn0.2NiCr		
	PIT	AIT0.15	AIT0.35	PIT	AIT0.15	AIT0.35
$d_{\gamma}, \mu m$	48 ± 1.5	43 ± 3.3	35 ± 2.1	56 ± 0.9	49 ± 1.4	44 ± 2.2
T_{iso}, K		673			673	
$T_{h\bar{x}}, K$		753			983	
C_1		2304			2205	
$T'_{0,\bar{x}}, K$		763			778	
C_2		8911			8537	

4.2.3. Kinetics of Bainitic Phase Transformation

Figure 4 displays the kinetics of the bainitic transformation of MC1.5Mn1NiCr and LC2.5Mn0.2NiCr steels under PIT and AIT conditions at different ausforming strains. It shows that the calculation results fitted very well with the experimental data. The transformation kinetics presented in Figure 4a,b could be divided into three stages, namely onset, growth, and cessation. The onset was indicated at a locus, at which the first BF sub-units were formed. After that, the growth driven by the shear was kinetically captured by the progress of the BF sheaves. Finally, the transformation stopped when the decomposition of austenite was supersaturated as it reached its plateau. Ausforming had a strong influence on an acceleration of the transformation onset and a reduction in the BF volume fraction. However, for MC1.5Mn1NiCr/AIT0.35 steel, the transformation was somewhat sluggish compared to the other conditions for the same material. This circumstance could be precisely explained by the nucleation rate activity and the driving energy, as given in the next section. According to the fact that ausforming enhances the austenite stability, even though the deformation simultaneously accelerated the transformation, the drastic increase in defect density in UA during the initial progress of bainitic transformation resulted in a

reduction in the BF fraction. The results were consistent with those reported in [18,53,54], particularly in the MC1.5Mn1NiCr steel. It can be seen that increasing the ausforming strain in LC2.5Mn0.2NiCr steel gave a slight difference in the lowering of the fraction of BF. In light of the chemical variations, LC2.5Mn0.2NiCr steel with a lower carbon content with adjusted Cr and Ni alloying elements possessed higher BF fractions than MC1.5Mn1NiCr steel, regardless of the applied ausforming. It could be verified from their bulk carbon contents and the effective enrichment of carbon in austenite. Hence, it was not surprising that the lower carbon steel exhibited smaller fractions of BF, which is similar to [55].

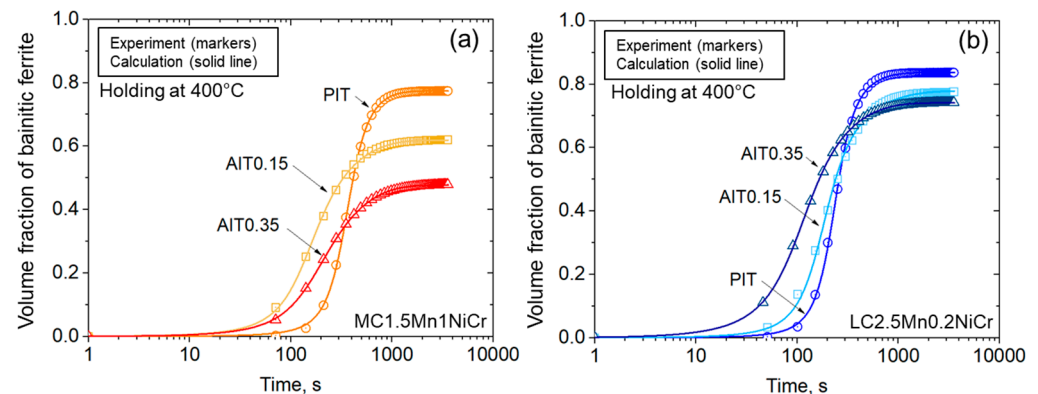
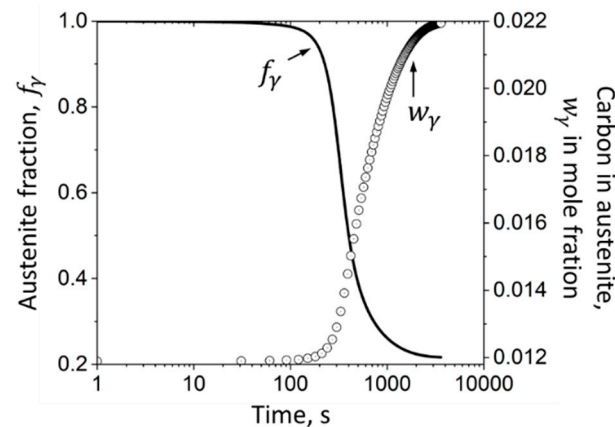


Figure 4. The kinetics of bainitic transformation of (a) MC1.5Mn1NiCr and (b) LC2.5Mn0.2NiCr steels under PIT and AIT with the strain of 0.15 and 0.35.

The fitted values of w_α , d_s , Q_0^* , and K_1 obtained from the proposed model are shown in Table 5. Only w_α and Q_0^* were well explicable with their physical meaning. The reduction of Q_0^* values signified a decreased energy barrier of the nucleation reaction and seemed remarkably diminished by the ausforming. This parameter was associated with the kinetics acceleration of the BF transformation due to the increased number of existing nucleation sites per unit volume in UA. Considering the lower value of Q_0^* presented in the MC1.5Mn1NiCr/AIT0.15 compared with that in the MC1.5Mn1NiCr/AIT0.35, it could be described by the higher number of nucleation sites or defect densities, which essentially contributed in the later stage of the bainitic transformation. In this respect, it was not surprising that the average amount of carbon concentration in the BF supersaturation (w_α) became constricted with regard to the higher kinetics acceleration at the beginning and was most likely associated with more carbon enrichment. However, the w_α values gathered for the present model were invariably smaller than the mean carbon concentration in the mole fraction of both of the examined MC1.5Mn1NiCr and LC2.5Mn0.2NiCr steels, namely 0.01185 and 0.00824, respectively, which is similar to Ravi's work [27]. The silicon and aluminum additions allowed the specific energy for carbon enrichment and enabled austenite to consume with a certain amount of carbon during the enrichment process, as illustrated in Figure 5. By this model, the evolution of carbon enrichment could be evaluated by the rejection of carbon from the supersaturated BF sub-unit during the austenite decomposition. The presence of RA evidenced the effectiveness of the incomplete reaction that occurred when the austenite was stabilized by the carbon enrichment. Nonetheless, the net carbon value calculated from this model could not be directly compared with the corresponding experimental values in Table 2, because the remaining available carbon may be further partitioned during the subsequent transformation of FM.

Table 5. Fitting parameters obtained for the used model.

Parameter	MC1.5Mn1NiCr			LC2.5Mn0.2NiCr		
	PIT	AIT0.15	AIT0.35	PIT	AIT0.15	AIT0.35
w_{α} , mole fraction	0.0091	0.0056	0.00081	0.0060	0.0048	0.0031
Q_0^* , kJ/mole	172.98	166.48	170.9	167.53	164.83	145.74
d_s	1.47	19.26	12.03	1.81	4.36	9.73
K_1	0.46	4.86	7.32	0.36	0.69	1.29

**Figure 5.** Relationship between the austenite decomposition and the degree of carbon enrichment in austenite of MC1.5Mn1NiCr steel with PIT condition.

As previously mentioned in Section 3.1.1, the kinetics of bainitic transformation was governed by the nucleation rate mechanism, i.e., the grain boundary nucleation and the autocatalytic nucleation. The initial nucleation rate was activated by the grain boundary nucleation, which depended only on the density of the nucleation sites. Subsequent nucleation rates were then controlled by the autocatalytic nucleation with regard to the spontaneous dissociation of the specific dislocation defects and the accumulated stored energy of the corresponding dislocations [56]. Moreover, a generation of additional defects by ausforming presumably provided more available sites while simultaneously deteriorating the activation energy of the nucleation. Enhancing the defect densities thus increased the nucleation rate by triggering the transformation onset. The nucleation kinetics of examined steels subjected to different conditions are presented in Figure 6. It was hereby agreed that at the earliest stage of BF formation the driving energy for nucleation was higher than the stabilization effect, owing to the potential nucleation sites, which were generated during either the ausforming or the cooling to the transformation temperature. The formation of BF continued until the driving energy for nucleation and stored energy due to the mechanically stabilized austenite, which became identical at the maximum nucleation rate. Hereafter, the deceleration kinetics occurred, implying that the stability of the neighboring austenite was increased by the successive formations of the BF sub-units, which resulted in a reduction in stored energy for the transformation. This occurrence could be verified by the relationship between the driving energy for the autocatalytic nucleation and the corresponding number of nucleation sites, as depicted in Figure 7. It is noteworthy that the nucleation rates and the driving energy values of LC2.5Mn0.2NiCr steel were all lower than those of the MC1.5Mn1NiCr steels, regardless of the heat-treated condition. This result was likely caused by the elemental distribution, which was similar to that observed in an experimental validation proposed by Wang et al. [4].

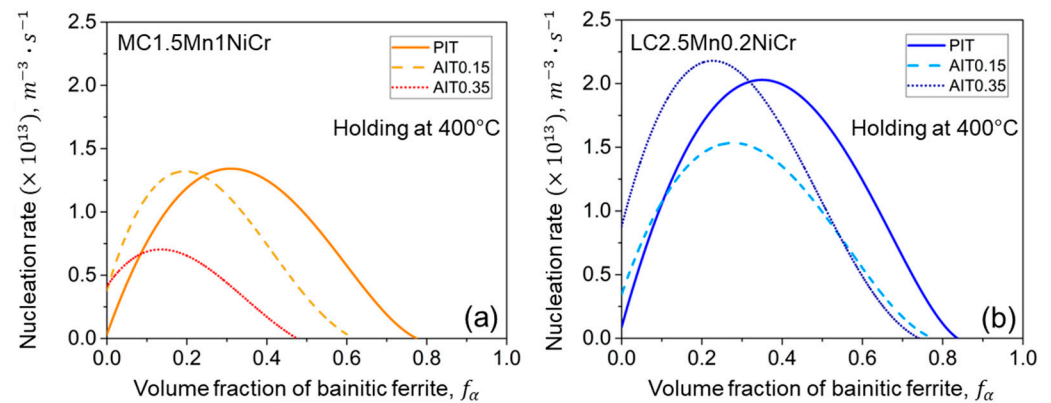


Figure 6. Nucleation rate as a function of BF volume fraction for (a) MC1.5Mn1NiCr and (b) LC2.5Mn0.2NiCr steels under various conditions.

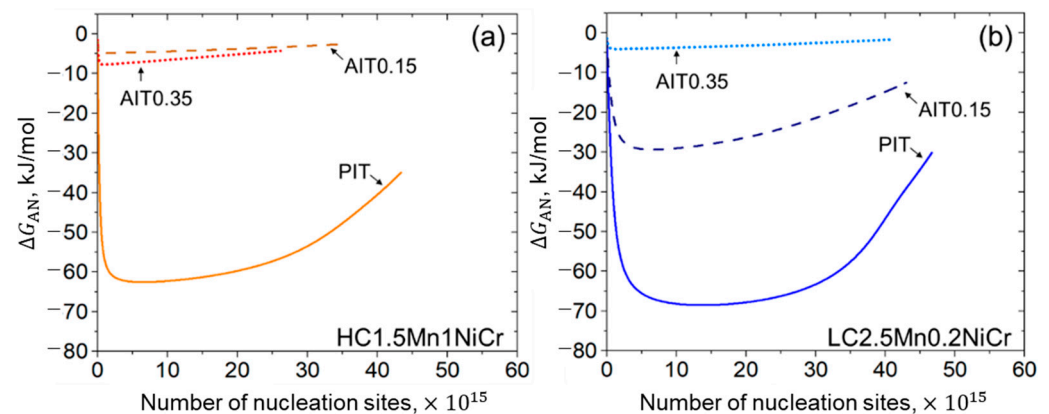


Figure 7. Driving force for autocatalytic nucleation as a function of density of nucleation sites of (a) MC1.5Mn1NiCr and (b) LC2.5Mn0.2NiCr steels under various conditions.

The autocatalytic driving energy could be also considered as an important factor for controlling the nucleation event. When the austenite stability became more dominant, the total driving energy stored for the phase transformation decreased. It can be observed that the driving energy was drastically increased at the initial stage of nucleus formation and then decreased gradually during the developing of the nucleation sites. The effect of ausforming almost caused degenerations of the nucleus development, accordingly, except that they occurred in MC1.5Mn1NiCr/AIT0.35 steel. The number of nucleation sites developed in the MC1.5Mn1NiCr/AIT0.15 steel was more extensive than in the MC1.5Mn1NiCr/AIT0.35 steel, which corresponded with lower driving energy, as presented in Figure 7a. Even though the MC1.5Mn1NiCr steel consumed less driving energy than the LC2.5Mn0.2NiCr steel, it had a small number of nucleation sites due to the existence of more dislocations. Interestingly, the driving energy of the LC2.5Mn0.2NiCr steels shown in Figure 7b was significantly sensitive to ausforming, and was well described, especially at the high degree of ausforming. From the correlation between the activation energy and the driving force defined in Equation (9), it was inevitable that the initial activation energy required to overcome any obstacles played an essential role in all the nucleation events. Nevertheless, in order to extract and consider only the activation energy influenced by the other mechanisms, regardless of the energy contributed by ausforming, it was reasonable to take the activation energy difference in Equation (15) into account so that a discussion of only the effect of chemical contribution on the variation of the activation energy difference, ΔQ^* was conceivable.

In Figure 8, the variations of the total activation energy difference with the evolution of the BF formation of MC1.5Mn1NiCr and LC2.5Mn0.2NiCr steels under PIT and AIT

conditions are illustrated. The carbon enrichment was presumed to be the main contributor for BF formation. It was found that the ΔQ^* energies required in all the conditions of the MC1.5Mn1NiCr steel were somewhat higher than those of the LC2.5Mn0.2NiCr steel. Such a tendency corresponded well with those shown in [27,56], in which it was reported that the activation energy was dependent, on one hand, on the undercooling temperature. It was decreased with the increasing of the temperature as a higher defect density was generated. On the other hand, ΔQ^* was partially governed by the chemical element addition. In particular, those containing more carbon content acting as an austenite stabilizing element could directly lead to suppression of the bainitic transformation, accompanied by the raising of the energy required for the nucleation event. The maximum ΔQ^* energies obtained for both the MC1.5Mn1NiCr and the LC2.5Mn0.2NiCr steels with PIT treatment were consistently higher than those with other heat-treating conditions. It was because of the small number of potential nucleation sites in PIT steel. In this sense, the reduction of the ΔQ^* energy with respect to the evolution of the BF formation should be associated with the increased number of nucleation sites, while the termination of BF development could be associated with an overconsumption of nucleation sites in UA. Hence, the result gave rise to more stable austenite.

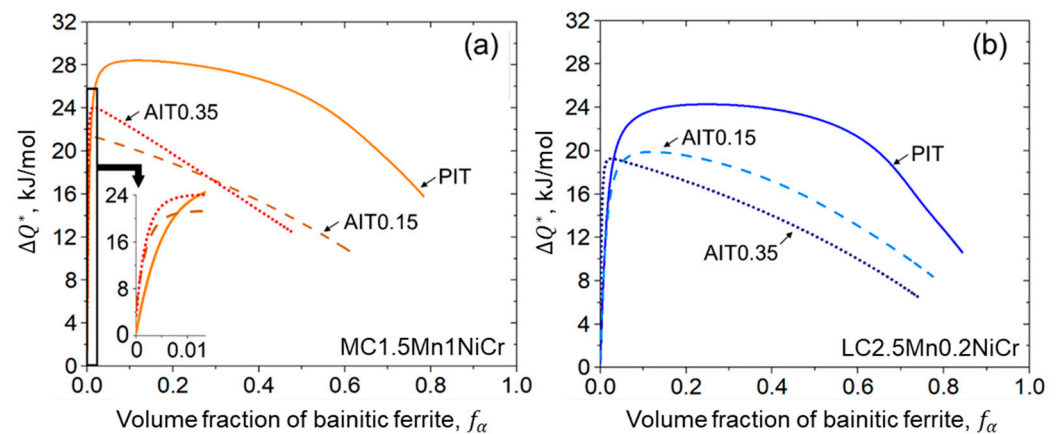


Figure 8. Variation of total activation energy difference with bainite formation evolution of (a) MC1.5Mn1NiCr and (b) LC2.5Mn0.2NiCr steels under various conditions.

4.2.4. Dislocation Density Estimation

Figure 9a,b shows the estimated dislocation density and the PAGs of the steels under PIT, AIT0.15, and AIT0.35 conditions, respectively. As can be seen, the decreases in the PAGs were not the only factors affecting the density development of the dislocations in this study. The contribution of hard phases such as BF and FM should also be included as the formation of such structures was in fact accompanied by the accumulation of stress [57], particularly when the average dislocation density values estimated from the PIT specimens of individual steels were compared. However, the effect of carbon content on such PAG reduction could be described by the carbon-controlled nucleation mechanism during the solid solution treatment [58]. The influence of the PAGs was more pronounced in the ausformed specimens than in the PIT specimen, and thus it would be reasonable to describe it by the Hall–Petch relation [59].

Under the ausforming conditions, besides the PAGs reduction that came along with the pre-existing density of dislocations, the enhancement of the dislocation density was also associated with the fractions of the hard phase, as mentioned previously. The density of the pre-existing dislocation in the austenite was directly dependent on the ausforming strain, while the formations of BF and FM were governed by the thermodynamic stability of austenite and the degree of carbon enrichment, respectively. In addition, the pre-existing dislocation density affected by ausforming could be evaluated by subtracting the average density of the dislocations of any AIT specimen from the value estimated from the PIT specimen. For the LC2.5Mn0.2NiCr steel, the additional dislocations introduced by

the 0.15 and 0.35 strains were 2.4×10^{14} and $3.6 \times 10^{14} \text{ m}^{-2}$, respectively. Likewise, the estimated values of the MC1.5Mn1NiCr steel in accordance with the ausforming strains were 1.3×10^{15} and $1.5 \times 10^{15} \text{ m}^{-2}$, accordingly. Such extra dislocations can be inherited further to the tempering region and change the nucleation activity during the bainitic transformation. Therefore, it could be concluded that the presence of higher dislocations in the MC1.5Mn1NiCr steel was likely due to a strong hindrance of the nucleation reaction, in which the effect of the dislocation-induced mechanical stabilization of austenite was more pronounced. However, the conclusion with respect to ausforming the enhanced thermal stability of austenite may not be applicable for the MC1.5Mn1NiCr steel as more FM was formed. In contrast, the deformation encouraged a higher nucleation activity and was mostly available for a greater formation of nucleation sites during bainitic transformation for the LC2.5Mn0.2NiCr steel. The results hereby enabled UA to be better stabilized after the transformation, although the ausformed LC2.5Mn0.2NiCr steels had a much lower density of dislocations. As a consequence, it seems that the relationship between nucleation sites and dislocation density evolutions could not be concluded as two different trends were seen in two different materials. Nevertheless, the LC2.5Mn0.2NiCr steel, with a substantial BF fraction due to the large degree of ausforming, effectively resisted the formation of FM by improving the thermal stability of austenite.

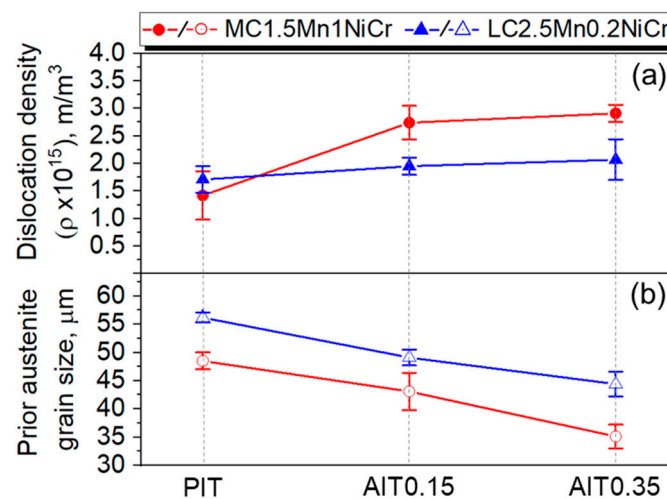


Figure 9. (a) Dislocation density estimation and (b) prior austenite grain size of MC1.5Mn1NiCr and LC2.5Mn0.2NiCr steels under PIT, AIT0.15, and AIT0.35 treatments.

5. Conclusions/Summary

A model was formulated in this study to describe the effect of ausforming on the kinetics of isothermal bainitic transformation. The behavior of two low-carbon steels can be described based on nucleation control and the Koistinen–Marburger relationship. Different levels of ausforming were systematically characterized in experiments and further used to develop, calibrate, and validate the model. The model distinguishes grain boundary and autocatalytic nucleation. The associated driving energies are controlled by the chemical energy, interfacial energy, and stress-field energy caused by the formation of bainitic ferrite sub-units. The major conclusions are drawn in the following:

- The formation of bainitic ferrite is mainly governed by two factors: carbon enrichment in austenite and the activation energy as an energy barrier required for nucleation.
- Ausforming accelerates the onset of the bainitic phase transformation but results in sluggish transformation due to the mechanical stabilization of austenite. A higher degree of ausforming is more applicable in the steel with lower carbon content. With the substantial development of nucleation sites, even though they provide a slightly lower fraction of bainitic ferrite, the result effectively resists the formation of fresh martensite by improving the thermal stability of austenite.

- A fitting parameter representing the initial energy barrier can be used to examine the activation energy change caused by ausforming. A decrease in the energy barrier allows the acceleration of the transformation. While the transformation progresses, the driving energy for autocatalytic nucleation becomes smaller due to the enhancement of the dislocation density.
- The impact of carbon content plays a slight role in the onset period, but it is more pronounced during the progress of bainitic transformation. Minimizing carbon concentration in steel gives rise to a decrease in the net activation energy difference with the increasing of the nucleation rate. The result allocates a higher density of nucleation sites with more bainitic ferrite fractions.

Author Contributions: Conceptualization, T.K.; methodology, T.K.; validation, T.K., W.B., J.L. and V.U.; formal analysis, T.K.; data curation, T.K. and J.L.; writing—original draft preparation, T.K.; writing—review and editing, T.K., W.B., J.L. and V.U. All authors have read and agreed to the published version of the manuscript.

Funding: This research received no external funding.

Institutional Review Board Statement: Not applicable.

Informed Consent Statement: Not applicable.

Data Availability Statement: Not applicable.

Acknowledgments: The authors wish to thank Jiali Zhang from the Institute for Materials Applications in Mechanical Engineering, RWTH-Aachen University, for her assistance in using XRD measurement.

Conflicts of Interest: The authors declare no conflict of interest.

References

1. Bhadeshia, H.; Edmonds, D.V. Bainite in silicon steels: New composition–property approach Part 1. *Met. Sci. J.* **1983**, *17*, 411–419. [CrossRef]
2. Caballero, F.G. Carbide-free bainite in steels. In *Phase Transformations in Steels*; Elsevier: Amsterdam, The Netherlands, 2012; pp. 436–467, ISBN 9781845699703.
3. Bhadeshia, H. *Bainite in Steels: Transformations, Microstructure and Properties*, 2nd ed.; IOM Communications: London, UK, 2001; ISSN 9781861251121.
4. Wang, S.C.; Yang, J.R. Effects of chemical composition, rolling and cooling conditions on the amount of martensite/austenite (M/A) constituent formation in low carbon bainitic steels. *Mater. Sci. Eng. A* **1992**, *154*, 43–49. [CrossRef]
5. Hofer, C.; Bliznuk, V.; Verdiere, A.; Petrov, R.; Winkelhofer, F.; Clemens, H.; Primig, S. Correlative microscopy of a carbide-free bainitic steel. *Micron* **2016**, *81*, 1–7. [CrossRef] [PubMed]
6. Hofer, C.; Leitner, H.; Winkelhofer, F.; Clemens, H.; Primig, S. Structural characterization of “carbide-free” bainite in a Fe–0.2C–1.5Si–2.5Mn steel. *Mater. Charact.* **2015**, *102*, 85–91. [CrossRef]
7. Hu, F.; Wu, K.M. Isothermal transformation of low temperature super bainite. *Adv. Mater. Res.* **2010**, *146–147*, 1843–1848. [CrossRef]
8. Li, C.W.; Han, L.Z.; Luo, X.M.; Liu, Q.D.; Gu, J.F. Fine structure characterization of martensite/austenite constituent in low-carbon low-alloy steel by transmission electron forward scatter diffraction. *J. Microsc.* **2016**, *264*, 252–258. [CrossRef]
9. Shimanov, M.; Korpala, G.; Terzic, A.; Kawalla, R. Bainitic steels: Their characteristics and applications. *Key Eng. Mater.* **2016**, *684*, 104–110. [CrossRef]
10. Takahashi, M.; Bhadeshia, H. A model for the microstructure of some advanced bainitic steels. *Mater. Trans.* **1991**, *32*, 689–696. [CrossRef]
11. Garcia-Mateo, C.; Sourmail, T.; Caballero, F.G. Bainitic Steel: Nanostructured. In *Encyclopedia of Iron, Steel, and Their Alloys*; Colás, R., Totten, G.E., Eds.; CRC Press: Boca Raton, FL, USA, 2016; pp. 271–290, ISBN 978-1-4665-1104-0.
12. Caballero, F.G.; Santofimia, M.J.; García-Mateo, C.; Chao, J.; De Andrés, C.G. Theoretical design and advanced microstructure in super high strength steels. *Mater. Des.* **2009**, *30*, 2077–2083. [CrossRef]
13. Garcia-Mateo, C.; Caballero, F.G. Advanced high strength bainitic steels. In *Comprehensive Materials Processing*; Elsevier: Amsterdam, The Netherlands, 2014; pp. 165–190, ISBN 9780080965338.
14. Yao, Z.; Xu, G.; Hu, H.; Yuan, Q.; Tian, J.; Zhou, M. Effect of Ni and Cr addition on transformation and properties of low-carbon bainitic steels. *Trans. Indian Inst. Met.* **2019**, *72*, 1167–1174. [CrossRef]
15. Changle, Z.; Hanguang, F.; Shengqiang, M.; Dawei, Y.; Jian, L.; Zhenguo, X.; Yongping, L. Effect of Mn content on microstructure and properties of wear-resistant bainitic steel. *Mater. Res. Express* **2019**, *6*, 86581. [CrossRef]

16. Kumnorkaew, T.; Lian, J.; Uthaisangasuk, V.; Bleck, W. Effect of ausforming on microstructure and hardness characteristics of bainitic steel. *J. Mater. Res. Technol.* **2020**, *9*, 13365–13374. [CrossRef]
17. Lee, C.H.; Bhadeshia, H.; Lee, H.-C. Effect of plastic deformation on the formation of acicular ferrite. *Mater. Sci. Eng. A* **2003**, *360*, 249–257. [CrossRef]
18. Hase, K.; Garcia-Mateo, C.; Bhadeshia, H. Bainite formation influenced by large stress. *Mater. Sci. Technol.* **2004**, *20*, 1499–1505. [CrossRef]
19. Matsuda, H.; Bhadeshia, H. Kinetics of the bainite transformation. *Proc. R. Soc. Lond. A* **2004**, *460*, 1707–1722. [CrossRef]
20. Rees, G.I.; Bhadeshia, H. Bainitic transformation kinetics: Part 1. Modified model. *Mater. Sci. Technol.* **1992**, *8*, 985–993. [CrossRef]
21. Magee, C.L. The kinetics of martensite formation in small particles. *Metall. Mater. Trans. B* **1971**, *2*, 2419–2430. [CrossRef]
22. van Bohemen, S.M.C.; Sietsma, J. Modeling of isothermal bainite formation based on the nucleation kinetics. *Int. J. Mater. Res.* **2008**, *99*, 739–747. [CrossRef]
23. Ghosh, G.; Olson, G.B. Kinetics of F.C.C. → B.C.C. heterogeneous martensitic nucleation-I. The critical driving force for athermal nucleation. *Acta Metall. Mater.* **1994**, *42*, 3361–3370. [CrossRef]
24. Ghosh, G.; Olson, G.B. Kinetics of F.C.C. → B.C.C. heterogeneous martensitic nucleation-II. Thermal activation. *Acta Metall. Mater.* **1994**, *12*, 3371–3379. [CrossRef]
25. Meng, Q.P.; Rong, Y.H.; Hsu, T.Y. Effect of internal stress on autocatalytic nucleation of martensitic transformation. *Metall. Mater. Trans. A* **2006**, *37*, 1405–1411. [CrossRef]
26. Zou, H.; Hu, H.; Xu, G.; Xiong, Z.; Dai, F. Combined effects of deformation and undercooling on isothermal bainitic transformation in an Fe-C-Mn-Si alloy. *Metals* **2019**, *9*, 138. [CrossRef]
27. Ravi, A.M.; Sietsma, J.; Santofimia, M.J. Exploring bainite formation kinetics distinguishing grain-boundary and autocatalytic nucleation in high and low-Si steels. *Acta Mater.* **2016**, *105*, 155–164. [CrossRef]
28. Rees, G.I.; Shipway, P.H. Modelling transformation plasticity during the growth of bainite under stress. *Mater. Sci. Eng. A* **1997**, *223*, 168–178. [CrossRef]
29. Zhou, M.; Xu, G.; Wang, L.; Xue, Z.; Hu, H. Comprehensive analysis of the dilatation during bainitic transformation under stress. *Met. Mater. Int.* **2015**, *21*, 985–990. [CrossRef]
30. Lee, S.; Lee, S.J.; de Cooman, B.C. Austenite stability of ultrafine-grained transformation-induced plasticity steel with Mn partitioning. *Scr. Mater.* **2011**, *65*, 225–228. [CrossRef]
31. Mahieu, J.; de Cooman, B.C.; Maki, J. Phase transformation and mechanical properties of si-free CMnAl transformation-induced plasticity-aided steel. *Metall. Mater. Trans. A* **2002**, *33*, 2573–2580. [CrossRef]
32. Abrams, H. Grain size measurement by the intercept method. *Metallography* **1971**, *4*, 59–78. [CrossRef]
33. Dyson, D.J.; Holmes, B. Effect of Alloying Additions on the Lattice Parameter of Austenite. *J. Iron Steel Inst.* **1970**, *208*, 469–474.
34. Lutterotti, L.; Scardi, P. Simultaneous structure and size-strain refinement by the Rietveld method. *J. Appl. Crystallogr.* **1990**, *23*, 246–252. [CrossRef]
35. Popa, N.C. The (hkl) dependence of diffraction-line broadening caused by strain and size for all Laue groups in Rietveld refinement. *J. Appl. Crystallogr.* **1998**, *31*, 176–180. [CrossRef]
36. Warren, B.E. *X-ray Diffraction*; Dover Publications Inc.: New York, NY, USA, 1969; ISBN 9780201085242.
37. Williamson, G.K.; Smallman, R.E., III. Dislocation densities in some annealed and cold-worked metals from measurements on the X-ray debye-scherrer spectrum. *Philos. Mag.* **1956**, *1*, 34–46. [CrossRef]
38. Fielding, L.C.D. The Bainite Controversy. *Mater. Sci. Technol.* **2013**, *29*, 383–399. [CrossRef]
39. Caballero, F.G. Bainitic Steel: Transformation Mechanisms and Properties. In *Encyclopedia of Iron, Steel, and Their Alloys*; Colás, R., Totten, G.E., Eds.; CRC Press: Boca Raton, FL, USA, 2016; pp. 291–305, ISBN 978-1-4665-1104-0.
40. Ali, A.; Bhadeshia, H. Nucleation of Widmanstätten ferrite. *Mater. Sci. Technol.* **1990**, *6*, 781–784. [CrossRef]
41. Bhadeshia, H.; Edmonds, D.V. The mechanism of bainite formation in steels. *Acta Mater.* **1980**, *28*, 1265–1273. [CrossRef]
42. Tszeng, T.C. Autocatalysis in bainite transformation. *Mater. Sci. Eng. A* **2000**, *293*, 185–190. [CrossRef]
43. Koistinen, D.; Marburger, R. A general equation prescribing the extent of the Austenite-Martensite transformation in pure iron-carbon alloys and plain carbon steels. *Acta Metall.* **1959**, *7*, 59–60. [CrossRef]
44. Olsen, G.B.; Cohen, M. Dislocation theory of martensitic transformations. In *Dislocations in Solids*; Nabarro, F.R.N., Ed.; Elsevier Science Publishers B.V.: Amsterdam, The Netherlands, 1986; pp. 293–408.
45. Dong, H.; Sun, X. Deformation Induced Ferrite Transformation. In *Ultra-Fine Grained Steels*; Weng, Y., Ed.; Springer: Berlin/Heidelberg, Germany, 2009; pp. 86–136, ISBN 978-3-540-77230-9.
46. Ghosh, G.; Raghavan, V. The kinetics of isothermal martensitic transformation in an Fe-23.2wt.%Ni2.8wt.%Mn alloy. *Mater. Sci. Eng. A* **1986**, *80*, 65–74. [CrossRef]
47. Bhadeshia, H. MAP Program MAP_STEEL_MUCG83. Available online: <http://www.phase-trans.msm.cam.ac.uk/map/steel/programs/mucg83.html> (accessed on 12 July 2021).
48. van Bohemen, S.M.C.; Sietsma, J. Kinetics of martensite formation in plain carbon steels: Critical assessment of possible influence of austenite grain boundaries and autocatalysis. *Mater. Sci. Technol.* **2014**, *30*, 1024–1033. [CrossRef]
49. Santofimia, M.J.; van Bohemen, S.; Sietsma, J. Combining bainite and martensite in steel microstructures for light weight application. *J. S. Afr. Inst. Min. Metall.* **2013**, *113*, 143–148.

50. Capdevila, C.; Caballero, F.G.; De Andrés, C.G. Determination of Ms temperature in steels: A bayesian neural network model. *ISIJ Int.* **2002**, *42*, 894–902. [CrossRef]
51. Lee, J.S.; van Tyne, C.J. A kinetics model for martensite transformation in plain carbon and low-alloyed steels. *Metall. Mater. Trans. A* **2012**, *43*, 422–427. [CrossRef]
52. Wirths, V. Prozessführung und Zyklisches Werkstoffverhalten von Karbidfreien Bainitischen Stählen. Ph.D. Thesis, Rheinisch-Westfälischen Technischen Hochschule Aachen, Aachen, Germany, 2016.
53. Shipway, P.H.; Bhadeshia, H. Mechanical stabilisation of bainite. *Mater. Sci. Technol.* **1995**, *11*, 1116–1128. [CrossRef]
54. Hu, H.; Xu, G.; Wang, L.; Zhou, M.; Xue, Z. Effect of ausforming on the stability of retained austenite in a C-Mn-Si bainitic steel. *Met. Mater. Int.* **2015**, *21*, 929–935. [CrossRef]
55. Soliman, M.; Palkowski, H. Development of the low temperature bainite. *Arch. Civ. Mech. Eng.* **2016**, *16*, 403–412. [CrossRef]
56. Shah, M.; Kumar, D.S.; Ankita, P. Phenomenological kinetic model of the nano-bainitic steels to characterize the dynamics of the autocatalytic nucleation process. *SN Appl. Sci.* **2020**, *2*, 635. [CrossRef]
57. PEET, M.J.; Bhadeshia, H. Surface relief due to bainite transformation at 473 K (200 °C). *Metall. Mater. Trans. A* **2011**, *42*, 3344–3348. [CrossRef]
58. Castro Cerda, F.M.; Sabirov, I.; Goulas, C.; Sietsma, J.; Monsalve, A.; Petrov, R.H. Austenite formation in 0.2% C and 0.45% C steels under conventional and ultrafast heating. *Mater. Des.* **2017**, *116*, 448–460. [CrossRef]
59. Narutani, T.; Takamura, J. Grain-size strengthening in terms of dislocation density measured by resistivity. *Acta Metall. Mater.* **1991**, *39*, 2037–2049. [CrossRef]

Article

Microstructural Evolution in Large-Section Plastic Mould Steel during Multi-Directional Forging

Xuan Chen, Boya Wu, Jiayuan Li, Xiaoxiao Zhang, Pengpeng Zuo, Xiaochun Wu and Junwan Li *

School of Materials Science and Engineering, Shanghai University, Shanghai 200444, China; chenxuan9311@163.com (X.C.); boyao03@163.com (B.W.); lijiaoyuan_0129@163.com (J.L.); zhangxx1020@163.com (X.Z.); zpp0513@163.com (P.Z.); wuxiaochun@shu.edu.cn (X.W.)

* Correspondence: lijunwan@shu.edu.cn

Abstract: To obtain excellent mechanical properties from large cross-sections of plastic mould steel (SDP1), we conducted multi-directional forging (MDF) to control the microstructure of ingots. To investigate the microstructural evolution of SDP1 steel during MDF, we performed hot forging at 1150 °C using a THP01–500A hydraulic press. The dimensions of the specimens were $\Phi 38$ mm \times 80 mm. The microstructure of the specimens after forging was observed under a metallographic microscope. Furthermore, the results of the finite element method (FEM) simulations were employed to improve the quality of the forgings. The predicted results agreed well with the experimental ones, indicating that FEM is effective for analysing microstructural evolution during MDF. Thus, MDF for large cross-sections of SDP1 steel ($\Phi 1000$ mm \times 2200 mm) was simulated. The results showed that the average grain size of SDP1 steel at the core of an ingot after MDF ranged from 40.6 to 43.3 μ m. Although this was slightly higher than the grain size of the sample after traditional upsetting and stretching forging (TUSF) (35.7–46.0 μ m), the microstructure of the SDP1 steel sample after MDF was more uniform than that after TUSF. Compared with TUSF, MDF not only refines the grain size but also improves the microstructure uniformity of the sample.

Citation: Chen, X.; Wu, B.; Li, J.; Zhang, X.; Zuo, P.; Wu, X.; Li, J. Microstructural Evolution in Large-Section Plastic Mould Steel during Multi-Directional Forging. *Metals* **2022**, *12*, 1175. <https://doi.org/10.3390/met12071175>

Academic Editors: Shuwen Wen, Yongle Sun and Xin Chen

Received: 12 June 2022

Accepted: 8 July 2022

Published: 10 July 2022

Publisher's Note: MDPI stays neutral with regard to jurisdictional claims in published maps and institutional affiliations.



Copyright: © 2022 by the authors. Licensee MDPI, Basel, Switzerland. This article is an open access article distributed under the terms and conditions of the Creative Commons Attribution (CC BY) license (<https://creativecommons.org/licenses/by/4.0/>).

Keywords: multi-directional forging; large cross-section plastic mould steel; microstructure evolution; FEM simulation

1. Introduction

During the fabrication of large plastic mould steel blooms, the low impact toughness of the product is a major quality issue. Through microstructural analysis, this phenomenon is attributed to the coarse grain and nonuniform grain size [1–3]. As the most important manufacturing process for plastic mould steel, microstructural control in free forging processes determines product quality. Discontinuous dynamic recrystallisation (DRX), which occurs during hot deformation processes, is an important microstructural evolution behaviour. Recently, severe plastic deformation (SPD) methods have been widely studied owing to their ability to provide fairly good grain refinement in metallic alloys [4]. These techniques improve mechanical fatigue, corrosion, wear and creep properties of various alloys [5,6]. Several SPD methods, such as accumulative roll bonding, equal-channel angular pressing, friction stir processing and constrained groove pressing and multi-directional forging (MDF) [7–17], have found industrial applications. MDF has various advantages, such as repeatability, cost effectiveness, simplicity and the possibility of fabricating large parts [18–21].

MDF is a strong plastic deformation process improved by hammer forging compared with traditional unidirectional forming processes [22–25]. During MDF, the ingot is continuously elongated or compressed along the x -, y - and z -axes with changing loading direction, which has a great influence on the flow stress behaviour and the microstructure [26–28]. Although MDF of a large number of ferrous and nonferrous alloys have already been studied, there are few investigations on plastic mould steel available in the literature. For

example, Moghanaki et al. [24] studied the effect of solution treatment on the mechanical properties of Al-Cu-Mg alloy during multi-directional forging. The hardness of solution treated samples after MDF was strongly increased from 84 to 163 HV, which is attributed to both dynamic formation of Guinier-Preston-Bagaryatsky (GPB) zones/Cu-Mg co-clusters and dislocation storage. Nakao et al. [27], based on experiments on microstructure and mechanical properties, proved that the MDF can improve the level of grain refinement of stainless steel. In the process of MDF, the grain fragmentation degree increased due to the coordination of mechanical twins and martensitic transformation. With the increase in strain, the tensile strength significantly improved. Soleymani et al. [29] conducted multi-directional forging experiments on low-carbon steel modules and found that the grain refinement mechanism was static recrystallisation when the forging temperature was 500 °C. The new grains nucleated within the deformed grains, grew and consumed the deformed tissues until the material was completely recrystallised.

MDF has been studied and verified by many scholars, but in the manufacturing process of plastic mould steel, MDF technology has not been studied and applied. In this paper, both MDF and the traditional upsetting and stretching forging (TUSF) were carried out on the forging of large cross-sections of plastic mould steel. Based on the numerical simulation of the forging processes, the strain state and the evolutionary law of the microstructure during MDF and TUSF were investigated and discussed to provide effective guidance for the production of forgings.

2. Materials and Methods

2.1. Material

The material used in this study was as-forged micro-alloyed plastic mould steel (SDP1®), and its normal chemical composition is listed in Table 1. The steel sheet was manufactured by air and spray cooling after forging, and its thickness was 700 mm. The microstructure was observed and captured using an optical microscope (OM, Nikon, LV 150, Tokyo, Japan) and a field-emission scanning electron microscope (Carl Zeiss SUPRA 40, Oberkochen, Germany). For OM observation, the samples were mechanically ground using sandpaper, polished, and etched in a 4% nital solution.

Table 1. Normal chemical composition of SDP1 plastic mould steel (wt.%).

Element	C	Cr	Mn	Mo	Si	N	Nb	S	P	Fe
Wt.%	0.30	1.40	2.00	0.30	0.20	0.008	0.035	≤0.003	≤0.015	Bal.

2.2. MDF Procedure

Cylindrical samples (38 mm in diameter and 80 mm in length) were prepared by wire-electrode cutting, followed by homogenisation at 1150 °C for 2 h. MDF was performed to refine the grains of the SDP1 steel, and it was performed based on three-step forging (Figure 1a) using a THP01-500A hydraulic press (Tianduan, Tianjin, China). MDF was performed at an initial forging temperature of 1150 °C and a speed of 5 mm·s^{−1} with a controllable deformation speed. During the process, the reduction was controlled at 50%. The ingots were reheated to 1150 °C for 0.5 h between every pass. In Figure 1a, P1 is located in the centre of the upper surface of the cylinder, P2 in the centre of the cylinder body, and P3 in the middle of the cylinder side surface. The samples were repeatedly deformed up to three passes by changing the loading direction in each pass by 90°. Prior to the second forging step, the pancake produced in the first step was rotated by 90° around the *x*-axis to press the *y*-plane of the ingot. The third forging process step was similar to the second step. Thus, the *z*-, *y*- and *x*-planes of the sample were compressed, in turn, to obtain fine grains. After the MDF process, to prevent the forged samples from cracking due to the rapid cooling, the ingots were pre-cooled until the temperature of the centre surface was below 850 °C, after which they were quenched in water. Samples 1–3 (Figure 1b) corresponded to the first, second and third steps of the forged ingots. To investigate the microstructure

of the MDF samples at different regions, three positions on the samples were selected for microstructural observation (Figure 1a). The samples were cut from the middle section of the forged billets. The middle area was representative of the entire sample and convenient for comparison. Austenite grain boundaries were shown by the oxidation method. The average grain size of the samples under different hot deformation positions was calculated based on the volume average of the grain using the three-circle truncated-point method. Several metallographic photographs were recorded at each sampling point to create grain size data statistics, and Image-pro Plus (version 6.0, Media Cybernetics, Rockville, MD, USA) was used to revise the data to obtain accurate and reliable average grain-size data.

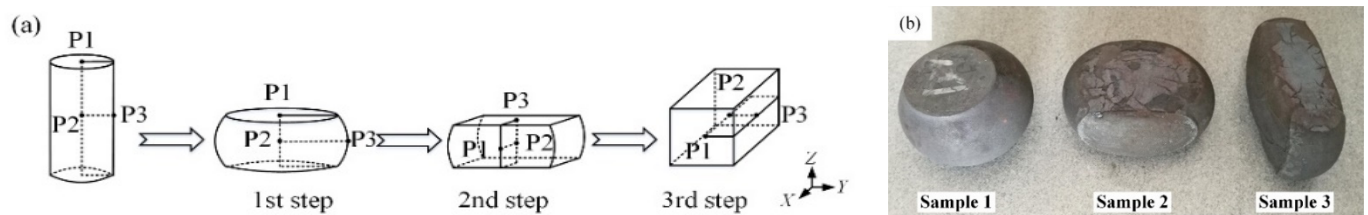


Figure 1. MDF experiment: (a) sequence of MDF steps; (b) state of SDP1 steel after MDF.

3. Experimental Results and Analysis

Figure 2 shows the grain size and morphology of the ingot before forging. The microstructure revealed fairly equiaxed grain morphology delineated with definite grain boundaries. The microstructure was characterised dominantly by coarse grains; the average grain size of the ingots was 120 μm , indicating coarse grains before the forging process. The ingots were collected from the hydraulic press after plastic deformation, but no crack was observed at the surface of the billets, suggesting that the alloy exhibited good workability at 1150 $^{\circ}\text{C}$.

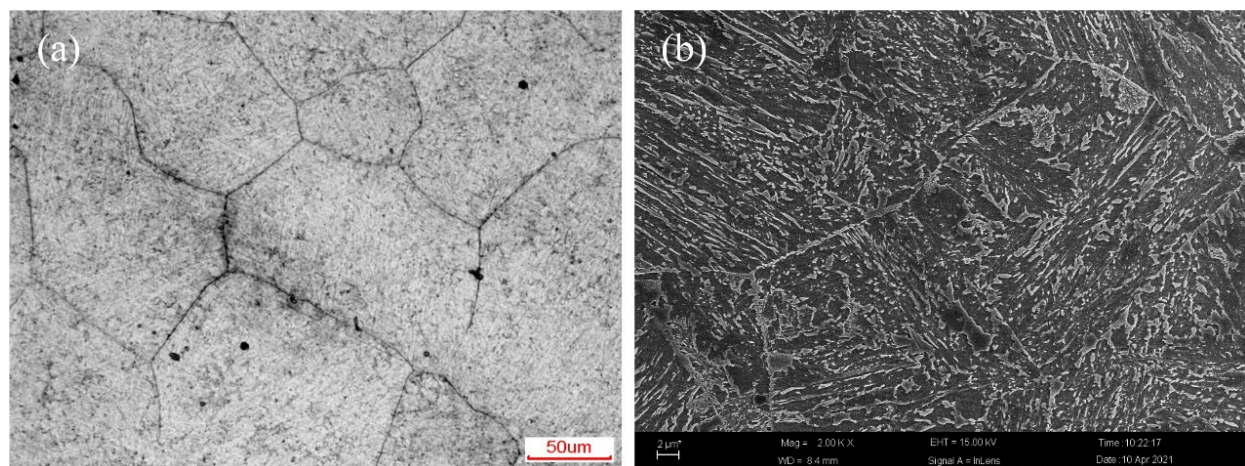


Figure 2. (a) initial grain size and (b) morphology of the SDP1 steel.

Figure 3 shows deformation microstructures of the samples after MDF, and Figure 4 shows the grain size distribution statistics of the SDP1 steel samples after MDF. The black area in the metallographic photographs shows an unpolished oxide layer, which does not affect the evaluation of the grain size. The grain size varied significantly with location during the MDF process (Figure 4a). Many deformed fine grains were observed in Sample 1, indicating recrystallisation during the MDF process. After the first step in the MDF process, many coarse grains were observed at point P1, and it was difficult to obtain more grain refinement. However, the grain size of points P2 and P3 decreased sharply. The average grain sizes of points P1, P2 and P3 of Sample 1 decreased from 120 to 119.0, 28.2 and 29.7 μm , respectively. The MDF first step slightly affected the

average grain size of point P1, and more grain refinement could only be achieved by increasing the number of MDF passes. After the second step in MDF, the size distribution of point P1 showed significant refinement, and the distribution was dominated by 30–40 μm grains (approximately 42.86%); in addition, grains in the range of <10 μm and ≥ 40 μm constituted approximately 5.71% and 22.86%, respectively. After the third MDF step, the size distribution of point P1 was dominated by 20–40 μm grains (approximately 70.73%), and grains ≥ 40 μm constituted only 2.44%.

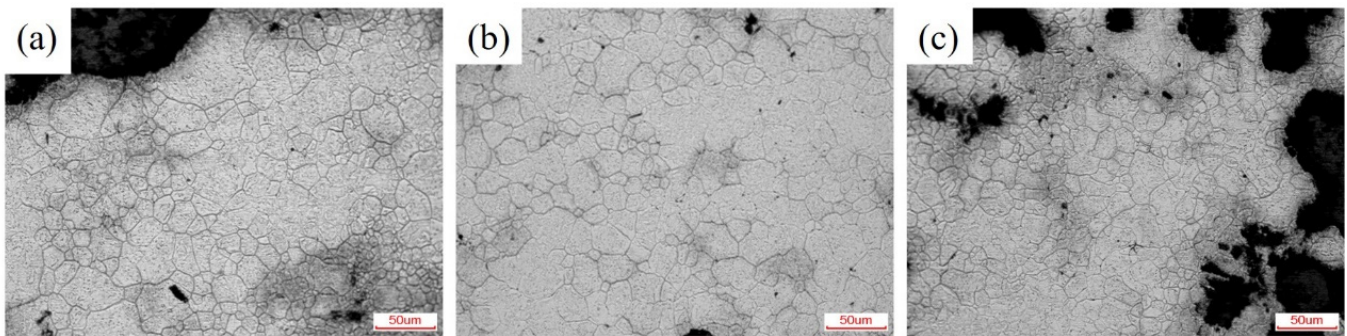


Figure 3. Microstructures of point P2 in (a) Sample 1; (b) Sample 2; (c) Sample 3.

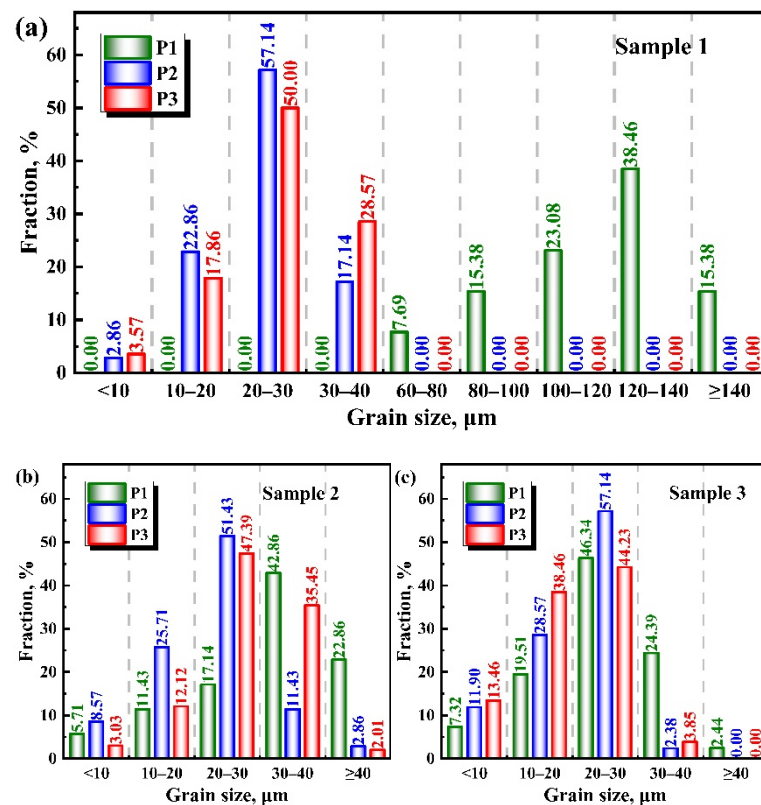


Figure 4. Grain size distribution and statistics of (a) Sample 1; (b) Sample 2; (c) Sample 3 at different tracking points.

All MDF steps resulted in remarkable grain refinement. With an increase in the MDF passes, the number fraction of the fine recrystallised grains increased (Figure 4b), and the recrystallisation grains became much finer than those obtained after one MDF pass. The grain size distribution of point P2 (Figure 4b) showed a broad distribution between 20 and 30 μm , and the average grain size was 26.5 μm . The number fraction of fine grains at point P2 increased compared with that of Sample 1. With a further increase in MDF passes, the

number fraction of fine recrystallised grains further increased (Figure 4c). A uniform fine grain structure evolved in Sample 3. The deformation microstructure was almost composed of mainly equiaxed fine grains considered to be recrystallisation grains. Homogeneous microstructures with average grain sizes of 28.7, 25.0 and 22.9 μm were obtained at points P1, P2 and P3, respectively. Few grains larger than 40 μm were obtained only at P1. The corresponding grain size distribution was characterised by a relative peak against the grain sizes ranging from 20 to 30 μm . The number fractions of the grains ranging from 20 to 30 μm in Sample 3 processed at points P1, P2 and P3 were 46.34%, 57.14% and 44.23%, respectively. The results show that MDF improved grain refinement. In addition to local coarse grains, the grains of the ingot were fine and uniform.

4. Numerical Procedure

4.1. Microstructural Evolution Model

Recrystallisation is a process by which deformed grains are replaced by new sets of grains that nucleate and grow until the original grains have been entirely consumed. Recrystallisation is important in developing microstructures in deformation-processed metals. Recrystallisation may occur during or after deformation; the former is termed dynamic, and the latter is termed static. The microstructure evolution model of SDP1 steel used in this simulation was derived from our previous calculations (Table 2) [30]. Combining the recrystallisation kinetic model and FE simulation of SDP1 steel, including the DRX, static recrystallisation (SRX) and meta recrystallisation (MRX), the effects of MDF and TUSF on the microstructural evolution of the ingots were investigated.

Table 2. Microstructural evolution model of SDP1 steel.

Quantity	Equation
Zener–Hollomon parameter	$Z = 1.06 \times 10^{12} [\sinh(0.0094\sigma_p)]^{5.35}$
DRX grain size evolution	$D_{\text{DRX}} = 21400.5 \left[\dot{\epsilon} \exp\left(\frac{257325}{RT}\right) \right]^{-0.26}$
DRX rate	$\epsilon_{0.5} = 0.0059 \dot{\epsilon}^{0.23} \exp\left(\frac{46187}{RT}\right)$
Peak strain	$\epsilon_p = 0.0011 \left[\dot{\epsilon} \exp\left(\frac{257325}{RT}\right) \right]^{0.22}$
DRX fraction	$X = 1 - \exp\left[-0.693 \left(\frac{\epsilon - \epsilon_c}{\epsilon_{0.5} - \epsilon_c}\right)^2\right]$
Time for 50% SRX	$t_{0.5} = 4.5 \times 10^{-8} \epsilon^{-1.27} \dot{\epsilon}^{-0.25} \exp\left(\frac{151231}{RT}\right)$
SRX volume fraction	$X_{\text{SRX}} = 1 - \exp\left[-0.693 \left(\frac{t}{t_{0.5}}\right)^{1.1}\right]$
Time for 50% MRX	$t_{0.5} = 1.22 \times 10^{-6} \dot{\epsilon}^{-0.41} \exp\left(\frac{126605}{RT}\right)$
MRX volume fraction	$X_{\text{MRX}} = 1 - \exp\left[-0.693 \left(\frac{t}{t_{0.5}}\right)^{0.6}\right]$
Grain growth	$d_g^{8.18} = d_0^{8.18} + 6.03 \times 10^{54} t \exp\left(\frac{-800866}{RT}\right)$

σ_p —peak stress, MPa; ϵ —strain; $\dot{\epsilon}$ —strain rate; ϵ_c and $\epsilon_{0.5}$ —critical strain rate and the DRX rate; R —gas constant, 8.314 J mol^{−1} K^{−1}; T —deformation temperature, K; t —time, s; d_0 —initial grain size, μm .

4.2. FEM Model

A comparative experiment was conducted to verify the accuracy of the recrystallisation model. To compare with the hot compression test, a cylindrical ingot ($\Phi 38 \text{ mm} \times 80 \text{ mm}$) was used for MDF. The speed of the press was approximately 5 mm s^{−1}. During MDF, the height of the ingot after each pass was reduced to 40, 27 and 35 mm along the z , y and x central axes of the ingot, respectively.

As shown in Figure 5, a hexahedron element was used to discrete the ingot during FEM simulations. The suitable mesh ensured simulation precision and saved computing resources. The as-homogenised SDP1 steel had an average grain size of 120 μm . Based on the experimental data, the average initial grain size of the ingot was set to 120 μm , and other simulation parameters were also consistent with the experimental values. Combining

the recrystallisation kinetic model and the FEM of SDP1 steel, the effects of MDF on the microstructural evolution in forgings were simulated.

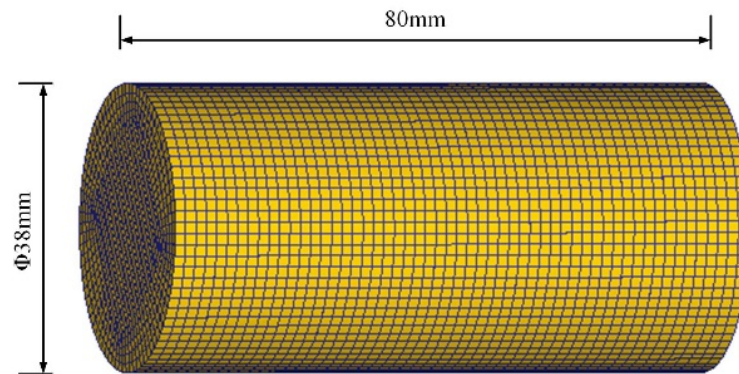


Figure 5. Three-dimensional finite element (FE) model of the specimen.

Microstructural evolution is not a major concern in the FE simulation of hot forging; thus, hot forging numerical theory only considers the coupling effect of the temperature and stress/strain fields. The coupling effect between the temperature and stress/strain evolution is described as follows. On the one hand, the plastic-deformation work accumulated in forging is converted into an internal heat source at a certain proportion. On the other hand, because of the existence of a temperature gradient, the expansion is different. Finally, a thermal strain is induced.

The instantaneous temperature field of the forging blank in a forging process can be expressed by the Fourier heat-transfer equation in a rectangular coordinate system.

$$\frac{\partial}{\partial X}(\lambda \frac{\partial T}{\partial X}) + \frac{\partial}{\partial Y}(\lambda \frac{\partial T}{\partial Y}) + \frac{\partial}{\partial Z}(\lambda \frac{\partial T}{\partial Z}) + \frac{\partial Q_2}{\partial t} = \rho c \frac{\partial T}{\partial t} \quad (1)$$

where X , Y and Z are the three directions of the rectangular coordinate system; ρ , c and λ are the density, specific heat capacity, and thermal conductivity of the materials, respectively; and Q_2 and t are the internal heat source and time, respectively. The change rate of the heat source can be expressed as follows:

$$\frac{\partial Q_2}{\partial t} = \dot{q} = kq \cdot \bar{\sigma} \cdot \dot{\bar{\epsilon}} \quad (2)$$

where kq is the conversion ratio of the heat-to-plastic deformation work; $\bar{\sigma}$ is the effective stress; $\dot{\bar{\epsilon}}$ is the effective strain rate. This equation realizes unilateral coupling of the stress/strain field to the temperature field.

Initial and boundary conditions must be determined to solve the transient-heat-conduction problem. The initial temperature of the forging blank was uniform and not less than 1150 °C. It can be expressed as:

$$T(X, Y, Z)|_{t=0} = T_0(X, Y, Z) \quad (3)$$

The boundary condition of the forging blank can be divided into two categories depending on whether the forging blank is in contact with the die. The boundary condition of a free surface that is not in contact with the model is expressed as follows:

$$qf = Hf(T_f - T_E)(S \in Sf) \quad (4)$$

where S is the module surface; Sf is a free surface; q_f and T_f are the heat flow and temperature of the free surface, respectively; T_E is the environment temperature; Hf is the total heat-transfer coefficient including convection and radiation heat transfer. Thus, the boundary condition of the free surface belongs to the second boundary condition.

For the surface in contact with the die, the heat-transfer mechanism was very complex, which can be roughly divided into the following two heat-transfer mechanisms. On the one hand, heat conduction was achieved through the contact points between the blank and anvil and solid interstitials (oxide skin, etc.). In addition, the friction heat generation between the die and forging blank should be considered. Thus, the boundary condition of the contact surface can be written as:

$$q_c = H_c(T_c - T_d) + q_\mu(S \in S_c) \quad (5)$$

where S_c represents the contact surface; q_c and q_μ are the total and friction heat flows of the contact surface, respectively; H_c denotes the total heat-transfer coefficient of the contact surface; T_c and T_d are the temperatures of the contact and die surfaces, respectively.

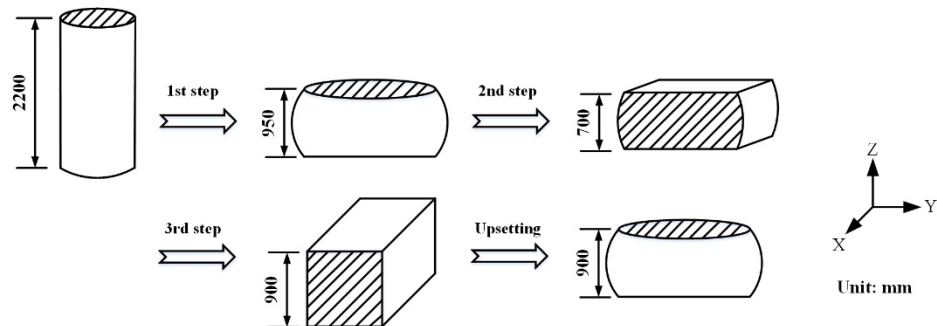
The stress/strain field of hot forging satisfies the assumption and basic equation of a rigid-plastic material. In addition, we need to specify the coupling effect of the temperature field on the stress/strain field.

$$\Delta \epsilon^T = \alpha_2(\Delta T) \quad (6)$$

where ϵ^T and ΔT are the thermal strain and temperature increments, respectively; α_2 is the thermal expansion coefficient of the forging blank.

The forging blank is cylindrical with dimensions of $\Phi 1000 \text{ mm} \times 2200 \text{ mm}$ (Figure 6). Because the forging blank is formed in different directions, instead of simplifying the model using a symmetrical relationship, we used the entire model. The geometry of the forging blank was meshed using a hexahedral element, and more than 10,000 hexahedral elements were obtained. To simulate the heat transfer between the forging blank and the mould, meshing the forging blank is insufficient; thus, a discrete mould geometry was employed.

(a) Multi-directional forging (MDF)



(b) Traditional upsetting and stretching forging (TUSF)

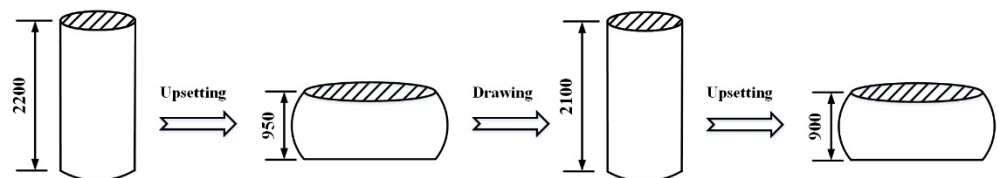


Figure 6. Schematic of (a) MDF and (b) traditional upsetting and stretching forging (TUSF) processes.

Furthermore, TUSF was conducted to compare with MDF. In these two forging processes, the first step was to upset the z -direction. Thus, the forging blank height could be forged from 2200 to 950 mm. In the second TUSF step, the blank was forged in the y -direction using a small smith anvil, and the height was reversed to 2200 mm. In the drawing process, the feed and reduction rates were maintained at 50% and 25%, respectively. In the second and third MDF steps, the blank was forged to 700 and 900 mm in the y - and x -direction, respectively, by successively using a large Smith anvil. A TUSF pass consisted of upsetting and elongation in the z - and y -directions, respectively, whereas one MDF pass

involved upsetting in the z -direction and compression in the y - and x -directions. Finally, the MDF and TUSF samples were upset to a height of 900 mm. Thus, TUSF and MDF differ in terms of the steps after z -direction upset. Upset in the z -direction has attracted attention because it is the first step and results in maximum deformation.

For both TUSF and MDF, a compressive speed of 10 mm/s was adopted. The friction and heat transfer coefficients of the anvil and blank were 0.3 and 11, respectively. The initial temperature of the forging blank was 1150 °C, and the temperature of the anvil and the ambient temperature were 150 °C and 20 °C, respectively. Before each step, the temperature of the blank was reset to 1150 °C. Based on the austenite grain size in the high-temperature homogenisation state, the average initial grain size of the ingot was set to 200 μm . Combining these two forging procedures and the FE model of hot forging, we simulated two-pass TUSF and MDF to analyse the distribution of temperature, effective stress and effective strain in the forging blank.

5. Results and Discussion

When the sample was compressed with a flat anvil, the metal flew around as the height decreased because of the friction between the specimen and the anvils, making it difficult for the metal to deform near the contact surface. Thus, the compressed specimen formed a drum shape, resulting in different grain sizes at different positions on the specimen. During the first MDF step (i.e., upsetting), the deformed specimen is divided into three regions (Figure 7). Region I is located near the interface between the specimen and the anvils, which is greatly affected by friction, reducing plastic deformation [25]. Region II is far from the end surface and is subject to less friction. It is in the most favourable deformation area at an angle of 45° to the vertical force and prone to plastic deformation. Region III is a small deformation zone, which is close to the surface of the specimen and around region I, and the extent of deformation is between that in regions I and II.

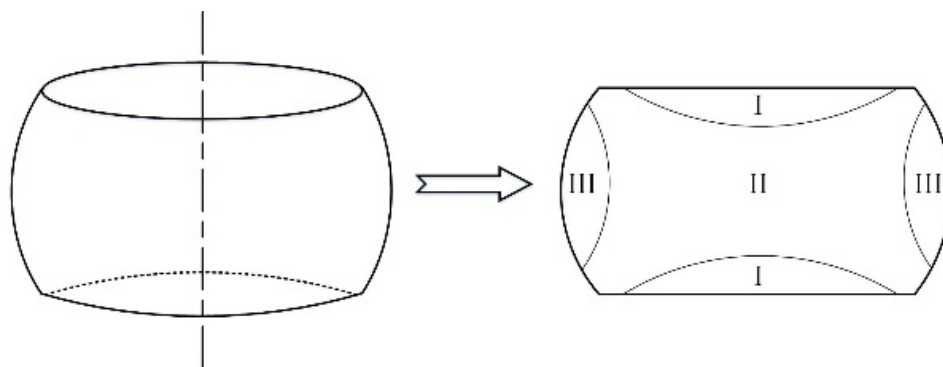


Figure 7. Schematic of difficult (I), large (II) and small (III) deformation areas of the specimen after upsetting.

5.1. Comparative Analysis of Experimental and Simulation Results

Figure 8 shows the experimental and simulated specimens after MDF. The arrows in Figure 8a–c indicate the flow state of the material during plastic deformation. Comparing the two sets of data, we find that FEM could well predict the shape and size of deformation forgings, which can guide the forging process. Figure 9 shows the average grain size distribution of the specimen after different forging steps. The samples show regular shapes after different forging steps, and a drum shape was formed on the side of each sample, which was similar to the shape of the ingot used in the experiment. Figure 9a shows the grain size distribution after the first step of MDF. Compared with Figure 4, the average grain size near the interface was quite large. The grain size near the centre of the interface (i.e., point P1) was the largest (119 μm), which is consistent with the initial grain size without refinement. The core of Sample 1 had the smallest grain size of 24.2 μm . The grain size of point P3 was close to but not as uniform as that of point P2. After MDF,

the grain of Sample 3 was tiny and distributed uniformly. For some areas with uneven grain distribution, secondary forging or other heat-treatment processes can be carried out. The simulation results were in good agreement with the experimental results. The FEM simulation results showed that the evolutionary law of the average grain size can well reflect the microstructural evolution of recrystallisation. Meanwhile, FEM is an effective method for analysing the thermal compression process, and the obtained recrystallisation model of SDP1 is reliable and effective.

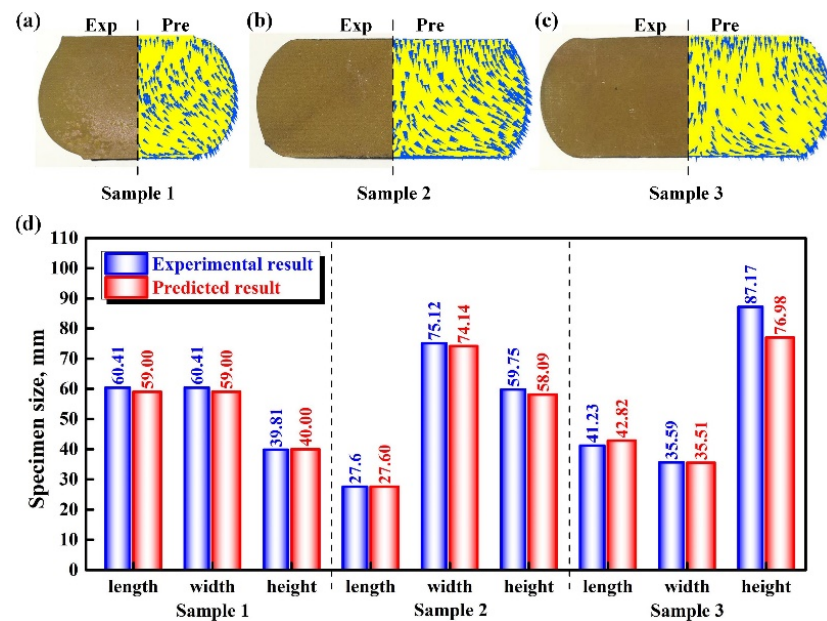


Figure 8. Experimental and simulated specimen sizes after MDF. (a) sample 1, (b) sample 2, (c) sample 3, (d) three-dimensional comparison.

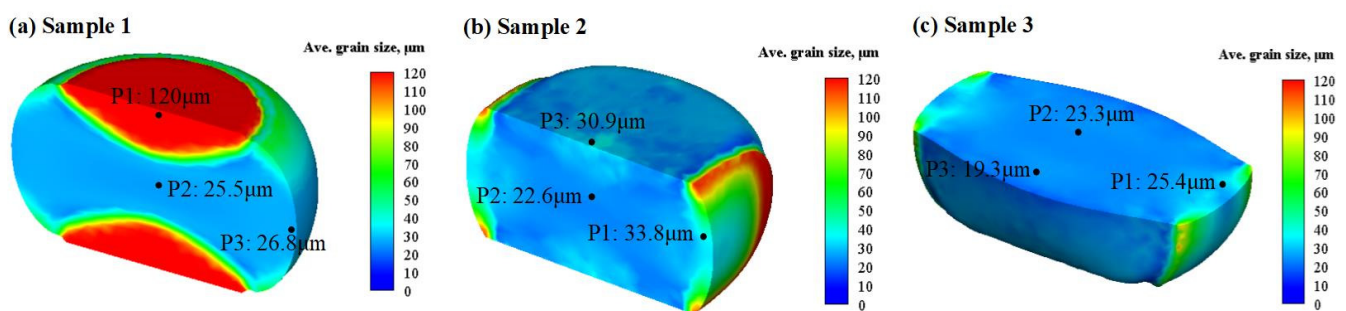


Figure 9. Average grain size of (a) Sample 1; (b) Sample 2; (c) Sample 3 at different tracking points obtained from FEM results.

5.2. Microstructural Evolution during the First MDF Step

Figure 10 shows the effective strain and stress contour plots of the deformed specimen after MDF at 1150 °C. The results show an inhomogeneous distribution of effective strain in the samples during MDF. The nonuniform strain distribution after upsetting agreed with the characteristics of the three deformation zones in the specimen. The accumulated strain in region I was higher than that in the other two regions. During upsetting, the strain distribution was extremely uneven, and the strain value decreased gradually from the centre along the radius to the side surface. In region I, where the specimen was in contact with the anvils, due to the friction resistance and heat transfer, the deformation was very small, because the magnitude of friction varied inversely with the distance, and region I was a cone. The outer drum part of region III was a free surface, which was less affected by friction resistance and depended on the expansion of region I; thus, longitudinal bulging was observed. With the same reduction, the deformation decreased from the centre to the end face. The maximum effective strain inside the sample reached 1.78, and the minimum effective strain was 0.03 after upsetting.

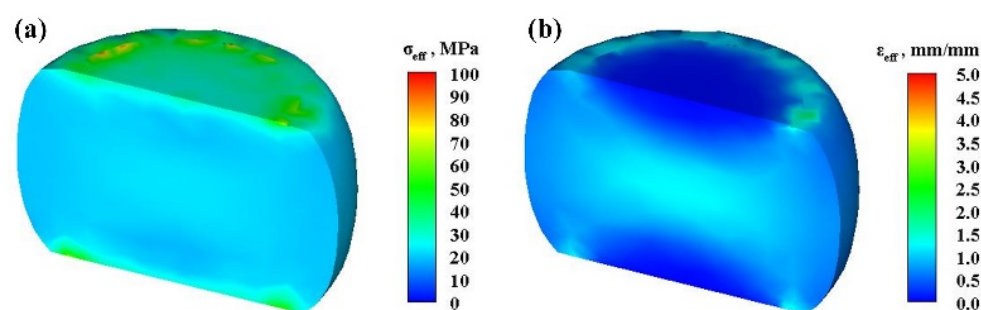


Figure 10. (a) Effective stress and (b) strain distributions of specimens after upsetting.

Grain refinement due to the fact of recrystallisation during the forging process determines the final grain size of an alloy. As shown in Figure 11a, the uneven distribution of deformation resulted in a difference in grain size in different regions. The as-homogenised coarse grain structure underwent significant grain refinement during the upsetting process. The recrystallisation volume fraction of region I was small because of the small strain, and there was no recrystallisation at the centre of the region. The grain size of the region was the same as the initial grain size, and recrystallisation occurred only in some regions. Due to the severe deformation in region II, there was adequate recrystallisation in the region, the grain size was uniform, and the centre of the region was completely recrystallised. The grain size of region III was not uniform, unlike in regions I and II. Compared with other regions, region II showed the largest deformation and the most sufficient recrystallisation. Compared to the edge region, the accumulated strain at the centre was larger, and recrystallisation occurred at the initial stage of the MDF process, providing more potential sites for recrystallisation nuclei. A higher accumulated strain indicates higher stored energy and an increased driving force for recrystallisation [31]. Consequently, a finer and more homogeneous grain structure was formed at the centre region after upsetting. In addition, due to the heat transfer between the specimen and the dies and that between the specimen and the environment, the final temperature around the specimen was much lower than that of the specimen core after upsetting. Consequently, finer and more homogeneous grain with an average grain size range of 45.7–49.9 μm developed at the centre region after upsetting.

Recrystallisation is a process that can induce stress relaxation to varying extents in a deformed metal by releasing the stored energy arising from the deformation process when heat-treated at an appropriate temperature [32]. Recrystallisation is important in microstructural development in deformation-processed metals [33]. During upset simulation, three types of recrystallisation behaviour, including DRX, SRX and MRX, may occur within

the sample. DRX occurs during high-temperature deformation, and it aids grain refinement and homogenisation. Figure 11b shows that the DRX volume fraction in region II was sufficient for grain refinement. The DRX fraction at the core of the sample reached 100%, and the grains were uniformly distributed. The microstructure agreed with the stress–strain field. SRX occurs in high-temperature multi-pass deformation gaps of materials. MRX differs from SRX. It occurs with DRX at the core and continues to grow within the gap time. As shown in Figure 11c,d, neither SRX nor MRX occurred during upsetting. This was because upsetting was a one-off finish, and there was no time for deformation gaps. Thus, it cannot provide sufficient conditions for SRX or MRX [34–40].

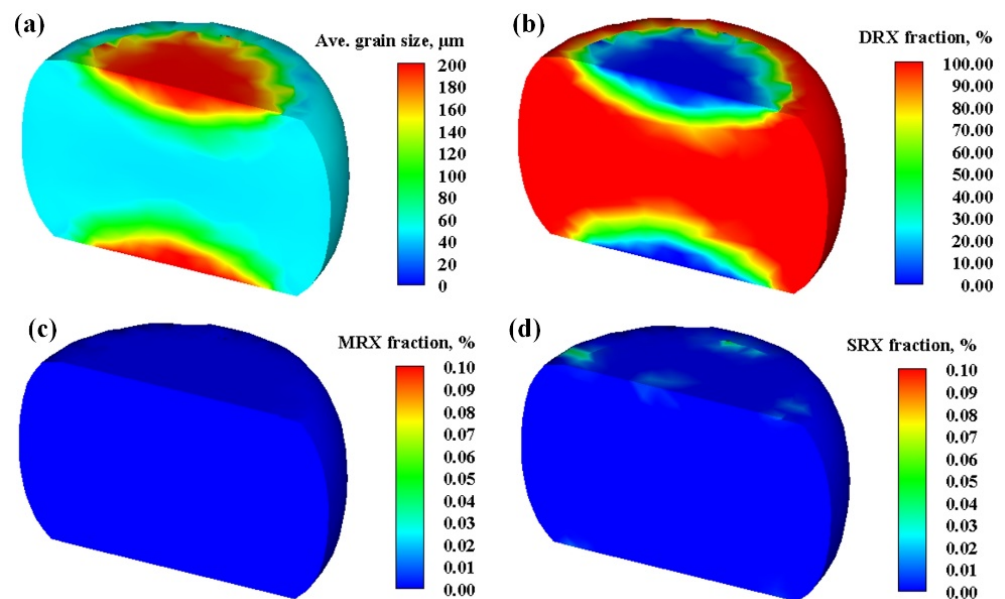


Figure 11. (a) Average grain size; (b) dynamic recrystallisation (DRX); (c) meta-recrystallisation (MRX); (b,d) static recrystallisation (SRX) fractions in the specimen after upsetting.

To further investigate the grain evolution, different points on the specimen were observed as shown in Figure 12a. With an increase in reduction during the MDF process, both the effective strain at the centre (P2) and side (point P3) regions increased, and the difference in the accumulated strain between the centre and side regions increased, but there was a little change in the effective strain at P1. After upsetting, the effective strain at points P1, P2 and P3 were approximately 0.03, 1.24 and 0.72, respectively. The average grain sizes at points P2 and P3 decreased as the reduction exceeded a certain value (Figure 12c). Point P2 recrystallised in 17 s, which was earlier than that at P3 (18 s), and the rate of grain refinement at P2 was greater than that at P3. Compared with P3, P2 showed a better grain refinement effect, and the final average grain size was obtained first. In contrast, P1 was restricted by friction resistance, the strain was always lower than the critical strain, and no recrystallisation occurred. The final average grain size at P1, P2 and P3 was 200, 45.4 and 45.6 μm , respectively. The DRX volume fractions at P2 and P3 (Figure 12d) increased when the reduction exceeded a certain value, which is consistent with Figure 12b,c. At 17 s, that is, when the strain reached 0.15, the recrystallisation fraction at P2 increased first. Complete recrystallisation occurred at P2 and P3 after upsetting, but no DRX occurred at P1, which is in a difficult deformation zone. The final DRX fractions at P1, P2 and P3 were 0%, 100% and 100%, respectively.

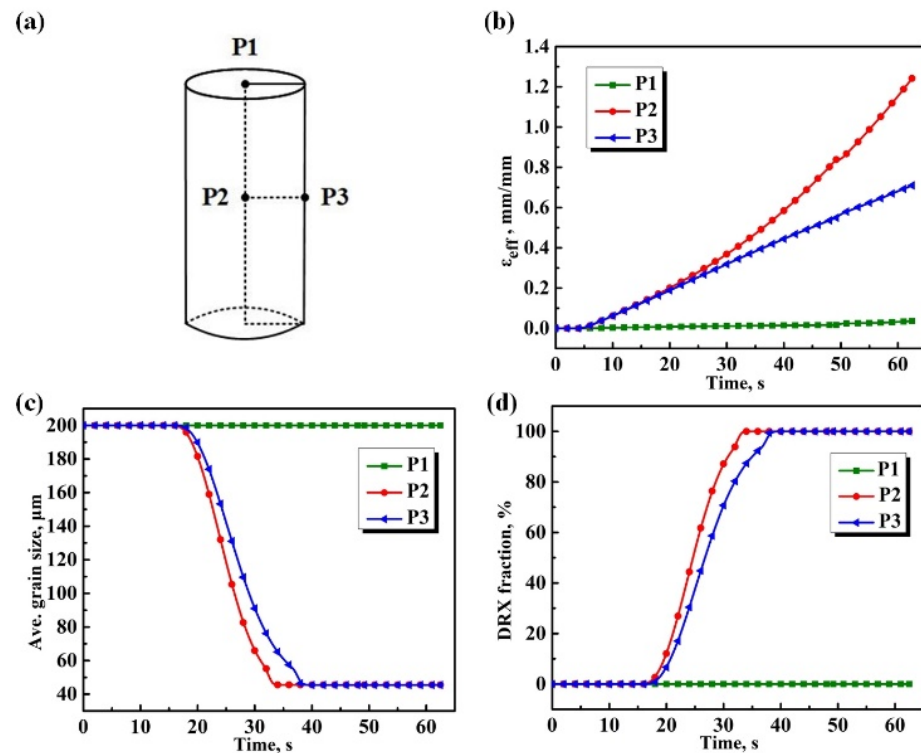


Figure 12. (a) Different tracking points; (b) effective strain; (c) average grain size; (d) DRX fraction curves.

5.3. Comparison of Microstructural Evolution between MDF and TUSF

Drawing is a forging process in which the cross-sectional area of a blank is reduced, and the length is increased by deformation. According to the strain during each compression deformation, drawing increases the length through continuous accumulation of axial strain. The end surface of the specimen was in contact with an anvil; thus, it was affected by friction resistance, resulting in limited deformation and smaller strain at the region. On the other hand, friction resistance decreased towards the specimen centre, resulting in more deformation at the centre (Figure 13). Herein, the maximum and minimum strains after MDF were 3.86 and 0.6, respectively. Compared with MDF, the feeding amount of each drawing step was small in TUSF, and it was necessary to rotate the specimen to achieve deformation. Therefore, the TUSF process was more complex and inefficient. After TUSF, the maximum and minimum strains were 3.43 and 0.32, respectively.

The average grain size varied from 40.6 to 43.3 μm at the centre of the specimen after MDF (Figure 14a) and from 35.7 to 46.0 μm after TUSF (Figure 14b). The average grain size of the specimen core after TUSF was slightly smaller, but the range was higher than that of the sample after MDF. The DRX of MDF was more adequate, and the grain at the centre was more uniform; meanwhile, the surface of the sample was neater after MDF than after TUSF. The minimum and maximum grain sizes were 1 and 60 μm , respectively after MDF. However, the surface of the sample after TUSF was not smooth. The minimum and maximum grain sizes were 12 and 132 μm , respectively. The large span of the grain size and incomplete recrystallisation in the local region after upsetting and drawing affected the comprehensive performance of forging and, subsequent, processing. The SRX and MRX volume fractions of the MDF ingot were much lower than those of traditional forging, because MDF is a continuous compression deformation process. The ingot showed DRX during deformation, and the DRX fraction in most regions of the ingot reached 100%. In contrast, the conditions were provided for SRX and MRX during the TUSF process. In general, grain refinement was mainly achieved by DRX; grain refinement and dynamic softening caused by the SRX and MRX were relatively low.

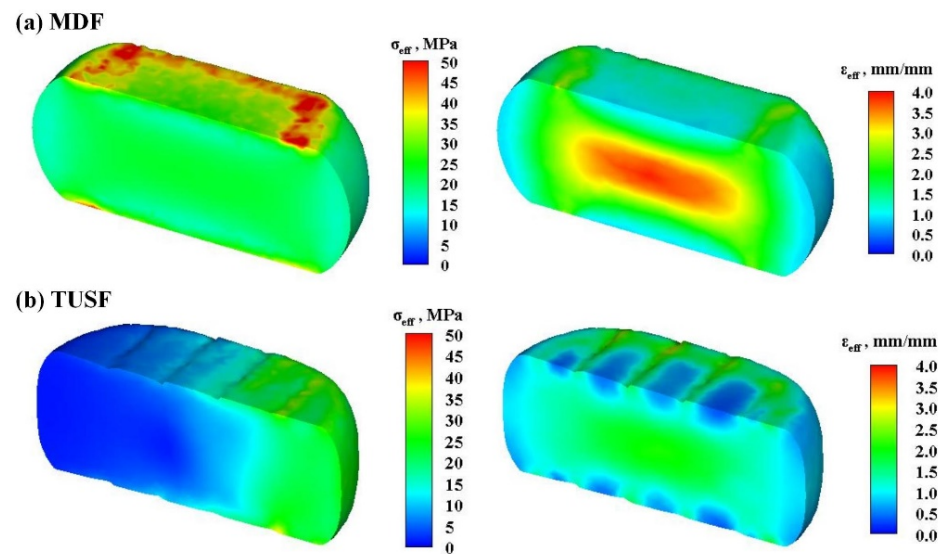


Figure 13. Effective stress and strain distributions of specimens after (a) MDF and (b) TUSF.

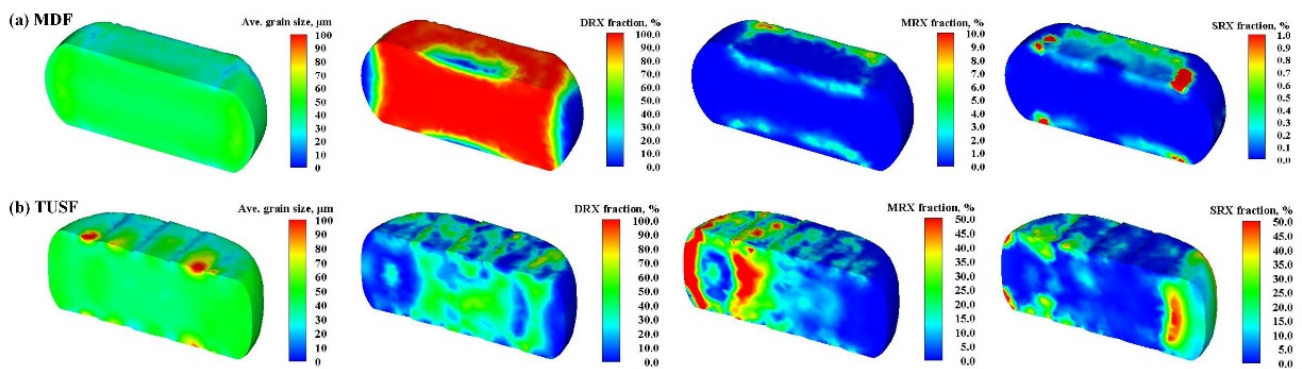


Figure 14. Schematic diagram of the microstructural distribution and recrystallisation behaviour after (a) MDF and (b) TUSF.

Second upsetting deformation was carried out after a complete MDF and TUSF to compare and analyse the effects of MDF and TUSF on subsequent deformation of ingots. Due to the influence of friction resistance on the end surface of the specimen, the nonuniform deformation of the specimen showed a drum shape. The distribution of effective stress and strain was consistent with the characteristics of the three deformation regions in the upsetting process (Figure 15). As shown in Figure 16, with an increase in reduction, strain at the three points increased gradually and reached a maximum. The initial effective strains at P1, P2 and P3 in the MDF sample were 0.86, 3.89 and 1.88, respectively, and the final strains were 1.15, 5.02 and 2.10, respectively. The initial values at P1, P2 and P3 in the TUSF sample were 0.91, 2.07, 1.18, and the final strain values were 1.07, 3.18 and 1.63, respectively.

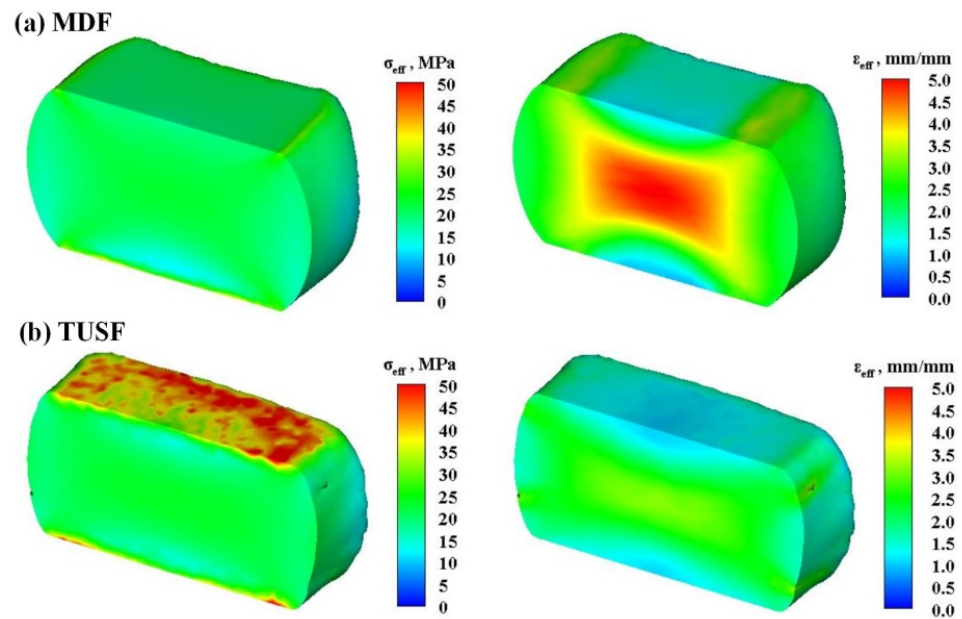


Figure 15. Effective stress and strain distributions in (a) MDF and (b) TUSF specimens.

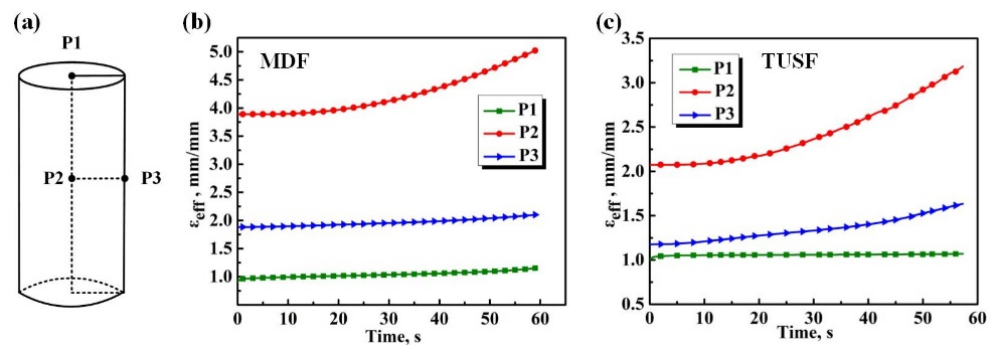


Figure 16. Time-dependent effective strain curves for (b) MDF and (c) TUSF specimens at (a) different tracking points.

The average grain size ranged from 40.2 to 41.8 μm in the core of the MDF specimen and from 38.7 to 42.2 μm in that of the TUSF specimen. Their average values were similar. The grain size in the core of the TUSF specimen was slightly smaller, but the range was slightly higher. Analysing and comparing Figure 17a,b, we can find that DRX in the MDF sample was more sufficient. The recrystallisation volume fraction in the core of the MDF specimen reached 100%, and the grain size was more uniform than that of the TUSF specimen. The minimum and maximum grain sizes of the entire sample were 12 and 52 μm , respectively. However, the surface of the TUSF specimen was not smooth, and the minimum and maximum grain sizes were 13 and 63 μm , respectively. The grain size of a traditional forging specimen was large, the grain of the sample centre was not uniform and there were mixed crystals, which can affect the overall performance of forged samples and subsequent processing.

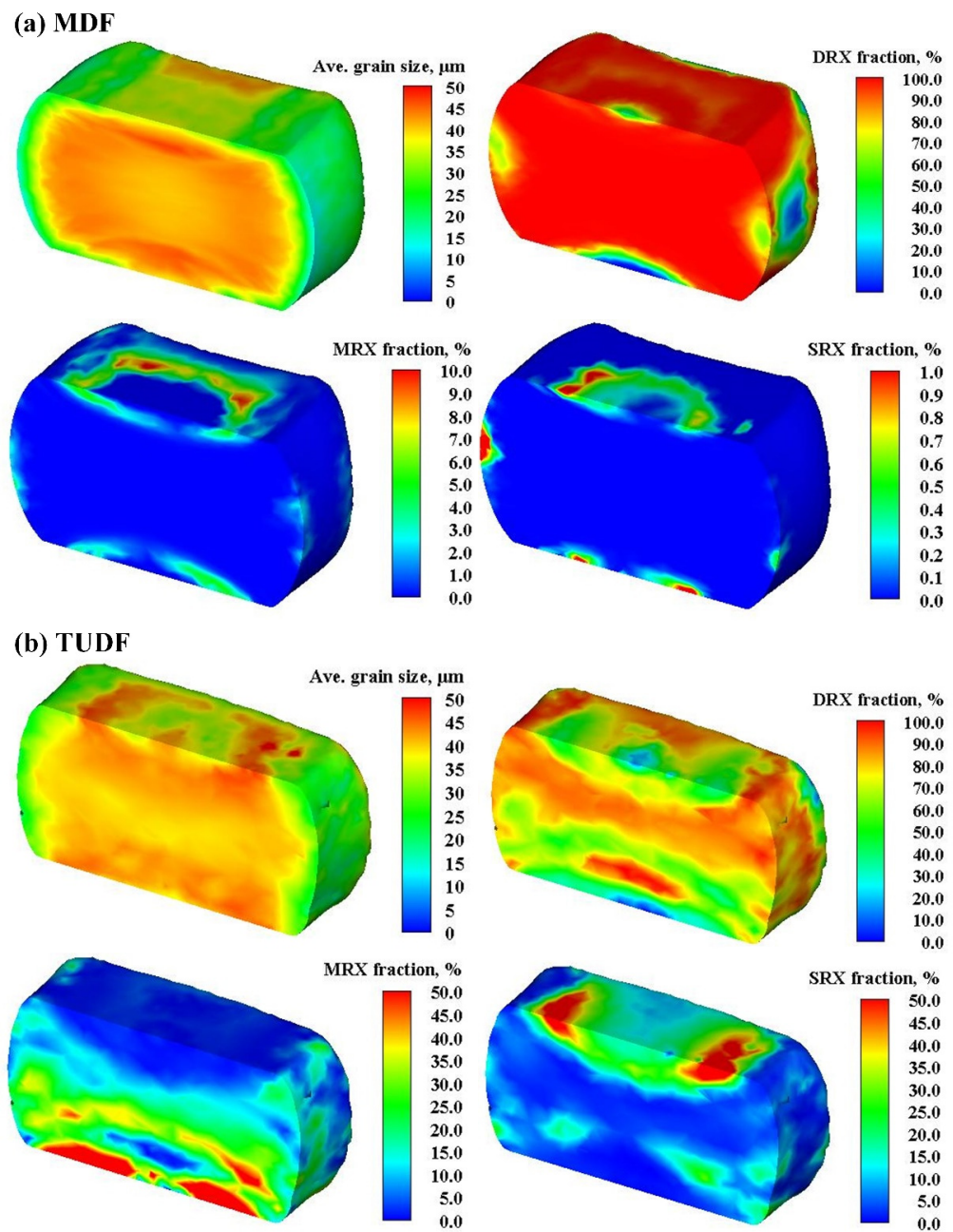


Figure 17. Microstructural distribution contours for the (a) MDF and (b) TUSF specimens.

The initial grain sizes at P1, P2 and P3 in the MDF specimen were 39, 40 and 17 μm , and the final grain sizes were 36, 40 and 14 μm , respectively (Figure 18). The grain size at P2 was almost unchanged, and that at P1 and P3 decreased significantly, possibly because the deformation on the side surface was relatively large, and the grains on the surface were easily broken. However, the temperature of the core remained at the initial temperature of 1150 $^{\circ}\text{C}$, the grain plasticity was good, and the grains would not fracture during plastic deformation. On the other hand, the initial grain sizes at P1, P2 and P3 on the TUSF specimen were 46, 39 and 41 μm , and the final grain sizes were 42, 39 and 24 μm , respectively. After further treatment, the grain structure at P2 remained unchanged, and the average grain size was 39 μm . There are more variations in the average grain size and DRX volume fraction in the TUSF specimen (Figure 18b), attributed to the uneven distribution of grain size and DRX during drawing.

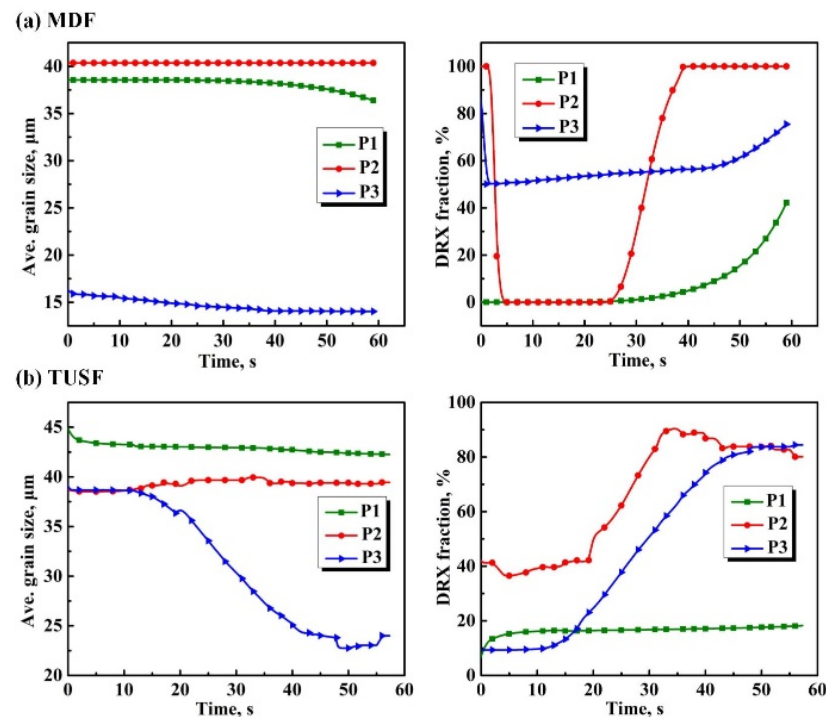


Figure 18. Time-dependent average grain size and DRX fraction curves for (a) MDF and (b) TUSF specimens at different tracking points.

6. Conclusions

- (1) The grain size distribution in the MDF specimen was inhomogeneous. During the first step of MDF, the microstructure undergoes significant grain refinement, but an inhomogeneous grain structure was obtained due to the inhomogeneous strain distribution at the centre and edge regions. Finer grains developed at the centre region during forging. Based on experimental results, the microstructural evolutionary model used in this study is reliable;
- (2) The forged ingot had an inhomogeneous grain distribution, and the average grain size at the core of the SDP1 steel sample after MDF was approximately 40.6–43.3 μm . Although this was slightly greater than the post-TUSF grain size (35.7–46.0 μm), the microstructure of the SDP1 steel sample after MDF was more uniform than that after TUSF;
- (3) After MDF, the grains at the core of the sample were completely recrystallised (a recrystallisation volume fraction of 100%). In contrast, after TUSF, the grains at the centre of the sample were completely recrystallised, resulting in a nonuniform grain structure. Insufficient recrystallisation can result in mixed crystals;
- (4) The average grain size of the SDP1 steel sample after MDF was 11.0–60.0 μm , which was smaller than that of the post-TUSF sample (12.0–132.0 μm). In addition, the surface of the sample after TUSF was not smooth, which can affect the overall performance of the sample and subsequent processing.

Author Contributions: Conceptualisation, X.C. and J.L. (Junwan Li); methodology, X.Z.; software, X.Z.; validation, X.C., B.W. and J.L. (Jiayuan Li); formal analysis, X.C.; investigation, X.C.; resources, X.W.; data curation, B.W.; writing—original draft preparation, X.C. and X.Z.; writing—review and editing, J.L. (Junwan Li) and P.Z.; visualisation, X.C.; supervision, J.L. (Junwan Li); project administration, X.C.; funding acquisition, X.W. All authors have read and agreed to the published version of the manuscript.

Funding: This research was funded by National Key R&D Program of China (grant numbers: 2016YFB0300400 and 2016YFB0300404).

Data Availability Statement: The data presented in this study are available upon request from the corresponding author. The data are not publicly available due to the fact of technical or time limitations.

Acknowledgments: The authors are grateful to Xiaocheng Li., Xijuan He. and Jie Ji. for their contribution to the discussion.

Conflicts of Interest: The authors declare no conflict of interest.

References

1. Zheng, Y.-F.; Wu, R.-M.; Li, X.-C.; Wu, X.-C. Continuous cooling transformation behaviour and bainite formation kinetics of new bainitic steel. *Mater. Sci. Technol.* **2016**, *33*, 454–463. [CrossRef]
2. Wu, R.M.; Zheng, Y.; Wu, X.C.; Li, X.C. Effect of titanium on the microstructure and hardness uniformity of non-quenched and tempered prehardened steel for large-section plastic mould. *Ironmak. Steelmak.* **2016**, *44*, 17–22. [CrossRef]
3. Xiaoxiao, Z.; Xuan, C.; Xiaocheng, L.; Yushu, H.; Junwan, L.; Xiaochun, W. Numerical Study on Microstructure Evolution of Large Cross-section SDP1 Plastic Die Steel during Multi-directional Forging. *Shanghai Metals* **2020**, *42*, 57–62. [CrossRef]
4. Xiao, Z.; Yang, X.; Wang, J.; Fang, Z.; Guo, C.; Zhang, D.; Yang, Y.; Zhang, X. Influence of Fe addition on annealing behaviors of a phosphorus containing brass. *J. Alloys. Compd.* **2017**, *712*, 268–276. [CrossRef]
5. Tang, L.; Liu, C.; Chen, Z.; Ji, D.; Xiao, H. Microstructures and tensile properties of Mg–Gd–Y–Zr alloy during multidirectional forging at 773K. *Mater. Des.* **2013**, *50*, 587–596. [CrossRef]
6. Bahmani, A.; Arthanari, S.; Shin, K.S. Achieving a high corrosion resistant and high strength magnesium alloy using multi directional forging. *J. Alloys Compd.* **2020**, *856*, 158077. [CrossRef]
7. Heidarzadeh, A.; Saeid, T.; Klemm, V. Microstructure, texture, and mechanical properties of friction stir welded commercial brass alloy. *Mater. Charact.* **2016**, *119*, 84–91. [CrossRef]
8. Miura, H.; Yu, G.; Yang, X. Multi-directional forging of AZ61Mg alloy under decreasing temperature conditions and improvement of its mechanical properties. *Mat. Sci. Eng. A-Struct.* **2011**, *528*, 6981–6992. [CrossRef]
9. Zharebtsov, S.V.; Salishchev, G.A.; Galeev, R.M.; Valiakhmetov, O.R.; Mironov, S.Y.; Semiatin, S.L. Production of submicrocrystalline structure in large-scale Ti–6Al–4V billet by warm severe deformation processing. *Scripta Mater.* **2004**, *51*, 1147–1151. [CrossRef]
10. Miura, H.; Maruoka, T.; Yang, X.; Jonas, J.J. Microstructure and mechanical properties of multi-directionally forged Mg–Al–Zn alloy. *Scripta Mater.* **2012**, *66*, 49–51. [CrossRef]
11. Gubicza, J.; Dobatkin, S.; Khosravi, E.; Kuznetsov, A.; Lábár, J.L. Microstructural stability of Cu processed by different routes of severe plastic deformation. *Mater. Sci. Eng. A* **2011**, *528*, 1828–1832. [CrossRef]
12. Sitdikov, O.; Sakai, T.; Miura, H.; Hama, C. Temperature effect on fine-grained structure formation in high-strength Al alloy 7475 during hot severe deformation. *Mater. Sci. Eng. A* **2009**, *516*, 180–188. [CrossRef]
13. Nunes, L.G.d.S.; Machado, M.L.P. Simulation of the Accumulative Roll-Bonding process through warm torsion test. *J. Mater. Res. Technol.* **2018**, *7*, 326–330. [CrossRef]
14. Wang, H.; Su, L.; Yu, H.; Lu, C.; Tieu, A.K.; Liu, Y.; Zhang, J. A new finite element model for multi-cycle accumulative roll-bonding process and experiment verification. *Mater. Sci. Eng. A-Struct.* **2018**, *726*, 93–101. [CrossRef]
15. Kulagin, R.; Beygelzimer, Y.; Ivanisenko, Y.; Mazilkin, A.; Straumal, B.; Hahn, H. Instabilities of interfaces between dissimilar metals induced by high pressure torsion. *Mater. Lett.* **2018**, *222*, 172–175. [CrossRef]
16. Li, P.; Lin, Q.; Wang, X.; Tian, Y.; Xue, K.-M. Recrystallization behavior of pure molybdenum powder processed by high-pressure torsion. *Int. J. Refract. Met. Hard Mater.* **2018**, *72*, 367–372. [CrossRef]
17. Martynenko, N.; Lukyanova, E.; Serebryany, V.; Gorshenkov, M.; Shchetinin, I.; Raab, G.; Dobatkin, S.; Estrin, Y. Increasing strength and ductility of magnesium alloy WE43 by equal-channel angular pressing. *Mater. Sci. Eng. A-Struct.* **2018**, *712*, 625–629. [CrossRef]
18. Wei, J.; You, J.; Zhang, D.; Jiang, S.; Chen, Z.; Liu, C. Reducing yield asymmetry in a wrought Mg–9Al alloy by randomized texture achieved via multi-directional forging. *Mat. Sci. Eng. A-Struct.* **2020**, *796*, 140003. [CrossRef]
19. Manjunath, G.A.; Shivakumar, S.; Fernandez, R.; Nikhil, R.; Sharath, P.C. A review on effect of multi-directional forging/multi-axial forging on mechanical and microstructural properties of aluminum alloy. *Mater. Today. Proc.* **2021**, *47*, 2565–2569. [CrossRef]
20. Bagherpour, E.; Pardis, N.; Reihanian, M.; Ebrahimi, R. An overview on severe plastic deformation: Research status, techniques classification, microstructure evolution, and applications. *Int. J. Adv. Manuf. Technol.* **2018**, *100*, 1647–1694. [CrossRef]
21. Xing, J.; Yang, X.; Miura, H.; Sakai, T. Mechanical Properties of Magnesium Alloy AZ31 after Severe Plastic Deformation. *Mater. Trans.* **2008**, *49*, 69–75. [CrossRef]
22. Zhang, R.; Wang, D.; Yuan, S. Effect of multi-directional forging on the microstructure and mechanical properties of TiBw/TA15 composite with network architecture. *Mater. Des.* **2017**, *134*, 250–258. [CrossRef]
23. Zhang, Z.; Qu, S.; Feng, A.; Shen, J. Achieving grain refinement and enhanced mechanical properties in Ti–6Al–4V alloy produced by multidirectional isothermal forging. *Mater. Sci. Eng. A-Struct.* **2017**, *692*, 127–138. [CrossRef]
24. Khani Moghanaki, S.; Kazeminezhad, M.; Logé, R. Mechanical behavior and texture development of over-aged and solution treated Al–Cu–Mg alloy during multi-directional forging. *Mater. Charact.* **2018**, *135*, 221–227. [CrossRef]

25. Huang, H.; Zhang, J. Microstructure and mechanical properties of AZ31 magnesium alloy processed by multi-directional forging at different temperatures. *Mater. Sci. Eng. A-Struct.* **2016**, *674*, 52–58. [CrossRef]
26. Seshacharyulu, T.; Medeiros, S.; Morgan, J.; Malas, J.; Frazier, W.; Prasad, Y. Hot deformation mechanisms in ELI Grade Ti-6Al-4V. *Scr. Mater.* **1999**, *41*, 283–288. [CrossRef]
27. Nakao, Y.; Miura, H. Nano-grain evolution in austenitic stainless steel during multi-directional forging. *Mater. Sci. Eng. A-Struct.* **2011**, *528*, 1310–1317. [CrossRef]
28. Zharebtsov, S.; Murzinova, M.; Salishchev, G.; Semiatin, S. Spheroidization of the lamellar microstructure in Ti-6Al-4V alloy during warm deformation and annealing. *Acta Mater.* **2011**, *59*, 4138–4150. [CrossRef]
29. Soleymani, V.; Eghbali, B. Grain Refinement in a Low Carbon Steel Through Multidirectional Forging. *J. Iron Steel Res. Int.* **2012**, *19*, 74–78. [CrossRef]
30. Li, X.; Duan, L.; Li, J.; Wu, X. Experimental study and numerical simulation of dynamic recrystallization behavior of a microalloyed plastic mold steel. *Mater. Des.* **2015**, *66*, 309–320. [CrossRef]
31. Kim, W.J.; Hong, S.I.; Kim, Y.S.; Min, S.H.; Jeong, H.T.; Lee, J.D. Texture development and its effect on mechanical properties of an AZ61 Mg alloy fabricated by equal channel angular pressing. *Acta Mater.* **2003**, *51*, 3293–3307. [CrossRef]
32. Sakai, T.; Belyakov, A.; Kaibyshev, R.; Miura, H.; Jonas, J.J. Dynamic and post-dynamic recrystallization under hot, cold and severe plastic deformation conditions. *Prog. Mater. Sci.* **2014**, *60*, 130–207. [CrossRef]
33. Lu, Y.; Ma, R.; Wang, Y.-n. Texture evolution and recrystallization behaviors of Cu–Ag alloys subjected to cryogenic rolling. *T. Nonferr. Metal. Soc.* **2015**, *25*, 2948–2957. [CrossRef]
34. Dehghan-Manshadi, A.; Barnett, M.R.; Hodgson, P.D. Recrystallization in AISI 304 austenitic stainless steel during and after hot deformation. *Mat. Sci. Eng. A-Struct.* **2008**, *485*, 664–672. [CrossRef]
35. Montheillet, F.; Lurdos, O.; Damamme, G. A grain scale approach for modeling steady-state discontinuous dynamic recrystallization. *Acta Mater.* **2009**, *57*, 1602–1612. [CrossRef]
36. Eghbali, B. Effect of strain rate on the microstructural development through continuous dynamic recrystallization in a microalloyed steel. *Mater. Sci. Eng. A-Struct.* **2010**, *527*, 3402–3406. [CrossRef]
37. Li, D.; Guo, Q.; Guo, S.; Peng, H.; Wu, Z. The microstructure evolution and nucleation mechanisms of dynamic recrystallization in hot-deformed Inconel 625 superalloy. *Mater. Des.* **2011**, *32*, 696–705. [CrossRef]
38. Vervynckt, S.; Verbeken, K.; Thibaux, P.; Houbaert, Y. Recrystallization–precipitation interaction during austenite hot deformation of a Nb microalloyed steel. *Mat. Sci. Eng. A-Struct.* **2011**, *528*, 5519–5528. [CrossRef]
39. BadJena, S.; Park, J. Effect of particles on the dynamic recrystallization behavior of Al–V–N microalloyed medium carbon steel. *Mater. Sci. Eng. A-Struct.* **2012**, *548*, 126–133. [CrossRef]
40. Mehtonen, S.; Karjalainen, L.; Porter, D. Hot deformation behavior and microstructure evolution of a stabilized high-Cr ferritic stainless steel. *Mater. Sci. Eng. A-Struct.* **2013**, *571*, 1–12. [CrossRef]

Article

A Study of Aluminum Honeycomb Structures under Dynamic Loading, with Consideration Given to the Effects of Air Leakage

Radosław Ciepielewski and Danuta Miedzińska *

Faculty of Mechanical Engineering, Military University of Technology, Kaliskiego 2 Street, 00-908 Warsaw, Poland; radoslaw.ciepielewski@wat.edu.pl

* Correspondence: danuta.miedzinska@wat.edu.pl

Abstract: Aluminum honeycomb structures are used in the construction of protective materials due to the positive relationship between their mass and their energy-absorbing properties. Applying such materials in the construction of large machinery, such as military vehicles, requires the development of a new method of finite element modeling, one that considers conditions with high strain rates, because a material model is currently lacking in the available simulation software, including LS-DYNA. In the present study, we proposed and verified a method of numerically modeling honeycomb materials using a simplified Y element. Results with a good level of agreement between the full core model and the Y element were achieved. The obtained description of the material properties was used in the subsequent creation of a homogeneous model. In addition, we considered the influence of increases in pressure and the leakage of the air entrapped in the honeycomb cells. As a result, we were able to attain a high level of accuracy regarding the stress values across the entire range of progressive failure, from the loss of stability to full core densification, and across a wide range of strain rates.

Keywords: honeycomb; numerical modelling; dynamic compression; structure; air leakage

Citation: Ciepielewski, R.; Miedzińska, D. A Study of Aluminum Honeycomb Structures under Dynamic Loading, with Consideration Given to the Effects of Air Leakage. *Materials* **2023**, *16*, 2211. <https://doi.org/10.3390/ma16062211>

Academic Editors: Shuwen Wen, Yongle Sun and Xin Chen

Received: 27 January 2023

Revised: 6 March 2023

Accepted: 7 March 2023

Published: 9 March 2023



Copyright: © 2023 by the authors. Licensee MDPI, Basel, Switzerland. This article is an open access article distributed under the terms and conditions of the Creative Commons Attribution (CC BY) license (<https://creativecommons.org/licenses/by/4.0/>).

1. Introduction

Functional, cell-oriented structures, including honeycombs, have a long history of successful application. For example, they were used in the initial period of space exploration, specifically in the Apollo 11 [1] project, to build elements of the crew and technical compartments. NASA and others [2–4] concluded that the honeycomb structure has the best energy-absorbing properties in relation to its specific mass. Due to this feature, honeycomb structures are used across a wide range of industries, including the automotive industry [5,6] and the military [7,8].

Sandwich structures with honeycomb cores are commonly used because of their high stiffness-to-weight ratio. Moreover, they have predictable progressive folding (stress–strain) characteristics in the case of static loading. This feature has made it possible to derive a mathematical model that enables the calculation of the so-called average value of crushing stress (plateau) to the core (occurring from the moment of stability loss to the beginning of the increase in force due to the structure’s densification) on the basis of the known, basic values characterizing honeycomb structures, such as the yield point of the core material, the wall thickness, and the cell size [9]. However, in [10,11], the authors show that the strength of the structure can increase by up to 50% with dynamic loading. In addition, there are a number of aspects that, if simplified, may make it impossible to effectively predict a honeycomb’s structural behavior, such as the air trapped inside the cells [12].

Modern tools, such as the finite element method (FEM) used in industry and science, allow for the effective prediction of the effects of dynamic loading, including fast-changing ones such as those that a shock wave from the detonation of an explosive may have on protective structures. In order to ensure a high-quality representation of the real conditions

and the properties of the materials used, the data used in the preparation of the model should be as reliable as possible.

Scientific publications dealing with the numerical modeling of honeycomb structures can be divided into several groups, according to the subject covered by the authors. The most popular subjects include modeling the phenomenon of the loss of stability, modeling the local phenomena that occur during structural deformation, the determination of strength characteristics based on full geometric models and submodels, and observations of the phenomenon of energy absorption by structures modeled as homogeneous, using special constitutive models.

In [13], the authors focused on modeling the buckling process and progressive folding by comparing the effects obtained by using geometry to represent the samples, containing 16 single cells, used in their experimental tests, with results obtained from a four-cell compression analysis. The authors indicate that, by applying the appropriate boundary conditions—that is, by ensuring that the free edges of the walls maintained symmetry with respect to the plane perpendicular to them—the authors were able to obtain the same characteristics regardless of the number of individual cells that were modeled.

Similarly, in [14], the authors focused on determining the characteristics of dynamically loaded aluminum cores. The structures were modeled by retaining the full geometry corresponding to that which was used in the experimental research. Their test results show that successive walls inside the core deformed symmetrically in relation to their longer axes of symmetry.

In scientific nomenclature, the behavior of the core as a single-cell sector is referred to as the Y element. Among others, this modeling method was used in [15]. The authors presented the results of numerical analyses, the subject of which was the static compression of honeycomb cores as modeled in two different ways—by fully mapping the honeycomb geometry, and by solely modeling one single-unit sector. The main advantage of the method, in addition to the simple construction of the model and the significant reduction in the time needed to perform the calculations, is the ability to determine the full characteristics of the core, including the elastic range and the compaction range. The oscillations observed in the area of progressive folding represent a noticeable disadvantage.

A different approach to reducing the so-called numerical cost of the analysis of the strength of a cell core in an aluminum honeycomb is presented by the authors of [16], which is devoted to modeling the structure by using a structure consisting of joint-connected short beams. The authors used a Discrete Beam Method (DBM) and proved that the approach is correct and that it provides results that demonstrate a high level of agreement with those obtained experimentally.

Another approach often found in the literature [17,18]—which allows for a significant simplification of the metallic honeycomb geometric modeling process and a reduction of the time needed to perform the calculations—is the use of one of the constitutive models designed to reproduce the behavior of the loaded structure, which is modeled as homogeneous, usually using eight-node cubic elements. This method allows for a significant simplification of the core-modeling process, especially when it is applied to structures with large dimensions in relation to the characteristic dimensions of the structure. Modeling fine walls using elements with a small characteristic dimension, thus ensuring a reliable representation of the deformation of the core, reduces the time step in the case of dynamic analyses, leading to a significant increase in the time needed to perform the calculations.

In such cases, the MAT_HONEYCOMB constitutive material model, which is applied in FEM calculation systems (including LS-DYNA), can be used [19]. Its application allows for a full representation of the global stiffness of a structure, both axial and shear, in terms of elasticity, progressive folding, and complete compression, accompanied by its linear elastic characteristics. This model has been used to successfully predict the behavior of materials in which thin-walled, anisotropic-oriented structures were used, e.g., honeycombs, as well as in foamed metals and plastics. However, a significant simplification of the structural

modeling process using MAT_HONEYCOMB requires the knowledge of a number of the parameters and characteristics of a particular core.

On the basis of the work presented in [20] produced by researchers at Toyota Motors®, the LS-DYNA system has been equipped with an additional constitutive model called MAT_MODIFIED_HONEYCOMB, which is designed to describe transversely isotropic bodies, the mechanical properties of which are symmetrical with respect to the axis normal to the isotropic plane. Honeycomb-type geometric structures have such a feature. However, industrially manufactured structures of this type are double-walled in one direction; therefore, treating them as transversely isotropic may be considered an oversimplification. Nevertheless, due to trends in the design of energy-consuming elements, including ones with regular spatial structures that have been created using additive manufacturing techniques, it is necessary to mention this material model as well. Because none of the material models described above have the ability to account for increases in stress caused by the pressure of compressed air trapped inside the cells, there is a need for a solution to that problem.

The aim of the present study was to develop and verify a method of modeling a homogenous honeycomb structure—as subjected to dynamic loads—using the characteristics obtained from a fast Y-element model. Such an approach has allowed us to obtain valuable results from FEM analysis, based on material models of the MAT_HONEYCOMB type, across a wide range of strain rates, thus minimizing the need for experimental research. The authors of [21] present experimental studies on the static and dynamic compression of honeycomb structures. The conclusion we drew from their work was that the strengthening of the structure is related to the volume of air trapped inside the closed cells.

2. Materials

Seven types of structures, all available from the catalogs of the manufacturers of these materials, were selected. The geometrical parameters of the individual structures are presented in Table 1. The name given to each structural type includes the following information: cell size–aluminum type–wall thickness. All dimensions used in the names are expressed in inches. An example of the studied material, along with the characteristic dimensions of its core, is shown in Figure 1.

Table 1. Geometrical parameters of the studied honeycomb structures.

No.	Type	Declared * Cell Size S [mm]	Declared * Wall Thickness t [mm]	Height T [mm]
1	1/8-5052-0.0007	3.1750	0.01778	10
2	1/8-5052-0.001	3.1750	0.02540	10
3	1/8-5052-0.0015	3.1750	0.03810	10
4	3/16-5052-0.0007	4.7625	0.01778	10
5	3/16-5052-0.001	4.7625	0.02540	10
6	3/16-5052-0.0015	4.7625	0.03810	10
7	1/4-5052-0.001	6.3500	0.02540	10

* data provided by the producer’s catalogue [21].

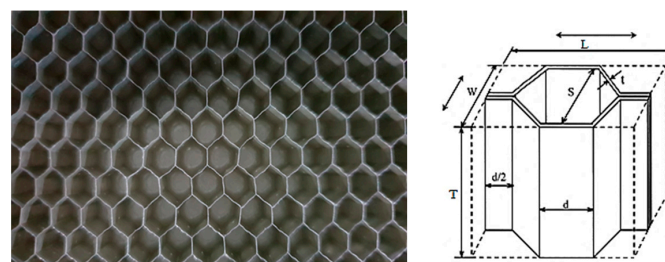


Figure 1. An example of the analyzed honeycomb structure (left), and the basic designations of the honeycomb’s structural elements (right) [9].

3. Research Methodology

The research was conducted in the following stages:

First, a numerical analysis of the static compression of a simplified model of the honeycomb structure (the Y element) was completed with the introduction of imperfections related to the geometry of the real structure (based on computed tomography (CT) studies); validation of the model using experimental research was achieved.

Second, numerical analyses of the honeycomb structures were performed, using a homogeneous model and characteristics obtained from the calculations of the Y element, including the influence of the air trapped within the cells of the structure.

The scheme of the research stages is presented in Figure 2.

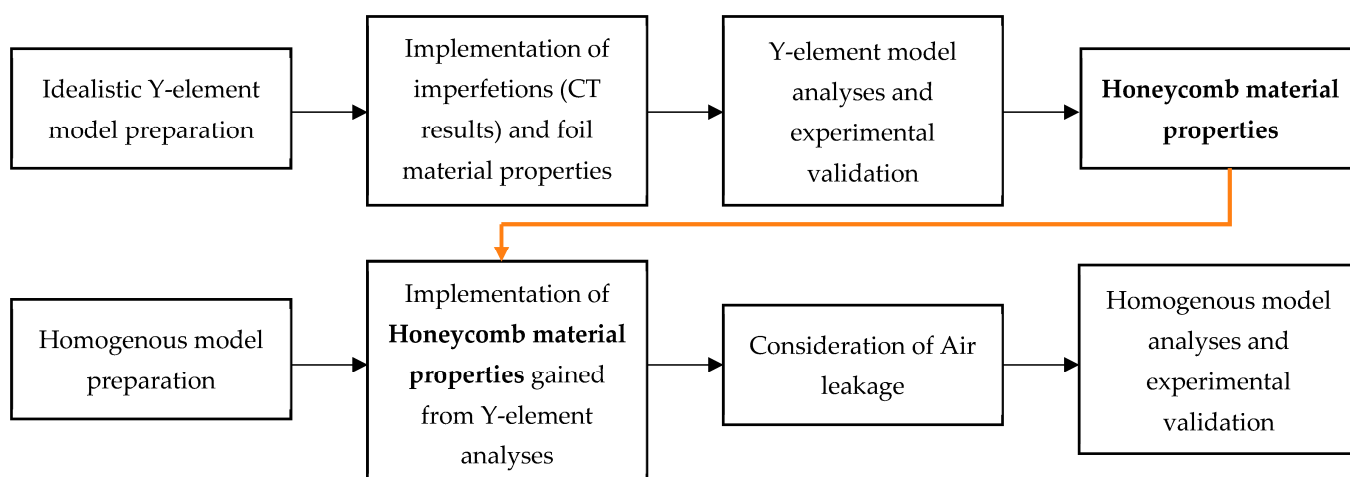


Figure 2. Research methodology scheme.

4. Models

In this section, the preparation of the model and its validation are presented. The conditions for the numerical analyses of static compression using the simplified Y element and those using the homogenous model are presented in Sections 4.1 and 4.2, respectively.

4.1. Numerical Analyses of Static Compression Using the Simplified Y Element

The smallest, repetitive subarea that can be separated from a structure is a cell with the base of an equilateral triangle, the sides of which are perpendicular to the walls of three adjacent honeycomb cells. A separated single cell (the Y element) is shown in Figure 3.

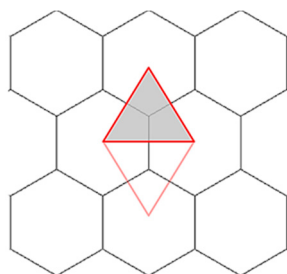


Figure 3. A single cell (Y element), as contained within a honeycomb structure.

As indicated in [13–15], structures consisting of repeating elements can be analyzed by solely focusing on a model that has been simplified down to the level of a segment, using appropriate boundary conditions. In the case of the analyzed structures, these conditions were limited to the treatment of the sides of the subarea as planes of symmetry.

The geometric model shown in Figure 4a, when prepared for discretization, consisted of three walls connected to each other in line with one of the longer edges. The walls were connected to each other at an opening angle of 120° .

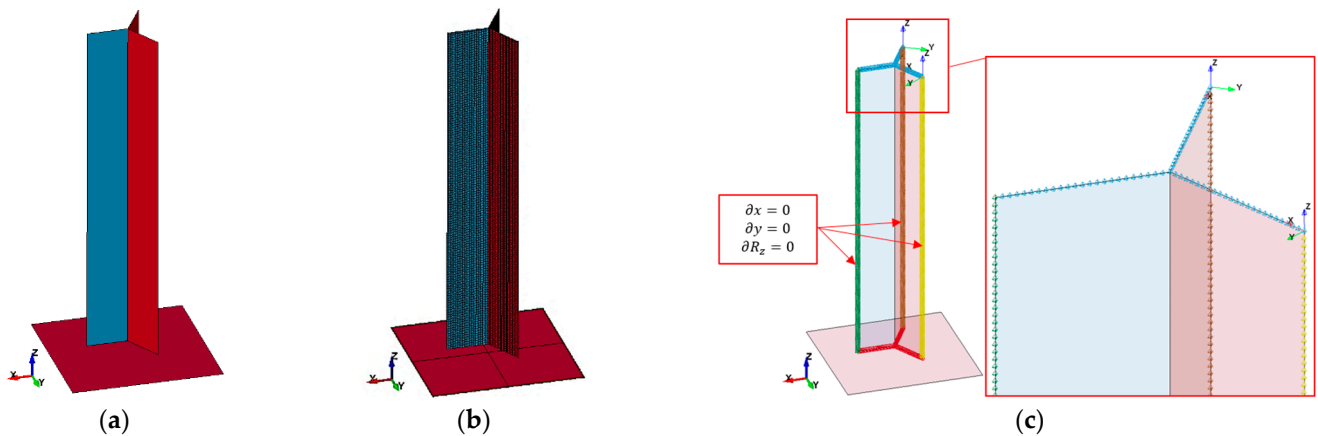


Figure 4. Y element: (a) geometric model, (b) finite element model, (c) boundary conditions.

Four-node, fully integral shell elements with five integration points across the element thickness were used to build the finite element mesh, as presented in Figure 4b. The characteristic dimension of the element was 0.23 mm, and there were 100 of them at the wall height. The selection of the element size was preceded by an analysis of the impacts that changing this parameter would have. At levels below the dimensions described above, no improvements were observed. The Belytschko–Tsay elements were used. To carry out the static compression analysis, all degrees of freedom were fixed in the top nodes and in the nodes next to the plane that forces motion (except that which was translational in the Z-axis). The boundary conditions, along with the symmetry conditions and the local coordinate systems, are shown in Figure 4c.

In order to accurately reproduce the actual structure and identify imperfections, the tested samples were subjected to computed tomography (CT) studies.

A SkyScan 1174 tomograph was used for this task. The obtained point clouds were processed to reduce noise, and then they were used to generate a polygonised structure; discrete, triangular surfaces were created between the closest points. In this way, spatial models of the cores were obtained, which was useful for making measurements. The axonometric views of the CT models for the 1/8-0.0015 and 3/16-0.0015 samples are shown in Figure 5.

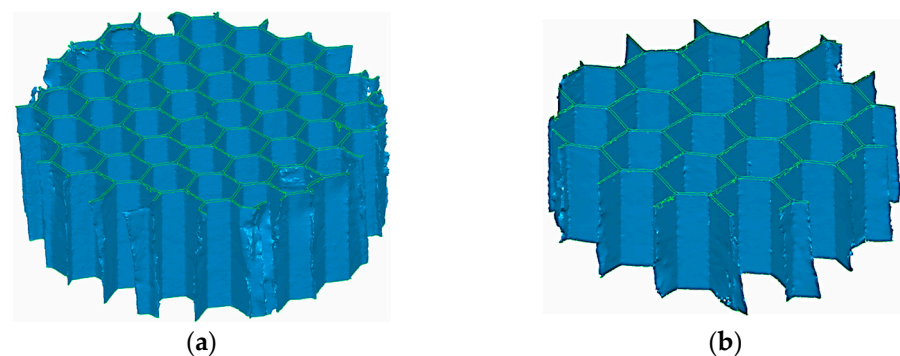


Figure 5. CT models of two of the studied materials: (a) 1/8-0.0015 and (b) 3/16-0.0015.

Analyzing the actual structures of the cores via the creation of three-dimensional models using computed tomography allowed for the examination of the basic geometric parameters, e.g., the length of individual walls, the size of the cell, and the bending radii of the walls near the joints. Exemplary measurement results are shown in Figure 6.

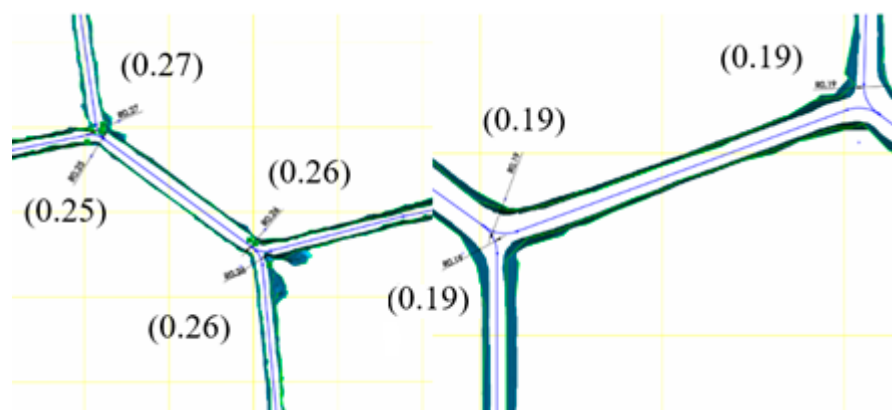


Figure 6. Examples of the measurement results of the geometrical parameters of the actual cores.

The results of the geometric measurements, averaged for individual samples, are presented in Table 2.

Table 2. List of characteristic dimensions obtained by measuring actual structures.

Measured Value	1/4-5052-0.001	3/16-5052-0.0007	3/16-5052-0.001	3/16-5052-0.0015	1/8-5052-0.0007	1/8-5052-0.001	1/8-5052-0.0015
R [mm]-bending radius of a single wall	0.27	0.22	0.28	0.39	0.19	0.26	0.37
d_{theor} [mm] theoretical wall width *	3.67	2.75	2.75	2.75	1.83	1.83	1.83
d_1 [mm] single-wall width	3.57	3.02	3.06	3.14	2.19	2.11	2.14
d_2 [mm] double-wall width	3.84	2.72	2.62	2.53	1.63	1.75	1.71

* provided in the manufacturer's catalog card [21].

On the basis of the data presented above, it can be seen that the double walls have a smaller width and the single walls have a higher width than those declared in the catalog cards. Moreover, the portion of the wall that is arched is a distinct part of it. The obtained measurement results allowed us to conclude that the bend radii of the walls depend mainly on their thickness, and that the dimensions are linked by a ratio of approximately 10:1.

In order to check the impact of the above-described geometric parameters, models of the structure of the sample designated as 1/8-0.0015 were built, one using a simple, idealized version, and the other constructed using the mapped shape of the walls according to the parameters described in Table 2. Both versions are shown in Figure 7, which demonstrates that, in addition to the visible rounding of the edges of the single wall (marked in red), the width of the double wall (marked in blue) has been reduced in favor of the single wall.

The introduced change in the geometry resulted in differences in the form of structural deformation that were apparent as early as the initial loss-of-stability phases. As can be seen in Figure 8, there are seven ridges on the flat core walls, and there are six smaller ridges on the rounded sides.

Minor differences in the geometry of the compared models were also reflected in the stress–strain characteristics obtained via the compression test. The value of the critical stress decreased by 11.6% (from 8.65 MPa to 7.64 MPa), and the value of the mean breaking stress decreased by 15.5% (from 5.98 MPa to 5.05 MPa). The value of the longitudinal modulus of elasticity before loss of stability also changed by 28.1% (from 3.11 GPa to 3.24 GPa). These are significant differences, thus the change in the model's geometry should be taken into

account in simulations. A comparison of the discussed characteristics, with reference to those obtained experimentally [21], is presented in Figure 9.

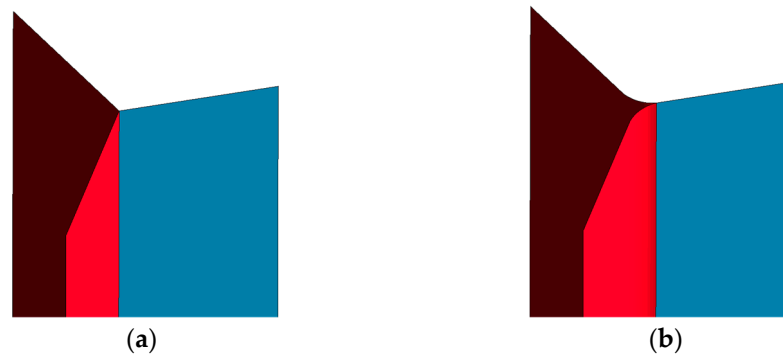


Figure 7. Geometric models of the core for the following versions: (a) simple/idealized; (b) showing the mapped shape of the rounded walls.

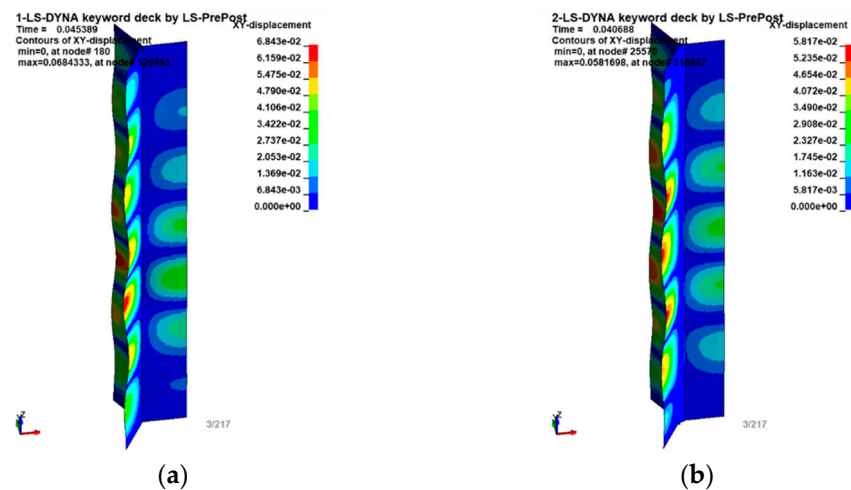


Figure 8. Maps of displacements [in mm] in the X–Y plane of the model in (a) the straight/idealized version; and (b) with the mapped shape of the rounded walls.

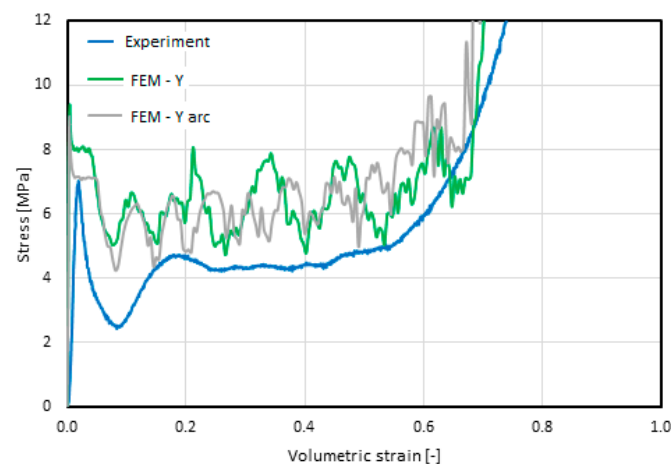


Figure 9. Comparison of the stress–volumetric strain characteristics of material 1/8-5052-0.0015 obtained for the following versions of the models: straight/idealized (FEM–Y, green line); with the mapped shape of the rounded walls (FEM–Y arc, gray line); and experimentally obtained characteristics, blue line [21].

The constitutive model MAT_003_PLASTIC_KINEMATIC [19] was used to reflect the behavior of the material from which the tested Y element was made: aluminum alloy Al 5052-H39. It is a bilinear model, the stress–strain relationship of which is described by defining the tangent of the angle of the elastic part and the part of the kinematic strengthening. The parameters and mechanical properties of the material were taken from a report published by NASA [22] because the parameters of the thin, multi-rolled foil significantly differ from the parameters of the material from which it was made. In [22], the results of tests of the foil composed of the Al 5052-H39 alloy, as well as those of the foil fragments cut from the finished structure of the cellular core, are presented.

The basic parameters of aluminum Al 5052-H39, as used to make cores with a honeycomb topology in the untreated form [23], in the form of foil [22], and in the form of a fragment of the core [24], are presented in Table 3. After plastic processing, the material is characterized by significantly lower strength parameters. In the form of a film, it has a 19% lower Young's modulus, a 30% lower yield point, and a 25% lower tensile strength. The sample cut from the core fragment has a Young's modulus that is up to 46% lower, a 32% lower yield point, and a 35% lower tensile strength.

Table 3. Comparison of the mechanical properties of aluminum Al 5052-H39, a foil composed of Al 5052-H39, and a fragment of a honeycomb core composed of that foil.

Parameter	Symbol	Unit	5052-H39 [23]	Foil 5052-H39 [24]	Core Fragment [24]
Density	ρ	kg/m ³	2.7×10^3	2.7×10^3	2.7×10^3
Elastic modulus	E	GPa	70.00	56.53	37.92
Yield stress	R_e	MPa	325.0	227.5	220.6
Tensile strength	R_m	MPa	330.0	248.2	234.4
Elongation at break	ϵ_u	%	4.0	1.6	4.7

Due to the fact that the developed Y-element models were used to determine the mechanical properties of the statically compressed aluminum honeycombs without the need for experimental testing, the properties of the Al 5052-H39 foil were considered in the subsequent numerical calculations.

4.2. Numerical Analysis of the Honeycomb Structures Using the Homogenous Model

The aim of the tests described below was to assess the effectiveness of using the results of the simulation of the Y element in models that describe the global response of this type of material without a detailed analysis of the behavior of their internal structure.

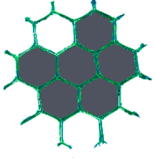
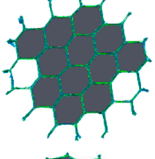
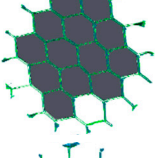
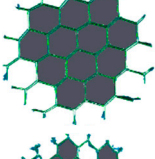
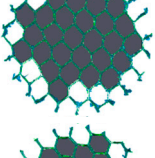
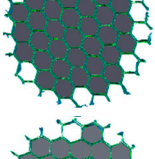
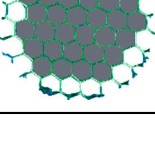
Geometric models, as shown in Figure 5, were analyzed in order to identify fully closed cells and the possible damage resulting in the formation of open cells. Then, the volumes of the solids bounded by the closed walls of the cores were measured. Measurement results for the same types of samples were averaged. A visualization of an example of the discussed process is presented in Table 4. The samples with smaller core sizes had a noticeably higher proportion of closed-cell volume, considering that they had the same global dimensions.

The previous experimental research of honeycomb structures under various levels of strain rate loading carried out by the authors [21] was used to develop the assessments for this paper. By presenting the experimentally obtained, absolute increases in plateau stress [21] in the domain of the air volume locked in by the cell walls, an almost-linear characteristic was obtained, which can be observed in Figure 10. This observation may indicate that the main factor influencing the final shape of the stress–volumetric strain characteristic is the increase in the pressure of the air trapped inside the cells, especially for dynamic testing (strain rate of 3.8×10^2 and 3.3×10^3 1/s).

Another argument for the correctness of this assertion is the conclusion made on the basis of the observation of images recorded with a high-speed camera in the dynamic test using a split Hopkinson pressure bar (3.3×10^3 1/s). As shown in Figure 11, the gas began to leak from the inside of the sample during the final compression phase ($t = 333.30 \mu\text{s}$). It became visible due to a dust cloud—a mixture of air escaping from the inside of the

sample and fine particles of the damaged core and resin. This phenomenon took place in each case after reaching approximately 50% of the deformation; it continued after the maximum displacement of the initiating bar face, and this continued even after its plane lost contact with the sample plane. The described phenomenon may prove that, during the test, strong air compression takes place inside the core, which is released only after complete compression.

Table 4. Measurement results of the volume of air limited by walls in the real models of the samples.

	Graphical Representation	Wall Thickness t [mm]	Cell Size S [mm]	Closed Air Volume V_a [mm ³]
1/4-5052-0.001		0.02540	6.3500	2264.5
3/16-5052-0.0007		0.01778	4.7625	2556.8
3/16-5052-0.001		0.02540	4.7625	2702.0
1/8-5052-0.0015		0.03810	4.7625	2744.9
1/8-5052-0.0007		0.01778	3.1750	3426.4
1/8-5052-0.001		0.02540	3.1750	3548.8
1/8-5052-0.0015		0.0381	3.175	3662.1

The above conclusion is important because none of the constitutive models available in commercially used computing environments take into account this kind of phenomenon's influence on the change in the global mechanical properties of the structure.

Therefore, in order to describe the behavior of aluminum honeycomb structures in terms of strain rates higher than quasi-static, it is necessary to take an approach that will account for both the reaction of the deformed, thin-walled core and that of the air pressure inside the cells.

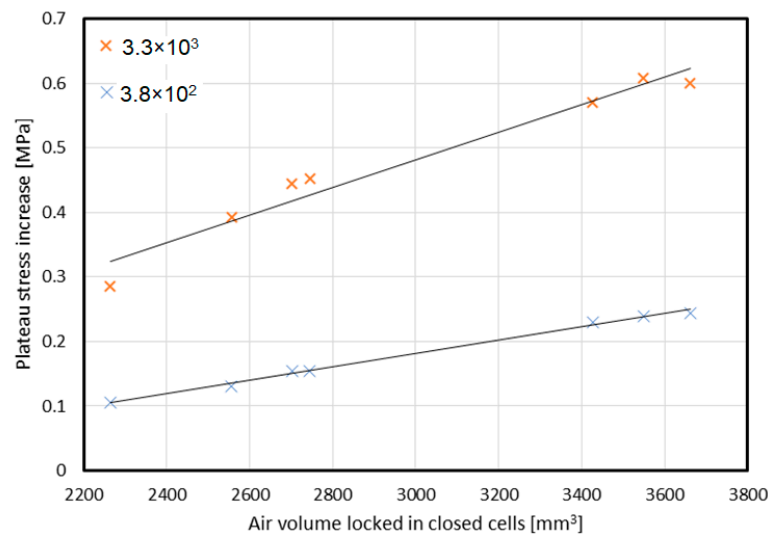


Figure 10. Increase in plateau stress depending on the volume of air trapped inside cells (based on results obtained in [21]).

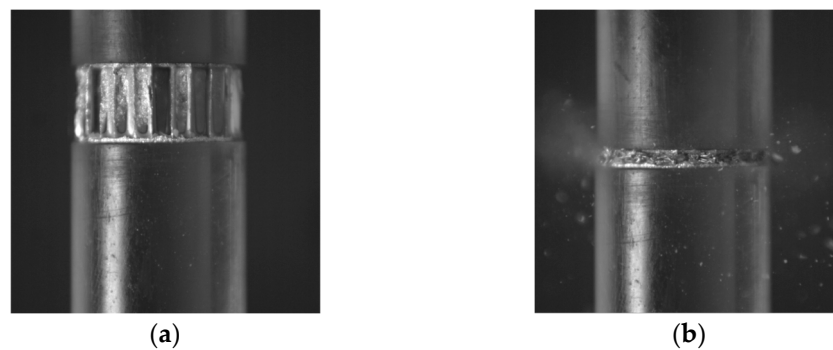


Figure 11. Deformation of sample 1/8-5052-0.0015 in the following time steps: (a) $t = 0$, and (b) $t = 333.30 \mu s$ (based on results obtained in [21]).

Assuming, as a simplification, that the air closed inside the cells is compressed without heat exchange, the increase in pressure ΔP can be described by a simple equation [25],

$$\Delta P = P_0 \left(\frac{V_0}{V} - 1 \right) \quad (1)$$

where P_0 is the initial pressure (atmospheric).

Then, the indirectly measured stress value of the real structure would be the sum of the stress value in the structure (treating it as homogeneous according to the assumption made) and the pressure at a given time step. Due to the fact that the deformation of the core takes place only in the direction of displacement, the change in volume can be treated as a change in the height of the sample; as a result, the expected value of the measured stress is described by the formula [25]

$$\sigma = \sigma_r + P_0 \left(\frac{T_0}{T_0 - u} - 1 \right) \quad (2)$$

where σ_r is the stress in the core of the sample treated as a continuous medium, and T_0 is the initial core height.

The assumptions formulated above lead to the conclusion that the air trapped inside the cells causes an increase in the noted stress value, regardless of the strain rate. There are studies [24] which prove that the key aspect linking the structure's response with the

duration of its destruction are air leakages resulting from imperfections in the structure and the material discontinuities formed in the process of deformation. The assumption can be modified in accordance with research carried out by Xu et al. [24] and Hu et al. [25], in which it was shown that the cross-sectional area of a honeycomb block also changes during axial compression. The air leakage δ is determined by the relationship [21]

$$\delta = 1 - \frac{PV}{P_0V_0} \quad (3)$$

Therefore, the pressure value can be determined by the formula

$$P = P_0 \frac{1 - \delta}{1 - \varepsilon_v} \quad (4)$$

where ε_v is the volumetric strain.

It is assumed that δ is the core failure time of the t' function and differentiating Equation (4) over time, assuming that one obtains

$$\dot{P} = \frac{P_0}{1 - \varepsilon_v} \left(\frac{1 - \delta}{1 - \varepsilon_v} \cdot \dot{\varepsilon}_v - \dot{\delta} \right) \quad (5)$$

and the leakage rate is

$$\dot{\delta} = \frac{1}{P_0} \left[P \dot{\varepsilon}_v - \dot{P} (1 - \varepsilon_v) \right] \quad (6)$$

Based on the relations presented above, it can be noticed that the pressure value and the rate of the leakage are related to the strain rate $\dot{\varepsilon}_v$. Researchers developing analytical models for this type of issue [12], using the assumption that the strain rate is constant during the test, derived a relationship that links the pressure change inside the core with the strain and the leakage rate

$$\Delta P = P_0 \left(\frac{1}{1 - \varepsilon_v} - 1 \right) \cdot \left(1 - \frac{\dot{\delta}}{\dot{\varepsilon}_v} \right) \quad (7)$$

Equation (16) does not contain any unknown parameters other than the leakage rate. The authors of [25] state that this rate should be determined empirically by comparing the stress–volumetric strain results obtained during the compression of the samples with the cores tightly closed between covers, and those with openings releasing air during the test. The leakage intensity is very similar when the results of testing honeycomb structures with the same t/d ratio are compared, and its value depends on the strain rate. The obtained characteristics of the leakage intensity as a function of the strain rate for one of the cases analyzed in [25] (1/8-5052-0.001) is presented in Figure 12. In this case, the leakage rate increased almost in direct proportion to the value of the strain rate. This means that a tenfold increase in strain rate resulted in at least a tenfold increase in the leakage rate.

To perform simulation tests of the uniaxial compression of the homogenous honeycomb materials, a model with a cylinder geometry with a diameter of 25 mm and a height of 10 mm was used, reflecting the global geometry of the sample core. It consisted of 525 elements with a hexagonal topology.

The material model MAT_26_HONEYCOMB, available in the LS-DYNA system, was used to map the core, which was treated as a homogeneous material [19].

In MAT_26, in the uncompressed state (initial state, loss of stability, and progressive folding), the material retains its orthotropic properties, and the stress tensor components remain unconnected from each other so that the strain component in one local direction does not cause reaction forces in the others. Modules of the longitudinal and shear stiffness in particular directions depend on the given modules of the initial stiffness and the stiffness of a fully compressed (compacted) structure. These dependencies are as follow [19]:

$$E_{aa} = E_{aa0} + \beta(E - E_{aa0}) \quad (8)$$

$$E_{bb} = E_{bb0} + \beta(E - E_{bb0}) \quad (9)$$

$$E_{cc} = E_{cc0} + \beta(E - E_{cc0}) \quad (10)$$

$$G_{ab} = G_{ab0} + \beta(G - G_{ab0}) \quad (11)$$

$$G_{bc} = G_{bc0} + \beta(G - G_{bc0}) \quad (12)$$

$$G_{ca} = G_{ca0} + \beta(G - G_{ca0}) \quad (13)$$

where

$$\beta = \max \left[\min \left(\frac{1 - V}{1 - V_f}, 1 \right), 0 \right] \quad (14)$$

and E is the modulus of elasticity of the core material; G is the shear modulus of the core material; E_{aa0} , E_{bb0} , and E_{cc0} are the modules of elasticity of the uncompressed cores; G_{ab0} , G_{bc0} , and G_{ca0} are the shear modules of the uncompressed cores; V is the relative volume (the ratio of the current volume to the initial volume), and V_f is the relative volume at which the core is considered fully compressed and it transforms into a linear elastic characteristic (the relative volume of total compaction).

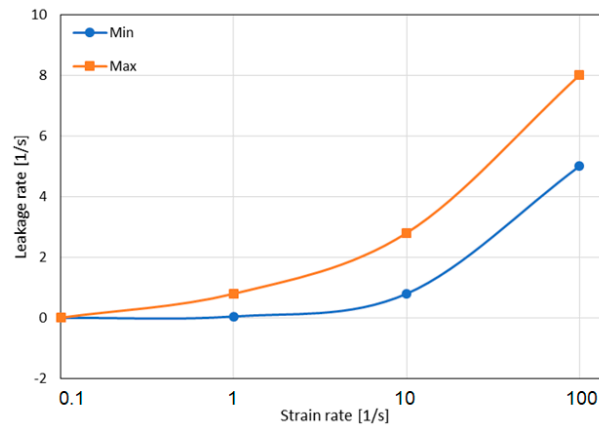


Figure 12. Leakage rate vs. strain rate for 1/8-5052-0.001 (based on [25]).

In addition, the material model requires the definition of a set of curves that present the material characteristics obtained in the experimental tests: compression in each of the basic directions and shear in each of the base planes. There are two ways to define these characteristics. The first one is to determine the magnitude of stresses as a function of the relative volume (V). It is also possible to determine the magnitude of stresses as a function of volumetric strains, defined as

$$\varepsilon_V = 1 - V \quad (15)$$

Finally, the components of the stress tensor are calculated according to the following relationship:

$$\sigma_{ij}^{n+1} = s_{ij}^{n+1} - p^{n+1} \delta_{ij} \quad (16)$$

After the process of updating the stress values is completed, they are converted into a global form.

For the modeling of individual structure types, the parameters presented in Table 4 were adopted. In each case, the $\sigma_{ij} - \varepsilon_{ij}$ characteristics were developed by selecting characteristic points from the curves obtained by the FEM simulation using the Y-element model.

The development of a model capable of taking into account the change in the nature of the response of the change of the initial conditions causing the strain-rate increase was based on one of the available methods describing the behavior of air-filled elements.

The model should allow us to describe the change in gas pressure, along with the change in the volume inside where it was located. It should also take into account the leakage in the calculation of the pressure changes and the application to the surface and the spatial boundary of the element. All of the possibilities mentioned above are offered by one of the simplest models: AIRBAG_SIMPLE_AIRBAG_MODEL [19]. The current value of the pressure acting on the boundaries of the vessel domain is calculated using the equation of state [19]:

$$P = (\gamma - 1)\rho e \quad (17)$$

where P is the pressure, ρ is the density, and e is the internal energy of gas.

The γ coefficient is the adiabatic exponent: the ratio of specific heat at a constant pressure c_p to specific heat at a constant volume c_v [25]

$$\gamma = \frac{c_p}{c_v} \quad (18)$$

The rate of changes in the air mass m inside the volume, with time, is described by the relationship [26]

$$\frac{dm}{dt} = \frac{dm_i}{dt} - \frac{dm_o}{dt} \quad (19)$$

The value of the air mass, which flows in via subsequent time steps m_i , is defined by the appropriate characteristic. There are two options for determining the mass of the outflowing air m_o : by defining the area of the holes through which the air leaks and their shape coefficient, and by defining the mass characteristics over time. There is also a possibility of making the size of the surface of the holes and the shape factor dependent on the value of the pressure inside.

In the discussed approach, the components of the energy balance [26]

$$\dot{e} = \dot{e}_i - \dot{e}_o - P\dot{V} \quad (20)$$

are as follows: \dot{e}_i is energy change caused by the mass of inflowing gas, \dot{e}_o is the change in energy caused by the mass of the outflowing gas, $P\dot{V}$ is work achieved by the pressure per volume change.

The described boundary condition was applied to the surfaces of the elements on the outer walls of the cylinder, as shown in Figure 13. This allowed for a direct transfer of the forces resulting from the increase in pressure to the sample boundaries. The parameters used to describe the air enclosed inside the sample are presented in Table 5. All parameters related to the influence of the air mass were omitted.

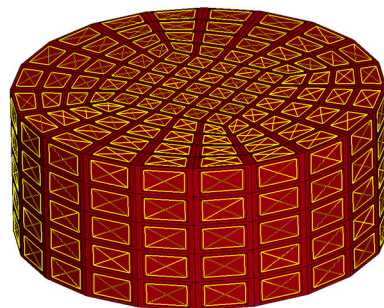
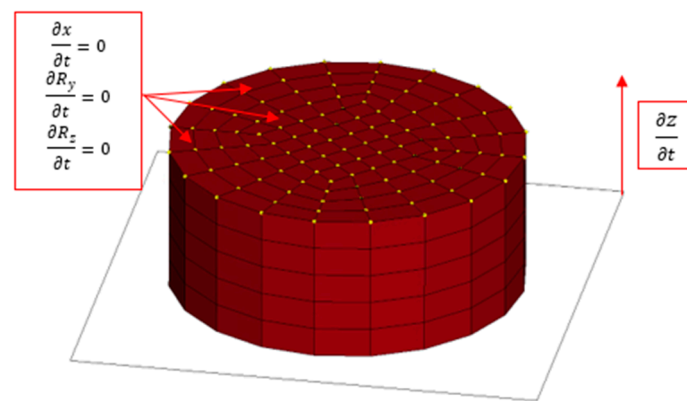


Figure 13. Numerical model of the homogeneous honeycomb material, with surfaces used as air-leakage boundaries.

Table 5. Parameters of the air enclosed inside the cores, according to the assumptions of the AIRBAG_SIMPLE_AIRBAG_MODEL [27].

Parameter	Symbol	Unit	Value
Density	ρ	kg/m ³	1.2
Specific heat at constant volume	c_v	J/(kg·K)	713.00
Specific heat at constant pressure	c_p	J/(kg·K)	1000.00
Ambient pressure	P_e	MPa	0.1
Temperature	T	K	293
Area of holes	A_o	m ²	0.004

The initial boundary conditions are presented in Figure 14. An explicit scheme of the integration of the equations of motion was used for the calculations.

**Figure 14.** Scheme of the initial boundary conditions applied in the model.

5. Results

The results are presented in two subsections in accordance with the descriptions of models presented in Section 3. The results of the numerical analyses for the quasi-static compression tests are described, first for the simplified Y element, and then for the homogenous model, in which the material characteristics gained via analyses of the Y element were implemented.

5.1. Results of the Numerical Analyses of the Static Compression of the Y-Element

The basic result of the performed analyses was the characteristic of the change in the stress value as a function of the volumetric strain and the list of resulting parameters. The characteristics obtained in the static and experimental FEM analyses [21], presented in Figure 15, reveal a consistent course of changes in the stress value, with an increase in the strain value. The similarity is especially visible in the elastic phase until it reaches critical stress, progressive folding, and compaction. The most pronounced difference in the stress values occurred just after the loss of stability. In each of the experimentally tested cases, a subsequent deep decrease occurred, up to about one-half of the subsequent progressive folding stress. The characteristics obtained by the FEM analysis did not include this feature. After the loss of stability, the force value decreased and stabilized until the compaction phase. Another effect that was recorded only during the simulation was the oscillation of the stress value in the progressive folding and compaction phases. The first of the causes mentioned above should be viewed as being involved with the local nature of such phenomena: as a loss of stability, the formation of a single fold, its closing, the mutual contact of walls, the subsequent loss of stability, etc. In the real structure, the local effects compensated for each other and there were no oscillations. Another noteworthy feature of the recorded oscillations of the stress value in the progressive folding phase was the

increase in the amplitude with an increase in the wall thickness and a decrease in frequency with an increased cell size. In contrast, the oscillations in the densification phase were related to the occurrence of contact forces and friction due to the contact of the progressively larger surfaces of the walls with each other and their sliding over one another.

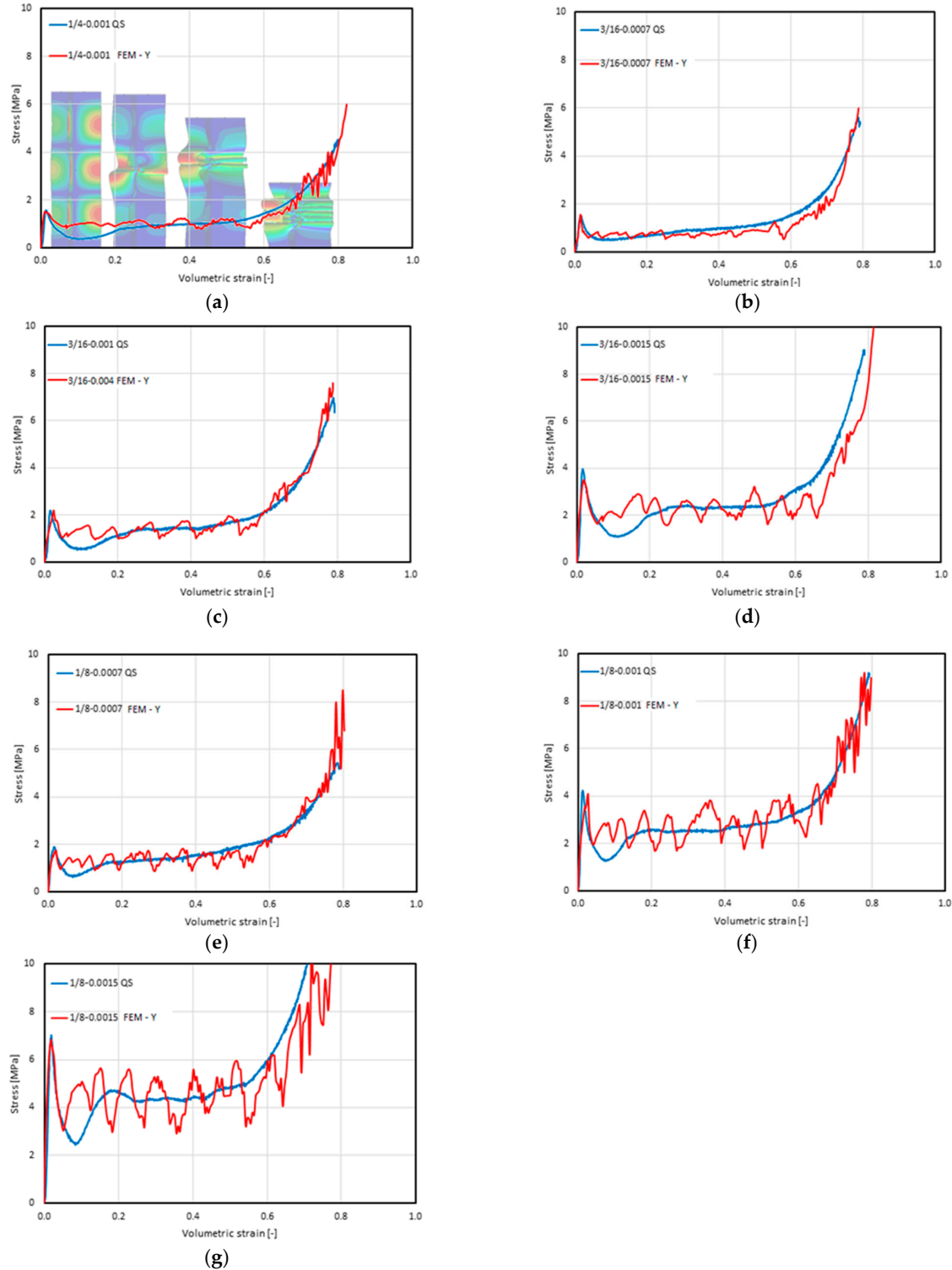


Figure 15. Summary of the stress–volumetric strain characteristics obtained using the FEM–Y model (FEM–Y) and experimentally in the quasi-static compression (QS) test [21] of the following material types: (a) 1/4-5052-0.001; (b) 16-5052-0.0007; (c) 3/16-5052-0.001; (d) 3/16-5052-0.0015; (e) 1/8-5052-0.0007; (f) 1/8-5052-0.001; and (g) 1/8-5052-0.0015.

The obtained characteristics of the full range of deformations allowed for the identification and determination of the basic parameters of the individual types of honeycomb cores. Table 6 presents a summary and comparison between our results and those obtained through empirical research. Values included within parentheses denote the percentage of difference between those obtained through experimentation and those obtained through FEM analyses.

Table 6. List of the basic parameters of the examined structures.

Parameter	Plateau Stress σ_{pl} [MPa]	Elastic Modulus E_H [MPa]	Critical Stress σ_{cr} [MPa]	Relative Volume of Total Compaction V_F [-]
1/4-5052-0.001	0.99 (−8.8%)	261.16 (−6.5%)	1.42 (9.6%)	0.28 (9.7%)
3/16-5052-0.0007	0.95 (3.1%)	168.22 (−6.7%)	1.60 (−6.0%)	0.28 (−7.7%)
3/16-5052-0.001	1.42 (3.4%)	247.73 (5.8%)	2.22 (−1.4%)	0.29 (−7.4%)
1/8-5052-0.0015	2.28 (2.6%)	397.34 (4.7%)	3.54 (10.6%)	0.21 (27.6%)
1/8-5052-0.0007	1.49 (2.6%)	251.34 (3.8%)	1.72 (9.5%)	0.27 (−8.0%)
1/8-5052-0.001	2.70 (−2.3%)	474.06 (8.8%)	4.11 (3.1%)	0.24 (7.7%)
1/8-5052-0.0015	4.41 (1.3%)	591.11 (−1.9%)	6.82 (3.0%)	0.21 (30.0%)

5.2. Results of the Numerical Analyses of the Honeycomb Structures Using the Homogenous Model

The stress–volumetric strain characteristics obtained through experimental tests [21] and those obtained via numerical analyses using the solid (homogenous) model are presented in Figure 16. Each of the graphs contains the results obtained during the tests carried out at three strain rates: 8.3×10^{-2} , marked as QS; 3.8×10^2 , marked as DH; and 3.3×10^3 , marked as SHPB. The summaries are grouped according to the type of structure under study. In order to emphasize the characteristics obtained in the FEM calculations, the previously shown characteristics from empirical studies [21] are marked with dashed lines.

Characteristics obtained by means of the FEM analyses were consistent with their equivalents obtained experimentally, and the tendency to strengthen with an increase in the strain rate was maintained. Additionally, the nature of this tendency is similar; that is, in the plateau stress range, no hardening of a constant, proportional value occurred. It can therefore be assumed that the use of the material characteristics obtained via the static tests of the model—and the inclusion of the air enclosed inside the core under the test conditions in the model—brought about the intended results.

No vibrations occurred in any of the analyzed cases, and no other symptoms of wave phenomena were observed, which were recorded during the experiments using the split Hopkinson pressure bar. However, it should be mentioned that the method of determining the stress value was indirect and consisted of the measurement of the deformation of a long, slender bar that is also susceptible to oscillation in directions other than longitudinal. Therefore, the oscillations did not result from the response of the material being tested, but from the method of measurement and reading. The characteristics obtained in the FEM tests were smooth, devoid of sinusoidal components characterized by high amplitudes or low frequencies.

It should be pointed out that the characteristics obtained experimentally and numerically differ significantly in the initial range. While the elastic range had a similar course in all cases, as well as in terms of the nature of the stress build-up in the initial range, after reaching the value defined by the $\sigma_{ij} - \varepsilon_{ij}$ curve characteristic for the MAT_HONEYCOMB constitutive model used, the stress value stabilized; in the remaining further range of strain, it followed the values defined by it. Importantly, we observed no phenomenon where a clear plateau value was achieved that was much higher than that of the critical stress, followed (in the case of a real structure) by a loss of stability and the kind of breakdown of the structure's stability, as manifested by a decrease in the stress value to a level below the plateau value that was achieved and maintained at a later stage in most of the compression tests. A more precise observation of this issue is shown in Figure 17, which presents the

stress–volumetric strain characteristics of the 1/8-5052-0.0015 sample with the displayed range of volumetric strain limited to 20%.

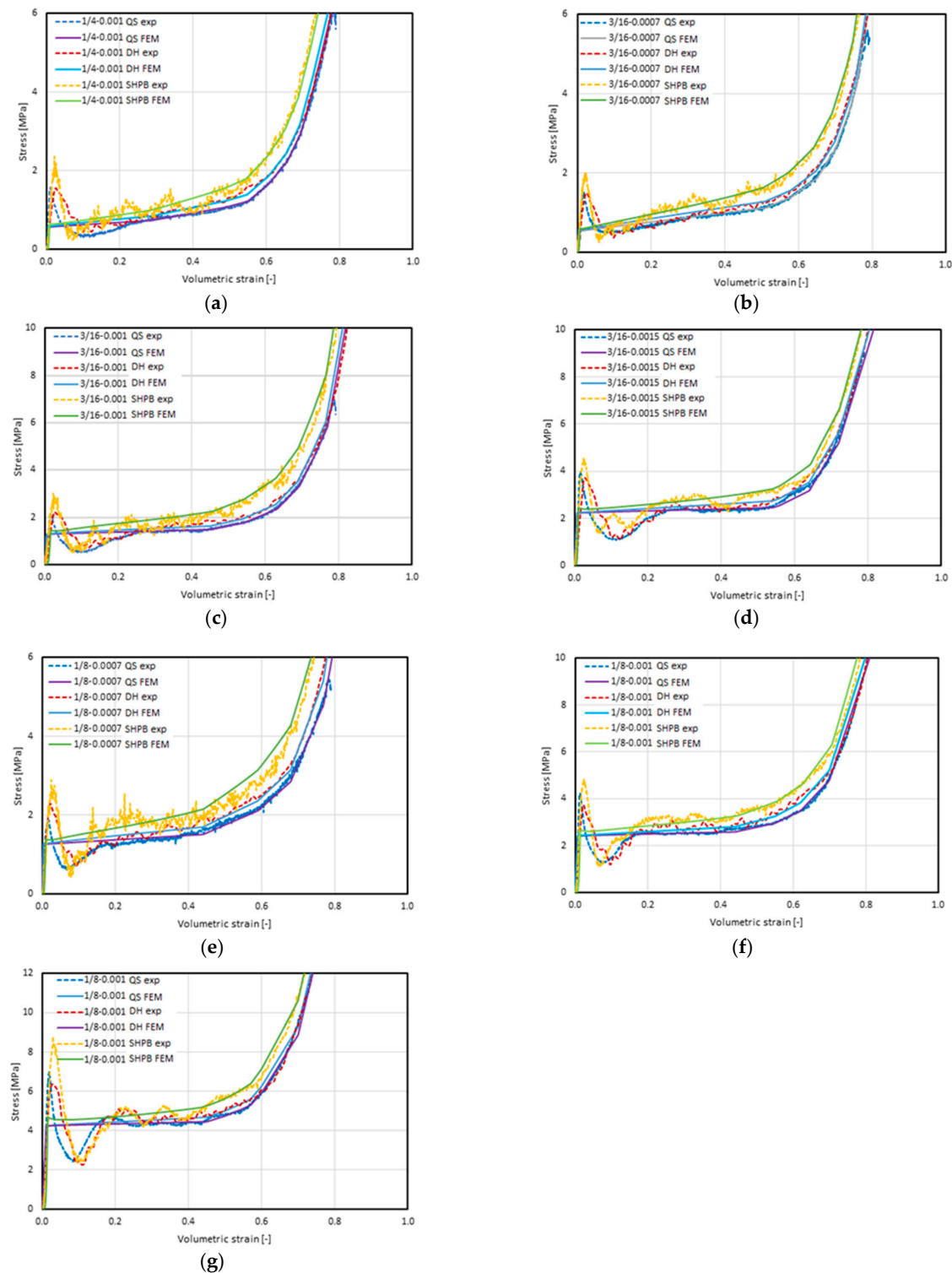


Figure 16. Summary of the stress–volumetric strain characteristics obtained using the FEM–homogeneous model (FEM) and experimentally (exp) [21] at a quasi-static load (QS) strain rate of 8.3×10^{-2} 1/s, at a dynamic load (DH) strain rate of 3.8×10^2 1/s, and using a Split Hopkinson Pressure Bar (SHPB) with a strain rate of 3.3×10^3 1/s of the materials, including (a) 1/4-5052-0.001; (b) 3/16-5052-0.0007; (c) 3/16-5052-0.001; (d) 3/16-5052-0.0015; (e) 1/8-5052-0.0007; (f) 1/8-5052-0.001; and (g) 1/8-5052-0.0015.

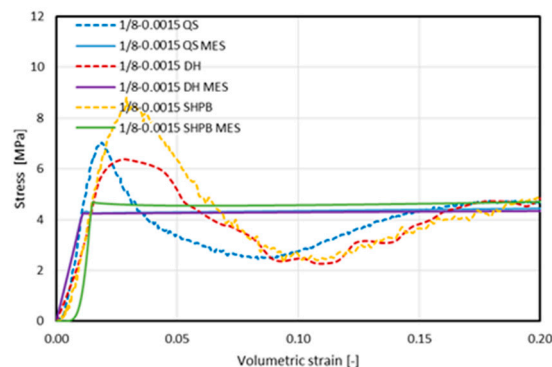


Figure 17. Summary of stress–volumetric strain characteristics obtained using the FEM–homogeneous model (FEM) and experimentally (exp) [21] at a quasi-static load (QS) strain rate of 8.3×10^{-2} 1/s, at a dynamic load (DH) strain rate of 3.8×10^2 1/s, and using a Split Hopkinson Pressure Bar (SHPB) at a strain rate of 3.3×10^3 1/s of the sample 1/8-5052-0.0015 for a strain limited to $<0.2>$ scope.

6. Conclusions

The MAT_HONEYCOMB model does not include an option that allows for the consideration of the phenomenon by indicating a scalar stress value, up to which the material response would be dependent on the modulus of longitudinal elasticity, followed by assuming a value consistent with the indicated characteristic.

In order to obtain the full stress–strain characteristics of a metallic honeycomb, a numerical model can be used, the geometry of which will be limited to a single Y element. In order to obtain descriptions of the stress–volumetric strain characteristics and the scalar parameters, one must make sure that the following conditions are met. Regardless of the assumed strain rate, it is appropriate to apply the characteristics from static tests and achieve correct simulation results under a wide range of strain rates, assuming that the model takes into account the pressure change due to the potential compression of the air enclosed in the core volume.

In this study, the effectiveness of one of the simpler methods was tested: the definition of the boundary condition of uniform pressure distribution over a limited area. This enables the development of a model that faithfully reproduces the responses of a honeycomb structure at different strain rates.

Author Contributions: Conceptualization, R.C. and D.M.; methodology, R.C. and D.M.; validation, R.C.; formal analysis, R.C. and D.M.; investigation, R.C.; resources, R.C. and D.M.; data curation, R.C.; writing—original draft preparation, R.C. and D.M.; writing—review and editing, R.C. and D.M.; visualization, R.C.; supervision, D.M. All authors have read and agreed to the published version of the manuscript.

Funding: The paper was written as part of the implementation of the university research grant No. 22-838.

Institutional Review Board Statement: Not applicable.

Informed Consent Statement: Not applicable.

Data Availability Statement: The data presented in this study are available on request from the corresponding author.

Conflicts of Interest: The authors declare no conflict of interest.

References

1. Dotts, R. *Apollo Experience Report—Spacecraft Heating Environment and Thermal Protection for Launch Through the Atmosphere of the Earth*, NASA TN D-7085; National Aeronautics and Space Administration: Washington, DC, USA, 1973.
2. McFarland, R. *The Development of Metal Honeycomb Energy-Absorbing Elements*; Technical Report no. 32-639; California Institute of Technology: Pasadena, CA, USA, 1964.

3. Xiang, Y.; Yu, T.; Yang, L. Comparative analysis of energy absorption capacity of polygonal tubes, multi-cell tubes and honeycombs by utilizing key performance indicators. *Mater. Des.* **2016**, *89*, 689–696. [CrossRef]
4. Zhang, D.; Lu, G.; Ruan, D.; Fei, Q.; Duan, W. Quasi-static combined compression-shear crushing of honeycombs: An experimental study. *Mater. Des.* **2019**, *167*, 107632. [CrossRef]
5. Quoc, P.M.; Krzikalla, D.; Mesicek, J.; Petru, J.; Smirau, J.; Sliva, A.; Poruba, Z. On Aluminum Honeycomb Impact Attenuator Designs for Formula Student Competitions. *Symmetry* **2020**, *12*, 1647. [CrossRef]
6. Zhang, S.; Chen, W.; Gao, D.; Xiao, L.; Han, L. Experimental study on dynamic compression mechanical properties of aluminum honeycomb structures. *Appl. Sci.* **2020**, *10*, 1188. [CrossRef]
7. Reyno, T.; Underhill, P.R.; Krause, T.W.; Marsden, C.; Wowk, D. Surface Profiling and Core Evaluation of Aluminum Honeycomb Sandwich Aircraft Panels Using Multi-Frequency Eddy Current Testing. *Sensors* **2017**, *17*, 2114. [CrossRef] [PubMed]
8. Jedral, A. Review of testing methods dedicated for sandwich structures with honeycomb core. *Trans. Aerosp. Res.* **2019**, *2*, 7–20. [CrossRef]
9. Wierzbicki, T. Crushing analysis of metal honeycombs. *Int. J. Impact Eng.* **1983**, *1*, 157–174. [CrossRef]
10. Goldsmith, W.; Sackman, L. An experimental study of energy absorption in impact on sandwich plates. *Int. J. Impact Eng.* **1992**, *12*, 241–262. [CrossRef]
11. Baker, W.E.; Togami, T.C.; Weydert, J.C. Static and dynamic properties of high-density metal honeycombs. *Int. J. Impact Eng.* **1998**, *21*, 149–163. [CrossRef]
12. Xu, S.; Beynona, J.H.; Ruan, D.; Yu, T.X. Strength enhancement of aluminium honeycombs caused by entrapped air under dynamic out-of-plane compression. *Int. J. Impact Eng.* **2012**, *47*, 1–13. [CrossRef]
13. Wilbert, A.; Jang, W.Y.; Kyriakides, S.; Floccari, J.F. Buckling and progressive crushing of laterally loaded honeycomb. *Int. J. Solids Struct.* **2011**, *48*, 803–816. [CrossRef]
14. Deqiang, S.; Weihong, Z.; Yanbin, W. Mean out-of-plane dynamic plateau stresses of hexagonal honeycomb cores under impact loadings. *Compos. Struct.* **2010**, *92*, 2609–2621. [CrossRef]
15. Khoshhravan, M.R.; Najafi Pour, M. Numerical and experimental analyses of the effect of different geometrical modelings on predicting compressive strength of honeycomb core. *Thin-Walled Struct.* **2014**, *84*, 423–431. [CrossRef]
16. Jost, T.; Heubrandtner, T.; Ruff, C.; Fellner, B. A new method to model Aluminium honeycomb based crash barriers in lateral and frontal crash load cases. *LS-DYNA Anwend.* **2008**, *B-III*, 13–24.
17. Shkolnikov, M.B. Honeycomb modeling for side impact moving deformable barrier (MDB). In Proceedings of the 7th International LS-DYNA@Users Conference, Detroit, MI, USA, 1–14 July 2002.
18. Jackson, K.E. Predicting the Dynamic Crushing Response of a Composite Honeycomb Energy Absorber Using Solid-Element Based Models in LS-DYNA®. In Proceedings of the 11th International LS-DYNA@Users Conference, Detroit, MI, USA, 1–10 January 2020.
19. Hallquist, J. *LS-DYNA® Theory Manual*; Livermore Software Technology Corporation: Livermore, CA, USA, 2006.
20. Kojima, S.; Yasuki, R.; Mikutsu, S.; Takasudo, T. A study on yielding function of aluminum honeycomb. In Proceedings of the 5th European LS-DYNA Users Conference, Birmingham, UK, 25–26 May 2005.
21. Ciepielewski, R.; Gieleta, R.; Miedzińska, D. Experimental Study on Static and Dynamic Response of Aluminum Honeycomb Sandwich Structures. *Materials* **2022**, *15*, 1793. [CrossRef]
22. Yamashita, M.; Gotoh, M. Impact behavior of honeycomb structures with various cell specifications—Numerical simulation and experiment. *Int. J. Impact Eng.* **2005**, *32*, 618–630. [CrossRef]
23. Matweb—Your Source for Materials Information. 2015. Available online: <https://www.matweb.com/> (accessed on 10 November 2022).
24. HexWeb® Rigidcell™, Corrosion Resistant Aluminum Corrugated Honeycomb; Product Data; Hexcel Corporation: Stamford, CT, USA, 2020; p. 24.
25. Shanqing, X.; Beynona, J.; Ruana, D.; Lu, G. Experimental study of the out-of-plane dynamic compression of hexagonal honeycombs. *Compos. Struct.* **2012**, *94*, 2326–2336.
26. Mattern, S. *Overview on Airbag-Modelling Possibilities in LS-DYNA*; DYNAmore Express, DYNAmore GmbH: Stuttgart-Vaihingen, Germany, 2020.
27. Available online: engineeringtoolbox.com/individual-universal-gas-constant-d_588v (accessed on 20 November 2021).

Disclaimer/Publisher’s Note: The statements, opinions and data contained in all publications are solely those of the individual author(s) and contributor(s) and not of MDPI and/or the editor(s). MDPI and/or the editor(s) disclaim responsibility for any injury to people or property resulting from any ideas, methods, instructions or products referred to in the content.

Article

The Mechanism of In-Situ Laser Polishing and Its Effect on the Surface Quality of Nickel-Based Alloy Fabricated by Selective Laser Melting

Yanhua Zhao ^{1,*}, Chuanbin Du ¹, Peifu Wang ², Wei Meng ¹ and Changming Li ³

¹ School of Mechanical and Electronic Engineering, Shandong Jianzhu University, Fengming Road, Jinan 250101, China; 2020070101@stu.sdjzu.edu.cn (C.D.); 2020075115@stu.sdjzu.edu.cn (W.M.)

² Jinan Special Equipment Inspection Institute, Jinan 250100, China; wangpeifu2001@sohu.com

³ Hangzhou Optimax Tech Co., Ltd., Hangzhou 310000, China; h2378649304@163.com

* Correspondence: zyh@sdjzu.edu.cn; Tel.: +86-189-5416-9696

Abstract: Laser polishing (LP) is an effective method to improve the surface quality of an additively manufactured nickel-based alloy. In this paper, the in-situ laser polishing (ILP) experiment is performed on the selective laser melting (SLM) IN718 samples. The white light interferometer is used to test the three-dimensional surface profile and surface roughness of samples. The results show that the surface quality of as-SLMed samples by ILP is improved. In particular, the surface roughness is decreased by 33.5%. To reveal the mechanism of ILP, a three-dimensional numerical model is established based on the finite volume method (FVM). The model can accurately simulate the mesoscopic scale physical phenomena when the laser interacts with the metal. The temperature field, the melt pool flow, and the evolution of the surface morphology during the ILP process are predicted using this model. The mechanism of ILP is revealed based on the dynamics of the molten pool. The contribution of capillary and thermocapillary forces to the reduction of bulge curvature at different stages is studied. Furthermore, the effect of ILP power on the surface quality is investigated, and the mechanism of bulges and depressions on the track surface during high-power ILP is revealed.

Keywords: selective laser melting; in-situ laser polishing; mesoscopic simulation; temperature change; surface morphology evolution

Citation: Zhao, Y.; Du, C.; Wang, P.; Meng, W.; Li, C. The Mechanism of In-Situ Laser Polishing and Its Effect on the Surface Quality of Nickel-Based Alloy Fabricated by Selective Laser Melting. *Metals* **2022**, *12*, 778. <https://doi.org/10.3390/met12050778>

Academic Editors: Shuwen Wen, Yongle Sun, Xin Chen and Alexandre Emelyanenko

Received: 17 March 2022

Accepted: 29 April 2022

Published: 30 April 2022

Publisher's Note: MDPI stays neutral with regard to jurisdictional claims in published maps and institutional affiliations.



Copyright: © 2022 by the authors. Licensee MDPI, Basel, Switzerland. This article is an open access article distributed under the terms and conditions of the Creative Commons Attribution (CC BY) license (<https://creativecommons.org/licenses/by/4.0/>).

1. Introduction

Nickel-based alloys have been widely used in the nuclear industry [1], aerospace [2], and other industries due to their excellent yield strength, structural stability, and resistance to oxidation and corrosion [3] at elevated temperatures. Nickel-based alloy parts often have complex structures that are difficult to manufacture by traditional methods. Additive manufacturing (AM) technology is one of the most efficient means of manufacturing complex parts. Among them, SLM technology is particularly suitable for the manufacture of complex components [4], such as centrifugal compressor blades [5]. However, the surface quality of SLM alloys is still poorer compared to subtractive manufacturing. Subsequent subtractive processing is required to meet the needs of assembly [6]. It also seriously affects the fatigue performance of parts [7]. These factors limit the popularization and application of SLM to a certain extent [8].

1.1. Polishing and LP

Polishing can effectively improve the surface quality of parts. The traditional polishing methods for IN718 materials mainly include electrochemical polishing and abrasive flow polishing. Electrochemical polishing can reduce the surface roughness of AM IN718 parts to 0.25 microns [9]. Abrasive flow polishing is good at grinding the inner surface of complex parts [10]. However, traditional polishing methods also have their disadvantages.

Traditional mechanical polishing is not suitable for the complex parts manufactured by SLM [8]. Chemical polishing is dangerous and has environmental concerns [11]. In addition, abrasive flow polishing has material loss [9].

As an eco-friendly manufacturing method, LP does not pollute the environment, does not harm the health of workers [12], does not affect mechanical properties, and has a high degree of automation [13]. LP has begun to be used to improve the surface quality of SLM parts [14]. Li et al. [3] studied the thermodynamic behavior and porosity change of SLM IN718 parts subjected to LP. The results showed that the polishing zone temperature was above 1683 K, the cooling rate was about 2.46×10^6 K/s, and the porosity decreased by 65.7% after polishing. Fang et al. [15] carried out LP on the laser additive manufacturing of IN718 parts. In addition, it was reported that the surface roughness can be reduced from 7 μm to less than 1 μm by the LP process. The microhardness increased from 345 HV to 440 HV. Cwikła et al. [16] used LP to reduce the surface roughness of AM IN718 parts by 87.9% and proved that the argon environment is more conducive to the improvement of surface quality than the air environment. Ma et al. [17] performed LP on AM TC4, and the surface roughness was decreased from 5 μm to 1 μm after polishing. Due to the formation of the α' martensitic phase in the polishing zone, the surface microhardness was increased by 32%, and the wear resistance was also greatly improved. Chen et al. [18] used LP as a post-processing technique to improve the mechanical properties of 316 L stainless steel parts fabricated by SLM. The research showed that the average grain size of the polished zone was 17.3 μm . A hardened layer of 50–70 μm was formed. In addition, the tensile strength and ductility were also significantly improved. Liang et al. [19] studied the effect of LP on the surface quality of SLM aluminum alloy. The results showed that LP can repair the cracks on the surface of the alloy, fuse the pores on the surface, melt the powders on the surface, and greatly reduce the surface roughness. It can be seen that LP can effectively improve the surface quality of SLM parts. Immediately before the work environment is cooled and ventilated, the surface of parts made with SLM is subjected to an LP process, namely, ILP. ILP technology can not only improve the surface quality of parts but also improve processing efficiency and avoid oxidation during LP [20].

1.2. Mechanism of LP

In order to improve the surface quality of parts more effectively, many scholars have devoted themselves to the study of the LP mechanism. Because it is difficult to observe the interaction between laser and material during LP-only by experimental means, it is even more difficult to reveal the mechanism of LP. Therefore, some scholars have carried out LP numerical simulation research to try to explain the mechanism of LP. Marimuthu et al. [8] used experiments and numerical simulation to prove the importance of energy input on LP surface quality. The surface roughness of the LP region strongly depends on the flow velocity of the molten pool, which is also directly related to the energy input. Xu et al. [21] established a two-dimensional numerical model to study the mechanism of bulge formation during the LP process. The main reason for this was that the molten material on both sides of the track flows toward the center of the track. Zhang et al. [22] established a model to describe the flow behavior of the molten pool during LP and mainly studied the effects of capillary force and thermocapillary force in the LP process. The results showed that capillary forces play a leading role and were responsible for eliminating surface defects with large curvatures. Li et al. [23] used numerical simulation to explain why the defects cannot be completely eliminated during LP. Due to the rapid cooling rate of the molten pool, the flow time of the molten pool was too short to completely eliminate the surface defects. Li et al. [24] established a two-dimensional axisymmetric numerical model for LP. The process of cooling was simulated. The model observed that the top of the peak starts to melt first, and the molten liquid flows from the peak to the trough. At the same time, the flow velocity would suddenly increase, and the molten pool was in an unstable state. As the study revealed, an unstable melt pool might prevent the flow of liquid from the bulge to the depression, which is detrimental to the improvement of surface quality.

1.3. Scope of This Research

The surface morphology of SLM-fabricated parts has a significant impact on the process of LP and the final surface quality [25]. Few current LP numerical simulation studies take this into account. The purpose of this study is to fill in the knowledge gap so as to reveal the mechanism of the effect of LP on the surface quality of SLM parts more realistically and effectively.

To this end, the fabrication of SLM samples and ILP experiments were carried out first. The macro- and micro-surface morphologies of the samples were observed. Based on FVM, a three-dimensional numerical model, including the SLM and LP stages, was established. The physical phenomena, such as capillary force, thermocapillary force, vaporization, recoil pressure, convective heat transfer, thermal radiation, and latent heat of phase change, were fully considered. Based on this model, the temperature field, molten pool dynamics, and surface morphology evolution during the ILP were simulated. The mechanism of the reduction of bulge curvature and the generation of new bulges and depressions after ILP on the SLM surface was revealed.

2. In-Situ Laser Polishing (ILP) Experiment

2.1. Experiment Methods

The material used in this study was the IN718 powder obtained by gas atomization. The size of the powder was 15–53 μm , and the base material was 304 stainless steel. The SLM and ILP equipment was a LATEC LAM-150V 3D printer, with a maximum power of 1000 W, and the oxygen content could be controlled within 100 ppm.

The purpose of the experimental work was to study the influence of LP on the surface quality of parts fabricated using SLM. Similar process parameters (i.e., power, speed, etc.) were used for both the SLM and ILP processes. According to our previous experimental exploration, the SLM processing parameters were determined to be 185 W of laser power and a 0.6 m/s scanning speed, and the ILP processing parameters were 180 W of laser power and a 0.6 m/s scanning speed. The spot diameter was 0.05 mm. The laser energy distribution was a Gaussian distribution. The layer thickness was 0.04 mm. In addition, the hatch spacing was 0.01 mm. The time-lapse between SLM and ILP was about 0.023 s. The ILP was carried out immediately after the SLM. The size of the samples was 10 mm \times 10 mm \times 5 mm. The samples were printed in 125 layers, each with 500 tracks. The ILP scanning was consistent with the SLM. In this experiment, a single laser was used, and the ILP was performed after the SLM was completed. The as-SLMed and ILPed samples are shown in Figure 1a,b, respectively.

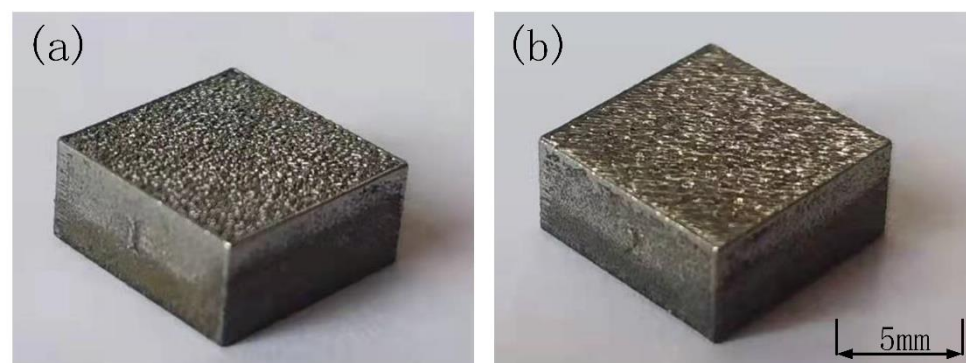


Figure 1. Macroscopic morphology of sample. (a) As-SLMed; (b) ILPed. The parameters of SLM were 185 W, 0.6 m/s and 0.05 mm and 0.01mm (power, speed, spot diameter and hatch spacing). The parameters of ILP were 180 W, 0.6 m/s and 0.05 mm and 0.01mm (power, speed, spot diameter and hatch spacing).

A total of 8 samples were prepared, as-SLMed samples 1–4, ILPed samples 1–4, and the surface roughness was tested, respectively. Sample No. 1 was measured four times each.

All measurement results are shown in Figure 2. The errors of the measurement data are all within the allowable range, which proves the repeatability of processing and measurement is good. All as-SLMed and ILPed samples' test results are averaged together and obtained surface roughness with uncertainty.

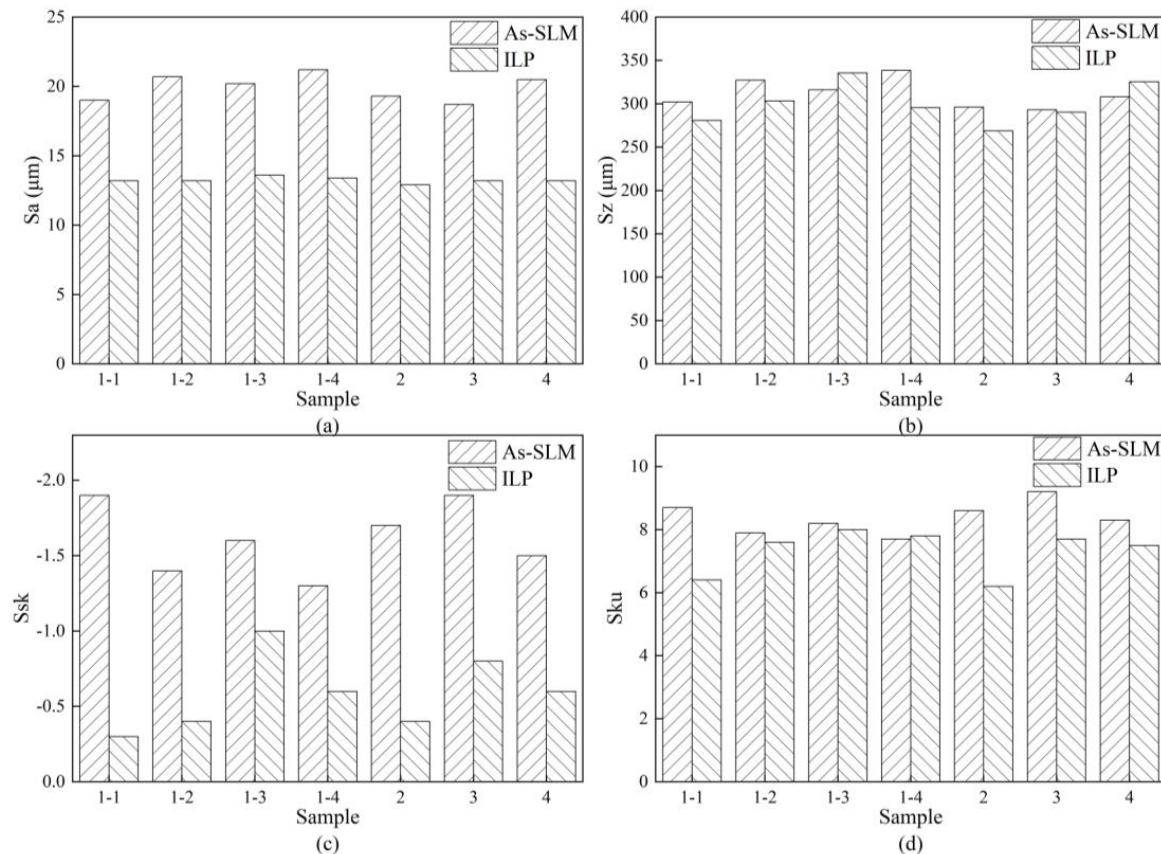


Figure 2. Surface roughness data. (a) S_a ; (b) S_z ; (c) S_{sk} ; (d) S_{ku} . The parameters of SLM were 185 W, 0.6 m/s and 0.05 mm and 0.01mm (power, speed, spot diameter and hatch spacing). The parameters of ILP were 180 W, 0.6 m/s and 0.05 mm and 0.01mm (power, speed, spot diameter and hatch spacing).

A Morphology Elite K white light interferometer was used to test the surface morphology and surface roughness of the samples. The surface area of the samples is 10 mm \times 10 mm. Due to the limitation of the measuring range of the equipment, and in order to facilitate the positioning of the sample during measurement, the measurement was carried out in an area of 1.302 mm \times 1.735 mm in the center of the sample. There were 305,000 data points. According to the research results of scholar Przemysław [26], high-frequency noise will seriously affect the measurement results of the surface topography. When using the white light interferometer for 3D surface measurement, the main sources of noise are shot noise, positioning noise, and discretization noise [27]. In this study, the Fourier filtering technology was used to deal with high-frequency noise in the raw data.

2.2. Results of Experiment

Figure 3 shows the microscopic three-dimensional contour of the samples. Figure 3a,b are as-SLMed and ILPed, respectively. Compared with an as-SLMed sample, the height difference in the ILPed sample is reduced, and the number of bulges is also reduced. The surface roughness results are shown in Figure 2. S_a represents the difference between the

height of each point and the arithmetic mean of the entire surface. The calculation formula is the following:

$$Sa = \frac{1}{A} \iint_A |Z(x,y)| dx dy \quad (1)$$

where A is the area of the sample, and Z(x,y) is the height of the point.

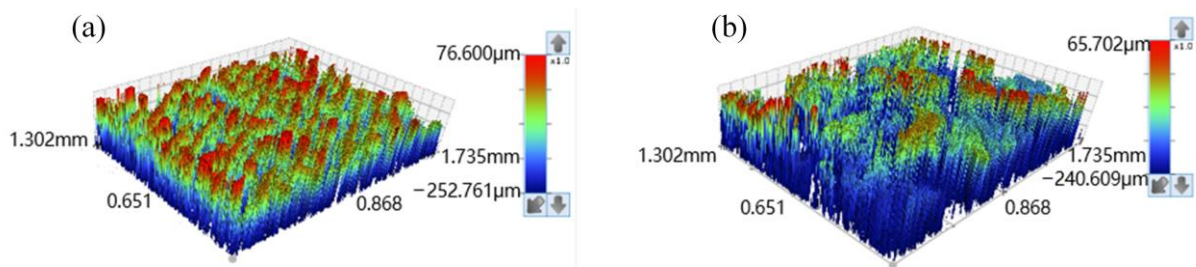


Figure 3. Three-dimensional surface morphology measured by white light interferometer. (a) As-SLMed; (b) ILPed. The parameters of SLM were 185 W, 0.6 m/s and 0.05 mm and 0.01mm (power, speed, spot diameter and hatch spacing). The parameters of ILP were 180 W, 0.6 m/s and 0.05 mm and 0.01mm (power, speed, spot diameter and hatch spacing).

Sa is the extension of Ra from a straight line to a curved surface, which is more suitable for evaluating the surface quality of a curved surface. In addition, compared with other surface quality parameters, Sa is more comprehensive and can better represent the smoothness of the entire surface. Sz represents the height difference of the surface. As shown in Table 1, compared with the as-SLMed sample, the ILPed samples have a great decrease in Sa, but not much in Sz. Even some ILP samples have a larger Sz. The Sa of the additive part is $20.0 \pm 1.25 \mu\text{m}$, and the Sz is $315.9 \pm 22.75 \mu\text{m}$. The Sa after ILP is $13.3 \pm 0.35 \mu\text{m}$, and the Sz is $302.2 \pm 33.35 \mu\text{m}$. The skewness (Ssk) of the two samples is less than 0, and the kurtosis (Sku) is greater than 3, indicating that the surface morphology of SLMed sample is mainly characterized by ‘peak’. The shape of the peak is narrow and sharp, and LP does not change this surface morphology feature. The Ssk increased by 62.5%, closer to 0, indicating a more uniform height distribution of the ILP sample. The Sku decreased by 13.1%, indicating that the ILP sample was smoother. LP improves the surface quality that is, the metal surface is remelted under the irradiation of the laser. The molten metal liquid is redistributed on the surface by the combined driving of capillary force and thermocapillary force, and the molten material at the bulge will fill the depression, making the surface becomes smooth. This ultimately reduces surface roughness. The experimental results show that ILP can improve the surface quality of the SLMed samples.

Table 1. Average value of surface roughness.

Label	As-SLMed	ILP	Change Percentage
Sa (μm)	20.0 ± 1.25	13.3 ± 0.35	33.5%
Sz (μm)	315.9 ± 22.75	302.2 ± 33.35	4.3%
Ssk	-1.6 ± 0.3	-0.6 ± 0.3	62.5%
Sku	8.4 ± 0.75	7.3 ± 0.90	13.1%

3. Numerical Model and Validation

3.1. Model Establishment

The processes of SLM and LP include heat conduction between laser and metal, phase transformation of metal, molten pool flow, heat conduction and convection, vaporization, thermal radiation, latent heat of phase change, and other mechanisms [28]. These factors constitute the numerical model.

To simplify the physical model, the following assumptions are made: (1) The fluid is assumed to be an incompressible Newtonian fluid. (2) The heat flux is assumed to be Gaussian distribution.

The three-dimensional model of the computational domain is shown in Figure 4. The size of the computational domain was $1\text{ mm} \times 0.4\text{ mm} \times 0.24\text{ mm}$. The size of the powder bed was $1\text{ mm} \times 0.4\text{ mm} \times 0.04\text{ mm}$. The thickness of the powder bed was the same as in the experiment. The powder bed was established by the discrete element software EDEM 2018. Its thickness was controlled by the distance between the blade and the base. The powder bed was placed on the base. The model was placed in an argon environment and contained 868,602 grids with a uniform grid size of $5\text{ }\mu\text{m}$. A single-track simulation and three-track simulation were performed in this study. The three-track simulation only appeared in Section 4.4. The simulation used a single laser, and the ILP scan would wait until the SLM scan of the whole layer was completed.

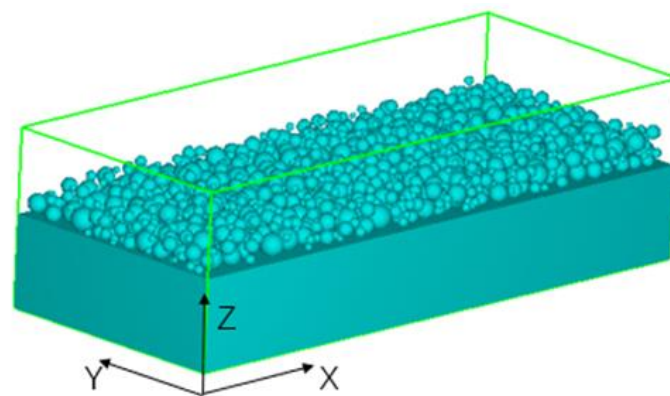


Figure 4. Computational domain.

The modeling was carried out using FLOW-3D V11.1 [29], a commercial computational fluid dynamics (CFD) code, on a GTS2-RIS212Q workstation with 24 cores and 24 threads. Using the FVM method to simulate the SLM and ILP, information such as surface morphology evolution, molten pool flow, and temperature distribution can be obtained. However, the information on stress evolution during processing cannot be obtained. This is a limitation of the FVM approach.

3.2. Governing Equations

The metal solid is melted under the role of laser. In addition, the fluid flow in the molten pool satisfies continuity, momentum conservation, and energy conservation.

Continuity equation [30]:

$$\nabla \cdot (\rho \vec{v}) = 0 \quad (2)$$

Momentum conservation equation [30]:

$$\frac{\partial}{\partial t}(\rho \vec{v}) + \nabla(\rho \vec{v} \otimes \vec{v}) = \nabla \cdot (\mu \nabla \vec{v}) - \nabla P + \rho \vec{g} \quad (3)$$

Energy conservation [31]:

$$\frac{\partial h}{\partial t} + (\vec{v} \cdot \nabla)h = \frac{1}{\rho}(\nabla \cdot k \nabla T) \quad (4)$$

In Equations (2)–(4), ρ is the density of the material, μ is the viscosity, v is the fluid velocity, g is the acceleration of gravity, h is enthalpy, t is the time, k is the thermal conductivity, and T is temperature of the material.

The volume of fluid (VOF) method is used to capture the free surface. The free surface is viewed as a material surface, and the fluid volume fraction is used to represent the

proportion of fluid occupying space in the grid, so as to realize the capturing of the free surface. The volume fraction function satisfies the following transportation equation [32]:

$$\frac{\partial F}{\partial t} + \nabla \cdot (F \vec{v}) = 0 \quad (5)$$

where F is the volume fraction of the fluid, $F = 1$, $F = 0$, $0 < F < 1$ represent fluid-filled, fluid-free, and partially fluid-filled with free surface, respectively [32].

As the laser moves, the temperature in the computational domain changes sharply. The heat conduction obeys the energy conservation law and the Fourier law. It is a typical three-dimensional transient heat conduction process, which satisfies the following equation [29]:

$$\rho c \frac{\partial T}{\partial t} = \frac{\partial}{\partial x} \left(k \frac{\partial T}{\partial x} \right) + \frac{\partial}{\partial y} \left(k \frac{\partial T}{\partial y} \right) + \frac{\partial}{\partial z} \left(k \frac{\partial T}{\partial z} \right) + Q \quad (6)$$

In the formula, c is the specific heat capacity of the material and Q is the source term.

3.3. Gaussian Heat Source and Boundary Conditions

Since the energy of free photoelectrons in the laser is relatively low, it is difficult to reach a deeper position directly through the metal surface, so the surface heat source model is adopted. The following is the heat source formula [33]:

$$q(r) = \frac{2\alpha P}{\pi\omega^2} \exp\left(-2\frac{r^2}{\omega^2}\right) \quad (7)$$

where $q(r)$ is the heat flux, P is the laser power, α is absorption, ω is the heat source radius, and r is the distance from any point in the plane to the laser center point. In this study, α was 0.38 and ω was 0.025 mm. α is cited from the paper by Li et al. [31], ω is consistent with the experiment. They are used for all simulations. (These parameters are used for all performed simulations).

Thermal boundary conditions at the free surface of the molten pool are as follows [34]:

$$q_{in} = q(r) - h_c(T - T_0) - \varepsilon_r \sigma (T^4 - T_0^4) - q_{ev} \quad (8)$$

In the formula, q_{in} is the heat flux variation at the free interface of the molten pool, h_c is the natural convection heat transfer coefficient, ε_r is the emissivity, σ is the Stefan-Boltzmann constant, T is the temperature, T_0 is the ambient temperature, and q_{ev} is the evaporation heat.

In the process of SLM and ILP, the metal phase is melted rapidly and even reach the boiling temperature, evaporation occurs, and heat dissipation to the environment. The following is the evaporative heat equation [31,35]:

$$q_{ev} = 0.82 \frac{\Delta H^*}{\sqrt{2\pi MRT}} p_0 \exp\left(\Delta H^* \frac{T - T_{lv}}{RTT_{lv}}\right) \quad (9)$$

In the formula, ΔH^* is the escape metal vapor, M is the molar mass of the material, R is the ideal gas constant, p_0 is the environmental pressure, and T_{lv} is the boiling temperature. Metal vapor will exert recoil pressure on free interface as follows [35]:

$$p_r = 0.54 p_0 \exp\left(L_{lv} \frac{T - T_{lv}}{RTT_{lv}}\right) \quad (10)$$

L_{lv} is the latent heat of vaporization of metallic materials.

3.4. Process Parameters and Material Properties

The SLM process and four ILP process parameters are shown in Table 2. The purpose of the modeling study is to reveal the mechanism of ILP. Modeling should try to ensure the

quality of the track. And there must be no excessive computing time. The typical computing time of a single track SLM is about 40 hours (h) [30]. To choose suitable parameters, the parameters of Yuan et al. [36], using 0.8 m/s and 200 W, were referred to. A series of simulations were performed by varying the power. Finally, the scanning speed was 0.8m/s and the power used was 150W. Using these parameters, good track quality is obtained with suitable computing time.

Table 2. Process parameters used in the modelling computation of SLM followed by ILP with different power.

Sample	Power (W)	Scanning Speed (m/s)
SLM	150	0.8
ILP	50	0.8
ILP	90	0.8
ILP	130	0.8
ILP	170	0.8

The thermophysical properties of IN718 are shown in Figure 5. The other material properties are shown in Table 3.

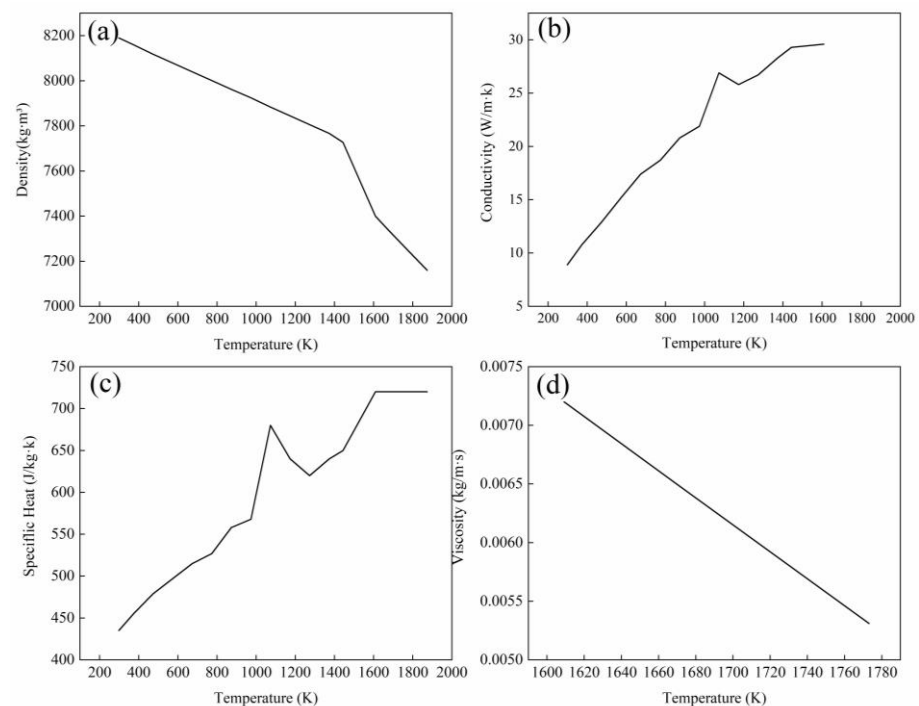


Figure 5. Temperature-dependent thermophysical properties of IN718. (a) Density; (b) Conductivity; (c) Specific Heat; (d) Viscosity. Reprinted with permission from [31]. Copyright 2016 Elsevier.

Table 3. IN718 material properties. Data from [30].

Property	Value	Units	Property	Value	Units
Reflection coefficient	0.7	K	Marangoni coefficient	1.1×10^{-4}	$\text{N} \cdot \text{m}^{-1} \cdot \text{K}^{-1}$
Solidus temperature	1523	K	Latent heat of fusion	270	$\text{kJ} \cdot \text{kg}^{-1}$
Liquidus temperature	1608	K	Latent heat of vaporisation	6300	$\text{kJ} \cdot \text{kg}^{-1}$
Boiling temperature	3188	K	Surface tension coefficient	1.89	$\text{N} \cdot \text{m}^{-1}$

3.5. Validation

To demonstrate the viability of the modelling techniques adopted in the current study, a single-layer, single-track SLM process was simulated, using the same processing

parameters as for the SLM experiment in Section 2.1. The simulated surface topography was compared with that of the experiment that was characterized using the white light interferometer. The section location, line profile and line roughness of the experimental surface are shown in Figure 6a. The section location, line profile and line roughness of the simulated surface are shown in Figure 6b. The roughness of the experimental surface was compared with the roughness of the simulated surface. The error of R_a is 6.06%; the error of R_z is 1.33%, and the variation trend of the line profile of the simulated and experimental surfaces is consistent. That is, the simulated surface is in good agreement with the experimental surface.

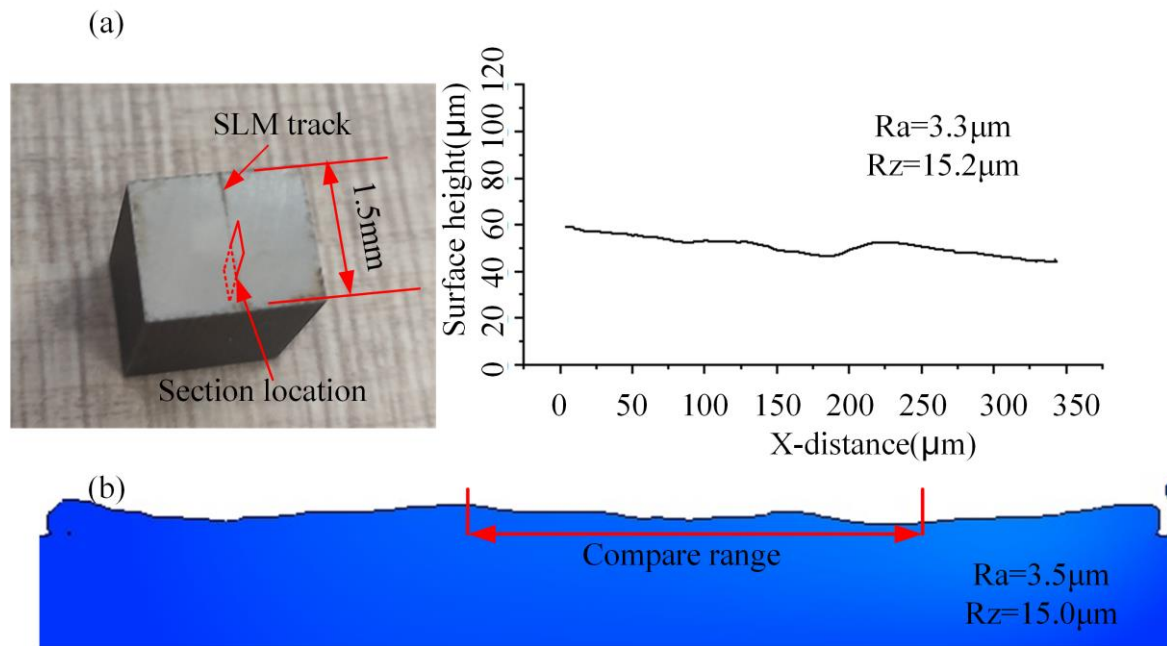


Figure 6. Simulation and experimental surface comparison. (a) experiment; (b) simulation. Obtained at 185 W, 0.6 m/s and spot diameter were 0.05 mm (power, speed and spot diameter).

In order to further verify the validity of the simulation model. The surface topography of a 1 mm-long SLM single track obtained by the simulated was compared with the surface topography of the track obtained by the SLM test [37]. The simulation and experiment use the same parameters, as shown in Figure 7. The contour of Figure 7a represents the boundary of the track. It can be seen that the width of the track obtained by experiment and simulation is gradually reduced along the laser scanning direction. The shape of the width reduction area is approximately conical. The experimental track and the simulated track show good agreement. The variation trend of the track width is related to the inherent heat and mass transfer characteristics during the SLM process [37], and the LP also depends on the heat and mass transfer of the molten pool [36,38]. Therefore, the numerical model established in this paper can well predict the changing trend of the SLM track and can be used to simulate the ILP process.

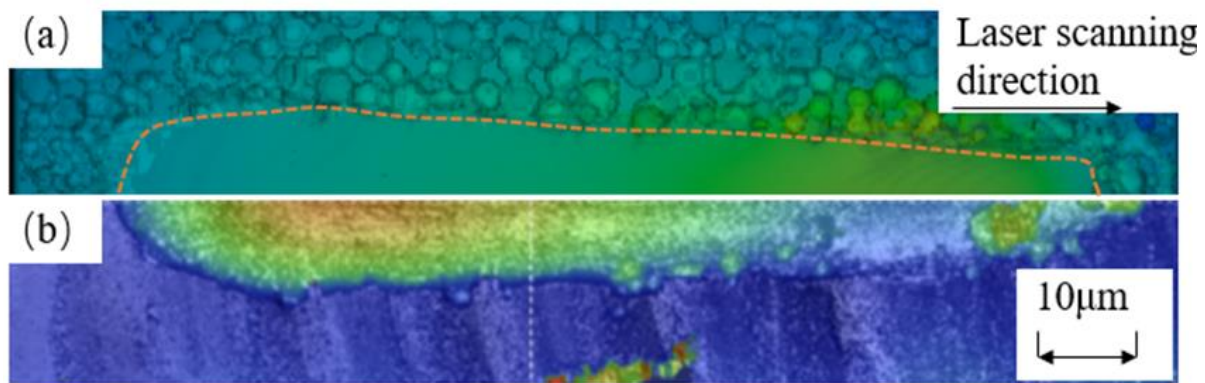


Figure 7. Track morphology comparison. (a) The simulated track morphology, obtained at 195 W, 0.4 m/s and 0.05 mm; (b) Experimental track morphology, obtained at 195 W, 0.4 m/s and 0.05 mm (power, speed and spot diameter). Reprinted with permission from [37]. Copyright 2021 The Society of Manufacturing Engineers.

4. Results and Discussion of Numerical Simulation

4.1. Temperature Change in ILP Process

The temperature change curve of the monitoring point under different ILP powers is shown in Figure 8. The monitoring point is located below the center point of the top surface of the track. The simulation was performed in the computational domain shown in Figure 4. The temperature in the powder bed and the solidified layers changed rapidly during SLM. The peak temperature of the SLM stage is 4309 K and reaches its peak at 0.55 ms. The peak temperature is above the evaporation temperature, indicating that the monitoring point is in the direct-action area of the laser at this time. The liquid at the monitoring point is evaporated. At 1.65 ms, because the ILP laser moves to this point, the temperature of the monitoring point reaches a peak again. With the increase in ILP power, the peak temperature of the monitoring point of the ILP stage gradually increased.

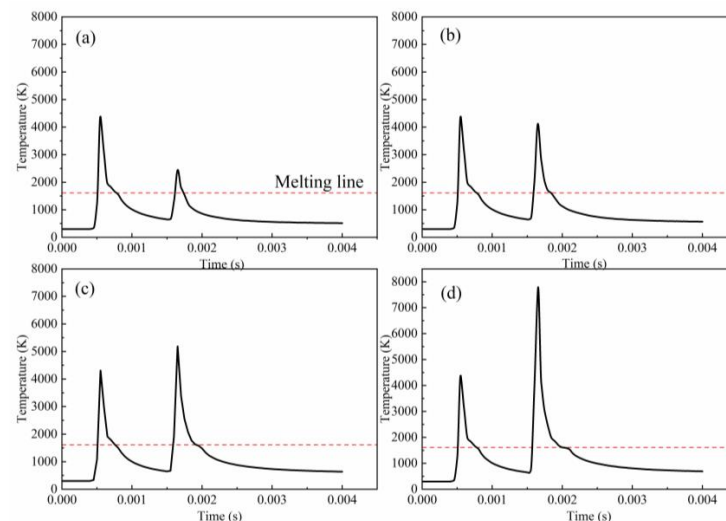


Figure 8. The temperature change of ILP with different ILP power. (a) 50 W; (b) 90 W; (c) 130 W; (d) 170 W.

When the ILP power is 50 W, although there is heat residue in the SLM stage, the second temperature peak is only 2448 K, which is far lower than the first peak of 4309 K (as shown in Figure 8a). Mainly due to the energy density of the ILP laser being much lower than the SLM laser. When the ILP power is 90 W, the second peak temperature is increased greatly to 4052 K, which is still below the first peak temperature. When the molten pool of the monitoring point cools down, the cooling rate tends to decrease gradually. From

Figure 8b, it can be seen that the slope of the curve above the liquid line in the ILP stage is gradually decreasing. This is because as the laser moves, the monitoring point is positioned further back in the molten pool.

The temperature contours on the vertical plane through the center of the ILP track predicted by the numerical simulation under different powers are shown in Figure 9. The black horizontal lines are the paths along which the temperature gradient curves are derived and plotted in Figure 10. As shown in Figure 10, in the molten pool, the more backward (the opposite direction of the X direction), the smaller the temperature gradient, and the slower the temperature change rate of the monitoring point. When the ILP power is 50 W, the cooling rate does not change significantly, because, under this processing condition, the temperature gradient in the molten pool changes very little. After the molten pool at the monitoring point is solidified, the cooling rate is significantly accelerated. From Figure 8, it can be seen that the sudden change in the slope of the curve at the liquid line in the ILP stage. This is because the heat transfer rate from liquid to solid is lower than the heat transfer rate between solids, so the metal phase dissipates heat to the base faster after solidification. When the ILP power is 130 W, the first peak temperature is exceeded by the second, and the second peak temperature is 5184 K. Although the ILP power is less than the SLM power, the working temperature is higher than the latter. This phenomenon occurs because the thermal conductivity of a continuous solid is greater than that of powder [39], and the heat of the laser is more easily transferred to the monitoring point. In addition, there is residual heat on the track after SLM, and the initial temperature of the monitoring point during ILP is 660 °C. When the ILP power is 170 W, the second peak temperature is 7710 K due to the increase in input energy density.

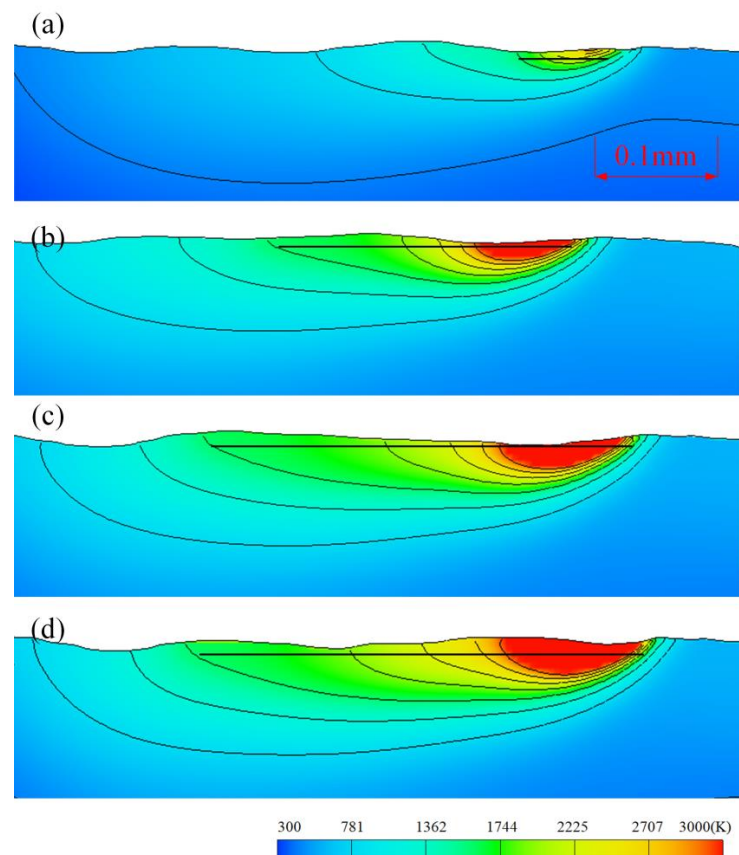


Figure 9. The temperature contours of ILP with different ILP power. (a) 50 W; (b) 90 W; (c) 130 W; (d) 170 W. The scanning speed was 0.8 m/s, and the spot diameter was 0.05 mm. The entire domain is 0.6 mm long and 0.13 mm high.

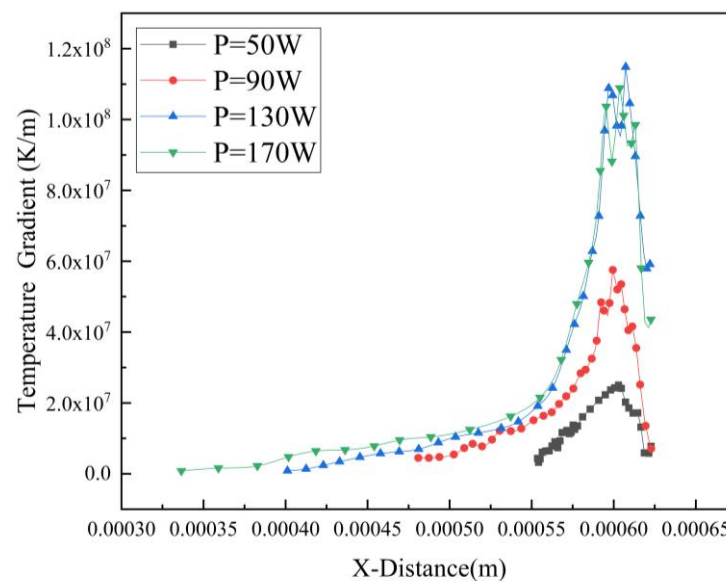


Figure 10. The temperature gradient in the X direction of the molten pool during the ILP process with four processing parameters.

In the ILP process, the working temperature of the molten pool is increased with increasing power. The larger working temperature can increase the fluidity of the molten pool so that the liquid at the bulge can fully flow in the molten pool and redistribute evenly. However, too high of a working temperature also greatly increases the instability of the molten pool [40], which may impair the surface quality.

4.2. Surface Morphology Evolution and Molten Pool Dynamics during ILP

To reveal the mechanism of ILP, the evolution of the surface morphology and the molten pool dynamics in the ILP process were studied. Taking the large bulge in the middle of Figure 11c as an example, it is described how the surface topography of the SLMed track is altered by ILP. Figure 11 is a x-z view of the center of the track, the contour is the temperature contour, and the arrow is the molten pool velocity vector. Figure 11a shows the initial state of the powder bed. Figure 11b shows the surface profile after SLM. When $t = 1.35$ ms, the track of the SLM has been completely solidified, but the temperature of the original molten pool area is still about 1000 K, and the temperature of other areas is also higher than the ambient temperature. The temperature accumulation in the SLM stage is beneficial for the ILP process. At this time, the ILP molten pool has not yet touched the bulge. The laser is just acting on the track, and the energy input is low, and the temperature gradient of the molten pool is low.

Among the internal forces in the molten pool, surface tension (capillary force) plays a leading role. As shown in Figure 11, the velocity vectors of the molten pool surface mostly point to the center of the molten pool. The surface area of the molten pool tends to be reduced by surface tension, which may lead to balling [35]. When $t = 1.40$ ms, as shown in Figure 11d, the molten pool is elongated at this time, and the Marangoni flow effect appears behind it. These indicate that there is a surface tension gradient at the gas-liquid interface. A vortex appears in the middle of the molten pool. The circulation of the liquid in the molten pool can be accelerated by the vortex, thereby the cooling and solidification of the molten metal are also accelerated [28]. At the front of the molten pool, the velocity vector points to the bulge. The molten pool begins to wet the bulge and the heat transfers to the bulge. This is the accumulation of heat for the molten pool to swallow the bulge. When $t = 1.45$ ms, as shown in Figure 11e, with the forward movement of the laser and the influence of the wetting behavior of the molten pool, the left half of the bulge has been swallowed by the molten pool [41]. The molten pool does not diffuse downward to the SLM track at the bulge area but flows into the valley under the action of the capillary

force [21,22,24], thereby filling the valley. This flow trend can be seen in Figure 11, which is in the surface shallow melting (SSM) state of LP [42]. When $t = 1.50$ ms, as shown in Figure 11f, most of the bulge area has been melted. Since the liquid in the bulge area flows to the lower left of the bulge under the action of capillary force, the bulge in Figure 11e has been flattened at this moment.

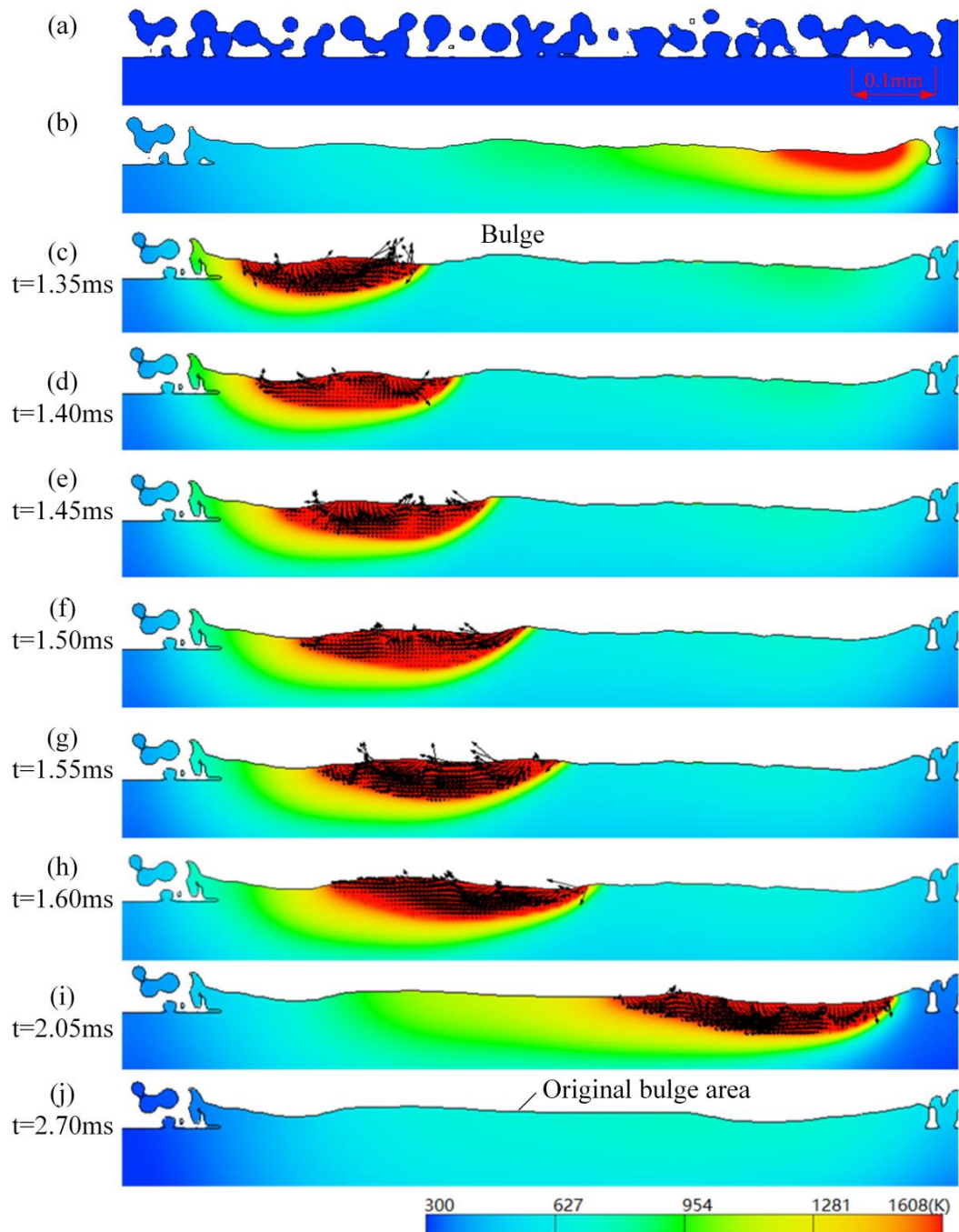


Figure 11. Surface topography evolution. (a) Powder bed; (b) surface profile after SLM; (c–j) are the ILP process. The parameters of SLM were 150 W, 0.8 m/s and 0.05 mm (power, speed and spot diameter). The parameters of ILP were 130 W, 0.8 m/s and 0.05 mm (power, speed and spot diameter). The entire domain is 1 mm long and 0.15 mm high.

At this moment, the remaining bulge area wetted by the molten pool also has this flow to the lower left. When $t = 1.55$ ms, as shown in Figure 11g, the bulge has been completely swallowed by the molten pool, which is in the surface over melting (SOM) state

of LP [42]. The capillary force and thermocapillary force work together [22,24,41] in the molten pool. There is a downward flow driven by capillary force and a tangential flow driven by thermocapillary force. The capillary force plays a major role, which gradually reduces the curvature of the bulge. When $t = 1.60$ ms, the original bulge was eliminated under the driving of capillary force. At this time, the thermocapillary force plays a major role, as shown in Figure 11h. When $t = 2.05$ ms, as shown in Figure 11i, the molten pool at the original bulge area is completely solidified and becomes flat under the action of ILP. When $t = 2.7$ ms, as shown in Figure 11j, the laser no longer acts on the track, and the molten pool is completely solidified. Several bulges in the as-SLMed track disappear, and the track becomes smooth. However, there are depressions at both ends of the track, indicating that new surface defects will also be generated during the ILP process.

The main driving force in the molten pool changes with the development of the molten pool. When the bulge begins to be swallowed by the molten pool, capillary force dominates, causing the liquid in the molten pool to flow to the lower left of the bulge along the slope. When the bulge is completely swallowed by the molten pool, the capillary force continues to dominate, causing a downward normal flow of the molten pool to reduce the curvature of the bulge. As the curvature of the bulge decreases, the effect of capillary force is gradually weakened, and the thermocapillary force becomes the main driving force in the molten pool.

The surface roughness of SLMed parts is reduced by ILP. That is, as the laser advances and under the action of the wettability of the molten pool, the bulges on the surface of the SLMed part are constantly swallowed by the molten pool. The molten material at the bulge is moved backward by the combined action of capillary force and thermal capillary force and is redistributed in the molten pool. The surface becomes flat.

4.3. Effect of ILP Power on the Surface Quality of as-SLMed Track and Its Mechanism

ILP simulations at 50 W, 90 W, 130 W, and 170 W were carried out, and the surface morphology characteristics of all samples and the underlying mechanism were analyzed. Figure 12 shows the cross-sectional of the samples. Figure 12a shows the morphology of the track before ILP, and the track shows an uneven wavy shape, which is caused by the bulge caused by the laser scanning and the lack of fusion and spatter of the powder [18,42]. The surface roughness of the as-SLMed track is $4.9 \mu\text{m}$. The coordinate data of the surface points were extracted in the simulation software, and S_a was calculated by the formula (1). The track morphology at an ILP power of 50 W is shown in Figure 12b. It can be seen that the length and height of each bulge are reduced, but the overall surface roughness changes little, only $0.1 \mu\text{m}$ less than the as-SLMed surface roughness. When the power of the ILP is 90 W, as shown in Figure 12c, the length and height of each bulge are further reduced. Due to the short life of the molten pool, the bulges do not completely disappear [23], and the surface roughness is reduced to $4.0 \mu\text{m}$. From the three-dimensional surface morphology of Figure 12, the surface morphology of 50 W and 90 W has no significant change compared with the as-SLMed. When the ILP power is 130 W, the life of the molten pool is increased. As shown in Figure 12d, the original bulges are eliminated after ILP, but new bulges are generated, and depressions are generated at both ends of the track surface. From Figure 12d, the surface morphology has changed greatly compared with the as-SLMed, and a new surface morphology has been formed. The surface morphology is closely related to the molten pool flow velocity, and too fast flow velocity is not conducive to the formation of good surface morphology [8]. The molten pool flow velocity during ILP was investigated. The location of the monitoring of the molten pool flow velocity point is shown in Figure 12a. This point is melted under all processing conditions. In addition, in the fluctuating melt pool, this point is always in a liquid state. Figure 13 shows the velocity fluctuation during the ILP. As the laser moves, the position of the monitoring point in the molten pool is constantly changing. The flow velocity of the fluid at the monitoring point is also constantly changing, and the flow velocity curve fluctuates accordingly. When the flow velocity is 0, the monitoring point is solidified. The ILP powers are 50 W, 90 W, 130 W, and 170 W,

and they solidify at 0.0018 s, 0.0019 s, 0.0020 s, and 0.0022 s, respectively. When the ILP power is at 170 W, the melt pool flow velocity is increased greatly, and the growth range is also greater compared to the first two groups. The large increase in the molten pool velocity makes the molten pool extremely unstable. During the ILP process, the surface morphology of the molten pool changes rapidly, and some bulges will be generated on the surface of the molten pool. Some of the molten materials at the bulges will be brought to other areas during the flow of the molten pool, and some will have solidified before they are redistributed in the molten pool. Periodic waves are generated at the track surface due to the high energy input, as shown in Figure 12e. These waves severely affect the surface roughness. At this time, the surface roughness is 13.4 μm .

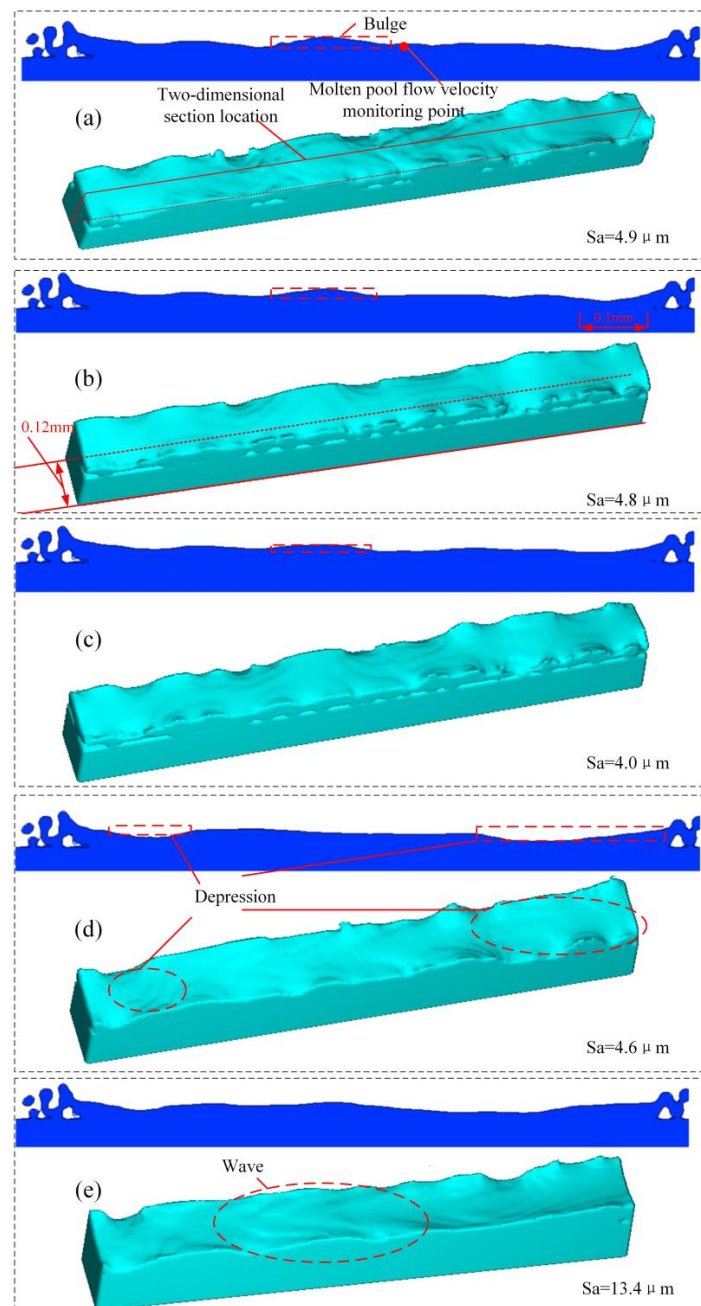


Figure 12. Surface morphology. (a) As received; (b) 50 W; (c) 90 W; (d) 130 W; (e) 170 W. The parameters of SLM were 150 W, 0.8 m/s and 0.05 mm. The other parameters of ILP were 0.8 m/s and 0.05 mm. The length of the plane domain is 1 mm, and the height is 0.15 mm. The size of the 3D domain is 1 mm \times 0.12 mm \times 0.2 mm.

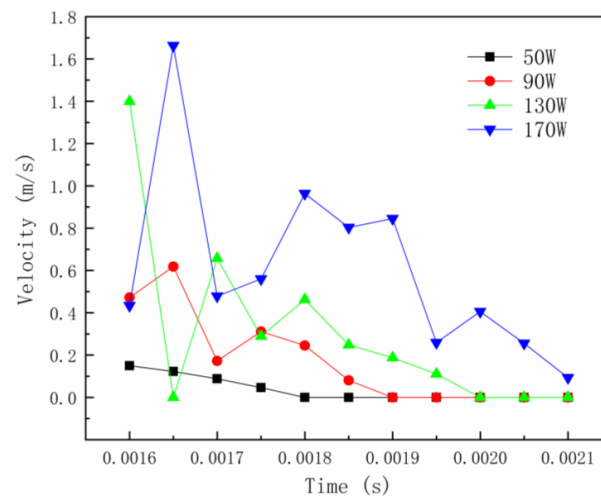


Figure 13. The flow velocity of the molten pool of the monitoring point fluctuates with time under different ILP power.

The mechanism of depression generation during ILP can be revealed by analyzing the melt pool fluid dynamics results from modelling with 130W laser power. As shown in Figure 14, when $t = 1.30$ ms, the molten pool at the left end of the track generates a depression under the action of capillary force. When $t = 1.40$ ms, there is a liquid flow from the bulge to the depression. When $t = 1.60$ ms, the depression has been solidified but not flattened. This is because when $t = 1.40$ ms, due to the insufficient heat accumulation, the molten pool size is small and the life is short, which causes the depression to not have enough time to be filled [23]. At $t = 1.60$ ms, the depression is further deepened due to the accumulation of material on the right side of the depression by the Marangoni flow. The depression on the right side of the track is generated because the material is continuously transported to the left by the Marangoni flow during the laser movement. The depression area transports material to the left area, but the depression area does not receive the material, resulting in a depression, is generated at the right end of the track.

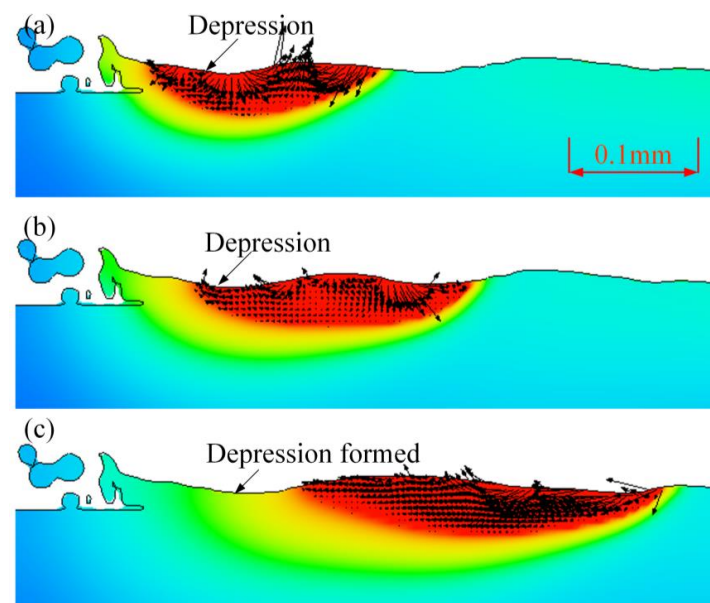


Figure 14. The cause diagram of the left end depression of the track when the ILP power is 130 W. (a) $t = 1.30$ ms; (b) $t = 1.40$ ms; (c) $t = 1.60$ ms. The parameters of SLM were 150 W, 0.8 m/s and 0.05 mm. The parameters of ILP were 130 W, 0.8 m/s and 0.05 mm. The entire domain is 0.54 mm long and 0.15 mm high.

The molten pool flow is used to reveal the mechanism of the formation of the new bulges in the ILP process. Figure 15 shows the velocity fields of the y-z section when the ILP power is 130 W. As shown in Figure 15a, when $t = 1.7$ ms, the surface tension gradient of the molten pool is greater than 0. The velocity vector points from both sides of the laser scanning track to the center of the track. The molten material on both sides of the track is delivered to the center of the track [21]. At this time, it is in the heating stage of molten pool formation. As shown in Figure 15b, when $t = 1.85$ ms, the size of the molten pool is the largest, and the molten pool begins to cool at this time. The surface tension gradient is still greater than 0. Both sides of the track transport material to the center of the track, and a bulge has been generated in the center at this time. When $t = 1.90$ ms, as shown in Figure 15c, the surface tension gradient of the molten pool becomes negative. The bulge in the center of the track begins to transport material to both sides of the track. When $t = 1.95$ ms, as shown in Figure 15d, the molten pool surface becomes flat under the action of the previous negative surface tension gradient. However, at this time, the surface tension gradient of the molten pool becomes positive, and both sides of the track transport materials to the center of the track. At $t = 2.0$ ms, a bulge is generated in the center of the track in the melt pool, as in Figure 15e, and the bulge is dragged up by the velocity vector. When the molten pool is completely solidified, as shown in Figure 15f, the bulge still exists. The formation of the bulge has a great relationship with the surface tension gradient, and the final formation of the surface bulge depends on the surface tension gradient during the cooling stage of the molten pool. The thermal capillary force affected by surface-active elements is the driving force for the tangential flow of the molten pool [24], and it plays a major role in the formation of bulges [21,37]. If the bulge created in the transverse direction is hemispherical, it will also be seen in the longitudinal direction. If it is semi-cylindrical, it will not be seen in a longitudinal direction. However, both will increase the surface roughness. The bulge in Figure 15 resembled a semi-cylindrical shape. When the ILP power is 130 W, there is no further reduction in surface roughness due to the presence of new depressions and new bulges. However, the surface roughness is still reduced to $4.6 \mu\text{m}$.

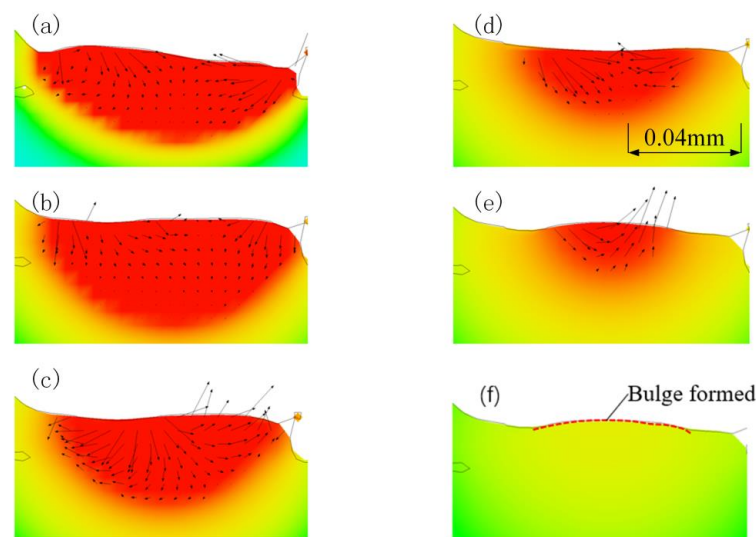


Figure 15. The formation of bulge in LP process. (a) $t = 1.70$ ms; (b) $t = 1.85$ ms; (c) $t = 1.90$ ms; (d) $t = 1.95$ ms; (e) $t = 2.00$ ms; (f) $t = 2.15$ ms. The parameters of SLM were 150 W, 0.8 m/s and 0.05 mm. The parameters of ILP were 130 W, 0.8 m/s and 0.05 mm. The entire domain is 0.11 mm long and 0.06 mm high.

The ILP power is a key factor in improving surface quality. At the appropriate power, the molten material will be redistributed on the metal surface under the combined action of capillary and thermocapillary forces. The curvature of the bulges is reduced, and the depressions are filled, thereby the surface roughness is reduced, as shown in Figure 12c. As the laser power increases, the life of the molten pool is increased and the molten material

has more time to be redistributed on the surface, resulting in the surface roughness being further reduced. However, after the laser power exceeds a certain value, the surface roughness is not reduced but increased. Increasing the input energy increases the life and instability of the molten pool. During the flow of the molten pool, although the original defects are eliminated, new defects are also created, as shown in Figure 12d,e. Eventually, this leads to the surface roughness being increased.

4.4. Influence of the Interaction between the Tracks on Surface Quality

In order to investigate the effect of the interaction between the tracks on the final surface quality, two three-track simulations were performed. One was for SLM, and the other was for ILP after the SLM with an elapsed time of 0 ms. The processing parameters were the same as those of SLM and Sample-2 in Table 1. The results are shown in Figure 16. The multiple-track has a great improvement in the surface quality compared with single-track. In the single-track simulation, the S_a of the as-SLM sample is $4.9\text{ }\mu\text{m}$, and the S_a of the ILPed sample is $4.0\text{ }\mu\text{m}$. While in the multi-track simulation, the two numbers are $3.9\text{ }\mu\text{m}$ and $3.0\text{ }\mu\text{m}$. In the multiple-track simulation, the surface roughness after ILP is reduced by 23%, which is greater than the 18.4% of the single track. This is because in the multiple-track simulation, the laser heats up and melts the tracks on both sides, which results in the surface having been remelted several times and the surface quality being improved. Therefore, the interaction between the tracks is beneficial to the improvement of the surface quality.

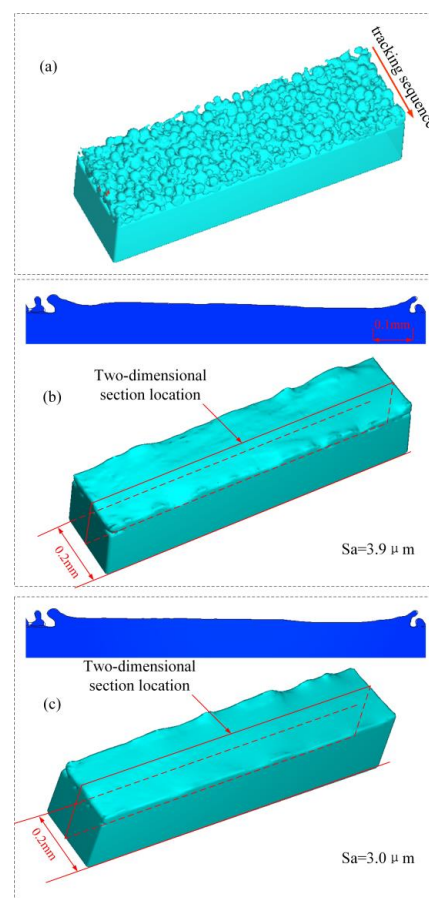


Figure 16. Multi-track simulation surface profile. (a) Powder bed; (b) As-SLMed; (c) ILPed. The parameters of SLM were 150 W, 0.8 m/s and 0.05 mm. The parameters of ILP were 90 W, 0.8 m/s and 0.05 mm. The hatch spacing was 0.01 mm. The length of the plane domain is 1 mm, and the height is 0.15 mm. The size of the 3D domain is 1 mm \times 0.2 mm \times 0.2 mm.

In addition, during SLM and ILP, the interaction between tracks is affected by hatch spacing and spot diameter. If the hatch spacing is too large or the spot diameter is too small, the tracks will not overlap, and they will not affect each other. So, the surface quality of the samples is affected by the hatch spacing and spot diameter, which deserves further study.

5. Conclusions

This paper demonstrates the effectiveness of ILP to improve the surface quality of nickel-based alloys fabricated by SLM. The temperature field, molten pool flow, and surface morphology evolution of the ILP process were studied by numerical simulation. The mechanisms of ILP for surface quality improvement and new defect formation were revealed. The following results were obtained:

- (1) SLM and ILP experiments were performed, respectively. The surface roughness of the SLM samples after ILP is reduced from $20.0 \pm 1.25 \mu\text{m}$ to $13.3 \pm 0.35 \mu\text{m}$. The quality of the surface is significantly improved, which proves the effectiveness of ILP in improving the surface quality of nickel-based alloys fabricated by SLM;
- (2) During the ILP process, the peak temperature in the ILP stage increases with increasing power, and the life of the molten pool also increases. When the ILP power is 130 W, the peak temperature in the ILP stage exceeds the peak temperature in the SLM stage. The high temperature of the molten pool will make the molten pool unstable, which is not conducive to the improvement of surface quality;
- (3) The mechanism of ILP improving the surface quality of SLM parts is that capillary force and thermal capillary force drive the molten pool flow to reduce the curvature of the bulge. During the initial stage of the molten pool swallowing the bulge, capillary force drives the liquid to the left of the bulge. When the bulge is completely swallowed by the molten pool, capillary force drives the molten pool to flow downward. As the curvature of the bulge decreases, the thermocapillary force becomes the main driving force, and the liquid is driven to the back of the molten pool;
- (4) The ILP power has a great influence on the surface quality. If the ILP power is too small, the molten pool life will be short, which is not enough to make the surface bulge disappear, and the effect on the surface quality improvement is limited. If the ILP power is too large, new bulges and depressions will be produced on the track surface, which will affect the surface quality;
- (5) Capillary force during the ILP process leads to the formation of the depression in the molten pool. If the mass transfer caused by the thermocapillary force cannot fill the depression in time, it will cause the formation of a recessed defect on the track surface. The material exchange between the center and both sides of the track caused by the surface tension gradient leads to the formation of the bulges. The final surface bulge depends on the surface tension gradient in the cooling stage of the molten pool.

Author Contributions: Y.Z. designed the experimental plan and supervised the entire work. C.D. established the numerical model and carried out a numerical simulation analysis. P.W. completed the sample preparation, W.M. completed the model verification part, and C.L. completed the sample test. All authors have read and agreed to the published version of the manuscript.

Funding: This research was funded by National Natural Science Foundation of China (Grant No. 51975339, 51605262); China Postdoctoral Science Foundation (Grant No. 2019T120602, 2017M610439); Youth Innovation and Technology Support Program for University in Shandong Province (Grant No. 2019KJB003).

Informed Consent Statement: Not applicable.

Data Availability Statement: Not applicable.

Acknowledgments: The authors would like to thank Shandong Leishi Intelligent Manufacturing Co., Ltd. for providing the technical support.

Conflicts of Interest: The authors declare no conflict of interest.

References

1. Wang, Z.; Guan, K.; Gao, M.; Li, X.; Chen, X.; Zeng, X. The microstructure and mechanical properties of deposited-IN718 by selective laser melting. *J. Alloys Compd.* **2011**, *513*, 518–523. [CrossRef]
2. Qiu, C.; Chen, H.; Liu, Q.; Yue, S.; Wang, H. On the solidification behaviour and cracking origin of a nickel-based superalloy during selective laser melting. *Mater. Charact.* **2018**, *148*, 330–344. [CrossRef]
3. Li, Y.; Zhang, Z.; Guan, Y. Thermodynamics analysis and rapid solidification of laser polished Inconel 718 by selective laser melting. *Appl. Surf. Sci.* **2020**, *511*, 145–152. [CrossRef]
4. Li, N.; Huang, S.; Zhang, G.; Qin, R.; Liu, W.; Xiong, H.; Shi, G.; Blackburn, J. Progress in additive manufacturing on new materials: A review. *J. Mater. Sci. Technol.* **2018**, *35*, 242–269. [CrossRef]
5. Zhao, Y.; Sun, J.; Li, J.; Yan, Y.; Wang, P. A comparative study on Johnson-Cook and modified Johnson-Cook constitutive material model to predict the dynamic behavior laser additive manufacturing FeCr alloy. *J. Alloys Compd.* **2017**, *723*, 179–187. [CrossRef]
6. Zhao, Y.; Sun, J.; Li, J.; Wang, P.; Zheng, Z.; Chen, J.; Yan, Y. The stress coupling mechanism of laser additive and milling subtractive for FeCr alloy made by additive–subtractive composite manufacturing. *J. Alloys Compd.* **2018**, *769*, 898–905. [CrossRef]
7. Cao, L.; Zhou, Q.; Han, Y.; Song, B.; Nie, Z.; Xiong, Y.; Xia, L. Review on intelligent monitoring of defects and process control of selective laser melting additive manufacturing. *Acta Aeronaut. Astronaut. Sin.* **2020**, *65*, 199–233. [CrossRef]
8. Jain, S.; Corliss, M.; Tai, B.; Hung, W. Electrochemical polishing of selective laser melted Inconel 718. *Procedia CIRP* **2019**, *34*, 239–246. [CrossRef]
9. Marimuthu, S.; Triantaphyllou, A.; Antar, M.; Wimpenny, D.; Morton, H.; Beard, M. Laser polishing of selective laser melted components. *Int. J. Mach. Tools. Manuf.* **2015**, *95*, 97–104. [CrossRef]
10. Tsai, M.; Yang, W. Combined ultrasonic vibration and chemical mechanical polishing of copper substrates. *Int. J. Mach. Tools Manuf.* **2012**, *53*, 69–76. [CrossRef]
11. Guo, J.; Au, K.; Sun, C.; Goh, M.; Kum, C.; Liu, K.; Wei, J.; Suzuki, H.; Kang, R. Novel rotating-vibrating magnetic abrasive polishing method for double-layered internal surface finishing. *J. Mater. Process. Technol.* **2019**, *264*, 422–437. [CrossRef]
12. Pereira, O.; Rodríguez, A.; Fernández-Abia, A.; Barreiro, J.; López de Lacalle, L.N. Cryogenic and minimum quantity lubrication for an eco-efficiency turning of AISI 304. *J. Clean. Prod.* **2016**, *139*, 440–449. [CrossRef]
13. Habibzadeh, S.; Li, L.; Shum-Tim, D.; Davis, E.C.; Omanovic, S. Electrochemical polishing as a 316L stainless steel surface treatment method: Towards the improvement of biocompatibility. *Corros. Sci.* **2014**, *87*, 89–100. [CrossRef]
14. Yao, Y.; Zhou, R.; Zhang, C.; Mei, T.; Wu, M. Surface polishing technology for additive manufacturing complex metal components. *Acta Aeronaut. Astronaut. Sin.* **2020**, *78*, 1–14. [CrossRef]
15. Fang, Z.; Lu, L.; Chen, L.; Guan, F. Laser Polishing of Additive Manufactured Superalloy. *Procedia CIRP* **2018**, *71*, 150–154. [CrossRef]
16. Cwikła, M.; Dziedzic, R.; Reiner, J. Influence of Overlap on Surface Quality in the Laser Polishing of 3D Printed Inconel 718 under the Effect of Air and Argon. *Materials* **2021**, *14*, 1479. [CrossRef] [PubMed]
17. Ma, C.; Guan, Y.; Zhou, W. Laser polishing of additive manufactured Ti alloys. *Opt. Laser. Eng.* **2017**, *93*, 171–177. [CrossRef]
18. Chen, L.; Richter, B.; Zhang, X.; Bertsch, K.; Thoma, D.; Pfefferkorn, F. Effect of laser polishing on the microstructure and mechanical properties of stainless steel 316L fabricated by laser powder bed fusion. *Mater. Sci. Eng. A* **2021**, *802*, 140–154. [CrossRef]
19. Liang, C.; Hu, Y.; Liu, N.; Zou, X.; Wang, H.; Zhang, X.; Fu, Y.; Hu, J. Laser Polishing of Ti6Al4V Fabricated by Selective Laser Melting. *Metals* **2020**, *10*, 191. [CrossRef]
20. Zhou, J.; Han, X.; Li, H.; Liu, S.; Shen, S.; Zhou, X.; Zhang, D. In-Situ Laser Polishing Additive Manufactured AlSi10Mg: Effect of Laser Polishing Strategy on Surface Morphology, Roughness and Microhardness. *Materials* **2021**, *14*, 393. [CrossRef]
21. Xu, J.; Zou, P.; Kang, D.; Wang, W. Theoretical and experimental study of bulge formation in laser polishing of 304 stainless steel. *J. Manuf. Process.* **2021**, *66*, 39–52. [CrossRef]
22. Zhang, C.; Zhou, J.; Shen, H. Role of Capillary and Thermocapillary Forces in Laser Polishing of Metals. *J. Manuf. Sci. Eng. Trans. ASME* **2017**, *139*, 41–56. [CrossRef]
23. Li, K.; Zhao, Z.; Zhou, H.; Zhou, H.; Yin, J.; Zhang, W.; Zhou, G. Numerical Simulation of Effect of Different Initial Morphologies on Melt Hydrodynamics in Laser Polishing of Ti6Al4V. *Micromachines* **2021**, *12*, 581. [CrossRef] [PubMed]
24. Li, K.; Zhao, Z.; Zhou, H.; Zhou, H.; Jin, J. Numerical analyses of molten pool evolution in laser polishing Ti6Al4V. *J. Manuf. Process.* **2020**, *58*, 574–584. [CrossRef]
25. Song, Y. *Research on Laser Polishing Mechanism and Process of SLM Additive Manufacturing Surface*; Shandong University: Jinan, China, 2021. [CrossRef]
26. Przemysław, P. Reduction of Influence of the High-Frequency Noise on the Results of Surface Topography Measurements. *Materials* **2021**, *14*, 333. [CrossRef]
27. Pavel, P.; Ondřej, H. White-light interferometry on rough surfaces—measurement uncertainty caused by noise. *Appl. Opt.* **2012**, *51*, 465–473.
28. Lv, F.; Liang, H.; Xie, D.; Mao, Y.; Wang, C.; Shen, L.; Tian, Z. On the role of laser in situ re-melting into pore elimination of Ti–6Al–4V components fabricated by selective laser melting. *J. Alloys Compd.* **2021**, *854*, 156–168. [CrossRef]
29. Khairallah, S.; Anderson, A.; Rubenchik, A.; King, W. Laser powder-bed fusion additive manufacturing: Physics of complex melt flow and formation mechanisms of pores, spatter, and denudation zones. *Acta Mater.* **2016**, *108*, 36–45. [CrossRef]

30. Ye, W. *Numerical Simulation of Temperature Field and Morphology Evolution of Molten Pool during Laser Selective Melting Process*; Xi'an University of Technology: Xi'an, China, 2019.
31. Lee, Y.; Zhang, W. Modeling of heat transfer, fluid flow and solidification microstructure of nickel-base superalloy fabricated by laser powder bed fusion. *Addit. Manuf.* **2016**, *12*, 178–188. [CrossRef]
32. Hu, Y.; Zhu, K.; Xi, B. A 3-dimensional volume of fluid method-PLIC3D. *Chin. Q. Mech.* **2003**, *18*, 238–243. [CrossRef]
33. Dai, D.; Gu, D. Influence of thermodynamics within molten pool on migration and distribution state of reinforcement during selective laser melting of AlN/AlSi10Mg composites. *Int. J. Mach. Tools Manuf.* **2016**, *100*, 14–24. [CrossRef]
34. Xiang, Y.; Zhang, S.; Li, J.; Wei, Z.; Yang, L.; Jiang, L. Numerical simulation and experimental verification for selective laser single track melting forming of Ti6Al4V. *J. Zhejiang Univ. (Eng. Sci.)* **2019**, *53*, 2102–2109. [CrossRef]
35. Gürtler, F.; Karg, M.; Leitz, K.H.; Schmidt, M. Simulation of Laser Beam Melting of Steel Powders using the Three-Dimensional Volume of Fluid Method. *Phys. Procedia* **2013**, *41*, 881–886. [CrossRef]
36. Yuan, W.; Chen, H.; Cheng, T.; Wei, Q. Effects of laser scanning speeds on different states of the molten pool during selective laser melting: Simulation and experiment. *Mater. Des.* **2020**, *189*, 108–129. [CrossRef]
37. Shrestha, S.; Chou, K. A study of transient and steady-state regions from single-track deposition in laser powder bed fusion. *J. Manuf. Process.* **2021**, *61*, 226–235. [CrossRef]
38. Xu, J.; Zou, P.; Wang, W.; Kang, D. Study on the mechanism of surface topography evolution in melting and transition regimes of laser polishing. *Opt. Laser. Technol.* **2021**, *139*, 106–118. [CrossRef]
39. Roberts, I.; Wang, C.J.; Esterlein, R.; Stanford, M.; Mynors, D. A three-dimensional finite element analysis of the temperature field during laser melting of metal powders in additive layer manufacturing. *Int. J. Mach. Tools Manuf.* **2009**, *49*, 916–923. [CrossRef]
40. Bayat, M.; Thanki, A.; Mohanty, S.; Yang, A.S.; Tiedje, J.N.; Hattel, J. Keyhole-induced porosities in Laser-based Powder Bed Fusion (L-PBF) of Ti6Al4V: High-fidelity modelling and experimental validation. *Addit. Manuf.* **2019**, *30*, 100–112. [CrossRef]
41. Leung, C.; Marussi, S.; Towrie, M.; Atwood, R.; Withers, P.; Lee, P. The effect of powder oxidation on defect formation in laser additive manufacturing. *Acta Mater.* **2019**, *166*, 294–305. [CrossRef]
42. Basha, S.; Bhuyan, M.; Basha, M.; Venkaiah, N.; Sankar, M. Laser polishing of 3D printed metallic components: A review on surface integrity. *Mater. Today Proc.* **2020**, *26*, 2047–2054. [CrossRef]

Article

Fatigue Crack Growth Analysis under Constant Amplitude Loading Using Finite Element Method

Abdulnaser M. Alshoaibi

Mechanical Engineering Department, Faculty of Engineering, Jazan University, P.O. Box 114, Jazan 45142, Saudi Arabia; alshoaibi@jazanu.edu.sa

Abstract: Damage tolerant design relies on accurately predicting the growth rate and path of fatigue cracks under constant and variable amplitude loading. ANSYS Mechanical R19.2 was used to perform a numerical analysis of fatigue crack growth assuming a linear elastic and isotropic material subjected to constant amplitude loading. A novel feature termed Separating Morphing and Adaptive Remeshing Technology (SMART) was used in conjunction with the Unstructured Mesh Method (UMM) to accomplish this goal. For the modified compact tension specimen with a varied pre-crack location, the crack propagation path, stress intensity factors, and fatigue life cycles were predicted for various stress ratio values. The influence of stress ratio on fatigue life cycles and equivalent stress intensity factor was investigated for stress ratios ranging from 0 to 0.8. It was found that fatigue life and von Mises stress distribution are substantially influenced by the stress ratio. The von Mises stress decreased as the stress ratio increased, and the number of fatigue life cycles increased rapidly with the increasing stress ratio. Depending on the pre-crack position, the hole is the primary attraction for the propagation of fatigue cracks, and the crack may either curve its direction and grow towards it, or it might bypass the hole and propagate elsewhere. Experimental and numerical crack growth studies reported in the literature have validated the findings of this simulation in terms of crack propagation paths.



Citation: Alshoaibi, A.M. Fatigue Crack Growth Analysis under Constant Amplitude Loading Using Finite Element Method. *Materials* **2022**, *15*, 2937. <https://doi.org/10.3390/ma15082937>

Academic Editors: Shuwen Wen, Yongle Sun and Xin Chen

Received: 23 March 2022

Accepted: 15 April 2022

Published: 18 April 2022

Publisher's Note: MDPI stays neutral with regard to jurisdictional claims in published maps and institutional affiliations.



Copyright: © 2022 by the author. Licensee MDPI, Basel, Switzerland. This article is an open access article distributed under the terms and conditions of the Creative Commons Attribution (CC BY) license (<https://creativecommons.org/licenses/by/4.0/>).

Keywords: fatigue analysis; equivalent stress intensity factor; linear elastic fracture mechanics; ANSYS; constant amplitude loading

1. Introduction

One of the most common catastrophic failures in mechanical structures is fatigue. Over the last few decades, researchers have strived to comprehend the mechanism of fatigue loading in materials that were exposed to dynamic loading, starting with the stress and strain life methodologies proposed by many researchers [1–6], which were curve-fitting-based approaches that used nominal and local stress–strain values. Another approach is the energy-based approach proposed by [7], which has since been used as the starting point for several experimental studies. However, such techniques are mostly limited to calculating the permissible number of load cycles before material failure instead of presenting characteristics of fatigue crack nucleation and propagation mechanisms. To properly study fatigue failure, several parameters, such as stress level, loading frequency, stress ratio ($R = \min/\max$), and material type, must be considered. In several studies, it has been demonstrated that the level of stress applied has a major impact on the fatigue failure of materials [8–11]. The linear elastic fracture mechanics (LEFM) theory was developed to identify the issue of fatigue crack growth [12–14]. The LEFM methods are commonly adopted for use on long cracks within small-scale yielding. The LEFM techniques are commonly used on long fractures with small-scale yielding behaviors near the crack tip, i.e., the Paris regime near the crack tip, i.e., the Paris regime [12,15]. Meanwhile, the Boundary Element Method [16,17], Meshless Method [18], Finite Difference Method [19], Finite Element Method (FEM), and Extended Finite Element Method (XFEM) [20–22] are the most

used methodologies for modeling crack propagation. The most common computational approach for simulating damage and failure under both static and dynamic loadings is the FEM, which obtained stress, strain, displacement, and stress intensity factor (SIF) solutions for a wide range of engineering problems. The FEM, commonly known as adaptive remeshing procedures, has proved to be highly effective and reliable. The adaptive remeshing procedures consist of four main steps: (1) existence of a demonstrative 3D finite element framework; (2) prediction of the equivalent SIFs along the crack front; (3) prediction of crack front progressions using appropriate fatigue crack growth law; and (4) specification of a new 3D finite element model considering the new crack front. These procedures are continued until a predetermined crack length or ultimate fracture is reached. Using the 3D FEM to compute the stress intensity factor at a set of points on the crack front, the fatigue crack growth analysis can be accomplished precisely. Nowadays, there is a variety of software to deal with the problem of fatigue crack growth, e.g., FRANC3D [23], ABAQUS [24], ANSYS [25–30], ZENCRACK [31], COMSOL [32], BEASY [33], and NAS-TRAN [34]. Three approaches have been commonly used to describe material fatigue analysis: the method of fracture mechanics proposed by Paris and Erdogan [35], the method of strain–life introduced by Coffin [36], and the method of stress–life introduced by Wöhler [37]. In this work, the first technique was used to estimate fatigue life, in which the crack tip was entirely described by the stress intensity factors. Various experimental procedures have been reported; however, the procedures are generally time-consuming and costly to implement. A numerical analysis approach such as the ANSYS Mechanical R19.2 is an effective process to save both time and money in the laboratory by reducing the amount of work, time, and expenses. Alternatively, there was also an analytical-based technique that was efficient in simulating fatigue growth [38,39]. The main motivation for this study was to make a significant contribution to the use of ANSYS as an effective tool for simulating crack growth under mixed-mode loading situations and monitoring the influence of the holes and crack location on the crack growth trajectory.

2. SMART Crack Growth Procedure

SMART is an efficient fracture mechanics simulation approach based on an adaptive meshing strategy in the surrounding area of the crack propagation path. At a certain loading level, the crack begins to grow as soon as a critical value is reached. The crack propagates either to a certain limit specified by the user or to the point where generating a new mesh is impossible, which generally corresponds to the total split of the body into sections. The Unstructured Mesh Method (UMM) was employed in ANSYS to reduce the consumption time in the pre-processing using the tetrahedral mesh generated automatically for the crack front instead of using the ideal hex mesh configuration, reducing the computational time from a few days to a few minutes. The UMM approach is described in detail in [40]. Tetrahedron meshes were used for the crack fronts in the SMART analysis, which were automatically updated as the crack front changed due to the crack growth. The crack propagation path is defined by an angle θ , which is estimated by the ratio of modes of SIF at the crack tip [41–43]. A mixed-mode loading condition is considered by ANSYS, and the maximum circumferential stress is used as a crack growth criterion in the present study. Based on this criterion, the following formula is used for the crack growth path in ANSYS [25,44]:

$$\theta = \cos^{-1} \frac{3(K_{II}^{\max})^2 + (K_I^{\max})\sqrt{(K_I^{\max})^2 + 8(K_{II}^{\max})^2}}{(K_I^{\max})^2 + 9(K_{II}^{\max})^2} \quad (1)$$

where:

K_I^{\max} = maximum values of the first mode of SIF under cyclic loading, and
 K_{II}^{\max} = maximum values of the second mode of SIF under cyclic loading.

The SIFs were calculated via interaction-integral evaluation at the solution phase of the analysis, and then the values were stored in the results file. The crack propagation

simulation in this ANSYS simulation is confined to region II of the typical crack propagation under fatigue loading, which may be expressed as:

$$\frac{da}{dN} = C(\Delta K_{eq})^m \quad (2)$$

where a = crack length, n = the number of fatigue life cycles, C = Paris constant, m = Paris exponent, and ΔK_{eq} = the equivalent range of stress intensity factor, which may be represented as [44,45]:

$$\Delta K_{eq} = \frac{1}{2} \cos\left(\frac{\theta}{2}\right) [\Delta K_I(1 + \cos \theta) - 3\Delta K_{II} \sin \theta] \quad (3)$$

where:

$$\begin{aligned} \Delta K_I &= K_I^{\max} - K_I^{\min} = (1 - R)K_I^{\max} \\ \Delta K_{II} &= K_{II}^{\max} - K_{II}^{\min} = (1 - R)K_{II}^{\max} \end{aligned} \quad (4)$$

as R represents the load ratio.

According to Equation (2), with a crack growth increment Δa , the fatigue life cycles can be expressed as:

$$\int_0^{\Delta a} \frac{da}{C(\Delta K_{eq})^m} = \int_0^{\Delta N} dN = \Delta N \quad (5)$$

Figure 1 illustrates a simplified flow chart for the ANSYS SMART procedures for fatigue crack propagation.

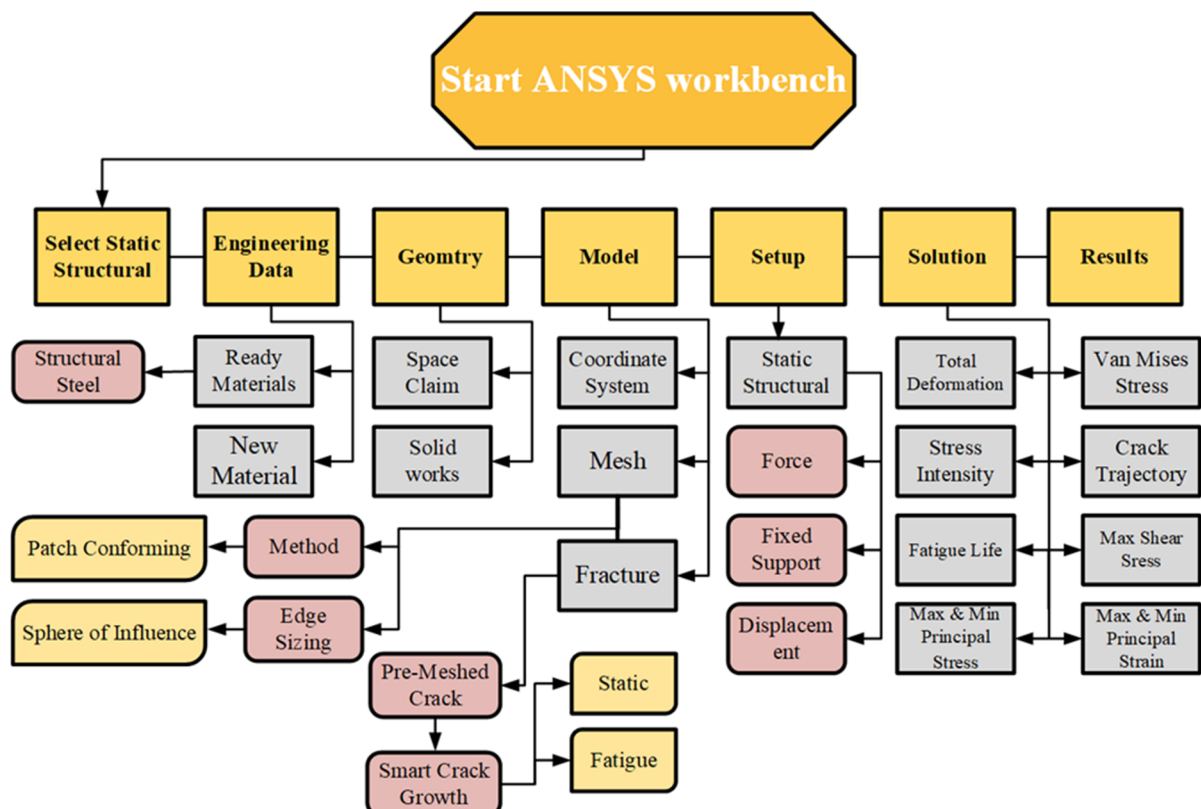


Figure 1. Flowchart for the ANSYS SMART procedures.

3. Results of Numerical Simulations

Modified Compact Tension with Different Pre-Crack Location

The modified compact tension specimen was studied in three distinct configurations in this study. The modified specimens vary from standard specimens in that they have three extra holes, as shown in Figure 2, which violate the standard specimens' symmetry

and result in curvilinear fatigue crack pathways. The actual crack initiation locations are compared to the nominal position of the notch tip in the geometries, as shown in Table 1. The considered material was a nickel-based superalloy with the following material properties shown in Table 1. The amount of the applied load was $p = 3.6$ kN with a stress ratio of $R = 0$ and cyclic frequency of 20 Hz. Changing the vertical location of the original notch (H) up or down its normal midline position, as illustrated in Table 2, leads to altering the path and ultimate destination of the crack growth. As shown in Figure 2, the vertical notch location (H) is defined relative to the geometry's top edge. The initial mesh generated by ANSYS, which had a 1 mm element size and generated 292,160 nodes and 192,860 elements, is shown in Figure 3, which employed the sphere of influence at the crack tip area. There are three different scenarios for the crack growth trajectory based on the nominal notch positions.

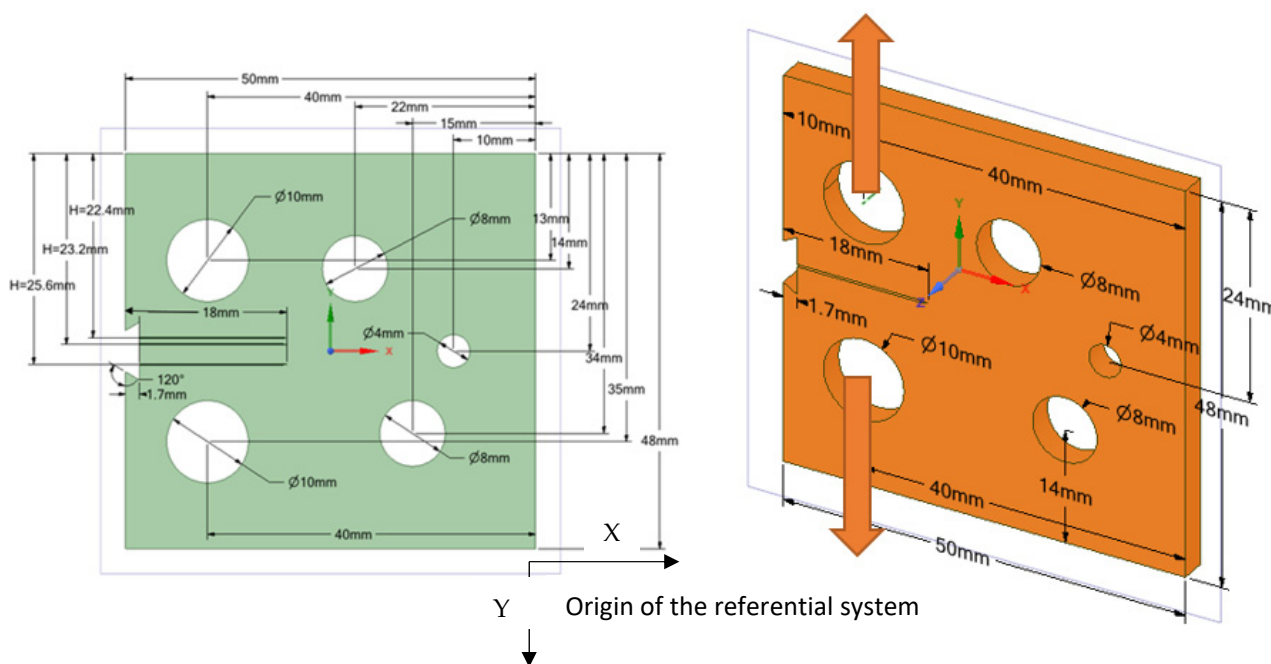


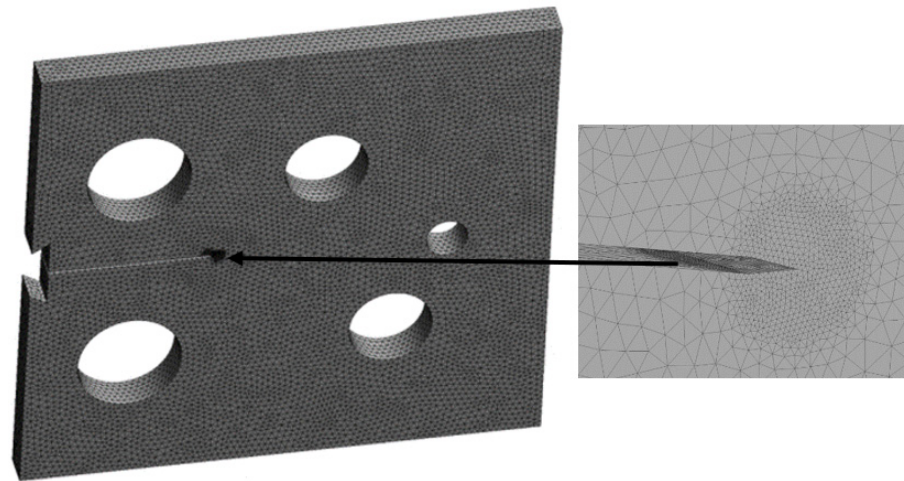
Figure 2. Modified compact tension geometrical dimensions.

Table 1. Mechanical properties of the nickel-based superalloy material.

Properties	Metric Units Value
Elasticity modulus, E	211 GPa
Poisson's ratio, ν	0.3
Yield strength, σ_y	422 MPa
Ultimate strength, σ_u	838 MPa
Fracture toughness, K_{IC}	130 MPa \sqrt{m}
Paris' law coefficient, C	1.02×10^{-11}
Paris' law exponent, m	2.5

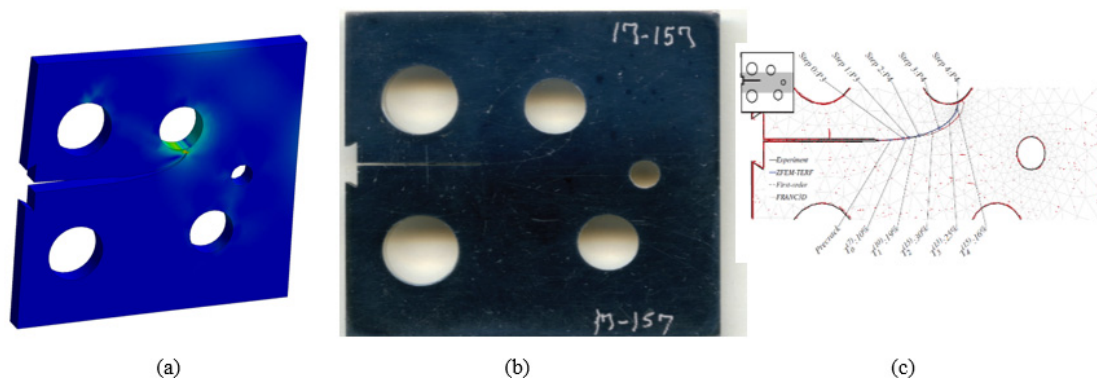
Table 2. Pre-crack position for the modified compact tension.

Specimen Number	Crack Tip Position (mm)		
	(H)	(x)	(y)
1	22.4	−32	25.6
2	25.6	−32	22.4
3	23.2	−32	24.8

**Figure 3.** Initial mesh for the modified compact tension.

Specimen 1

The initial crack in this specimen was located at 22.4 mm from the specimen's top edge. Comparisons of the simulated crack propagation trajectory using ANSYS to the reference experimental [46] and numerical [47] paths are shown in Figure 4a–c, respectively. Crack propagation trajectories in the numerical findings provided by [47] were predicted in three steps: the first step is to use the hyper-complex FEM trial energy response function (ZFEM-TERF) technique for crack trajectory estimation; at each step of crack growth, the model is updated with curvilinear crack path segments that are generated by the trial energy response function (TERF) approach. A finite element model was generated using the FRANC3D program in the second step before being solved using the Abaqus software in the final step. In comparison to the numerical crack growth paths presented in Figure 4c applying the ZFEM-TERF approach and FRANC3D [31], Figure 4a–b indicate that the estimated crack propagation trajectory in this study is very consistent with the experimental trajectory [46].

**Figure 4.** Specimen 1, crack propagation path (a) ANSYS results, (b) experimental results [46], and (c) numerical results [47].

Specimen 2

The initial crack in the second specimen was located at 25.6 mm from the specimen's top edge. The predicted crack propagation trajectory using ANSYS has matched the experimental trajectory reported by [46] more closely than the predicted trajectories estimated by [47], which had tighter curvature trajectories, as illustrated in Figure 5.

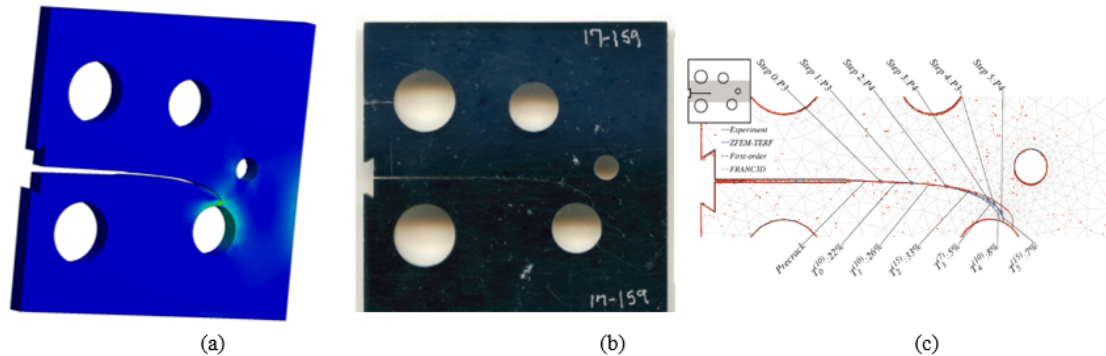


Figure 5. Specimen 2, crack propagation path (a) ANSYS results, (b) experimental results [46], and (c) numerical results [47].

Specimen 3

The initial crack in the second specimen was located at 23.2 mm from the specimen's top edge. As can be seen in Figure 6, the estimated crack propagation trajectory tightly matches the experimental crack growth trajectory reported by [46] compared to the predicted paths from the numerical results using ZFEM-TERF and FRANC3D conducted by [47], which deviated from the experimental path [46].

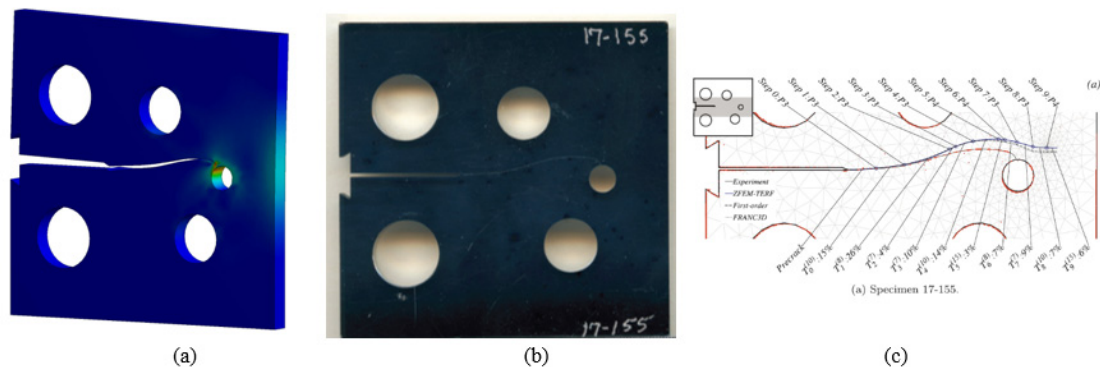


Figure 6. Specimen 3, crack propagation path (a) ANSYS results, (b) experimental results [46], and (c) numerical results [47].

Considering that, the von Mises stress as well as the maximum principal stress are essential parameters for crack propagation assessment, which indicate the regions of maximum and minimum stresses on the geometry. Figures 7 and 8 show the von Mises stress distribution stress contour as well as the maximum principal stress for each of the three specimens. The von Mises stresses and the maximum principal stress were higher in specimen one, where the top hole was located closer to the crack based on the original crack location. As the crack also sinks on the smallest hole near the right edge of the specimen, specimen two had the lowest values of the von Mises stresses and the maximum principal stress, whereas specimen three had the intermediate values of both stresses, as the crack also sinks on the second lower hole near the right edge of the specimen.

The results of the opening mode of SIF (K_I) for the three samples are shown in Figure 9. The maximum values of K_I are 1205 MPa mm^{0.5}, 4136 MPa mm^{0.5}, and 5800 MPa mm^{0.5} for a crack length of 12.97, 18.33 mm, and 21.161 mm for specimens one, two, and three,

respectively. Similarly, Figure 10 also displays the estimated values for the second mode of stress intensity factor (K_{II}). As the crack follows a curving trajectory toward the top hole, the K_{II} values for the first specimen increase to a maximum of $96.133 \text{ MPa mm}^{0.5}$ at the boundary of the hole. However, in specimens two and three, the values of K_{II} decreased with negative values as the crack propagated on a curved path in the opposite direction of specimen one, with minimum values of $-243 \text{ MPa mm}^{0.5}$ and $-230 \text{ MPa mm}^{0.5}$ for specimens two and three, respectively. In the mixed-mode situations, the direction of the tangential component of the applied load is attributed to the negative mode II stress intensity factor. The signs of SIFs depend on the orientation of the crack with the loading.

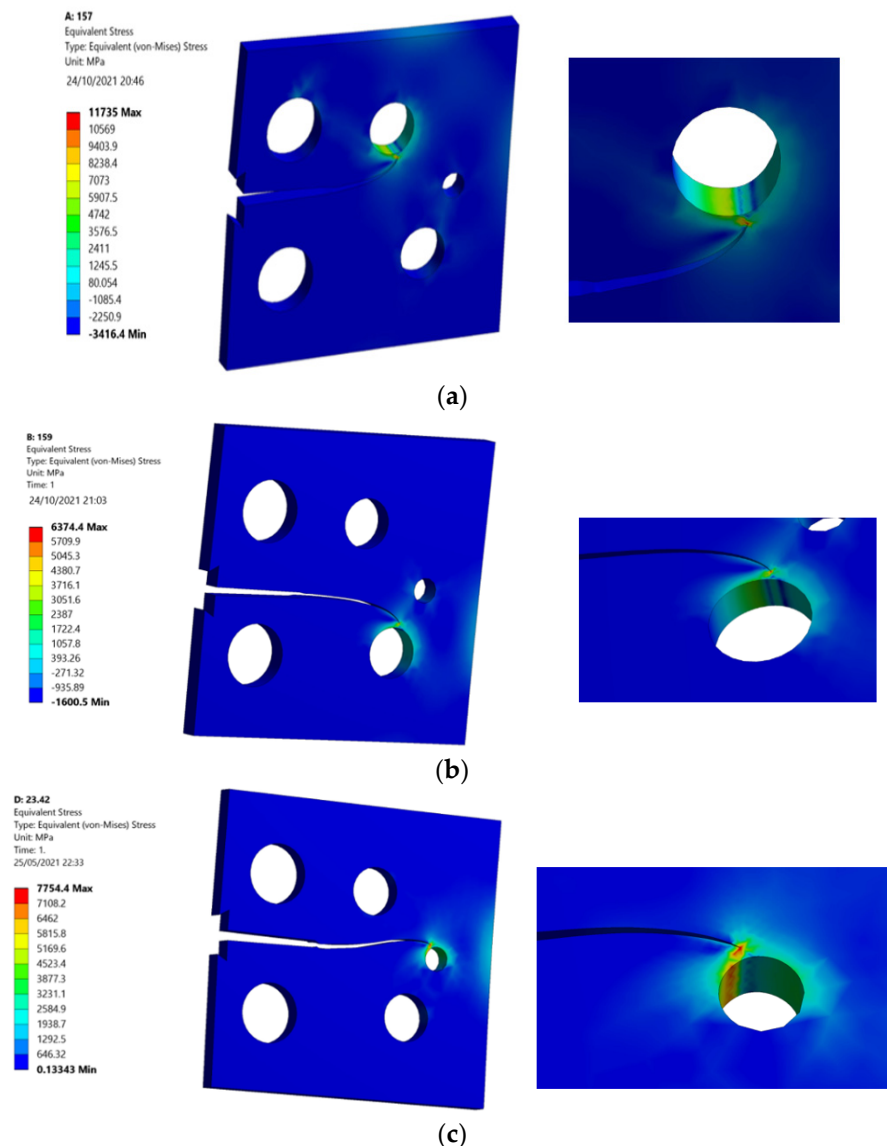


Figure 7. Von Mises stress distribution of (a) specimen 1, (b) specimen 2, and (c) specimen 3.

To determine fatigue life under constant amplitude loading circumstances with a stress ratio of $R = 0$, a step-by-step simulation of crack propagation was performed according to the associated SIFs. Figure 11 displays the predicted fatigue life cycles for each specimen; as seen in this figure, the fatigue life cycles were gradually increased from specimens one to three, since the stress intensity factors were also increased to the same extent for all of the specimens.

The third specimen was simulated at various stress ratios ranging from $R = 0.1$ to 0.8 to correlate the stress ratio effects on the equivalent stress intensity factor as well as fatigue

crack growth rates. Almost at a given applied cyclic equivalent stress intensity, an increase in load ratio leads to an increase in fatigue crack growth rate. Equivalently, the observed equivalent stress intensity factor for fatigue crack growth decreases as the load ratio is increased, as shown in Figure 12. In other words, at high-stress ratios, less accumulated fatigue energy is necessary to support crack growth than at lower stress ratios. In contrast, the number of load cycles with respect to the crack growth extension increases as the stress ratio increases, as shown in Figures 13 and 14 for the stress ratios ranging from 0.1 to 0.8. This effect is proportional to the maximum concentration of von Mises stress and hence to the driving force of mode I cracking. According to the results shown in Figures 13 and 14, the percentages of increase in the equivalent stress intensity factors for different stress ratios ranging from 0.1 to 0.8 are not equal to the percentages of increase in the fatigue life cycles. Damage distributions differed depending on the stress ratios. Damage was equally distributed along with the specimens with larger stress ratios, but it was severe and concentrated at lower stress ratios (0.1–0.4), resulting in higher self-generated temperatures and specimen failure at shorter lifetimes. The von Mises stress distribution for specimen three under different stress ratios $R = 0.1$ –0.8 is shown in Figure 15. It is found that von Mises stress decreases as the stress ratio increases, which was also related to the increase in the fatigue life cycles.

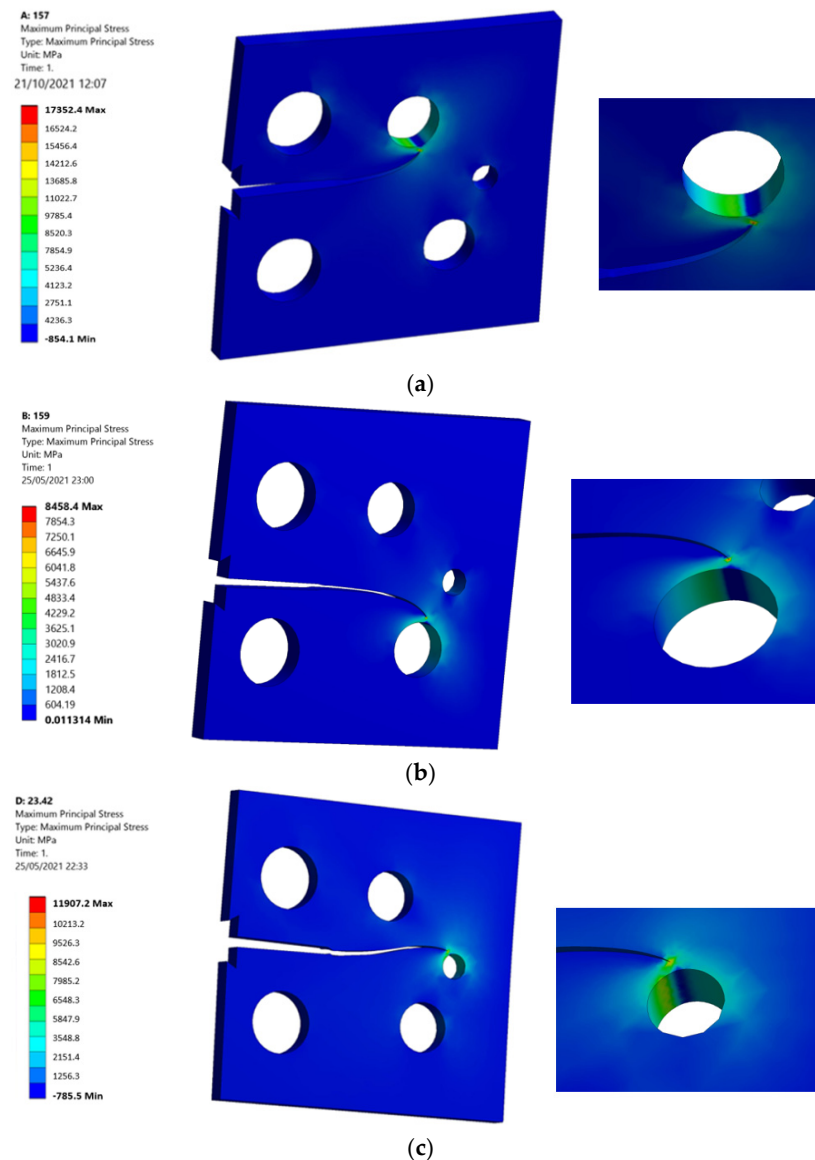


Figure 8. Maximum principal stress of (a) specimen 1, (b) specimen 2, and (c) specimen 3.

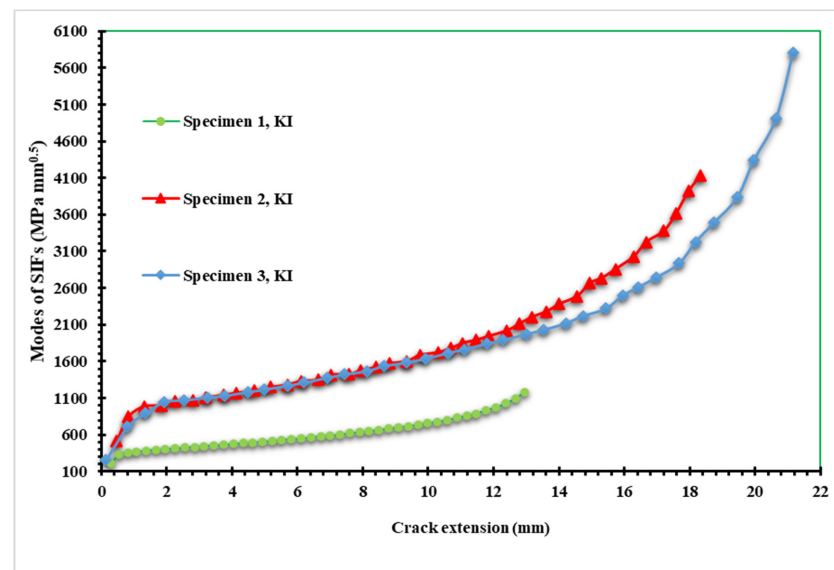


Figure 9. The first mode of SIFs versus crack length for the three specimens.

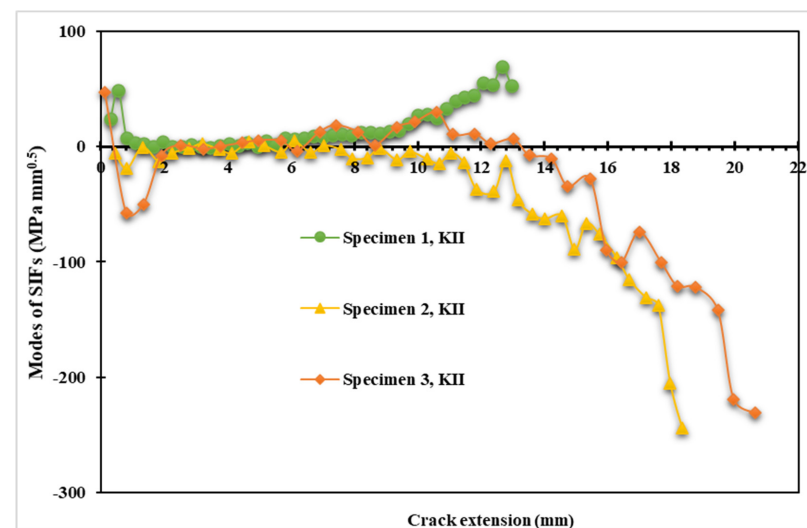


Figure 10. The second mode of SIFs versus crack length for the three specimens.

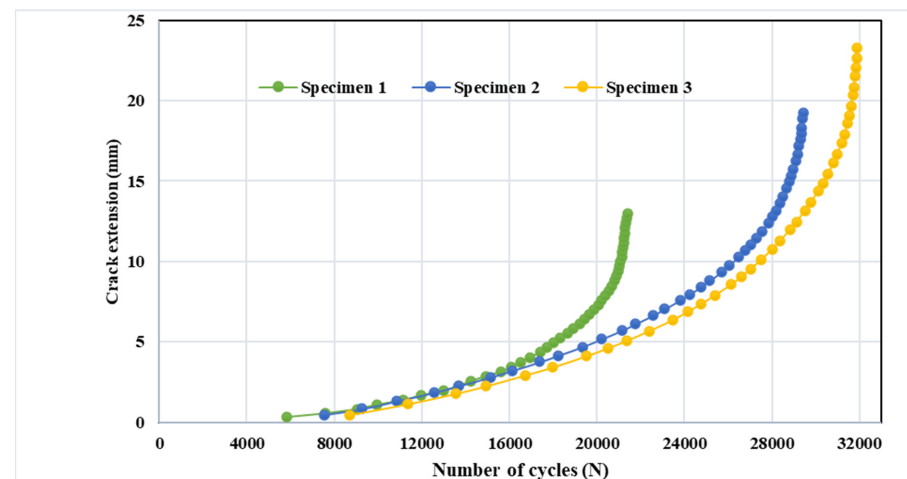


Figure 11. Predicted fatigue life cycles for the three specimens under stress ratio $R = 0$.

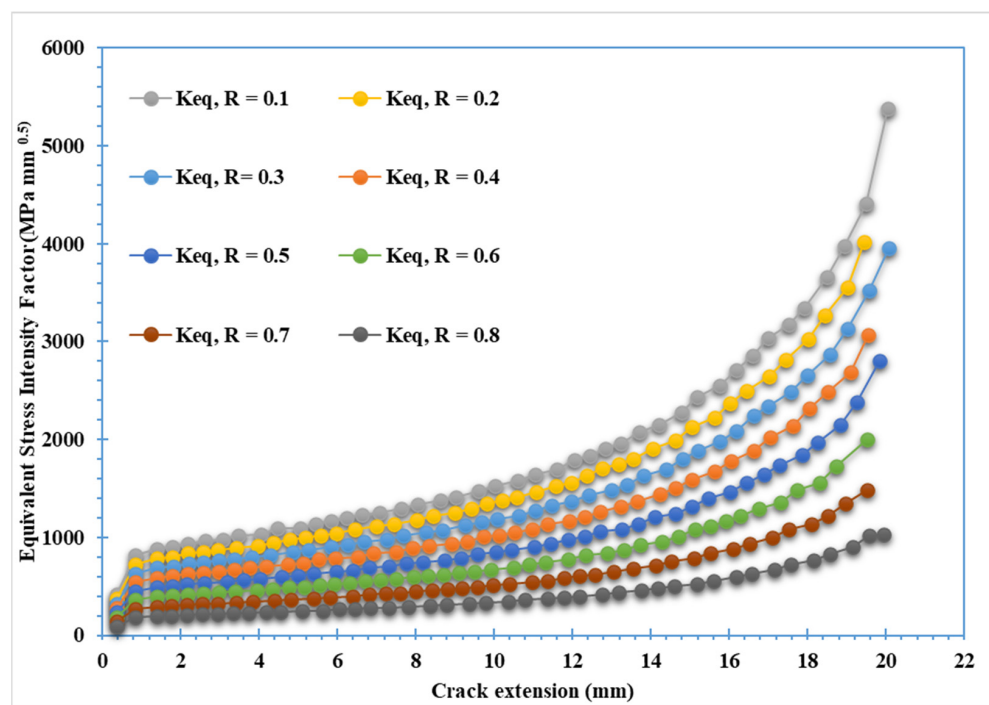


Figure 12. Equivalent stress intensity factor for specimen 3 with different stress ratios.

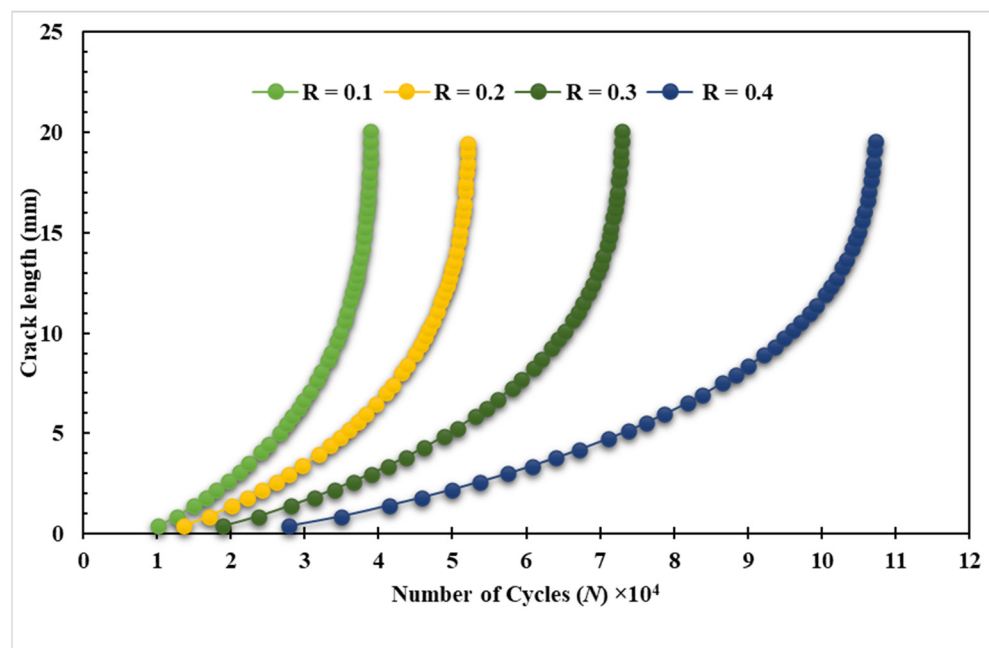


Figure 13. Predicted fatigue life cycles for specimen 3 with stress ratios, $R = 0.1$ – 0.4 .

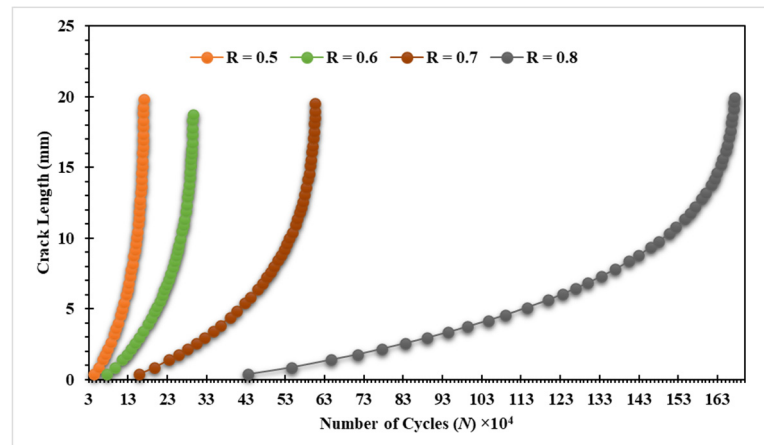


Figure 14. Predicted fatigue life cycles for specimen 3 with stress ratios, $R = 0.5$ – 0.8 .

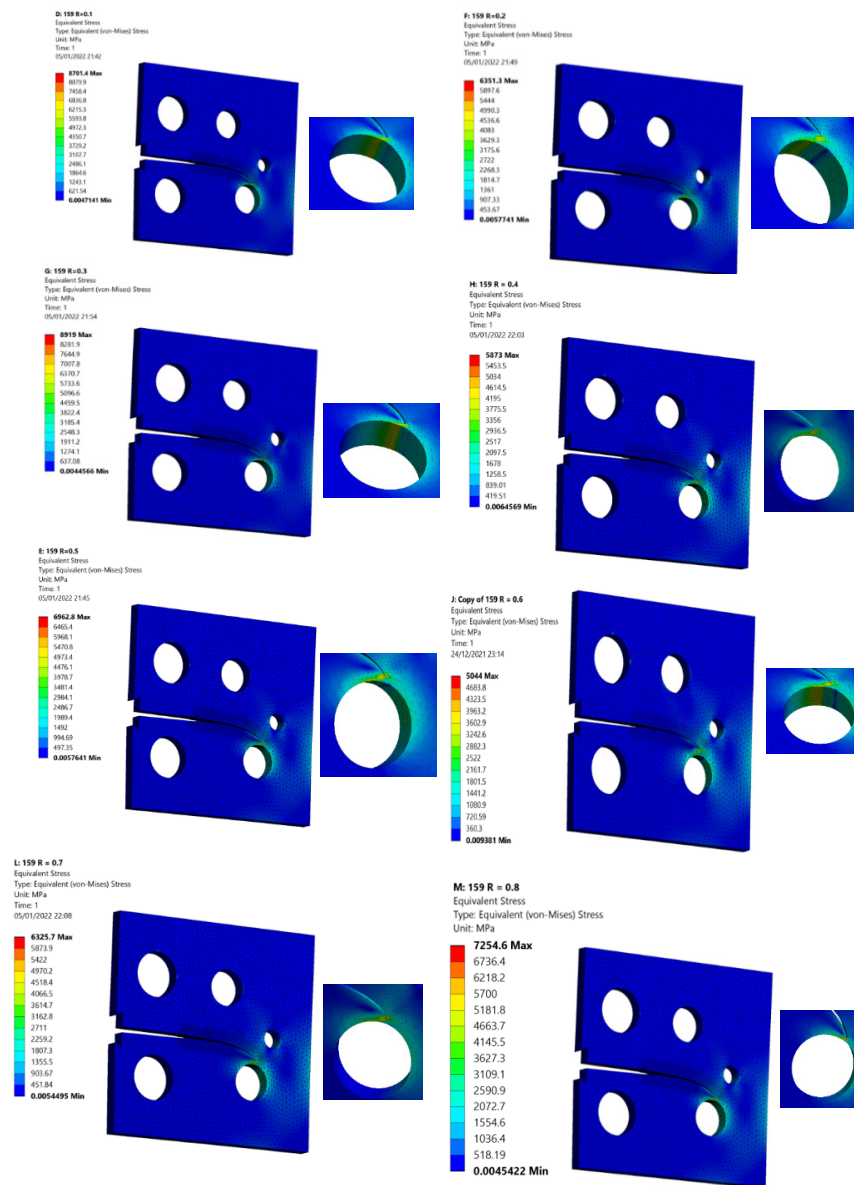


Figure 15. Von Mises stresses distribution for specimen 3 with various stress ratios, $R = 0.1$ – 0.8 .

4. Conclusions

This study investigated the fatigue crack growth in isotropic linear elastic materials under constant amplitude loading where some defects such as holes are intentionally introduced in the material and different load ratios are applied. For this purpose, the finite element software ANSYS was used. The topic of study is certainly very important and can result in a deeper understanding of crack propagation and material design. The fatigue crack propagation of a modified compact tension specimen with various pre-crack locations was simulated using the ANSYS SMART methodology. Based on the Paris law, the crack growth simulation in SMART used tetrahedral meshes for the crack fronts that were updated automatically when the crack front was modified as a consequence of crack propagation. Based on the position of the hole and the starting position of the crack tip, the growth of the crack was either attracted to the hole and changed its trajectory to reach the hole “sink in the hole behavior” or deviated away from the hole and grew when the hole was missing “missed hole behavior”. The influence of a wide range of load ratios ($R = 0, 0.1, 0.2, 0.3, 0.4, 0.5, 0.6, 0.7, 0.8$) on fatigue crack growth, fatigue life, and equivalent range of SIF was investigated. According to the predicted results, it was found that as the stress ratio increased and the fatigue life cycles rapidly increased, whereas von Mises stress decreased.

Funding: This research received no external funding.

Institutional Review Board Statement: Not applicable.

Informed Consent Statement: Not applicable.

Data Availability Statement: The data presented in this study are available upon request from the corresponding author.

Conflicts of Interest: The authors declare no conflict of interest.

References

- Gerber, W. Bestimmung der zulässigen eisen construcionen. *Z. Bayer Arch. Ing. Ver.* **1874**, *6*, 101–110.
- Smith, K.N. A stress-strain function for the fatigue of metals. *J. Mater.* **1970**, *5*, 767–778.
- Socie, D.; Morrow, J. Review of contemporary approaches to fatigue damage analysis. In *Risk and Failure Analysis for Improved Performance and Reliability*; Springer: Berlin/Heidelberg, Germany, 1980; pp. 141–194.
- Manson, S.; Halford, G.R. Practical implementation of the double linear damage rule and damage curve approach for treating cumulative fatigue damage. *Int. J. Fract.* **1981**, *17*, 169–192. [CrossRef]
- Ince, A.; Glinka, G. A modification of Morrow and Smith–Watson–Topper mean stress correction models. *Fatigue Fract. Eng. Mater. Struct.* **2011**, *34*, 854–867. [CrossRef]
- Ince, A.; Glinka, G. A generalized fatigue damage parameter for multiaxial fatigue life prediction under proportional and non-proportional loadings. *Int. J. Fatigue* **2014**, *62*, 34–41. [CrossRef]
- Weertman, J. Theory of fatigue crack growth based on a BCS crack theory with work hardening. *Int. J. Fract.* **1973**, *9*, 125–131. [CrossRef]
- Mansor, N.; Abdullah, S.; Ariffin, A. Effect of loading sequences on fatigue crack growth and crack closure in API X65 steel. *Mar. Struct.* **2019**, *65*, 181–196. [CrossRef]
- Stewart, A.T. The influence of environment and stress ratio on fatigue crack growth at near threshold stress intensities in low-alloy steels. *Eng. Fract. Mech.* **1980**, *13*, 463–478. [CrossRef]
- Hudson, C.M. *Effect of Stress Ratio on Fatigue-Crack Growth in 7075-T6 and 2024-T3 Aluminum-Alloy Specimens*; National Aeronautics and Space Administration: Washington, DC, USA, 1969.
- Noroozi, A.; Glinka, G.; Lambert, S. A study of the stress ratio effects on fatigue crack growth using the unified two-parameter fatigue crack growth driving force. *Int. J. Fatigue* **2007**, *29*, 1616–1633. [CrossRef]
- Paris, P.C.; Tada, H.; Donald, J.K. Service load fatigue damage—A historical perspective. *Int. J. Fatigue* **1999**, *21*, S35–S46. [CrossRef]
- Pook, L.P. *Linear Elastic Fracture Mechanics for Engineers: Theory and Applications*; WIT Press: London, UK, 2000.
- Irwin, G.R. Analysis of stresses and strains near the end of a crack transversing a plate. *Trans. ASME Ser. E J. Appl. Mech.* **1957**, *24*, 361–364. [CrossRef]
- Bang, D.; Ince, A.; Noban, M. Modeling approach for a unified crack growth model in short and long fatigue crack regimes. *Int. J. Fatigue* **2019**, *128*, 105182. [CrossRef]

16. Giannella, V.; Dhondt, G.; Kontermann, C.; Citarella, R. Combined static-cyclic multi-axial crack propagation in cruciform specimens. *Int. J. Fatigue* **2019**, *123*, 296–307. [CrossRef]
17. Giannella, V.; Fellingner, J.; Perrella, M.; Citarella, R. Fatigue life assessment in lateral support element of a magnet for nuclear fusion experiment “Wendelstein 7-X”. *Eng. Fract. Mech.* **2017**, *178*, 243–257. [CrossRef]
18. Anaei, M.M.; Khosravifard, A.; Bui, T. Analysis of fracture mechanics and fatigue crack growth in moderately thick plates using an efficient meshfree approach. *Theor. Appl. Fract. Mech.* **2021**, *113*, 102943. [CrossRef]
19. Nejad, R.M.; Liu, Z.; Ma, W.; Berto, F. Reliability analysis of fatigue crack growth for rail steel under variable amplitude service loading conditions and wear. *Int. J. Fatigue* **2021**, *152*, 106450. [CrossRef]
20. Huynh, H.D.; Nguyen, M.N.; Cusatis, G.; Tanaka, S.; Bui, T.Q. A polygonal XFEM with new numerical integration for linear elastic fracture mechanics. *Eng. Fract. Mech.* **2019**, *213*, 241–263. [CrossRef]
21. Surendran, M.; Natarajan, S.; Palani, G.; Bordas, S.P. Linear smoothed extended finite element method for fatigue crack growth simulations. *Eng. Fract. Mech.* **2019**, *206*, 551–564. [CrossRef]
22. Rozumek, D.; Marciniak, Z.; Lesiuk, G.; Correia, J. Mixed mode I/II/III fatigue crack growth in S355 steel. *Procedia Struct. Integr.* **2017**, *5*, 896–903. [CrossRef]
23. Carter, B.; Wawrzynek, P.; Ingraffea, A. Automated 3-D crack growth simulation. *Int. J. Numer. Methods Eng.* **2000**, *47*, 229–253. [CrossRef]
24. *Abaqus User Manual*; Version 6.14; Abacus: Providence, RI, USA, 2020.
25. ANSYS. Academic Research Mechanical, Release 19.2, Help System. In *Coupled Field Anal. Guide*; ANSYS, Inc.: Canonsburg, PA, USA, 2020.
26. Lee, H.-H. *Finite Element Simulations with ANSYS Workbench 2021: Theory, Applications, Case Studies*; SDC publications: Mission, KS, USA, 2021.
27. Alshoaibi, A.M. Computational Simulation of 3D Fatigue Crack Growth under Mixed-Mode Loading. *Appl. Sci.* **2021**, *11*, 5953. [CrossRef]
28. Alshoaibi, A.M.; Fageehi, Y.A. 3D modelling of fatigue crack growth and life predictions using ANSYS. *Ain Shams Eng. J.* **2022**, *13*, 101636. [CrossRef]
29. Alshoaibi, A.M. Numerical Modeling of Crack Growth under Mixed-Mode Loading. *Appl. Sci.* **2021**, *11*, 2975. [CrossRef]
30. Fageehi, Y.A.; Alshoaibi, A.M. Numerical Simulation of Mixed-Mode Fatigue Crack Growth for Compact Tension Shear Specimen. *Adv. Mater. Sci. Eng.* **2020**, *2020*, 1–14. [CrossRef]
31. Hou, J.; Wescott, R.; Attia, M. Prediction of fatigue crack propagation lives of turbine discs with forging-induced initial cracks. *Eng. Fract. Mech.* **2014**, *131*, 406–418. [CrossRef]
32. Jafari, A.; Broumand, P.; Vahab, M.; Khalili, N. An eXtended Finite Element Method Implementation in COMSOL Multiphysics: Solid Mechanics. *Finite Elem. Anal. Des.* **2022**, *202*, 103707. [CrossRef]
33. Giannella, V.; Sepe, R.; De Michele, G.; Esposito, R. Deterministic fatigue crack-growth simulations for a railway axle by Dual Boundary Element Method. In *IOP Conference Series: Materials Science and Engineering*; IOP Publishing: Bristol, UK, 2021; p. 012080.
34. Fajdiga, G.; Sraml, M. Fatigue crack initiation and propagation under cyclic contact loading. *Eng. Fract. Mech.* **2009**, *76*, 1320–1335. [CrossRef]
35. Paris, P.; Erdogan, F. A critical analysis of crack propagation laws. *J. Fluid. Eng.* **1963**, *85*, 528–534. [CrossRef]
36. Coffin, L. *Cyclic deformation and fatigue of metals*; Elsevier: Amsterdam, The Netherlands, 1963; pp. 257–272.
37. Wöhler, A. Versuche zur Ermittlung der auf die Eisenbahnwagenachsen einwirkenden Kräfte und die Widerstandsfähigkeit der Wagen-Achsen. *Z. Bauwes.* **1860**, *10*, 583–614.
38. Zakavi, B.; Kotousov, A.; Branco, R. An analytical-based approach for simulating fatigue crack growth in round bars. *Int. J. Fract.* **2021**, *7*, 1–12. [CrossRef]
39. Zakavi, B.; Kotousov, A.; Khanna, A.; Branco, R. A new method for analysis of part-elliptical surface cracks in structures subjected to fatigue loading. *Theor. Appl. Fract. Mech.* **2019**, *103*, 102258. [CrossRef]
40. Alshoaibi, A.M.; Fageehi, Y.A. Finite Element Simulation of a Crack Growth in the Presence of a Hole in the Vicinity of the Crack Trajectory. *Materials* **2022**, *15*, 363. [CrossRef]
41. Wawrzynek, P.; Carter, B.; Banks-Sills, L. *The M-Integral for Computing Stress Intensity Factors in Generally Anisotropic Materials*; National Aeronautics and Space Administration, Marshall Space Flight Center: Huntsville, AL, USA, 2005.
42. Citarella, R.; Giannella, V.; Lepore, M.; Dhondt, G. Dual boundary element method and finite element method for mixed-mode crack propagation simulations in a cracked hollow shaft. *Fatigue Fract. Eng. Mater. Struct.* **2018**, *41*, 84–98. [CrossRef]
43. Dhondt, G.; Hackenberg, H.-P. Use of a rotation-invariant linear strain measure for linear elastic crack propagation calculations. *Eng. Fract. Mech.* **2021**, *247*, 107634. [CrossRef]
44. Bjørheim, F. Practical comparison of crack meshing in ANSYS mechanical APDL 19.2. Master’s Thesis, University of Stavanger, Stavanger, Norway, 2019.
45. Xiangqiao, Y.; Shanyi, D.; Zehua, Z. Mixed-mode fatigue crack growth prediction in biaxially stretched sheets. *Eng. Fract. Mech.* **1992**, *43*, 471–475. [CrossRef]

46. Wagner, D. A finite element-based adaptive energy response function method for curvilinear progressive fracture. Ph.D. Thesis, The University of Texas at San Antonio, San Antonio, TX, USA, 2018.
47. Wagner, D.; Garcia, M.J.; Montoya, A.; Millwater, H. A Finite Element-based Adaptive Energy Response Function Method for 2D Curvilinear Progressive Fracture. *Int. J. Fatigue* **2019**, *127*, 229–245. [CrossRef]

Article

Buckling Analysis of Thin-Walled Circular Shells under Local Axial Compression using Vector Form Intrinsic Finite Element Method

Wenliang Ma ^{1,2}, Zihan Sun ^{2,3,*}, Han Wu ³, Leige Xu ², Yong Zeng ⁴, Yanxing Wang ⁵ and Guangyin Huang ⁵

¹ School of Water Conservancy, North China University of Water Resources and Electric Power, Zhengzhou 450046, China

² School of Civil Engineering and Communication, North China University of Water Resources and Electric Power, Zhengzhou 450046, China

³ Key Laboratory for Mechanics in Fluid Solid Coupling Systems, Institute of Mechanics, Chinese Academy of Sciences, Beijing 100190, China

⁴ Henan Provincial Communications Planning, Survey & Design Institute Co., Ltd., Zhengzhou 450046, China

⁵ Department of Capital Construction, North China University of Water Resources and Electric Power, Zhengzhou 450046, China

* Correspondence: sunzihan621@163.com

Abstract: The buckling failure of thin-walled circular shells under local axial compression is common in engineering. This study uses the vector form intrinsic finite element (VFIFE) method to investigate the buckling behavior of thin-walled circular shells under local axial compression by introducing a multilinear hardening model, taking into account geometric and material nonlinearity. A buckling analysis program based on the VFIFE method was developed and verified by comparison with experimental results. The buckling mode and postbuckling behavior of thin-walled circular shells were studied by using the verified program. The results show that the VFIFE method with a multilinear hardening model can accurately calculate the buckling load of local axially compressed thin-walled circular shells, and effectively simulate the buckling development process, which offers great advantages in predicting the postbuckling of structures.

Keywords: vector form intrinsic finite element; thin-walled circular shells; local axial compression buckling; postbuckling; multilinear hardening model

Citation: Ma, W.; Sun, Z.; Wu, H.; Xu, L.; Zeng, Y.; Wang, Y.; Huang, G. Buckling Analysis of Thin-Walled Circular Shells under Local Axial Compression using Vector Form Intrinsic Finite Element Method. *Metals* **2023**, *13*, 564. <https://doi.org/10.3390/met13030564>

Academic Editors: Shuwen Wen, Yongle Sun and Xin Chen

Received: 15 February 2023

Revised: 6 March 2023

Accepted: 8 March 2023

Published: 10 March 2023



Copyright: © 2023 by the authors. Licensee MDPI, Basel, Switzerland. This article is an open access article distributed under the terms and conditions of the Creative Commons Attribution (CC BY) license (<https://creativecommons.org/licenses/by/4.0/>).

1. Introduction

As a basic structural unit, a thin-walled circular shell has strong functionality and is simple to process which is widely used in aerospace, marine engineering, civil engineering, and other fields [1–4]. Thin-walled circular shells are prone to buckling failure under axial loading, and this kind of buckling is essentially the buckling of thin-shell structures. The whole buckling process involves geometric nonlinearity, material nonlinearity, and contact nonlinearity, and its buckling behavior is difficult to predict. To accurately predict the buckling behavior of thin-shell structures, Horrigmoe et al. [5] deduced the buckling analysis of thin-shell structures under the condition of linear elasticity in the early stage, Combescure [6] studied the buckling behavior of thin-shell structures with elastoplastic constitutive equations while considering large deformations. Spagnoli [7] deduced the postbuckling behavior of linear elastic conical shells. Abambres [8] used generalized beam theory (GBT) to predict steel pipe buckling and compared the results with the finite element calculation. Kadkhodayan [9] predicted the buckling of a thin-walled shell under uniform and linearly varying inplane loading by incremental theory. In practical engineering, the stress of thin-walled circular shells is mainly subject to axial pressure and is very prone to uneven force phenomenon [10,11]. Jiao et al. [12,13] studied the influence of local axial compression of different degrees on the buckling load and buckling mode of

thin-walled circular shells through experiments and the finite element method (FEM). Hossein Nassiraei et al. [14], based on the FEM, conducted and analyzed a total of 138 collar plates with strengthened and unstrengthened tubular X-joints, and a theoretical equation was proposed based on the yield volume model to predict the ultimate capacity of the X-connections strengthened with collar plates under brace compression. Then, the formula was confirmed by the acceptance criteria of the UK Department of Energy [15]. Wu et al. [16] used modified couple stress theory to study the buckling and postbuckling of symmetric functionally graded microplate lying on a nonlinear elastic foundation. Liu et al. [17] studied the buckling of hydroformed toroidal pressure hulls with octagonal cross sections. Peng et al. [18] studied the numerical and experimental buckling and postbuckling analyses of sphere-segmented toroidal shell subject to external pressure.

In the process of buckling, the materials of thin-walled circular shells will undergo a transition from the elastic stage to the plastic stage. The stress–strain relationship in the plastic stage is complex, and it is difficult to accurately simulate the complete stress–strain relationship of materials. Generally, the hardening stage during plastic is commonly simplified as ideal elastoplasticity, the bilinear hardening model [19–21], the power hardening model [22,23], and the Ramberg–Osgood model [24–26]. Different hardening models have different characteristics, among which is ideal elastoplasticity, which will not harden after the material enters the plastic stage, and the stress–strain curve is parallel to the strain axis. The bilinear hardening model simplifies the constitutive curve into two broken lines, and the stress–strain curve in the hardening stage is a broken line with a fixed slope. In the power hardening model, the stress–strain curve in the hardening stage of the material is a power curve. The Ramberg–Osgood model simulates the stress–strain curve as a power curve for the material as a whole. The above four models all simplify the full elastoplastic curve into a finite polyline or curve, which is not accurate enough to describe the stress–strain relationship of the entire elastoplastic stage. To describe the stress–strain relationship in the entire elastoplastic stage more accurately, this paper uses a multilinear hardening model, that is, a model based on the incremental elastic-plastic flow law, where the constitutive curve after the material enters the plastic stage is discretized into multiple points, and then each point is connected with a straight line.

FEM is often used to predict the structural buckling behavior of elastic-plastic materials [27–29]. Structural buckling is a large deformation problem, and the FEM needs to constantly update the element stiffness matrix and boundary conditions to solve this kind of problem, which makes the calculation complicated. For the elastic-plasticity of materials, only the above four simplified hardening models can be used in most cases, so compatibility with the multilinear hardening method of constantly updating the tangent modulus of the constitutive is difficult. Additionally, the thin-shell structure will collapse after local buckling, resulting in a large degree of displacement of the structure. In this case, the simple statics problem-solving error of the FEM is so large that the small deformation assumption is no longer applicable. Statics and dynamics are often combined to deal with such geometric nonlinear problems, although Shih et al. pointed out that if the FEM calculation of rigid body displacement is much larger than the pure deformation, this may lead to unstable results [30]. Due to the deficiency of the FEM in analyzing large deformation and displacement problems such as the local axial buckling of thin-shell structures, the VFIFE is used for simulation analysis.

VFIFE is an innovative method developed based on vector mechanics and the finite particle method, which was first proposed by Ting et al. [30–32]. The VFIFE discretizes the structure into particles, calculates the displacement within the path element through Newton's second law, and then calculates the pure deformation and internal force of the structure through the inverse motion. The VFIFE does not need to solve the complex stiffness matrix and has its geometric nonlinearity, so it has a great advantage in dealing with large deformation and large displacement. Currently, the VFIFE has been developed into a beam element [33], membrane element [34], plate element [35], solid element [36], etc. Wu et al. [37] introduced the Cowper–Symonds (C-S) viscoplastic constitutive model

into the VFIFE, and Wang formed the shell element by linear superposition of the plate element and membrane element [38].

Due to the characteristics of dynamic analysis, compared with the FEM which can only calculate the structural modes through the singular matrix method, the VFIFE can directly predict the development of postbuckling of the structure and has a great advantage over the FEM in predicting the postbuckling behavior of the structure. The method of predicting structural buckling by VFIFE was originally derived by Wang [39,40], who calculated the buckling of a thin-shell structure under linear elasticity by force-control and displacement-control methods, respectively, then compared the calculated results with the classical linear elastic buckling derivation and ABAQUS software, which verified that the calculation accuracy of the buckling of a thin-shell structure by VFIFE with the displacement-control method was higher. Xu et al. introduced the von Mises yield criterion to correctly predict the local buckling of buried pipelines subjected to reverse fault motion [41]. Yu et al. [42] discussed the buckling of subsea pipelines with integral buckle arrestors and then introduced soil springs to study the buckling failure of buried subsea pipelines under reverse fault displacement [43]. The above research enriches the content of VFIFE and demonstrates its advantages.

This paper, based on the vector form intrinsic finite thin-shell element, simulates the buckling of a thin-walled circular shell under local axial compression, calculates the tensile internal force of the thin-shell element using the constant strain triangle membrane element (CST) and the bending internal force of the thin-shell element using the discrete Kirchhoff triangle thin-plate element (DKT), and the two elements are linearly superimposed to form a complete shell element. Geometric nonlinearity and material nonlinearity are considered in the buckling process of the structure. The multilinear hardening model was applied to the triangular shell element, and the corresponding tangent modulus is found according to the equivalent von Mises stress calculated in each calculation step to carry out the elastoplastic calculation. The Fortran calculation program for the vector form intrinsic finite thin-shell element and circular tube buckling was compiled and OpenMP [44] technology was used to improve the calculation efficiency. The simulation results were compared with existing experiments to verify the reliability of the analysis method and program. Then, the postbuckling process of the thin-walled circular shell was analyzed, and the reliability of thin-shell structure buckling was verified by the introduction of a multilinear hardening model, which provides a new and reliable idea for the buckling analysis of a thin-shell structure.

2. Analysis Model

2.1. Circular Tube under Localized Axial Compression Loads

The research object of this paper is a thin-walled circular shell under axial compression loads. Figure 1 is a schematic diagram of a thin-walled circular shell under local axial compression loads. The left figure is a three-dimensional diagram of the circular tube, with red arrows representing the local axial compression loads exerted on the end face of the circular tube in a certain angle range. On the right are a top-down view of the circular tube, the black areas where it is not stressed, and the red areas representing the axial compression loads at an axial pressure angle of $2 \times \theta$, which simulates the experiment in reference [12], by adding a convex flange with a certain angle to the top of the cylindrical shell, the specimen was subjected to the axial compression buckling test system.

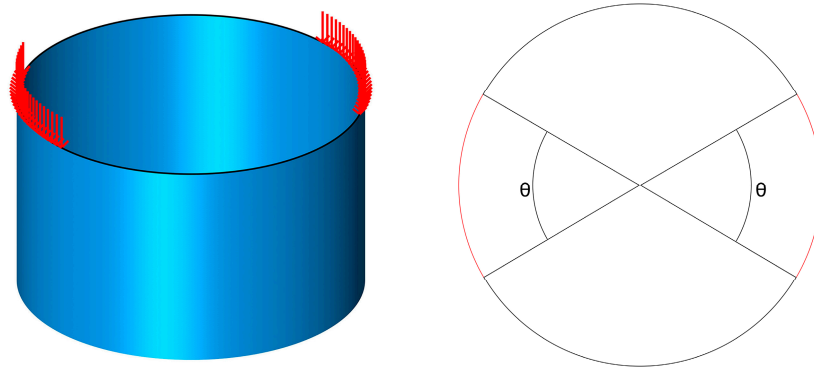


Figure 1. Tube under localized axial compression loads.

The tube has a thickness of 1.2 mm, a diameter of 1000 mm, and a height of 600 mm, and is made of DC01 cold-rolled steel with an elastic modulus of 206 GPa and a yield strength of 158.7 MPa.

2.2. Governing Equations

Different from the FEM, the VFIFE discretizes the structure into finite particles to describe the deformation and motion of the structure under loads, and the mass (moment of inertia) of each particle is the point at which the structure is concentrated after equivalence. The motion of a particle is described by Newton's second law:

$$\mathbf{M}\ddot{\mathbf{x}} + c\mathbf{M}\dot{\mathbf{x}} = \mathbf{F} \quad (1)$$

$$\mathbf{I}\ddot{\theta} + c_{\theta}\mathbf{I}\dot{\theta} = \mathbf{F}_{\theta} \quad (2)$$

where \mathbf{M} and \mathbf{I} are the mass and moment of the inertia matrix of the particle, $\ddot{\mathbf{x}}$ and $\ddot{\theta}$ are the acceleration and angular acceleration of the particle, $\dot{\mathbf{x}}$ and $\dot{\theta}$ are the velocity and angular velocity of the particle, and \mathbf{F} and \mathbf{F}_{θ} are the resultant force and the external force on the particle. The damping of the particle on translational and rotational degrees of freedom are c and c_{θ} , and generally, the particle is damped the same in all directions.

Refer to the derivation of existing scholars, substituting Equations (1) and (2) into the central difference method, the particle motion formula can be obtained as follows:

$$\mathbf{x}_{n+1} = c_1\left(\frac{\Delta t^2}{m}\right)\mathbf{F}_n + 2c_1\mathbf{x}_n - c_2\mathbf{x}_{n-1} \quad (3)$$

$$\theta_{n+1} = c_1\Delta t^2\mathbf{I}^{-1}\mathbf{F}_{\theta n} + 2c_1\theta_n - c_2\theta_{n-1} \quad (4)$$

where \mathbf{x}_n and θ_n are the position vector and the corner vector of the particle at step n , \mathbf{F}_n and $\mathbf{F}_{\theta n}$ are the resultant force and resultant moment of the particle at step n , Δt is the time step of a single loading step, and c_1 and c_2 are the constants associated with damping.

2.3. Internal Force

Unlike the FEM, which solves the internal force by solving linear equations, the VFIFE solves the internal force by decomposing the element displacement into the rigid body displacement and solving the internal force by using pure deformation through the virtual work principle.

2.3.1. Inverse Motion

VFIFE solves the pure deformation of the structure by inverse motion. The inverse motion of a shell element is represented in Figure 2:

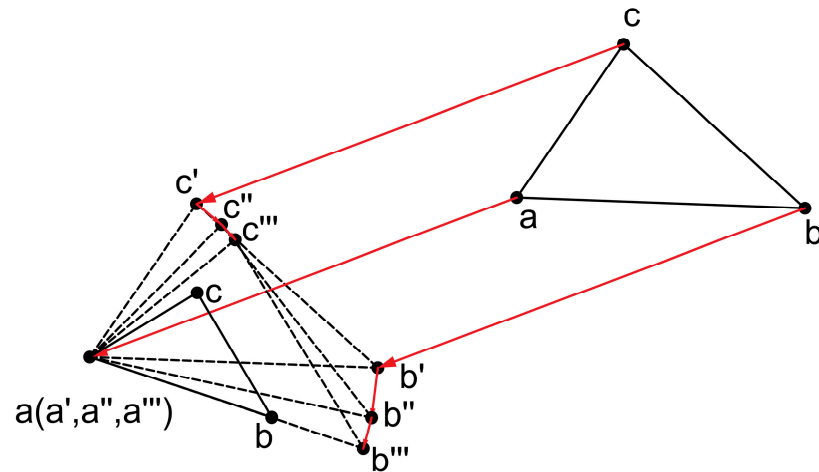


Figure 2. Inverse motion of a shell element.

The inverse motion in space undergoes rigid body translation ($abc \rightarrow a'b'c'$), out of the plane to inplane ($a'b'c' \rightarrow a''b''c''$), and rotation inplane ($a''b''c'' \rightarrow a'''b'''c'''$), and finally, the pure deformation of each particle on the element is obtained:

$$\begin{cases} \Delta \eta_a^d = 0, \Delta \eta_i^d = (u_i - u_a) + \Delta \eta_{i-op}^r + \Delta \eta_{i-ip}^r, i = b, c \\ \Delta \eta_{\theta i}^d = u_{\theta i} + \Delta \eta_{\theta i-op}^r + \Delta \eta_{\theta i-ip}^r, i = a, b, c \end{cases} \quad (5)$$

where $\Delta \eta_i^d$ and $\Delta \eta_{\theta i}^d$ represent the pure deformation line displacement and angular displacement of the particle, $\Delta \eta_{i-op}^r$ and $\Delta \eta_{\theta i-op}^r$ represent the pure deformation line and angular displacements out of the plane, and $\Delta \eta_{i-ip}^r$ and $\Delta \eta_{\theta i-ip}^r$ represent the pure deformation line and angular displacements in the plane.

2.3.2. Solution of Internal Force

The internal force calculation on VFIFE is based on pure deformation by the virtual work principle. Through the virtual work principle, the internal forces at each node of the shell element can be obtained by linear superposition of the bending internal forces obtained by the DKT thin plate element and the tensile and compressive internal forces obtained by the CST membrane element. The internal forces are solved by the following formula:

$$\sum_i \delta(\hat{u}_i)^T \hat{f}_i + \sum_i \delta(\hat{u}_{\theta i})^T \hat{f}_{\theta i} = \int_V \delta(\Delta \hat{\epsilon}_m)^T \hat{\sigma}_m dV + \int_V \delta(\Delta \hat{\epsilon}_p)^T \hat{\sigma}_p dV \quad (6)$$

where $\Delta \hat{\epsilon}$ and $\hat{\sigma}$ represent the strain increment and stress of the node, respectively, and m stands for the membrane element and p for the plate element.

2.4. Determination of Buckling

This paper determines whether the structure is buckling according to the axial-force-displacement relationship. Before the structure buckling, the axial force gradually increases with the increase of displacement, with the two having a linear relationship. When the structure buckles, the axial force at the buckling point will decrease with the increase of displacement, and the axial force at the buckling point is considered as the buckling load of the structure. Due to the dynamic characteristics of the process of VFIFE analysis, the method of gradually increasing the axial force needs to wait until the result converges, which is not effective for the prediction of buckling. Therefore, the method of imposing forced displacement on the structure is adopted to push back the axial force of the structure,

to draw the axial-force–displacement relationship curve of the buckling process. Formula (7) is the calculation formula of the axial force in reverse derivation:

$$\begin{cases} f_n^{ext} = \frac{1}{c_1 \Delta t^2} \mathbf{M}(x_{n+1} + c_2 x_{n-1} - 2c_1 x_n) - f_n^{int} \\ f_{\theta n}^{ext} = \frac{1}{c_1 \Delta t^2} \mathbf{M}(\theta_{n+1} + c_2 \theta_{n-1} - 2c_1 \theta_n) - f_{\theta n}^{int} \end{cases} \quad (7)$$

where f_n^{ext} and $f_{\theta n}^{ext}$ represent the external force and moment of the particle at loading step n , and f_n^{int} and $f_{\theta n}^{int}$ represent the internal force and internal moment of the particle at loading step n .

2.5. Nonlinearity

2.5.1. Geometric Nonlinearity

Based on Newton's second law, VFIFE discretizes the structure into a finite number of particles to describe the deformation and motion state of the structure. The state of the structure is related to the velocity and acceleration direction of the particles under the force. The motion state of the points in the path element can be clearly described, so it is not necessary to correct the geometric nonlinearity of a structure with a large deformation and a large displacement.

2.5.2. Material Nonlinearity

When the deformation is small, the material will recover its original state after the load is removed, so this stage belongs to the elastic stage of the material. When the deformation exceeds the range of elastic deformation, it will produce permanent deformation from which the material cannot recover. However, the stress–strain relationship of the material in the plastic stage is relatively complex, and the plasticity of the material in the numerical simulation is a material nonlinear problem, which requires a separate method to describe.

In the existing VFIFE study, there is only the bilinear hardening model and the power hardening model, which cannot accurately simulate the elastoplasticity of the materials. In order to accurately describe the strain state of the element under different stress states, a multilinear hardening model was used to discretize the material constitutive curve into multiple points, and the points were connected into broken lines. The elastic-plastic matrix under the state was updated according to the stress state of different load steps to accurately predict the elastic-plastic stress–strain of the material.

The von Mises yield criterion was used to judge whether it was plastic or not, and each integration layer is considered as a plane stress state while integrating according to thickness. When the stress satisfies the following formula,

$$F = \bar{\sigma} - \sigma_s^2 = 0 \quad (8)$$

The material is considered to have reached the yield point, if $F > 0$, and the material enters the plastic stage. Equation (8), $\bar{\sigma}$ is equivalent to von Mises stress, and σ_s is the yield limit;

At time t , the strain increment $\Delta \epsilon$ can be calculated according to the existing node displacement. Assuming that the increment step is elastic, the stress increment can be calculated according to the existing strain increment, and the elastic predicted stress at a time $t + \Delta t$ can be calculated by superimposing the stress at time t , as shown in Equation (9),

$${}^{t+\Delta t}\sigma^{pr} = {}^t\sigma + \mathbf{D}_e \Delta \epsilon \quad (9)$$

where ${}^{t+\Delta t}\sigma^{pr}$ represents elastic predictive stress at the time $t + \Delta t$, ${}^t\sigma$ represents the stress at time t , and \mathbf{D}_e represents the elastic matrix;

The equivalent treatment of elastic predicted stress solved by the elastic prediction method is introduced into the von Mises yield formula. If the result is greater than zero, the node is in an elastic state and continues to be solved according to linear elasticity. If the result is less than zero, it means that it has entered a plastic state. Here, the elastic factor m ,

which is the proportion of elasticity at the integration point, is introduced. The solution of m is:

$$m = (-a_1 + \sqrt{a_1^2 + 4a_0a_2}) / 2a_2 \quad (10)$$

where, for isotropic hardening materials, a_0 is the von Mises yield function at time t . Therefore, a_1 and a_2 are obtained by the following formula:

$$\begin{cases} a_1 = \mathbf{S}^T \Delta \mathbf{S} \\ a_2 = \frac{1}{2} \Delta \mathbf{S}^T \Delta \mathbf{S} \end{cases} \quad (11)$$

where \mathbf{S} presents the tensor of deviation stress at time t and $\Delta \mathbf{S}$ represents the increment of deviation stress at time t , and the superscript T stands for matrix transpose.

It should be noted that the m value calculated here should be greater than zero and less than one. If it is not in this interval, all the values are set as plastic, that is, $m = 0$;

The update of and material hardening modulus of the elastic-plastic matrix are closely related, and the mathematic expression of the hardening modulus is:

$$E_p = \frac{EE_t}{E - E_t} \quad (12)$$

where E_t represents the tangent modulus, which is the slope of the tangent at the point corresponding to the constitutive curve of the material under this stress state. The multilinear hardening model in this paper simplifies the constitutive curve of materials into multiple broken lines, and the tangent modulus is taken as the slope of the corresponding interval broken line on the simplified constitutive curve where the stress is at time $t - \Delta t$. At the same time, according to the flow rule of isotropic hardening, the hardening of materials can only go outward along the circular tangent line of von Mises stress, not inward, and the slope of the actual constitutive curve will be less than zero when it reaches tensile strength, and therefore, in this paper, the tangent modulus of the part with a slope less than zero in the constitutive curve is taken as 1000, which can not only ensure the continuous hardening of the material but also keep a small error with the actual material.

After solving the hardening modulus, the elastic-plastic matrix can be updated. The plastic matrix is calculated as follows:

$$\mathbf{D}_p = \frac{E}{B(1-\nu^2)} \begin{bmatrix} (s_x + \nu s_y)^2 & (s_x + \nu s_y)(s_y + \nu s_x) & (1-\nu)(s_x + \nu s_y)\tau_{xy} \\ (s_x + \nu s_y)(s_y + \nu s_x) & (s_y + \nu s_x)^2 & (1-\nu)(s_y + \nu s_x)\tau_{xy} \\ (1-\nu)(s_x + \nu s_y)\tau_{xy} & (1-\nu)(s_y + \nu s_x)\tau_{xy} & (1-\nu)^2\tau_{xy}^2 \end{bmatrix} \quad (13)$$

where,

$$B = s_x^2 + s_y^2 + 2\nu s_x s_y + 2(1-\nu)\tau_{xy}^2 + \frac{2(1-\nu)E_p\sigma_s}{9G} \quad (14)$$

In the formula, G is the shear modulus and s_x and s_y is the deviation stress.

After the plastic matrix is calculated, the elastic-plastic matrix can be calculated:

$$\mathbf{D}_{ep} = \mathbf{D}_e - \mathbf{D}_p \quad (15)$$

First, calculate the plastic strain increment according to the strain increment

$$\Delta \epsilon_p = (1 - m)\Delta \epsilon \quad (16)$$

Finally, the plastic stress is calculated:

$${}^{t+\Delta t}\boldsymbol{\sigma} = {}^t\boldsymbol{\sigma} + m^{t+\Delta t}\boldsymbol{\sigma}^{pr} + \mathbf{D}_{ep}\Delta \epsilon_p \quad (17)$$

Based on the VFIFE principles, the buckling program of the thin-shell structure is compiled, and the model data, boundary conditions, and loads are input into the calculation program. In each analysis step, the element displacement and internal force are calculated

first, and then the equivalent stress and strain are calculated and introduced into the subprogram of the multilinear hardening model. First, the elastic prediction is carried out to determine whether the plastic stage has been entered, and if it has entered into the plastic stage, plastic correction is required. Finally, the next analysis step is carried out. The program flow of each elastic-plastic incremental step is shown in Figure 3.

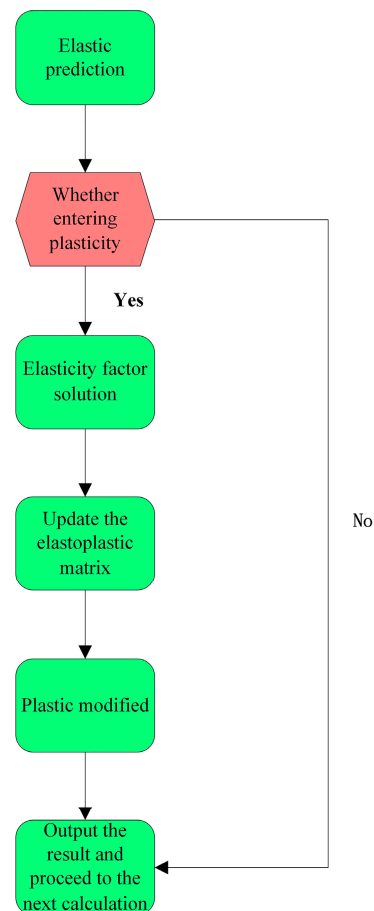


Figure 3. Multilinear hardening model program. Green represents process flow and red represents logical judgment.

3. Model Verification and Parameter Setting

3.1. Multilinear Hardening Model Verification

To verify the feasibility of the multilinear hardening model, the axial tensile process of cold-rolled steel was simulated by an analysis program, and the simulated stress–strain curve was compared with the experimental stress–strain curve. The simulation material selected was DC01 cold rolled steel, with an elastic modulus of $E = 206$ GPa, a yield strength of $\sigma_s = 158.7$ MPa, and an established specimen model, as shown in Figure 4. The simulation results were compared with the tensile test results [12]. To simulate the situation close to the test, the bottom of the specimen was fixed, and the top of the specimen was restricted except for the degree of freedom in the tensile direction. A forced upward displacement was applied to the top of the specimen. The stress–strain curve drawn by taking the equivalent stress–strain of the central node of the specimen was compared with the test results, as shown in Figure 5.

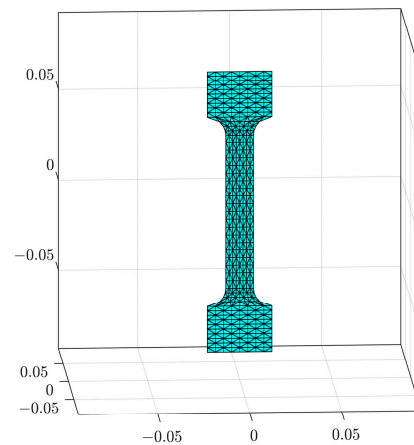


Figure 4. Tensile test model.

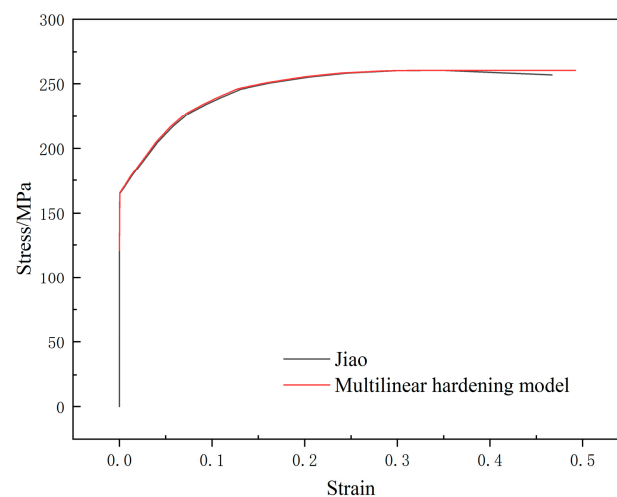


Figure 5. Comparison of stress–strain curves.

It can be seen from the above comparison results that the simulation results are in good agreement with the experimental results, which proves that the multilinear hardening model introduced in this paper can accurately predict the stress value of the material under a given strain in the VFIFE.

3.2. Calculation Parameters

Based on the above description, the buckling behavior of a circular tube under local axial compression is simulated by the VFIFE method. The axial compression of the structure is derived by applying the forced displacement, that is, a fixed constraint is applied to the bottom node of the tube, and a forced axial displacement is applied to the top node, limiting the other degrees of freedom except the forced axial displacement. The time step is $\Delta t = 1 \times 10^{-6}$ s. The multilinear hardening model is adopted. The material of the tube is DC01 cold-rolled steel, and the material parameters are set according to the test in Section 3.1.

A triangular shell element is adopted for the circular tube model. As shown in Figure 6, the element is discretized into three mass points distributed at the element nodes. Each triangular element is an isosceles right triangle.

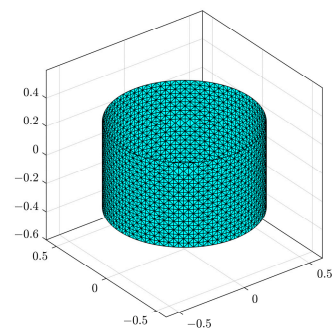


Figure 6. Cylindrical shell model under VFIFE.

Based on the analysis of the buckling load of a thin-walled circular shell under a $2 \times 90^\circ$ local axial compression load under different mesh sizes, the appropriate mesh is determined. The simulation calculation refers to the experimental setting of Jiao [12], with triangular meshes with side lengths of 20 mm, 30 mm, 40 mm, and 50 mm were analyzed respectively, loaded at 2 mm/s. The simulation and experimental errors obtained are shown in Table 1.

Table 1. Buckling loads and errors were calculated from the mesh of different sizes.

Meshing Size/mm	Buckling Load/kN	Error/%
50	272.7	5.50
40	263.6	2.24
30	258.6	0.35
20	258.1	0.15

In the experiment, the first buckling load is 257.7 kN, as can be seen in Table 1, when the mesh size is 30 mm, the calculation error becomes small and the margin of error decreases slightly as the mesh size decreases, so the mesh size in this paper is 30 mm.

The forced displacement of the top node needs to be loaded at a certain speed, and the loading speed will affect the calculation results. The axial force–displacement curves at different speeds are analyzed, the optimal loading speed is selected by comparison., and the loading angle is $2 \times 90^\circ$, with a triangular shell element, and the length of the right angle side of the element is 30 mm, loaded the top displacement at the speeds of 30 mm/s, 10 mm/s, 2 mm/s, and 1 mm/s, respectively, and the calculated displacement axial force curve is shown in Figure 7.

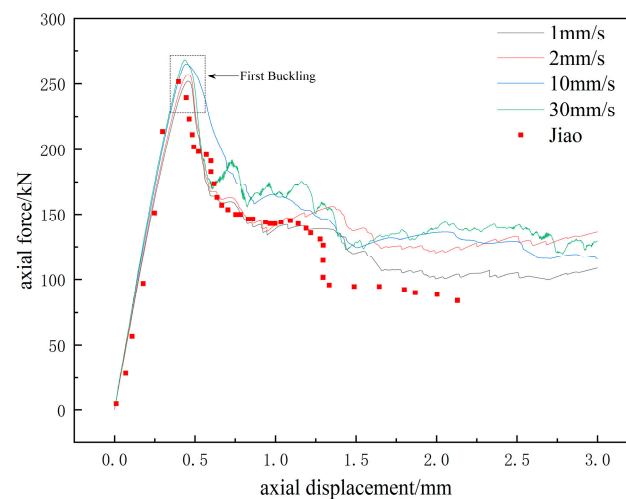


Figure 7. Displacement-load curves under different loading rates.

In the experiment, the first buckling load is 257.7 kN, and the first buckling load loaded at 30 mm/s is 265.6 kN, with an error of 3.07%, the first buckling load loaded at 10 mm/s is 263.6 kN, with an error of 2.28%, the first buckling load loaded at 2 mm/s is 258.6 kN, with an error of 0.34%, and the first buckling load loaded at 1 mm/s is 256.9 kN, with an error of 0.31%. It can be seen from the analysis results that before the buckling of the structure, each loading rate can be very close to the experimental results. However, due to the influence of inertial force, a faster loading rate means a greater buckling load. When the loading rate is reduced to 2 mm/s, the agreement between the first buckling load and the experiment reaches a relatively ideal level, however, there is still a large gap between the subsequent curve and the experiment. After loading at the rate of 1 mm/s, the result is improved, so this paper adopted the rate of 1 mm/s for loading.

It should be pointed out that there are often many small gaps between the experimental process and the expected design, such as the initial defects of the specimen and the uneven control of the load. These conditions are in an ideal state in the numerical simulation, and the small gap between the two will cause non-negligible errors in the buckling structure. For the subsequent buckling behavior after the first buckling, it is very difficult to simulate results that are very consistent with the experiment. However, if subsequent buckling similar to the experiment can be simulated, it has a very important value for guiding the structural design.

4. Results and Discussion

In this paper, based on the simulation program, buckling loads under different degrees of local axial compression are calculated, and the buckling modes are predicted. Finally, postbuckling is visualized by drawing a displacement contour of the tube at different stages in the deformation process, and the development of buckling under local axial compression load is explored.

4.1. First Buckling Load Buckling Modes

Simulations were performed for circular tubes with axial compression angles of $2 \times 30^\circ$, $2 \times 60^\circ$, $2 \times 90^\circ$, $2 \times 120^\circ$, $2 \times 150^\circ$, and $2 \times 180^\circ$ (overall axial compression), and the calculated results were plotted as displacement–axial force curves to compare with the experimental results, as shown in Figure 8.

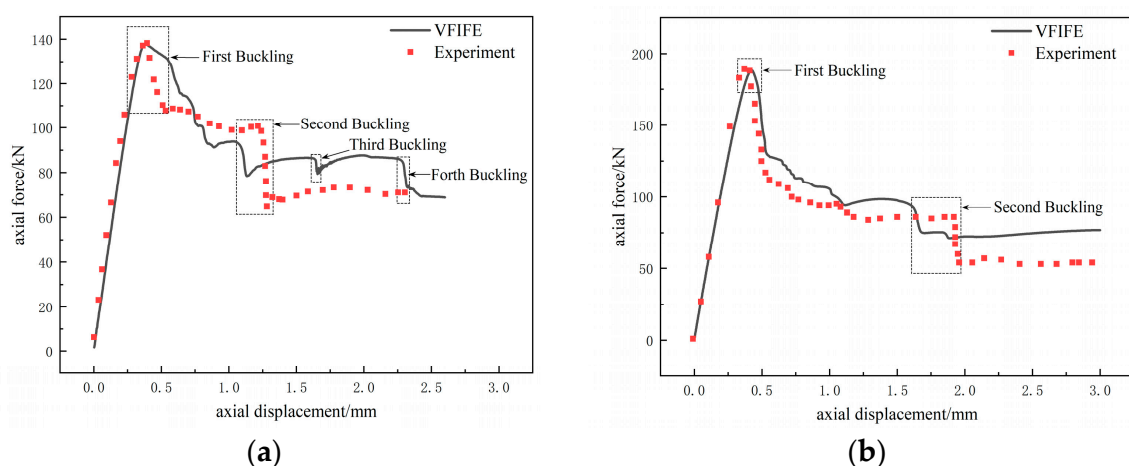


Figure 8. Cont.

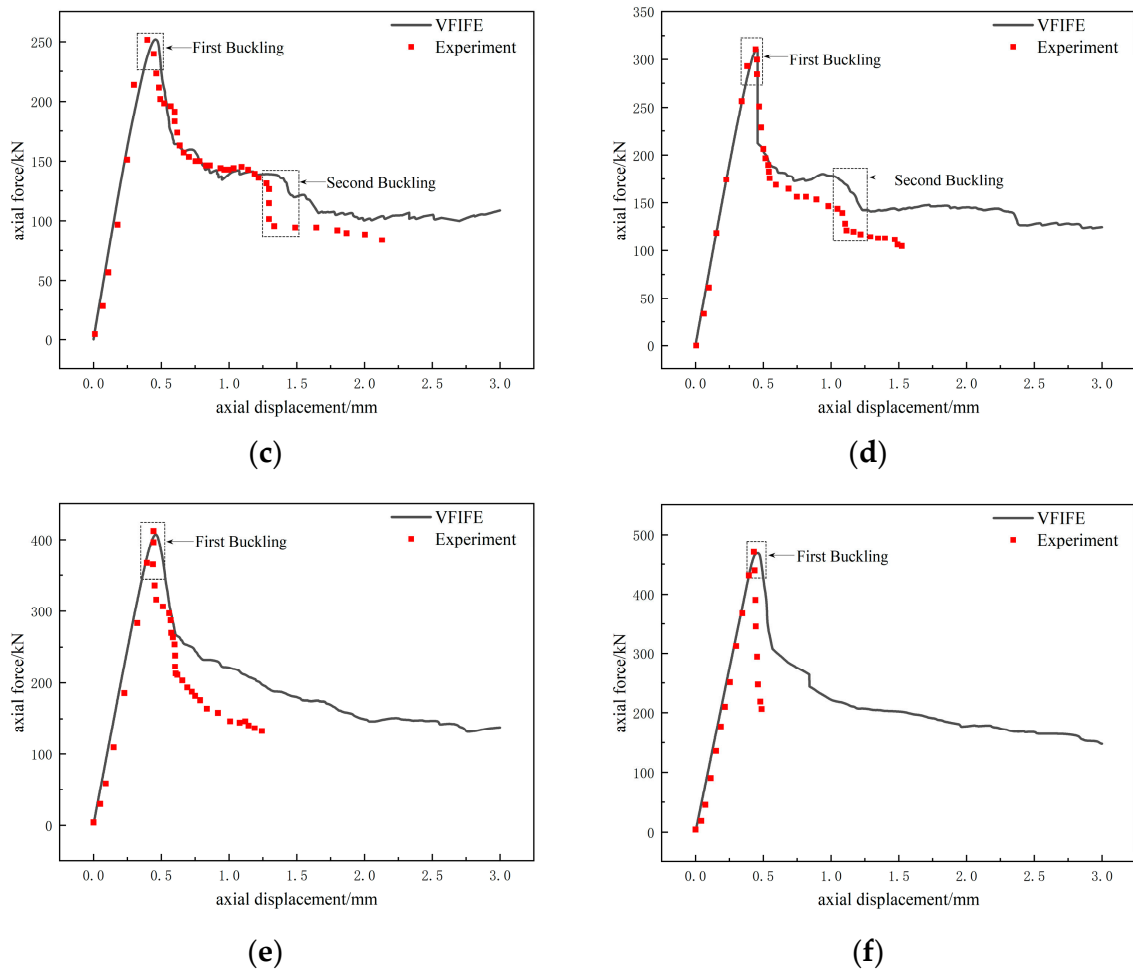


Figure 8. Axial displacement-force curve: (a) $2 \times 30^\circ$, (b) $2 \times 60^\circ$, (c) $2 \times 90^\circ$, (d) $2 \times 120^\circ$, (e) $2 \times 150^\circ$, (f) $2 \times 180^\circ$.

Table 2 shows the comparison between the first buckling load calculated by VFIFE and the experiments in the literature. The error between the first buckling load predicted by VFIFE and the experimental results is less than 1%.

Table 2. Comparison of results.

Axial Compression Angle	Experiment/kN	VFIFE/kN	Error/%
$2 \times 30^\circ$	138.9	137.9	0.72
$2 \times 60^\circ$	191.0	192.3	0.68
$2 \times 90^\circ$	257.7	256.9	0.31
$2 \times 120^\circ$	310.3	313.1	0.99
$2 \times 150^\circ$	409.1	406.3	0.68
$2 \times 180^\circ$	466.3	468.4	0.45

When the angle of local axial comparison is $2 \times 30^\circ$, $2 \times 60^\circ$, $2 \times 90^\circ$, and $2 \times 120^\circ$, secondary buckling occurs in both the experimental and the simulation results, as seen in the abrupt change of the displacement-axial force curve in Figure 9. VFIFE predicts four buckling of the structure for a local axial comparison angle of $2 \times 30^\circ$, two buckling for local axial comparison angles of $2 \times 60^\circ$, $2 \times 90^\circ$, and $2 \times 120^\circ$, and only one buckling for axial comparison angles of $2 \times 150^\circ$ and $2 \times 180^\circ$. It is inferred that the smaller the local

axial comparison angle, the more likely the structure is to buckle several times, so every engineering project should try to avoid a local axial pressure load on the circular tube.

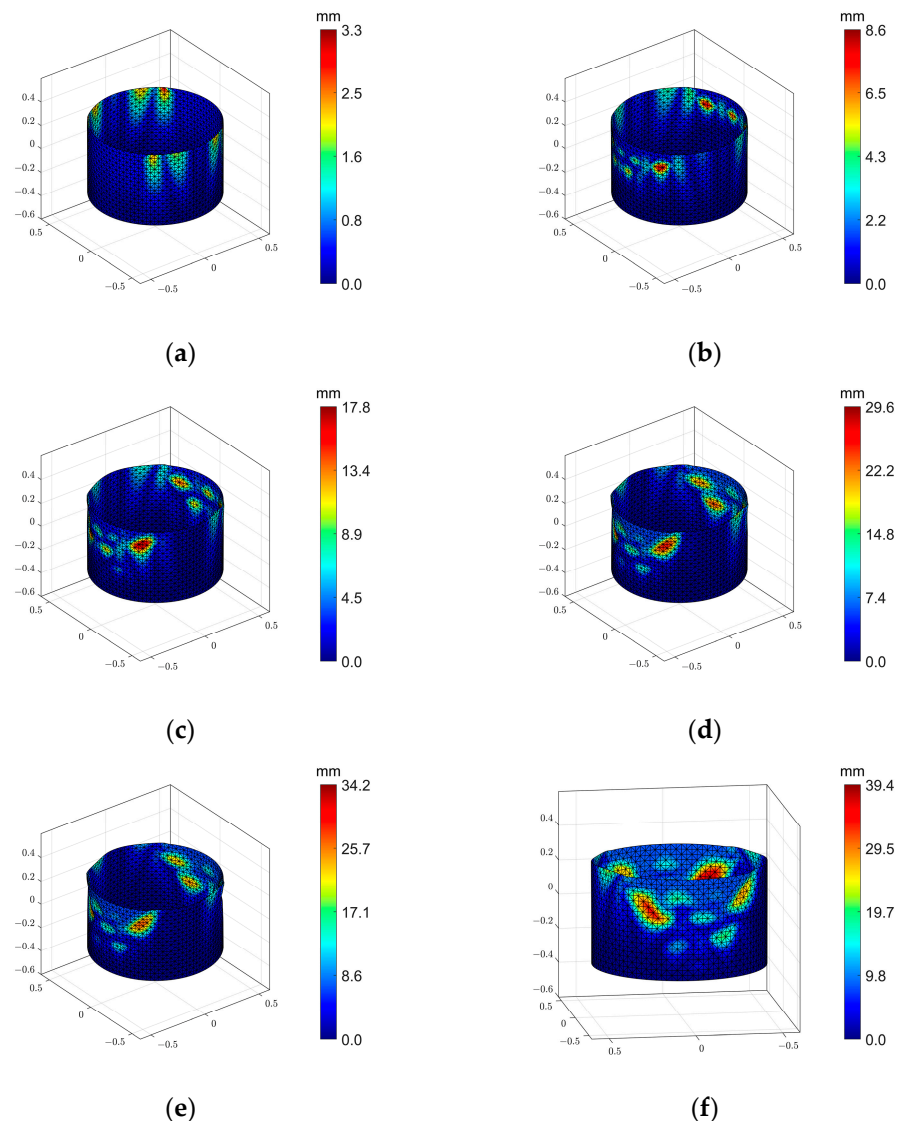


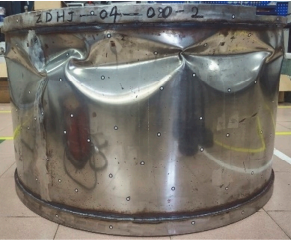
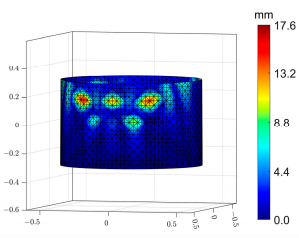

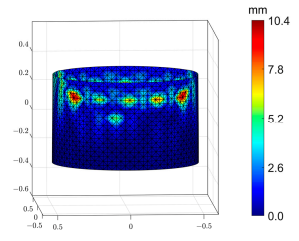

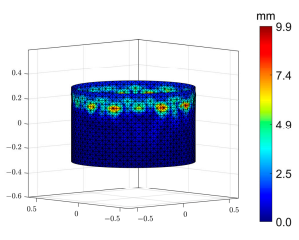
Figure 9. Postbuckling of $2 \times 90^\circ$ local axial compression: (a) before buckling, (b,c) first buckling, (d–f) second buckling.

The prediction of modal and postbuckling behavior of thin-shell structure buckling has far-reaching significance for practical engineering. The FEM prediction of postbuckling buckling is done by first solving a linear equation system, then calculating different modal orders according to different eigenvalues, and then adding different modalities to the structure according to geometric defects, all in order to predict the postbuckling behavior of the structure, which is a complicated process to solve. VFIFE with its dynamic solution predicts the buckling behavior of thin-shell structures after buckling without additional modal analysis operations and predicts the structural modalities at different stages of buckling and accurately predicts the loads in this state.

Table 3 shows the comparison between the buckling modes calculated by VFIFE near the first buckling of the circular tube under $2 \times 90^\circ$ and $2 \times 120^\circ$ local axial compression loads, and $2 \times 180^\circ$ overall axial compression load, and the experimental results [12]. In the table, the buckling modes calculated by VFIFE are represented by a displacement contour, in which the color bar from blue to red represents the change of the overall displacement

from large to small, and the buckling deformation is generally larger, and it is easy to distinguish the deformation direction, so deformation size is taken as an absolute value.

Table 3. Comparison of buckling mode. Pictures of the experiment are reproduced with the permission of [12], copyright@Thin-Walled Structures, 2021.

Angle	Experiment	VFIFE
$2 \times 90^\circ$		
$2 \times 120^\circ$		
$2 \times 180^\circ$		

Based on the buckling modes near the first buckling, it can be seen that the location and deformation of the buckling deformation calculated by VFIFE are more similar to the experiments, and the predictions of the buckling deformation of the thin-shell structure by VFIFE are more appropriate to the actual situation.

4.2. Buckling Modes and Postbuckling

The calculation of the first buckling load is of great value for guiding the structural design, however, it is still difficult to avoid buckling of the structure in actual engineering. The prediction of the postbuckling behavior of the structure is also of high value for guiding engineering. Most commercial software based on FEM can solve the structural buckling load by solving linear equations with the eigenvalue method and solve the postbuckling modes by the explicit dynamics method, though the process is cumbersome, and VFIFE can do these calculations directly. According to previous studies, the validity and accuracy of the VFIFE method proposed in this paper are verified in the buckling analysis of thin-walled circular shells. Based on developed analytical procedures, this section investigates the postbuckling behavior of thin-walled circular shells.

The postbuckling behavior under local axial compression load was analyzed, and the postbuckling of $2 \times 90^\circ$ local axial compression and $2 \times 120^\circ$ local axial compression were analyzed, respectively. The forced displacement of 8 mm downward was applied to the end of the pipe through different local axial compression angles, and the postbuckling behavior was studied according to the displacement contour after deformation, with the color in the displacement contour the same as in Section 3, the blue to red representing the

change of the total displacement from large to small, and the deformation size is taken as an absolute value.

Figure 9 depicts the postbuckling of the circular tube under the local axial compression load of $2 \times 90^\circ$. Figure 9a–e is the unified view angle, and in Figure 9f, the view angle is adjusted to the side of the axial compression applied more conveniently. Figure 9a shows the state of the structure when buckling is about to occur, under a local axial compression load of $2 \times 90^\circ$, the figure shows that the locations where obvious folds appear were not under compression, and the larger deformations occur in the regions outside the axial compression locations where folds appear. Figure 9b,c are after the first buckling occurs, as the second buckling of the structure appears and develops, and the third buckling occurs in Figure 9d,e, where the depression deformation only becomes larger inward, no new depressions appear, and there is no load position where the fold of the structure gradually becomes larger. Similar to the overall axial compression, depressions still occur in the structure from above and downwards, however, the depressions only occur near the axial compression load. Figure 9f is the state of the structure after the 8 mm forced displacement is applied, the depression finally closes and occurs at the location of the axial compression load, and the rest is folded deformation. It can be predicted that if the load continues to be applied to it, the depression deformation at the position where the forced displacement is applied and the fold at the position where the load is not applied will continue to increase, and eventually, all the deformation will coincide, and then new deformation or even structural fracture may occur.

Figure 10 depicts the postbuckling of the circular tube under a local axial compression load of $2 \times 120^\circ$. Figure 10a shows the state of the structure when buckling is about to occur, and the location where a clear fold appears can be seen in the figure as being without pressure, Figure 10b shows the depressed deformation of the structure after the first buckling, Figure 10b–d show the second buckling of the structure, and the deformations are developing and tend to merge, Figure 10e shows the third buckling of the structure, however, the buckling deformation is smaller than the first two bucklings, and Figure 10f shows the state of the structure after 8 mm forced displacement is applied, as the depressions finally merge and occur at the locations of the axial compression load, while at the locations without axial compression load, the structure has a large inward fold, and the deformation of the structure is already very serious at this time. As can be seen from the postbuckling of $2 \times 90^\circ$ local axial compression, the development of buckling is very similar to the postbuckling of $2 \times 90^\circ$ local axial compression and folds appear in areas where no axial compression is applied before buckling occurs. When the fold continues to expand after buckling, depression deformation occurs at the location where the axial compression is applied.

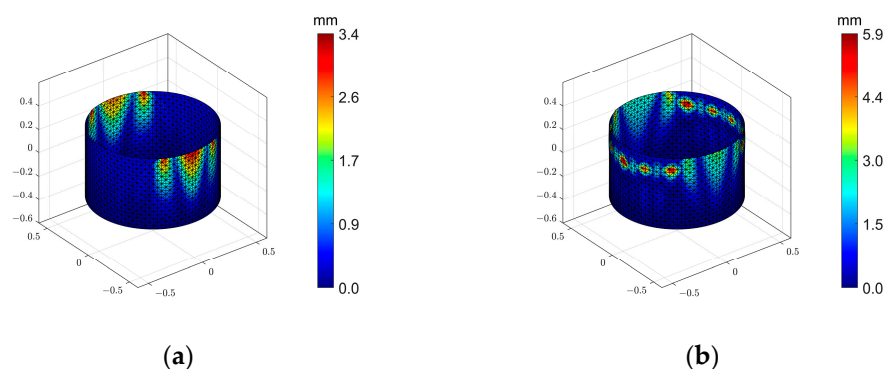


Figure 10. Cont.

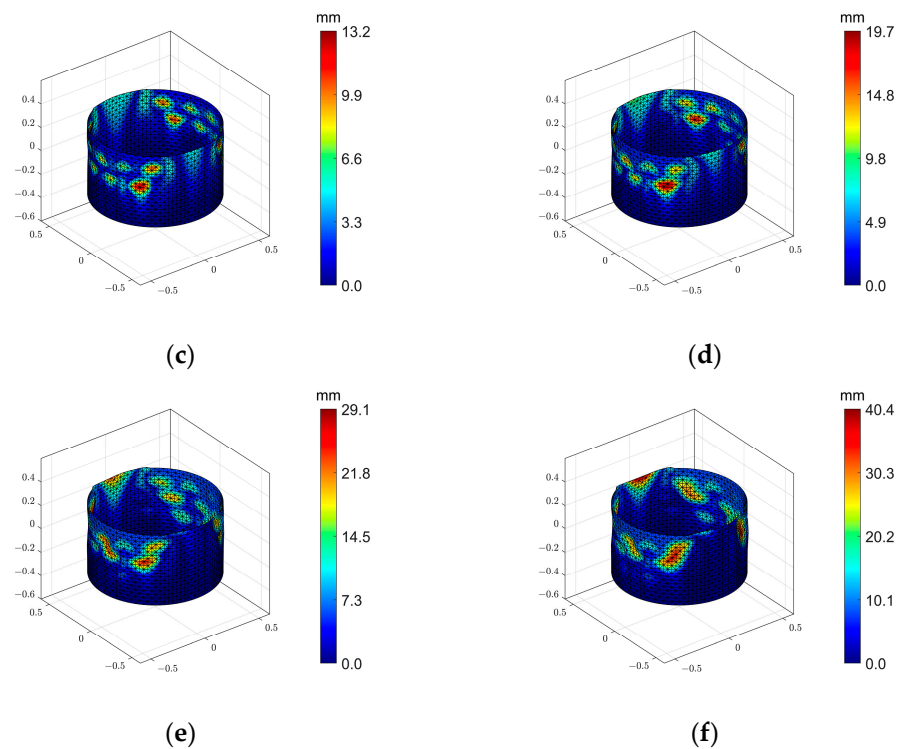


Figure 10. Postbuckling of $2 \times 120^\circ$ local axial compression: (a) before buckling, (b) first buckling, (c–f) second buckling.

Finally, the postbuckling behavior of overall axial compression is simulated as a control, and the postbuckling of the circular tube is achieved by applying a forced axial displacement of 8 mm downward from the end of the tube to the circular tube. Figure 11 is the displacement contour of the structure in the whole loading process after buckling, Figure 11a shows that the first buckling occurs just at the beginning, the element extrusion deformation first appears at the location where the depression is about to occur, Figure 11b depicts the gradual formation of the depression at the extrusion location to the inside of the tube, the deformation of the depression gradually expands and then the second buckling appears at Figure 11c and the third buckling at Figure 11d. At this time, the depression formed by the third buckling has covered the entire round tube. The deformation of the depression in Figure 11e gradually increases and eventually merges into a larger depression in Figure 11f, and as the buckling deformation continues to develop, contact between elements will appear. At this time, boundary nonlinearity needs to be introduced. The shell element adopted in this paper does not include boundary nonlinearity and fracture determination, so subsequent developments are not within the scope of this paper.

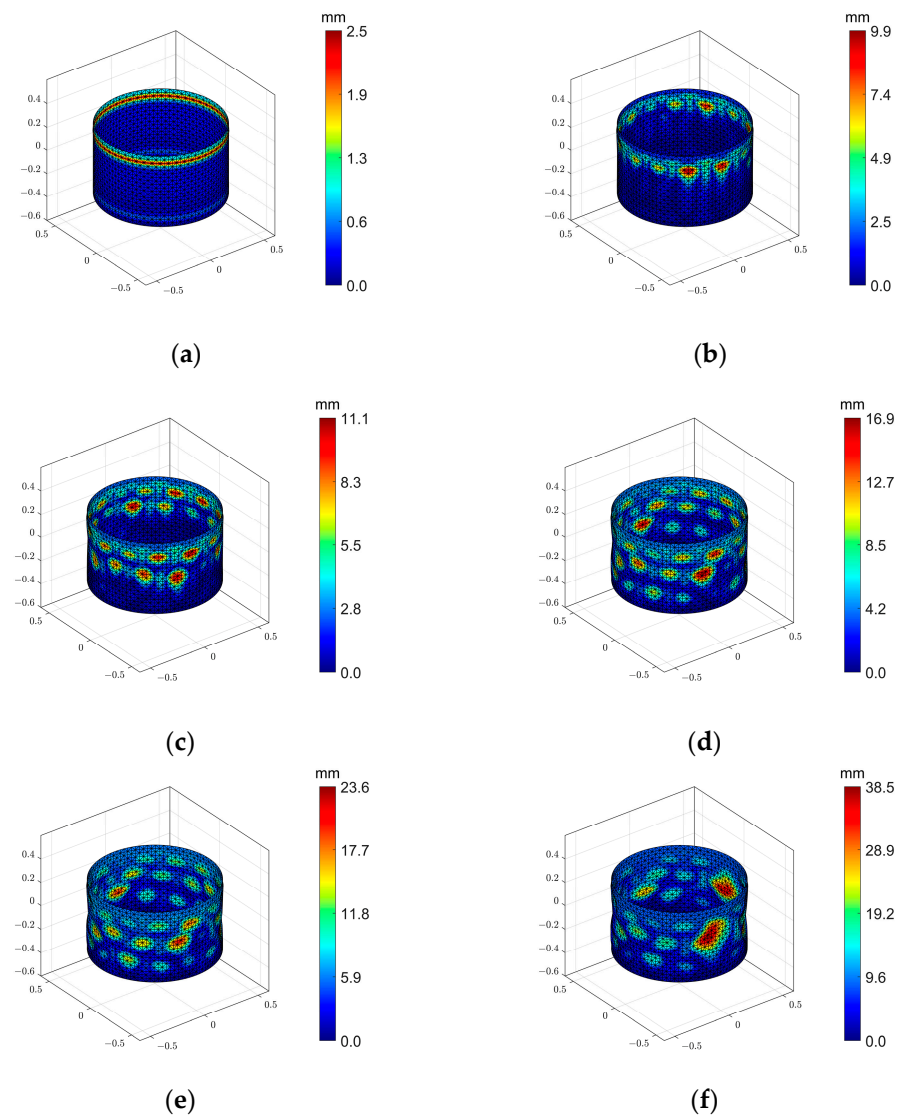


Figure 11. Postbuckling of the overall axial compression: (a) before buckling, (b) first buckling, (c) second buckling, (d–f) third buckling.

The three examples of postbuckling above show that a circular tube subjected to axial compression loading will deform in a top-down depression after buckling occurs. Compared with the overall axial compression, the deformation of the local axial compression circular tube is more irregular, the deformation of the region under load is mostly an inward sag, the region without axial compression will fold, and the fold will gradually increase with the axial displacement, resulting in the shape of the top of the circular tube becoming irregular, and as the mechanical characteristics of such irregular shapes are difficult to predict, such phenomenon should be avoided as much as possible in practical engineering.

5. Conclusions

Based on the vector form intrinsic finite element theory, this paper developed a program for calculating and analyzing the buckling of the structure, considering the multilinear hardening model, verified the multilinear hardening model according to the experimental data, and then simulated the buckling of a thin-walled circular shell under a local axial compression load. Compared with the experimental results, the postbuckling behavior of the thin-walled circular shell was as predicted. The following conclusions can be drawn:

- (1) The multilinear hardening model based on the von Mises yield criterion can divide the elastic-plastic constitutive curve of materials into multiple broken lines and can approach the elastic-plastic constitutive curve of some materials infinitely closely. The stress–strain relationship of materials can be simulated accurately when the model is applied to VFIFE. Compared with the ideal elastoplasticity, bilinear hardening model, power hardening model, and Ramberg–Osgood model used in most numerical simulations, the structural strain under a given stress can be simulated more accurately.
- (2) The VFIFE introduces the multilinear hardening model, which predicts the first buckling load of the local axial compression tube with high accuracy, and the error between the simulation and experiment in this paper is less than 1%. For the buckling mode, after the first buckling occurs, the results of the VFIFE simulation are more consistent with the experiment, which verifies the effectiveness and accuracy of VFIFE in predicting structural buckling.
- (3) For the prediction of the postbuckling of structures, VFIFE has great advantages. Different from the complex settings of most commercial software based on FEM, VFIFE can directly predict the postbuckling behavior of structures under the action of force.
- (4) When a circular tube is subjected to local axial compression loads, the smaller the local axial compression angle, the smaller the buckling load will be. If the load is in the form of overall axial compression, the depression deformation will appear uniformly along the circular tube ring, while if the load is in the form of local axial compression, the depression will occur at the location of the load, and the rest of the location of the fold, so that the geometry of the force side of the circular tube becomes irregular, affecting the mechanical properties of the structure. Such situations should be avoided in engineering wherever possible.

Author Contributions: Conceptualization, W.M. and Z.S.; Data curation, Z.S.; Funding acquisition, W.M. and L.X.; Methodology, W.M., Z.S., H.W., L.X. and Y.Z.; Project administration, W.M.; Software, Z.S. and L.X.; Supervision, W.M.; Validation, H.W., Y.Z. and G.H.; Visualization, Z.S. and H.W.; Writing—original draft, Z.S.; Writing—review & editing, W.M., Z.S., H.W. and Y.W. All authors have read and agreed to the published version of the manuscript.

Funding: This research was supported by the Science and Technology Project of Henan Province (Grant No. 192102310210); The Science and Technology Project of Henan Province (Grant No. 212102310951).

Data Availability Statement: Data will be available upon reasonable request.

Conflicts of Interest: The authors declare no conflict of interest.

References

1. Wagner, H.N.R.; Hühne, C. Robust knockdown factors for the design of cylindrical shells under axial compression: Potentials, practical application and reliability analysis. *Int. J. Mech. Sci.* **2018**, *135*, 410–430. [CrossRef]
2. Trivedi, N.; Singh, R.K. Fracture characterization studies of concrete structures through experiments on reinforced concrete cylindrical shell specimens. *Ann. Nucl. Energy* **2020**, *140*, 107338. [CrossRef]
3. Su, R.; Li, X.; Xu, S.-Y. Axial behavior of circular CFST encased seawater sea-sand concrete filled PVC/GFRP tube columns. *Construct. Build. Mater.* **2022**, *353*, 129159. [CrossRef]
4. Chung, C.-C.; Lee, K.-L.; Pan, W.-F. Collapse of Sharp-Notched 6061-T6 Aluminum Alloy Tubes under Cyclic Bending. *Int. J. Struct. Stab. Dyn.* **2016**, *16*, 1550035. [CrossRef]
5. Horrigmoe, G.; Bergan, P.G. Nonlinear analysis of free-form shells by flat finite elements. *Comput. Methods Appl. Mech. Eng.* **1978**, *16*, 11–35. [CrossRef]
6. Combescure, A.; Galletly, G.D. Plastic buckling of complete toroidal shells of elliptical cross-section subjected to internal pressure. *Thin-Walled Struct.* **1999**, *34*, 135–146. [CrossRef]
7. Spagnoli, A.; Chryssanthopoulos, M.K. Elastic buckling and postbuckling behaviour of widely-stiffened conical shells under axial compression. *Eng. Struct.* **1999**, *21*, 845–855. [CrossRef]
8. Abambres, M.; Camotim, D.; Silvestre, N. GBT-based elastic–plastic post-buckling analysis of stainless steel thin-walled members. *Thin-Walled Struct.* **2014**, *83*, 85–102. [CrossRef]

9. Kadkhodayan, M.; Maarefdoust, M. Elastic/plastic buckling of isotropic thin plates subjected to uniform and linearly varying in-plane loading using incremental and deformation theories. *Aerosp. Sci. Technol.* **2014**, *32*, 66–83. [CrossRef]
10. Song, C.Y.; Teng, J.G.; Rotter, J.M. Imperfection sensitivity of thin elastic cylindrical shells subject to partial axial compression. *Int. J. Solids Struct.* **2004**, *41*, 7155–7180. [CrossRef]
11. Changyong, S. Buckling of un—Stiffened cylindrical shell under non—Uniform axial compressive stress. *J. Zhejiang Univ. Sci.* **2002**, *3*, 520–531. [CrossRef]
12. Jiao, P.; Chen, Z.; Ma, H.; Ge, P.; Gu, Y.; Miao, H. Buckling behaviors of thin-walled cylindrical shells under localized axial compression loads, Part 1: Experimental study. *Thin-Walled Struct.* **2021**, *166*, 108118. [CrossRef]
13. Jiao, P.; Chen, Z.; Ma, H.; Ge, P.; Gu, Y.; Miao, H. Buckling behaviors of thin-walled cylindrical shells under localized axial compression loads, Part 2: Numerical study. *Thin-Walled Struct.* **2021**, *169*, 108330. [CrossRef]
14. Nassiraei, H.; Zhu, L.; Gu, C. Static capacity of collar plate reinforced tubular X-connections subjected to compressive loading: Study of geometrical effects and parametric formulation. *Ships Offshore Struct.* **2019**, *16*, 54–69. [CrossRef]
15. Nassiraei, H.; Rezadoost, P. Static capacity of tubular X-joints reinforced with fiber reinforced polymer subjected to compressive load. *Eng. Struct.* **2021**, *236*, 112041. [CrossRef]
16. Wu, C.; Lou, J.; He, L.; Du, J.; Wu, H. Buckling and Post-Buckling of Symmetric Functionally Graded Microplate Lying on Nonlinear Elastic Foundation Based on Modified Couple Stress Theory. *Int. J. Struct. Stab. Dyn.* **2018**, *18*, 1850110. [CrossRef]
17. Liu, X.; Zhang, J.; Di, C.; Zhan, M.; Wang, F. Buckling of Hydroformed Toroidal Pressure Hulls with Octagonal Cross-Sections. *Metals* **2022**, *12*, 1475. [CrossRef]
18. Peng, Y.; Kong, Z.; Dinh, B.H.; Nguyen, H.-H.; Cao, T.-S.; Papazafeiropoulos, G.; Vu, Q.-V. Web Bend-Buckling of Steel Plate Girders Reinforced by Two Longitudinal Stiffeners with Various Cross-Section Shapes. *Metals* **2023**, *13*, 323. [CrossRef]
19. Barham, W.S.; Idris, A.A. Flexibility-based large increment method for nonlinear analysis of Timoshenko beam structures controlled by a bilinear material model. *Structures* **2021**, *30*, 678–691. [CrossRef]
20. Zhang, C.; Yang, X. Bilinear elastoplastic constitutive model with polyvinyl alcohol content for strain-hardening cementitious composite. *Constr. Build. Mater.* **2019**, *209*, 388–394. [CrossRef]
21. Turkalj, G.; Lanc, D.; Brnic, J. Large displacement beam model for creep buckling analysis of framed structures. *Int. J. Struct. Stab. Dyn.* **2009**, *9*, 61–83. [CrossRef]
22. Xiao, G.; Yang, X.; Qiu, J.; Chang, C.; Liu, E.; Duan, Q.; Shu, X.; Wang, Z. Determination of power hardening elastoplastic constitutive relation of metals through indentation tests with plural indenters. *Mech. Mater.* **2019**, *138*, 103173. [CrossRef]
23. Lu, X.; Huang, F.; Zhao, B.; Keer, L.M. Contact Behaviors of Coated Asperity with Power-Law Hardening Elastic–Plastic Substrate During Loading and Unloading Process. *Int. J. Appl. Mech.* **2018**, *10*, 1850034. [CrossRef]
24. Chen, L.; Yu, Y.; Song, W.; Wang, T.; Sun, W. Stability of geometrically imperfect struts with Ramberg–Osgood constitutive law. *Thin-Walled Struct.* **2022**, *177*, 109438. [CrossRef]
25. Huang, Z.; Chen, Y.; Bai, S.-L. An Elastoplastic Constitutive Model for Porous Materials. *Int. J. Appl. Mech.* **2013**, *5*, 50035. [CrossRef]
26. Mourlas, C.; Khabele, N.; Bark, H.A.; Karamitros, D.; Taddei, F.; Markou, G.; Papadrakakis, M. Effect of Soil–Structure Interaction on Nonlinear Dynamic Response of Reinforced Concrete Structures. *Int. J. Struct. Stab. Dyn.* **2020**, *20*, 2041013. [CrossRef]
27. Ruocco, E.; Reddy, J.N. Buckling analysis of elastic–plastic nanoplates resting on a Winkler–Pasternak foundation based on nonlocal third-order plate theory. *Int. J. Non-Linear Mech.* **2020**, *121*, 103453. [CrossRef]
28. Zhou, W.; Shi, Z.; Li, Y.; Rong, Q.; Zeng, Y.; Lin, J. Elastic-plastic buckling analysis of stiffened panel subjected to global bending in forming process. *Aerosp. Sci. Technol.* **2021**, *115*, 106781. [CrossRef]
29. Zou, Z.; Liu, D.; Song, C.; Jin, M.; Guo, B.; Zhang, H. Elastic-Plastic Finite Element New Method for Lower Bound Shakedown Analysis. *Int. J. Struct. Stab. Dyn.* **2022**, *22*, 2250171. [CrossRef]
30. Shih, C.; Wang, Y.-K.; Ting, E.C. Fundamentals of a Vector Form Intrinsic Finite Element: Part III. Convected Material Frame and Examples. *J. Mech.* **2011**, *20*, 133–143. [CrossRef]
31. Ting, E.C.; Shih, C.; Wang, Y.-K. Fundamentals of a Vector Form Intrinsic Finite Element: Part I. Basic Procedure and A Plane Frame Element. *J. Mech.* **2011**, *20*, 113–122. [CrossRef]
32. Ting, E.C.; Shih, C.; Wang, Y.-K. Fundamentals of a Vector Form Intrinsic Finite Element: Part II. Plane Solid Elements. *J. Mech.* **2011**, *20*, 123–132. [CrossRef]
33. Wu, H.; Zeng, X.; Xiao, J.; Yu, Y.; Dai, X.; Yu, J. Vector form intrinsic finite-element analysis of static and dynamic behavior of deep-sea flexible pipe. *Int. J. Nav. Archit. Ocean Eng.* **2020**, *12*, 376–386. [CrossRef]
34. Wu, T.-Y.; Ting, E.C. Large deflection analysis of 3D membrane structures by a 4-node quadrilateral intrinsic element. *Thin-Walled Struct.* **2008**, *46*, 261–275. [CrossRef]
35. Wu, T.-Y. Dynamic nonlinear analysis of shell structures using a vector form intrinsic finite element. *Eng. Struct.* **2013**, *56*, 2028–2040. [CrossRef]
36. Zhen, W.; Yang, Z.; Xuelin, Y. Nonlinear behavior analysis of entity structure based on vector form intrinsic finite element. *J. Build. Struct.* **2015**, *36*, 133–140. [CrossRef]
37. Wu, T.-Y.; Tsai, W.-C.; Lee, J.-J. Dynamic elastic–plastic and large deflection analyses of frame structures using motion analysis of structures. *Thin-Walled Struct.* **2009**, *47*, 1177–1190. [CrossRef]

38. Zhen, W.; Yang, Z.; Xuelin, Y. Collision-contact, crack-fracture and penetration behavior analysis of thin-shell structures based on vector form intrinsic finite element. *J. Build. Struct.* **2016**, *37*, 53–59. [CrossRef]
39. Zhen, W.; Yang, z.; Xuelin, Y. Vector form intrinsic finite element method for buckling analysis of thin-shell structures. *J. Cent. South Univ. (Sci. Technol.)* **2016**, *47*, 2058–2064.
40. Zhen, W.; Yang, Z.; Xuelin, Y. Analisis of buckling behavior of planar membrane structures based on vector form intrinsic finite element. *J. Zhejiang Univ. (Eng. Sci.)* **2015**, *49*, 1116–1122.
41. Xu, L.; Lin, M. Analysis of buried pipelines subjected to reverse fault motion using the vector form intrinsic finite element method. *Soil Dyn. Earthq. Eng.* **2017**, *93*, 61–83. [CrossRef]
42. Yu, Y.; Li, Z.; Yu, J.; Xu, L.; Zhao, M.; Cui, Y.; Wu, H.; Duan, Q. Buckling analysis of subsea pipeline with integral buckle arrestor using vector form intrinsic finite thin shell element. *Thin-Walled Struct.* **2021**, *164*, 107533. [CrossRef]
43. Yu, Y.; Li, Z.; Yu, J.; Xu, L.; Cheng, S.; Wu, J.; Wang, H.; Xu, W. Buckling failure analysis for buried subsea pipeline under reverse fault displacement. *Thin-Walled Struct.* **2021**, *169*, 108350. [CrossRef]
44. The OpenMP API Specification for Parallel Programming. Available online: <https://www.openmp.org> (accessed on 1 June 2022).

Disclaimer/Publisher’s Note: The statements, opinions and data contained in all publications are solely those of the individual author(s) and contributor(s) and not of MDPI and/or the editor(s). MDPI and/or the editor(s) disclaim responsibility for any injury to people or property resulting from any ideas, methods, instructions or products referred to in the content.

Article

Effect of Quenching Parameters on Distortion Phenomena in AISI 4340 Steel

Ricardo Daniel Lopez-Garcia ^{1,*}, Israel Medina-Juárez ^{2,*} and Araceli Maldonado-Reyes ¹

¹ Department of Mechanical Engineering, Tecnológico Nacional de México/Campus Cd. Victoria, Blvd. Emilio Portes Gil No. 1301 Pte., C.P. 87010 Cd. Victoria, Tamaulipas, Mexico; araceli.mr@cdvictoria.tecnm.mx

² Postgraduate and Research Department, Tecnológico Nacional de México/Campus Cd. Victoria, Blvd. Emilio Portes Gil No. 1301 Pte., C.P. 87010 Cd. Victoria, Tamaulipas, Mexico

* Correspondence: ricardo.lg@cdvictoria.tecnm.mx (R.D.L.-G.); israel.mj@cdvictoria.tecnm.mx (I.M.-J.)

Abstract: During quenching heat treatment, the formation of high residual stress values and the presence of distortion are phenomena which are difficult to control and accurately predict, their effects being extremely important to the components or pieces of complex and robust geometry that are commonly used in the industry. The latter is mainly due to the mixture of the high temperature levels formed between the surface and the cores of the components and the martensitic transformation during quenching. In this research, an experimental and simulated analysis of the process of the quenching heat treatment of AISI 4340 steel, using geometrically complex components, was undertaken with the objective of studying and understanding the effect of quenching process parameters on distortion, stress generation, and mechanical properties. A model that applied the finite elements method (FEM), in which entry data such as thermo-physical and mechanical properties were obtained through experimental techniques that were reported in the literature, made it possible to simulate the cooling process under different conditions, which helped to explain the origins of the distortion in the quenched parts. The results show a close relationship between various quenching parameters such as heat extraction speed, the immersion orientation in the liquid, and the component's geometry. The data obtained could contribute to accelerating the design process of the heat processing routes for quenching components by taking into consideration both the classic process variables and, due to the increased precision resulting from mathematical modeling, additional factors such as the geometry of real applications.

Keywords: distortion; quenching; FEM; residual stresses

Citation: Lopez-Garcia, R.D.; Medina-Juárez, I.; Maldonado-Reyes, A. Effect of Quenching Parameters on Distortion Phenomena in AISI 4340 Steel. *Metals* **2022**, *12*, 759. <https://doi.org/10.3390/met12050759>

Academic Editors: Shuwen Wen, Yongle Sun and Xin Chen

Received: 23 March 2022

Accepted: 22 April 2022

Published: 28 April 2022

Publisher's Note: MDPI stays neutral with regard to jurisdictional claims in published maps and institutional affiliations.



Copyright: © 2022 by the authors. Licensee MDPI, Basel, Switzerland. This article is an open access article distributed under the terms and conditions of the Creative Commons Attribution (CC BY) license (<https://creativecommons.org/licenses/by/4.0/>).

1. Introduction

The purpose of the quenching heat treatment is to modify the initial microstructure of steel by means of cooling the heated parts through the austenitizing temperatures of different liquid quenchants, such as brine, water, or oil. The high cooling rate achieved during the quenching process suppresses diffusion-controlled phase transformations (ferrite, perlite, and bainite) and favors non-diffusional transformations such as martensite, a desirable phase in quenched steel which is responsible for reaching optimum levels of mechanical properties [1,2], followed by a complementary tempering heat treatment. Quenching heat treatment on steel adequately meets the requirements that the modern industry demands. This is mainly in the automotive and aerospace industries, where the strict control of the specifications of mechanical properties and residual stresses are required in order to reduce the possibility of failures and to increase the service life of various components with differing complex geometries. For this reason, distortion control plays a determining role in the dimensional precision of massive production parts when it comes to reducing waste.

Most of the rejection problems of hardened parts are related to the quenching process and caused by poor heat treatment design; because of this, in the metal–mechanical industry, optimal control of the quenching process becomes essential in reducing economic losses [3]. Quenching process design must consider the strict control of the involved process variables, such as the cooling rate, the orientation of the component during immersion, the agitation of the quenching media, the quenching bath temperature, and the component's geometry, all of which influence the dimensional accuracy of hardened parts [4]. The AISI 4340 alloy is a widely used heat-treatable steel because of its high fatigue strength and toughness. Therefore, this type of steel is widely used for the manufacturing of components with high demands for mechanical properties; such components include gears, bolts, torsion bars, and crankshafts, among others [5,6].

On an industrial level, the manufacturing of robust, long or geometrically complex parts is traditionally sensitive to the distortion effects present in the manufacturing process. Therefore, the control of distortion is a research topic widely studied by academics and researchers. The development of distortion not only involves the effect of volumetric expansion induced by the phase transformation (austenite–martensite) but also the complex interaction between different variables such as the austenitizing temperature, immersion velocity and direction, the temperature and agitation of the quenching media, and the geometry of the treated components, among other factors, which results in a complex phenomenon that is difficult to predict and control [7–10]. Due to the complex geometry and the non-homogeneous temperature distribution, the uncontrolled variables of the quenching process could cause the appearance of various undesirable phenomena such as high residual stresses, variations in dimensional precision, cracking and fractures that compromise the component's integrity during its service life [11], and the many other types of waste that can occur during the manufacturing process. Although a significant number of studies have been conducted on this topic, and their results have helped to improve processes in manufacturing industries, failures still occur in the quenching process when the parts or components are heavy or have complex geometries, as is the case with gears, molds, crankshafts, and springs, among many others [12].

In recent years, an important number of numerical tools, such as the finite element method (FEM), have been developed and can be used for the analysis and understanding of the behavior of materials under different processing conditions, and which currently allow a first approach in the design of new heat treatments, the evaluation of residual stress, and the understanding of distortion [13–18]. These investigations have focused on studying variables such as chemical composition, the heat transfer coefficient (HTC), austenitic grain size, component geometry, the temperature of the quenching bath, the agitation of the liquid quenchants, and the immersion direction and immersion velocity. However, despite numerous studies' attempts to understand the relationship between such variables, there are still questions related to their influence on the distortion phenomenon.

Currently, there is little information in the literature on the experimental validation of distortion formation during the quenching of geometrically complex steel parts [19], and these studies have focused on small parts with simple geometries that can be simplified to model and measure the generated distortion [20–25]. Some of these studies that used FEM to predict distortion did not perform experimental measurements [10,26,27].

In the present investigation, a study of the quenching process of AISI 4340 steel samples of complex geometry and also uses an FEM model is presented in order to predict the dimensional behavior, the evolution of internal stresses, and the mechanical properties obtained during the quenching heat treatment, in which the magnitude of the distortion was experimentally measured. The study focuses on the relationships between the immersion speed, the direction of immersion into the quenching media, the mechanical properties, the microstructure, the thermal history, and the final stress profile and distortion.

2. Materials and Methods

2.1. Materials and Experimental Procedure

The material used in this research was an AISI 4340 steel of medium carbon content, of which its main alloyings were Cr and Ni. The chemical composition of the steel is presented in Table 1. For the quenching tests, probes were fabricated with a geometry similar to the one shown in Figure 1. There was a dimensional control of the specimens prior to and after the heat treatment with an interior gauge, a Starrett 700MA with a precision of 0.01 mm, for the purpose of quantifying the dimensional changes in the A, B, and C gaps of the specimens that were caused by the distortion during quenching; see Figure 1.

Table 1. Chemical composition of AISI 4340 steel.

Element	C	Cr	Mo	Ni	Mn	Si	S	P	Fe
% wt.	0.4	0.89	0.25	1.80	0.7	0.3	0.021	0.005	Balance

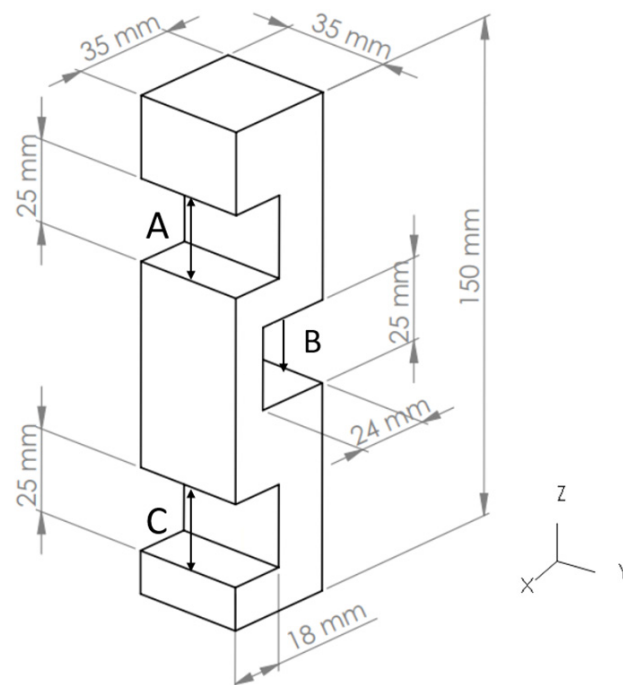


Figure 1. Geometry and dimensions of the part studied.

2.2. Heat Treatment Process

For all the quenching tests, the samples used were instrumented with type K thermocouples attached to their surfaces and connected to a data acquisition card with 10 channels: OMB-DAQ 54. The pieces were heated at a rate of 5 °C/min in a Thermolyne 3500 muffle-type furnace (Thermo Scientific, Waltham, MA, USA) until reaching an austenitization temperature of 860 °C; once reached, it was kept for 45 min to achieve a homogeneous austenitic microstructure. The quenching was performed in two liquid quenching media, oil and water. The commercial quenching oil Equiquench 770 of Equimsa brand was used at a temperature of 60 °C, while the aqueous media was tap water at a temperature of 25 °C. In both cases, the quenching media were kept in constant agitation by the action of a peripheral pump of $\frac{1}{2}$ HP, and the immersion speed used was 40 mm/s, controlled through a robotic arm with stepper motor controls; the conditions of the process are summarized in Table 2. The direction of the immersions occurred in the direction “-z” in the case of the quenching probes in a vertical mode and in the “x” direction for the quenching probes in a horizontal mode; see Figure 1.

Table 2. Quenching process conditions for AISI 4340 steel.

Sample	Temp. (°C)	Soaking Time	Quenching Media	Immersion Rate (mm/s)	Orientation
V-OQ	860	45	Oil	40	Vertical
H-OQ	860	45	Oil	40	Horizontal
V-WQ	860	45	Water	40	Vertical
H-WQ	860	45	Water	40	Horizontal

2.3. Microstructural Analysis

The microstructure of the heat-treated samples was analyzed using an optical microscope (Velab, Ecatepec, Mexico) with a prior standard metallographic preparation according to the norm ASTM E3 [28], while the microstructure was revealed using a 2% Nital etchant according to ASTM E407 [29].

2.4. Hardness Evaluation

The hardness of the treated specimens was measured with a TIME TH-500 model hardness tester (Time Group Inc., Beijing, China) in Rockwell C scale along an axial cut in the “z” axis.

3. Modeling of the Quenching Process

The simulation of the finite elements in the quenching process involved three main aspects: the heat transfer coefficient, the phase transformations, and the residual stresses plus the deformations that had to be properly taken into account [14,16,30,31].

The mathematical model presented in this research considered the relationships between the thermal phenomena, the microstructural changes, mechanical properties, and the residual stresses generated both by thermal origin stress and those due to the phase transformations. The research considered a component of complex geometry through FEM simulation; therefore, thermal gradients existed at the same instant in time. This temperature distribution in the component depends on factors such as the quenching severity, thermal conductivity, heat capacity and latent heat.

Modeling the phase transformations was considered through the evolution of the phase volume fraction during its solid-state transformation as a function of the cooling time and temperature; because of this, diagrams for time–temperature–transformation (TTT) were necessary in modeling. On the other hand, internal stresses produced in the material were calculated by elasto-plastic analysis that assumed small deformations in the part.

3.1. Heat Transfer

The quenching heat treatment can be defined as a transient heat conduction problem that involves all possible means of heat extraction (conduction, radiation, and convection). However, the effect of thermal radiation was not considered in the simulation model used because the treated piece was exposed to the environment for an extremely short time, and the loss of heat by radiation was not considerable; therefore, only the heat conduction and convection equations are described below, using the law of Fourier [32] in Equation (1):

$$q = -k\nabla T \quad (1)$$

where q is the heat flux, k is the thermal conductivity, and ∇T is the temperature gradient field inside the part. According to Fourier’s law, the heat conduction equation of the transient problem that contains the phase transformation can be defined using the conservation of energy balance in the rectangular coordinate system presented in Equation (2):

$$\frac{\partial}{\partial x} \left(k \frac{\partial T}{\partial x} \right) + \frac{\partial}{\partial y} \left(k \frac{\partial T}{\partial y} \right) + \frac{\partial}{\partial z} \left(k \frac{\partial T}{\partial z} \right) + q_v = \left(\frac{\partial T}{\partial t} \right) \rho C_p \quad (2)$$

where k is the thermal conductivity, T is the quenching part temperature, q_v is the heat generation rate from the steel phase transformations, ρ is the material density, C_p is the specific heat capacity at a constant pressure, t is the time, and (x, y, z) are the rectangular coordinates.

To calculate the heat transmission by convection between the part's surface and the cooling media, the cooling equation of Newton is used, as described in Equation (3):

$$Q = hA\Delta T \quad (3)$$

where Q is the heat flux density, h is the heat transfer coefficient, A is the surface area of the part, and ΔT is the temperature difference between the part's surface and the quenching media.

3.2. Phase Transformation

Because phase transformations have a strong relationship with the thermal and mechanical behavior of the material, they should be considered when finite element simulations are used. In the first place, the temperature ranges where the phase transformations occur and which are limited by the critical temperatures must be defined. Commonly these temperatures can be calculated using time–temperature–transformation (TTT) diagrams or through analytical expressions.

TTT diagrams describe the relationship between the beginning and end of a transformation and indicate a transformed volume fraction during the isothermal process at different temperatures. The isothermal kinetic equation, known as the Johnson–Mehl equation [33], is a fundamental variable in the numerical simulation of thermal processes, although it cannot be directly applied to calculate the volume fraction during non-isothermal processes. Due to this restriction, the Avrami equation was proposed, which has been widely used in these type of processes [34], Equation (4):

$$\xi = 1 - \exp(-bt^n) \quad (4)$$

where ξ is the volume fraction of the new phase, t is the isothermal time duration, b is a temperature, chemical composition of parent phase, and grain size dependent constant, and n is a constant dependent on the type of phase transformation, varying from 1 to 4.

In the case of displacive transformation (martensite), there is a stage of nucleation and growth; however, the growth rate is so high that the volume of transformation of the phase is almost entirely controlled by nucleation, and as a result, its transformation kinetics are not influenced by the cooling speed. Because of this, it cannot be explained by Avrami's equation. Therefore, the amount of martensite formed is calculated using the equation established by Koistinen and Marburger [35], Equation (5):

$$\xi = 1 - \exp[-\alpha(M_s - T)] \quad (5)$$

where ξ is the martensite transformed volume fraction, T is the temperature, M_s is the martensite transformations beginning temperature, and α is a constant that indicates the transformation rate and depends on the chemical composition of steel. It is important to mention that through the TTT and CCT diagrams it is possible to obtain the martensitic transformation temperature at a critical cooling rate.

3.3. Mechanical Interactions

The formation of residual stresses during quenching can occur in different manners—high temperature gradients, martensitic transformations, or the combination of both. In the first, the differences in temperature between the surface and the core of the part cause the surface to cool faster than the core, and therefore a volume contraction of the part begins on the surface with the presence of tension from the residual stresses, while in the core, to balance the entire part state of the residual stresses, there should be compression. In the second case, when a martensitic transformation is involved, stresses appear immediately

after the martensitic transformation occurs on the surface of the piece, causing compressive residual stresses and tension-types in the core. The end of the residual stress behavior finishes as soon as the martensitic transformation occurs in the core of the part; at this point, the surface of the part is completely transformed and has reached room temperature [36]. Assuming that steel behaves like a thermo-elasto-plastic material, the total strain rate on the steel during quenching can be expressed in terms of the five deformation sources in Equation (6).

$$\dot{\epsilon}_{ij} = \dot{\epsilon}_{ij}^e + \dot{\epsilon}_{ij}^p + \dot{\epsilon}_{ij}^{th} + \dot{\epsilon}_{ij}^{pt} + \dot{\epsilon}_{ij}^{tr} \quad (6)$$

where $\dot{\epsilon}_{ij}^e, \dot{\epsilon}_{ij}^p, \dot{\epsilon}_{ij}^{th}, \dot{\epsilon}_{ij}^{pt}, \dot{\epsilon}_{ij}^{tr}$ terms are the elastic, plastic, thermal, phase transformation, and plasticity transformation strain rates, respectively. Equations (7)–(11) are used individually in the simulation model to calculate the addition of deformations due to the different physical origins considered in this study.

$$\dot{\epsilon}_{ij}^e = \frac{1}{E} [(1 + \nu)\sigma_{ij} - \delta_{ij}\nu\sigma_{ii}] \quad (7)$$

$$\dot{\epsilon}_{ij}^p = d\lambda \frac{\partial \varphi}{\partial \sigma_{ij}} \quad (8)$$

where $E, \nu, \sigma_{ij}, d\lambda, \delta_{ij}$, and φ are the elastic modulus, Poisson's ratio, Cauchy stress tensor, the plastic multiplier, Kronecker delta, and the yield functional using temperature, respectively.

$$\dot{\epsilon}_{ij}^{th} = \sum_{\kappa=1}^p \zeta_{\kappa} \int_0^T \alpha_{\kappa} dT \quad (9)$$

where α_{κ} is the thermal expansion coefficient of the phase κ , and ζ_{κ} is the volume fraction of phase κ .

$$\dot{\epsilon}_{ij}^{pt} = \sum_{\kappa=1}^p \frac{1}{3} \delta_{ij} \Delta_{\kappa} \dot{\zeta}_{\kappa} \quad (10)$$

where Δ_{κ} is the structural dilation due to the phase transformation.

$$\dot{\epsilon}_{ij}^{tr} = \frac{3}{2} K_{\kappa} \dot{\zeta}_{\kappa} (1 - \zeta_{\kappa}) S_{ij} \quad (11)$$

where K_{κ} is a constant due to the transformation-induced plasticity (TRIP), $\dot{\zeta}_{\kappa}$ is the transformation rate of the phase κ , and S_{ij} is the stress deviator tensor.

Once the previous sources of deformation have been established, the internal stresses can be reconstructed using Hooke's law for isotropic materials.

Hardness values can be calculated using a simple rule of mixtures, assuming a constant hardness value for each phase.

$$\bar{H} = f_1(H_1) + f_2(H_2) + \dots + f_n(H_n) \quad (12)$$

where \bar{H} is the weighted average of hardness in any element of the simulated geometry, $H_{(1-n)}$ are typical values of hardness for each phase, and $f_{(1-n)}$ values are the calculated volume fraction for each present phase.

3.4. Finite Element Simulation Conditions

The quenching process was simulated using the finite elements method (FEM). Table 3 summarizes the simulation parameters used. The compute domain of geometry is shown in Figure 2, representing a tridimensional model with 165,000 tetrahedral elements and 36,500 nodes, which was chosen so the results did not depend on the refinement degree of the mesh. The input data of the thermal and transformation properties of the material can be appreciated in Figure 3; these thermophysical properties of the material were the ones available in the literature for AISI 4340 steel. The model considered the thermal interactions,

the formation of internal stress, the elasto-plastic deformation, and the microstructural evolution.

Table 3. Simulation parameters.

Simulation Parameters	Value (s)
Number of simulation steps	800
Number of elements	165,000
Number of nodes	36,500
Initial temperature of the nodes (°C)	860
Environment temperature (°C)	25
Quenching oil temperature (°C)	55
Cooling water temperature (°C)	25
Immersion rate (mm/s)	40
Immersion direction	−Z and X
Iteration method	Newton–Raphson
Heat transfer coefficient	$f(T)$, shown in Figure 3e,f

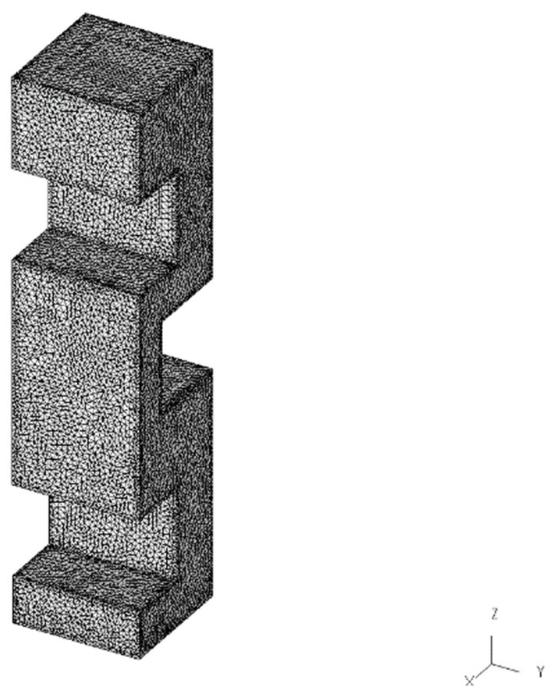
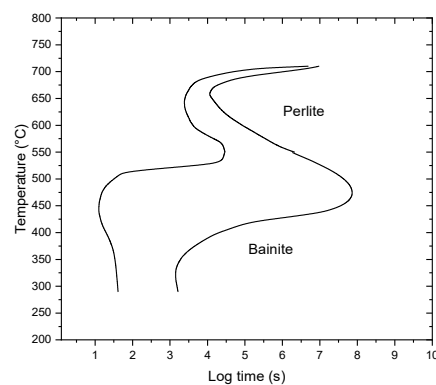
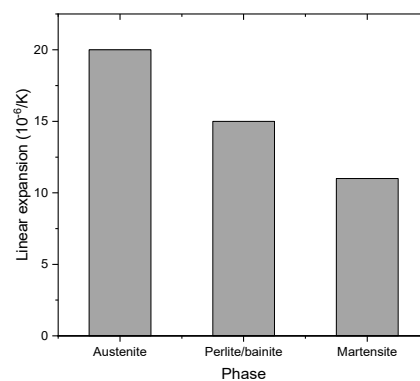


Figure 2. Mesh used in FEM simulation.



(a)



(b)

Figure 3. Cont.

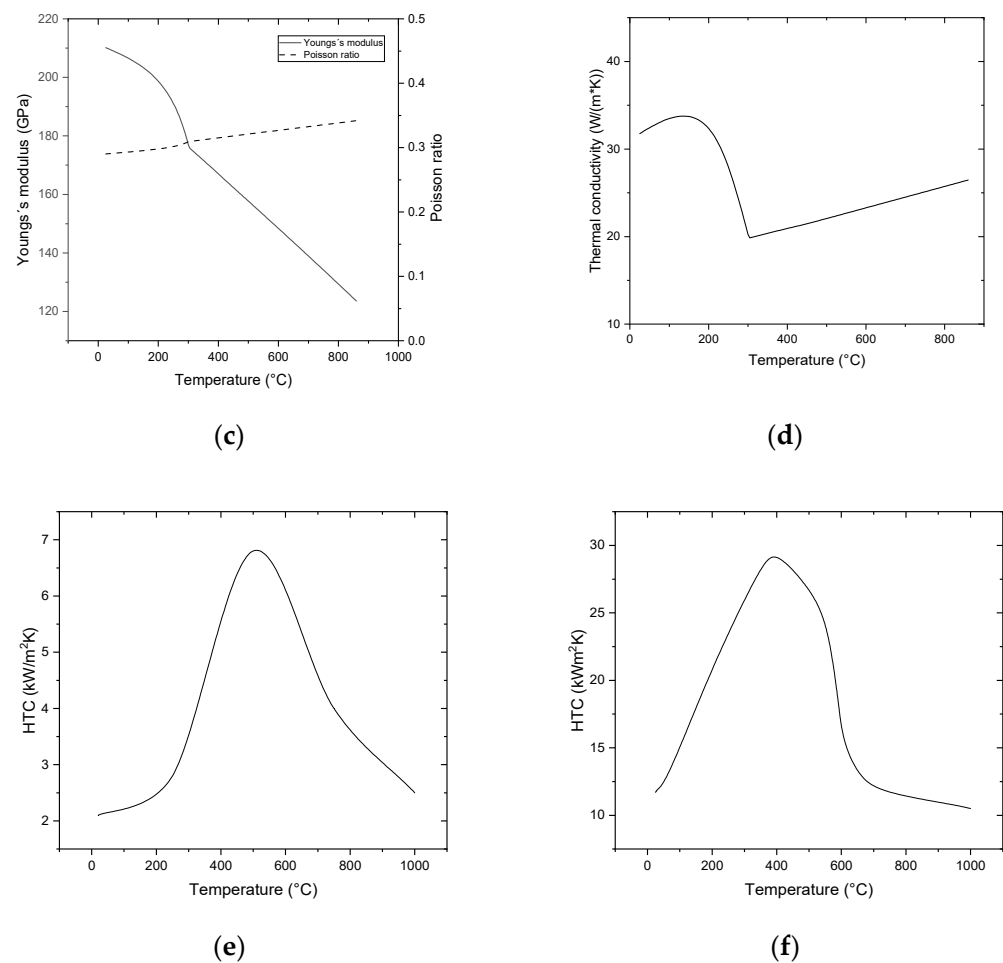


Figure 3. Thermophysical properties for AISI 4340 steel used in FEM simulation: (a) TTT diagram [37]; (b) thermal expansion [38]; (c) Young's modulus and Poisson's ratio [38]; (d) thermal conductivity [38]; (e) HTC (oil) adapted with permission from [39] 2022, Elsevier; and (f) HTC (water) [40].

4. Results and Discussion

4.1. Thermal Analysis

In Figure 4, the experimental results of the temperature evolution during the cooling on the surface of the quenched parts from 860 °C until reaching the quenching media temperature are shown; oil and water with temperatures of 55° and 25°, respectively, in the two directions of immersion, vertical and horizontal.

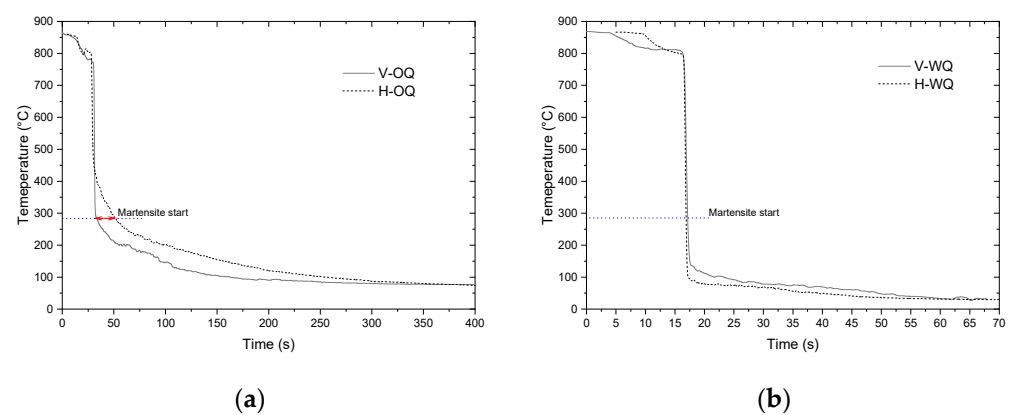


Figure 4. Thermal history of studied pieces in tow immersion modes: (a) oil quenching and (b) water quenching.

At the beginning of the cooling for all the studied cases, it was observed that there was a downfall in the cooling curve temperature of 860 °C until 770 °C, and this downfall was related to the stage of convection cooling followed by a severe cooling caused by the immersion into the used liquid. Just as expected, the water-quenched samples showed an extremely rapid decrease in temperature, quickly reaching the martensitic transformation, as shown in Figure 4b, while the time required for the samples to reach thermal equilibrium with the quenching media was 70 s in the case of the quenching in oil, with the time extending asymptotically until 400 s, as shown in Figure 4a. Additionally, it could be observed that the relative cooling times of the oil immersion mode were reduced when the specimen was submerged in a vertical position (V-OQ), which is explained by the austenite–martensite transformation beginning before expected and by the transformation being completed in a shorter span of time for all the specimens. However, for the horizontal immersion (H-OQ), this timing was delayed for an approximated period of 30 s to begin the martensite transformation (see Figure 4a). Figure 5 shows the thermal history and the maximum cooling rates reached in each stage until the completion of cooling for all the studied conditions. Figure 5a,b represents the oil immersion conditions of the tested specimens, the maximum cooling rates of 55° and 45 °C/s for the vertical direction immersion (V-OQ) and horizontal (H-OQ), respectively. On the other hand, the maximum cooling rate was observed in the vertical immersion position, with water as the cooling medium. The maximum cooling rates were 150 and 250 °C/s for the vertical direction immersions (V-WQ) and horizontal (H-WQ), respectively; see Figure 5c,d. Cooling rates in that order of magnitude typically cause problems such as cracking or fracture of the samples because of the high temperature gradient formed at different points in the component.

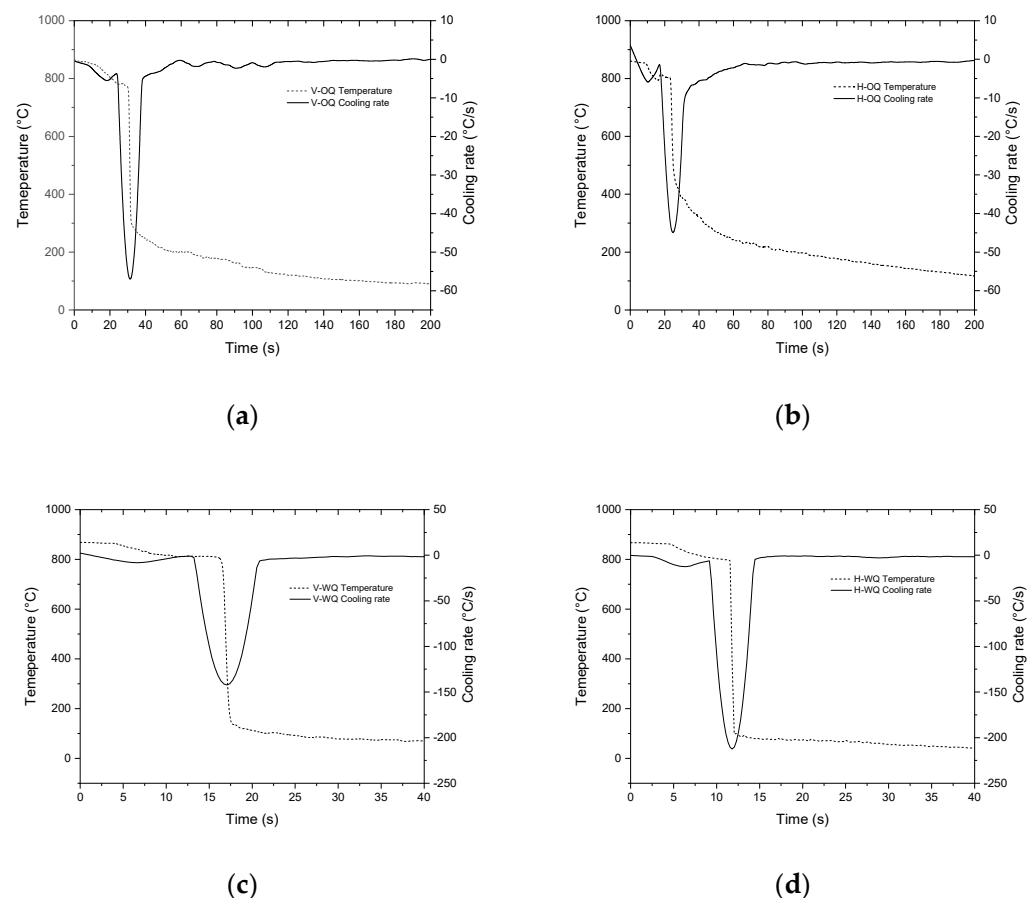


Figure 5. Maximum cooling rates in quenched AISI 4340 steel samples: (a) V-OQ; (b) H-OQ; (c) V-WQ; and (d) H-WQ.

During the cooling of the quenched samples, it was desirable that the temperature changes along the samples occurred in a uniform way between the surface and the core in order to avoid the formation of high thermal gradients, which can be the origin of high stress of thermal origin. Even though the formation of residual stresses depends on a complex interaction among the diverse thermal–physical–mechanical phenomena, for the specific case of the quenching treatment, the homogeneous distribution of temperature along the component is a critical condition. Because of this, it becomes an issue of great interest to evaluate the temperature gradient intensity formed between the surface and core zones during the cooling, which can partially inform the stress profiles found through the mathematical model at the end of the heat treatment and in the presence of the diverse unwanted phenomena of excessive distortion and the occurrence of fractures. These thermal gradients were evaluated in six positions (surface and core) during the whole cooling stage for all the simulated cases, and the results are presented in Figure 6. The results show that the highest thermal gradients were present when water was used as the quenching medium; see Figure 6c,d. Values of $\Delta T \approx 650^\circ\text{C}$ were found between the surface and the core of the piece, showing non-homogeneous temperature profile behavior due to the fast heat extraction in its surface and a heat extraction slower in the core, increasing the possibility of the presence of cracks and subsequent fractures. Figure 6a,b shows the thermal gradients in the samples quenched in oil as the quenching medium. It can be observed that the lowest thermal gradients, $\Delta T \approx 350^\circ\text{C}$, are found on the points (P3 vs. P6) which corresponded to the thinnest zone of the piece, while in the other studied points, the maximum values of ΔT were $\approx 440^\circ\text{C}$, increasing the probability of a major concentration of thermal origin stresses and the presence of distortions that compromised the dimensional precision of the pieces and caused the generation of cracks and fractures in real quenched components.

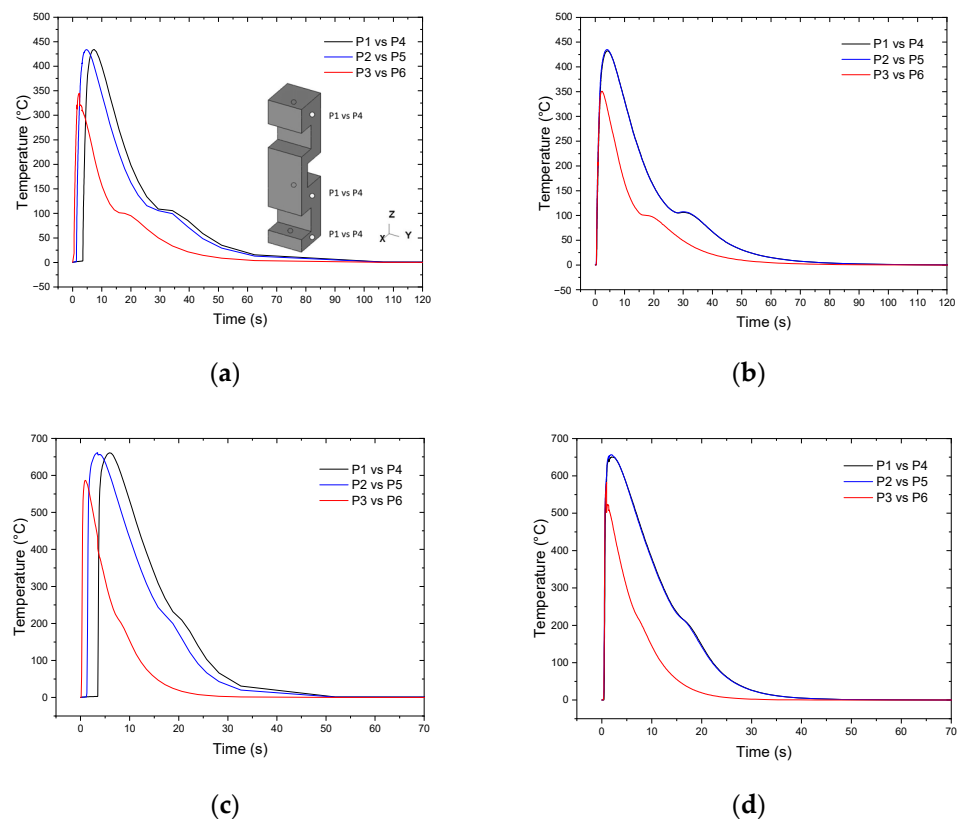


Figure 6. Temperature gradient (ΔT) between surface and core points during cooling of AISI 4340: (a) VOQ; (b) H-OQ; (c) V-WQ; and (d) H-WQ.

The cooling profiles obtained experimentally were compared with the simulation results and are presented in Figure 7. It is evident that the model could predict the necessary time for the piece to reach the thermal balance with the quenching media; however, the model needs to be perfected to obtain the same cooling rates in the inferior parts of the cooling curves corresponding to the convection cooling stage. In a general way, the implemented model overestimated the cooling rates in the oil cases and underestimated the cooling rates in the water quenched case estimations.

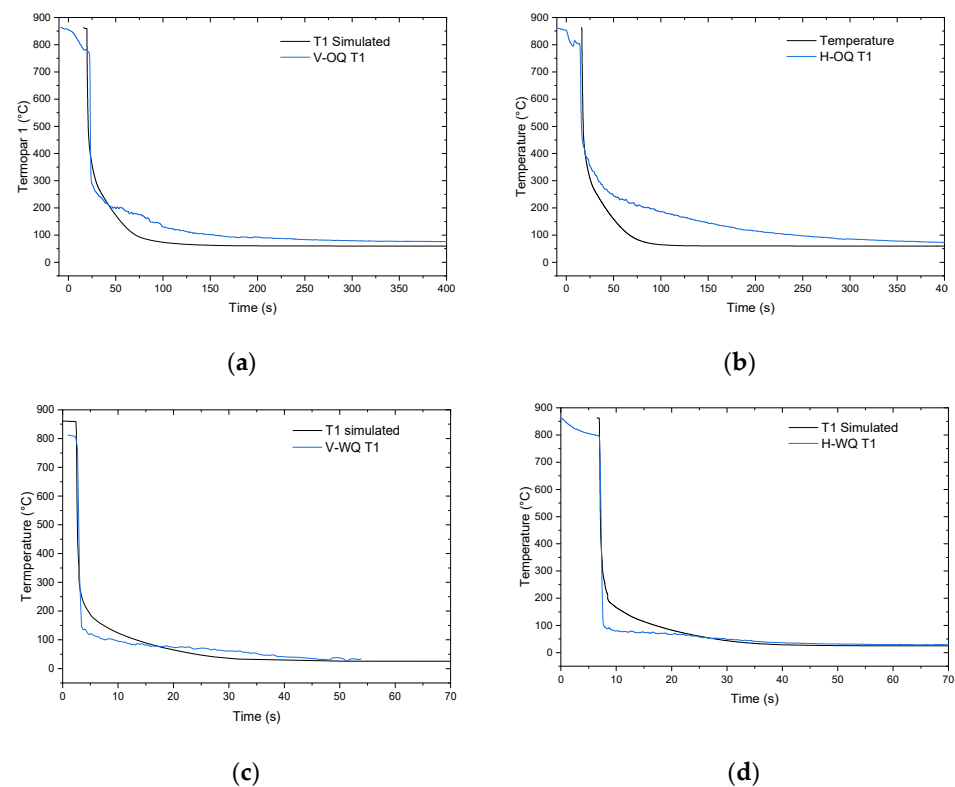


Figure 7. Comparison between simulated cooling curves and those measured with thermocouples in different quenching media and immersion modes: (a) V-OQ; (b) H-OQ; (c) V-WQ; and (d) H-WQ.

4.2. Microstructure and Hardness

Figure 8 shows images through optical microscopy of the obtained microstructure from the quenched AISI 4340 steel in oil and water and two immersion directions. In all studied cases, an almost complete martensite transformation could be observed, which was expected according to the steel chemistry and the used quenching conditions.

After the microstructural characterization, a simulation analysis through FEM modeling was made to compare the results of the austenite–martensite transformation during the cooling stage. According to the results shown in the histograms in Figure 9a,b, which represents the martensite distribution in all the 36,500 nodes of the model, 93% transformed martensite was obtained for the quenching condition in oil; these results are similar for the vertical immersion condition (V-OQ) and horizontal condition (H-OQ). Moreover, with the quenching treatment using water as the quenching medium, the martensite transformation reached 97% in both vertical immersion (V-WQ) and horizontal immersion modes (H-WQ). In addition to the histograms in Figure 9, for the distribution of martensite in the pieces studied at the end of the modeled cooling for the different studied conditions of immersion, see Figure 10. It can be seen that despite the similarities in the amount of final martensite transformation for both immersion cases, the most homogeneous distribution was found in the vertical immersion cases without consideration of the quenching media, indicating a more uniform cooling under this condition when compared to the cooling in a horizontal position that generates less symmetrical martensite distributions.

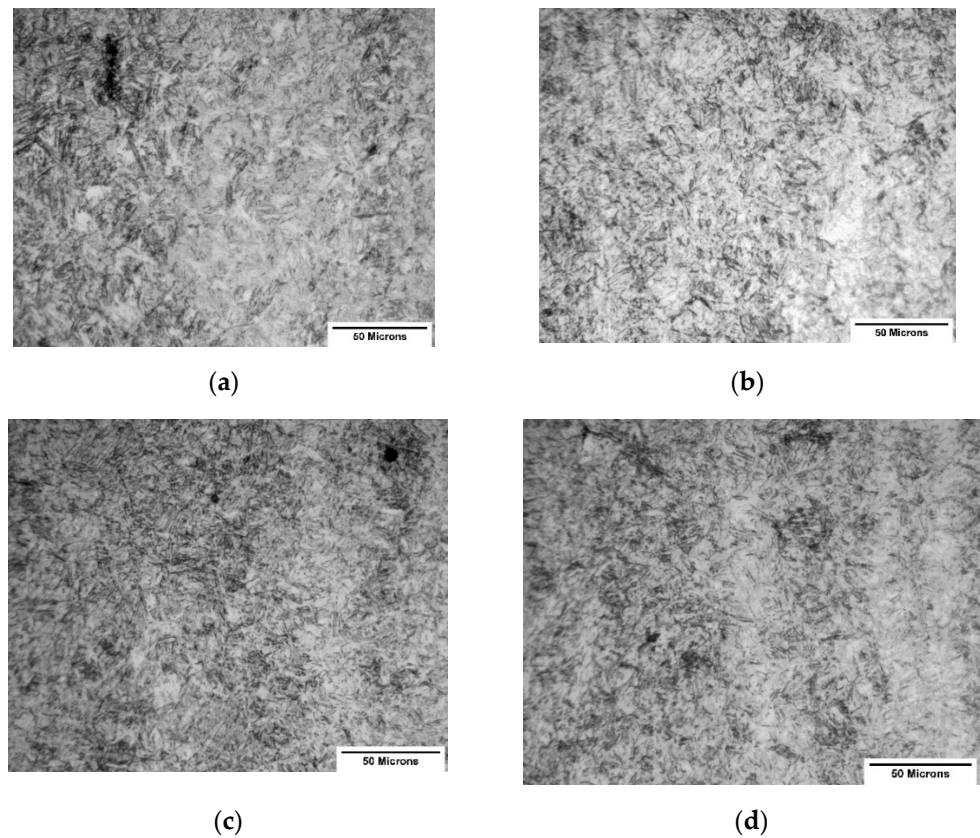


Figure 8. Obtained microstructure after quenching treatment of AISI-4340 steel at 500 \times : (a) V-OQ; (b) H-OQ; (c) V-WQ; and (d) H-WQ.

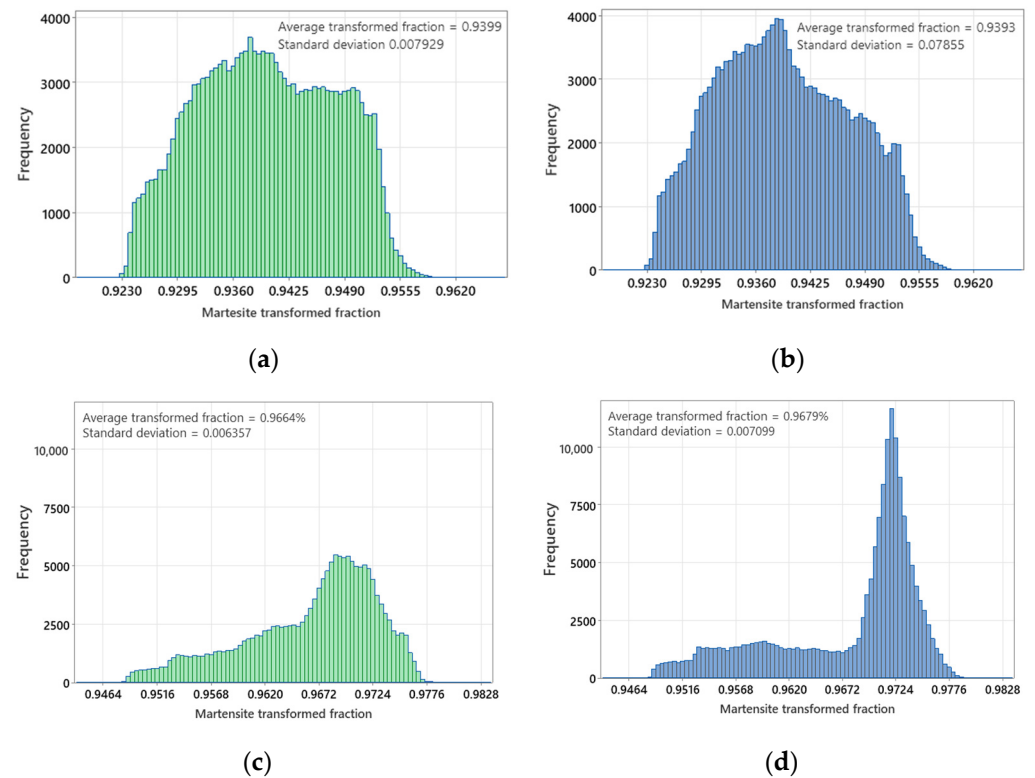


Figure 9. Nodal transformed fraction in quenched samples: (a) V-OQ; (b) H-OQ; (c) V-WQ; and (d) H-WQ.

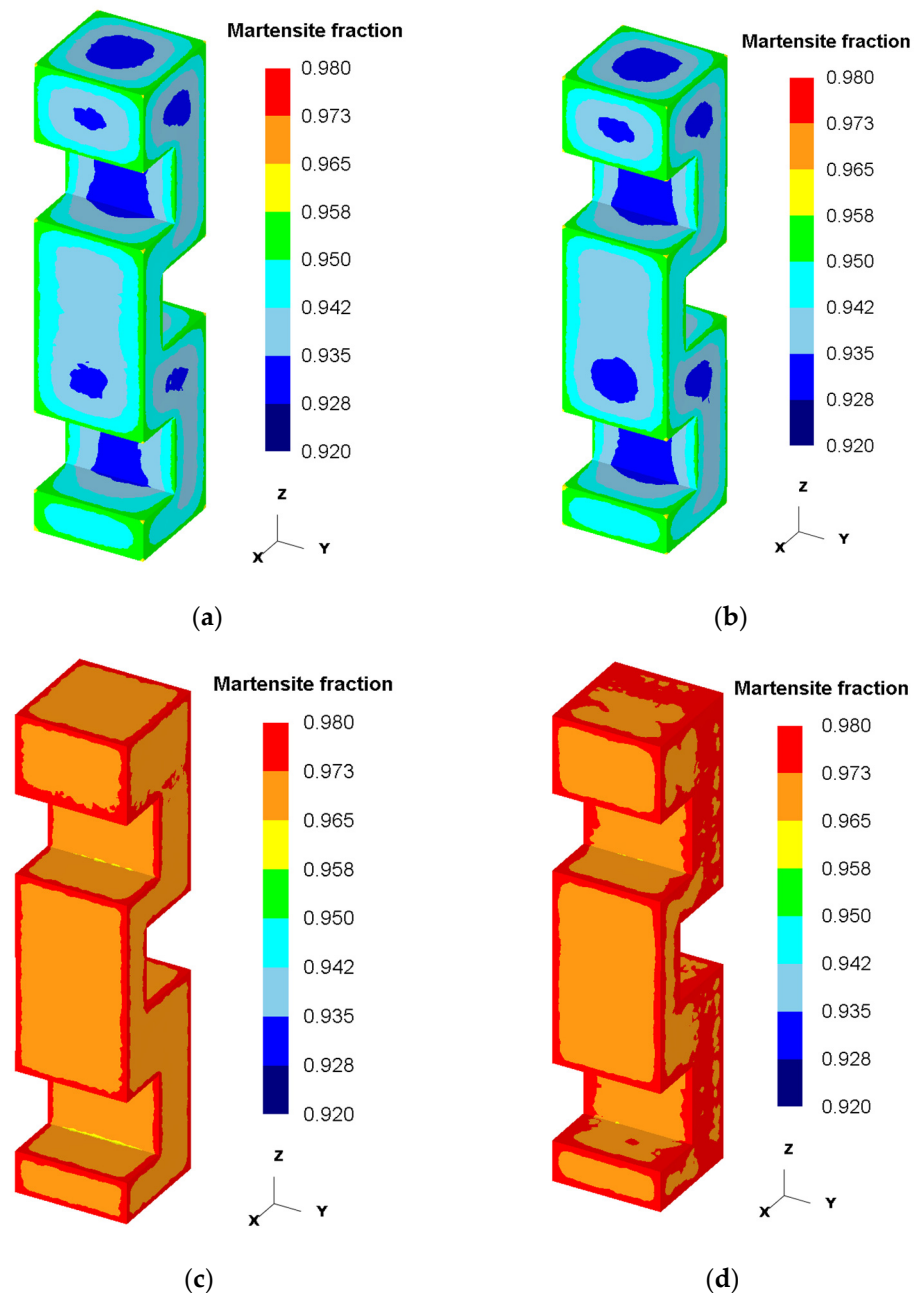


Figure 10. Martensite distribution in samples: (a) vertical oil quench; (b) horizontal oil quench; (c) vertical water quench; and (d) horizontal water quench.

The difference between the results lies mainly in the quenching media; when water was used, the quenching severity was more aggressive and a major cooling rate was obtained, promoting the austenite–martensite phase transformation to occur early in most nodes in the simulation model. By contrast, for the oil quenched cases, the cooling rate was minor, and the martensite complete transformation was affected by variables such as the oil temperature, agitation of the liquid, and the rate and the immersion direction of the pieces.

The hardness of the quenched pieces was measured in a longitudinal section along the axis “z” in the coordinate system. Figure 11 shows the average hardness in three zones in the studied samples of AISI 4340 steel under different immersion modes in oil and water. The water-cooled pieces showed more hardness in both immersion modes in the three analyzed zones, and the hardness levels obtained were 57.3–59.1 HRC. By contrast, for the oil cooling and the vertical immersion conditions, a major hardness was obtained

with hardness magnitudes between 51.9 and 54 HRC. On the other hand, the quenching condition in oil and horizontal immersion showed the lowest hardness magnitude for the experiments performed. The hardness results obtained through FEM showed a more uniform distribution compared with the experimental results for all the types of immersion and quenching media, and the latter can be observed in Figure 12, which shows the hardness distribution of the 36,500 nodes that formed the mesh through histograms. These hardness fluctuations could be explained by the variations in the transformation kinetics used in the model in addition to the HTC used, which could be optimized using the experimental data collected in this research for future works.

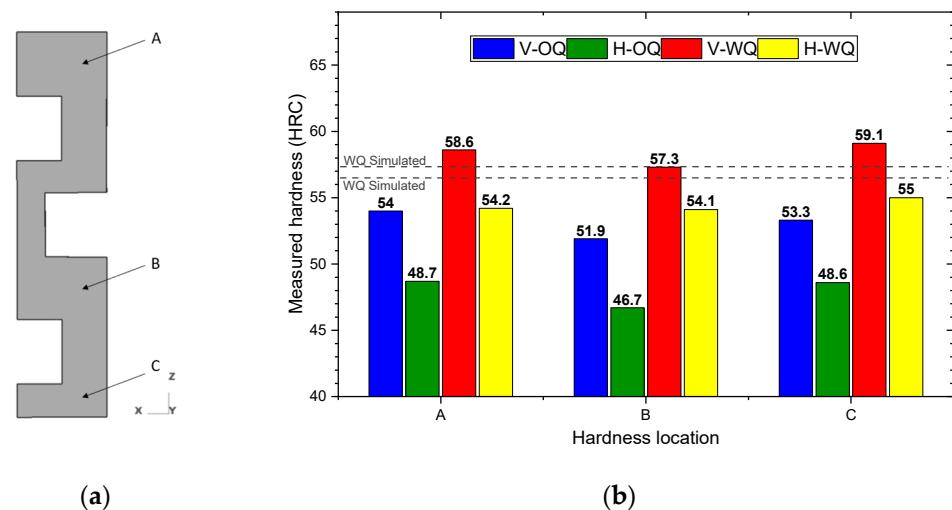


Figure 11. Measured and calculated hardness in quenched samples: (a) measured zones and (b) experimental hardness results.

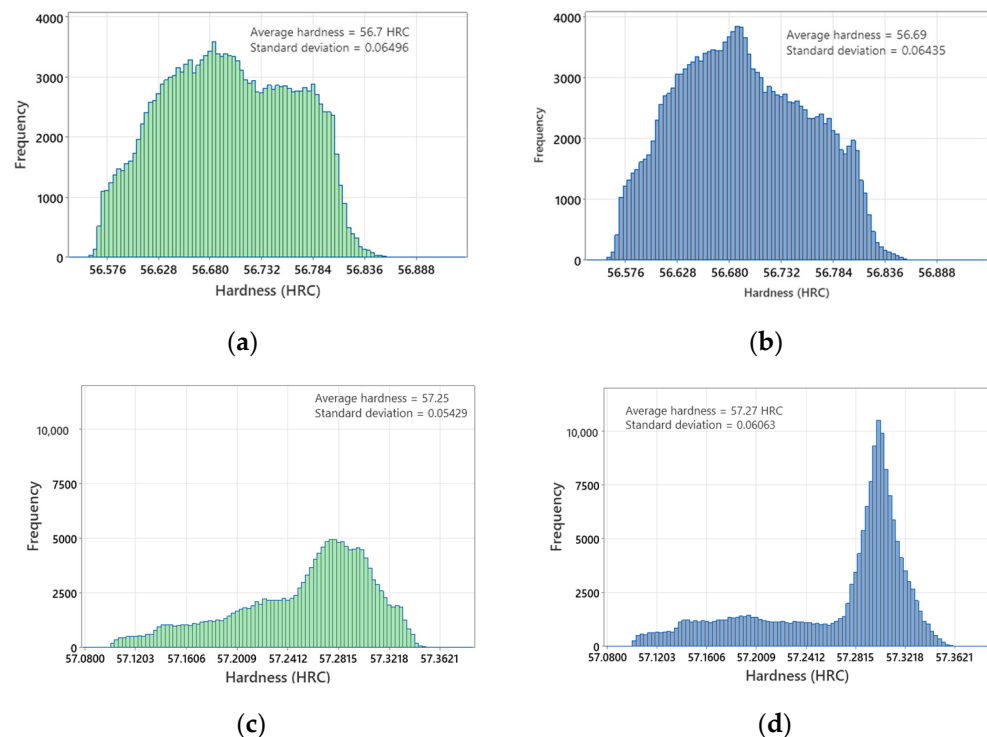


Figure 12. Nodal hardness distribution in entire FEM model: (a) V-OQ; (b) H-OQ; (c) V-WQ; and (d) H-WQ.

4.3. Distortion

Figure 13 shows the distortion generated the studied samples after the quenching treatment measured in a quantitative way in three zones identified as: A, B, and C, which correspond to the nominal 25 mm gaps prior to the heat treatment (see Figure 1).

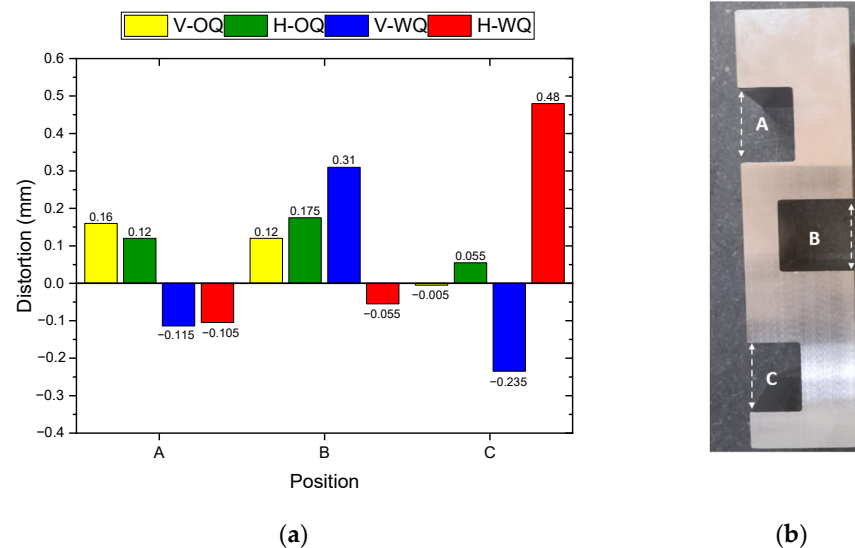


Figure 13. (a) Measured distortion after quench and (b) measured gaps in geometry.

It can be seen that the major distortion was presented in the water-quenched samples in the direction of horizontal immersion (H-WQ), and the magnitude of the measured distortion was ≈ 0.48 mm, while the minor distortion was found for the case of the oil-quenched samples and when the piece enters the quenching media in a vertical direction (V-OQ), with a magnitude of just $|0.005|$ mm. In both cases, these values occurred in the thinnest region of the piece, identified as zone C. Furthermore, it was observed that for the quench in water and in the direction of the vertical immersion (V-WQ), a distortion was obtained in the range of 0.23–0.31 mm for the gaps B and C, while for A it corresponded to the thickest region of the piece and presented the lowest distortion levels, regardless the cooling media used. In a general way, the tendency to increase the magnitude of the distortion was presented when using the direction of horizontal immersion and using water as the quenching medium, while when using oil, which is the less severe quenching medium, and a vertical direction immersion, the decrease of the distortion effect is favored.

In contrast, the distortion values obtained in the simulation presented in Figure 14 are in good agreement with the experimental results in the V-OQ and H-OQ specimens. Less consistent values are found with specimen V-WQ due to the difference found in the gap “A” that shows an inverted distortion with respect to the corresponding experimental result. Finally, the H-WQ specimen was the one with the worst concordance with the experimental results. This difference between results shows the difficulty in modeling processes with many variables, and in this case, even the slightest deviation during immersion in the quenching medium creates an inadequate value for the heat transfer coefficient due to the different convection conditions generating such resultant discrepancies.

The austenite to martensite phase transformation is accompanied by a volumetric expansion and promotes the formation of internal stresses, and similarly, the thermal gradients during the cooling process produce the correspondent thermal origin stresses. In such a way, the dimensional change in the geometry of the studied pieces was related to the combined effect of these phenomena. Both are difficult to avoid; however, these are possible to predict and control through the design of a quenching system that allows the manipulation of each one of the critical variables along with numeric techniques, such as FEM models, which make the design of heat treatments as efficient and controllable as possible.

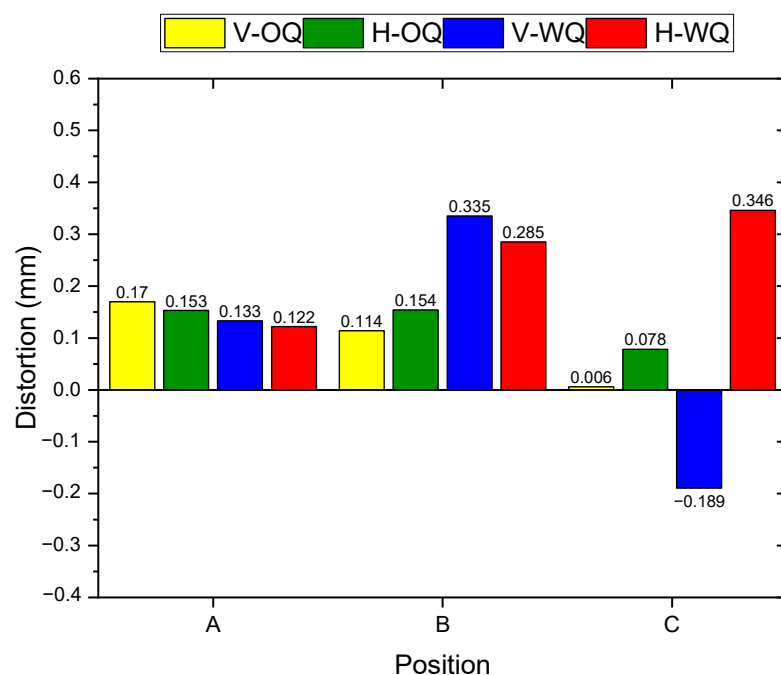


Figure 14. Simulated distortion after quench.

4.4. Simulated Residual Stresses and Precense of Cracks

The accumulation of internal stresses of thermal origins due to the high temperature gradients is added to the stresses generated by the volumetric expansion during the martensitic transformation, generating not only a decrease in the dimensional precision due to distortion but also, if these stresses overcome the yield stress, cracks or fractures in the material may occur. That is the reason why it becomes important to study the evolution of these stresses to know their magnitude and distribution related to cooling time. Figure 15 shows the stress distribution in the pieces at the end of the simulation, pointing out the residual stress concentrators obtained in each case studied.

Figure 15 shows the stress concentration along the geometry of the piece for all the studied cases. It can be appreciated that the vertical quenching modes produced more minor stress values than the corresponding horizontal quenching cases. Showing the mode V-OQ, Figure 15a shows minor stresses at the end of the quenching. The mode H-WQ, in Figure 15d, is the sample that reached stress values on the order of 530 MPa. This last value was far from overcoming the elastic limit of AISI 4340 steel; however, analyzing the stress history along the cooling time, peak values can be found very close to the yield limit of the material, at least in the water-quenched simulated samples.

In Figure 16 are shown the maximum values of residual stresses related to the simulation time in different zones of the studied pieces in both directions of immersion for water-quenched samples. Figure 16a represents the vertical immersion condition when the maximum effective stresses were reached at 10 s after beginning the quenching process, while, for the horizontal direction, the average time after the immersion started was 7 s; see Figure 16c. This difference in times is caused by the fact that in the horizontal immersion mode, the time for the total immersion of the sample is less than that for the the horizontal way, exposing a greater heat transfer area that accelerates the cooling process of the entire piece in relation to the vertical immersion, and reaching major cooling rates; see Figure 16c,d. In Figure 16a,b (V-WQ), it can be observed that there are a few critical zones that can compromise the integrity of the entire piece, and the magnitudes of the stresses in these zones are found between 800 and 1100 MPa; in contrast, observe zone P4, where even though it underwent a quick cooling process, it was not exposed to a sustained thermal gradient such as that in zones P1–P3, which developed high values for stress. On the contrary, the horizontal mode immersion in Figure 16c,d, shows a major number of

zones with elevated stress values along the whole piece due to the immersion condition. The magnitudes of such stresses are in the range of 750–1100 MPa and are found in all the geometrical concentrators (sharp edges corners), unlike the vertical immersion case.

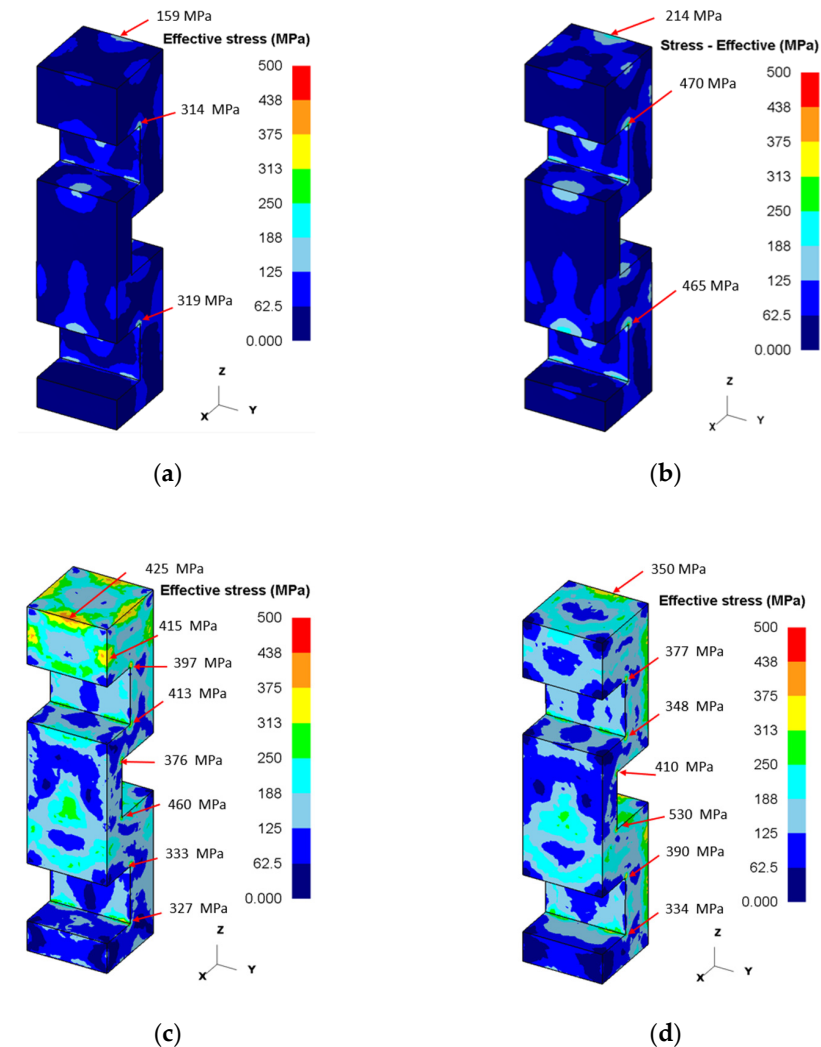


Figure 15. Final stress profiles after quench: (a) vertical oil quench; (b) horizontal oil quench; (c) vertical water quench; and (d) horizontal water quench.

Most of the steels are susceptible to fragilization when they are exposed to severe temperature changes, such as those in the quenching process. In this research, the formation of cracks in the water-quenched samples was detected for both modes of immersion, and this effect was not observed in the oil-quenched samples. In Figure 17 are shown some images of fractures found in a full section cut along the “z” axis during the metallographic preparation of the pieces; in both cases, they were of the intergranular type, finding their origins in the surface with a propagation direction towards the core of the samples.

The appearance and location of the cracks could be explained from the previously exposed results in which the evolution of the residual stresses are related to the occurrence time, therefore reaching values close to the yield limit of AISI 4340 steel in the quenched condition, as reported by Li [41]. It is possible that the real stresses in the pieces are bigger than the calculated values by the FEM model; however, such simulated stresses predict the zones of the piece where the material is prone to fail and correspond to the zones of high thermal gradients and geometric concentrators. Because of this, the accuracy of the model is able to be improved in future works, including the experimental measurement data of residual stresses, the mechanical properties, and heat transference coefficient optimization.

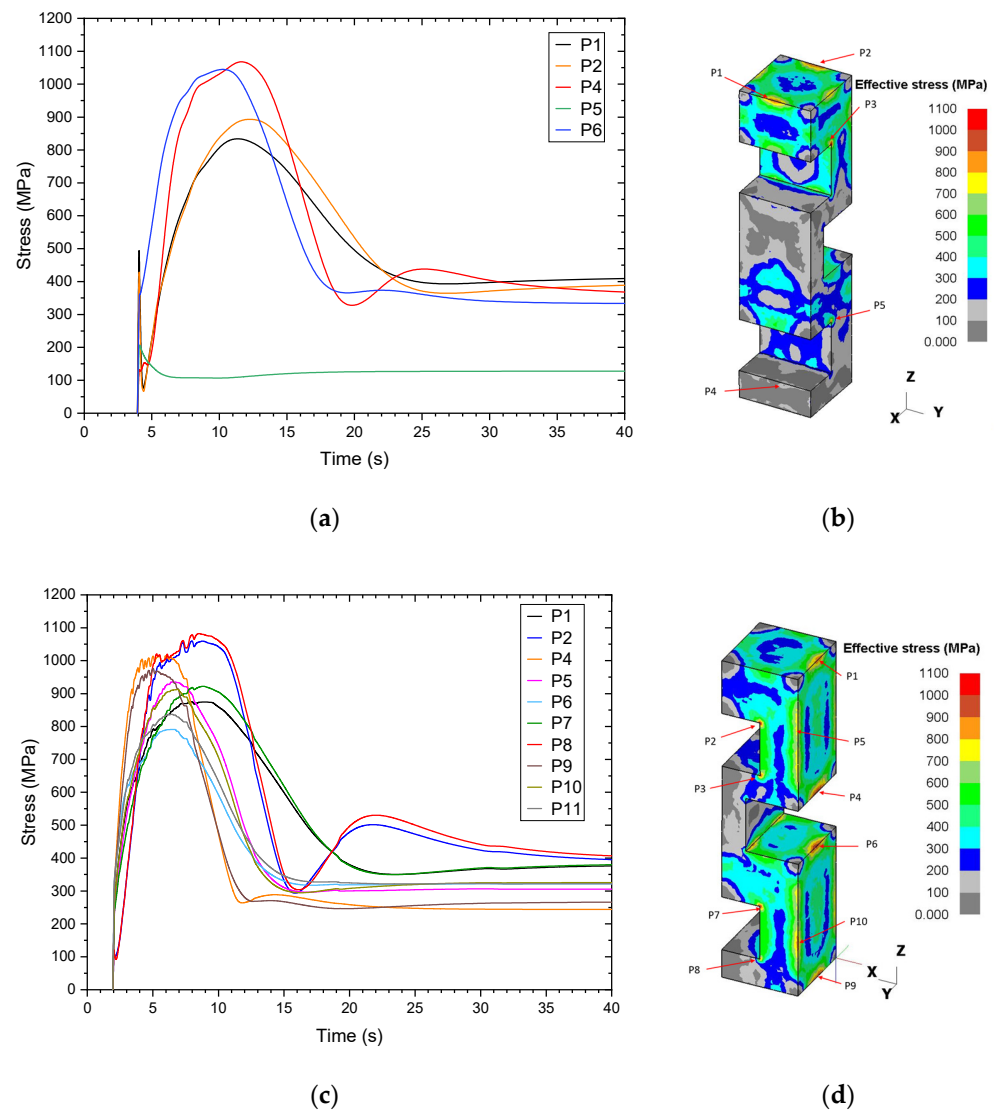


Figure 16. Stress evolution during quenching: (a) internal stress vs quenching time in V-WQ sample; (b) stress profile at 10 s after quenching starts in V-WQ sample; (c) internal stress vs. quenching time in H-WQ sample; (d) stress profile at 7 s after quenching starts in H-WQ sample.

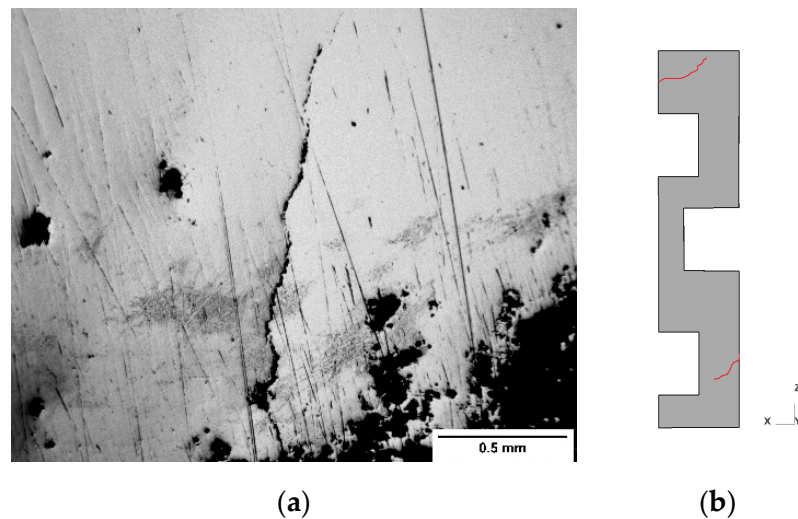


Figure 17. Cont.

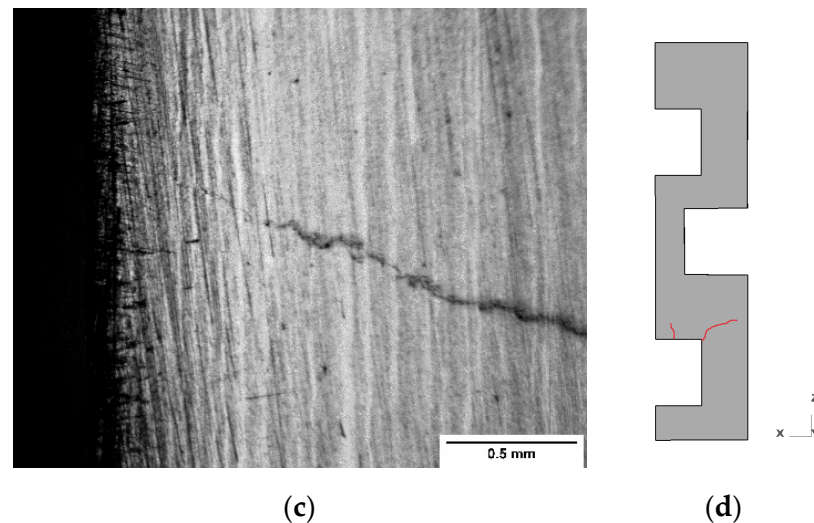


Figure 17. Developed cracks during water quenching: (a) V-WQ sample crack; (b) location of V-WQ crack; (c) H-WQ sample crack; and (d) location of H-WQ crack.

5. Conclusions

Quenching heat treatment was characterized under controlled conditions relying on an FEM model which is able to reproduce the thermal history, phase transformations, hardness, and the formation of residual stresses during the simulated quenching process of a geometrically complex piece of AISI 4340 steel. The direction of immersion and the cooling media used were the studied variables. Considering the obtained results, it can be concluded:

- The highest magnitude of thermal gradients was present when using water as the cooling medium and the direction of horizontal immersion, increasing the presence of high values of stress with thermal origin and decreasing the dimensional precision and its mechanical properties;
- There are favorable conditions during the quenching process to reduce those phenomena that affect the quality of the quenched pieces. The condition of vertical immersion and the employment of oil at 60 °C presented a lower magnitude of effective stresses according to the FEM model used, as well as more minor distortion and higher hardness values when compared with the horizontal immersion in both quenching media;
- The present research allowed us to analyze the distortion behavior in a geometrically non-conventional piece under two different quenching media using FEM modeling, becoming a potent tool in the design of heat treatments for real engineering elements with complex geometries;
- Once certain variables have been defined, such as the immersion direction and the quenching media, in which a low level of residual stresses and distortion can be obtained, it is advisable to continue researching other critical conditions in the process that contribute to reducing and predicting the distortion and cracking in quenched steels.

Author Contributions: Conceptualization, R.D.L.-G. and I.M.-J.; methodology, R.D.L.-G. and I.M.-J.; formal analysis, R.D.L.-G., I.M.-J. and A.M.-R.; investigation, I.M.-J.; resources, R.D.L.-G.; writing—original draft preparation, R.D.L.-G., I.M.-J. and A.M.-R.; writing—review and editing, R.D.L.-G., I.M.-J. and A.M.-R.; supervision, I.M.-J.; project administration, R.D.L.-G. and I.M.-J.; funding acquisition, R.D.L.-G. All authors have read and agreed to the published version of the manuscript.

Funding: This research was funded by Tecnológico Nacional de México under the grant number 11358.21-P.

Institutional Review Board Statement: Not applicable.

Informed Consent Statement: Not applicable.

Data Availability Statement: Not applicable.

Acknowledgments: The authors are very grateful to the Tecnológico Nacional de México campus Ciudad Victoria for the use of its facilities and laboratories.

Conflicts of Interest: The authors declare no conflict of interest.

References

1. Denis, S.; Sjöström, S.; Simon, A. Coupled Temperature, Stress, Phase Transformation Calculation; Model Numerical Illustration of the Internal Stresses Evolution During Cooling of a Eutectoid Carbon Steel Cylinder. *Metall. Trans. A Phys. Metall. Mater. Sci.* **1987**, *18*, 1203–1212. [CrossRef]
2. Li, Z.; Freborg, A.M.; Hansen, B.D.; Srivatsan, T.S. Modeling the Effect of Carburization and Quenching on the Development of Residual Stresses and Bending Fatigue Resistance of Steel Gears. *J. Mater. Eng. Perform.* **2012**, *22*, 664–672. [CrossRef]
3. Šolić, S.; Podgornik, B.; Leskovek, V. The occurrence of quenching cracks in high-carbon tool steel depending on the austenitizing temperature. *Eng. Fail. Anal.* **2018**, *92*, 140–148. [CrossRef]
4. Da Silva, A.; Pedrosa, T.; Gonzalez-Mendez, J.; Jiang, X.; Cetlin, P.; Altan, T. Distortion in quenching an AISI 4140 C-Ring—Predictions and experiments. *Mater. Des.* **2012**, *42*, 55–61. [CrossRef]
5. Jami, M.; Gil, E.; Ushiña, E.; Cabrera, V.H.; Cartagena, A. Determine hardness and torsional resistance of AISI/SAE 4340 steel, treated by quenching at 860 °C and tempering at 300 °C, 350 °C and 400 °C. *Mater. Today Proc.* **2021**, *49*, 35–42. [CrossRef]
6. Fakir, R.; Barka, N.; Brousseau, J.; Caron-Guillemette, G. Analysis of the Mechanical Behavior of AISI 4340 Steel Cylindrical Specimens Heat Treated with Fiber Laser. *J. Manuf. Process.* **2020**, *55*, 41–56. [CrossRef]
7. Huang, D.; Arimoto, K.; Lee, K.; Lambert, D.; Narazaki, M. Prediction of Quench Distortion on Steel Shaft with Keyway by Computer Simulation. In Proceedings of the ASTM Proceedings: Heat Treating, St. Louis, MO, USA, 9–12 October 2000; pp. 708–712.
8. Watanabe, K.; Yamada, M.; Nakasaki, M.; Matsumoto, R.; Utsunomiya, H. Determination of Transformation Transformation Plasticity Plasticity Coefficient of Steel Steel by Horizontal Quenching of Shaft. *Procedia Manuf.* **2020**, *50*, 498–502. [CrossRef]
9. De Oliveira, W.P.; Savi, M.A.; Pacheco, P.M.C.L. Finite element method applied to the quenching of steel cylinders using a multi-phase constitutive model. *Arch. Appl. Mech.* **2013**, *83*, 1013–1037. [CrossRef]
10. Kang, S.-H.; Im, Y.-T. Three-dimensional thermo-elastic-plastic finite element modeling of quenching process of plain-carbon steel in couple with phase transformation. *Int. J. Mech. Sci.* **2007**, *49*, 423–439. [CrossRef]
11. He, L.; Li, H. FEM simulation of quenching residual stress for the plane strain problems. In Proceedings of the 2010 International Conference on Computer Design and Applications, Qinhuaangdao, China, 25–27 June 2010; Volume 3, pp. 119–123. [CrossRef]
12. Decroos, M.; Seefeldt, M. The Effect of Size on the Distortion Behavior After Carburisation and Quenching Processes of Gears. *Int. J. Met. Mater. Eng.* **2017**, *139*, 1–10. [CrossRef]
13. Jung, M.; Kang, M.; Lee, Y.-K. Finite-element simulation of quenching incorporating improved transformation kinetics in a plain medium-carbon steel. *Acta Mater.* **2012**, *60*, 525–536. [CrossRef]
14. Basak, A.; Levitas, V.I. Finite element procedure and simulations for a multiphase phase field approach to martensitic phase transformations at large strains and with interfacial stresses. *Comput. Methods Appl. Mech. Eng.* **2019**, *343*, 368–406. [CrossRef]
15. Lopez-Garcia, R.D.; Garcia-Pastor, F.A.; Castro-Roman, M.J.; Alfaro-Lopez, E.; Acosta-Gonzalez, F.A. Effect of Immersion Routes on the Quenching Distortion of a Long Steel Component Using a Finite Element Model. *Trans. Indian Inst. Met.* **2016**, *69*, 1645–1656. [CrossRef]
16. Şimşir, C.; Gür, C.H. 3D FEM simulation of steel quenching and investigation of the effect of asymmetric geometry on residual stress distribution. *J. Mater. Process. Technol.* **2008**, *207*, 211–221. [CrossRef]
17. Lee, S.-J.; Lee, Y.-K. Finite element simulation of quench distortion in a low-alloy steel incorporating transformation kinetics. *Acta Mater.* **2008**, *56*, 1482–1490. [CrossRef]
18. Medina-Juárez, I.; Araujo de Oliveira, J.; Moat, R.J.; García-Pastor, F.A. On the Accuracy of Finite Element Models Predicting Residual Stresses in Quenched Stainless Steel. *Metals* **2019**, *9*, 1308. [CrossRef]
19. Şimşir, C. Modeling and Simulation of Steel Heat Treatment-Prediction of Microstructure, Distortion, Residual Stress, and Cracking. In *Steel Heat Treating Technologies*; Dossett, J.L., Totten, G.E., Eds.; ASM International: Metals Park, OH, USA, 2014; pp. 409–466. ISBN 978-1-62708-166-5.
20. Nie, Z.; Wang, G.; Lin, Y.; Rong, Y. (Kevin) Precision Measurement and Modeling of Quenching-Tempering Distortion in Low-Alloy Steel Components with Internal Threads. *J. Mater. Eng. Perform.* **2015**, *24*, 4878–4889. [CrossRef]
21. Sonar, T.; Lomte, S.; Gogte, C.; Balasubramanian, V. Minimization of Distortion in Heat Treated AISI D2 Tool Steel: Mechanism and Distortion Analysis. *Procedia Manuf.* **2018**, *20*, 113–118. [CrossRef]
22. Li, Z.; Grandhi, R.V.; Srinivasan, R. Distortion minimization during gas quenching process. *J. Mater. Process. Technol.* **2006**, *172*, 249–257. [CrossRef]
23. Li, Z.; Zhan, M.; Fan, X.; Wang, X.; Ma, F.; Li, R. Multi-mode distortion behavior of aluminum alloy thin sheets in immersion quenching. *J. Mater. Process. Technol.* **2019**, *279*, 116576. [CrossRef]
24. Farivar, H.; Prah, U.; Hans, M.; Bleck, W. Microstructural adjustment of carburized steel components towards reducing the quenching-induced distortion. *J. Mater. Process. Technol.* **2019**, *264*, 313–327. [CrossRef]

25. Cho, J.; Kang, W.; Kim, M.; Lee, J.; Lee, Y.; Bae, W. Distortions induced by heat treatment of automotive bevel gears. *J. Mater. Process. Technol.* **2004**, *153*, 476–481. [CrossRef]
26. Bouissa, Y.; Bohlooli, N.; Shahriari, D.; Champiaud, H.; Morin, J.-B.; Jahazi, M. FEM modeling and experimental validation of quench-induced distortions of large size steel forgings. *J. Manuf. Process.* **2020**, *58*, 592–605. [CrossRef]
27. Nallathambi, A.K.; Kaymak, Y.; Specht, E.; Bertram, A. Sensitivity of material properties on distortion and residual stresses during metal quenching processes. *J. Mater. Process. Technol.* **2010**, *210*, 204–211. [CrossRef]
28. ASTM Standard E3. In *Standard Guide for Preparation of Metallographic Specimens*; ASTM International: West Conshohocken, PA, USA, 2017.
29. ASTM Standard E407. In *Standard Practice for Microetching Metals and Alloys*; ASTM International: West Conshohocken, PA, USA, 2017.
30. Mirzakhani, S.; Javanbakht, M. Phase Field-Elasticity Analysis of Austenite-Martensite Phase Transformation at the Nanoscale: Finite Element Modeling. *Comput. Mater. Sci.* **2018**, *154*, 41–52. [CrossRef]
31. Feulvarch, E.; Fontaine, M.; Bergheau, J.-M. XFEM investigation of a crack path in residual stresses resulting from quenching. *Finite Elements Anal. Des.* **2013**, *75*, 62–70. [CrossRef]
32. Fourier, J.B.J. *Théorie Analytique de La Chaleur*; Cambridge University Press: Cambridge, UK, 2009; ISBN 9780511693229.
33. Johnson, W.A. Reaction Kinetics in Processes of Nucleation and Growth. *Am. Inst. Min. Met. Petro. Eng.* **1939**, *135*, 416–458.
34. Avrami, M. Kinetics of Phase Change. I General Theory. *J. Chem. Phys.* **1939**, *7*, 1103–1112. [CrossRef]
35. Koistinen, D.P.; Marburger, R.E. A general equation prescribing the extent of the austenite-martensite transformation in pure iron-carbon alloys and plain carbon steels. *Acta Metall.* **1959**, *7*, 59–60. [CrossRef]
36. Todinov, M.T. Mechanism for formation of the residual stresses from quenching. *Model. Simul. Mater. Sci. Eng.* **1998**, *6*, 273–291. [CrossRef]
37. Vander Voort, G.F. *Atlas of Time-Temperature Diagrams for Irons and Steels*; ASM International: Metals Park, OH, USA, 1991; ISBN 978-0871704153.
38. JMatPro 13.0 Demo Version. Available online: <https://www.sentsoftware.co.uk/demo> (accessed on 20 March 2022).
39. Buczek, A.; Telejko, T. Investigation of heat transfer coefficient during quenching in various cooling agents. *Int. J. Heat Fluid Flow* **2013**, *44*, 358–364. [CrossRef]
40. Sugianto, A.; Narazaki, M.; Kogawara, M.; Shirayori, A. Validity of Heat Transfer Coefficient Based on Cooling Time, Cooling Rate, and Heat Flux on Jominy End Quench Test. In *Proceedings of the MS&T 2007, Materials Science and Technology*, Detroit, MI, USA, 16–20 September 2007; pp. 171–180.
41. Li, H.F.; Duan, Q.Q.; Zhang, P.; Zhang, Z.F. The Relationship between Strength and Toughness in Tempered Steel: Trade-off or Invariable? *Adv. Eng. Mater.* **2019**, *21*, 1801116. [CrossRef]

Article

Web Bend-Buckling of Steel Plate Girders Reinforced by Two Longitudinal Stiffeners with Various Cross-Section Shapes

Yongli Peng ¹, Zhengyi Kong ², Ba Huu Dinh ³, Huu-Hue Nguyen ⁴, Truong-Son Cao ⁴, George Papazafeiropoulos ^{5,*} and Quang-Viet Vu ^{6,*}

¹ Department of Civil Engineering, Ma'anshan University, Ma'anshan 243100, China

² Department of Civil Engineering, Anhui University of Technology, Ma'anshan 243032, China

³ Department of Civil Engineering, Chonnam National University, Yongbong-ro 77, Buk-gu, Gwangju 61186, Korea

⁴ Faculty of Civil Engineering, Thuyloi University, 175 Tay Son, Dong Da, Hanoi 100000, Vietnam

⁵ Department of Structural Engineering, National Technical University of Athens, Zografou, 15780 Athens, Greece

⁶ Faculty of Civil Engineering, Vietnam Maritime University, 484 Lach Tray Street, Le Chan District, Hai Phong 180000, Vietnam

* Correspondence: gpapazafeiropoulos@yahoo.gr (G.P.); vietvq@vimaru.edu.vn (Q.-V.V.); Tel.: +30-6983507762 (G.P.); +84-974-282222 (Q.-V.V.)

Abstract: This work performs an investigation into the optimal position of two longitudinal stiffeners with different cross-section shapes such as open section (L-shaped and T-shaped) and closed section (rectangular and triangular shapes) shapes of stiffened plate girders under bending loading through an optimization procedure using a gradient-based interior point (IP) optimization algorithm. The stiffener optimum locations are found by maximizing the bend-buckling coefficient, k_b , generated from eigenvalue buckling analyses in Abaqus. The optimization procedure efficiently combines the finite element method and the IP optimization algorithm and is implemented using the Abaqus2Matlab toolbox which allows for the transfer of data between Matlab and Abaqus and vice versa. It is found that the proposed methodology can lead to the optimum design of the steel plate girder for all stiffener cross-section types with an acceptable accuracy and a reduced computational effort. Based on the optimization results, the optimum positions of two longitudinal stiffeners with various cross-section shapes are presented for the first time. It is reported that the optimum locations of two longitudinal stiffeners with open cross-section shapes (T- and L-shaped) are similar to that of flat cross-section, while the optimum positions of two longitudinal stiffeners with closed cross-section types (rectangular and triangular sections) are slightly different. One of the main findings of this study is that the bend-buckling coefficient of the stiffened girder having stiffeners with triangular cross-section shape is highest while that with flat cross-section shape is lowest among all considered stiffener types and this latter case has minimum requirement regarding the web thickness.

Citation: Peng, Y.; Kong, Z.; Dinh, B.H.; Nguyen, H.-H.; Cao, T.-S.; Papazafeiropoulos, G.; Vu, Q.-V. Web Bend-Buckling of Steel Plate Girders Reinforced by Two Longitudinal Stiffeners with Various Cross-Section Shapes. *Metals* **2023**, *13*, 323. <https://doi.org/10.3390/met13020323>

Academic Editor: Xin Chen

Received: 11 January 2023

Revised: 31 January 2023

Accepted: 2 February 2023

Published: 5 February 2023

Keywords: Abaqus2Matlab; longitudinal stiffeners; optimization procedure; steel plate girders; web bend-buckling



Copyright: © 2023 by the authors. Licensee MDPI, Basel, Switzerland. This article is an open access article distributed under the terms and conditions of the Creative Commons Attribution (CC BY) license (<https://creativecommons.org/licenses/by/4.0/>).

1. Introduction

Longitudinal stiffeners have been extensively used to improve the buckling strength of steel plates or steel plate girders subject to different loading conditions such as compression, patch loading, combined bending and shear, pure bending, etc. As a result of the significant increase in strength that stiffeners offer when placed at steel plates or steel plate girders, research related to members of this type has been widely conducted. Regarding steel plates reinforced by one or more longitudinal stiffeners under compression, Haffar et al. [1] proposed two new mathematical models for buckling resistance prediction of a steel plate with a closed longitudinal stiffener. Both proposed methods gave similar results, leading to load resistance values of satisfactory precision. Kovesdi et al. [2] investigated the

buckling resistance of longitudinally stiffened plates subjected to compression using the shell finite element (FE) method. The author suggested an alternative design procedure to improve the economy of the practical design. Regarding plate girders under patch loading, Loaiza et al. [3] investigated buckling and post buckling behavior of longitudinally stiffened I-girders using an FE simulation. Various hypotheses regarding the effect of vertical and out-of-plane displacements of the web panel on the determination of the critical buckling load of the stiffened plate girder were taken into consideration. The analysis results showed that a full restriction of the vertical and out-of-plane displacements at the stiffener location led to improved patch load resistance at the ultimate load level. Demari et al. [4] performed a numerical study of slender I-girders strengthened with one longitudinal stiffener under patch loading. They reported that the optimum stiffener location for patch loading resistance is closer to the loaded flange when compared to girders under pure bending. Recently, based on an experimental database, Truong et al. [5] proposed an efficient machine learning method, namely the XGBoost algorithm, for predicting the patch load resistance of longitudinally stiffened plate girders. The efficiency and accuracy of the proposed method were demonstrated by comparing its performance with other machine learning methods as well as design equations from the existing standards. Regarding stiffened girders under combined bending and shear, by analyzing various FE models, Truong et al. [6] investigated the influence of multiple longitudinal stiffeners on the ultimate strength of plate girders. It was reported in this research that the variation in the ultimate strength of the girder was almost constant against the various dimensionless geometric parameters. Chen and Yuan [7] conducted a comprehensive experimental and numerical investigation into the local buckling behavior of longitudinally stiffened stainless steel plate girders subjected to combined bending and shear loading. It was observed that the existing M–V interaction curves recommended in EN 1993-1-4 for determining the bending and shear endpoints provide safe-sided estimations with a good level of consistency and accuracy for such structures.

Regarding the case of stiffened girders subjected to pure bending loads, in recent decades, longitudinal stiffeners have been widely utilized in girder webs to enhance the bending strength of the stiffened girder with slender sections. It has been reported that longitudinal stiffeners with various cross-section types, consisting of open cross-sections (flat, T, and L sections) and closed sections (rectangular, triangular, and trapezoidal sections) have been used for this purpose. Research related to the bending response of plate girders strengthened by longitudinal stiffeners has been extensively conducted all over the world, especially for flat stiffeners. Regarding the optimization problem of a single longitudinal stiffener with a flat cross-section, many researchers have proposed that the optimum position of a single longitudinal stiffener is placed at $0.2D$ from the girder compression flange (D is the depth of girder web), assuming the longitudinal edges of the girder web are simply supported [8–11]. Recently, through the finite element method, several researchers have found that the optimum location of a single stiffener for the stiffened girder under bending loading is at about $0.42D_c$ from the compression flange (D_c is the depth of girder web in compression), regardless of any asymmetric cross-section [12–15]. By investigating the elastic bend-buckling response of symmetric and asymmetric I-section girders with a single longitudinal stiffener using FE modeling, Cho and Shin [16] suggested the optimum stiffener position to be $0.425D_c$ from the compression flange. These optimal values are slightly different with those mentioned in AASHTO LRFD [17], in which the optimum stiffener position is at $0.4D_c$. On the other hand, research related to the optimization problems of multiple longitudinal stiffeners are still limited in the literature. Based on theoretical solutions, Rockey and Cook [18,19] proposed an optimum placement of multiple longitudinal stiffeners with flat cross-section plate girders. It was reported in these studies that the boundary conditions of longitudinal edges of the girder web were presumed to be either simply supported or clamped, whilst its vertical edges were assumed to be simply supported. By using numerical simulations, Kim et al. [20] proposed the optimum placement of two stiffeners with a flat cross-section girder under bending. An empirical

formula to calculate the buckling coefficient of the stiffened girder under bending was recommended as well. Kim et al. [15] conducted a comprehensive work related to the optimum location of a single and two longitudinal stiffener(s) of a stiffened girder subjected to pure bending. Finally, the optimum stiffener locations and the minimum flexural rigidity for both the single and two stiffener(s) were suggested and presented a good comparison with the previous works. All the research mentioned above adequately provided the optimum position of a stiffener with a flat shape.

Furthermore, research related to the optimal stiffener position considering various stiffener cross-section types is still limited. Through finite element analysis, Maiorana et al. [21] investigated the buckling behavior of stiffened plate subjected to bending loading. Based on analysis results, the authors suggested the optimum position for all considered cross-section types of the stiffeners (flat, T, L, rectangular, triangular, and trapezoidal sections) to be at $0.2D$. However, the presence of flanges of the girder affecting the bend-buckling response and optimal stiffener placement was not taken into consideration. Recently, George et al. [22] suggested the optimal location of a single stiffener with open and closed cross-section types for stiffened girders subjected to bending loading. The presence of girder flanges was taken into consideration. However, the optimum location of two longitudinal stiffeners with various cross-section shapes has not been considered elsewhere.

Although the issue of the optimum stiffener position on steel plate girders has been addressed as mentioned in the previous paragraphs, consideration of multiple stiffeners has been limited only to flat stiffener shapes, whereas the studies that have investigated the effect of the stiffener shape on the buckling response of the girder have not taken into account the case of two or more stiffeners. This work tries to bridge this research gap, i.e., explore the case of multiple stiffeners with various cross-section shapes and their effect on the buckling load capacity and design efficiency of the steel plate girder. In this study, the optimal positions of two longitudinal stiffeners with open and closed section types along the web height of the stiffened girder subjected to bending loading are investigated by maximizing the critical buckling load of the latter. We develop various optimum designs depending on the cross-section type. The efficiency of the latter among the various aforementioned optimum designs is explored in terms of the maximum buckling coefficient and the minimum web thickness of the stiffened girder. The gradient-based interior point (IP) optimization algorithm, coupled with an appropriate FE model, is used for calculating the aforementioned optimum designs. The proposed numerical procedure proves to have low requirements in terms of implementation and computational effort, given that the Abaqus2Matlab [23] toolbox which automatically combines Abaqus [24] and Matlab [25] in a loop is employed. Based on the analysis results, the optimum stiffener locations and minimum web thickness for various stiffener types are suggested.

2. Existing Design Standards

2.1. AASHTO LRFD Standards

The AASHTO LRFD standards [17] for optimum stiffener position and the bend-buckling coefficient of a stiffened girder web were based on the research reported by Frank and Helwig [26], in which the boundary conditions of the longitudinal edges of the girder web were assumed to be simply supported at flanges, and its vertical edges were presumed to be simply supported by vertical stiffeners as well. The critical buckling load recommended by the AASHTO LRFD standards is presented in the following equation:

$$F_{crw} = \frac{0.9kE}{\left(\frac{D}{t_w}\right)^2} \quad (1)$$

where k is the bend-buckling coefficient, E represents the steel elastic modulus, D is the web depth, and t_w is the web thickness.

In the AASHTO LRFD standards, the bend-buckling coefficient was recommended as follows:

$$k = \begin{cases} \frac{11.64}{\left(\frac{D_c - d_s}{D}\right)} & \text{if } \frac{d_s}{D_c} < 0.4 \\ \frac{5.17}{\left(\frac{d_s}{D}\right)^2} & \text{if } \frac{d_s}{D_c} \geq 0.4 \end{cases} \quad (2)$$

where D_c and d_s are the web depth in compression in the elastic range and the distance of the stiffener from the compression flange, respectively. The optimum position of a single flat stiffener is at $0.4D_c$ from the compression flange, regardless of the asymmetry of the girder section. It is noted that in the AASHTO LRFD standards, Equation (2) can be conservatively utilized for girder webs with multiple longitudinal stiffeners. No specific equations were provided for girder webs with two or more stiffeners.

2.2. Eurocode 3 Standard

In the Eurocode 3 standard [27], the bending strength of the stiffened girder can be calculated by taking into consideration the combination of the effective widths of the stiffened girder web and the compression flange. In this standard, the buckling coefficients are also determined based on similar assumptions as the AASHTO LRFD standards. The bend-buckling coefficients were defined as a function of $\psi = \sigma/\sigma_c$, in which σ is the maximum stress at other web edges and σ_c represents the maximum compressive stress. The bend-buckling coefficient is given as follows:

$$k = \begin{cases} \frac{8.2}{(1.05 + \psi)} & \text{for } 0 < \psi < 1 \\ 7.81 - 6.29\psi + 9.78\psi^2 & \text{for } -1 < \psi < 1 \\ 5.98(1 - \psi)^2 & \text{for } -3 < \psi < -1 \end{cases} \quad (3)$$

The optimum position of a single stiffener is consistent with that recommended by the AASHTO LRFD standards (at $0.4D_c$ from the compression flange). However, the design philosophy for bend-buckling resistance mentioned in the Eurocode 3 standard is intrinsically different from that considered in the AASHTO LRFD standards.

3. Methodology

3.1. Elastic Buckling Analysis

In this work, a linear elastic buckling analysis is implemented for the evaluation of the critical load, F_{cr} , of the longitudinally stiffened plate girders with open (T and L sections) and closed (rectangular and triangular sections) cross-sections of the stiffeners subject to bending. The lowest positive value of λ , which is the buckling eigenvalue, called λ_{cr} , can be obtained by solving Equation (1) as follows:

$$(K + \lambda K_G)u = 0 \quad (4)$$

where K presents the model stiffness matrix, K_G is the geometric stiffness matrix, λ stands for the multiplier of the reference load pattern F , and u is the buckling mode shape.

The buckling load is computed by Equation (5) as follows:

$$F_{cr} = \lambda_{cr} F \quad (5)$$

On the other hand, based on the classical buckling theory of plates under pure compression, the critical buckling load of a plate girder under bending loading can be computed as follows:

$$F_{cr} = k_b \frac{\pi^2 E t_w^3}{12(1 - \nu^2) D} \quad (6)$$

where E represents the elastic modulus, t_w stands for the thickness of girder web, ν represents the Poisson's ratio, and D is the depth of girder web.

Based on Equations (5) and (6), the buckling coefficient, k_b , can be determined.

3.2. Problem Statement for Optimization of Longitudinally Stiffened Plate Girders

It is known that the optimum stiffener location can be obtained when the critical buckling load of a stiffened plate girder is maximized. Hence, the optimal stiffener position is determined by maximizing the bend-buckling coefficient, k_b . The optimization problem can be presented in the following form:

Find:

$$x = [d_{s1}, d_{s2}] \quad (7)$$

so that

$$k_b(x) = \frac{12(1 - \nu^2)D}{\pi^2 E t_w^3} F_{cr}(x) \quad (8)$$

is maximized, subject to:

$$0.1D \leq d_{s1} \leq 0.5D \quad (9)$$

$$0.1D \leq d_{s2} \leq 0.5D \quad (10)$$

$$d_{s2} - d_{s1} \geq 18t_w \quad (11)$$

with the following values assigned to parameters:

$$b_{s,1} = b_{s,2} = 0.08D \quad (12)$$

$$\frac{b_{s,1}}{t_{s,1}} = \frac{b_{s,2}}{t_{s,2}} = 8 \quad (13)$$

In Equations (9) and (10), the limits are selected based on structural constraints, i.e., the stiffener location cannot exceed the half-depth of the web and it must be at least 10% of the height depth apart from the compression flange. In the latter case, for lower distances from the web, it is generally preferable to increase the stiffness of the plate girder through increasing the cross-section of the compression flange rather than placing a stiffener, which will require additional material and workmanship while additionally not contributing much to the increase in the girder plate stiffness. Moreover, Equation (11) takes into account the fact that each stiffener cross-section integrates with part of the web section to which it is attached, equal to $9t_w$, as designated in AASHTO LRFD standard part 6.10.11.3.3 [17]. Equations (12) and (13) specify the dimensions of the stiffeners in relation to the web depth. The dimensions of the stiffener cross-section remain constant during the optimization procedure and are selected so that the stiffeners are assumed to form a nodal line at the stiffener–plate junction to provide the highest buckling coefficient. To ensure the condition of nodal line formation, the out of plane displacements along the nodal line are restrained. The out of plane displacements do not exceed the following nonzero positive tolerances:

$$r \leq r_{tol} \quad (14)$$

where r_{tol} represents the tolerance and the normalized parameter, r , is provided by the relation:

$$r = \frac{\max(|w_s|)}{\max(|w_w|)} \quad (15)$$

In Equation (15), w_s represents the out-of-plane displacement of the stiffener and w_w stands for the out-of-plane displacement of the girder web.

3.3. Optimization Procedure

In order to provide the solution of the optimization problem presented in Equations (4)–(7), an interior point algorithm (IPA), adopted in some references [28–30], was utilized. The optimization procedure is conducted in Abaqus [24] and Matlab [25] through Abaqus2Matlab toolbox [23,31] that integrates these software within the optimization loop. Detailed steps are presented as follows:

1. Establish a Matlab function so that an Abaqus input file (*.inp) is automatically created when it runs inside Matlab;
2. Define input variables (longitudinal stiffener positions) in the Matlab function above;
3. Define the objective function mentioned in Section 3.2 for the optimization problem;
4. Build a main Matlab function consisting of the starting point value for the solution, lower and upper bound values of the stiffener position, and an optimization algorithm (using the `fmincon` function available in Matlab). The starting point is an initial guess and can be any arbitrary selection which satisfies the lower and upper bounds as well as any other constraints that may apply;
5. Compute the objective function defined in step 3;
6. Perform the optimization procedure;
7. Check the stopping criterion. This criterion is a maximization of k_b . If the criterion is satisfied, the optimization procedure will complete. Otherwise, it will go to the next step;
8. Change the design variable value to create a new Abaqus input file;
9. Run the analysis in Abaqus again;
10. Repeat steps 6–9 until convergence is attained, satisfying the specific tolerance;
11. The optimization result obtained is the final solution.

The optimization procedure for finding the optimal position of two longitudinal stiffeners is described in Figure 1. The optimization problem is essentially convex, without any local optima. For the case of more than one stiffener, this has been suggested by simplified analytical methods published in the literature (see, e.g., [19]). It is assumed that there are no large deviations in the optimization space considered in this study from the optimization space of such simplified approaches, since their results can approximate the actual result very well. On the other hand, it has been shown in many studies (see, e.g., [32,33]) that the variation in the buckling coefficient of a plate girder with a single stiffener with varying stiffener locations does not yield local optima, and the optimum position of the single stiffener is unique. Therefore, from the aforementioned points it can be deduced that the optimum configuration in the case of two stiffeners is unique and independent of the starting guess of the solution.

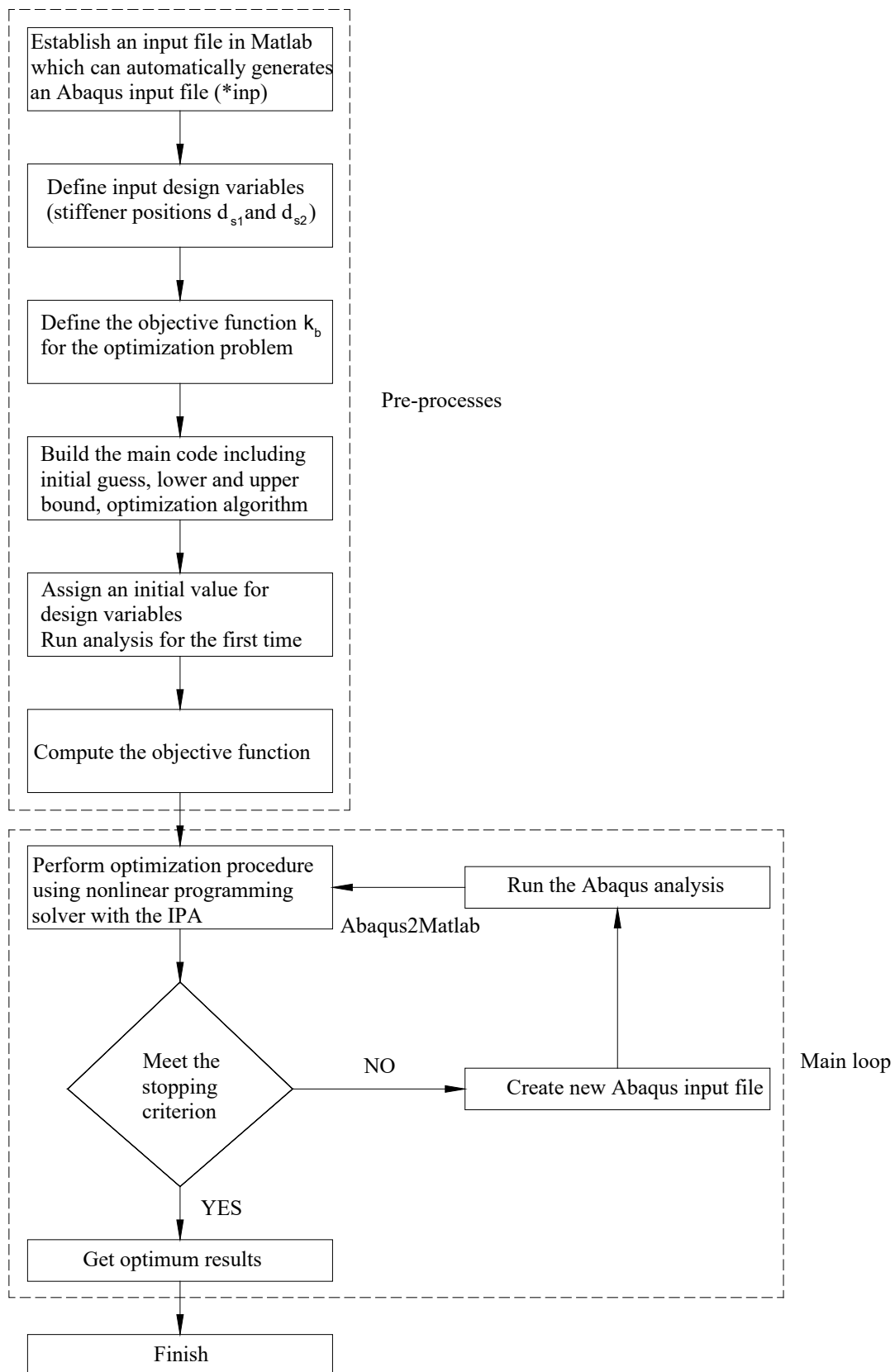


Figure 1. The optimization procedure flowchart [10,11].

4. Finite Element Modeling

The bend-buckling behavior of a stiffened plate girder presented in Figure 2 was computed based on finite element (FE) analysis of the structure using ABAQUS commercial software [24]. In this work, FE models of the girder with two longitudinal stiffeners with open (T-shaped and L-shaped) and closed (triangular and rectangular) cross-sections are based on the FE model mentioned in [14,15,22,34]. For instance, all descriptions of geometric dimensions of the girder (except the dimensions of longitudinal stiffeners), material properties, and FE modeling procedure are consistent with those of model 2 reported in [14,15]. Particularly, the web depth was selected as 3.0 m, while the web thickness was 9.0 mm. The flange width and flange thickness were 600 mm and 54 mm, respectively. The length-to-depth ratio (panel aspect ratio) of the girder was chosen to be 1.0. All materials were considered to be in the elastic range with an elastic modulus of 210 GPa and a Poisson's ratio of 0.3. The vertical edges of the girder web were assumed to be simply supported. All elements were simulated using 4-node shell elements S4R with a mesh size of 40 mm [14,15]. Figures 3 and 4 display the loading and boundary conditions for all stiffener cross-section types. Based on these FE models developed and the procedure mentioned in Section 3.3, the optimum stiffener position of two longitudinal stiffeners with open and closed cross-sections will be investigated in Sections 5 and 6 of this study. It is noted that, although the load distribution, which is specified in the Abaqus model, follows the linear shape which appears in Figure 3, in Figure 4, due to the notation followed in Abaqus/CAE interface, the length of the force vectors appears as fixed for visualization purposes.

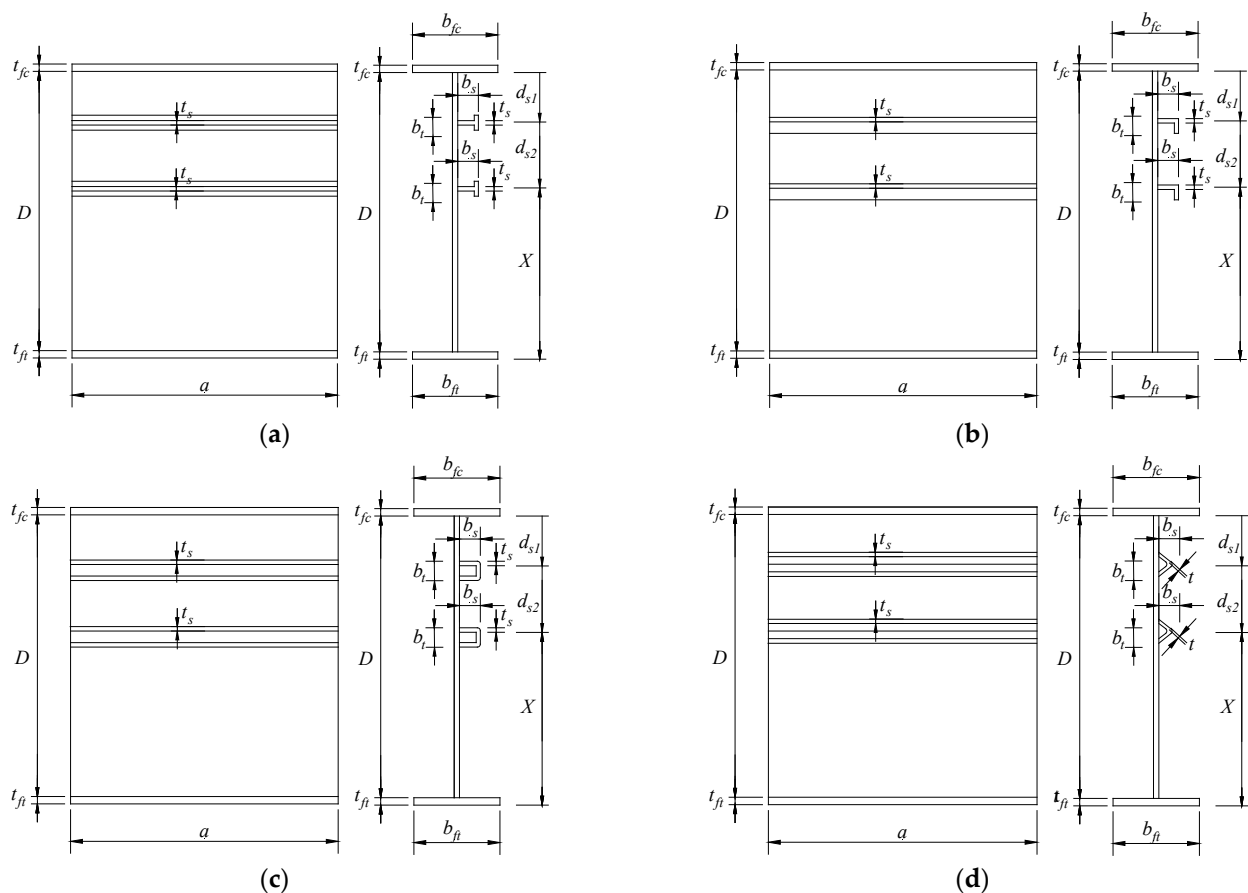
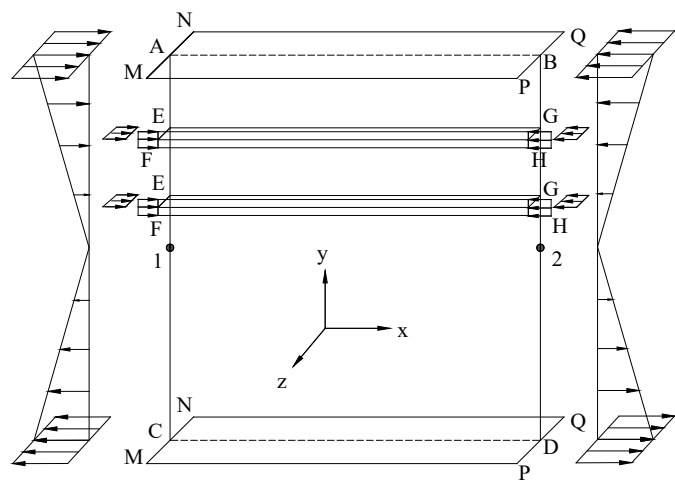
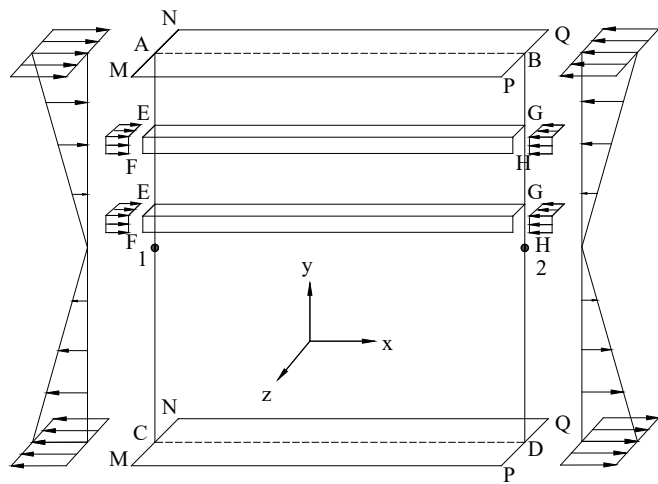


Figure 2. Geometric dimensions of stiffened plate girders with various stiffener cross-section shapes. (a) T-shaped; (b) L-shaped; (c) Rectangular-shaped; (d) Triangular-shaped.



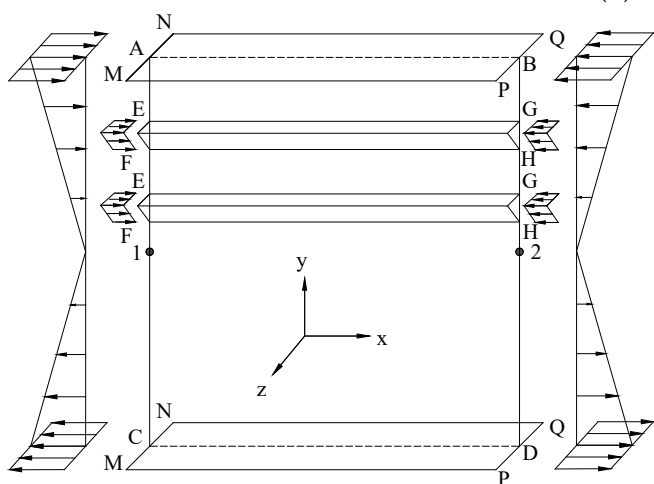
Edge	U_x	U_y	U_z	θ_x	θ_y	θ_z
AB & CD	-	-	-	-	-	-
AC & BD	-	-	R	-	-	-
MN & PQ	-	-	R	R	R	-
EF & GH	-	-	R	R	R	-
Point 1	R	R	-	-	-	-
Point 2	-	R	-	-	-	-
-	Free		R Restrained			

(a)



Edge	U_x	U_y	U_z	θ_x	θ_y	θ_z
AB & CD	-	-	-	-	-	-
AC & BD	-	-	R	-	-	-
MN & PQ	-	-	R	R	R	-
EF & GH	-	-	R	R	R	-
Point 1	R	R	-	-	-	-
Point 2	-	R	-	-	-	-
-	Free		R Restrained			

(b)



Edge	U_x	U_y	U_z	θ_x	θ_y	θ_z
AB & CD	-	-	-	-	-	-
AC & BD	-	-	R	-	-	-
MN & PQ	-	-	R	R	R	-
EF & GH	-	-	R	R	R	-
Point 1	R	R	-	-	-	-
Point 2	-	R	-	-	-	-
-	Free		R Restrained			

(c)

Figure 3. Cont.

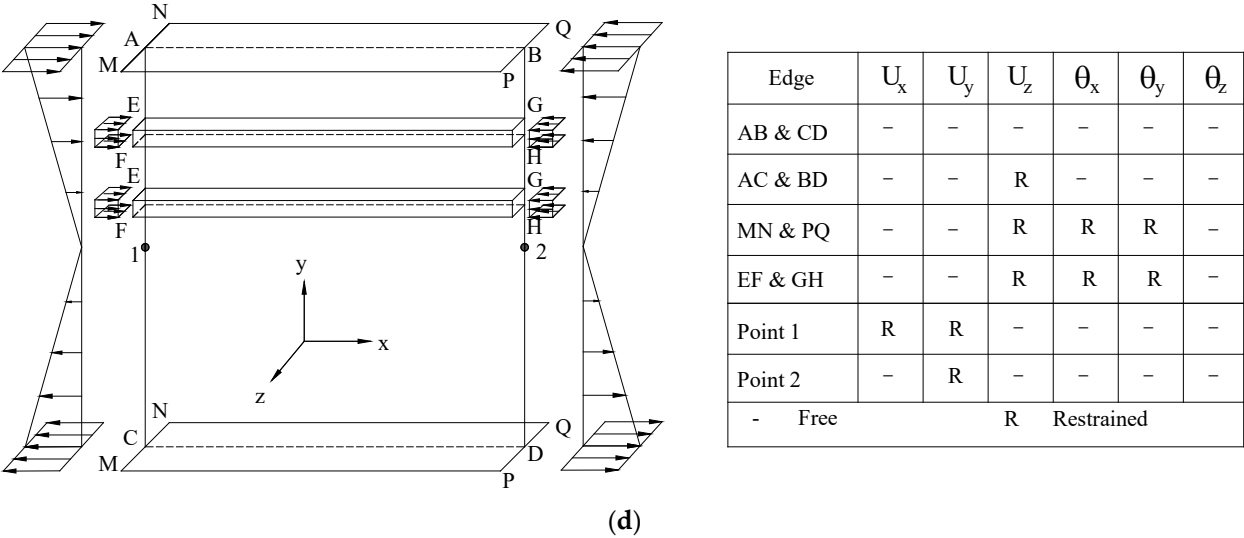


Figure 3. Loading and boundary conditions for various plate girder configurations: (a) T section, (b) L section, (c) triangular section, (d) rectangular section.

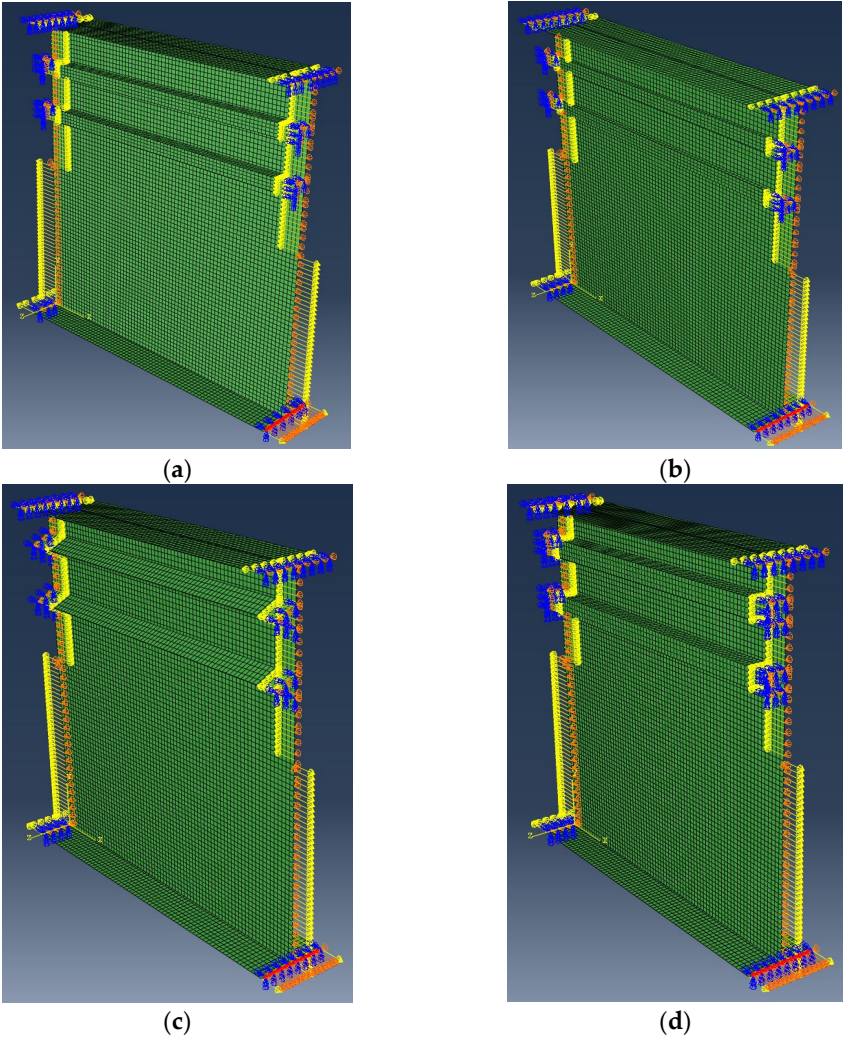


Figure 4. Loading and boundary conditions for various plate girder configurations in Abaqus: (a) T section, (b) L section, (c) triangular section, (d) rectangular section.

5. Optimum Location of 2 Stiffeners with Open Cross-Section Types

In this section, the optimization procedure presented in Section 3.3 is employed for finding the optimal positions of two longitudinal stiffeners with open cross-section types (T and L sections) along the web depth of the stiffened girder subjected to pure bending loading.

The optimum placement of two stiffeners having flat, T-shaped and L-shaped cross-sections is presented in Table 1, in which the results for the flat shape were taken from Kim et al. [15] for comparison. The aspect ratio of the panel ($\varphi = a/D$) was fixed as 1.0 and the slenderness ratio of girder web (D/t_w) was fixed as 333 for all stiffener cross-section types. From Table 1, it can be observed that the optimal positions of longitudinal stiffeners 1 and 2 for both T-shaped and L-shaped cross-sections are at around $0.25D_c$ and $0.55D_c$, respectively. It is apparent that the optimum values are similar with those obtained for the flat stiffener cross-section type reported by Kim et al. [15]. In addition, it can be observed that the buckling coefficient, k_b , of the stiffener with a T-shaped cross-section is slightly higher than that of the stiffener with an L-shaped cross-section. However, both stiffeners with T-shaped and L-shaped cross-sections yield much higher buckling coefficients compared with the flat cross-section. Therefore, using stiffeners with T-shaped or L-shaped cross-sections significantly enhances the bend-buckling strength of the stiffened plate girder compared to stiffeners with a flat cross-section. Figure 5 shows the convergence history for stiffeners with open cross-section shapes, while Figure 6 shows the mode shapes of the girders with stiffeners of T-shaped and L-shaped cross-section types obtained from the optimization procedure.

Table 1. Optimal values for two longitudinal stiffeners for both cross-section types.

Stiffener Type	φ	d_{s1}/D_c	d_{s2}/D_c	k_b	Note
Flat-shaped	1.0	0.244	0.566	437.02	[15]
T-shaped	1.0	0.25	0.55	501.62	Present study
L-shaped	1.0	0.25	0.55	500.25	Present study

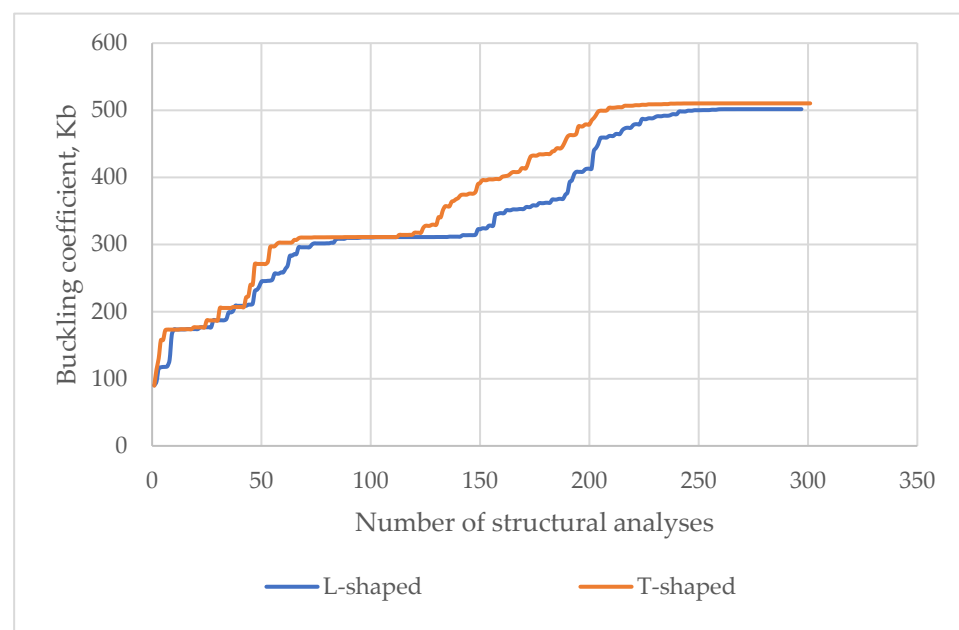


Figure 5. Convergence history for stiffeners with open cross-section shapes.

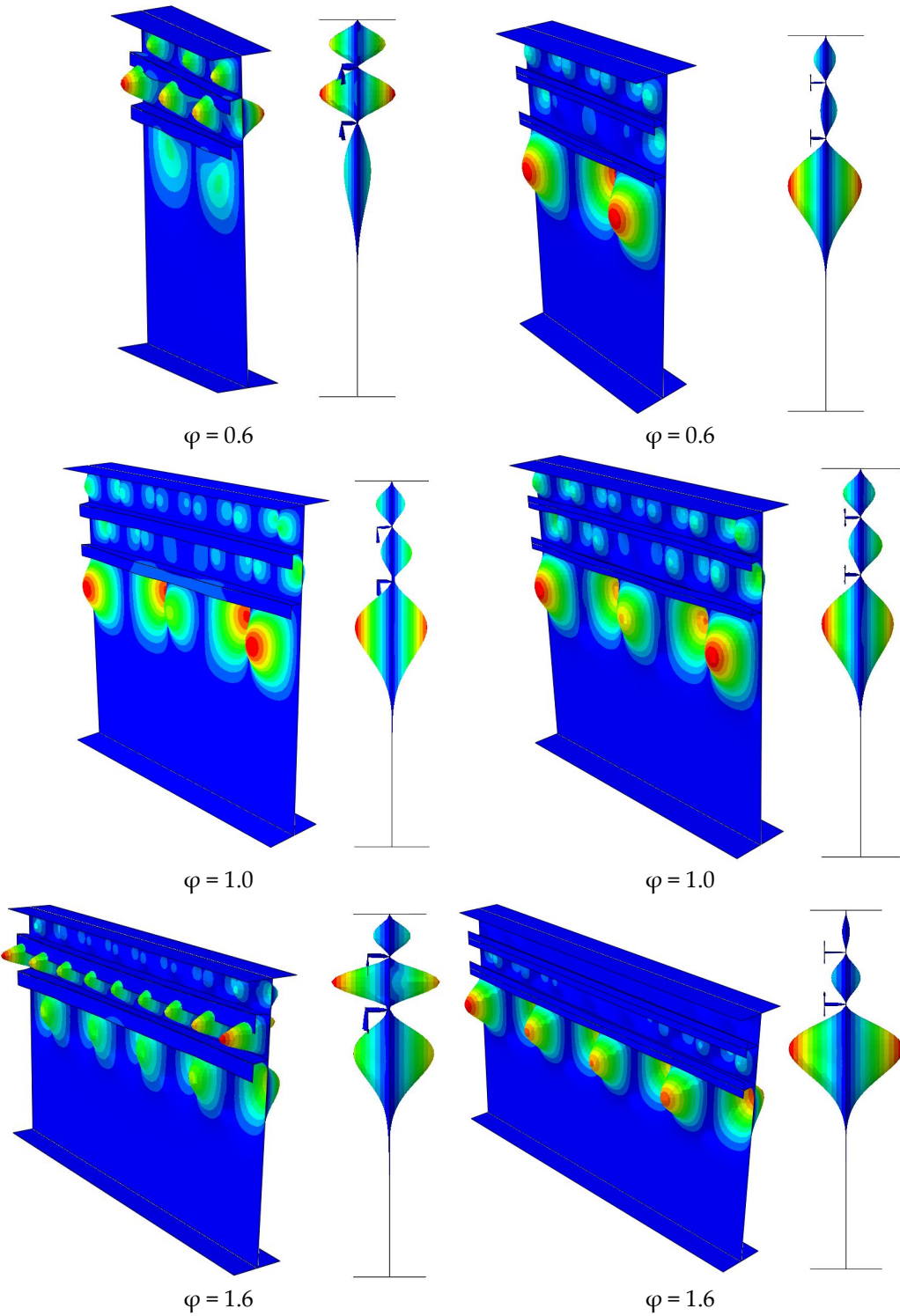


Figure 6. Cont.

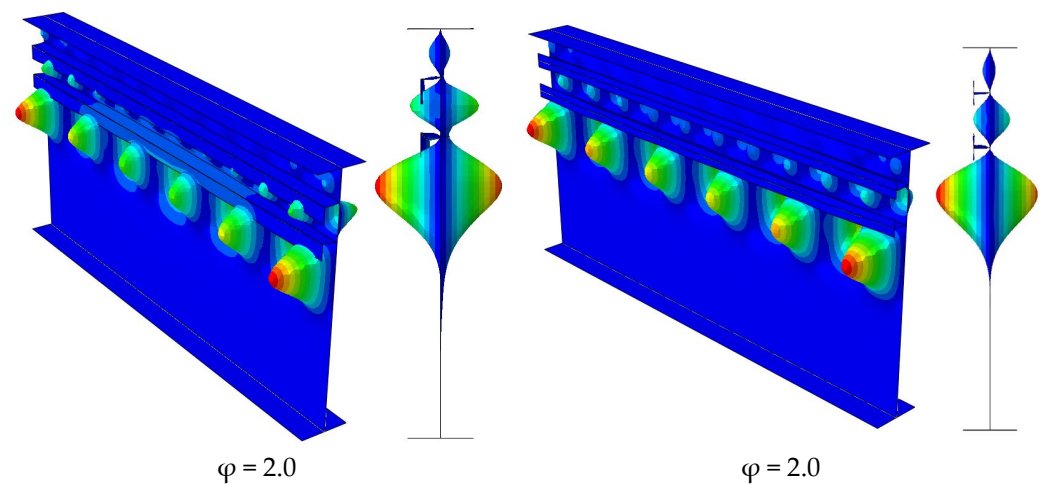


Figure 6. Buckling mode shapes of the stiffened girder with T-shaped and L-shaped stiffeners.

Table 2 discloses the effect of the panel aspect ratio on the optimal stiffener locations with the aspect ratios of 0.6, 1.0, 1.6, and 2.0. It can be seen that there is only a small effect of the panel aspect ratio on the optimal stiffener locations for both stiffener types. It was also observed that the buckling coefficients of the stiffeners corresponding to $\varphi = 0.6$ and $\varphi = 1.0$ were almost identical, while the buckling coefficients of the stiffeners corresponding to $\varphi = 1.6$ and $\varphi = 2.0$ were almost identical as well. The reason is because the flexural rigidity used for the stiffeners with $\varphi = 1.6$ and 2.0 is higher than that for the stiffeners with $\varphi = 0.6$ and 1.0.

Table 2. Effect of panel aspect ratio on the optimum stiffener locations.

φ	Stiffener Type	d_{s1}/D_c	d_{s2}/D_c	k_b
0.6	T-shaped	0.25	0.55	501.48
	L-shaped	0.25	0.55	500.1
1.0	T-shaped	0.25	0.55	501.62
	L-shaped	0.25	0.55	500.25
1.6	T-shaped	0.24	0.53	582.76
	L-shaped	0.24	0.53	578.59
2.0	T-shaped	0.24	0.53	582.96
	L-shaped	0.24	0.53	579.32

6. Optimum Location of Two Stiffeners with Closed Cross-Section Types

This section examines the optimum placements of two longitudinal stiffeners with closed cross-section types consisting of triangular and rectangular shapes for a stiffened girder subjected to bending by performing the procedure presented in Section 3.3.

The optimal positions of two longitudinal stiffeners with rectangular and triangular cross-section types are indicated in Table 3 for different aspect ratios. It is seen from this table that the optimal stiffener positions for these cross-section types are similar regardless of the aspect ratio. The optimum placements of stiffeners 1 and 2 are at around $0.23D_c$ and $0.55D_c$ from the compression flange of the girder, respectively. These optimum values are slightly different from the optimum locations of stiffeners with open cross-section types. Therefore, it can be concluded that the optimum positions of two longitudinal stiffeners with open and closed cross-section configurations are quite similar. In addition, it can be observed from Table 3 that the bend-buckling coefficients of the stiffeners with triangular shape are about 5% higher than those with rectangular shape. The convergence histories obtained from the optimization procedure for stiffeners with triangular and rectangular cross-section shapes are presented in Figure 7, while the mode shapes of these stiffeners

are illustrated in Figure 8. It is noted that the mode shapes obtained from these stiffener types are similar.

Table 3. Optimum results for the longitudinal stiffeners with closed cross-section types.

φ	Stiffener Types	d_{s1}/D_c	d_{s2}/D_c	k_b
0.6	Triangular	0.23	0.55	1109.33
	Rectangular	0.23	0.54	1049.47
1.0	Triangular	0.23	0.55	1112.28
	Rectangular	0.23	0.54	1050.66

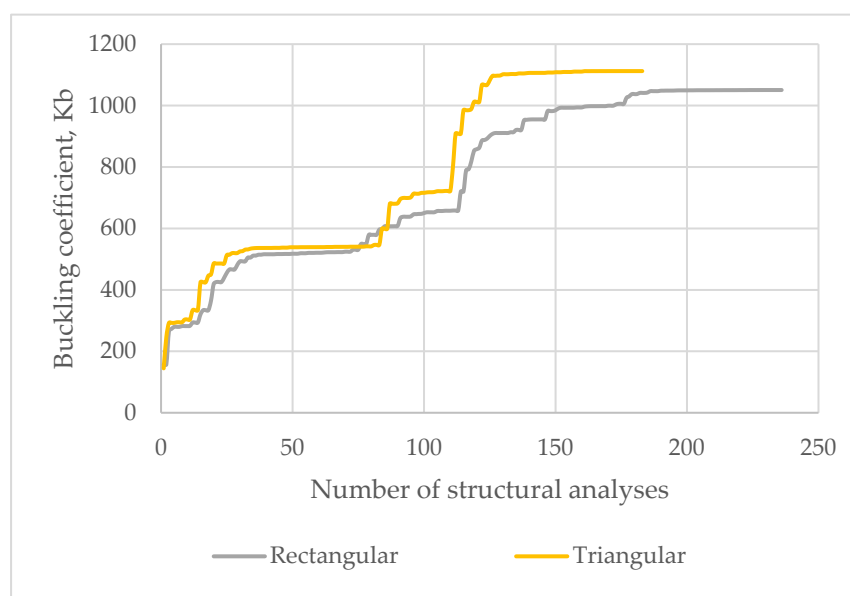


Figure 7. Convergence history for stiffeners with closed cross-section shapes.

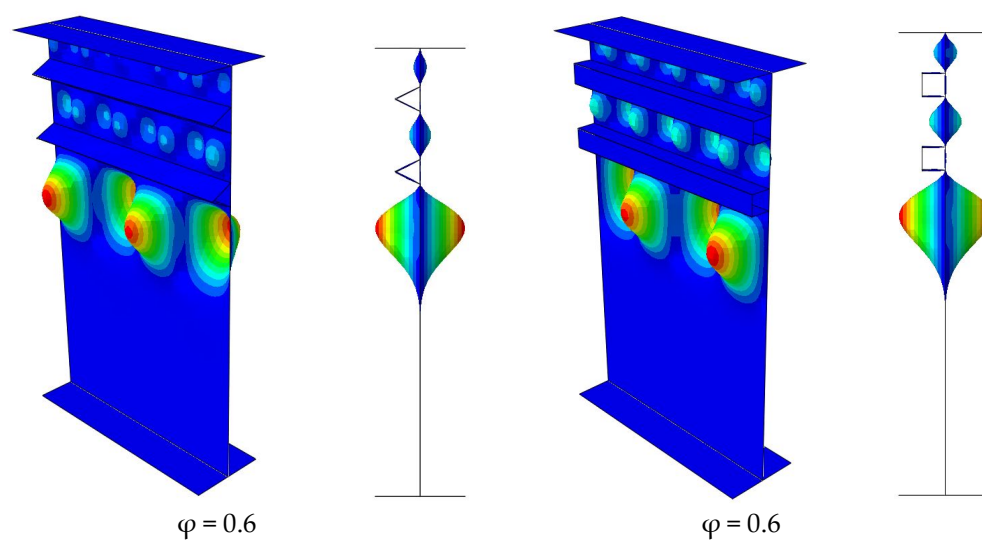


Figure 8. Cont.

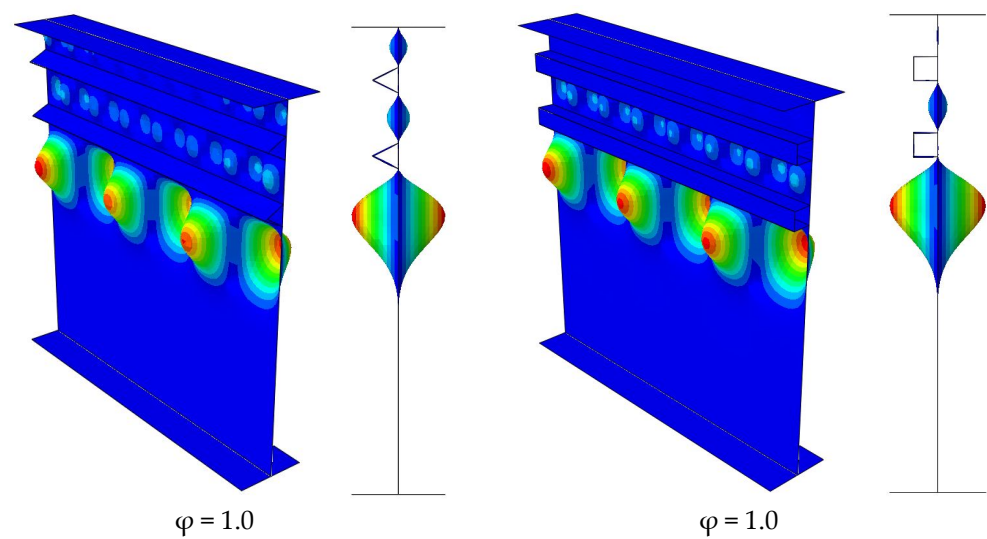


Figure 8. Bend-buckling mode shapes of a stiffened girder with triangular and rectangular stiffener cross-sections.

7. Comparison of the Efficiency of Longitudinal Stiffener Types

This section compares the efficiency of two longitudinal stiffeners with various cross-section shapes in terms of buckling coefficient and minimum web thickness of the stiffened girder. Regarding the buckling coefficient, Figure 9 presents a comparison of the buckling coefficient for two longitudinal stiffeners with flat, T, L, rectangular, and triangular cross-section shapes with respect to a panel aspect ratio of 1. It can be observed that the buckling coefficients of stiffeners with closed section shapes are significantly higher than those with open cross-section shapes. In particular, the triangular shape provides the highest buckling coefficient, while the flat shape gives the lowest buckling coefficient.

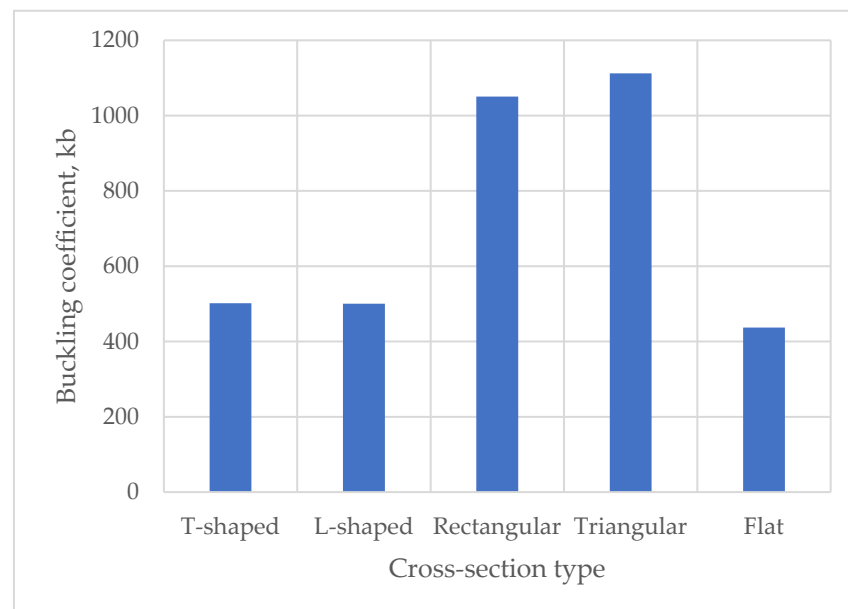


Figure 9. Comparison of buckling coefficient for two longitudinal stiffeners with various cross-section shapes ($\varphi = 1.0$).

Regarding the minimum web thickness of the stiffened girder, the limit of the slenderness ratio of stiffened webs should satisfy the requirements mentioned in AASHTO LRFD [17] as follows:

$$\frac{D}{t_w} \leq 0.95 \sqrt{\frac{Ek_b}{F_y}} \quad (16)$$

where

k_b represents the bend-buckling coefficient of the stiffened girder;

F_y stands for the steel yield strength;

F_y is assumed to be 315 MPa;

E is elastic modulus, where $E = 210$ GPa.

From Equation (13), the minimum thickness of the stiffened web is computed as follows:

$$t_w \geq \frac{D}{0.95 \sqrt{\frac{Ek_b}{F_y}}} \quad (17)$$

From Equation (17), a comparison of the minimum thicknesses of the girder web computed for various stiffener shapes is given in Table 4. It is observed in Table 4 that the flat stiffener needs the highest minimum web thickness, while the triangular stiffener requires the lowest minimum web thickness among all stiffener types considered. It is noteworthy that the required web thickness of the girder web reinforced by two stiffeners with closed cross-section shapes is significantly reduced compared to those reinforced by two stiffeners with open cross-section shapes. In particular, when the web girder is reinforced by two stiffeners with a triangular section shape, the required web thickness decreases by at least 37.26% compared with the case in which the web is reinforced by two stiffeners with a flat cross-section shape.

Table 4. Comparison of minimum stiffened web thickness.

Stiffener Type	D (mm)	k_b	t_{\min} (mm)
Flat-shaped	3000	437.02	5.85
T-shaped	3000	501.62	5.46
L-shaped	3000	500.25	5.47
Triangular	3000	1112.28	3.67
Rectangular	3000	1050.66	3.77

8. Conclusions

In this work, the optimum positions of two longitudinal stiffeners with different cross-section shapes placed at the web of stiffened girders under bending are examined through an optimization procedure performed by coupling Abaqus and Matlab through the Abaqus2Matlab toolbox. Based on the optimization results, the optimum locations of two longitudinal stiffeners with open and closed cross-section types are obtained. An advantage of the proposed methodology is that it simulates the structural optimization problem with a robust numerical procedure which combines FEA and optimization, and it proves to be able to yield meaningful results for all structural configuration cases with an acceptable accuracy and a reduced computational effort. Some conclusions can be drawn as follows:

- The optimum positions of the stiffeners with open cross-section shapes (T- and L-shaped) are around $0.25Dc$ and $0.55Dc$, which are similar to the optimum location of the flat stiffener.
- The optimum positions of the stiffeners with closed cross-section shapes (triangular and rectangular shapes) are around $0.23Dc$ and $0.54Dc$, which are slightly different to the stiffeners with open cross-sections.

- The bend-buckling coefficient of the stiffened girder with stiffeners with a triangular cross-section shape is highest, while that with a flat cross-section shape is lowest in all considered stiffener types.
- The required web thickness of the girder web reinforced by two stiffeners with closed section shapes is remarkably reduced compared with those reinforced by two stiffeners with open cross-section shapes.

The main objective of this study is to investigate the effect of the stiffener location and shape on the buckling load and configuration of steel plate girders reinforced by two longitudinal stiffeners due to bending loading. Maximizing the buckling coefficient leads to the optimum design, since this maximizes the load capacity in each structural configuration of the steel plate girder. The optimization procedure that is implemented in this study has led to the discovery of optimum configurations which maximize the buckling load capacity. Therefore, the optimum locations of the two stiffeners proposed in this study should be taken into account for maximizing the safety of the structure, as should other constraints in construction. A major observation is that stiffeners with triangular cross-sections lead to the highest buckling coefficient compared with other cross-section shapes. Apart from this, it is proven in this study that a suitable selection of stiffener cross-section type and location can lead to a substantial construction cost reduction compared to the usual state of practice designs, since the web thickness can be reduced by as much as 37.26%.

Future work could address issues such as investigating the effect on the buckling load capacity of the plate girder of various loading types (shear loading, patch loading, biaxial bending, etc.), structural constraints (e.g., presence of bolts at the web or flanges), stiffener orientations (vertical or oblique), and cutouts (circular or rectangular) at the web body.

Author Contributions: Conceptualization, Y.P.; methodology, Z.K.; software, G.P.; validation, Z.K.; formal analysis, Y.P.; investigation, Q.-V.V.; resources, B.H.D.; data curation, T.-S.C.; writing—original draft preparation, G.P.; writing—review and editing, H.-H.N.; visualization, B.H.D.; supervision, Q.-V.V.; project administration, Q.-V.V.; funding acquisition, Q.-V.V. All authors have read and agreed to the published version of the manuscript.

Funding: This research was funded by Vietnam National Foundation for Science and Technology Development (NAFOSTED) under grant number 107.01-2019.322.

Data Availability Statement: Data will be available upon reasonable request.

Conflicts of Interest: The authors declare no conflict of interest.

References

1. Haffar, M.Z.; Kövesdi, B.; Adany, S. Buckling of compressed plates with closed-section longitudinal stiffeners: Two new mathematical models for resistance prediction. *Structures* **2021**, *33*, 3526–3539. [CrossRef]
2. Kövesdi, B.; Haffar, M.; Adany, S. Buckling resistance of longitudinally stiffened plates: Eurocode-based design for column-like and interactive behavior of plates with closed-section stiffeners. *Thin-Walled Struct.* **2021**, *159*, 107266. [CrossRef]
3. Loaiza, N.; Graciano, C.; Casanova, E. Web slenderness for longitudinally stiffened I-girders subjected to patch loading. *J. Constr. Steel Res.* **2019**, *162*, 105737. [CrossRef]
4. Demari, F.E.; Mezzomo, G.P.; Pravia, Z.M.C. Numerical study of slender I-girders with one longitudinal stiffener under patch loading. *J. Constr. Steel Res.* **2020**, *167*, 105964. [CrossRef]
5. Truong, V.-H.; Papazafeiropoulos, G.; Vu, Q.-V.; Pham, V.-T.; Kong, Z. Predicting the patch load resistance of stiffened plate girders using machine learning algorithms. *Ocean Eng.* **2021**, *240*, 109886. [CrossRef]
6. Truong, V.-H.; Papazafeiropoulos, G.; Pham, V.-T.; Vu, Q.-V. Effect of multiple longitudinal stiffeners on ultimate strength of steel plate girders. *Structures* **2019**, *22*, 366–382. [CrossRef]
7. Chen, Z.; Yuan, H. Local buckling behaviour of longitudinally stiffened stainless steel plate girders under combined bending and shear. *Thin-Walled Struct.* **2023**, *184*, 110541. [CrossRef]
8. Azhari, M.; Bradford, M. Local buckling of I-section beams with longitudinal web stiffeners. *Thin-Walled Struct.* **1993**, *15*, 1–13. [CrossRef]
9. Alinia, M.; Moosavi, S. A parametric study on the longitudinal stiffeners of web panels. *Thin-Walled Struct.* **2008**, *46*, 1213–1223. [CrossRef]
10. Vu, Q.-V.; Papazafeiropoulos, G.; Graciano, C.; Kim, S.-E. Optimum linear buckling analysis of longitudinally multi-stiffened steel plates subjected to combined bending and shear. *Thin-Walled Struct.* **2018**, *136*, 235–245. [CrossRef]

11. Vu, Q.-V.; Truong, V.-H.; Papazafeiropoulos, G.; Graciano, C.; Kim, S.-E. Bend-buckling strength of steel plates with multiple longitudinal stiffeners. *J. Constr. Steel Res.* **2019**, *158*, 41–52. [CrossRef]
12. Elbanna, A.; Ramadan, H.; Mourad, S. Buckling enhancement of longitudinally and vertically stiffened plate girders. *J. Eng. Appl. Sci.* **2014**, *61*, 351–370.
13. HKim, S.; Park, Y.; Kim, B.; Kim, K. Numerical investigation of buckling strength of longitudinally stiffened web of plate girders subjected to bending. *Struct. Eng. Mech.* **2018**, *65*, 141–154.
14. Hoàn, P.; Trung, P.; Vi, V. Nghiên cứu xác định vị trí tối ưu của sườn tăng cường dọc của dầm cầu thép chịu uốn. Tạp chí Khoa học Công nghệ Xây dựng. *NUCE* **2020**, *14*, 29–38.
15. Kim, S.-E.; Papazafeiropoulos, G.; Graciano, C.; Truong, V.-H.; Do, Q.T.; Kong, Z.; Vu, Q.-V. Optimal design of longitudinal stiffeners of unsymmetric plate girders subjected to pure bending. *Ocean Eng.* **2021**, *221*, 108374. [CrossRef]
16. Cho, E.-Y.; Shin, D.-K. Elastic web bend-buckling analysis of longitudinally stiffened I-section girders. *Int. J. Steel Struct.* **2011**, *11*, 297–313. [CrossRef]
17. AASHTO. *AASHTO LRFD Bridge Design Specifications*, 7th ed.; American Association of State Highway and Transportation Officials: Washington, DC, USA, 2014.
18. Rockey, K.; Cook, I. Optimum reinforcement by two longitudinal stiffeners of a plate subjected to pure bending. *Int. J. Solids Struct.* **1965**, *1*, 79–92. [CrossRef]
19. Rockey, K.; Cook, I. The buckling under pure bending of a plate girder reinforced by multiple longitudinal stiffeners. *Int. J. Solids Struct.* **1965**, *1*, 147–156. [CrossRef]
20. Kim, B.J.; Park, Y.; Kim, K.; Choi, B. Web bend-buckling strength of plate girders with two longitudinal web stiffeners. *Struct. Eng. Mech.* **2019**, *69*, 383–397.
21. Maiorana, E.; Pellegrino, C.; Modena, C. Influence of longitudinal stiffeners on elastic stability of girder webs. *J. Constr. Steel Res.* **2010**, *67*, 51–64. [CrossRef]
22. Papazafeiropoulos, G.; Vu, Q.-V.; Nguyen, V.-S.; Truong, V.-H. Optimum location of a single longitudinal stiffener with various cross-section shapes of steel plate girders under bending loading. *J. Sci. Technol. Civ. Eng. (STCE)—NUCE* **2022**, *16*, 65–75. [CrossRef]
23. Papazafeiropoulos, G.; Muñoz-Calvente, M.; Martínez-Pañeda, E. Abaqus2Matlab: A suitable tool for finite element post-processing. *Adv. Eng. Softw.* **2017**, *105*, 9–16. [CrossRef]
24. ABAQUS. *Analysis User's Manual*, Version 6.14; Dassault Systems: Los Angeles, CA, USA, 2014.
25. MathWorks, Inc. *MATLAB R2017b*; MathWorks, Inc.: Natick, MA, USA, 2017.
26. Frank, K.H.; Helwig, T.A. Buckling of webs in unsymmetric plate girders. *Eng. J. Second Quart.* **1995**, *32*, 43–53.
27. CEN. *EN 1993-1-5; Eurocode 3: Design of Steel Structures-Part 1-5: Plated Structural Elements*. European Committee for Standardization: Brussels, Belgium, 2006.
28. Byrd, R.H.; Gilbert, J.C.; Nocedal, J. A trust region method based on interior point techniques for nonlinear programming. *Math. Program.* **2000**, *89*, 149–185. [CrossRef]
29. Byrd, R.H.; Hribar, M.E.; Nocedal, J. An Interior Point Algorithm for Large-Scale Nonlinear Programming. *SIAM J. Optim.* **1999**, *9*, 877–900. [CrossRef]
30. Waltz, R.; Morales, J.; Nocedal, J.; Orban, D. An interior algorithm for nonlinear optimization that combines line search and trust region steps. *Math. Program.* **2006**, *107*, 391–408. [CrossRef]
31. Pham, V.T.; Vu, Q.V.; Papazafeiropoulos, G.; Ngo, V.T. Efficiency of Abaqus2Matlab toolbox for structural optimization problems. *IOP Conf. Ser. Mater. Sci. Eng.* **2020**, *869*, 022025. [CrossRef]
32. Ghorashi, M.; Askarian, A.; Gashtasby, M. Optimal design of stiffened plates for buckling under in-plane forces and bending moments. In Proceedings of the Eighth International Conference on the Application of Artificial Intelligence to Civil and Structural Engineering Computing, Stirling, UK, 19–21 September 2001; pp. 83–84.
33. Silva, D.A.B.; Filho, J.O.F.; Barreto, R. Numerical study for optimization of the buckling behavior of longitudinally stiffened plates under pure bending. In Proceedings of the 1st International Congress on Structural Integrity and Maintenance—SIM 2021, Online, 8–9 April 2021.
34. Papazafeiropoulos, G.; Vu, Q.-V.; Truong, V.-H.; Luong, M.-C.; Pham, V.-T. Prediction of buckling coefficient of stiffened plate girders using deep learning algorithm. *Lect. Notes Civ. Eng.* **2019**, *54*, 1143–1148. [CrossRef]

Disclaimer/Publisher's Note: The statements, opinions and data contained in all publications are solely those of the individual author(s) and contributor(s) and not of MDPI and/or the editor(s). MDPI and/or the editor(s) disclaim responsibility for any injury to people or property resulting from any ideas, methods, instructions or products referred to in the content.

Article

Numerical Simulation Study of Expanding Fracture of 45 Steel Cylindrical Shell under Different Detonation Pressure

Zhenwei Huang¹ and Xinlu Yu^{1,2,*}
¹ Key Laboratory of Impact and Safety Engineering, Ningbo University, Ministry of Education, 818 Fenghua Road, Jiangbei District, Ningbo 315211, China; hzw961020@163.com

² College of Science & Technology, Ningbo University, Wenwei Road 521, Ningbo 315300, China

* Correspondence: yuxinlu@nbu.edu.cn; Tel.: +86-152-574-92195

Abstract: Detonation and fragmentation of ductile cylindrical metal shells is a complicated physical phenomenon of material and structural fracture under a high strain rate and high-speed impact. In this article, the smoothed particle hydrodynamics (SPH) numerical model is adopted to study this problem. The model's reliability is initially tested by comparing the simulation findings with experimental data, and it shows that different fracture modes of cylindrical shells can be obtained by using the same model with a unified constitutive model and failure parameters. By using this model to analyze the explosive fracture process of the cylindrical shells at various detonation pressures, it shows that when the detonation pressure decreases, the cylindrical metal shell fracture changes from a pure shear to tensile–shear mixed fracture. When the detonation pressure is above 31 GPa, a pure shear fracture appears in the shell during the loading stage of shell expansion, and the crack has an angle of 45° or 135° from the radial direction. When the pressure is reduced to 23 GPa, the fracture mode changes to tension–shear mixing, and the proportion of tensile cracks is about one-sixth of the shell fracture. With the explosion pressure reduced to 13 GPa, the proportion of tensile cracks is increased to about one-half of the shell fracture. Finally, the failure mechanism of the different fracture modes was analyzed under different detonation pressures by studying the stress and strain curves in the shells.

Keywords: cylindrical shell fracture; 45 steel; SPH numerical simulation

Citation: Huang, Z.; Yu, X. Numerical Simulation Study of Expanding Fracture of 45 Steel Cylindrical Shell under Different Detonation Pressure. *Materials* **2022**, *15*, 3980. <https://doi.org/10.3390/ma15113980>

Academic Editors: Shuwen Wen, Yongle Sun and Xin Chen

Received: 25 April 2022

Accepted: 31 May 2022

Published: 3 June 2022

Publisher's Note: MDPI stays neutral with regard to jurisdictional claims in published maps and institutional affiliations.



Copyright: © 2022 by the authors. Licensee MDPI, Basel, Switzerland. This article is an open access article distributed under the terms and conditions of the Creative Commons Attribution (CC BY) license (<https://creativecommons.org/licenses/by/4.0/>).

1. Introduction

In modern explosion research, the study of expanding fracture mode of cylindrical shells under high-speed impact loading has always been a hot topic [1–5]. A large number of researchers have observed the fragmentation process by changing variables in detonation experiments and used the recovered fragments to study the influencing factors of the fracture mode of the cylindrical shell. The detonation of a cylindrical shell is a process under a high-impact, high-strain rate. Cylindrical shell fracture is a difficult subject that involves both material and structural damage. Based on experiments and simulations, several researchers have proposed related assumptions and findings.

As early as 1943, Gurney [6] proposed an empirical formula for the velocity of cylindrical shell fragments based on the law of energy balance. The velocity relates to the mass of explosives, the mass of cylindrical shells, and the Gurney energy. In 1944, Taylor [7] observed the fracture process of the metal cylindrical shell under a certain explosion pressure through a high-speed camera, believed that the fracture of the cylindrical shell was a tensile fracture process and he proposed the Taylor criterion. However, the criterion did not consider other influencing factors, such as explosion pressure, shell dimensions, and loading method. Besides, the control mechanism is relatively simple. Based on the Taylor criterion, Hoggatt et al. [8] found another mode of expansion fracture under different explosion pressure. They thought that the fracture process of the cylindrical shell was

a competitive fracture between tensile fracture and shear fracture, under high explosive pressure, the shell is prone to pure shear fracture. Through experiments and numerical simulation studies, Martineau [9] found that the cylindrical shell had an adiabatic shear phenomenon in the expansion process when the strain rate was 104 s^{-1} and the strain was about 150%, the thickness of the cylindrical shell also affected adiabatic shear. Studies on microscopic characterization of metal materials [10], metal thermodynamic properties [11], and the influence of impurities in steel materials on the properties of the material [12] have shown the metal failure process is affected by many factors. In recent years, Liang et al. [13] studied the expansion ring's fracture by numerical simulation, and found that with low notch depth conditions, the expansion ring is prone to pure shear fracture. Tensile fracture dominated when the notch depth was higher, this result indicated that fracture mode was affected by defect factors. Under the guidance of the dynamic fragmentation theory of solids and the fragmentation theory of continuum energy, Grady [5] analyzed that the distribution of shell fragments was related to the ductility of the material itself. Hu et al. [14] and Hu et al. [15] carried out experimental research on the damage to metal cylindrical shells of 45 steel, TC4, and WTG05 tungsten alloys with different geometric dimensions driven by explosive detonation. They found that factors such as the thickness of the shell and loading detonation pressure would affect the fracture process of cylindrical shells. Generally speaking, thin-walled shells are prone to pure shear fracture under high detonation pressure loading, and fracture strain and strain rate would be relatively higher. When the explosion pressure is decreased or the shell thickness is increased, the fracture mode of the shell would change to shear–tensile mixed fracture, and the fracture strain and strain rate would be lower. Through numerical simulation research, Liu et al. [16] also found that different initiation methods of the explosion would affect the fracture of the cylindrical shell because the incident angle of the detonation wave to the inner wall of the cylindrical shell varied under different initiation methods of explosion; the pressure experienced by the inner surface of the cylindrical shell differs greatly. The results show that the peak pressure of the centerline detonation is the maximum, the single-point detonation is the second, and the plane detonation is the minimum. Arnold [4] studied the experimental results of metal cylindrical shells with different materials, wall thicknesses, and processing techniques, and proposed a calculation formula for predicting the distribution of shell fragments. Arnold found that medium-strength steel casings produced the largest fragments. In the axial direction, medium-strength steel casings produced the longest fragments. In terms of numerical simulation, Yu et al. [17] studied the pure shear fracture mechanism of TA2 cylindrical metal shells loaded with different explosives. Liu et al. [18] considered heterogeneity of the material and introduced a material shear failure constitutive model with probability, and discussed the initiation of cracks and propagation of multiple adiabatic shears in metal cylindrical shells.

However, the traditional numerical simulation method, especially the finite element method (FEM), can only analyze the deformation process, stress, and strain state of a cylindrical shell under an explosive shock wave, but by using the FEM method, various fracture modes such as pure shear fracture and the tensile–shear mixed fracture cannot be reproduced at present [17–19]. When using the traditional method (FEM) to analyze the fracture of a cylindrical shell, because the element produces extreme deformation and sudden change in the interface, it always appears that the failed element is deleted, which affects the fracture evolution process of a cylindrical metal shell in a subsequent calculation [20,21]. In addition, a large number of deleted elements lead to excessive loss of mass, momentum, and energy in the system. The method of smoothed particle hydrodynamics (SPH) adopted in this paper is a meshless method with Lagrangian particle configuration [22]; it avoids the mesh distortion of the Lagrangian method and the difficulty of the Euler method to capture the boundary. In the SPH method, the state of the system is described by discrete particles, and the smooth particles are used to bear their unique material properties so that they can work according to the law of the governing equation. By solving the integral expression of kernel function interpolation in the form of discrete

particle weighted summation, a stable and smooth approximation is obtained. In addition, when the distance between two particles exceeds a failure threshold, the particles are not deleted when the material fractures. The conservation of mass, momentum, and energy of the system is guaranteed; thus, the SPH simulation method has great applications in the fields of ultra-high-speed impact, explosion, crack propagation, and metal forming [23–25]. Therefore, this article selected the smoothed particle hydrodynamics method to establish the cylindrical shell explosion model.

2. Experimental Phenomenon of Fracture of Metal Cylindrical Shell

Many experimental studies have been carried out in China and worldwide on the fracture phenomenon and fragmentation characteristics of metal cylindrical shells under explosive loads [26–28]. Research shows that, for different materials and different detonation pressures, the fracture of the cylindrical shell demonstrates the following characteristics (in Figure 1): (1) Under high explosive pressure, the cylindrical shell undergoes shear fracture. When the detonation pressure decreases, it becomes a tensile–shear mixed fracture. The proportions of tensile cracks in the fracture are different; the lower the detonation pressure, the higher the proportion of tensile cracks in the fracture. (2) The shear cracks are formed by the unstable slip of the adiabatic shear belt. The direction is 45° or 135° to the radial direction. The cross-section is relatively flat (S area); the direction of the tensile cracks is along the radial direction, and the cross-section is uneven and rough (R area). (3) Cylindrical shell fragments can be divided into two types: large fragments of type A and small fragments of type B, as shown in Figure 1. Large fragments of type A include two surfaces of the cylindrical shell: the inner surface and the outer surface. Small fragments of type B only contain one surface of the cylindrical shell, according to whether the contained surface is the inner surface or the outer surface; it can be divided into B' and B''.

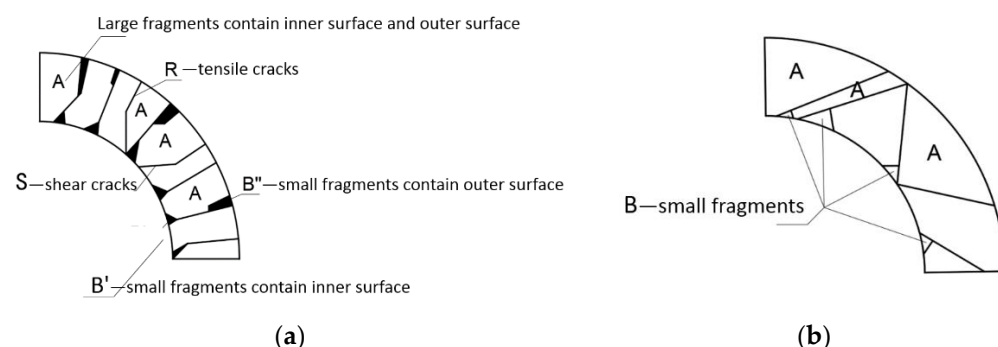


Figure 1. Main fragments: “A”—large fragments contain inner surface and outer surface and “B”—small fragments only contain one surface of the cylindrical shell; (a) tensile–shear mixed fracture mode; (b) pure shear fracture mode.

However, scholars have different understandings of the fracture process and the formation mechanism of fragments [3,29,30]. It is generally acknowledged that under low detonation pressure, the radial cracks initially occur on the outer surface under circumferential stress, and the thermoplastic shear band appears close to the inner wall, forming shear–tensile mixed fracture phenomenon. Under high detonation pressure, the inner wall undergoes thermoplastic adiabatic shear instability under compressive stress. The inward development of the radial cracks in the outer surface is inhibited and it develops along the shear direction; it shows pure shear fracture at last [6]. However, Zhang et al. [31] used numerical simulation to analyze the equivalent plastic strain evolution of the cylindrical metal shell in its explosion. They believed that the fracture of the ideal cylindrical shell cannot start from the outer surface. The tensile fracture starting from the outer surface may have a geometrical relationship with the defects in the surface of the shell. Zhen et al. [32] analyzed the metallographic structure of the exploding fracture fragments of the thick-walled cylinder, and believed that under low explosive detonation pressure, the microcrack

damage zone was first generated inside the wall thickness of the cylindrical shell, with the explosion pressure loading, the shell fractures. Since the zone near the inner wall of the cylindrical shell is under a state of compressive stress and the outer wall is under a state of tensile stress, the crack expands along radially outwards and expands along the shear concentration zone toward the inner surface, forming a tensile–shear mixed fracture.

Since most experimental research does not systematically design the experimental loading conditions, it is difficult to carry out a univariate comparison by verification analysis of the literature results. In China, Hu et al. [15], Tang et al. [33], and Hu et al. [34] carried out a series of comparative experimental studies on cylindrical shells and found different fracture modes, such as shear fracture and tensile–shear mixed fracture; there is also a single-rotation adiabatic shear fracture phenomenon under high detonation pressure. It can be seen that there is broad understanding of the fracture process of cylindrical shells under different explosion pressures, but the fracture mechanism is not yet clear.

In Tang's [34] experiment, JOB-9003 and hollow RHT-901 explosives were used to carry out a series of experimental studies on the explosion and fragmentation of a 45 steel cylindrical shell. Under different detonation pressures and charging conditions, the cylindrical shells of the same material, explosion, and fragmentation had pure shear fractures and tensile–shear mixed fractures.

The 45 steel cylindrical shell shows pure shear fracture under JOB-9003 explosive loading. A cylindrical shell with 4 mm thickness shows tensile–shear mixed fracture under the hollow RHT-901 explosive loading; the proportion of tensile cracks is extremely low, so it is almost pure shear fracture; when the wall thickness is 5 mm, the proportion of tensile cracks accounts for one-third of the shell thickness [33]. The cylindrical shell size, loading conditions, and fracture phenomenon are listed in Table 1. (Relative sized δ_d = shell thickness h /inner radius R of cylindrical shell). The average strain and strain rate of the cylindrical shell at time t were calculated using the formula: $\varepsilon_t = (R(t) - R_0)/R_0$, $\dot{\varepsilon} = d\varepsilon_t/dt \approx V_t/R_0$. The statistical experimental data are shown in Table 1 [15,33,34].

Table 1. Experimental cylindrical shell, loading conditions, and explosion–expansion fracture phenomenon, Refs. [15,33,34].

Types of Explosives	Wall Thickness/Inner Radius/d/R	δ_d	ε_c	$t_c/\mu s$	ε_f	$t_f/\mu s$	$\dot{\varepsilon}/10^4 s^{-1}$	Fracture Mode
RHT-901	5/30	0.17	0.18	7.8	0.37	15.8	2.5	tensile–shear mixed fracture
	4/30	0.13	0.24	8.8	0.43	15.4	2.9	tensile–shear mixed fracture
	3/30	0.10	0.30	10.1	0.45	14.1	3.5	pure shear
JOB9003	6/20	0.30	0.44	11.5	0.89	23.5	4.5	pure shear
	5/20	0.25	0.42	9.5	1.24	22.5	6.0	pure shear
	4/20	0.20	0.40	7.5	1.31	19.5	7.1	pure shear
	3/20	0.15	0.38	6.5	0.88	13.5	8.4	pure shear

Relative sized δ_d = shell thickness h /inner radius R of cylindrical shell ε_c —initial fracture strain, the radial strain at the moment t_c when cracks appear on the outer wall of the cylindrical shell. ε_f —product leakage strain, the radial strain at the moment t_f when the explosion products leak $\dot{\varepsilon}$ —strain rate.

3. SPH Numerical Simulation Model and Verification

3.1. Model Construction

When building the SPH model, the arrangement method of the particles is very important, which affects the accuracy of the result. LS-DYNA software provides automatic polar coordinate point distribution mode and the rectangular coordinate point distribution mode, but these two methods cause local uniform particle dispersion on the contact surface of the explosive metal that are not in one-to-one correspondence. Therefore, while building the cylindrical metal shell model, it is necessary to simultaneously satisfy the uniform dispersion of particles in the explosive propagation process and the symmetry of the interface contact between the annular explosive and the metal cylinder shell. It is required

that the particle arrangement and spacing of the SPH model should be kept as uniform as possible, and the interparticle symmetrical arrangement of the interface should be maintained. For this reason, the initial geometrical arrangement of particles is controlled by geometric grid cell division during modeling. Then, the method of generating particles at the grid cell center is used to ensure that the final arrangement and distribution of SPH particles are uniform and the particle pairs at the interface are symmetrically arranged, as shown in Figure 2.

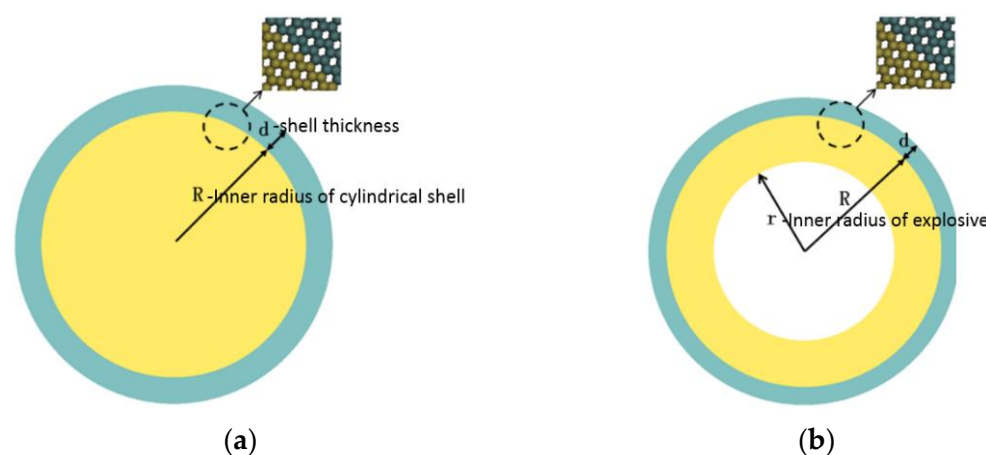


Figure 2. SPH numerical model: (a) JOB9003 packing ($R = 30$ mm) and (b) RHT-901 hollow packing ($R/r = 30$ mm/20 mm).

According to the literature [35,36], SPH particles have the same performance as atoms, that is, they diverge when they are close to each other and attract each other when they are far apart, thus resulting in particle aggregation during the process of calculation. Therefore, the artificial stress represented by Monaghan can effectively eliminate the tensile instability caused by SPH, so that the SPH method can maintain continuity in higher-order calculations. Monaghan artificial viscosity is controlled by parameters α and β in practical application. The β coefficient controls the penetration of interfacial particles (as shown in Figure 3). When the simulated detonation pressure is very high, it is necessary to increase the value of β to prevent nonphysical penetration, but the increase in β decreases the peak detonation pressure, increases the calculation time, and also changes the shear band development.

To improve the accuracy and tensile stability, moving least-squares-based formulation is used. This method is suitable for large deformation models, but it requires a large computational cost. MPP simulation needs to set the maximum and minimum smooth length scale factor at 1.00 to ensure that the calculation is correct, then by adjusting a quasi-linear approximation term QL in the algorithm. To the combination of precision and stability in an extremely large deformation simulation, if QL is set too small, the model will have higher accuracy, but the stability problem is outstanding; if QL is too large, the model will inhibit instability but have lower precision. By comparison, $QL = 0.01$ was chosen to achieve a good compromise between stability and accuracy.

The setting of β changes the detonation pressure. With the increase in β , the value of interface load decreases (as shown in Figure 4), changing the distribution, distance, and development of the shear band in the shell thickness. When the stability of contact between particles is satisfied, no particle penetration occurs at the interface; β is required to be as small as possible to obtain a clear shear band. Therefore, $\beta = 1$ was selected as the value of its viscosity coefficient in this paper. In this way, the stability of the particles can be controlled and the failure of the shell can be accurately reflected.

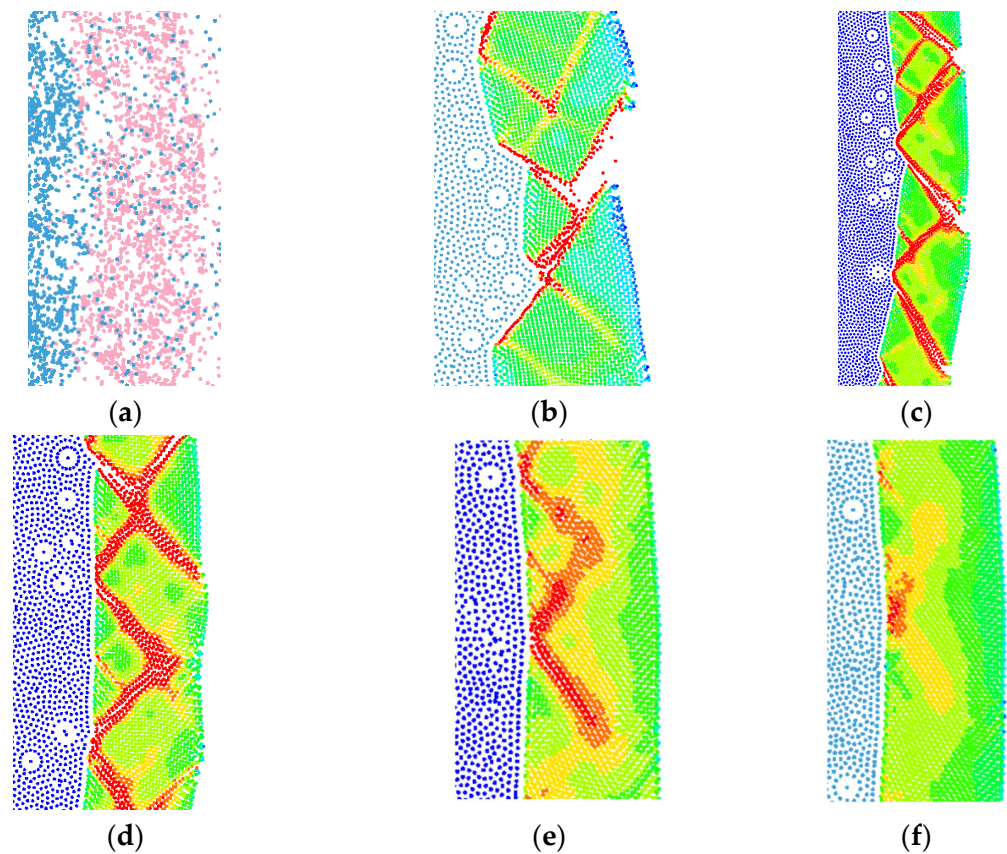


Figure 3. Comparison of the effects of different β values: (a) 14.2 μs , $\beta = 0.8$; (b) 14.2 μs , $\beta = 1$; (c) 14.2 μs , $\beta = 2$; (d) 14.2 μs , $\beta = 3$; (e) 14.2 μs , $\beta = 7$; (f) 14.2 μs , $\beta = 10$.

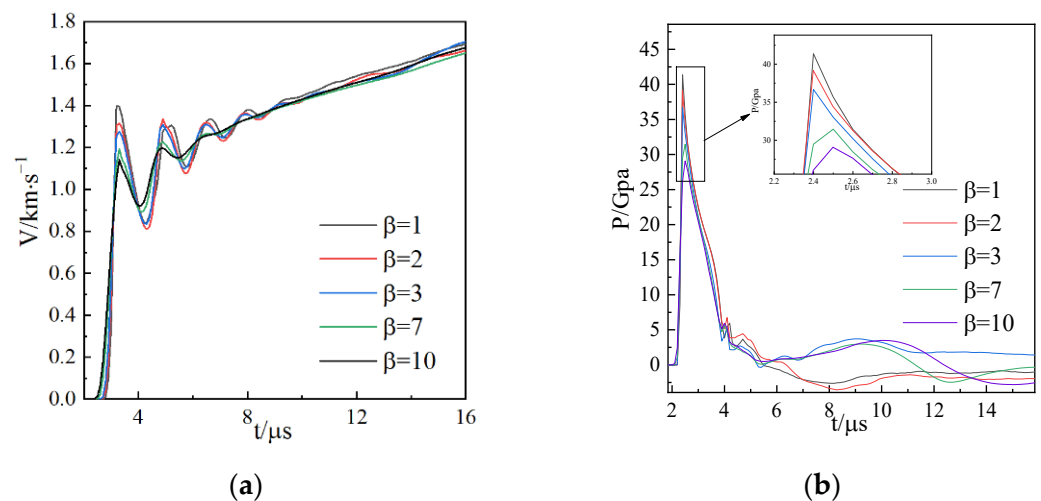


Figure 4. Comparison of data from different models: (a) velocity of the outer wall of the cylindrical shell and (b) internal hydrostatic pressure.

The SPH distribution distance has an impact on the model accuracy and internal stress propagation. If the particle spacing distribution distance decreases, the model accuracy is improved slightly, but the calculation amount is increased greatly. Finally, the model SPH distribution distance of 50 μm is chosen; it is close to the experimental result and requires less calculation.

3.2. Material Parameters of the Model

The 45 steel's rate of change under high pressure is described by the Gruneison equation of state [37]. The plasticity is described by the Johnson–Cook constitutive equation considering strain hardening, strain rate hardening, and thermodynamic softening effects.

$$\tilde{\sigma} = (A + B\bar{\sigma}^n) \left(1 + C \ln \frac{\dot{\epsilon}}{\dot{\epsilon}_0} \right) (1 - T^{*m}) \quad (1)$$

Adapting the experimental results of Hu [38], from the same institute as Tang, he conducted an experimental study on the strain hardening, strain rate hardening, and thermodynamic softening characteristics of 45 steel, and obtained the parameters of the Johnson–Cook constitutive equation by fitting. Since the quasi-static yield strength $\sigma_{0.2} = 350$ MPa, the fracture strength $\sigma_b = 600$ MPa, and the elongation of 45 steel used for the experimental cylindrical shell are 17%, the yield strength is lower than that for materials reported in the literature [38]. The strain hardening term in the Johnson–Cook constitutive equation is $(A + B\bar{\sigma}^n)$; the quasi-static yield strength and fracture strength properties of 45 steel used in the experiment were used for fitting and correction. The following were obtained: parameter $A = 350$ MPa, $B = 600$ MPa, $n = 0.307$. Other parameters of strain rate hardening and thermal softening are adopted directly from those reported in the literature [38], as shown in Table 2.

Table 2. Constitutive parameter values of 45 steel cylindrical shell [38].

		Johnson–Cook				Grüneison State Equation		
A/MPa	B/MPa	n	m	C	$\dot{\epsilon}_0$	C/m·s ^{−1}	s	γ_0
350	600	0.307	0.804	0.07	2×10^{-4}	4600	1.49	2.17

To facilitate the analysis, the failure model of 45 steel adopts the simplified plastic damage accumulation softening failure criterion and does not consider the influence of stress state, strain rate, or temperature on the damage. The damage degree D is:

$$D = \begin{cases} 0, & \bar{\epsilon}^P < \epsilon_{cr} \\ \frac{\sum \Delta \bar{\epsilon}^P - \epsilon_{cr}}{\epsilon_f - \epsilon_{cr}}, & \bar{\epsilon}^P > \epsilon_{cr} \end{cases} \quad (2)$$

where D is the damage parameter, $\Delta \bar{\epsilon}^P$ is the plastic variable increment of a time step, ϵ_{cr} is the material plastic initial damage strain, and ϵ_f is the material failure strain. We take $\epsilon_{cr} = 0.48$ and material failure strain $\epsilon_f = 1.0$. Once damage occurs, the material softens:

$$\sigma = \tilde{\sigma}(1 - D) \quad (3)$$

The explosive uses the JWL equation of state. The specific parameters are shown in Table 3 [39].

Table 3. JWL EOS parameters of the explosives [39].

Types of Explosives	A/GPa	B/GPa	ω	R_1	R_2	E_0/GJm^{-3}	P_{cj}/GPa	$\rho/\text{Kg}\cdot\text{m}^{-3}$	D/m·s ^{−1}
JOB9003	842.0	21.81	0.28	4.6	1.35	1	35	1884	8740
RHT-901	503.0	9.065	0.35	4.3	1.1	7.6	27	1658	7800

3.3. Validation of Numerical Models

The experimental results of detonation and expansion of 45 steel cylindrical shell given in Table 1 are taken as the object for the SPH numerical simulation. Figure 5 is the plastic strain diagram of the fracture process for 45 steel under the loading of JOB9003.

The beginning of time in the figure is defined uniformly as the moment when the detonation wave reaches the inner wall of the cylindrical shell. The SPH numerical results show that the plastic damage and fracture of the material first start in the middle of the shell thickness. The crack expands to the inner and outer surfaces along the shear direction of 45° or 135° to the radial direction. When $t = 7.5 \mu\text{s}$, the shear crack penetrates the shell; at that time, the shear crack surface is loaded by the internal detonation products, so the detonation products cannot leak immediately under the action of compressive stress. When $t = 17.9 \mu\text{s}$, the shell fragments on both sides of the crack disengaged and the detonation products leaked from the opening. The numerical simulation fracture mode is consistent with the trend of the experimental phenomenon.

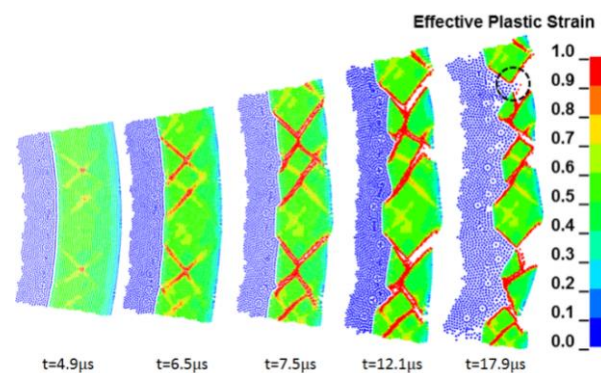


Figure 5. The evolution process of pure shear fracture under JOB9003 loading obtained by numerical simulation.

Figure 6 shows the comparison between the velocity–time history curve of the outer wall of the cylindrical shell obtained by SPH numerical simulation and the experimental DPS test results. They fit well; the time t_c of visible cracks on the outer surface of the cylindrical shell and the time of detonation particle leakage t_f are marked.

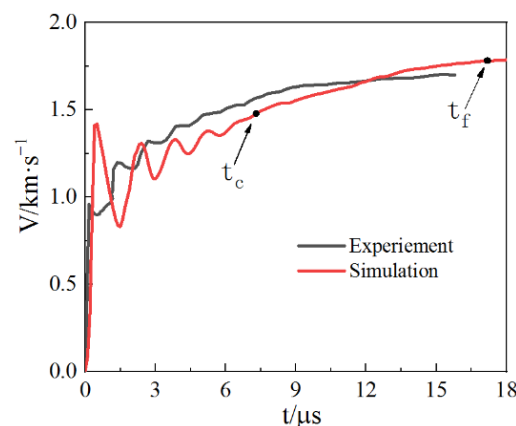


Figure 6. The radial expansion velocity for the outer surface of the cylindrical shell.

A numerical simulation of the fracture of 45 steel cylindrical shell with an inner diameter of 30 mm and wall thickness of 4 and 5 mm under the loading of hollow RHT-901 was carried out. The fracture model is a tensile–shear mixed fracture. Figure 7 shows the equivalent plastic strain and fracture evolution process of cylindrical shells with 4 and 5 mm thickness. It can be seen that the fracture of the cylindrical shell still starts from the middle of the wall thickness of the cylindrical shell and expands in the shear direction. In contrast to the shear evolution fracture under the action of the JOB9003 explosive, a similar “necking” phenomenon occurs at the joint of the shell when the shear crack develops close to the outer surface of the cylindrical shell. The crack direction turns to radial development. The final fracture presents a tensile–shear mixed fracture.

Among them, the shear fracture mainly occurs in the cylindrical shells with a thickness of 4 mm; tensile features can be seen locally, and the proportion of radial tensile cracks is very small, as shown in Figure 7a. The proportion of the cylindrical shell with a thickness of 5 mm has a significant increase in radial cracks, accounting for nearly one-third of the shell thickness, as shown in Figure 7b. This result is consistent with the experimental phenomenon and fracture characteristics described in the experiment [29].

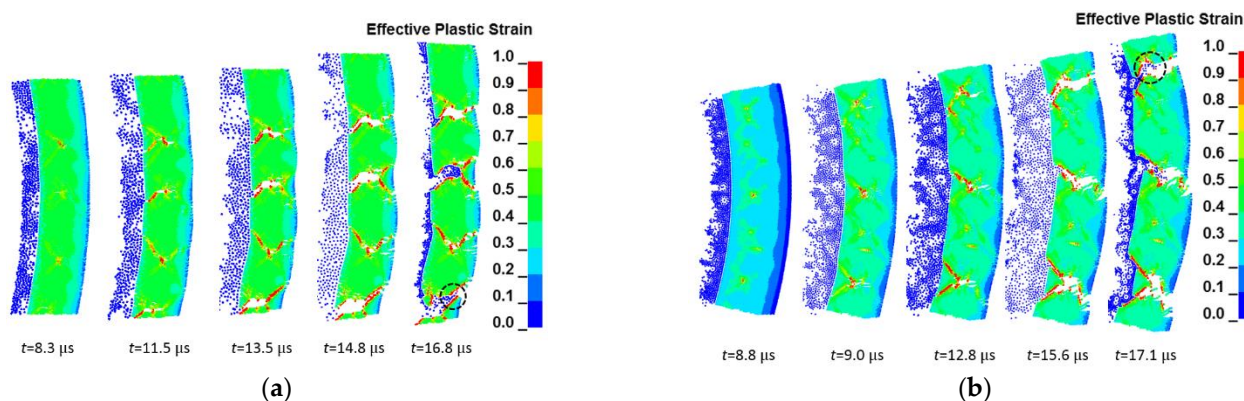


Figure 7. Simulation results of cylindrical shell expansion and fracture process with different R/h under a load of hollow RHT-901 explosive: (a) inner diameter 30 mm, shell thickness 4 mm; (b) inner diameter 30 mm, shell thickness 5 mm.

Taking the detonation wave reaching the outer surface of the cylindrical shell as $0 \mu s$, the numerical simulation results above are used in the same method as the experiment to obtain the apparent expansion strain of the cylindrical shell at the characteristic time: $\epsilon_t = (R(t) - R_0)/R_0$. R_0 is the initial radius of the cylindrical shell. $R(t)$ is the expansion radius of the cylindrical shell at the characteristic time t of the detonation loading process. Finally, the initial fracture strain ϵ_c at time t_c is obtained when visible cracks are on the outer surface, together with the shell fracture strain ϵ_r at time t_r and the product leakage strain ϵ_f at the explosion product leakage time t_f . The expansion strain rate $\dot{\epsilon}$ of the cylindrical shell is approximated by the formula: $\dot{\epsilon} = d\epsilon_t/dt \approx V_t/R_0$. V_t is the expansion velocity when the crack penetrates the shell thickness. Under the loading of JOB9003 and hollow RHT-901 explosives, the comparison between the SPH numerical experimental results and the experiment results [29] shows that the apparent initial fracture strain ϵ_c and the product leakage strain ϵ_f are in good agreement, as shown in Table 4.

Table 4. Comparison of numerical simulation and experiment results.

Types of Explosives	R/h		ϵ_c	$t_c/\mu s$	ϵ_r	$t_r/\mu s$	ϵ_f	$t_f/\mu s$	$\dot{\epsilon}/10^4 s^{-1}$	Fracture Mode
RHT-901	30/3	experiment *	0.30	10.1	/	/	0.45	14.1	3.5	pure shear
		simulation	0.39	13.2	0.39	13.3	0.45	15.2	3.1	pure shear
	30/4	experiment *	0.24	8.8	/	/	0.43	15.4	2.9	tensile–shear mixed fracture
		simulation	0.30	13.1	0.31	13.5	0.41	16.9	2.7	tensile–shear mixed fracture
	30/5	experiment *	0.18	7.8	/	/	0.37	15.8	2.5	tensile–shear mixed fracture
		simulation	0.21	11.9	0.23	12.8	0.30	15.6	2.1	tensile–shear mixed fracture
JOB9003	20/3	experiment *	0.38	6.5	/	/	0.88	13.5	8.4	pure shear
		simulation	0.36	6.0	0.37	6.1	0.89	12.9	8.2	pure shear
	20/4	experiment *	0.40	7.5	/	/	1.31	19.5	7.1	pure shear
		simulation	0.37	7.3	0.37	7.3	1.07	16.7	7.1	pure shear

Table 4. Cont.

Types of Explosives	R/h		ε_c	$t_c/\mu\text{s}$	ε_r	$t_r/\mu\text{s}$	ε_f	$t_f/\mu\text{s}$	$\dot{\varepsilon}/10^4 \text{ s}^{-1}$	Fracture Mode
	20/5	experiment *	0.42	9.5	/	/	1.24	22.5	6.0	pure shear
		simulation	0.41	9.4	0.42	9.6	1.21	22.3	6.4	pure shear
	20/6	experiment *	0.44	11.5	/	/	0.89	23.5	4.5	pure shear
		simulation	0.43	11.4	0.45	11.7	0.90	20.0	5.4	pure shear

ε_c —initial fracture strain, the radial strain at the moment t_c when cracks appear on the outer wall of the cylindrical shell; ε_f —products leakage strain, the radial strain at the moment t_f when the explosion products leak $\dot{\varepsilon}$ —strain rate; experiment *—data from the literature [30–32].

The results show that SPH can simulate the fracture mode of 45 steel cylindrical shell under different ways of filling and detonation pressure of JOB-9003 explosive and hollow RHT-901 explosive, which is consistent with the shear fracture, tensile–shear mixed fracture mode in experimental results. The changing trend of the fracture strain with the loading strain rate is also consistent with the experiment. The results show that the experimental end-state fragmentation phenomenon of shear and the tensile–shear mixed fracture mode under different explosive conditions can be well simulated by the SPH numerical model with the unified material constitutive and fracture model.

4. Fracture Results and Analysis of 45 Steel Cylindrical Shell under Different Detonation Pressure

4.1. Numerical Simulation Models

The abovementioned SPH simulation model (Figure 2a) was used to simulate the expansion fracture process of 45 steel cylindrical shell under four detonation pressures; the models of explosives are all fully filled SPH models with an inner diameter of 40 mm and shell thickness of $h = 4 \text{ mm}$.

The waveform is a triangular wave obtained by fitting the JWL high-pressure state equation (Figure 8). The explosive parameters are shown in Table 5.

Table 5. Parameters related to the JWL constitutive equation of explosives.

Types of Explosives	A/MPa	B/MPa	ω	R_1	R_2	E_0/GJm^{-3}	P_{cj}/GPa	$\rho/\text{Kg}\cdot\text{m}^{-3}$	$D/\text{m}\cdot\text{s}^{-1}$
JOB9003	842.0	21.81	0.28	4.6	1.35	10	35	1884	8740
RHT-901	503.0	9.065	0.35	4.3	1.1	7.6	27	1658	7800
TNT	371.2	3.231	0.30	4.15	0.95	3	21	1730	6930
HNS	162.7	10.82	0.25	5.4	1.8	4.1	7.9	1000	5100

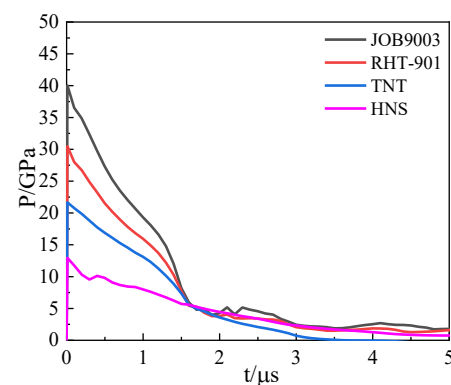


Figure 8. Loading history curves for the inner wall of the cylindrical shell under different explosion pressures.

It can be seen from the loading curve that the pulse width of the loading wave is the same, but the peaks of the loading pressures are different; the pressure peaks of the explosive detonation wave are about 40, 31, 21, and 13 GPa, and time to reach the shell inner wall was 2.2, 2.5, 2.8, and 3.8 μs . The following results take the time when the detonation wave reaches the inner wall as the starting time. Through the following results, the expansion and fracture evolution process of 45 steel under different explosive loads are analyzed.

4.2. Numerical Results and Analysis

Under the loading of JOB9003 explosive with high detonation pressure, the pressure propagation characteristics of the inner surface, the outer surface, and the mid-shell thickness of the 45 steel cylindrical shell with an inner diameter of 40 mm and shell thickness of 4 mm can be seen in Figure 9. Note that the inner surface is loaded with a peak value of about 40 GPa; t_i represents the initial damage time, t_c represents the cylinder shell penetration fracture time, and t_f represents the detonation products leakage time. (1) The inner surface of the shell is loaded by detonation products and is in a state of hydrostatic stress, the outer surface is in a state of tension under the tensile stress, and the middle of the shell thickness is in a tension–compression fluctuation state. The penetration fracture of the cylindrical shell occurs in the loading stage (the inner surface of the cylindrical shell is subjected to compressive stress and regarded as the loading stage; when the pressure drops to 0, the loading stage ends), as shown in Figure 9a. (2) Before the detonation shock wave is transmitted to the outer surface of the cylindrical shell, the effective plastic strain on the inner surface accumulates the most; the effective plastic strain has a decreasing distribution from the inner wall to the outer wall. When the shock wave reaches the outer surface and is reflected, the effective plastic strain in the middle of the metal shell is the largest, and the overall distribution is convex for the secondary plastic accumulation; the strain in the middle is always the position with the largest plastic strain. It is stipulated in the previous model establishment that, when the strain accumulation reaches $D = 0.48$, the cylindrical shell material becomes damaged and softened; when the strain accumulates rapidly to $D = 1.00$, the initial failure occurs, as shown in Figure 9b; when $t = 2.5 \mu\text{s}$, the material damage first forms in the middle of the wall thickness. When $t = 4.9 \mu\text{s}$, the failure particles appear in the middle of the shell thickness and expand to the inner and outer surfaces along the 45° and 135° directions; they extend to the inner and outer surfaces of the cylindrical shell when $t_c = 7.5 \mu\text{s}$, forming shear cracks and penetrating the cylindrical shell. When $t_f = 17.0 \mu\text{s}$, the detonation products leak from the opening fracture of the cylindrical shell, and the fragment fracture finally shows a pure shear shape, as indicated in Figure 9c.

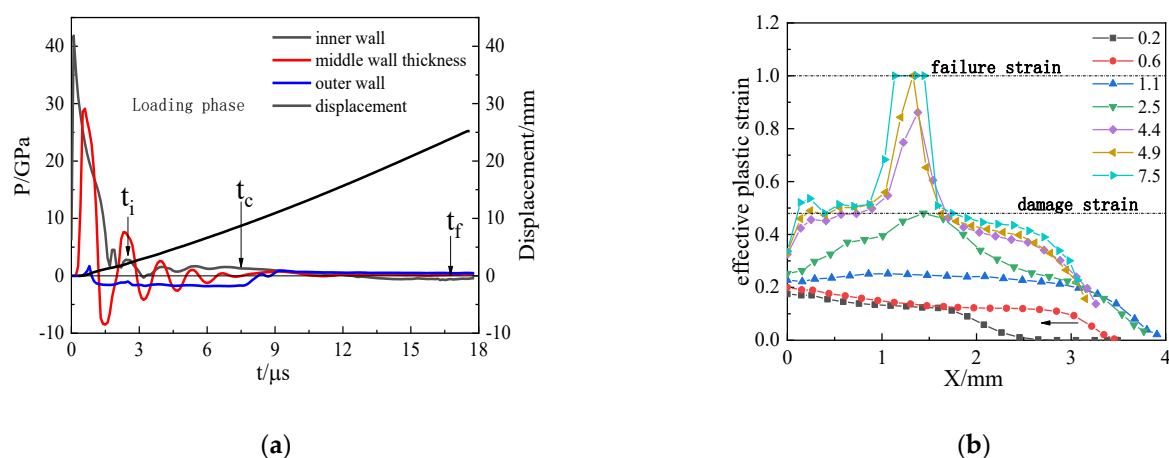


Figure 9. Cont.

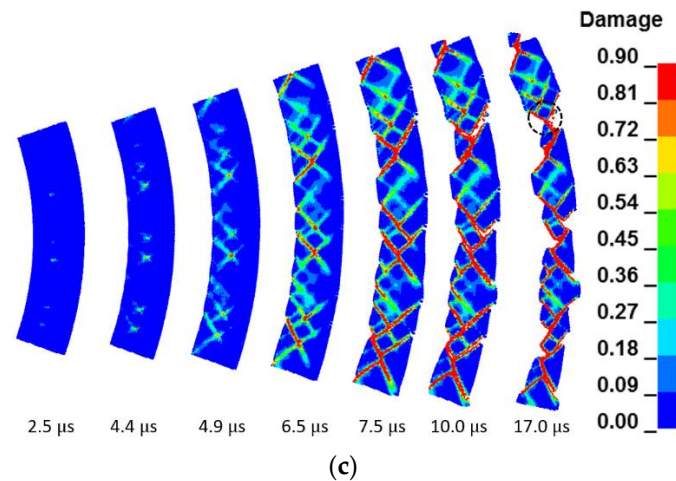


Figure 9. The explosive pressure, expanding deformation, and fracture for 45 steel cylinder shell under JOB9003 loading: (a) detonation wave propagation curves; (b) development of effective plastic strain in the shell thickness; (c) damage evolution for pure shear fracture.

The fracture process of 45 steel shell under RHT-901 loading is similar to JOB9003 loading. It shows pure shear fracture and fracture occurs in the loading stage. Under RHT-901 loading, the fracture and detonation product leakage time is later, as shown in Figure 10.

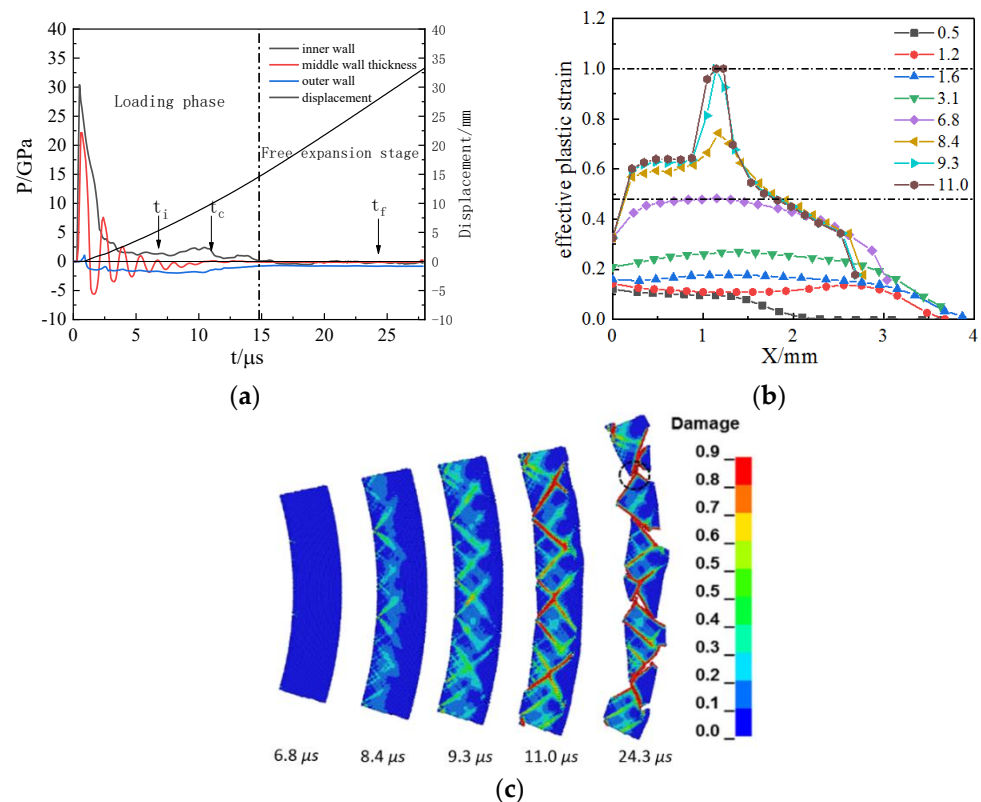


Figure 10. The explosive pressure, expanding deformation, and fracture for 45 steel cylinder shell under RHT-901 loading: (a) detonation wave propagation curves; (b) development of effective plastic strain in the shell thickness; (c) damage evolution for fracture.

Under the loading of TNT with a lower detonation pressure, the fracture mode of the cylindrical shell shows tensile–shear mixed fracture mode. The inner surface loaded by compressive stress ends at time $t = 11.2 \mu\text{s}$, and then the shell enters the free expansion

stage, as shown in Figure 11a. In the development of effective plastic strain in shell thickness, as shown in Figure 11b, the initial crack first forms near the inner wall; at this time, the cylindrical shell is still in the loading stage, and the crack along the 45° or 135° shear direction expands to the inner and outer surfaces. When the cylindrical shell enters the free expansion stage, $t = 11.2 \mu\text{s}$, the time–history curve of the triaxiality stress law at any position in the unbroken area is similar to position “A”, as shown in Figure 11d; the unbroken area of the cylindrical shell appears similar to the phenomenon of tensile “necking”—the crack development turns to the radial direction, finally becoming a tensile–shear mixed fracture. The proportion of tensile cracks is relatively small, about one-sixth, at time $t = 12.6 \mu\text{s}$. The cylindrical shell becomes a penetrative fracture when $t = 21.8 \mu\text{s}$, and detonation products leak.

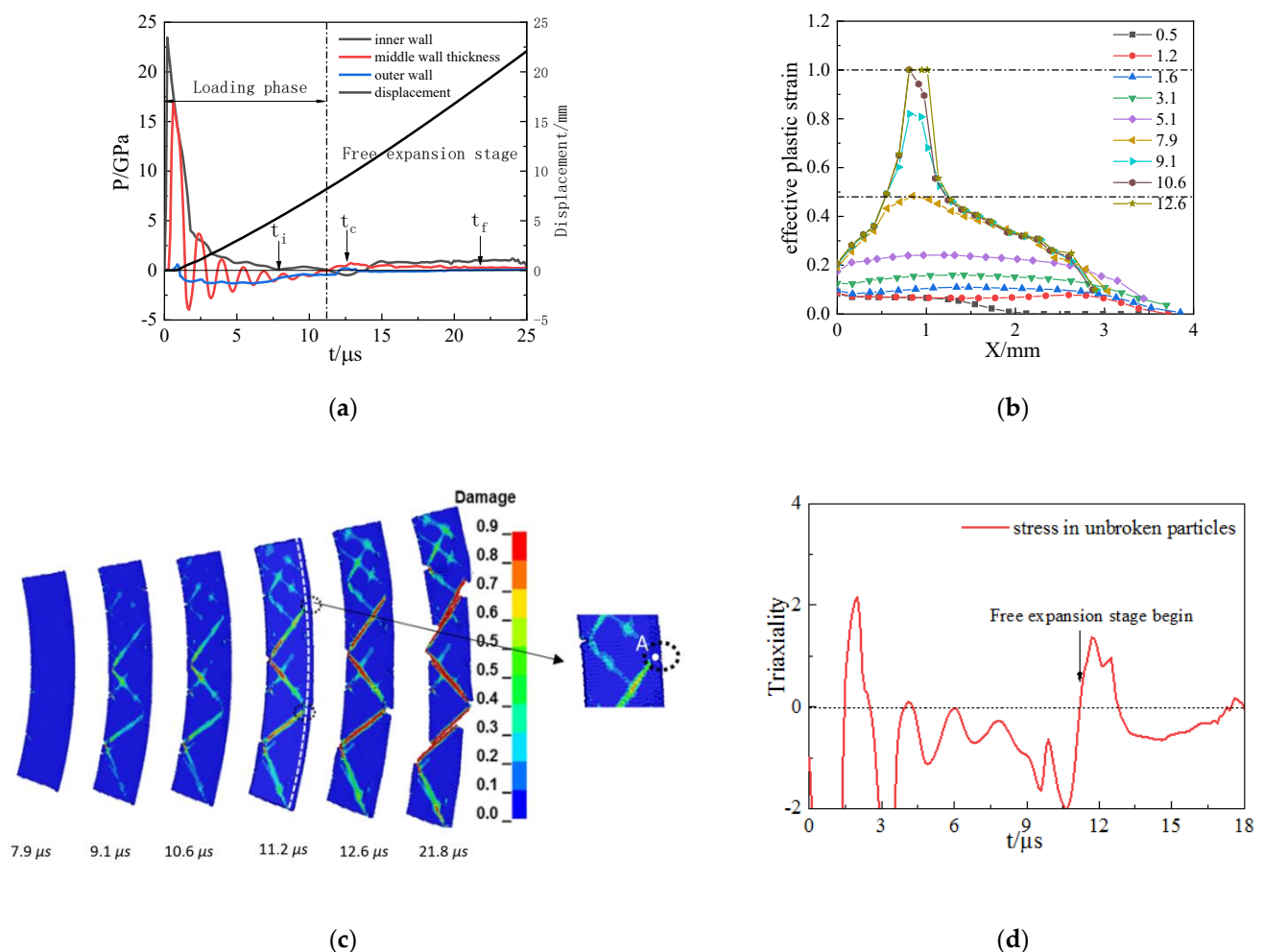


Figure 11. The explosive pressure, expanding deformation, and fracture for 45 steel cylinder shell under TNT loading: (a) detonation wave propagation curves; (b) development of effective plastic strain in the shell thickness; (c) damage evolution for fracture; (d) triaxial stress.

Under the loading of HNS with low detonation pressure, the 45 steel shell also undergoes tensile–shear mixed fracture, but tensile cracks accounted for a higher proportion in the fracture, about one-half. Shear cracks are less developed because fracture development takes less time during the loading phase, as shown in Figure 12.

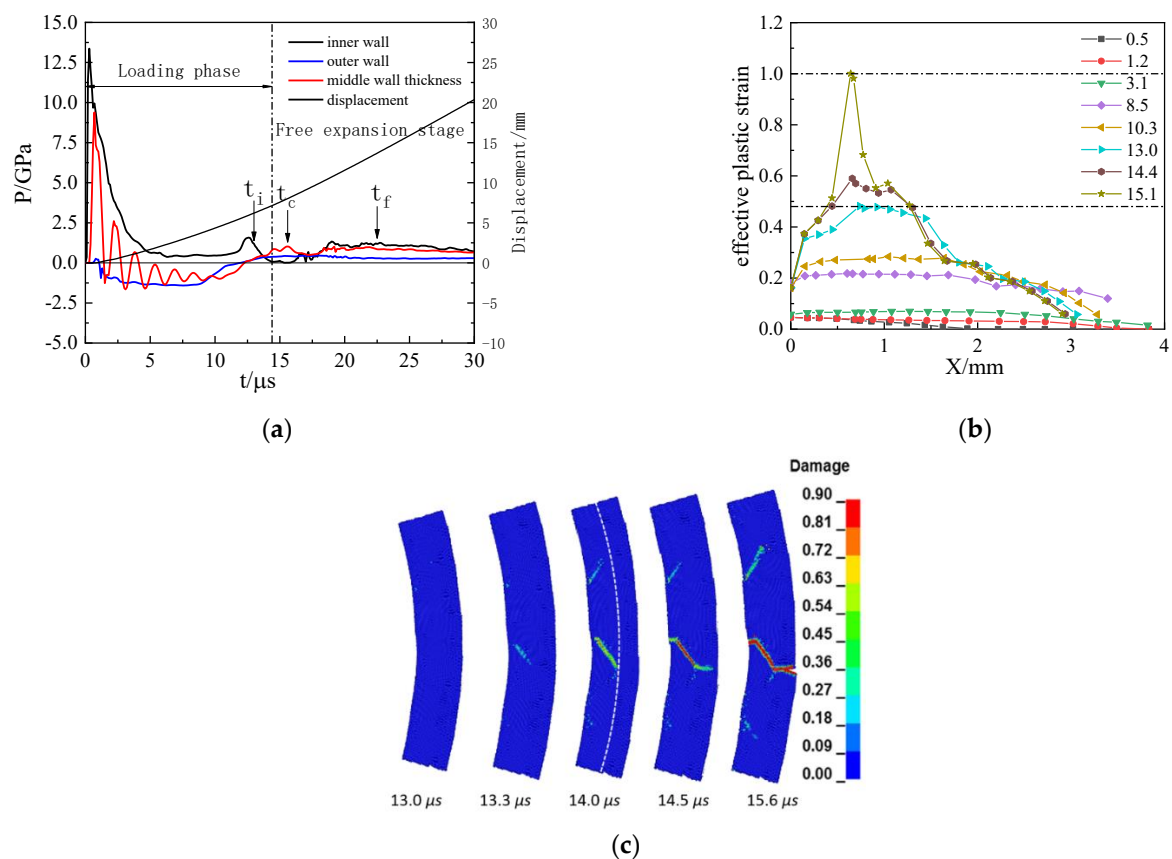


Figure 12. The explosive pressure, expanding deformation, and fracture for 45 steel cylinder shell under HNS loading: (a) detonation wave propagation curves; (b) development of effective plastic strain in shell thickness; (c) fracture damage evolution.

5. Conclusions

The following conclusions were drawn from the SPH numerical simulation analysis of the expansion fracture process of 45 steel cylindrical shell under different detonation pressure loading:

1. The experimental end-state fragmentation phenomenon of shear and tensile–shear mixed fracture under different explosive conditions can be simulated well by the SPH numerical model with a unified material constitutive and fracture model.
2. As the detonation pressure decreases, the fracture mode of 45 steel cylindrical shell changes from pure shear to tensile–shear mixed fracture. Cracks always form in the middle of shell thickness.
3. Under higher detonation pressure loading (JOB9003, RHT-901), the crack initiation and fracture of the 45 steel cylindrical shell occur during the loading stage; the failure of the cylindrical shell begins at mid-thickness in which the plastic strain accumulation is at its maximum. It spreads in the shear direction to the inner and outer walls, resulting in pure shear fracture mode.
4. As the detonation loading pressure decreases, loaded by explosives of TNT and HNS, on account of the initial fracture occurring during the loading stage, the fracture still begins from the middle of the shell thickness and spreads along the shear direction to the inner and outer walls. When the cylindrical shell expands to the free expansion stage, the unbroken area is under circumferential tensile stress, resulting in a phenomenon known as “necking”. The growing crack turns to the radial direction along the “necking” area, resulting in a tensile–shear mixed fracture mode. Furthermore, the lower the explosion pressure, the earlier the cylindrical shells enter the free expansion stage and the higher proportion of final tensile cracks.

Author Contributions: Conceptualization, Z.H., X.Y.; methodology, Z.H.; software, Z.H.; validation, Z.H.; formal analysis, Z.H.; investigation, Z.H.; resources, Z.H.; data curation, Z.H.; writing—original draft preparation, Z.H.; writing—review and editing, X.Y.; visualization, Z.H.; supervision, X.Y.; project administration, X.Y.; funding acquisition, Z.H. All authors have read and agreed to the published version of the manuscript.

Funding: This research received no external funding.

Institutional Review Board Statement: Not applicable.

Informed Consent Statement: Not applicable.

Data Availability Statement: Not applicable.

Conflicts of Interest: The authors declare no conflict of interest.

References

1. Mott, N.F. Fragmentation of shell cases. *Proc. R. Soc. Ser. A. Math. Phys. Sci.* **1947**, *189*, 300–308.
2. Beetle, J.C. SEM/1971(Part I). In Proceedings of the 4th Annual SEM Symposium, Chicago, IL, USA, 27–29 April 1971; IIT Research Institute: Chicago, IL, USA; pp. 137–144.
3. Singh, M.; Suneja, H.R.; Bola, M.S.; Prakash, S. Dynamic tensile deformation and fracture of metal cylinders at high strain rates. *Int. J. Impact Eng.* **2002**, *27*, 939–954. [CrossRef]
4. Arnold, W.; Rottenkolber, E. Fragment mass distribution of metal cased explosive charges. *Int. J. Impact Eng.* **2008**, *35*, 1393–1398. [CrossRef]
5. Grady, D.E. Length scales and size distributions in dynamic fragmentation. *Int. J. Fract.* **2010**, *163*, 85–99. [CrossRef]
6. Gurney, R.W. The initial velocities of fragments from bombs, shell, grenades. *Ballist. Res. Lab.* **1943**, *405*, 1–12.
7. Taylor, G.I. Analysis of the Explosion of a Long Cylindrical Bomb Detonated at One End. In *Mechanics of Fluids, Scientific Papers of G.I. Taylor*; Technical Report HO 195/10/193; Cambridge University Press: Cambridge, UK, 1941; Volume 2, pp. 277–286.
8. Hoggatt, C.R.; Recht, R.F. Fracture behavior of tubular bombs. *J. Appl. Phys.* **1968**, *39*, 1856–1862. [CrossRef]
9. Martineau, R.L.A. Viscoplastic Model of Expanding Cylindrical Shells Subjected to Internal Explosive Detonations. Ph.D. Thesis, Colorado State University, Fort Collins, CO, USA, 1998.
10. Jovičević-Klug, M.; Verbovšek, T.; Jovičević-Klug, P.; Šetina Batič, B.; Ambrožič, B.; Dražić, G.; Podgornik, B. Revealing the Pb whisker growth mechanism from Al-Alloy Surface and morphological dependency on material stress and growth environment. *Materials* **2022**, *15*, 2574. [CrossRef]
11. Hofmeister, A.M.; Criss, E.M.; Criss, R.E. Thermodynamic relationships for perfectly elastic solids undergoing steady-state heat flow. *Materials* **2022**, *15*, 2638. [CrossRef]
12. Sidorova, E.; Karasev, A.; Kuznetsov, D.; Jönsson, P.G. Investigation of the initial corrosion destruction of a metal matrix around different non-metallic inclusions on surfaces of pipeline steels. *Materials* **2022**, *15*, 2530. [CrossRef]
13. Liang, M.Z.; Li, X.; Lu, F. Effects of U-notches on the dynamic fracture and fragmentation of explosively driven cylinders. *Theor. Appl. Fract. Mech.* **2015**, *77*, 50–58. [CrossRef]
14. Hu, B.Y.; Dong, Q.D.; Han, C.S.; Hu, H.B.; Wang, D.S.; Gao, X.H. Macroscopic study on adiabatic shear fracture of explosive metal tubes. *Explos. Shock.* **1992**, *4*, 319–325.
15. Hu, H.B.; Tang, T.G.; Hu, B.Y.; Wang, D.S.; Han, C.S. The single-spin phenomenon of metallic cylindrical shells under blast loading and fracture. *Explos. Shock.* **2004**, *24*, 97–107.
16. Liu, M.T.; Tang, T.G.; Hu, H.B.; Li, Q.Z.; Hu, X.Z.; Li, Y.C. Numerical Simulation of explosive-driven cylindrical shell expansion fracture under different detonation modes. *Explos. Shock.* **2014**, *34*, 415–420.
17. Yu, X.L.; Dong, X.L.; Pan, S.J. Fracture behaviors of explosively driven TA2 alloy cylinders under different loadings. *Explos. Shock. Waves* **2018**, *38*, 148–154. [CrossRef]
18. Liu, M.T.; Ren, G.W.; Fan, C.; Tang, T.G.; Wang, X.Y.; Hu, H.B. Experimental and numerical studies on the expanding fracture behavior of an explosively driven 1045 steel cylinder. *Int. J. Impact Eng.* **2017**, *109*, 240–252. [CrossRef]
19. Zhang, S.W.; Jin, S.; Liu, C.L. Numerical simulation of detonation expansion fracture of a thick-walled circular tube with defects. *Chin. J. Appl. Mech.* **2010**, *27*, 622–625, 653.
20. Zhai, M.H.; Wang, Z.K.; Jiao, H.W. Comparative analysis of SPH method and finite element method in meshless method. *Mach. Des. Manuf.* **2008**, *7*, 32–34.
21. Wu, S.S.; Dong, X.L.; Yu, X.L. SPH simulation analysis of explosive expansion fracture of 45 steel cylindrical shell. *Explos. Shock.* **2021**, *41*, 67–77.
22. Liu, G.R.; Liu, M.B.; Li, S. *Smoothed Particle Hydrodynamics—A Meshfree Method*; World Science: Hackensack, NJ, USA, 2004.
23. Remington, T.P.; Owen, J.M.; Nakamura, A.M.; Miller, P.L.; Bruck Syal, M. Numerical simulations of laboratory-scale, hypervelocity-impact experiments for asteroid-deflection code validation. *Earth Space Sci.* **2020**, *7*, e2018EA000474. [CrossRef]
24. Jankowiak, T.; Łodygowski, T. Smoothed particle hydrodynamics versus finite element method for blast impact. *Bull. Pol. Acad. Sciences. Tech. Sci.* **2013**, *61*, 111–121. [CrossRef]

25. Kong, X.; Wu, W.; Li, J.; Liu, F.; Chen, P.; Li, Y. A numerical investigation on explosive fragmentation of metal casing using Smoothed Particle Hydrodynamic method. *Mater. Eng.* **2013**, *51*, 729–741. [CrossRef]
26. Zhou, F.; Molinari, J.F.; Ramesh, K.T. A cohesive model-based fragmentation analysis: Effects of strain rate and initial defects distribution. *Int. J. Solids Struct.* **2005**, *42*, 5181–5207. [CrossRef]
27. Wright, T.W.; Ockendon, H. A scaling law for the effect of inertia on the formation of adiabatic shear bands. *Int. J. Plast.* **1996**, *12*, 927–934. [CrossRef]
28. Grady, D.E.; Kipp, M.E. The growth of unstable thermoplastic shear with application to steady-wave shock compression in solids. *J. Mech. Phys. Solids* **1987**, *35*, 95–119. [CrossRef]
29. Xiao, Y.H. Normalized SPH without boundary deficiency and its application to transient solid mechanics problems. *Meccanica* **2020**, *55*, 2263–2283. [CrossRef]
30. Goto, D.M.; Becker, R.; Orzechowski, T.J.; Springer, H.K.; Sunwoo, A.J.; Syn, C.K. Investigation of the fracture and fragmentation of explosively driven rings and cylinders. *Int. J. Impact Eng.* **2008**, *35*, 1547–1556. [CrossRef]
31. Zhang, S.W.; Liu, C.L.; Yu, J.Q. Influence of microdefects on expansion fracture of round tube. *Explos. Shock.* **2008**, *28*, 316–323.
32. Zhen, K.; Dong, X.L. Tensile-shear failure of 20 steel cylindrical shells subjected to explosive loading. *Ordinance Mater. Sci. Eng.* **2018**, *41*, 61–64. [CrossRef]
33. Tang, T.G.; Li, Q.Z.; Sun, X.L.; Sun, Z.F.; Jin, S.; Gu, Y. Strain rate effect on expansion fracture of 45 steel cylindrical shell. *Explos. Shock.* **2006**, *26*, 129–133.
34. Hu, B.Y.; Dong, Q.D.; Han, C.S.; Hu, H.B.; Wang, D.S. A mesoscopic study on adiabatic shear fracture of explosive metal pipes. *Explos. Shock.* **1993**, *13*, 305–312.
35. Gray, J.P.; Monaghan, J.J.; Swift, R.P. SPH elastic dynamics. *Comput. Methods Appl. Mech. Eng.* **2001**, *190*, 49–50. [CrossRef]
36. Belytschko, T.; Yong, G.; Shao, P.X. A unified stability analysis of meshless particle methods. *Int. J. Numer. Methods Eng.* **2000**, *48*, 1359–1400. [CrossRef]
37. Wang, L.L. *Basics of Stress Waves*; National Defense Industry Press: Beijing, China, 2005.
38. Hu, C.M.; He, H.L.; Hu, S.S. A study on dynamic mechanical behaviors of 45 steel. *Explos. Shock. Waves* **2003**, *23*, 188–192. [CrossRef]
39. Sun, C.W. *Applied Detonation Physics*; National Defense Industry Press: Beijing, China, 2000.

Article

Influence of Mold Design on Shrinkage Porosity of Ti-6Al-4V Alloy Ingots

Tongzheng He ^{1,2} and Yuyong Chen ^{1,3,*}¹ School of Materials Science and Engineering, Harbin Institute of Technology, Harbin 150001, China² Pangang Group Panzhihua Research Institute of Iron & Steel Co., Ltd., Panzhihua 617000, China³ College Vanadium and Titanium, Panzhihua University, Panzhihua 617000, China

* Correspondence: yychen@hit.edu.cn; Tel.: +86-0451-86418802

Abstract: Mold design is one of the important ways to control shrinkage porosity. In this study, four mold forms with different tapers were first designed, the corresponding three-dimensional finite element models were built using the ProCAST software, and the influence of mold design on the filling and solidification processes of Ti-6Al-4V alloy was investigated. The results showed that the titanium alloy ingots exhibit typical characteristics of layer-by-layer solidification, and that the removal of the riser results in: (a) shortening the time it takes for molten metal to reach the bottom of the mold and the time needed to complete mold filling; (b) decreasing the maximum flow velocity and improving the filling stability; and (c) moving the shrinkage cavities up along the central axis of the ingot and decreasing the cavity volume. Meanwhile, it was also found that the shrinkage cavity volume decreases significantly with increasing mold taper, meaning a significant increase in ingot utilization rate. The shrinkage cavity formation mechanism was revealed through macrostructure analysis. During solidification, a grain frame is formed as a large number of equiaxed crystals intersect, thus creating an isolated liquid phase zone. When the liquid in this zone solidifies, the last zone to do so, its volume shrinkage cannot be compensated, thus leading to the formation of a shrinkage cavity.

Citation: He, T.; Chen, Y. Influence of Mold Design on Shrinkage Porosity of Ti-6Al-4V Alloy Ingots. *Metals* **2022**, *12*, 2122. <https://doi.org/10.3390/met12122122>

Academic Editors: Shuwen Wen, Yongle Sun and Xin Chen

Received: 11 November 2022

Accepted: 6 December 2022

Published: 9 December 2022

Publisher's Note: MDPI stays neutral with regard to jurisdictional claims in published maps and institutional affiliations.



Copyright: © 2022 by the authors. Licensee MDPI, Basel, Switzerland. This article is an open access article distributed under the terms and conditions of the Creative Commons Attribution (CC BY) license (<https://creativecommons.org/licenses/by/4.0/>).

Keywords: mold design; Ti-6Al-4V alloy ingot; mold taper; numerical simulation; shrinkage porosity

1. Introduction

Ti-6Al-4V (wt.%) alloy has been widely applied in aerospace, ocean engineering, biomedicine, and other fields owing to its good comprehensive mechanical properties and low production costs [1,2]. However, the defect of shrinkage porosity in Ti-6Al-4V alloy castings seriously reduces the serviceability of the alloy products and reduces the material utilization rate [3]. At present, researchers use various methods to control the formation of shrinkage cavities, including the hot isostatic pressing technique [3–5], optimizing the smelting method [6–11] and improving the casting process [12–16], and certain positive results have been achieved.

Research shows that the use of the hot isostatic pressing technique can effectively reduce shrinkage porosity in titanium alloy castings. Atkinson et al. [4] demonstrated clearly that reducing shrinkage porosity in as-cast microstructure is one of the main benefits of the hot isostatic pressing technique. Feng et al. [3] investigated the influence of the hot isostatic pressing technique on the shrinkage porosity of large, thin-walled Ti-6Al-4V alloy castings, finding that the method can not only effectively suppress the formation of shrinkage cavities, but can also significantly improve the bonding force of β grain boundaries, thus improving the toughness of the castings. However, the hot isostatic pressing process causes dimensional deformation of castings, and using the method it is difficult to eliminate shrinkage porosity completely [8,17–19]. With the continuous progress in casting technology in recent years, advanced processes such as centrifugal casting [6–8],

anti-gravity casting [9,10], and vacuum suction casting [11] have been widely used in the preparation of titanium alloy castings. Yang et al. [6] compared the effects of centrifugal and gravity casting on the shrinkage porosity of TiAl alloy castings by means of numerical simulation and experimental verification. The results show that centrifugal casting is more effective at suppressing the formation of isolated liquid phase zones and at reducing the volume of the shrinkage cavity. Suzuki et al. [7] investigated the effect of centrifugal speed on the shrinkage porosity of Ti-6Al-4V alloy castings, revealing that increasing centrifugal speed can effectively suppress the formation of shrinkage cavities. However, when the centrifugal speed is too high, the flow of molten metal may stop, resulting in the formation of shrinkage cavities [8]. In their study on the anti-gravity casting process of Ti-6Al-4V alloy, Ma et al. [9] clearly illustrated that the formation of shrinkage cavities can be effectively controlled by improving mold filling and adopting pressurized solidification. By examining the effect of filling pressure on the shrinkage porosity of TiAl alloy during anti-gravity casting, Yang et al. [10] clarified that increasing filling pressure can significantly increase the fluidity of molten metal and reduce heat loss, helping to suppress the formation of pre-solidification zones and effectively improve the feeding capacity of the molten metal. However, excessively high filling pressure is not conducive to the control of shrinkage porosity. It is worth noting that proper design of the casting process, such as setting a suitable pouring temperature and mold preheating temperature, is always important in reducing shrinkage porosity. Research shows [12–16] that these factors can effectively improve the fluidity of the molten metal and reduce heat loss, ensuring the high feeding capacity of the molten metal and suppressing the formation of shrinkage cavities. In addition, Gao et al. [20] significantly reduced the shrinkage cavity volume in a TiAl alloy ingot by adding a temperature gradient to the mold, pioneering a new path for controlling shrinkage porosity in titanium alloy ingots.

Unfortunately, relatively little effort has been made to study the influence of mold design on the shrinkage porosity of titanium alloy castings. In this study, the influence of mold design on the shrinkage porosity of Ti-6Al-4V alloy ingots was systematically investigated using four casting mold forms with slightly different shapes. Adopting an approach combining numerical simulation and experimental verification, the influence of a riser on alloy filling and solidification processes was studied, the quantitative relationship between the mold taper and shrinkage cavity (including shrinkage cavity volume and material utilization rate) was analyzed in depth, and the formation mechanism of shrinkage cavities in titanium alloy ingots was elucidated, thus providing an effective way to control shrinkage porosity in titanium alloy ingots.

2. Materials and Methods

2.1. Finite Element Model

In this study, the casting process of Ti-6Al-4V (wt.%) alloy was systematically explored using the ProCAST 2018 software (ESI Group, Paris, France). First, four common mold forms I–IV were designed (Figure 1) based on the casting equipment available, and the sample ingots prepared with the four mold forms were named alloys I–IV, respectively. Mold I features a riser with a height of 50 mm, and molds II–IV have no risers. The four ingots and molds have relative mass ratios of 0.56, 0.51, 0.55, and 0.47. Then, the sample ingots and molds were modeled in three dimensions and partitioned into meshes. The mesh of each ingot has an average cell size of 5 mm to ensure that there are at least two meshes at the thinnest part of the ingots, the mesh of each mold has an average cell size of 10 mm, and the number of volume mesh cells is about 334,737.

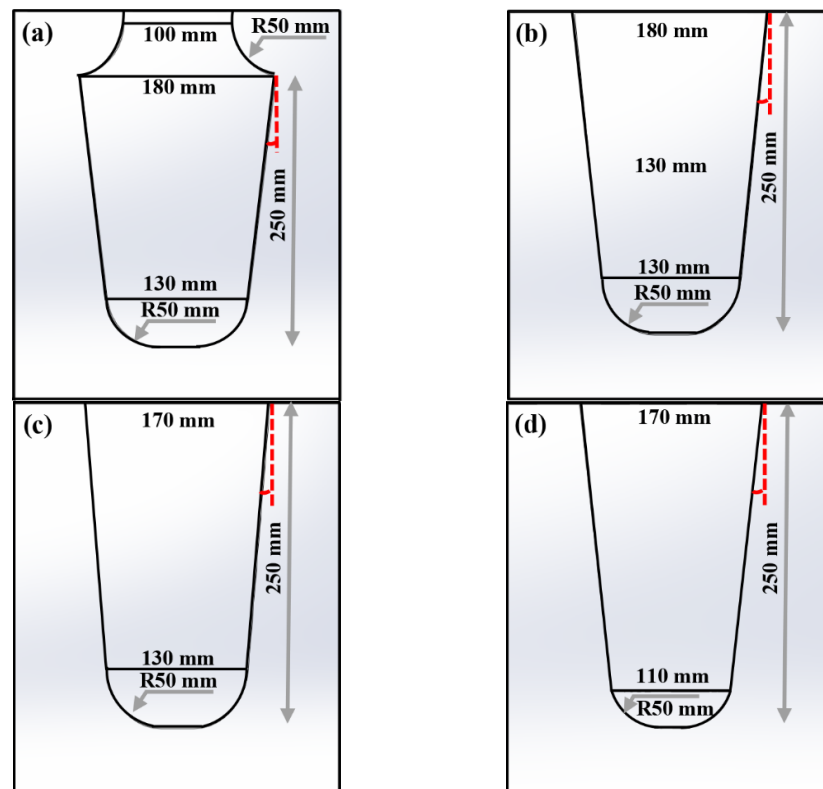


Figure 1. Mold design: (a) mold I; (b) mold II; (c) mold III; (d) mold IV.

2.2. Thermophysical Parameters and Boundary Conditions

Ti-6Al-4V alloy was chosen as the material for preparing the ingots and graphite was used as the mold material. The liquidus and solidus temperatures of Ti-6Al-4V alloy are 1660 °C and 1604 °C, respectively [5], and other thermophysical parameters were calculated using the ProCAST software, as shown in Table 1. Graphite has a density of 1690–1720 kg·m⁻³, a specific heat capacity of 0.72–2.89 kJ·kg⁻¹·K⁻¹, and a thermal conductivity of 12–108 W·m⁻¹·K⁻¹. In the calculation process, the pouring temperature was set to 1700 °C, the mold preheating temperature was 300 °C, and the pouring speed was 4.7 kg·s⁻¹. Meanwhile, the stress type of the Ti-6Al-4V alloy was set to “linear-elastic”, the stress type of graphite was “rigid”, and the cooling method was “air cooling”, with a heat transfer coefficient between the casting and the mold shell of 800 W·m⁻²·K⁻¹.

Table 1. Physical parameters of Ti-6Al-4V based on ProCAST calculation.

Temperature (°C)	Density (kg·m ⁻³)	Enthalpy (kJ·kg ⁻¹)	Viscosity (Pa·s)	Thermal Conductivity (W·m ⁻¹ ·K ⁻¹)
25	4430	11.8	-	7.87
200	4322	153.6	-	10.92
400	4297	214.4	-	12.54
600	4262	369.8	-	14.47
800	4231	464.3	-	16.49
1000	4189	585.9	-	18.68
1200	4138	741.3	-	20.95
1400	4094	856.1	-	24.56
1600	4039	1052.0	2.14	28.09
1700	3938	1416.7	1.76	33.56

In this study, the flowing molten metal was regarded as an incompressible Newtonian fluid, and the governing Equations (1)–(5) in the process of mold filling and solidification are as follows [6,10,21]:

The Navier-Stokes equations for viscous fluids are [6,21]:

$$\rho \left(\frac{\partial u}{\partial t} + u \frac{\partial u}{\partial x} + v \frac{\partial u}{\partial y} + w \frac{\partial u}{\partial z} \right) = -\frac{\partial P}{\partial x} + \rho g_x + \mu \left(\frac{\partial^2 u}{\partial x^2} + \frac{\partial^2 u}{\partial y^2} + \frac{\partial^2 u}{\partial z^2} \right) \quad (1)$$

$$\rho \left(\frac{\partial v}{\partial t} + u \frac{\partial v}{\partial x} + v \frac{\partial v}{\partial y} + w \frac{\partial v}{\partial z} \right) = -\frac{\partial P}{\partial y} + \rho g_y + \mu \left(\frac{\partial^2 v}{\partial x^2} + \frac{\partial^2 v}{\partial y^2} + \frac{\partial^2 v}{\partial z^2} \right) \quad (2)$$

$$\rho \left(\frac{\partial w}{\partial t} + u \frac{\partial w}{\partial x} + v \frac{\partial w}{\partial y} + w \frac{\partial w}{\partial z} \right) = -\frac{\partial P}{\partial z} + \rho g_z + \mu \left(\frac{\partial^2 w}{\partial x^2} + \frac{\partial^2 w}{\partial y^2} + \frac{\partial^2 w}{\partial z^2} \right) \quad (3)$$

Continuity equation [10,21]:

$$\frac{\partial(\rho u_x)}{\partial x} + \frac{\partial(\rho u_y)}{\partial y} + \frac{\partial(\rho u_z)}{\partial z} = 0 \quad (4)$$

Heat conduction equation [10,21]:

$$\rho C_p \left(\frac{\partial T}{\partial t} + u \frac{\partial T}{\partial x} + v \frac{\partial T}{\partial y} + w \frac{\partial T}{\partial z} \right) = \lambda \left(\frac{\partial^2 T}{\partial x^2} + \frac{\partial^2 T}{\partial y^2} + \frac{\partial^2 T}{\partial z^2} \right) + L \frac{\partial f_s}{\partial t} \quad (5)$$

where, ρ is the density of the molten metal; u , v , and w are the velocity vectors in the directions of x , y , and z respectively; P is pressure; g is the gravitational acceleration; μ is the viscosity; t is time; C_p is the specific heat capacity; T is the temperature; λ is the thermal conductivity coefficient; L is the latent heat of crystallization, and f_s is the solid fraction in the solidification stage.

2.3. Ingot Preparation and Macrostructure Characterization

Titanium alloy ingots weighing 20 kg each were prepared using a vacuum induction melting furnace. The raw materials include sponge titanium, pure Al, and Al-V alloy (V: 58.18wt.%). The iCAP 7400 ICP-OES analyzer (Thermo, Waltham, MA, USA) and the TCH600 N, H, and O analyzer (LECO, St. Joseph, MI, USA) were used to analyze the main elements (Al and V) and impurity elements (N, H, and O) of the ingots, respectively. The above test samples were all $\phi 4 \times 10$ mm discs weighing less than 30 mg, which were mechanically ground and ultrasonically cleaned in alcohol for 10 min. For each ingot, at least three positions were chosen for analysis, and the results are displayed in Table 2 to guarantee the correctness of the test results. Then, the ingots were dissected along the center line to show the distribution of shrinkage cavities. Meanwhile, the as-cast macrostructure of each ingot was observed. The metallographic etching solution used in the observation was Kroll reagent (5% HF + 10% HNO₃ + 85% H₂O).

Table 2. Measured chemical compositions (wt.%) of the Ti-6Al-4V.

Alloys	Al	V	H	N	O	Ti
I	6.2	4.3	0.002	0.011	0.096	Bal.
II	5.9	4.1	0.002	0.015	0.104	Bal.
III	6.1	4.2	0.003	0.011	0.101	Bal.
IV	6.2	4.2	0.002	0.010	0.098	Bal.

3. Results

3.1. Numerical Simulation of Mold I

Figure 2 shows the filling process and the flow velocity of molten metal when mold I is used. At 0.24 s, the molten metal quickly reached the bottom of the mold under the

action of gravity (Figure 2a), and the mold was completely filled at 4.09 s, with a filling rate of 98vol.% (Figure 2e). At the initial stage of mold filling, the molten metal has a high flow velocity ($2.394 \text{ m}\cdot\text{s}^{-1}$) and an obvious velocity gradient in the height direction (Figure 2g,h), but the mold filling stability is poor, which can easily lead to gas entrapment and molten metal splashing at the bottom of the mold. Xiong et al. [11] studied the influence of filling speed on the filling process of a TiAl alloy exhaust valve, reaching the following two conclusions. (1) A high filling speed causes a violent collision between the molten metal and the sprue, leading to the splashing of the molten metal. (2) A high filling speed causes serious turbulence at the surface of the molten metal, resulting in the entrapment of a large amount of gas. Liu et al. [22] also found in the investment casting process of a ZG310-570 steel bracket that an increase in filling speed significantly increases the probability of gas entrapment at the bottom of the casting. As the mold filling process progresses, the filling speed decreases obviously, the speed gradient weakens significantly, and the mold filling process stabilizes gradually (Figure 2d,i). At the late filling stage, the speed gradient disappears completely, and the filling proceeds stably (Figure 2j).

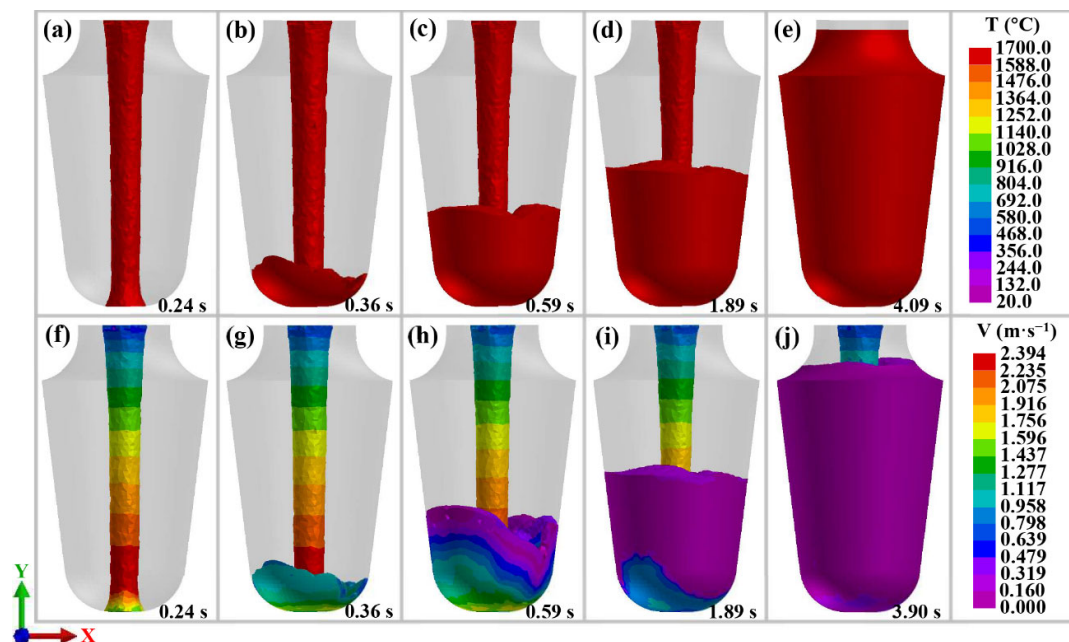


Figure 2. Filling process (a–e) and fluid velocity (f–j) of Ti-6Al-4V alloy in mold I.

Figure 3 shows the solidification process of molten metal and the distribution of shrinkage cavities when mold I is used. It can be seen from Figure 3a that at 1.13 s the part of the molten metal in contact with the mold wall solidifies first. As the mold-filling process progresses, the solidification zone gradually expands along the mold wall (the expansion direction is indicated by the gray arrow in Figure 3b). At 9.12 s, the part close to the mold wall approaches complete solidification (Figure 3c). This phenomenon further proves that the heat radiation of molten metal along the vertical wall is faster than in other directions. As the solidification process progresses, the part of the molten metal at the riser area reaches complete solidification first (Figure 3d), which means that the riser designed in this study cannot effectively fulfill the purpose of feeding. Meanwhile, the bottom part of the alloy ingot (where the cross-sectional area is smaller), under conditions of relatively good heat dissipation, reaches complete solidification earlier than the top part of the alloy ingot (where the cross-sectional area is larger). This leads to the formation of an isolated liquid phase zone at the central region of the top part of the alloy ingot, as shown in Figure 3e. Generally speaking, titanium alloy ingots exhibit typical characteristics of layer-by-layer solidification. It can be seen from Figure 3f that the shrinkage cavities are concentrated at the top part of the ingot, with a volume of 3.29 cm^3 , and the ingot utilization rate is

63.6% (where ingot utilization rate = the distance between the shrinkage cavity and the bottom of the ingot/mold height $\times 100\%$, and mold height = ingot height + riser height). It is worth noting that the zone of the shrinkage cavity almost completely coincides with the isolated liquid phase zone. Therefore, it can be concluded that the formation of the shrinkage cavity is closely related to the formation of the isolated liquid phase zone. The formation mechanism of the isolated liquid phase zone will be analyzed in detail later in this article.

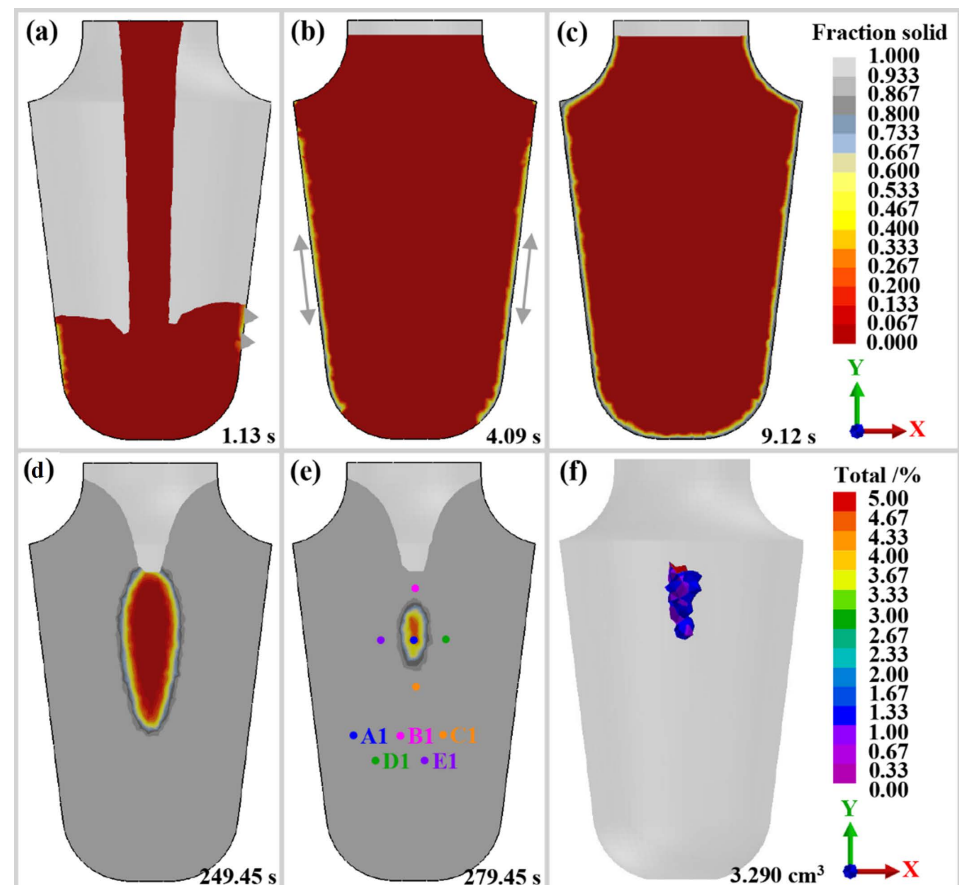


Figure 3. Solidification process (a–e) and shrinkage porosity (f) of Ti-6Al-4V alloy in mold I.

3.2. Numerical Simulation of Molds II, III, and IV

Mold I was optimized based on the above simulation results. Usually, to achieve proper feeding, the riser design can be optimized to ensure that it solidifies later than the casting. However, the use of a riser will significantly reduce the ingot utilization rate, especially when the mass of the ingot is small. Therefore, the riser in mold I was removed, resulting in mold II (Figure 1b). Figure 4a–e shows the mold filling process when mold II is used. It can be seen that when mold II is used, the molding filling has characteristics similar to those of mold I, but the bottom-reaching time of molten metal and filling time are shortened to 0.23 s and 3.57 s, respectively. As can be seen from the simulation results of molten metal flow velocity, Figure 5a–e, the maximum flow velocity of the molten metal decreases to $2.228 \text{ m}\cdot\text{s}^{-1}$ and the speed gradient difference at the initial stage of mold filling decreases, indicating that the mold II filling process is more stable than that of mold I. As demonstrated by the solidification process simulation results in Figure 6a–e, switching from mold I to mold II results in the formation position of the isolated liquid phase zone moving towards the top of the ingot along the central line. This is a desirable result. Figure 7a further proves that the use of mold II can not only effectively suppress the formation of shrinkage cavities (alloy II: 0.061 cm^3) but can also move the shrinkage cavity formation position towards the top of the ingot along the central line. In alloy I, the shrinkage cavity

is 46.8 mm from the top of the ingot, while this distance is shortened to 34.1 mm in alloy II, increasing the utilization rate of ingot II to 86.4%.

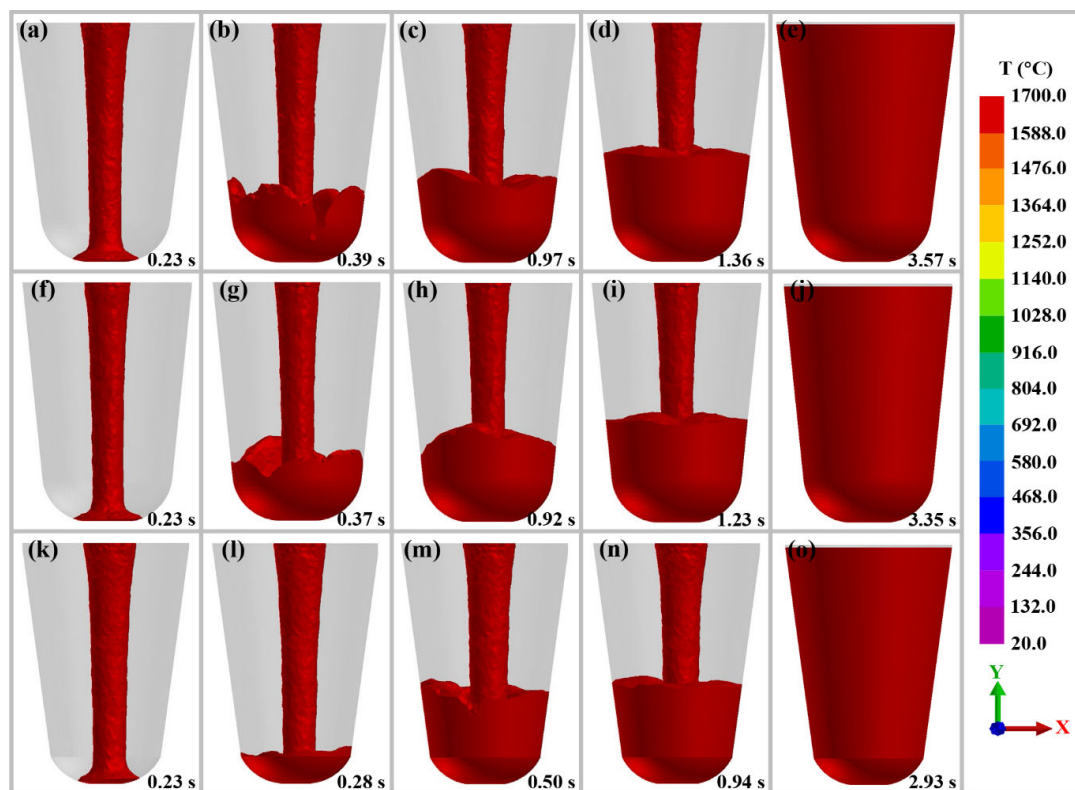


Figure 4. Filling process of Ti-6Al-4V alloy in mold II (a–e), III (f–j), and IV (k–o).

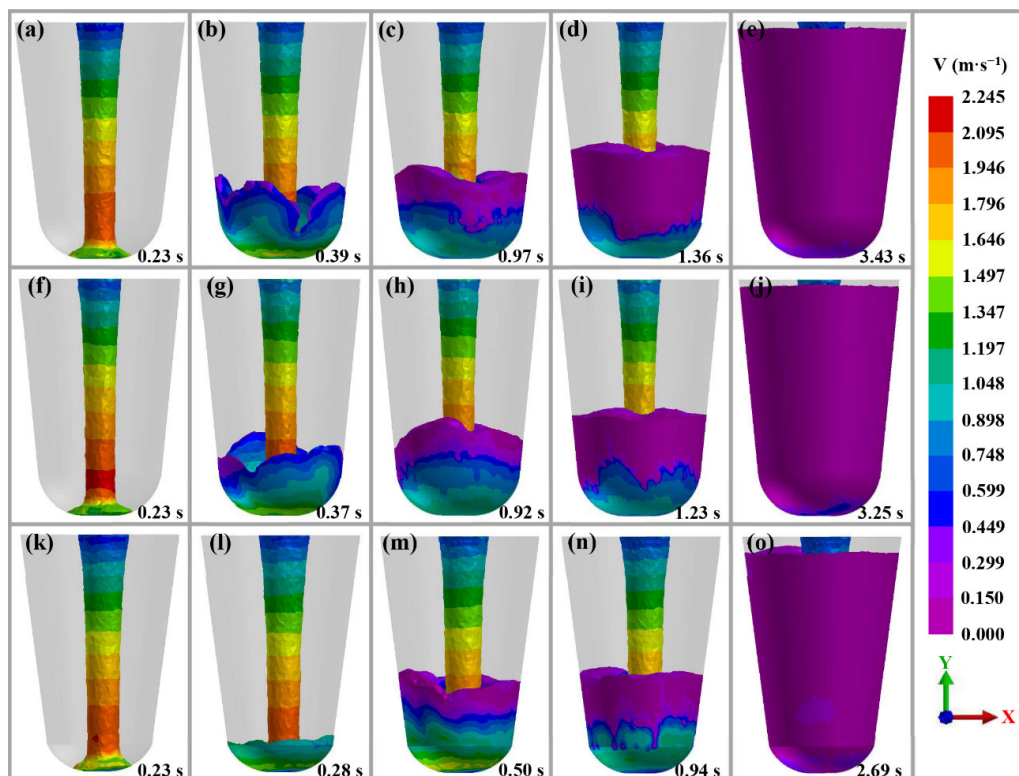


Figure 5. The fluid velocity of Ti-6Al-4V alloy in mold II (a–e), III (f–j), and IV (k–o).

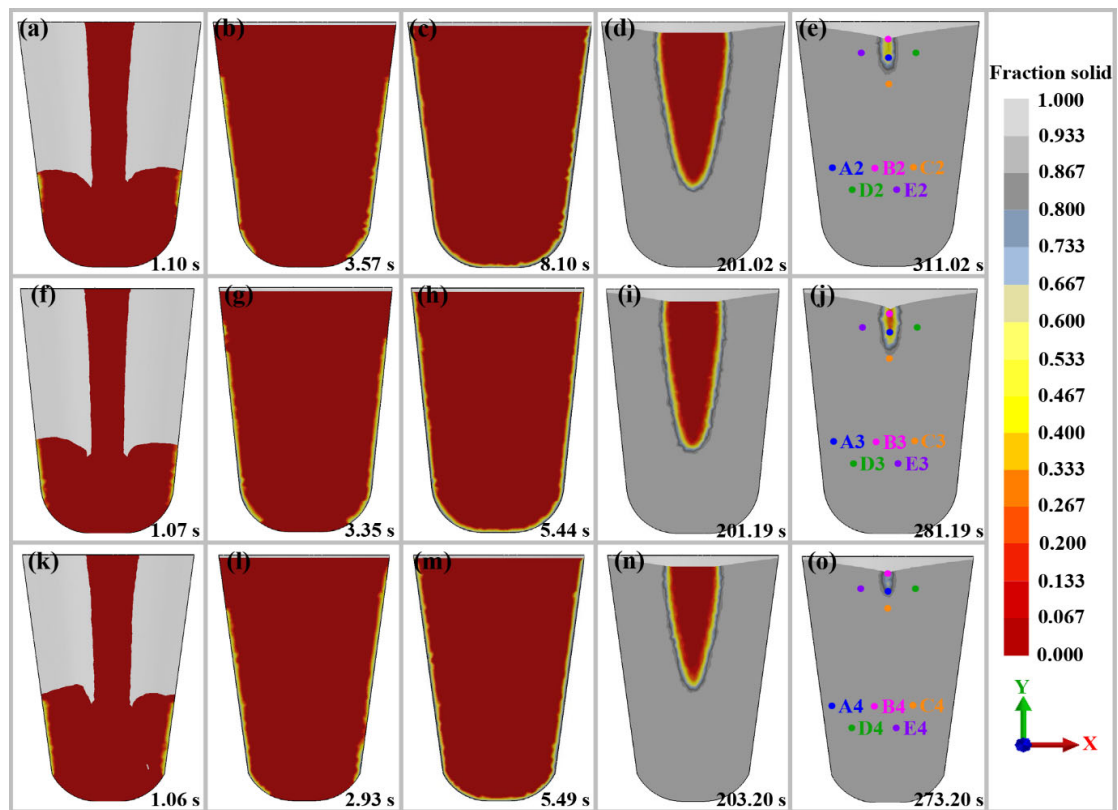


Figure 6. Solidification process of Ti-6Al-4V alloy in mold II (a–e), III (f–j), and IV (k–o).

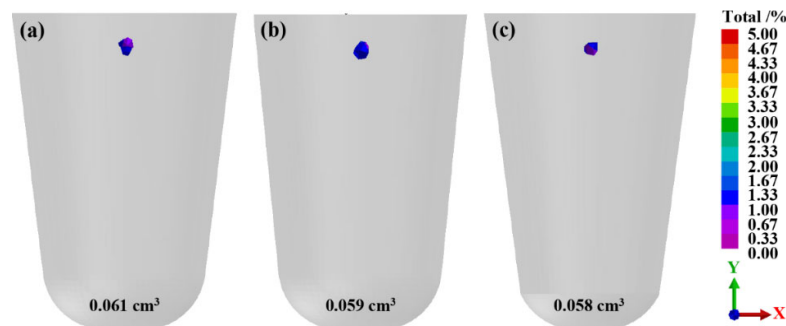


Figure 7. Distribution of shrinkage porosity for Ti-6Al-4V alloy in mold II–IV: (a) II; (b) III; (c) IV.

To further improve the mold filling and alloy casting solidification processes, an in-depth investigation on the key parameters of mold II was carried out, designing molds III and IV as shown in Figure 1c,d. The design of mold III reduces the top size of the ingot to 170 mm, and the design of mold IV reduces the bottom size of the ingot to 110 mm (smaller than mold III). It can be seen from Figures 4f–j and 5f–j that, when mold III is used, the molding filling has characteristics similar to those of mold II, but the maximum flow velocity of molten metal is slightly increased ($2.245 \text{ m}\cdot\text{s}^{-1}$). It can be seen from Figure 6f–j that, when mold III is used, the ingot solidification process exhibits no unique characteristics and that the shrinkage cavity volume is basically unchanged (0.059 cm^3), but that the ingot utilization rate is reduced to 85.8% (Figure 7b). It is worth noting that reducing the bottom size of the ingot lowers the maximum flow velocity of molten metal to $2.198 \text{ m}\cdot\text{s}^{-1}$, thus promoting smooth mold filling, as shown in Figures 4k–o and 5k–o. At the same time, this change has no obvious impact on shrinkage cavity volume (0.058 cm^3) and ingot utilization rate (86.7%), as shown in Figure 7c.

3.3. Experimental Verification

Figure 8 shows the Ti-6Al-4V alloy ingots prepared using molds I–IV. It can be seen that the actual distribution and volume variation pattern of shrinkage cavities in ingots I–IV are basically consistent with the simulation results. However, ingot I contains a large number of small shrinkage cavities and the riser can play a few roles in feeding. Ingot IV contains a small number of small shrinkage cavities. In order to visualize the morphology and distribution of the small shrinkage cavities, the blue rectangular boxed area in Figure 8a is enlarged appropriately and its important features are drawn at a certain scale, as shown in Figure 8b,c. The large shrinkage cavity is represented by the blue region, while the small shrinkage cavity is represented by the orange area. The statistical results show that ingot I has four large shrinkage cavities with an aspect ratio of 1.2–2.0 and nearly 100 small shrinkage cavities with a length of 0.37–2.94 mm that are concentrated around the large shrinkage cavities; in contrast, ingot IV has two large shrinkage cavities with an aspect ratio of 1.1 or 1.4 and a significantly smaller number (about 30) of small shrinkage cavities with a length of 0.5–1.94 mm. Noticeably, the utilization rates of ingots I–IV are 60.5%, 73.6%, 74.5%, and 80.5%, respectively, slightly different from the simulation results. Nonetheless, these figures prove that a rational mold design can effectively improve the material utilization rate. On the whole, numerical simulation results can provide some guidance for controlling the shrinkage porosity of titanium alloy ingots.

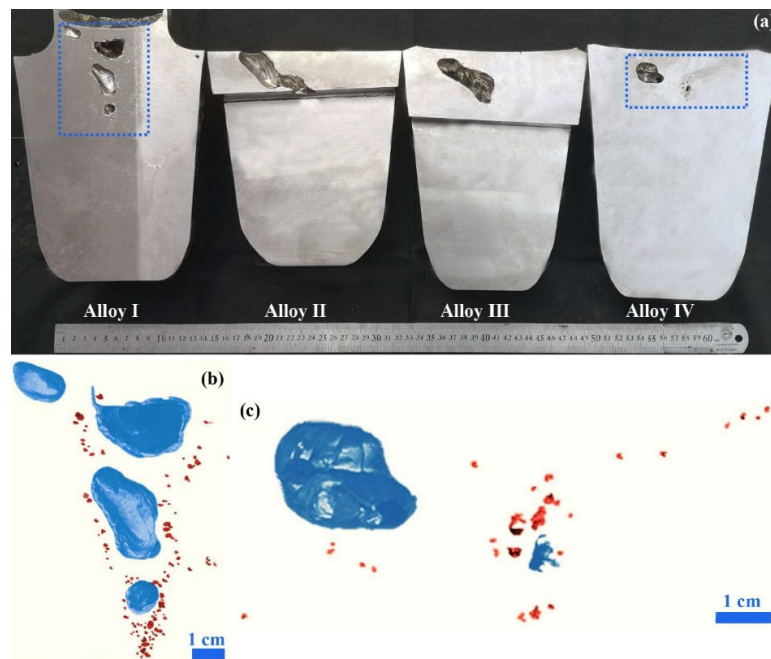


Figure 8. Shrinkage porosity of actual ingots (a) and local enlargement of ingot I (b) and IV (c).

4. Discussion

4.1. Formation Mechanism of Shrinkage Porosity

It can be seen from Figure 3, Figure 6, and Figure 7 that, at the initial stage of solidification, the molten metal solidifies layer by layer from the mold wall to the center of the ingot. The areas with good heat dissipation, such as the bottom of the ingot (where the cross-sectional area is relatively small), solidify first to form a solid surface layer. As the solidification process progresses, the solid shrinkage in the solidified area, the solidification shrinkage caused by solidification, and the liquid shrinkage in the core of the ingot caused by the temperature decrease occur simultaneously. At the late stage of solidification, an isolated liquid phase zone gradually forms in the top central part of the ingot (the area with a larger cross-sectional area). When the sum of the liquid shrinkage and solidification

shrinkage of the alloy is greater than the solid shrinkage, a shrinkage cavity will be formed in this area.

Zhang et al. [9] studied the anti-gravity casting process of Ti-6Al-4V alloy and discovered, through numerical simulation and experiment, that shrinkage cavities mostly occur in areas with relatively large cross sections, and that their locations are close to the sprue and riser. This is mainly because the area with a large cross-sectional area can better preserve heat. When other areas are completely solidified, cutting off the feeding channel, an isolated liquid phase zone will be formed in this area [11]. By studying the influence of TiB₂ on the fluidity of TiAl alloy, Han et al. [23] revealed that shrinkage cavities usually occur in the area that is the last part to solidify. In other words, at the late stage of solidification, the temperature of the isolated liquid phase zone is higher than its surrounding area. For each ingot, five points (A, B, C, D, and E) in the isolated liquid phase zone and the surrounding areas (Figures 3e and 6e,j,o) were picked, and the temperature variation of each point with time was analyzed. The results are shown in Figure 9. As the solidification process progresses, the temperature of point A gradually becomes higher than those of points B, C, D, and E, indicating that these solidify earlier than point A. This means that an isolated liquid phase region will be formed at point A and a shrinkage cavity will be formed at this location. In the same way, Yang et al. [24] explored the formation mechanism of shrinkage cavities in the casting process of TiAl alloy blades, finding that the formation of a shrinkage cavity is related to the presence of an isolated liquid phase zone (in the central region of the blade with larger thickness), and that the temperature of this zone was significantly higher than its surrounding area. Similarly, this formation mechanism was also discovered by Zheng et al. [25] in a study on the vacuum casting process of a brake drum made of Al-based composite materials.

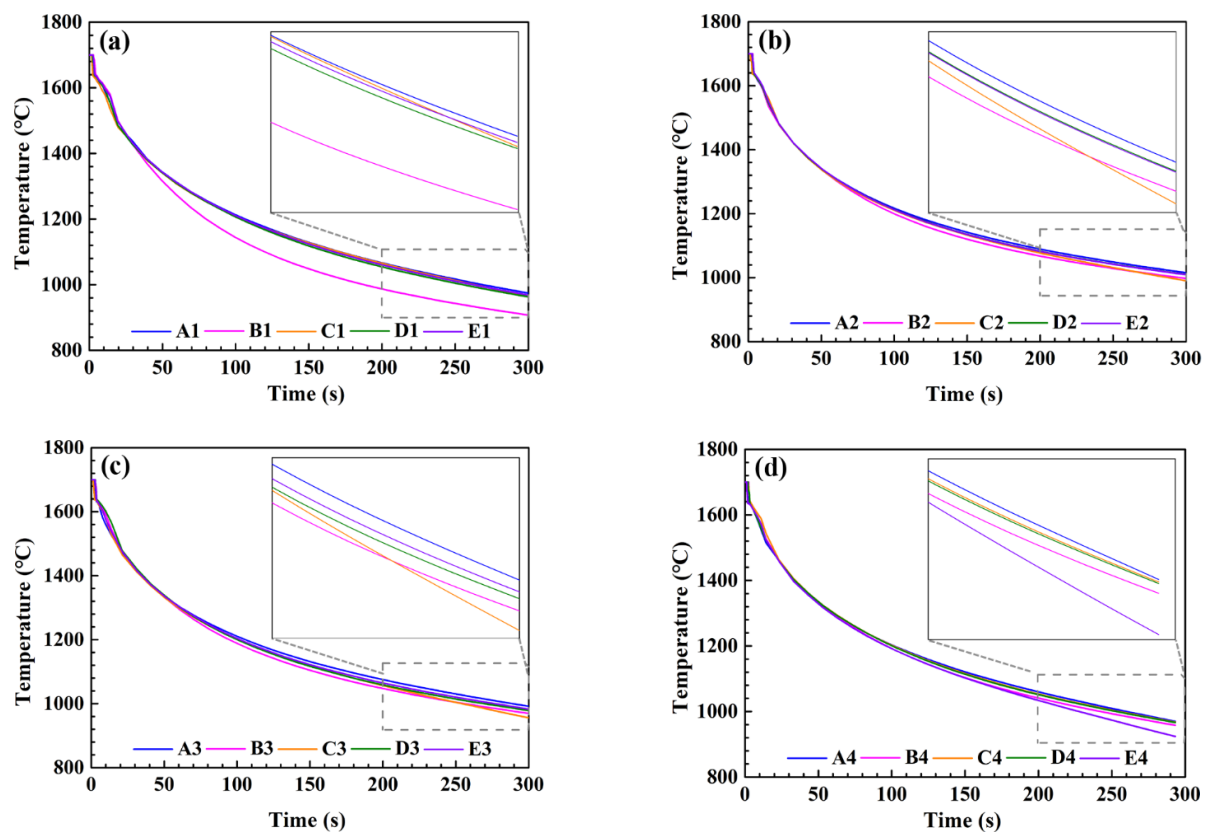


Figure 9. Temperature variation in the isolated liquid phase zones and their surrounding areas: (a) alloy I; (b) alloy II; (c) alloy III; (d) alloy IV.

Research shows [26] that the termination of melt metal flow of Ti-6Al-4V alloy exhibits the characteristics of alloys with a narrow crystallization temperature range. The formation of a shrinkage cavity in casting can be largely attributed to an isolated liquid phase zone resulting from the formation of a crystal grain frame comprising a large number of columnar crystal grains and a small number of equiaxed crystal grains. It was found through macrostructure observation (Figure 10) that the basic structure of the ingots prepared in this study is almost completely composed of equiaxed crystal grains. Therefore, it can be concluded that Ti-6Al-4V alloy ingots exhibit the characteristics of alloys with a wide crystallization temperature range. Analysis reveals that the difference in macrostructure characteristics is mainly attributed to the difference in the casting cooling rate which, in turn, can be traced to differences in the specifications of the castings. In the study [26], a spiral-shaped casting with a relatively small cross-sectional area was used, so the cooling speed was relatively high, providing favorable conditions for the formation of columnar crystal grains. By comparison, the near-cylindrical ingot in this study has a large thickness and relatively slow cooling speed (especially at the core), which seriously restricts the nucleation of columnar crystal grains. According to the characteristics of alloys with wide crystallization temperature ranges introduced by Dahle et al. [27], the formation of shrinkage cavities in this study is shown in Figure 11. In summary, the formation of shrinkage cavities in Ti-6Al-4V alloy ingots in this study is mainly due to (a) the formation of isolated liquid phase zones resulting from a grain frame comprising the intersection of a large number of equiaxed crystals, and (b) the inability of the last crystallization part to compensate for the volume shrinkage.



Figure 10. Macrostructure of Ti-6Al-4V alloy ingots.

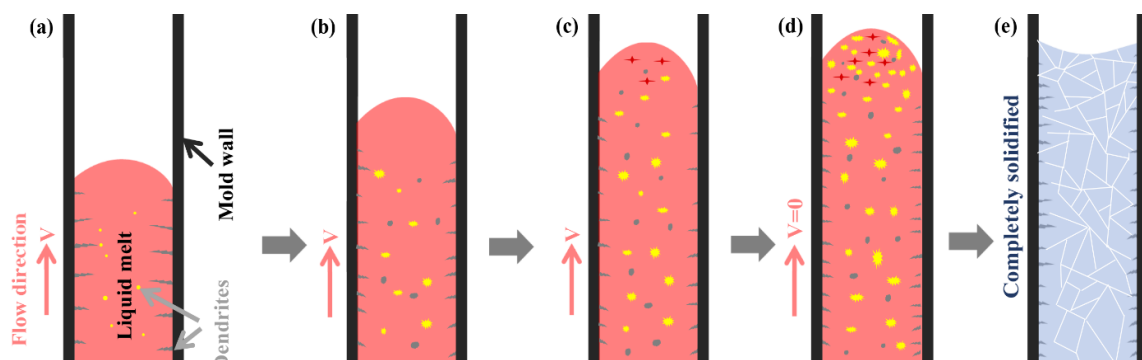


Figure 11. The cessation mechanism of flow for Ti-6Al-4V ingot: (a–c) filling step in which the liquid metal is in motion; (d) stagnant step in which the velocity of liquid metal is zero; (e) completely solidified step.

4.2. Influence of Mold Design on Shrinkage Porosity

In this study, the influence of riser removal on mold filling and the solidification process of Ti-6Al-4V alloy mainly causes the following three effects. (1) The bottom-reaching time of the molten metal and the mold filling completion time are shortened (Figures 2e and 4e). (2) The maximum flow velocity of the molten metal is decreased and the mold filling stability is improved (Figures 2f–j and 5 a–e). (3) The shrinkage cavities move up along the central axis of the ingot and the cavity volume decreases significantly (Figures 3f and 7a). On the one hand, the removal of the riser shortens the distance that the molten metal covers before reaching the bottom of the mold and reduces the total mass of the ingot, factors conducive to shortening the bottom-reaching time and the mold filling completion time. On the other hand, reducing the mold filling distance has the effect of decreasing the initial speed at which the molten metal reaches the bottom, slowing down the flow speed of the molten metal and improving the mold filling stability. Research shows that shortening the mold-filling time can effectively reduce heat loss in the mold-filling process and ensure good feeding during the solidification process [22,28]. These factors play an important role in reducing shrinkage cavity volume and changing the position of the shrinkage cavity. Based on this finding, Liu et al. [14] suggested that the filling time should be shortened as much as possible to ensure filling stability. In addition, after riser removal, the top area of the ingot can serve as a pool for feeding which is the fundamental reason why the shrinkage cavity moves up along the center line and its volume decreases. For mold I, the riser part solidifies earlier than any other part of the ingot in conformance with the layer-by-layer solidification pattern of titanium alloy ingots, cutting off the feeding channel earlier and promoting the formation of a shrinkage cavity. Huang et al. [29] explored the influence of the casting system on shrinkage porosity, and found that feeding becomes difficult when the sprue part solidifies earlier than the casting, resulting in a significantly increased probability of forming shrinkage cavities.

It can be seen from Figure 7 that when the top size of the ingot is reduced from 180 mm to 170 mm, while the volume of the shrinkage cavity is reduced from 0.061 cm³ to 0.059 cm³, the utilization rate of the ingot is reduced from 86.4% to 85.8%. When the bottom size of the ingot is reduced from 130 mm to 110 mm, the volume of the shrinkage cavity barely changes but the utilization rate of the ingot is increased to 86.7%. It is worth noting that changing the top or bottom size of the ingot means changing the mold taper. To further optimize the mold design, the influence of mold taper on the volume and distribution of shrinkage cavities was studied (Figure 12). It can be seen from Figure 12a,b that as the top size increases or the bottom size decreases (i.e., the mold taper increases), the shrinkage cavity volume decreases, and the ingot utilization rate increases, both significantly. Analysis reveals that increasing the top size is equivalent to increasing the volume of the pool for high-temperature molten metal, and decreasing the bottom size has the effect of increasing the solidification rate, both of which play an important role in promoting effective feeding, suppressing the formation of shrinkage cavities and making these move up along the central axis. Figure 12c,d show the quantitative relationship between mold taper and the shrinkage cavity, respectively. It is also found that the shrinkage cavity volume decreases significantly with increasing the mold taper, significantly increasing the ingot utilization rate.

In summary, it is advisable to remove the riser in the design of casting molds of titanium alloy ingots of small mass. This not only ensures that shrinkage cavities are concentrated at the top part of the ingot, thereby improving the utilization rate of the ingot, but also reduces the production cost. However, the removal of the riser increases the design requirements of the mold in order to suppress the formation of shrinkage cavities and to move them to the top part of the ingot.

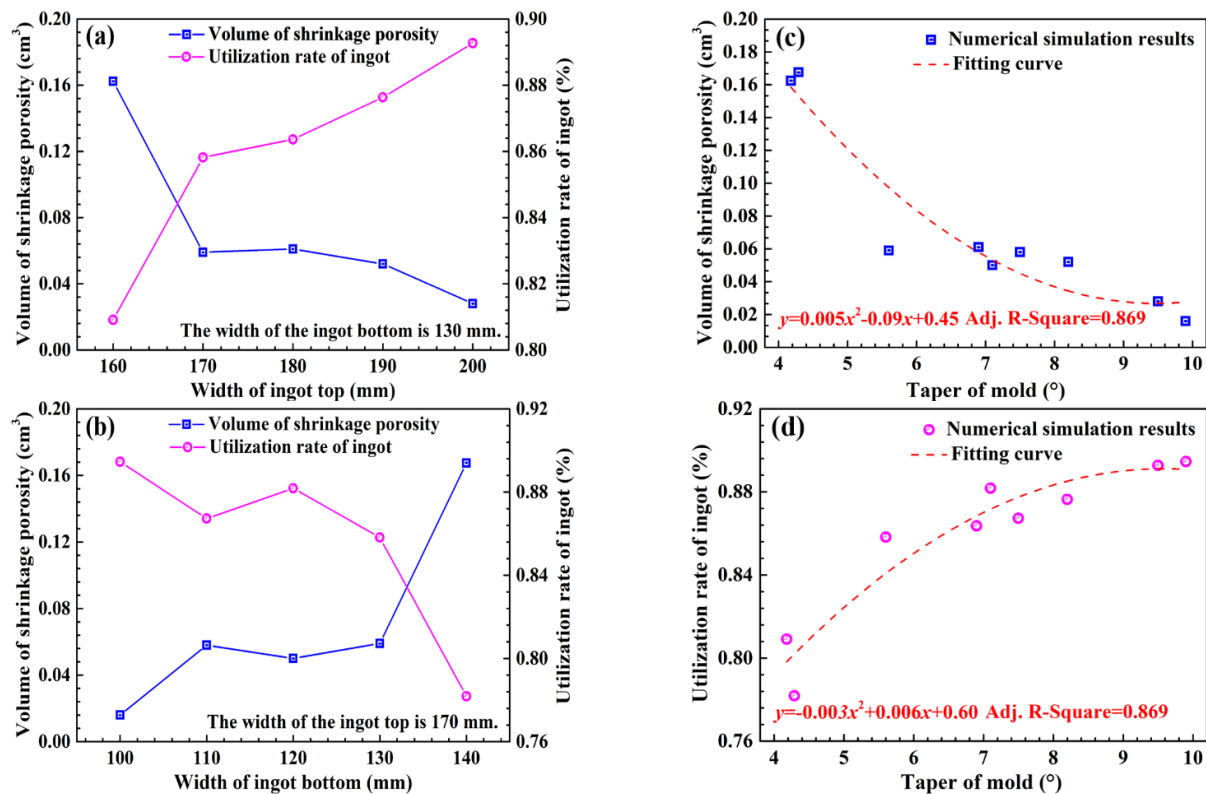


Figure 12. Effect of top width (a), bottom width (b), and mold taper (c,d) for ingots on shrinkage porosity and utilization rate of ingots.

5. Conclusions

The effect of mold design on the shrinkage porosity of Ti-6Al-4V alloy ingots has been thoroughly investigated using numerical simulation and experimental verification. The main conclusions are the following.

1. The presence of a riser in mold I results in a relatively high flow rate ($2.394 \text{ m} \cdot \text{s}^{-1}$) of molten metal, significantly reducing the stability of the mold-filling process. In addition, the riser part solidifies earlier than the main body of the ingot in conformance with the layer-by-layer solidification pattern of titanium alloy. The riser, therefore, cannot serve the purpose of feeding effectively, resulting in a significantly larger shrinkage cavity volume (3.29 cm^3) and a relatively low ingot utilization rate (63.6%).
2. The removal of the riser shortens the bottom-reaching time of the molten metal and the mold-filling completion time. Therefore, the maximum flow velocity decreases (alloy II–IV: $2.228 \text{ m} \cdot \text{s}^{-1}$, $2.245 \text{ m} \cdot \text{s}^{-1}$, $2.198 \text{ m} \cdot \text{s}^{-1}$) and the filling stability increases, effectively suppressing the formation of shrinkage cavities (alloy II–IV: 0.061 cm^3 , 0.059 cm^3 , 0.058 cm^3) and improving the ingot utilization rate significantly (alloy II–IV: 86.4%, 85.8%, 86.7%).
3. The formation of shrinkage cavities in Ti-6Al-4V alloy ingots in this study is mainly due to the formation of an isolated liquid phase zone. This zone results from the formation of a grain frame caused by the intersection of a large number of equiaxed crystals. The inability of this last crystallization part to compensate for volume shrinkage ultimately leads to the formation of shrinkage cavities.
4. With increasing top size or decreasing bottom size of the ingot (i.e., increasing mold taper), the volume of the shrinkage cavities decreases and the ingot utilization rate increases, both significantly. For instance, the shrinkage cavity volume of the ingot decreases from 0.162 cm^3 to 0.016 cm^3 , and the utilization rate increases from 80.9% to 89.5% when the mold taper is increased from 4.2° to 9.9° . Analysis reveals that increasing the top size is equivalent to increasing the volume of the pool of high-

temperature molten metal, and decreasing the bottom size has the effect of increasing the solidification rate, both of which play an important role in promoting effective feeding and suppressing the formation of shrinkage cavities.

Author Contributions: Conceptualization, T.H. and Y.C.; methodology, T.H.; software, T.H. and Y.C.; validation, T.H. and Y.C.; formal analysis, T.H.; investigation, T.H.; resources, Y.C.; data curation, T.H.; writing—original draft preparation, T.H.; writing—review and editing, T.H. and Y.C.; visualization, T.H.; supervision, Y.C.; project administration, Y.C.; funding acquisition, Y.C. All authors have read and agreed to the published version of the manuscript.

Funding: This work was financially supported by the Sichuan Science and Technology Program (No. 2019YFG0082).

Institutional Review Board Statement: Not applicable.

Informed Consent Statement: Not applicable.

Data Availability Statement: The data that support the findings of this study are available from the corresponding author, Yuyong Chen, upon reasonable request.

Conflicts of Interest: The authors declare that they have no conflict of interest.

References

- Williams, J.C.; Boyer, R.R. Opportunities and issues in the application of titanium alloys for aerospace components. *Metals* **2020**, *10*, 705. [CrossRef]
- Zhang, S.Y.; Li, J.S.; Kou, H.C.; Yang, J.R.; Yang, G.; Wang, J. Effects of thermal history on the microstructure evolution of Ti–6Al–4V during solidification. *J. Mater. Process. Technol.* **2016**, *227*, 281–287. [CrossRef]
- Feng, X.; Qiu, J.K.; Ma, Y.J.; Lei, J.F.; Cui, Y.Y.; Wu, X.H.; Yang, R. Influence of processing conditions on microstructure and mechanical properties of large thin-wall centrifugal Ti–6Al–4V casting. *J. Mater. Sci. Technol.* **2015**, *32*, 362–371. [CrossRef]
- Atkinson, H.V.; Davies, S. Fundamental aspects of hot isostatic pressing: An overview. *Metall. Mater. Trans. A* **2000**, *31*, 2981–3000. [CrossRef]
- Zhang, S.Y.; Li, J.S.; Kou, H.C.; Yang, J.R.; Yang, G.; Wang, J. Effect of mold temperature and casting dimension on microstructure and tensile properties of counter-gravity casting Ti–6Al–4V alloys. *China Foundry* **2016**, *13*, 9–14. [CrossRef]
- Yang, L.; Chai, L.H.; Liang, Y.F.; Zhang, Y.W.; Bao, C.L.; Liu, S.B.; Lin, J.P. Numerical simulation and experimental verification of gravity and centrifugal investment casting low pressure turbine blades for high Nb–TiAl alloy. *Intermetallics* **2015**, *66*, 149–155. [CrossRef]
- Suzuki, K.; Yao, M. Simulation of mold filling and solidification during centrifugal precision casting of Ti–6Al–4V alloy. *Met. Mater. Int.* **2004**, *10*, 33–38. [CrossRef]
- Jia, Y.; Xiao, S.L.; Tian, J.; Xu, L.J.; Chen, Y.Y. Modeling of TiAl alloy grating by investment casting. *Metals* **2015**, *5*, 2328–2339. [CrossRef]
- Zhang, S.Y.; Li, J.S.; Kou, H.C.; Yang, J.R.; Yang, G.; Wang, J. Numerical modeling and experiment of counter-gravity casting for titanium alloys. *Int. J. Adv. Manuf. Technol.* **2016**, *85*, 1877–1885. [CrossRef]
- Yang, J.R.; Wang, H.; Wu, Y.L.; Zhang, K.R.; Wang, X.Y.; Hu, R. Numerical calculation and experimental evaluation of counter-gravity investment casting of Ti–48Al–2Cr–2Nb alloy. *Int. J. Adv. Manuf. Technol.* **2018**, *96*, 3295–3309. [CrossRef]
- Xiong, C.; Ma, Y.C.; Chen, B.; Liu, K.; Li, Y.Y. Modeling of filling and solidification process for TiAl exhaust valves during suction casting. *Acta. Metall. Sin. Engl. Lett.* **2013**, *26*, 33–48. [CrossRef]
- Qi, Y.S.; Chen, L.L.; Chen, G.; Li, K.F.; Li, C.; Du, Z.M. Preparation and properties of special vehicle cover via a novel squeeze casting quantitative feeding system of molten metal. *Metals* **2020**, *10*, 266. [CrossRef]
- Dai, H.L.; Zhang, C.L.; Zhao, Q.; Zhu, H. The study of titanium alloy precision casting turbine blades based on Procast. *IOP Conf. Ser. Mater. Sci. Eng.* **2019**, *677*, 022090. [CrossRef]
- Liu, X.J.; Hao, Z.J.; Huang, M. Optimization of vacuum counter-pressure casting process for an aluminum alloy casing using numerical simulation and defect recognition techniques. *Int. J. Adv. Manuf. Technol.* **2020**, *107*, 2783–2795. [CrossRef]
- Shangguan, H.L.; Kang, J.W.; Yi, J.H.; Deng, C.Y.; Hu, Y.Y.; Huang, T. Controlled cooling of an aluminum alloy casting based on 3D printed rib reinforced shell mold. *China Foundry* **2018**, *15*, 210–215. [CrossRef]
- Zhao, J.; Zhang, Z.Y.; Liu, S.B.; Shi, K.; Bao, C.L.; Ning, Z.S.; Yan, P.; Wang, L.; Lou, Y.C. Elimination of misrun and gas hole defects of investment casting TiAl alloy turbocharger based on numerical simulation and experimental study. *China Foundry* **2020**, *17*, 29–34. [CrossRef]
- Eylon, D.; Keller, M.M.; Jones, P.E. Development of permanent-mold cast Ti–Al automotive valves. *Intermetallics* **1998**, *6*, 703–708. [CrossRef]
- Rishel, L.L.; Biery, N.E.; Raban, R.; Gandelsman, V.Z.; Pollock, T.M.; Cramb, A.W. Cast structure and property variability in gamma titanium aluminides. *Intermetallics* **1998**, *6*, 629–636. [CrossRef]

19. Lasalmonie, A. Why is it so difficult to introduce them in gas turbine engines? *Intermetallics* **2006**, *14*, 1123–1129. [CrossRef]
20. Gao, Y.; Zhang, L.J.; Gao, W.L.; Zhang, H. Prediction and improvement of shrinkage porosity in TiAl based alloy. *China Foundry* **2011**, *8*, 19–24.
21. Mi, G.F.; Liu, X.Y.; Wang, K.F.; Fu, H.Z. Application of numerical simulation technique to casting process of valve block. *J. Iron Steel Res. Int.* **2009**, *16*, 12–17. [CrossRef]
22. Liu, J.G.; Yang, L.; Fang, X.G.; Li, B.; Yang, Y.W.; Fang, L.Z.; Hu, Z.B. Numerical simulation and optimization of shell mould casting process for leaf spring bracket. *China Foundry* **2020**, *17*, 35–41. [CrossRef]
23. Han, J.C.; Dong, J.; Zhang, S.Z.; Zhang, C.J.; Xiao, S.L.; Chen, Y.Y. Effect of TiB₂ addition on microstructure and fluidity of cast TiAl alloy. *Vacuum* **2020**, *174*, 109210. [CrossRef]
24. Yang, L.; Chai, L.H.; Zhang, L.Q.; Lin, J.P. Numerical simulation and process optimization of investment casting of the blades for high Nb containing TiAl alloy. *Mater. Sci. Forum.* **2013**, *747*, 105–110. [CrossRef]
25. Zheng, H.S.; Zhang, Z.F.; Bai, Y.L. Numerical simulation and experimental study on compound casting of layered aluminum matrix composite brake drum. *Materials* **2021**, *14*, 1412. [CrossRef]
26. Wang, J.H.; Guo, X.L.; Wang, L.Q.; Lu, W.J. The influence of B₄C on the fluidity of Ti-6Al-4V-xB₄C composites. *Mater. Trans.* **2014**, *55*, 1367–1371. [CrossRef]
27. Dahle, A.K.; Karlsen, S.; Arnberg, L. Effect of grain refinement on the fluidity of some binary Al-Cu and Al-Mg alloys. *Int. J. Cast Metal. Res.* **1996**, *9*, 103–112. [CrossRef]
28. Xuan, D.P.; Zhou, C.; Zhou, Y.; Jiang, T.L.; Zhu, B.J.; Fan, W.H.; Jia, Y.G. Numerical simulation of the top side-pouring twin-roll casting of 6.5wt.% Si steel process. *Int. J. Adv. Manuf. Technol.* **2022**, *119*, 2355–2368. [CrossRef]
29. Huang, P.H.; Cheng, C.Y.; Huang, W.J.; Chou, C.S. Optimal design of investment casting system for toothed chain joint: Computer simulations and experimental verification. *Int. J. Adv. Manuf. Technol.* **2020**, *106*, 1931–1943. [CrossRef]

Article

A New Computational Method for Predicting Ductile Failure of 304L Stainless Steel

Myung-Sung Kim ¹, Hee-Tae Kim ², Young-Hwan Choi ², Jeong-Hyeon Kim ³, Seul-Kee Kim ^{3,*}
and Jae-Myung Lee ^{2,3,*}

¹ Department of Reliability Assessment, Korea Institute of Machinery and Materials, Daejeon 34103, Korea

² Department of Naval Architecture and Ocean Engineering, Pusan National University, Busan 46241, Korea

³ Hydrogen Ship Technology Center, Pusan National University, Busan 46241, Korea

* Correspondence: skkim@pusan.ac.kr (S.-K.K.); jaemlee@pusan.ac.kr (J.-M.L.); Tel.: +82-51-510-7953 (S.-K.K.); +82-51-510-2342 (J.-M.L.); Fax: +82-51-512-8836 (S.-K.K. & J.-M.L.)

Abstract: Austenitic stainless steel is useful for storing and transporting liquefied natural gas (LNG) at temperatures below $-163\text{ }^{\circ}\text{C}$ due to its superior low-temperature applications. This study develops a computational method for the failure prediction of 304L stainless steel sheet to utilize its usability as a design code for industrial purposes. To consider material degradation in a phenomenological way during the numerical calculation, the combined Swift–Voce equation was adopted to describe the nonlinear constitutive behavior beyond ultimate tensile strength. Due to the stress state-dependent fracture characteristics of ductile metal, a modified Mohr–Coulomb fracture criterion was adopted using stress triaxiality and Lode angle parameter. The numerical formulation of the elastoplastic-damage coupled constitutive model with fracture locus was implemented in the ABAQUS user-defined subroutine UMAT. To identify the material and damage parameters of constitutive models, a series of material tests were conducted considering various stress states. It has been verified that the numerical simulation results obtained by the proposed failure prediction methodology show good agreement with the experimental results for plastic behavior and fractured configuration.

Keywords: ductile fracture; elastoplastic constitutive model; modified Mohr–Coulomb model; numerical implementation; austenitic stainless steel

Citation: Kim, M.-S.; Kim, H.-T.; Choi, Y.-H.; Kim, J.-H.; Kim, S.-K.; Lee, J.-M. A New Computational Method for Predicting Ductile Failure of 304L Stainless Steel. *Metals* **2022**, *12*, 1309. <https://doi.org/10.3390/met12081309>

Academic Editors: Shuwen Wen, Yongle Sun and Xin Chen

Received: 29 June 2022

Accepted: 27 July 2022

Published: 4 August 2022

Publisher's Note: MDPI stays neutral with regard to jurisdictional claims in published maps and institutional affiliations.



Copyright: © 2022 by the authors. Licensee MDPI, Basel, Switzerland. This article is an open access article distributed under the terms and conditions of the Creative Commons Attribution (CC BY) license (<https://creativecommons.org/licenses/by/4.0/>).

1. Introduction

Austenitic stainless steel is recognized as a functional material in various industries due to its excellent strength, toughness, and superior corrosion resistance even in low-temperature environments [1–3]. In particular, 304L austenitic stainless steel, which is generally known as 18/8 steel, is useful for storing and transporting liquefied natural gas (LNG) at temperatures below $-163\text{ }^{\circ}\text{C}$ due to its superior low-temperature applications. Zheng et al. (2018) reported that the mechanical strength of low-temperature treated 304 stainless steel was increased up to 2.7 times compared to conventional as-received samples [4]. Mallick et al. (2017) reported that 10–20% low-temperature ($-196\text{ }^{\circ}\text{C}$) deformation leads to a higher level of strength (1306–1589 MPa) owing to the formation of a higher volume fraction of strain-induced martensite [5]. Singh et al. (2018) reported that the low-temperature mechanical strength was increased to 1200 MPa, which is much more than test results under ambient conditions. In addition, in low-temperature treatment, the micro-hardness was increased from 208 VHN to 520 VHN, which is more than double that of the as-received sample [6]. Oh et al. (2018) reported the low-temperature fatigue strength of 304 stainless steel was significantly improved compared to the ambient fatigue strength [7]. Thanks to these valuable studies, it has been established that 304(L) austenitic stainless steel is the optimal material in low-temperature applications because an enhanced mechanical performance was observed in terms such as strength, hardness, and fatigue strength at low temperatures.

Due to its superior low-temperature mechanical performance, 304L stainless steel is adopted as the main material for LNG carrier cargo holds. The primary barrier is corrugated because it undergoes repeated thermal shrinkage and contraction during operation in the LNG loading and unloading processes [8–11]. Therefore, some researchers have focused on the deformation and pressure resistance of 304L stainless steel-made corrugated membranes in experimental approaches. Kim et al. (2011) reported the pressure levels that induced the collapse of the corrugated walls via plastic buckling were six and twelve bar for the large and small corrugated containers, respectively [12]. Lee et al. (2015) reported the pressure-resisting capability of 304L-made stainless steel plate. The maximum deformation of the weakest corrugation was measured with respect to an applied exterior pressure and the pressure at the start of buckling failure was chosen as the pressure-resisting capability of the corrugations [13]. Jeong et al. (2021) reported the pressure-resisting capabilities of a 304L stainless steel corrugated membrane under hydrodynamic load [14]. Those research outcomes have helped improve the shape of the corrugated membrane. However, most evaluations of the pressure resistance performance and the deformation of the primary barrier of the LNG CCS were all conducted at room temperature. This is because it is very difficult to build a pressure test environment for large structures in low-temperature environments. Even so, it is important to evaluate the primary barrier in low-temperature environments, which is the main operating condition of 304L stainless steel primary barriers.

If difficulties are encountered in the experimental evaluation of low-temperature performance, failure evaluation techniques based on computational methods can be an excellent alternative. Evaluating the failure of ductile materials requires predicting the elastoplastic behavior and occurrence of failure. Among failure prediction approaches, the phenomenological failure model is defined as failure occurrence when the stress or strain of an element reaches a specific value. The strain-based failure model is more suitable than the stress-based failure model for dealing with structures undergoing severe plastic deformation and has proven quite useful in collision and failure problems [15–22].

Early studies to predict ductile failure explained the relationship between stress triaxiality and equivalent plastic strain [23–26]. In addition, it was found that the Lode angle, defined as the third invariant of the deviation stress tensor, also affects ductile failure [27–30]. The Mohr–Coulomb criterion is based on the maximum shear stress and is mainly used to determine the failure of rock, soil, and concrete. To eliminate the shortcoming of the absence of pressure dependency, Bai and Wierzbicki (2010) developed a modified Mohr–Coulomb criterion that is transformed from a local representation in terms of shear stress and normal stress to a mixed strain–stress representation of stress triaxiality, Lode angle parameter, and equivalent plastic strain for monotonic loading conditions [28]. The MMC criterion can predict the crack initiation point and the direction of crack propagation and its usefulness has already been verified in many previous studies [31–37].

Several studies have been conducted to predict the ductile fracturing of 304L stainless steel. Othmen et al. (2020) carried the prediction of the onset of rupture of austenitic stainless steel during its forming process [38]. Various fracture criteria, implemented in the finite element code Abaqus/Implicit via a user subroutine USDFLD, have been investigated. Pham and Iwamoto (2018) proposed the numerical fracture prediction of 304 stainless steel with the modified Johnson–Cook damage model [39]. Kim et al. (2013) proposed a viscoplastic model for 304L stainless steel considering the pre-strain and temperature effects [40]. These studies accurately predicted the occurrence of fractures and crack propagation but provided limited failure predictions due to their lack of consideration for various ranges of stress states.

Thus, the present study proposes the failure prediction methodology of 1.2 t 304L stainless steel sheet. An elastoplastic-damage coupled constitutive equation was developed to establish the failure criterion for the primary barrier and to propose a failure analysis technique. To establish the phenomenological ductile failure criterion for 304L stainless steel sheet, a series of material tests were performed considering various stress states. A modified

Mohr–Coulomb model was adopted to formulate ductile fracture criteria in accordance with the stress triaxiality and Lode angle of ductile materials. Numerical analysis with the completed ductile fracture criterion shows good agreement with experimental results.

2. Phenomenological Ductile Fracture Criteria

2.1. Characterization of Stress State

For a certain stress state $\{\sigma_1, \sigma_2, \sigma_3\}$ of an isotropic material, the stress tensor can be expressed as hydrostatic and deviatoric parts. The three main invariants of the stress tensor can be expressed as follow.

$$\sigma = s + pI \quad (1)$$

$$I_1 = \text{tr}[\sigma] \quad (2)$$

$$J_2 = \left(\frac{1}{2} s : s \right) \quad (3)$$

$$J_3 = \det[s] \quad (4)$$

where s, p is the deviatoric stress tensor and hydrostatic stress, respectively. I is the second-order identity tensor. From principal stress space, von-Mises yield surface circumscribes three-dimensional cylinder orthogonal to deviatoric plane (π -plane). To indicate a certain stress state on the deviatoric plane, a cylindrical coordinate system can be used to define the Lode angle from the hydrostatic stress and principal stress directions. The Lode angle can be defined as the angle of the principal stress axis on the deviatoric plane. The Lode angle is related to the normalized third invariant as follows [28].

$$\xi = \cos(3\theta) = \left(\frac{r}{q} \right)^3 \quad (0 \leq \theta \leq \pi/3) \quad (5)$$

$$r = \left[\frac{27}{2} (\sigma_1 - p)(\sigma_2 - p)(\sigma_3 - p) \right]^{1/3} = \left[\frac{27}{2} \det[s] \right]^{1/3} = \left[\frac{27}{2} J_3 \right]^{1/3} \quad (6)$$

$$\theta = \frac{1}{3} \arccos \left(\frac{27}{2} \frac{J_3}{[3J_2]^{3/2}} \right) \quad (7)$$

where ξ, r is the normalized third invariant and the third invariant, respectively. θ is the Lode angle expressed as stress invariants. Stress triaxiality is expressed as the ratio of hydrostatic stress ($\overline{OO'}$) and equivalent stress ($\overline{O'P}$) as follows.

$$\eta = \frac{p}{q} = \frac{\sqrt{2}}{3} \cot \left(\arctan \frac{\overline{O'P}}{\overline{OO'}} \right) \quad (8)$$

where q is the equivalent stress. From a viewpoint of principal stress coordinates, stress triaxiality represents the dominance of the hydrostatic stress in a certain stress state. The normalized Lode angle can be expressed as follows through the modified Haigh–Westergaard coordinate system [41].

$$\bar{\theta} = 1 - \frac{6\theta}{\pi} \quad (-1 \leq \bar{\theta} \leq 1) \quad (9)$$

In the planar stress condition, it is possible to convert a three-dimensional stress space into two dimensions.

2.2. Modified Mohr–Coulomb Model

Bai and Wierzbicki (2010) modified and extended Mohr–Coulomb (MC) fracture criterion to describe ductile fracture of isotropic crack-free solids in terms of equivalent plastic strain [28]. The Mohr–Coulomb fracture criterion has been widely used in rock and soil mechanics [42,43]. This criterion states that fracture occurs at a certain plane when the linear combination of shear and normal stress reaches a critical value [44]. Bai and

Wierzbicki (2010) assumed that the behavior of ductile materials can be described by the von-Mises yield condition and hardening power law [28]. The modified Mohr–Coulomb (MMC) fracture model can be expressed as follows in terms of the stress triaxiality and the normalized Lode angle.

$$\bar{\varepsilon}_i^p(\eta, \bar{\theta}) = \left\{ \frac{A}{c_2} \left[c_3 + \frac{\sqrt{3}}{2 - \sqrt{3}} (1 - c_3) \left(\sec\left(\frac{\bar{\theta}\pi}{6}\right) - 1 \right) \right] \times \left[\sqrt{\frac{1 + c_1^2}{3}} \cos\left(\frac{\bar{\theta}\pi}{6}\right) + c_1 \left(\eta + \frac{1}{3} \sin\left(\frac{\bar{\theta}\pi}{6}\right) \right) \right] \right\}^{-\frac{1}{n}} \quad (10)$$

where A , n are material parameters of swift equation, and c_i ($i = 1, 2, 3$) is fracture parameters. Three fracture parameters need to be calibrated from experimental results. In this study, with the following condition satisfied, the damage accumulation of the element is initiated.

$$\int_0^{\bar{\varepsilon}_i^p} \frac{d\bar{\varepsilon}^p}{\bar{\varepsilon}_i^p(\eta, \bar{\theta})} = 1 \quad (11)$$

where $\bar{\varepsilon}_i^p$ is equivalent plastic strain at damage initiation, and $\bar{\varepsilon}^p$ is equivalent plastic strain.

3. Elastoplastic-Damage Coupled Constitutive Model

3.1. Hardening Function

In this study, the Swift-Voce equation was adopted as a hardening function that expresses the isotropic hardening behavior according to the equivalent plastic strain for general ductile metal materials [41,45,46]. Swift-Voce equation can be described as follow.

$$\sigma_y(\bar{\varepsilon}^p) = \alpha k_s + (1 - \alpha) k_v k \quad (12)$$

$$k_s = A(\varepsilon_0 + \bar{\varepsilon}^p)^n \quad (13)$$

$$k_v = \sigma_{y0} + Q(1 - \exp(-\beta \bar{\varepsilon}^p)) \quad (14)$$

where k_s , k_v , and α is Swift equation, Voce equation, and weight parameter, respectively. A , ε_0 , n , σ_{y0} , Q , β is material parameters for Swift-Voce equation. Some ductile materials show yield plateau after yielding. Considering yield plateau strain (ε_{plat}), Swift-Voce equation can be described as follow.

$$k_s = \begin{cases} A(\varepsilon_0)^n & \bar{\varepsilon}^p \leq \varepsilon_{plat} \\ A(\varepsilon_0 + \bar{\varepsilon}^p - \varepsilon_{plat})^n & \bar{\varepsilon}^p > \varepsilon_{plat} \end{cases} \quad (15)$$

$$k_v = \begin{cases} \sigma_{y0} & \bar{\varepsilon}^p \leq \varepsilon_{plat} \\ Q\{1 - \exp[-\beta(\bar{\varepsilon}^p - \varepsilon_{plat})]\} & \bar{\varepsilon}^p > \varepsilon_{plat} \end{cases} \quad (16)$$

3.2. Damage Evolution Rules

In the present study, ductile materials undergo damage after damage initiation. For the isotropic hardening ductile material, damage manifests itself in two forms; softening of yield stress and degradation of elastic modulus as shown in Figure 1. Lemaitre (1985) explained that damage to the material affects the cross-sectional area due to the growth of pores and micro-cracks inside the material, leading to a decrease in the modulus of elasticity [47]. In this study, in order to define the phenomenological fracture, the damage variable is simply expressed in terms of the equivalent plastic strain rate as follows.

$$D = \begin{cases} 0 & (\bar{\varepsilon}^p < \bar{\varepsilon}_i^p) \\ D_s \times \bar{\varepsilon}^p & (\bar{\varepsilon}_i^p \leq \bar{\varepsilon}^p < \bar{\varepsilon}_f^p) \\ D_c & (\bar{\varepsilon}_f^p \leq \bar{\varepsilon}^p) \end{cases} \quad (17)$$

where D_s , D_c is damage accumulation control parameter and critical damage, respectively. Damage accumulation control parameter adjusts the degree of damage accumulation. Critical damage defines the thresholds for damage. $\bar{\varepsilon}_i^p$ and $\bar{\varepsilon}_f^p$ represents equivalent plastic strain at damage initiation and fracture, respectively.

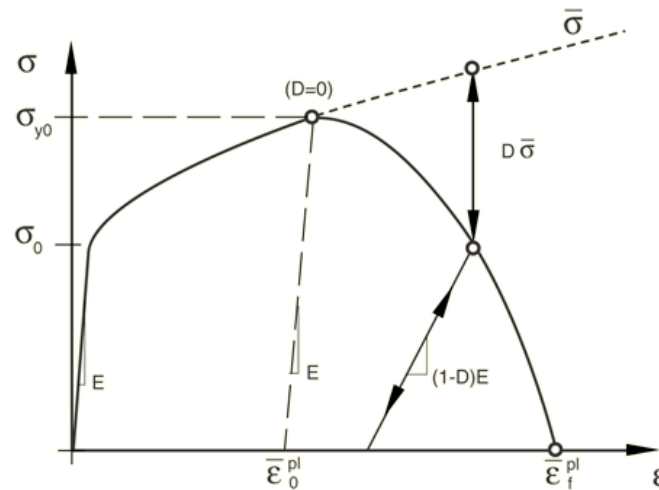


Figure 1. Stress-strain relationship with damage accumulation. With damage accumulation, critical equivalent plastic strain provokes damage initiation. After the onset of damage initiation, elastic modulus and strength are dramatically decreased.

3.3. Constitutive Model

In this study, an elastoplastic-damage coupled constitutive model is proposed to predict the damage of ductile material. The total strain tensor and strain rate tensor can be decomposed into elastic part and plastic part as follows.

$$\varepsilon = \varepsilon^e + \varepsilon^p \quad (18)$$

$$\dot{\varepsilon} = \dot{\varepsilon}^e + \dot{\varepsilon}^p \quad (19)$$

Using the concept of effective area and stress of damaged material proposed by Lemaitre (1985) [47], the general Hooke's law can be expressed as follows.

$$\sigma = (1 - D)D : \varepsilon^e \quad (20)$$

where σ , D represents the stress tensor and the stiffness tensor for isotropic materials, respectively. D is damage variable. Deviatoric stress and hydrostatic stress are as follows, respectively.

$$s = (1 - D)2G\varepsilon_d^e \quad (21)$$

$$p = (1 - D)K\varepsilon_v^e \quad (22)$$

where ε_d^e , ε_v^e is deviatoric strain tensor and volumetric strain, respectively. G and K represent shear modulus and volume modulus, respectively. Under the constant loading direction, the effect of kinematic hardening can be ignored. The yield function according to the von-Mises yield criterion is as follows.

$$\Phi = q - (1 - D)\sigma_y(\bar{\varepsilon}^p) \quad (23)$$

$$q = \sqrt{3J_2} = \sqrt{\frac{3}{2}s : s} = \sqrt{\frac{3}{2}}\|s\| \quad (24)$$

where q is the von-Mises equivalent stress expressed as the deviatoric stress, and $\sigma_y(\bar{\epsilon}^p)$ represents the isotropic hardening function expressing according to the equivalent plastic strain. According to the Prandtl-Reuss plastic law, flow rule is defined as follows [48].

$$\dot{\epsilon}^p = \dot{\gamma} \frac{\partial \Phi}{\partial \sigma} = \dot{\gamma} \sqrt{\frac{3}{2}} \frac{s}{\|s\|} \quad (25)$$

where $\dot{\epsilon}^p$, $\dot{\gamma}$ is the plastic strain rate and the plastic multiplier, respectively. Plastic strain rate is expressed as Prandtl-Reuss flow vector and plastic multiplier. Equivalent plastic strain rate is defined as follows.

$$\dot{\bar{\epsilon}}^p = \sqrt{\frac{2}{3} \dot{\epsilon}^p : \dot{\epsilon}^p} = \sqrt{\frac{2}{3}} \|\dot{\epsilon}^p\| = \dot{\gamma} \quad (26)$$

According to Equation (25), the equivalent plastic strain rate is the same as the plastic multiplier. The loading/unloading conditions of the constitutive model is as follows.

$$\Phi \leq 0, \quad \dot{\gamma} \geq 0, \quad \dot{\gamma} \Phi = 0 \quad (27)$$

3.4. Numerical Implementation Algorithm

In order to formulate the proposed elastoplastic-damage coupled constitutive model with fracture locus, ABAQUS/STANDARD, a commercial finite element analysis software, was adopted. ABAQUS with subroutine UMAT (user subroutine to define a material's mechanical behavior) provides the user to define material properties and provides values calculated at the integration point of each element.

In this study, the elastoplastic-damage coupled constitutive model was formulated with a fully implicit backward Euler integration scheme. A return mapping scheme with elasticity prediction and plastic correction was adopted. When the total strain increment ($\Delta \epsilon$) according to the time interval $[t_n, t_{n+1}]$ is determined at each integration point, the subroutine UMAT calculates unknown variables σ_{n+1} , ϵ_{n+1}^p , D_{n+1} , t_{n+1} using the known variables σ_n , ϵ_n^p , D_n , t_n [48,49]. When the total strain increment is determined, the trial stress and strain components can be expressed as follows.

$$\epsilon_{n+1}^{e \text{ trial}} = \epsilon_n^e + \Delta \epsilon \quad (28)$$

$$\bar{\epsilon}_{n+1}^{p \text{ trial}} = \bar{\epsilon}_n^p \quad (29)$$

$$D_{n+1}^{\text{trial}} = D_n \quad (30)$$

$$s_{n+1}^{\text{trial}} = (1 - D_n) 2G \epsilon_{v \text{ } n+1}^e \quad (31)$$

$$p_{n+1}^{\text{trial}} = (1 - D_n) K \epsilon_{v \text{ } n+1}^e \quad (32)$$

The corresponding trial yield function and trial equivalent stress are as follows.

$$\Phi^{\text{trial}} = q_{n+1}^{\text{trial}} - (1 - D_n) \sigma_y(\bar{\epsilon}_n^p) \quad (33)$$

$$q_{n+1}^{\text{trial}} = \sqrt{3J_2(s_{n+1}^{\text{trial}})} = \sqrt{\frac{3}{2} s_{n+1}^{\text{trial}} : s_{n+1}^{\text{trial}}} = \sqrt{\frac{3}{2}} \|s_{n+1}^{\text{trial}}\| \quad (34)$$

When the trial yield function is $\Phi^{\text{trial}} \leq 0$, the trial stress exists within the yield function, so it is regarded as an elastic region in which plastic increment does not occur. The state variables are updated as Equations (28)–(32) and the stress is updated as follows.

$$\sigma_{n+1} = s_{n+1}^{\text{trial}} + p_{n+1}^{\text{trial}} I \quad (35)$$

If the trial yield function is resulted in $\Phi^{trial} > 0$, plastic correction is required according to the incremental calculation of the equivalent plastic strain. First, strain and damage parameters can be defined by the Backward Euler method as follows.

$$\varepsilon_{n+1}^e = \varepsilon_{n+1}^{e\,trial} - \varepsilon_{n+1}^p = \varepsilon_{n+1}^{e\,trial} - \Delta\gamma \sqrt{\frac{3}{2}} \frac{\mathbf{s}_{n+1}}{\|\mathbf{s}_{n+1}\|} \quad (36)$$

$$\bar{\varepsilon}_{n+1}^p = \bar{\varepsilon}_n^p + \Delta\gamma \quad (37)$$

$$D_{n+1} = D_n + D_s \Delta\gamma \quad (38)$$

$$\varepsilon_{d\,n+1}^e = \varepsilon_{d\,n+1}^{e\,trial} - \Delta\gamma \sqrt{\frac{3}{2}} \frac{\mathbf{s}_{n+1}}{\|\mathbf{s}_{n+1}\|} \quad (39)$$

$$\varepsilon_{v\,n+1}^e = \varepsilon_{v\,n+1}^{e\,trial} \quad (40)$$

According to the definition of the strain tensor in the next step shown in Equation (36), deviatoric strain tensor and the volumetric strain of the next step are defined in Equations (39)–(40). The deviatoric stress and the hydrostatic stress are defined as follows.

$$\mathbf{s}_{n+1} = (1 - D_{n+1})2G\varepsilon_{d\,n+1}^{e\,trial} - (1 - D_{n+1})2G\Delta\gamma \sqrt{\frac{3}{2}} \frac{\mathbf{s}_{n+1}}{\|\mathbf{s}_{n+1}\|} \quad (41)$$

$$p_{n+1} = (1 - D_{n+1})K\varepsilon_{v\,n+1}^e \quad (42)$$

In order to represent the plastically corrected yield function at t_{n+1} , the deviatoric stress of the next step shown in Equation (43) must be calculated. This can be expressed as Equation (43) using the trial deviatoric stress shown in Equation (33), and because the trial deviation stress is proportional to the deviatoric stress of the next step, it can be summarized as Equation (44).

$$\mathbf{s}_{n+1} = \frac{1 - D_{n+1}}{1 - D_n} \mathbf{s}_{n+1}^{trial} - (1 - D_{n+1})2G\Delta\gamma \sqrt{\frac{3}{2}} \frac{\mathbf{s}_{n+1}}{\|\mathbf{s}_{n+1}\|} \quad (43)$$

$$\mathbf{s}_{n+1} = (1 - D_{n+1}) \left(\frac{1}{1 - D_n} - \frac{3G\Delta\gamma}{q_{n+1}^{trial}} \right) \mathbf{s}_{n+1}^{trial} \quad (44)$$

The yield function in the next step is defined as follows because it must satisfy the consistency condition.

$$\Phi_{n+1} = q_{n+1} - (1 - D_{n+1})\sigma_y \left(\bar{\varepsilon}_n^p + \Delta\gamma \right) \quad (45)$$

$$q_{n+1} = (1 - D_{n+1}) \left(\frac{1}{1 - D_n} q_{n+1}^{trial} - 3G\Delta\gamma \right) \quad (46)$$

The yield function can be expressed as a function of the plastic multiplier and the damage of the next step, and the return mapping method must be performed to calculate the plastic multiplier and the damage of the next step.

With Equation (38), Equation (45) can be simplified as Equation (47). The plastic multiplier is calculated through the Newton-Raphson method. The simplified yield function does not require the process of estimating the initial value of the plastic multiplier [48] in calculating the damage energy release rate like Lemaitre's damage composition equation.

$$\Phi_{n+1} = \frac{1}{1 - D_n} q_{n+1}^{trial} - 3G\Delta\gamma - \sigma_y \left(\bar{\varepsilon}_n^p + \Delta\gamma \right) \quad (47)$$

$$\sigma_{n+1} = \mathbf{s}_{n+1} + p_{n+1} \mathbf{I} \quad (48)$$

When all stress and state variables are updated, the yield function of the next step reaches an elastic region as a value close to zero. In finite element analysis, in order to calculate the tangent stiffness matrix of each element, a consistent tangent modulus of the material reaching the last updated plastic region is required. Through the relationship between stress and strain tensor, the consistent tangent modulus (D^{ep}) of the elastoplastic region is defined as follows [48].

$$D^{ep} \equiv \frac{\partial \sigma_{n+1}}{\partial \varepsilon_{n+1}^{e \text{ trial}}} \quad (49)$$

$$\sigma_{n+1} = \left[D^e - \frac{\Delta \gamma 6G^2}{q_{n+1}^{trial}} I_d \right] : \varepsilon_{n+1}^{e \text{ trial}} \quad (50)$$

$$D^e = 2GI_d + \left(K - \frac{2}{3}G \right) I \otimes I \quad (51)$$

$$I_d = I_s - \frac{1}{3}I \otimes I \quad (52)$$

$$I_s = I_{ijkl} = \frac{1}{2}(\delta_{ik}\delta_{jl} + \delta_{il}\delta_{jk}) \quad (53)$$

where I_s and I_d represent the fourth symmetric identity tensor and the deviatoric projection tensor, respectively, and δ_{ij} is Kröner delta. D^e is the consistent tangent modulus derived through Hooke's law in the elastic region where plastic correction was not performed. D^{ep} can be expressed as follows by partial unification of Equation (50).

$$D^{ep} = D^e - \frac{\Delta \gamma 6G^2}{q_{n+1}^{trial}} I_d - \frac{6G^2}{q_{n+1}^{trial}} \varepsilon_{n+1}^{e \text{ trial}} \otimes \frac{\partial \Delta \gamma}{\partial \varepsilon_{n+1}^{e \text{ trial}}} + \frac{\Delta \gamma 6G^2}{(q_{n+1}^{trial})^2} \varepsilon_{n+1}^{e \text{ trial}} \otimes \frac{\partial q_{n+1}^{trial}}{\partial \varepsilon_{n+1}^{e \text{ trial}}}. \quad (54)$$

$$D^{ep} = D^e - \frac{\Delta \gamma 6G^2}{q_{n+1}^{trial}} I_d + 6G^2 \left(\frac{\Delta \gamma}{q_{n+1}^{trial}} - \frac{1}{3G + \frac{d\sigma_y}{d\varepsilon^p} \Big|_{\varepsilon_n^p + \Delta \gamma}} \right) \frac{s_{n+1}^{trial}}{\|s_{n+1}^{trial}\|} \otimes \frac{s_{n+1}^{trial}}{\|s_{n+1}^{trial}\|}. \quad (55)$$

$$D^{ep} = 2G \left(1 - \frac{\Delta \gamma 6G^2}{q_{n+1}^{trial}} \right) I_d + 6G^2 \left(\frac{\Delta \gamma}{q_{n+1}^{trial}} - \frac{1}{3G + \frac{d\sigma_y}{d\varepsilon^p} \Big|_{\varepsilon_n^p + \Delta \gamma}} \right) \frac{s_{n+1}^{trial}}{\|s_{n+1}^{trial}\|} \otimes \frac{s_{n+1}^{trial}}{\|s_{n+1}^{trial}\|} + KI \otimes I. \quad (56)$$

4. Comparison with Experimental Results

4.1. Specimen

In order to perform the failure analysis of the primary barrier of Mark-III type LNG CCS, a series of material tests were performed on the same material applied to the primary barrier. 304L stainless steel was collected from 3500 mm × 1271 mm × 1.2 t of STS304L, and the chemical composition is presented in Table 1. As shown in Figure 2, five types of tensile specimen were prepared. The DB specimen, which means dogbone type tensile specimen, was fabricated to obtain the flow stress of 304L stainless steel. The width is 6 mm and the length of the reduced area is 30 mm. For NT05, NT10, and NT15 specimens, the radius of curvature of the notch in the middle was 5 mm, 10 mm, and 15 mm to obtain high-stress triaxiality. The minimum width at the center of the NT specimen is 6 mm. The CH03 specimen has a radius of curvature of 3 mm in the center hole. The central width of the NT and CH specimens is equal to 16 mm. The total length of all specimens is 110 mm, and the length and rolling direction of the specimens are the same.

Table 1. Chemical composition of 304L stainless steel.

C	Si	Mn	P	S	Cr	Ni
0.0152	0.379	1.130	0.0227	0.0017	18.653	10.178

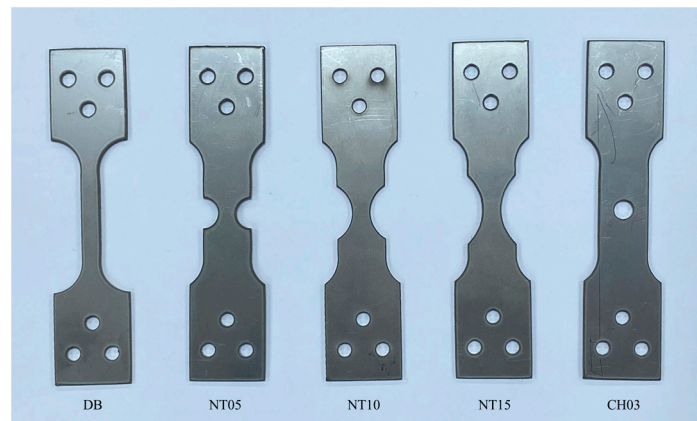


Figure 2. Material test specimens of 304L stainless steel sheet. DB specimen is used to acquire flow stress of 304L stainless steel, which has 6 mm width and 30 mm the length of reduced area. Other specimens are to identify the fracture strain. NT specimens have the radius of curvature of the notch to obtain high-stress triaxiality. The CH specimen has a radius of curvature of 3 mm in the center hole.

4.2. Experimental Set-Up

In this study, a universal testing machine was adopted to perform material testing. The maximum load capacity of UTM is 50 kN, and the speed of the crosshead can be controlled from 0.001 to 400.0 mm/min. In this study, the speed of the crosshead was controlled at 1.5 mm/min so that the initial strain rate for the DB specimen was 0.001/s. The displacement of all specimens was measured using an extensometer, and the gauge length was set to 25 mm. All material tests were performed at room temperature (13 °C). To verify repeatability, all tests were repeated three times and the results were shown as an average value.

4.3. Experimental Results

Figure 3a shows the results of the tensile test of the DB specimen at room temperature in terms of engineering stress and strain relationship. The elongation of the DB specimen was 0.7464, the 0.2% offset yield strength was 282 MPa, and the tensile strength was 679 MPa. The experimental result of the DB specimen was adopted only as a flow stress calculation. Figure 3b shows the force–displacement relationships of all specimens performed at room temperature. The smaller notch radius of the NT specimen increased the stress triaxiality and resulted in rapid failure. The CH03 specimen had a higher load because of the larger cross-sectional area at the center of the specimen.

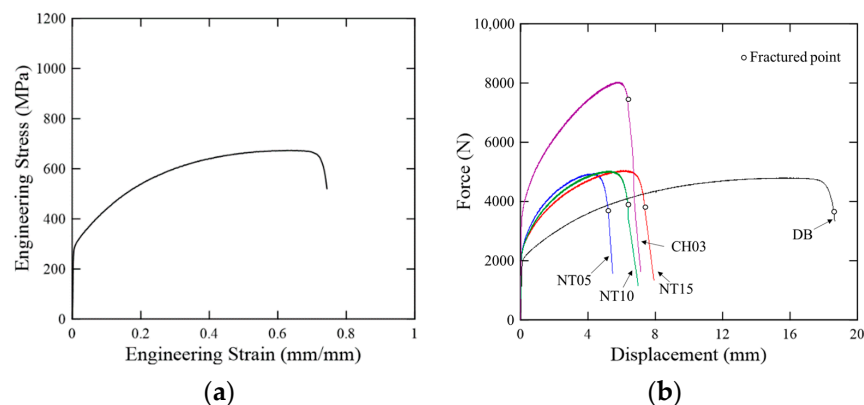


Figure 3. (a) Engineering stress–strain relationship at room temperature for DB specimen and (b) force–displacement relation. Given that the DB and NT specimens have the same minimum width, the maximum strength is almost the same. The smaller notch radius of the NT specimen caused increased stress triaxiality and rapid failure.

In order to observe the failure pattern of each specimen, the picture just before failure in the material test is shown in Figure 4. In the NT specimen, localized necking was observed in the center of the specimen, after which fracture progression was observed in the outer direction of the specimen. The CH03 specimen also begins to crack on both sides of the center hole and propagates outward. The fracture angle of all STS304L specimens was observed irregularly and it was judged that there was no tendency. As the purpose of the material test is to establish the ductile fracture criteria, no examination of the fracture surface of the specimen was conducted, nor was the effect of the notch radius on the material behavior analyzed through experimental results.

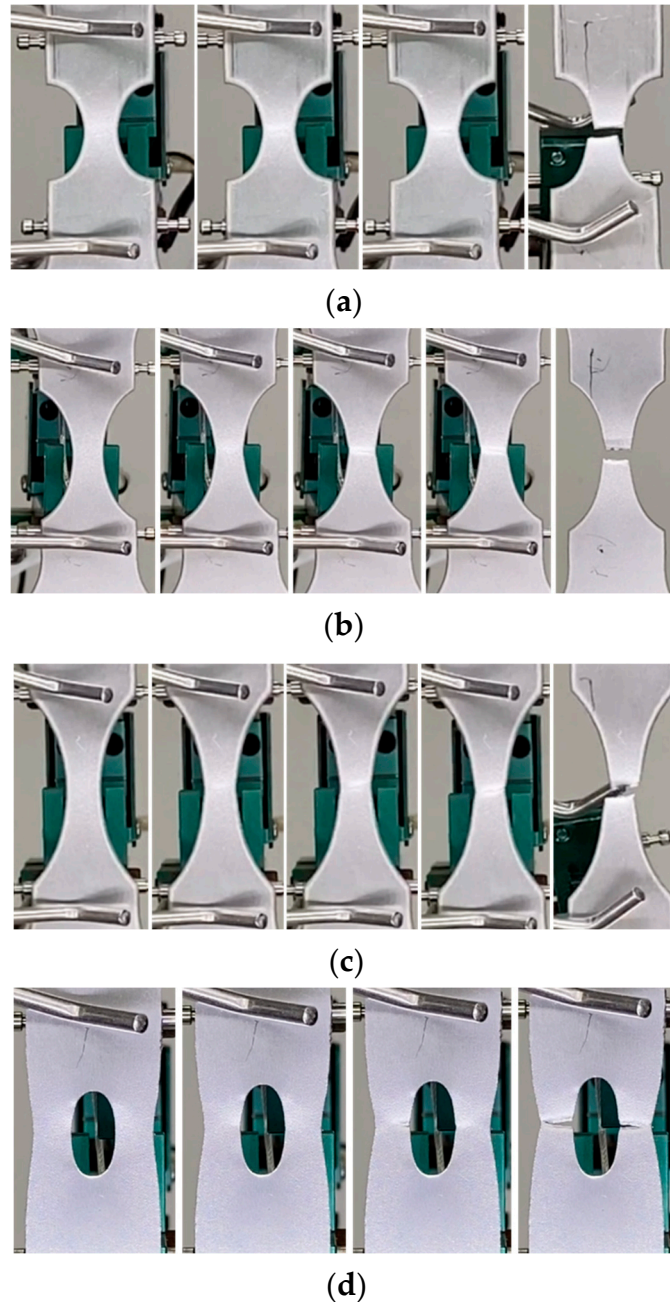


Figure 4. Ductile fracture configuration of 304L stainless steel: (a) NT05 specimen, (b) NT10 specimen, (c) NT15 specimen, and (d) CH03 specimen. Localized necking was clearly observed. The CH specimen showed a localized neck followed by crack propagation.

5. Calibration of Ductile Fracture Model

5.1. FE Model

In order to establish a ductile fracture model, the equivalent plastic strain at the fracture location is required during material testing. Bao-Wierzbicki (2004) proposed the procedure of comparing experimental results with detailed numerical simulations because it is difficult to obtain experimentally [50]. This procedure is very useful and easy to predict in evaluating the failure of a structure through a commercial finite element analysis program. With recent technological advances, many researchers are adopting a method of obtaining the strain contour of a material using a digital image correction technique without comparing numerical simulation and experimental results [31,51,52]. In this study, in order to evaluate the effectiveness of the proposed elastoplastic-damage coupled constitutive model, the DIC method is not adopted, and the equivalent plastic strain is obtained by comparing the experimental results and the numerical analysis results, and the ductile fracture model is formulated.

Parallel numerical simulations of all material tests were carried out using commercial finite element code ABAQUS/Standard. Material specimen modeling was performed as shown in Figure 5. Although all specimens had symmetry conditions in the thickness direction, width direction, and length direction, no symmetric model (1:1 modeling) was considered for the failure prediction. The modeling range was to be included from the center point of the specimen to 25 mm. Since the length of the reduced section of the DB specimen exceeded 25 mm, the entire specimen was modeled only for the DB specimen. Displacement control was performed by applying coupling constraints as reference points to the upper and lower surfaces of the finite element analysis model.

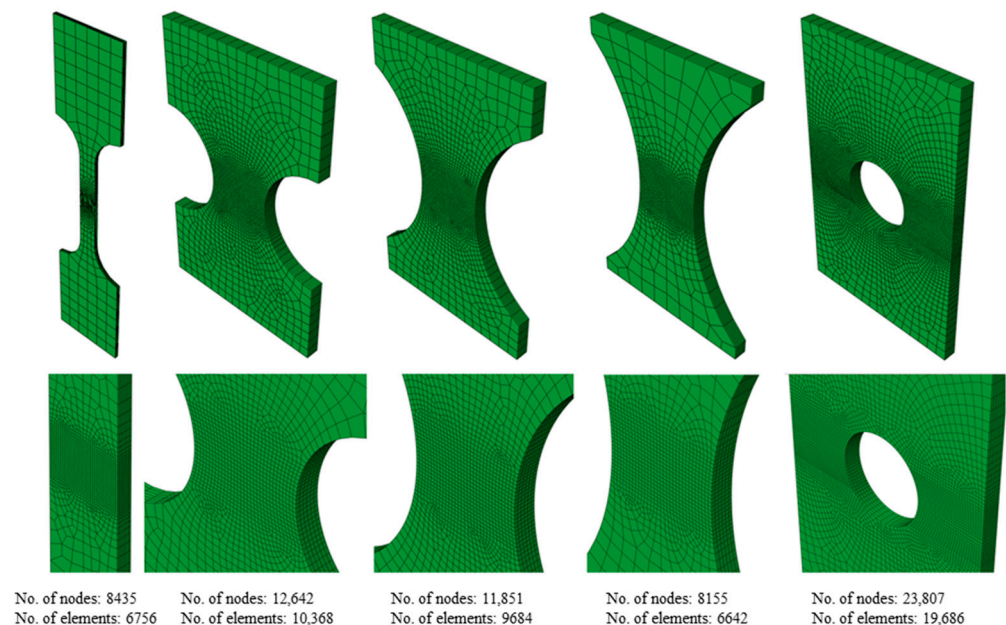


Figure 5. Finite element model for material test of 304L stainless steel. In order to accurately predict the ductile fracture at the failure location of all specimens, the element size was differentiated. In the region of interest, the element size was selected as 200 μm , and the number of elements in the thickness direction of the specimen was 6. To reduce computational cost, a coarse mesh was made outside the region of interest.

Eight-node brick element with reduced integration (C3D8R) was adopted for the finite element analysis model. When the ductile material undergoes plastic deformation and enters the necking range, the cross-sectional area decreases and the stress in the thickness direction cannot be ignored. Therefore, for precise prediction, the FE model was established using solid elements, not shell elements. The element size of the region of interest of each

element was selected as 200 μm , and the number of elements in the thickness direction of the specimen was 6. To simulate the specimen's fracture pattern, it is necessary to select a smaller element size [53–55]. However, this requires considerable computation cost, and it was difficult to observe a regular fracture pattern in the material test of 304L stainless steel.

5.2. Calculation of Flow Stress

Flow stress is calculated through the experimental results of 304L stainless steel. The engineering stress-strain relation obtained through the tensile test was converted into a true stress-strain relation, which was expressed by the Swift-Voce equation, a hardening function of the constitutive model proposed in this study. The experimental results and hardening equation fitting results are shown in Figure 6. Material parameters of 304L stainless steel are listed in Table 2.

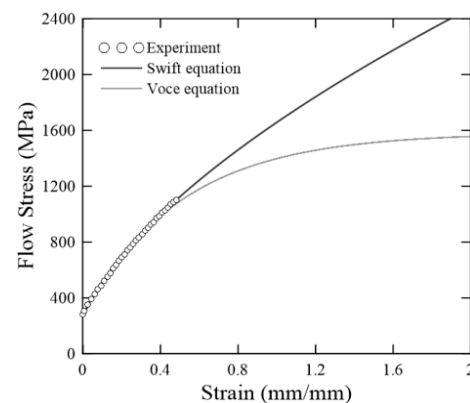


Figure 6. Flow stress of 304L stainless steel. Experimental results with engineering stress-strain relation are valid until the onset of the diffuse neck. In the domain of diffuse neck, the true stress is estimated through Swift equation and Voce equation.

Table 2. Material parameters of 304L stainless steel. In this study, 304L stainless steel did not show a yield plateau, so the yield plateau was set to zero.

Swift equation part	A	ϵ_0	n	ϵ_{plat}
	1610.0	0.0496	0.6	0.0
Voce equation part	α	σ_{y0}	Q	β
	1.0	282.0	1300.0	1.95

The Swift equation and Voce equation just estimate the post-necking behavior. The necessity of stress correction was reviewed by comparing the experimental results and the finite element analysis results applying flow stress. Figure 7 shows the comparison between the analysis result and the experimental result applying hardening equations. Through the flow stress calculated by the Swift equation, it was shown that the mechanical behavior of all specimens was well simulated. No yield plateau was observed in the tensile test at room temperature for 304L stainless steel, and failure occurred immediately after reaching the tensile strength.

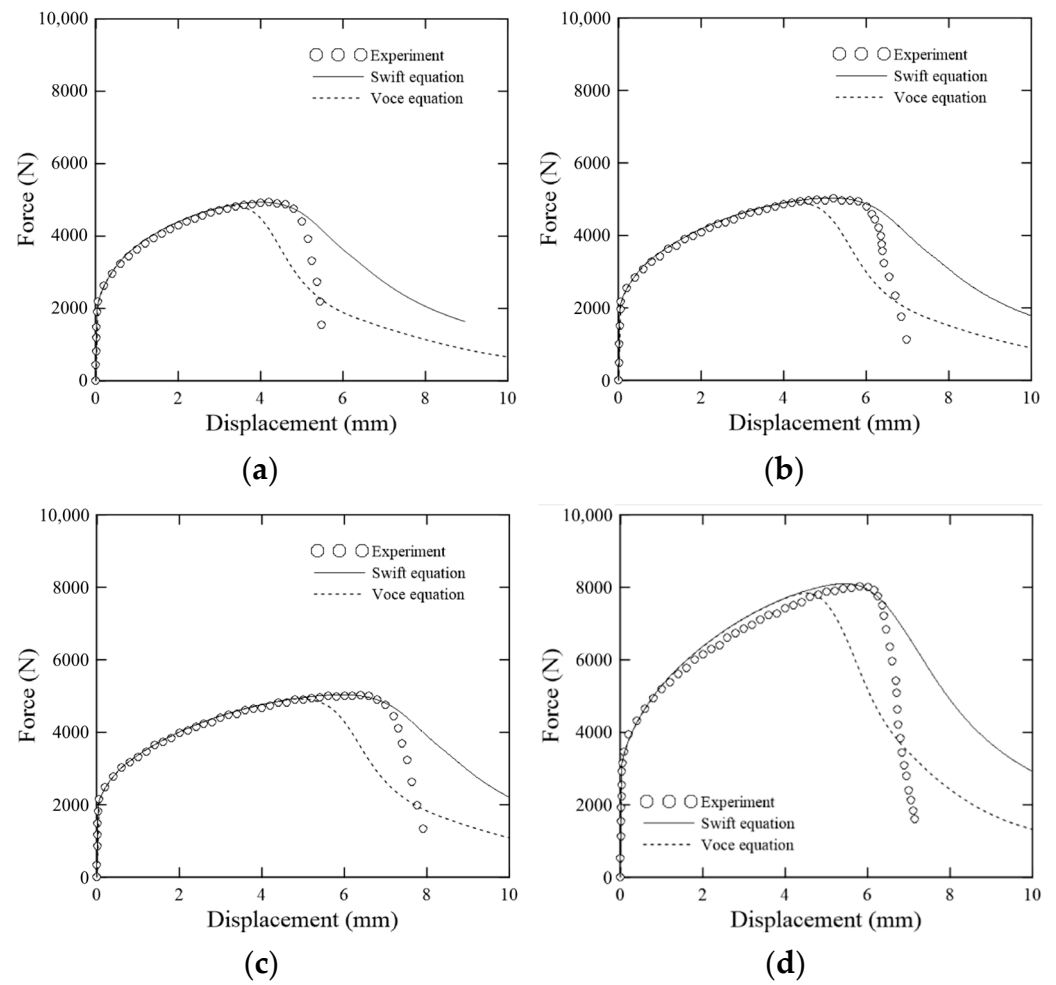


Figure 7. Comparison between experimental and simulation results of 304L stainless steel: (a) NT05 specimen, (b) NT10 specimen, (c) NT15 specimen, and (d) CH03 specimen. The flow stress using the Voce equation showed a strength drop before reaching the maximum strength. The flow stress calculation using the Swift equation is most appropriate.

5.3. Loading Path to Failure

To calibrate the ductile fracture model, the loading history at the predicted point of failure was investigated. In this study, when damage was initiated in the material test, the position of the largest equivalent plastic strain of the FE model was regarded as the predicted point of failure. The position of the highest equivalent plastic strain for the FE model is shown in Figure 8. This phenomenon can be observed at the same location in the experimental results shown in Figure 4.

As the equivalent plastic strain increases, the stress state is shown in Figure 9. If the growth of the equivalent plastic strain grows with a uniform stress triaxiality and Lode angle parameter, the fracture model can be easily calibrated. However, the stress triaxiality and Lode angle parameter of most ductile materials constantly fluctuate. Therefore, to consider the history of stress triaxiality and Lode angle parameter that appears as the specimen is deformed, and to reduce the sensitivity to fluctuations, the average value was introduced as follows.

$$\eta_{av} = \frac{1}{\bar{\epsilon}_i^p} \int_0^{\bar{\epsilon}_i^p} \eta(\bar{\epsilon}^p) d\bar{\epsilon}^p \quad (57)$$

$$\bar{\theta}_{av} = \frac{1}{\bar{\epsilon}_i^p} \int_0^{\bar{\epsilon}_i^p} \bar{\theta}(\bar{\epsilon}^p) d\bar{\epsilon}^p \quad (58)$$

where η_{av} , $\bar{\theta}_{av}$ are average stress triaxiality and average normalized Lode angle, respectively. $\bar{\epsilon}_i^p$ is the equivalent plastic strain at damage initiation and $\bar{\epsilon}^p$ is the equivalent plastic strain of the element. The average stress triaxiality, average normalized Lode angle, and equivalent plastic strain at damage initiation according to the specimen are listed in Table 3.

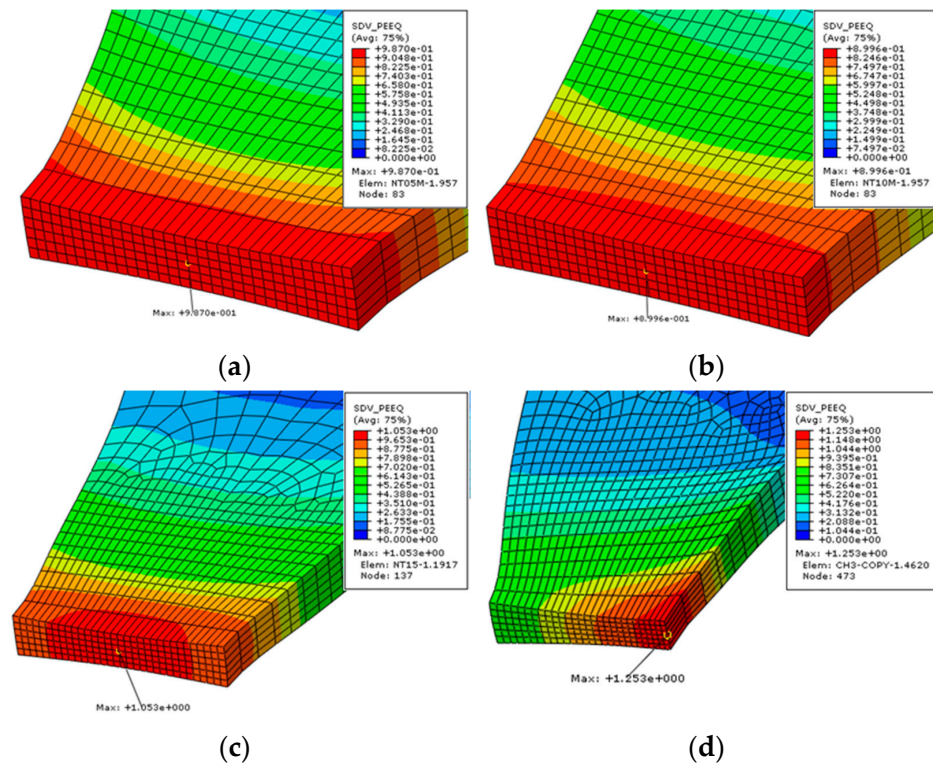


Figure 8. Equivalent plastic strain contour at damage initiation; (a) NT05 specimen, (b) NT10 specimen, (c) NT15 specimen, and (d) CH03 specimen. In the NT specimen, when the stiffness drop occurred rapidly, the maximum equivalent plastic strain appeared at the center of the specimen. In the CH specimen, the maximum equivalent plastic strain was observed in the direction of the hole diameter due to symmetric structure of specimen. A decrease in thickness was observed in the numerical analysis model of all specimens.

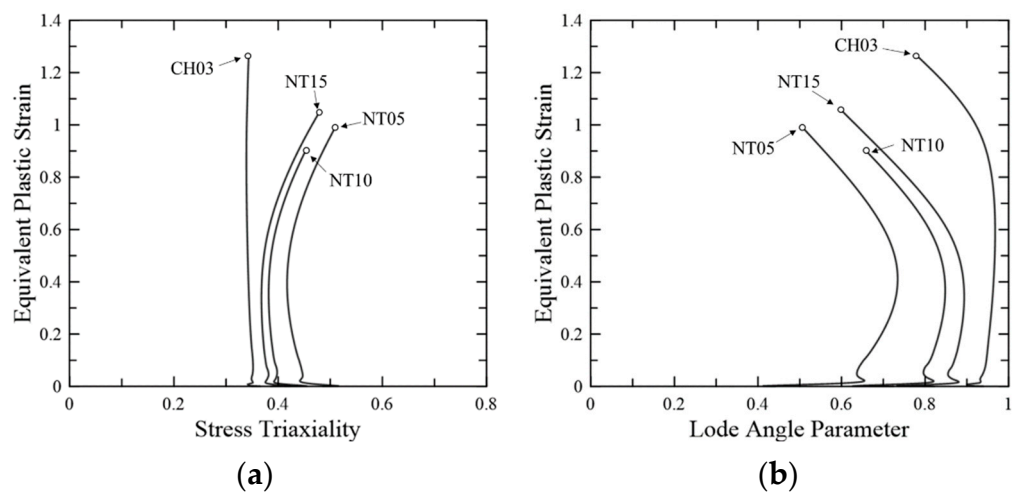


Figure 9. Equivalent plastic strain in accordance with (a) stress triaxiality and (b) Lode angle parameter. Black line white dot indicates equivalent plastic strain at damage initiation. As plastic strain accumulates, the stress triaxiality and Lode angle parameters were continuously changed.

Table 3. Average stress triaxiality, average normalized Lode angle, and equivalent plastic strain at damage initiation of 304L stainless steel. The average values were derived considering the loading history.

Specimen	Average Stress Triaxiality, η_{av}	Average Normalized Lode Angle, $\bar{\theta}_{av}$	Equivalent Plastic Strain at Damage Initiation, $\bar{\epsilon}_i^p$
NT05	0.442	0.665	0.987
NT10	0.399	0.799	0.900
NT15	0.395	0.817	1.053
CH03	0.343	0.936	1.262

5.4. Determination of Fracture Parameters

The fracture parameters of the modified Mohr–Coulomb fracture model were determined using the average stress triaxiality, average normalized Lode angle, and equivalent plastic strain at damage initiation for each specimen shown in Table 3. Fracture parameters were selected as the value with the least error from experimental data among fracture loci. The finally determined fracture parameters are summarized in Table 4. Figure 10 shows the 3D modified Mohr–Coulomb fracture locus of 304L stainless steel projected on the $\eta - \bar{\epsilon}^p$ plane and $\bar{\theta} - \bar{\epsilon}^p$ plane.

Table 4. Fracture parameters of the modified Mohr–Coulomb fracture model for 304L stainless steel sheet.

Fracture parameter	c_1	c_2	c_3
	0.016	961	1.05

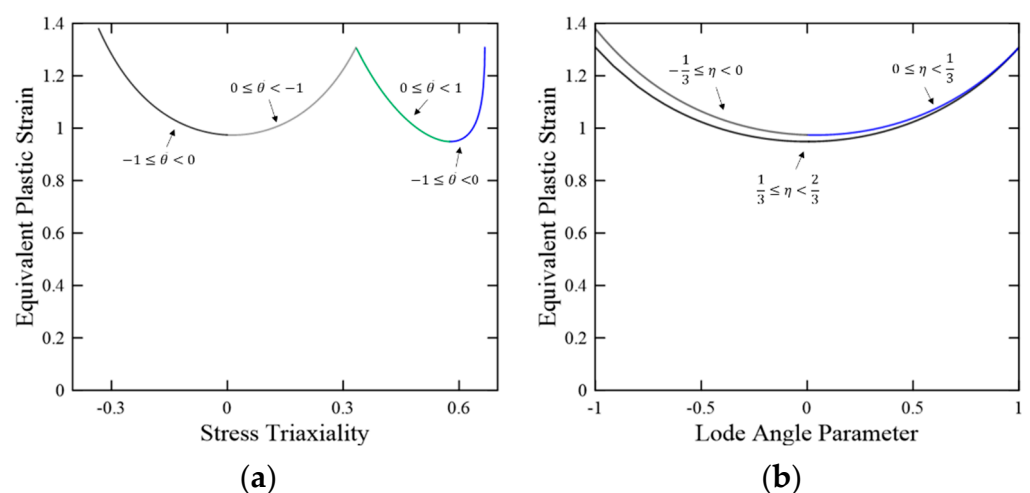


Figure 10. Fracture loci of the modified Mohr–Coulomb fracture model in accordance with (a) stress triaxiality and (b) Lode angle parameter of 304L stainless steel.

6. Prediction of Ductile Fracture

A ductile fracture simulation was performed to verify that the completed fracture locus was valid. The analysis model and boundary conditions are the same as those shown in chapter 5.1 FE model. Damage accumulation control parameter (D_s) and critical damage (D_c), which are damage parameters related to damage evolution, were set to 2.0 and 0.9, respectively. Figure 11a–d shows the comparison of the experimental results and analysis results for each test piece. In the deformed configuration shown in Figure 11e–h, the simulation results are shown after removing the element whose critical damage reached 0.9. All of the simulations show good agreement with experimental results.

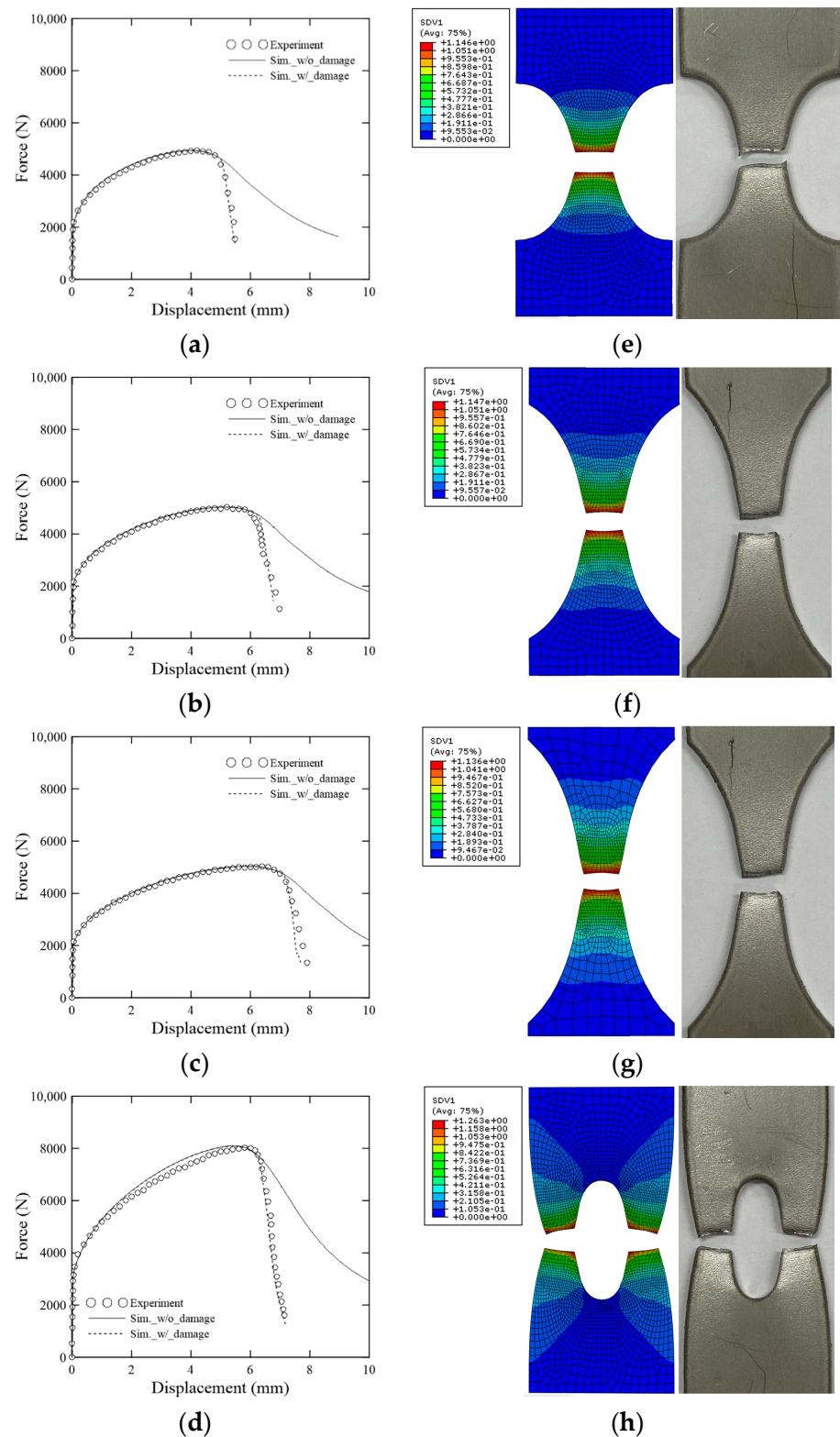


Figure 11. Comparison of force–displacement curve of (a) NT05, (b) NT10, (c) NT15, and (d) CH03 specimens and deformed configuration of (e) NT05, (f) NT10, (g) NT15, and (h) CH03 between experimental and simulation results (SDV1: equivalent plastic strain). With the Modified Mohr–Coulomb fracture criterion satisfied, crack propagation of the specimen occurs and complete failure follows. The fractured configurations between the numerical analysis and experiments are almost consistent.

7. Conclusions

In the present study, the failure prediction methodology was numerically developed to predict the ductile fracture of 304L stainless steel sheet. First of all, an elastoplastic constitutive model for a 304L stainless steel sheet was developed. To describe the constitutive behavior after diffuse necking, the combined Swift-Voce equation was adopted as a hardening function. The modified Mohr–Coulomb criterion based on the equivalent plastic strain was also adopted to describe the sudden fracture of the 304L stainless steel sheet. Numerical formulation of the elastoplastic-damage coupled constitutive model with fracture locus was implemented into ABAQUS user-defined subroutine UMAT.

To identify elastoplastic behavior and establish ductile fracture criterion, a series of material tests considering various stress states was performed. Five types of specimens were processed with 1.2 t 304L stainless steel, the raw material of the primary barrier of Mark-III type LNG CCS. Due to the ductility of 304L stainless steel, a considerable deformation occurred, and then a fracture was reached. After localized necking, fracture propagation was observed from the center point of the specimen. Since the modified Mohr–Coulomb model defines ductile fracture based on equivalent plastic strain, the equivalent plastic strain was obtained by comparing numerical analysis and experimental results in parallel. As plastic deformation accumulates, the stress triaxiality and Lode angle parameters fluctuate. To correct this problem, the average stress triaxiality and average Lode angle parameters were introduced. The modified Mohr–Coulomb fracture locus of 304L stainless steel was determined based on the material test results. Numerical analysis with ductile fracture criterion shows good agreement with experimental results.

The stainless steel exhibits outstanding mechanical performance in terms of the yield and tensile strength under cryogenic temperatures rather than at room temperature. However, ductility at a cryogenic temperature significantly decreases compared to room temperature. A fairly optimistic fracture analysis was performed based on fracture criteria based on equivalent plastic strain to the actual conditions in a LNG cargo tank. Therefore, the fracture criterion based on the experimental results at room temperature considered in this study is a fairly optimistic failure assessment result. Further studies will include failure prediction of the primary barrier of Mark-III type LNG CCS using the proposed numerical methodology in this study.

Author Contributions: Conceptualization, M.-S.K. and J.-M.L.; Data curation, M.-S.K., H.-T.K., Y.-H.C., J.-H.K. and S.-K.K.; Formal analysis, H.-T.K. and Y.-H.C.; Investigation, M.-S.K., H.-T.K., Y.-H.C., J.-H.K. and S.-K.K.; Methodology, M.-S.K.; Project administration, J.-M.L.; Supervision, J.-M.L.; Validation, H.-T.K., Y.-H.C., J.-H.K. and S.-K.K.; Writing—original draft, M.-S.K.; Writing—review & editing, J.-H.K., S.-K.K. and J.-M.L. All authors have read and agreed to the published version of the manuscript.

Funding: This work was supported by the Materials/Parts Technology Development Program (20017575, Development of Applicability Evaluation Technology for Cryogenic Insulation Material and Storage Vessel considering Operating Condition of Hydrogen Commercial Vehicle) funded By the Ministry of Trade, Industry & Energy (MOTIE, Korea). This work was supported by the R&D Platform Establishment of Eco-Friendly Hydrogen Propulsion Ship Program (No. 20006644) funded by the Ministry of Trade, Industry & Energy (MOTIE, Korea). This research was supported by the Development and demonstration of the on-board marine debris disposal modules program of the Korea Institute of Marine Science & Technology Promotion (KIMST) funded by the Ministry of Oceans and Fisheries (KIMST-20220494).

Institutional Review Board Statement: Not applicable.

Informed Consent Statement: Not applicable.

Data Availability Statement: The data presented in this study are available on request from corresponding author.

Conflicts of Interest: The authors declare no conflict of interest.

References

- Jia, S.; Tan, Q.; Ye, J.; Zhu, Z.; Jiang, Z. Experiments on dynamic mechanical properties of austenitic stainless steel S30408 and S31608. *J. Constr. Steel Res.* **2021**, *179*, 106556. [CrossRef]
- Kim, J.-H.; Park, W.-S.; Chun, M.-S.; Kim, J.-J.; Bae, J.-H.; Kim, M.-H.; Lee, J.-M. Effect of pre-straining on low-temperature mechanical behavior of AISI 304L. *Mater. Sci. Eng. A* **2012**, *543*, 50–57. [CrossRef]
- Kim, S.-K.; Lee, C.-S.; Kim, J.-H.; Kim, M.-H.; Lee, J.-M. Computational evaluation of resistance of fracture capacity for SUS304L of liquefied natural gas insulation system under cryogenic temperatures using ABAQUS user-defined material subroutine. *Mater. Des.* **2013**, *50*, 522–532. [CrossRef]
- Zheng, C.; Liu, C.; Ren, M.; Jiang, H.; Li, L. Microstructure and mechanical behavior of an AISI 304 austenitic stainless steel prepared by cold- or cryogenic-rolling and annealing. *Mater. Sci. Eng. A* **2018**, *724*, 260–268. [CrossRef]
- Mallick, P.; Tewary, N.; Ghosh, S.; Chattopadhyay, P. Effect of cryogenic deformation on microstructure and mechanical properties of 304 austenitic stainless steel. *Mater. Charact.* **2017**, *133*, 77–86. [CrossRef]
- Singh, R.; Sachan, D.; Verma, R.; Goel, S.; Jayaganthan, R.; Kumar, A. Mechanical behavior of 304 austenitic stainless steel processed by cryogenic rolling. *Mater. Today Proc.* **2018**, *5*, 16880–16886. [CrossRef]
- Oh, D.-J.; Kim, N.-K.; Song, S.-W.; Kim, Y.-D.; Kim, M.-H. Investigation of fatigue performance for new membrane-type LNG CCS at cryogenic temperature. *Mar. Struct.* **2018**, *62*, 90–105. [CrossRef]
- Park, S.Y.; Kim, W.T.; Choi, J.H.; On, S.Y.; Kim, S.S. Effects of process-induced residual stress and geometric characteristics on pressure-resisting capability of corrugation in primary barriers of liquefied natural gas carriers. *Ocean Eng.* **2021**, *237*, 109613. [CrossRef]
- Kim, J.-H.; Kim, S.-K.; Kim, M.-H.; Lee, J.-M. Numerical model to predict deformation of corrugated austenitic stainless steel sheet under cryogenic temperatures for design of liquefied natural gas insulation system. *Mater. Des.* **2014**, *57*, 26–39. [CrossRef]
- Kim, M.-S.; Kwon, S.-B.; Kim, S.-K.; Kim, J.-H.; Lee, J.-S.M. Impact failure analysis of corrugated steel plate in LNG containment cargo system. *J. Constr. Steel Res.* **2019**, *156*, 287–301. [CrossRef]
- Kim, M.-S.; Kim, J.-H.; Kim, S.-K.; Lee, J.-M. Experimental Investigation of Structural Response of Corrugated Steel Sheet Subjected to Repeated Impact Loading: Performance of LNG Cargo Containment System. *Appl. Sci.* **2019**, *9*, 1558. [CrossRef]
- Kim, B.C.; Yoon, S.H.; Gil Lee, D. Pressure resistance of the corrugated stainless steel membranes of LNG carriers. *Ocean Eng.* **2011**, *38*, 592–608. [CrossRef]
- Lee, D.; Kim, K.H.; Choi, I.; Gil Lee, D. Pressure-resisting capability of the knot area of the primary barrier for a LNG containment system. *Ocean Eng.* **2015**, *95*, 128–133. [CrossRef]
- Jeong, Y.-J.; Kim, H.-T.; Kim, S.-K.; Kim, J.-H.; Kim, Y.-T.; Heo, W.-S.; Lee, J.-M. Evaluation of the pressure-resisting capability of membrane-type corrugated sheet under hydrodynamic load. *Thin-Walled Struct.* **2021**, *162*, 107388. [CrossRef]
- Deng, X.; Wang, B. Peridynamic modeling of dynamic damage of polymer bonded explosive. *Comput. Mater. Sci.* **2020**, *173*, 109405. [CrossRef]
- Depaetere, R.; De Waele, W.; Hertelé, S. Fully-coupled continuum damage model for simulation of plasticity dominated hydrogen embrittlement mechanisms. *Comput. Mater. Sci.* **2021**, *200*, 110857. [CrossRef]
- Varandas, L.F.; Catalanotti, G.; Melro, A.R.; Falzon, B.G. On the importance of nesting considerations for accurate computational damage modelling in 2D woven composite materials. *Comput. Mater. Sci.* **2020**, *172*, 109323. [CrossRef]
- Paredes, M.; Wierzbicki, T.; Zelenak, P. Prediction of crack initiation and propagation in X70 pipeline steels. *Eng. Fract. Mech.* **2016**, *168*, 92–111. [CrossRef]
- Björklund, O.; Larsson, R.; Nilsson, L. Failure of high strength steel sheets: Experiments and modelling. *J. Mater. Process. Technol.* **2013**, *213*, 1103–1117. [CrossRef]
- Kim, S.-K.; Kim, J.-H.; Kim, J.-H.; Lee, J.-M. Numerical Model for Mechanical Nonlinearities of High Manganese Steel Based on the Elastoplastic Damage Model. *Metals* **2018**, *8*, 680. [CrossRef]
- Baltic, S.; Magnien, J.; Ganser, H.-P.; Antretter, T.; Hammer, R. Coupled damage variable based on fracture locus: Modelling and calibration. *Int. J. Plast.* **2019**, *126*, 102623. [CrossRef]
- Charoensuk, K.; Panich, S.; Uthaisangsuk, V. Damage initiation and fracture loci for advanced high strength steel sheets taking into account anisotropic behaviour. *J. Mater. Process. Technol.* **2017**, *248*, 218–235. [CrossRef]
- Hancock, J.W.; Mackenzie, A.C. On the mechanisms of ductile failure in high-strength steels subjected to multi-axial stress-states. *J. Mech. Phys. Solids* **1976**, *24*, 147–160. [CrossRef]
- Theocaris, P.S. Failure criteria for isotropic bodies revisited. *Eng. Fract. Mech.* **1995**, *51*, 239–255, 257–264. [CrossRef]
- Schiffmann, R.; Bleck, W.; Dahl, W. The influence of strain history on ductile failure of steel. *Comput. Mater. Sci.* **1998**, *13*, 142–147. [CrossRef]
- Schliiter, N.; Grimpe, F.; Bleck, W.; Dahl, W. Modelling of the damage in ductile steels. *Comput. Mater. Sci.* **1996**, *7*, 27–33. [CrossRef]
- Bai, Y.; Wierzbicki, T. A new model of metal plasticity and fracture with pressure and Lode dependence. *Int. J. Plast.* **2008**, *24*, 1071–1096. [CrossRef]
- Bai, Y.; Wierzbicki, T. Application of extended Mohr–Coulomb criterion to ductile fracture. *Int. J. Fract.* **2010**, *161*, 1–20. [CrossRef]
- Kim, S.-K.; Lee, C.-S.; Kim, J.-H.; Kim, M.-H.; Noh, B.-J.; Matsumoto, T.; Lee, J.-M. Estimation of Fatigue Crack Growth Rate for 7% Nickel Steel under Room and Cryogenic Temperatures Using Damage-Coupled Finite Element Analysis. *Metals* **2015**, *5*, 603–627. [CrossRef]

30. Kim, S.-K.; Kang, K.-Y.; Kim, M.-S.; Lee, J.-M. Low-Temperature Mechanical Behavior of Super Duplex Stainless Steel with Sigma Precipitation. *Metals* **2015**, *5*, 1732–1745. [CrossRef]
31. Paredes, M.; Grolleau, V.; Wierzbicki, T. On ductile fracture of 316L stainless steels at room and cryogenic temperature level: An engineering approach to determine material parameters. *Materialia* **2020**, *10*, 100624. [CrossRef]
32. Dunand, M.; Mohr, D. On the predictive capabilities of the shear modified Gurson and the modified Mohr–Coulomb fracture models over a wide range of stress triaxialities and Lode angles. *J. Mech. Phys. Solids* **2011**, *59*, 1374–1394. [CrossRef]
33. Luo, M.; Dunand, M.; Mohr, D. Experiments and modeling of anisotropic aluminum extrusions under multi-axial loading—Part II: Ductile fracture. *Int. J. Plast.* **2012**, *32–33*, 36–58. [CrossRef]
34. Chen, X.; Shi, M.F.; Shih, H.-C.; Luo, M.; Wierzbicki, T. AHSS Shear Fracture Predictions Based on a Recently Developed Fracture Criterion. *SAE Int. J. Mater. Manuf.* **2010**, *3*, 723–731. [CrossRef]
35. Granum, H.; Morin, D.; Børvik, T.; Hopperstad, O.S. Calibration of the modified Mohr–Coulomb fracture model by use of localization analyses for three tempers of an AA6016 aluminium alloy. *Int. J. Mech. Sci.* **2021**, *192*, 106122. [CrossRef]
36. Quach, H.; Kim, J.-J.; Nguyen, D.-T.; Kim, Y.-S. Uncoupled ductile fracture criterion considering secondary void band behaviors for failure prediction in sheet metal forming. *Int. J. Mech. Sci.* **2020**, *169*, 105297. [CrossRef]
37. Qian, L.-Y.; Fang, G.; Zeng, P. Modeling of the ductile fracture during the sheet forming of aluminum alloy considering non-associated constitutive characteristic. *Int. J. Mech. Sci.* **2017**, *126*, 55–66. [CrossRef]
38. Ben Othmen, K.; Haddar, N.; Jegat, A.; Manach, P.-Y.; Elleuch, K. Ductile fracture of AISI 304L stainless steel sheet in stretching. *Int. J. Mech. Sci.* **2020**, *172*, 105404. [CrossRef]
39. Pham, H.; Iwamoto, T. An evaluation of fracture properties of type-304 austenitic stainless steel at high deformation rate using the small punch test. *Int. J. Mech. Sci.* **2018**, *144*, 249–261. [CrossRef]
40. Kim, J.-H.; Lee, C.-S.; Kim, M.-H.; Lee, J.-M. Prestrain-dependent viscoplastic damage model for austenitic stainless steel and implementation to ABAQUS user-defined material subroutine. *Comput. Mater. Sci.* **2013**, *67*, 273–281. [CrossRef]
41. Mohr, D.; Marcadet, S.J. Micromechanically-motivated phenomenological Hosford–Coulomb model for predicting ductile fracture initiation at low stress triaxialities. *Int. J. Solids Struct.* **2015**, *67–68*, 40–55. [CrossRef]
42. Palchik, V. Application of Mohr–Coulomb failure theory to very porous sandy shales. *Int. J. Rock Mech. Min. Sci.* **2006**, *43*, 1153–1162. [CrossRef]
43. Zhao, J. Applicability of Mohr–Coulomb and Hoek–Brown strength criteria to the dynamic strength of brittle rock. *Int. J. Rock Mech. Min. Sci.* **2000**, *37*, 1115–1121. [CrossRef]
44. Kofiani, K.; Nonn, A.; Wierzbicki, T. New calibration method for high and low triaxiality and validation on SENT specimens of API X70. *Int. J. Press. Vessel. Pip.* **2013**, *111–112*, 187–201. [CrossRef]
45. Swift, H.W. Plastic Instability under Plane Stress. *J. Mech. Phys. Solids* **1952**, *1*, 1–18. [CrossRef]
46. Voce, E. The relationship between stress and strain for homogeneous deformation. *J. Inst. Met.* **1948**, *74*, 537–562.
47. Lemaitre, J. A continuous damage mechanics model for ductile fracture. *J. Eng. Mater. Technol.* **1985**, *107*, 83–89. [CrossRef]
48. Neto, E.A.; de Eduardo, S.; Perić, D.; Owen, D.R.J. *Computational Methods for Plasticity: Theory and Applications*; Wiley: Chichester, UK, 2008; ISBN 9780470694527.
49. Lian, J.; Wu, J.; Münstermann, S. Evaluation of the cold formability of high-strength low-alloy steel plates with the modified Bai–Wierzbicki damage model. *Int. J. Damage Mech.* **2015**, *24*, 383–417. [CrossRef]
50. Bao, Y.; Wierzbicki, T. On fracture locus in the equivalent strain and stress triaxiality space. *Int. J. Mech. Sci.* **2004**, *46*, 81–98. [CrossRef]
51. Sancho, A.; Cox, M.; Cartwright, T.; Davies, C.; Hooper, P.; Dear, J. An experimental methodology to characterise post-necking behaviour and quantify ductile damage accumulation in isotropic materials. *Int. J. Solids Struct.* **2019**, *176–177*, 191–206. [CrossRef]
52. Lou, Y.; Huh, H. Extension of a shear-controlled ductile fracture model considering the stress triaxiality and the Lode parameter. *Int. J. Solids Struct.* **2013**, *50*, 447–455. [CrossRef]
53. Xue, Z.; Pontin, M.; Zok, F.; Hutchinson, J. Calibration procedures for a computational model of ductile fracture. *Eng. Fract. Mech.* **2010**, *77*, 492–509. [CrossRef]
54. Erice, B.; Gálvez, F. A coupled elastoplastic-damage constitutive model with Lode angle dependent failure criterion. *Int. J. Solids Struct.* **2014**, *51*, 93–110. [CrossRef]
55. Kubík, P.; Šebek, F.; Hůlka, J.; Petruška, J. Calibration of ductile fracture criteria at negative stress triaxiality. *Int. J. Mech. Sci.* **2016**, *108–109*, 90–103. [CrossRef]

Article

Computational Design and Characterisation of Gyroid Structures with Different Gradient Functions for Porosity Adjustment

Leonie Wallat ^{1,*}, Patrick Altschuh ^{2,3}, Martin Reder ^{2,3}, Britta Nestler ^{2,3} and Frank Poehler ^{1,*}

¹ Institute of Materials and Processes, Karlsruhe University of Applied Sciences, Molkestr. 30, 76133 Karlsruhe, Germany

² Institute for Digital Materials Research, Karlsruhe University of Applied Sciences, Molkestr. 30, 76133 Karlsruhe, Germany; patrick.altschuh@h-ka.de (P.A.); martin_dominik.reder@h-ka.de (M.R.); britta.nestler@kit.edu (B.N.)

³ Institute for Applied Materials-Microstructure Modelling and Simulation, Karlsruhe Institute of Technology, Kaiserstraße 12, 76131 Karlsruhe, Germany

* Correspondence: leonie.wallat@h-ka.de (L.W.); frank.Poehler@h-ka.de (F.P.)

Abstract: Triply periodic minimal surface (TPMS) structures have a very good lightweight potential, due to their surface-to-volume ratio, and thus are contents of various applications and research areas, such as tissue engineering, crash structures, or heat exchangers. While TPMS structures with a uniform porosity or a linear gradient have been considered in the literature, this paper focuses on the investigation of the mechanical properties of gyroid structures with non-linear porosity gradients. For the realisation of the different porosity gradients, an algorithm is introduced that allows the porosity to be adjusted by definable functions. A parametric study is performed on the resulting gyroid structures by performing mechanical simulations in the linear deformation regime. The transformation into dimensionless parameters enables material-independent statements, which is possible due to linearity. Thus, the effective elastic behaviour depends only on the structure geometry. As a result, by introducing non-linear gradient functions and varying the density of the structure over the entire volume, specific strengths can be generated in certain areas of interest. A computational design of porosity enables an accelerated application-specific structure development in the field of engineering.

Keywords: TPMS structures; sheet-based gyroid; mechanical simulation; modelling; PACE3D

Citation: Wallat, L.; Altschuh, P.; Reder, M.; Nestler, B.; Poehler, F. Computational Design and Characterisation of Gyroid Structures with Different Gradient Functions for Porosity Adjustment. *Materials* **2022**, *15*, 3730. <https://doi.org/10.3390/ma15103730>

Academic Editors: Shuwen Wen, Yongle Sun and Xin Chen

Received: 20 April 2022

Accepted: 17 May 2022

Published: 23 May 2022

Publisher's Note: MDPI stays neutral with regard to jurisdictional claims in published maps and institutional affiliations.



Copyright: © 2022 by the authors. Licensee MDPI, Basel, Switzerland. This article is an open access article distributed under the terms and conditions of the Creative Commons Attribution (CC BY) license (<https://creativecommons.org/licenses/by/4.0/>).

1. Introduction

Triply periodic minimal surfaces (TPMS) are three-dimensional cell structures that occur in nature in many forms: for example, in butterfly wings [1] or on the skeletal plate of a sea urchin [2]. There are a variety of different structures: for example, gyroid, Schwarz diamond, and Schwarz primitive structures [3], which are defined by a mathematical periodic function and whose surfaces have a mean curvature of zero. This results in a smoothly curved surface, while the periodic cells are divided into two disjointed continuous channels that are intertwined. In addition to their lightweight potential, these cell structures are characterised by unique properties and shapes that make them attractive for a wide range of engineering applications. For example, the high surface-to-volume ratio and the two-phase system are very preferable properties for the development of heat exchangers [4–6]. In particular, the work by Weihong Li et al. [5] has shown that a comparison between a printed circuit heat exchanger (PCHE) and a heat exchanger with TPMS structures (Schwarz diamond and gyroid) shows both a higher thermal performance and a higher Nusselt number [5]. Furthermore, TPMS structures are of great interest in the field of tissue engineering, as their topological structure is similar to that of trabecular bone [7]. The introduction of a porosity gradient on the TPMS structures opens up new engineering

possibilities. In Dawei Li's research [8], for example, it was shown that sheet-based linear graded gyroid structures have a high energy absorption potential, which is a crucial property in applications with regard to crash safety. Moreover, the introduction of the gradient offers a new freedom of design. As such, the work of [9] aims to use linear graded cell gradients to replicate the natural environment of bones. Since structures with gradients have so far mostly been investigated with linear gradients and are interesting for a variety of applications, it is desirable to put more emphasis on non-linear porosity adjustments. In the following, the group of double gyroid structures is considered, which is exemplified in Figure 1, with the characteristic two-tunnel system. For example, in [8,10], this structure is referred to as 'sheet-based gyroid' (in the remainder of this article, it will only be referred to as 'gyroid').

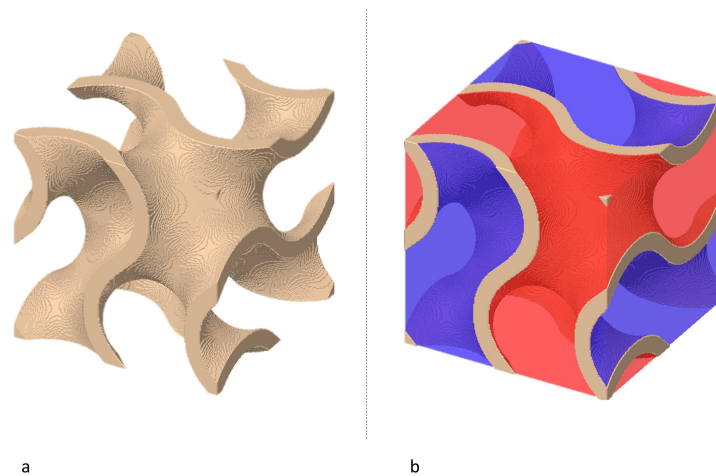


Figure 1. (a) Sheet-based gyroid structure; (b) gyroid structure with labelled two-tunnel system.

The following equation is used to approximate the surface of the gyroid structure by trigonometrical functions [4].

$$0 = \left[\sin \frac{2\pi x}{L_x} \cdot \cos \frac{2\pi y}{L_y} + \sin \frac{2\pi y}{L_y} \cdot \cos \frac{2\pi z}{L_z} + \sin \frac{2\pi z}{L_z} \cdot \cos \frac{2\pi x}{L_x} \right]^2 - t^2 \quad (1)$$

The number of cell repetitions in the x -, y -, and z -directions and the absolute sizes of the unit cells L_x , L_y , and L_z define the cell space [11]. The thickness of the cell wall is controlled by the variable t . Thus, t has an effect on the volume fraction (v^*) of the lattice structure [12]. According to [13,14], the volume fraction (v^*) and the closely related parameter porosity Φ are defined as follows:

$$\Phi = (1 - v^*) \cdot 100[\%] \quad (2)$$

with

$$v^* = \frac{v}{v_s}, \quad (3)$$

where v and v_s denote the volume of the pore structure and the volume of the solid structure, respectively [13,14]. In the literature, v^* is also referred to as 'relative density' [14,15]. As can be seen from equation (2), the higher the porosity, the thinner the cell walls. According to Gibson and Ashby [16], the mechanical properties of porous structures of the same topology are directly influenced by their porosity. They propose a correlation between the effective Young modulus and the relative density, which is known as Gibson–Ashby correlation. In addition to the porosity, the mechanical properties are also strongly influenced by the topology of the structure [11,17]. With respect to gyroid structures with imposed porosity gradients, the question therefore arises as to how different geometries with non-linear porosity gradients influence the resulting effective behaviour of the structures. Since

the complex manufacture of gyroid structures is cost and time intensive, it is desirable to answer these questions through digital modelling and simulations.

In this work, an algorithm for generating gyroid structures with imposed porosity gradients is introduced, and the resulting mechanical properties of the gyroids are investigated by performing a simulation study. For the structure generation, a constant porosity and two different functions are considered: a linear and a quadratic function. The numerical simulations are performed in the linear elastic regime, which is a common approach in the field of open cell foams. Kaoua et al. [18] use finite element (FE) simulations on Kelvin unit cells to investigate different ligament cross section geometries. In the work by Gan et al. [19] and Zhu et al. [17], elastic FE simulations are also applied to Voronoi-based foams, whereby in the latter work, the influence of geometry irregularities is investigated. The aim of the work is to enable the digital design of gyroid structures with tailored porosity gradients for specific applications.

2. Computational Design

Before mechanical simulations of the structures can be performed, the digital structures are created on the basis of a spatial algorithm. For the structure creation, a MatLab [20] source was programmed, which enables the creation of TPMS structures with and without gradients. The aim of the MatLab program is to create gyroid structures with adjustable porosities and definable porosity gradients, using mathematical functions. The TPMS structures are stored in vtk files, while the further preprocessing of the structures as well as the simulations are realised with the simulation framework PACE3D [21]. The simulation software “Parallel Algorithms for Crystal Evolution in 3D” (PACE3D) is a massive parallel in-house software package [21] which is developed at the Institute for Digital Materials Science (IDM) of the Karlsruhe University of Applied Sciences, Germany. The objective of PACE3D is to provide a package for large-scale multiphysics simulations, so as to solve coupled problems such as solidification, grain growth, mass and heat transport, fluid flow and mechanical forces (elasticity, plasticity), etc. The use of dimensionless quantities enables a scale-independent representation of the results, so that the simulations are performed with a non-dimensionalisation. With the help of a conversion table, physical quantities can be obtained from the results. The corresponding flowchart from the creation of the structures in the MatLab program to the mechanical simulation is summarised in Figure 2.

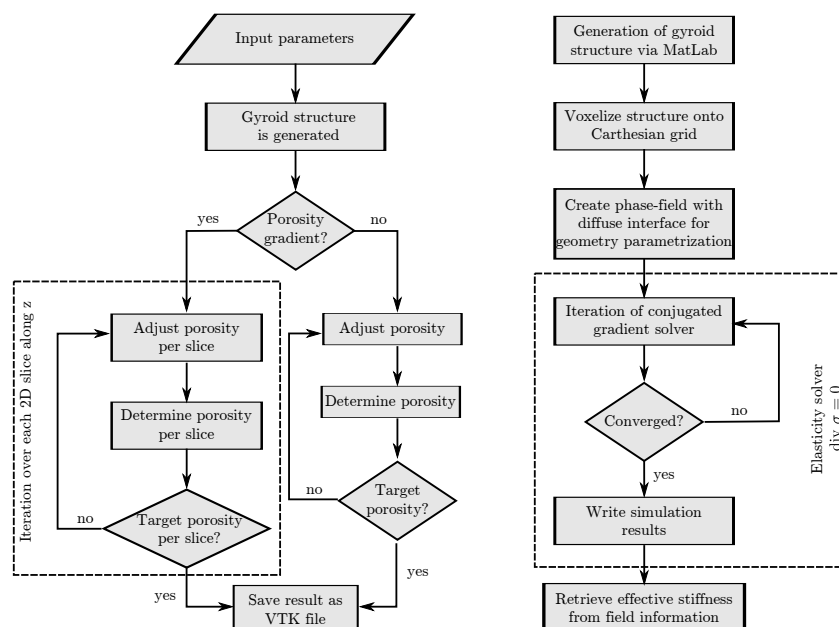


Figure 2. Schematic representation of the computational design of the structures. Generation of the gyroid structures in the MatLab program (left) and the workflow for the mechanical simulations with PACE3D (right).

2.1. Structure Generation

2.1.1. Input Parameters

The MatLab program offers the possibility of creating structures with constant and graded porosity. Table 1 lists and briefly describes the required input parameters for the the structure generation, while the individual parameters and their influence are discussed more specifically in the following.

Table 1. Input parameters of the MatLab program and their function for the creation of a gyroid structure.

Input Parameter	Function
num_x num_y num_z	Number of unit cells to be repeated in the x -, y -, and z -direction
$unitCellSize$	
n_{steps}	
Φ_{max} Φ_{min}	Maximum and minimum porosity of the cell
$func$	
$grad$	With/without gradient function (1, 0)
$delta$	Tolerance range

The input parameters num_x , num_y , and num_z specify the number of unit cells to be repeated in the corresponding direction, while the parameter $unitCellSize$ defines the physical dimension of the created gyroid unit cell. By multiplying $unitCellSize$ with the input parameters num_x , num_y , and num_z , the quantities L_x , L_y , and L_z of Equation (1) are obtained, which also represent the total domain size of the resulting structure in physical dimensions. The parameter n_{steps} defines the number of voxels that are used to discretise the gyroid in all directions of one spatial unit cell.

With Φ_{min} and Φ_{max} , the range of the minimum and maximum porosity is defined. In the MatLab program, the porosity is specified in the range between [0; 1], which represents the more commonly used expression of 0% and 100% for the porosity. When creating a gyroid structure with a constant overall porosity, the value from Φ_{max} is used. The porosity function is defined with the parameter $func$. The polynomial degree of the gradient function can be selected between 0 and 2, corresponding to a constant (0), a linear (1), and a quadratic (2) representation. The input parameter $grad$ determines whether the gyroid structure is generated with or without gradient by the integer values 1 and 0, respectively. Per default, the gradient occurs in the z -direction.

The parameter $delta$ is mainly responsible for the iterative adjustment of the actual porosity to the target porosity. A tolerance range is defined that describes the maximum permissible deviation between the actual porosity of the current layer and the target porosity. For instance, if the parameter is set to a value of 0.02, this corresponds to a deviation of the actual data of 2%, compared to the target porosity function. The smaller the number of this parameter, the more accurate and longer the program takes to calculate. The target porosity per cell layer is calculated by the gradient function.

Figure 3 shows four different gyroid unit cell structures with a cell size of 2.5 mm, which is generated with 200 steps and a $delta$ parameter of 0.02. Figure 3a,d illustrate a gyroid unit cell with a constant porosity of 0.8 (a) and 0.4 (d). By looking at the two structures, the influence of the porosity on the cell thickness becomes evident. The higher the porosity, the thinner the wall thickness. The structures Figure 3b,c refer to different gradient functions: linear (b) and quadratic (c) functions. The structures are in a porosity interval between 0.4 and 0.8.

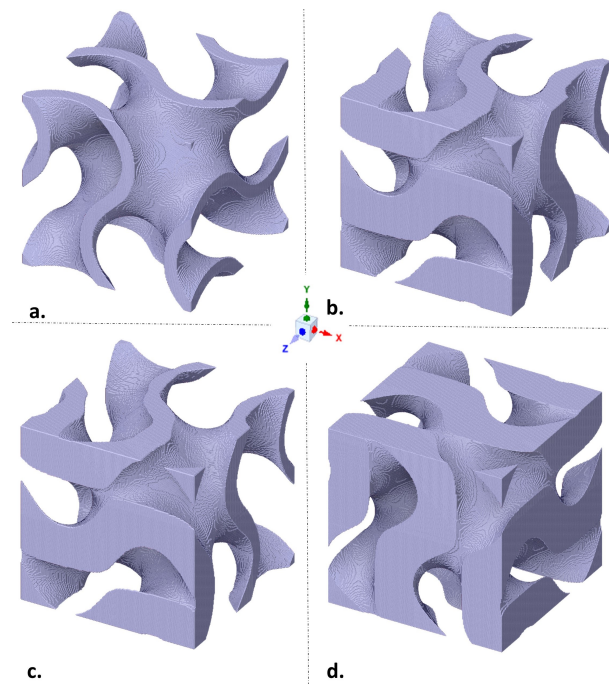


Figure 3. Unit cell of the gyroid structure; gradient with (a) constant function, with a porosity of 0.8; (b) linear function, with a porosity from 0.4 to 0.8; (c) quadratic function, with a porosity from 0.4 to 0.8; (d) constant function, with a porosity of 0.4.

2.1.2. Algorithm

In the algorithm, the porosity is adjusted step by step. First, the total volume of an initially generated cell structure is calculated as a starting point, while the discrete voxel values in the domain vary between -1 and 1 , according to Equation (1). Once the gradient function is selected, the superimposition begins in an iterative process. Three encapsulated for-loops are used to iterate over the spatial domain and a while-loop is responsible for adjusting the porosity to the target porosity. The adjustment is made by applying a threshold with values between -1 and 1 , which divides the domain into structure space and tunnels. The specified tolerance limits are used as the termination criterion of the while loop. In this way, the target porosity for each 2D layer of the 3D structure can be adjusted according to the gradient function. If no gradient is selected, the porosity adjustment is not applied per layer but to the entire cell structure. For the definition of the gradient function (Φ_{target}), a choice between the following three functions is possible so far.

Constant function:

$$\Phi_{\text{target}} = \Phi_{\text{max}} \quad (4)$$

Linear function:

$$\Phi_{\text{target}} = -\frac{\Phi_{\text{max}} - \Phi_{\text{min}}}{n_{\text{steps}_z}} \cdot q + \Phi_{\text{max}} \quad (5)$$

Quadratic function:

$$\Phi_{\text{target}} = -\frac{\Phi_{\text{max}} - \Phi_{\text{min}}}{(n_{\text{steps}_z} - 3)^2} \cdot (q - 2)^2 + \Phi_{\text{max}} \quad (6)$$

The constant function calculates a structure with a constant porosity along each spatial direction. For the linear cell gradient, a linear function with the usual linear structure $y = a \cdot x + b$ is used. The first part of the equation calculates the stepwise increase in the cell volume in each cell level (or the decrease in the porosity). Here, the calculation depends on the number of discrete points (n_{steps}) in whose direction the gradient is imposed. In this case, the gradient extends into the z -direction. The second part of the formula is used

to determine the initial porosity Φ_{\max} . In the first layer, the structure has the porosity of Φ_{\max} , which is gradually decreased until the final porosity Φ_{\min} is reached. q is the index parameter for the outermost for-loop and at the same time the spatial position of the current 2D layer.

For the quadratic cell gradient, a quadratic function of the structure $y = a * x^2 + b * x + c$ is used with $(b = 0)$. As with the linear function, a stepwise decrease in the porosity (increase in the cell volume) is determined at each cell level, except that the decrease should be quadratic. Since the quadratic gradient is defined as an inverted parabola with an offset on the y-axis, at the level of maximum porosity, the gyroid structure with a quadratic gradient is thickened more slowly than those with a thickening linear structure, as can be seen in Figure 4.

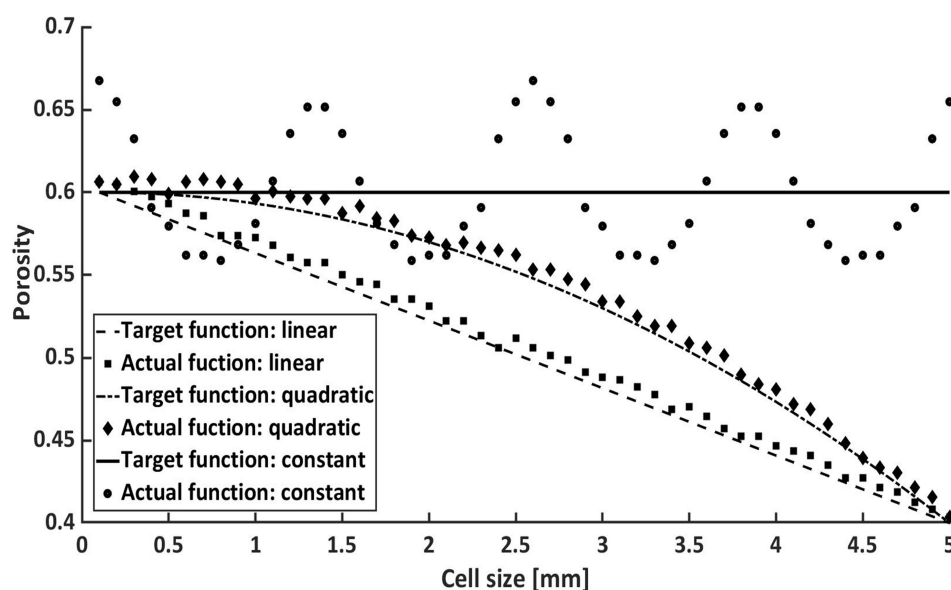


Figure 4. Porosity function of the constant, linear, and quadratic function.

In Figure 4, the three different gradients (constant, linear, and quadratic) are compared with their target and actual values of a single-cell gyroid structure. In each case, 50 actual and 50 target values per porosity function (input parameter: $n_{\text{steps}} = 50$) are mapped over 'Cell size' [5 mm], in the z-direction [x-axis], and 'Porosity' [y-axis]. The maximum porosity is 0.6, and the minimum porosity is 0.4. The actual values are an approximation of the target values. As already mentioned, the fit of the objective function mainly depends on the δ parameter.

2.2. Model and Setup for Mechanical Simulations

For the mechanical simulations, the static momentum balance in the small deformation regime is solved with a finite element discretisation. This is done using the PACE3D framework, which employs a phase-field method for the geometry parametrization. Therefore, the structures generated in the MatLab program (see Section 2.1) are discretised on a Cartesian grid, and a diffuse interface is employed between the metal and the surrounding air.

From the micromechanics-microstructure simulations, the stress tensor σ and the strain tensor ϵ are obtained as full field information. This gives rise to the normalised von Mises stresses σ_{VM} , whose maximum value determines the start of local plastification if it reaches the yield strength of the materials. Through homogenisation, an effective Young modulus can additionally be obtained from the stress and strain field [22]. This is done using the volume-averaged stress and strain over the whole computational domain and relating them via the effective Young modulus.

Simulations of compression tests are performed with the specified stress σ_{BC} , which is applied in the z-direction, as the boundary condition on both sides of the simulation

domain. All other boundaries are set to be stress-free. The domain is discretised using a Cartesian grid with $200 \times 200 \times 200$ elements. The air phase between the structure is modelled with a stiffness of zero, while the solid phase is considered to exhibit an isotropic elastic material behaviour.

3. Results and Discussion

3.1. Structure Consideration

Table 2 lists all 13 gyroid unit cells created for the subsequent investigation by mechanical simulations. Overall, the structures differ only in their porosity and gradient function. As can be seen from Table 2, the structures range in porosity from 0.4 to 0.8. For the structures with graded porosity (linear and quadratic), the thickening of the structures always ends at a porosity of 0.4. It should be mentioned that when the volume decreases, the influence on the mechanical stability should be considered, so as to optimise the lightweight potential. Since the porosity has a significant influence on the surface-to-volume ratio, and thus on the mechanical stability, it is also taken into account. The other input parameters that do not change are listed in Table 3. Assuming that the gyroid structures are characterised by the periodicity of their unit cell in all directions, it should be possible to apply the results of the mechanical simulation to multicell structures. In all three directions (x , y , z), the size of the analysed cell is set to 2.5 mm. A unit cell is divided into 200 voxels per spatial direction ($n_{\text{steps}} = 200$). The possible deviation from the target function is 2% ($\text{delta} = 0.02$).

Table 2. Created gyroid structures: constant gradient, linear gradient, quadratic gradient.

Constant Gradient	Linear Gradient	Quadratic Gradient
0.4	-	-
0.5	0.4 to 0.5	0.4 to 0.5
0.6	0.4 to 0.6	0.4 to 0.6
0.7	0.4 to 0.7	0.4 to 0.7
0.8	0.4 to 0.8	0.4 to 0.8

Table 3. Non-varying input parameters across all structures.

Input Parameter	Value
num_x	1
num_y	1
num_z	1
$unitCellSize$ [mm]	2.5
n_{steps}	200
delta	0.02

3.2. Surface Area-to-Volume Ratio

The surface area-to-volume (SA/V) ratio is an important technical aspect. A high SA/V ratio, for example, favours more efficient heat exchange [23] but usually has negative effects on the mechanical properties, which is why the SA/V ratio of the gyroid cells is investigated. To calculate the surface area-to-volume ratio, the stl files created in the MatLab program were imported into the Ansys workbench [24], where the volume and surface area of each structure were output.

The bar chart Figure 5 lists the SA/V ratio from the gyroid structures in ascending order, with and without gradients. There, it can be seen that a high porosity favours the ratio. For this reason, the gyroid cell with a constant porosity of 0.8 has the highest SA/V ratio of all structures. In contrast, the gyroid with a porosity of 0.4 has the lowest ratio. The structures with a quadratic gradient have a higher SA/V ratio than those with a linear gradient. This is due to the fact that the structure with a quadratic gradient thickens more

slowly, as can be seen in Figure 4. Between the gyroid structures with a constant porosity of 0.5 and 0.6, there are four structures with gradients. In the course of this work, a possible correlation between the SA/V ratio and the mechanical properties will be considered.

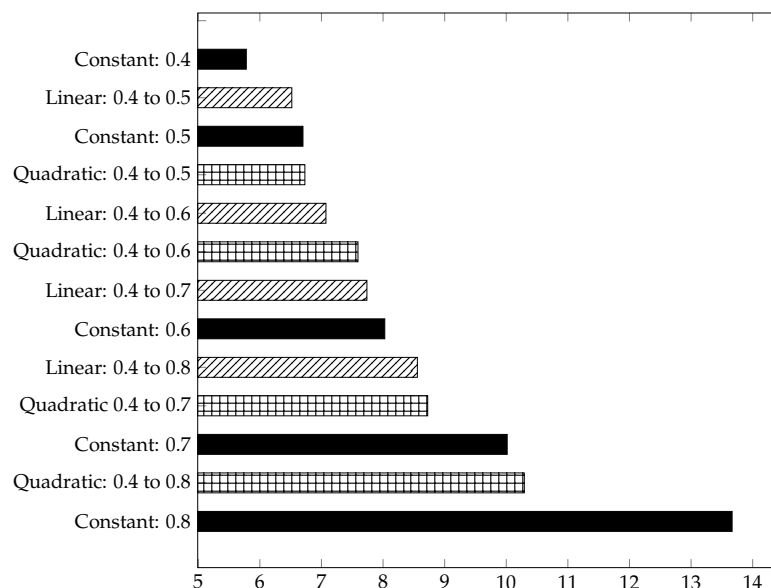


Figure 5. Surface [mm²]/volume [mm³] of gyroid structures in ascending order.

3.3. Mechanical Simulation

Material-independent and relative statements depending on the porosity type can be made about the structures with the same load scenario. For this reason, scaled data are used. For the analysis of the structures, a steady-state case with an applied load of $\sigma_{BC} = 400$ MPa is considered. Since the simulations are performed within the linear-elastic regime, the results are independent of the structure material and the characteristic length, due to the linear scalability. The effective Young modulo as well as the maximum and mean values of the von Mises stress are evaluated. The latter values correspond respectively to the volume average $\bar{\sigma}_{VM}$ of the von Mises equivalent stress field and its maximum value $\sigma_{VM,max}$ within the domain. Note that both quantities are given normalised with the load σ_{BC} and can thus be interpreted as mean and maximum values of a stress amplification factor. Dividing the yield strength of the material under consideration (e.g., AlMg7Si0.6) by this amplification factor gives the actual limit for local plastification and thus an effective yield strength. The effective Young modulus is given normalised with the one of the structure materials. In order to obtain physical quantities, a multiplication can be carried out with the material value under consideration. For example, $\bar{E}_{AlMg7Si0.6} = E_{AlMg7Si0.6} \bar{E}$, with $E_{AlMg7Si0.6} = 59$ GPa, if the structure is made of the alloy AlMg7Si0.6. The use of these normalised quantities allows a comparison between the structures without specifying the material or length scale.

Tables 4–6 represent the material-independent and scaled values of the respective structures. For better clarity and comprehensibility of the results, they are also shown in the bar charts Figures 6–8. The structures in the charts are all labelled according to the following pattern: ‘Type of gradient function: Porosity interval’. ‘Quadratic: 0.4 to 0.8’, for example, means that a gyroid structure with a quadratic gradient function and a porosity interval between 0.4 and 0.8 is considered.

Table 4. Scaled results of the gyroid structure with a constant gradient [dimensionless] of the normalised effective Young modules \bar{E} , a mean von Mises stress $\bar{\sigma}_{VM}$, and a maximum von Mises stress $\sigma_{VM,max}$, which is given for different porosities.

Porosity	\bar{E}	$\bar{\sigma}_{VM}$	$\sigma_{VM,max}$
0.4	0.10	0.88	10.40
0.5	0.05	0.99	14.92
0.6	0.03	1.09	19.50
0.7	0.02	1.18	23.94
0.8	0.01	1.24	28.74

Table 5. Scaled results of the gyroid structure with a linear gradient [dimensionless] of the normalised effective Young modules \bar{E} , a mean von Mises stress $\bar{\sigma}_{VM}$, and a maximum von Mises stress $\sigma_{VM,max}$, which is given for different porosities.

Porosity	\bar{E}	$\bar{\sigma}_{VM}$	$\sigma_{VM,max}$
from 0.4 to 0.5	0.06	0.97	14.99
0.6	0.04	1.02	18.94
0.7	0.03	1.07	22.82
0.8	0.02	1.11	28.01

Table 6. Scaled results of the gyroid structure with a quadratic gradient [dimensionless] of the normalised effective Young modules \bar{E} , a mean von Mises stress $\bar{\sigma}_{VM}$, and a maximum von Mises stress $\sigma_{VM,max}$, which is given for different porosities.

Porosity	\bar{E}	$\bar{\sigma}_{VM}$	$\sigma_{VM,max}$
from 0.4 to 0.5	0.06	0.99	15.07
0.6	0.04	1.05	18.75
0.7	0.02	1.11	23.86
0.8	0.02	1.16	29.64

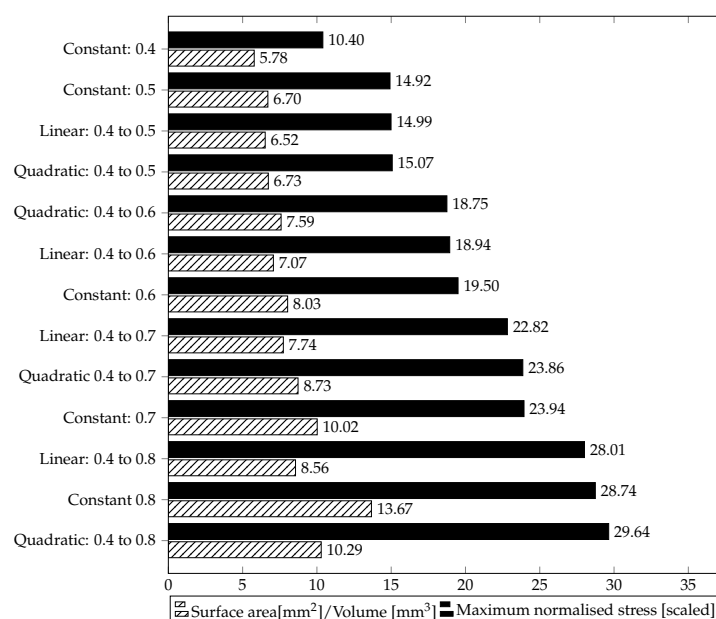


Figure 6. Dimensionless, scaled maximum normalised stress $\sigma_{VM,max}$ [scaled] of gyroid structures in ascending order, in comparison to the SA/V ratio of the same structure.

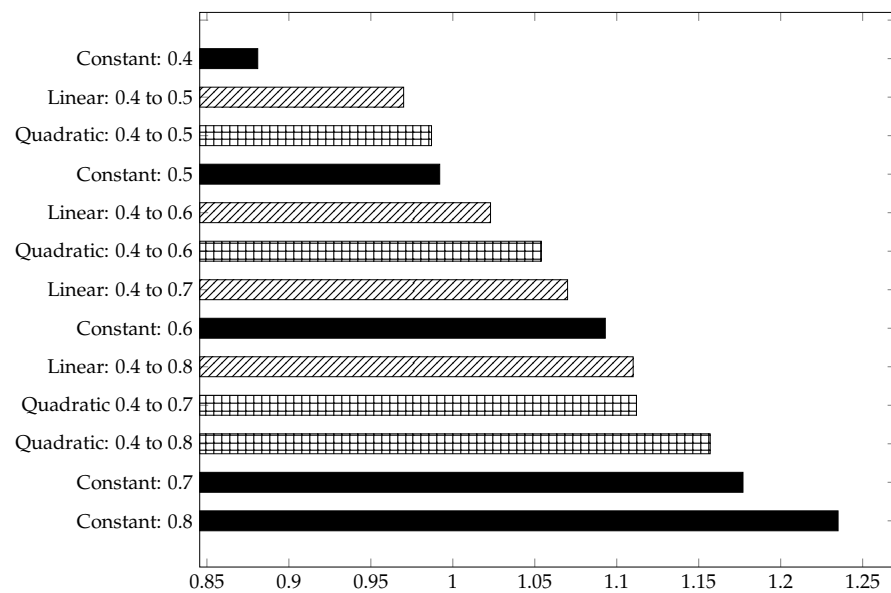


Figure 7. Dimensionless, scaled mean normalised stress $\bar{\sigma}_{VM}$ of gyroid structures in ascending order.

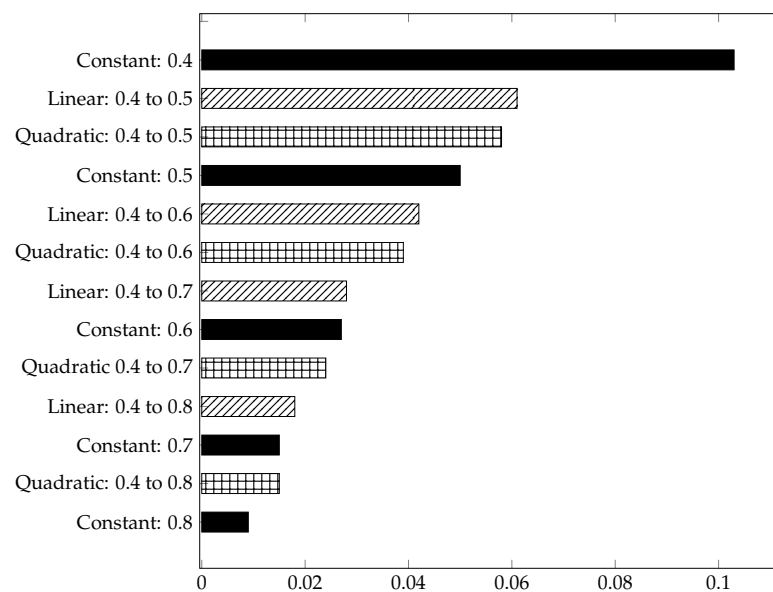


Figure 8. Dimensionless, scaled effective Young modulus \bar{E} of gyroid structures in decreasing order.

In Figure 6, the black bars represent the maximum normalised stresses ($\sigma_{VM,max}$) of the gyroid structures, sorted in ascending order. In addition, the corresponding SA/V ratio is shown in striped bars.

The gyroid structures with a quadratic porosity have the highest (quadratic: 0.4 to 0.8) and the gyroid structure with constant porosity has the lowest (constant: 0.4) maximum stresses, respectively. In addition, the bar graph illustrates that the linear gradient structures have lower scaled normalized maximum stresses than the quadratic gradient structures, but higher than the constant gradient structures. A structure with a linear porosity of 0.4 to 0.6 corresponds to an average of a constant porosity of 0.5. Here, it becomes clear that by adjusting the gradient, a higher SA/V ratio is achieved, but also higher maximum stresses. This observation also applies to the structure with a linear porosity from 0.4 to 0.8, which corresponds to an average porosity of 0.6.

As in Figure 6, the dimensionless, scaled, and normalised stresses [$\bar{\sigma}_{VM}$] of the structures are also sorted in ascending order in Figure 7. This allows for a faster comparison of the diagrams. The structural arrangements of the two diagrams are not in the same

order, since there is a deviation between the highest and the lowest values of the maximum normalised stress and the mean normalised stress.

Compared to the structures with quadratic or linear porosity, the structures with constant porosity have higher normalised stresses. The higher the porosity level of the structures, the higher the normalised stresses. This may indicate a more uniform stress distribution in the structures with gradients or that the structure has more unstressed regions. The gyroid structure 'quadratic: 0.4 to 0.8', for example, has a higher SA/V ratio than 'constant: 0.7', but a lower mean normalised stress.

The structures with a linear gradient generally exhibit the lowest mean stresses, compared to the other structures, which is also reflected in the scaled, dimensionless elastic modulus (see Figure 8).

The structures with a linear gradient have a higher effective Young modulus [\bar{E}] than the other structures in the same porosity range. This can be partly explained by the fact that the linear gradient structures are thickened more quickly and more evenly, which means that the initiating force can be better distributed. The Figure 8 lists the scaled and dimensionless effective Young modulus of the considered structures in decreasing order. It becomes clear that the porosity has a high influence on the effective Young modulus. Between the structures 'constant: 0.4' and 'constant: 0.8', for example, the effective Young modulus is reduced by a factor of about 11. In contrast, the effective Young modulus for the structures 'quadratic: 0.4 to 0.5' ('linear: 0.4 to 0.5') and 'quadratic: 0.4 to 0.8' ('linear: 0.4 to 0.8') decreases by a factor of 3.9 (quadratic) or 3.4 (linear). A clear relationship between the SV/A ratio and the effective Young modulus can be seen when comparing Figures 5 and 8. The sorted effective Young modulus is almost in the same order as the sorted SV/A ratio.

The evaluation of the von Mises stress field on the gyroid structures revealed that it is generally located at the rounded edges of the structure. It was noticed that the stress peaks for the gyroid structures with gradients are on the side with the highest porosity, due to the difference in porosity, while the stress peaks for the structures with constant porosity are on both sides, which can be seen in Figure 9. The stressed areas are marked in red and are located at the rounded edges, as described previously. Accordingly, the loaded edges are likely to fail first in compression tests. In addition, the one-sided loading of the structures with gradients would explain the higher stress distributions given in Figure 6.

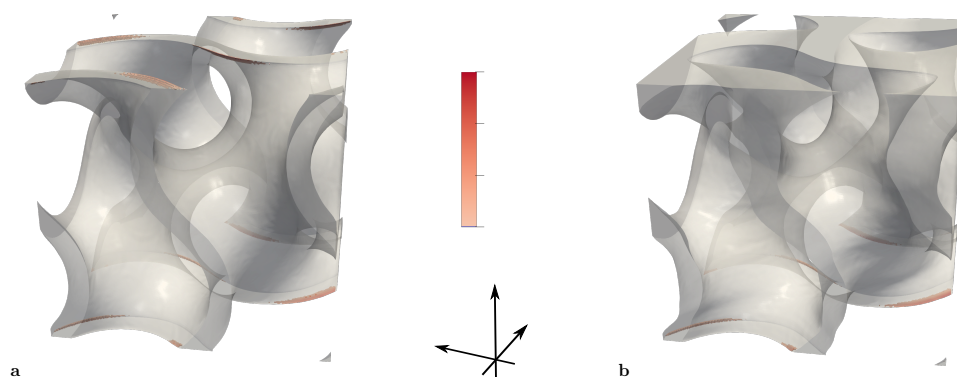


Figure 9. Maximum stresses on the surface of the gyroid structure with (a) a constant porosity of 0.8; (b) a quadratic porosity function between 0.4 and 0.8.

The mechanical simulation has shown that the structures with gradients enable new design and lightweight construction possibilities. The structures with gradients can be better adapted to the required properties. Depending on the choice of the new and the original structure, one property can be specifically improved, while another property can be reduced. In general, it can be said that the SA/V ratio increases with increasing porosity, while the effective Young modulus decreases. By choosing the structure 'linear: 0.4 to 0.5', for example, instead of 'constant: 0.5', the effective Young modulus increases by about 22% [quadratic gradient 16%], while the surface-to-SA/V ratio and the mean normalised stress would decrease by about 2% [quadratic about 0%].

If only the mechanical stability is of interest and not the lightweight potential or the surface area-to-volume ratio, the gyroid with the lowest porosity—in our case 0.4—is still unbeatable.

Likewise, the gyroid with a constant porosity of 0.8 would be interesting for applications where only the surface-to-volume ratio is of central importance, but not the mechanical properties.

4. Conclusions

In this study, gyroid structures, which are associated with the TPMS family, were investigated. In addition to the used structures with constant porosity, graded structures were produced. For the graded structures, a distinction was made between structures with linear and quadratic gradients. For the mechanical simulation, the created structures were imported into PACE3D. The results were converted into dimensionless, material-independent indices, so that a general statement could be made. In addition to the mechanical simulation, the SV/A ratio was also analysed.

The mechanical simulation shows that the introduction of the gradient multiplies the range of engineering design possibilities. Depending on the desired property and application, it is worthwhile to integrate a gradient into the structure. In general, it can be said that the structures with gradients usually have higher stress peaks, but lower mean normalised stresses.

For future applications, it would be interesting to create more gradient functions. One possibility, for example, would be to create a structure with a gradient which is thickened hourglass-like in terms of volume fraction, since the stress peaks all occur in the outer edge region. In addition, an experimental validation of the results would also be important, which is part of the ongoing work. The combination of experimental data and dimensionless indices will allow a tailor-made design for individual parts in the future.

Author Contributions: Conceptualization, B.N. and F.P.; Data Curation, P.A. and M.R.; Investigation, L.W.; Methodology, L.W.; Software, P.A. and M.R.; Supervision, B.N. and F.P.; Writing – original draft, L.W. All authors have read and agreed to the published version of the manuscript.

Funding: The paper was written as part of the project “InSeL—Innovative Schaumstrukturen für den effizienten Leichtbau” (Innovative foam structures for efficient lightweight construction), which is funded by the European Regional Development Fund (EFRE) and the state of Baden-Württemberg, as part of the Centre for Applied Research ZAFH. Furthermore, the authors would like to thank the Ministry of Science, Research, and Art Baden-Württemberg (MWK-BW) in the project MoMaF—Science Data Center, with funds from the state digitization strategy digital@bw (project number 57).

Institutional Review Board Statement: Not applicable.

Informed Consent Statement: Not applicable.

Data Availability Statement: Not applicable.

Acknowledgments: The authors thank Leon Geisen for his editorial support.

Conflicts of Interest: The authors declare no conflict of interest.

References

1. Michielsen, K.; Stavenga, D. Gyroid cuticular structures in butterfly wing scales: Biological photonic crystals. *J. R. Soc. Interface* **2008**, *5*, 85–94. [CrossRef] [PubMed]
2. Lai, M.; Kulak, A.N.; Law, D.; Zhang, Z.; Meldrum, F.C.; Riley, D.J. Profiting from nature: Macroporous copper with superior mechanical properties. *Chem. Commun.* **2007**, *34*, 3547–3549. [CrossRef] [PubMed]
3. Kladovasilakis, N.; Tsongas, K.; Tzetzis, D. Mechanical and FEA-Assisted Characterization of Fused Filament Fabricated Triply Periodic Minimal Surface Structures. *J. Compos. Sci.* **2021**, *5*, 58. [CrossRef]
4. Alketan, O.; Abu Al-Rub, R. Multifunctional mechanical-metamaterials based on triply periodic minimal surface lattices: A review. *Adv. Eng. Mater.* **2019**, *21*, 1900524. [CrossRef]
5. Li, W.; Yu, G.; Yu, Z. Bioinspired heat exchangers based on triply periodic minimal surfaces for supercritical CO₂ cycles. *Appl. Therm. Eng.* **2020**, *179*, 115686. [CrossRef]

6. Torquato, S.; Donev, A. Minimal surfaces and multifunctionality. *Proc. R. Soc. A Math. Phys. Eng. Sci.* **2004**, *460*, 1849–1856. [CrossRef]
7. Dong, Z.; Zhao, X. Application of TPMS structure in bone regeneration. *Eng. Regen.* **2021**, *2*, 154–162. engreg.2021.09.004. [CrossRef]
8. Li, D.; Liao, W.; Dai, N.; Xie, Y.M. Comparison of Mechanical Properties and Energy Absorption of Sheet-Based and Strut-Based Gyroid Cellular Structures with Graded Densities. *Materials* **2019**, *12*, 2183. [CrossRef]
9. Liu, F.; Mao, Z.; Zhang, P.; Zhang, D.Z.; Jiang, J.; Ma, Z. Functionally graded porous scaffolds in multiple patterns: New design method, physical and mechanical properties. *Mater. Des.* **2018**, *160*, 849–860. [CrossRef]
10. Jin, Y.; Kong, H.; Zhou, X.; Li, G.; Du, J. Design and Characterization of Sheet-Based Gyroid Porous Structures with Bioinspired Functional Gradients. *Materials* **2020**, *13*, 3844. [CrossRef]
11. Maskery, I.; Sturm, L.; Aremu, A.; Panesar, A.; Williams, C.; Tuck, C.; Wildman, R.; Ashcroft, I.; Hague, R. Insights into the mechanical properties of several triply periodic minimal surface lattice structures made by polymer additive manufacturing. *Polymer* **2018**, *152*, 62–71. SI: Advanced Polymers for 3DPrinting/Additive Manufacturing,
12. Maskery, I.; Aboulkhair, N.; Aremu, A.; Tuck, C.; Ashcroft, I. Compressive failure modes and energy absorption in additively manufactured double gyroid lattices. *Addit. Manuf.* **2017**, *16*, 24–29. [CrossRef]
13. Chen, Z.; Xie, Y.; Wu, X.; Wang, Z.; Li, Q.; Zhou, S. On hybrid cellular materials based on triply periodic minimal surfaces with extreme mechanical properties. *Mater. Des.* **2019**, *183*, 108109. [CrossRef]
14. Feng, J.; Liu, B.; Lin, Z.; Fu, J. Isotropic porous structure design methods based on triply periodic minimal surfaces. *Mater. Des.* **2021**, *210*, 110050. [CrossRef]
15. Zaharin, H.; Abdul-Rani, A.M.; Azam, F.; Ginta, T.; Sallih, N.; Ahmad, A.; Yunus, N.A.; Zulkifli, T.Z.A. Effect of Unit Cell Type and Pore Size on Porosity and Mechanical Behavior of Additively Manufactured Ti6Al4V Scaffolds. *Materials* **2018**, *11*, 2402. [CrossRef]
16. Gibson, L.J.; Ashby, M.F. *Cellular Solids: Structure and Properties*, 2nd ed.; Cambridge Solid State Science Series; Cambridge Univ. Press: Cambridge, UK, 1997. [CrossRef]
17. Zhu, H.; Hobdell, J.; Windle, A. Effects of cell irregularity on the elastic properties of open-cell foams. *Acta Mater.* **2000**, *48*, 4893–4900. [CrossRef]
18. Kaoua, S.A.; Boutaleb, S.; Dahmoun, D.; Azzaz, M. Numerical modelling of open-cell metal foam with Kelvin cell. *Comput. Appl. Math.* **2016**, *35*, 977–985. [CrossRef]
19. Gan, Y.; Chen, C.; Shen, Y. Three-dimensional modeling of the mechanical property of linearly elastic open cell foams. *Int. J. Solids Struct.* **2005**, *42*, 6628–6642. [CrossRef]
20. MATLAB. Version 9.6.0.1072779 (R2019a); The MathWorks Inc.: Natick, MA, USA, 2019.
21. Hötzer, J.; Reiter, A.; Hierl, H.; Steinmetz, P.; Selzer, M.; Nestler, B. The parallel multi-physics phase-field framework Pace3D. *J. Comput. Sci.* **2018**, *26*, 1–12. [CrossRef]
22. John, A.; John, M. Foam metal and honeycomb structures in numerical simulation. *Ann. Fac. Eng. Hunedoara* **2016**, *14*, 27–32.
23. Planinsic, G.; Vollmer, M. The surface-to-volume ratio in thermal physics: From cheese cube physics to animal metabolism. *Eur. J. Phys.* **2008**, *29*, 369. [CrossRef]
24. Ansys. Version 2021 R2; Ansys Inc.: Canonsburg, PA, USA, 2021.

Article

An Improved Particle-Swarm-Optimization Algorithm for a Prediction Model of Steel Slab Temperature

Ming Liu ^{1,2}, Peng Yan ³, Pengbo Liu ^{1,2}, Jinwei Qiao ^{1,2} and Zhi Yang ^{1,2,*}

¹ School of Mechanical & Automotive Engineering, Qilu University of Technology (Shandong Academy of Sciences), Jinan 250353, China

² Shandong Institute of Mechanical Design and Research, Jinan 250353, China

³ Key Laboratory of High-Efficiency and Clean Mechanical Manufacture, Ministry of Education, School of Mechanical Engineering, Shandong University, Jinan 250061, China

* Correspondence: yangzhi@qlu.edu.cn; Tel.: +86-13066769976

Abstract: Aiming at the problem of the low accuracy of temperature prediction, a mathematical model for predicting the temperature of a steel billet is developed. For the process of temperature prediction, an improved particle-swarm-optimization algorithm (called XPSO) is developed. XPSO was designed based on a multiple swarm scheme to improve the global search capability and robustness; thus, it can improve the low accuracy of prediction and overcome the problem of easy entrapment into local optima. In the XPSO, the multiple swarm scheme comprises four modified components: (1) the strategy of improving the positional initialization; (2) the mutation strategy for particle swarms; (3) the adjustment strategy of inertia weights; (4) the strategy of jumping out local optima. Based on widely used unimodal, multimodal and composite benchmark functions, the effectiveness of the XPSO algorithm was verified by comparing it with some popular variant PSO algorithms (PSO, IPSO, IPSO2, HPSO, CPSO). Then, the XPSO was applied to predict the temperatures of steel billets based on simulation data sets and measured data sets. Finally, the obtained results show that the XPSO is more accurate than other PSO algorithms and other optimization approaches (WOA, IA, GWO, DE, ABC) for temperature prediction of steel billets.

Keywords: optimization; particle swarm optimization algorithm; reheating furnace; temperature prediction

Citation: Liu, M.; Yan, P.; Liu, P.; Qiao, J.; Yang, Z. An Improved Particle-Swarm-Optimization Algorithm for a Prediction Model of Steel Slab Temperature. *Appl. Sci.* **2022**, *12*, 11550. <https://doi.org/10.3390/app122211550>

Academic Editors: Shuwen Wen, Yongle Sun and Xin Chen

Received: 10 September 2022

Accepted: 6 November 2022

Published: 14 November 2022

Publisher's Note: MDPI stays neutral with regard to jurisdictional claims in published maps and institutional affiliations.



Copyright: © 2022 by the authors. Licensee MDPI, Basel, Switzerland. This article is an open access article distributed under the terms and conditions of the Creative Commons Attribution (CC BY) license (<https://creativecommons.org/licenses/by/4.0/>).

1. Introduction

In the steel industry, the reheating furnace must reheat the material (slabs) to the desired uniformity temperature profiles at the exit. However, the slab reheating furnace's operation is a complex physical and chemical process [1]. To better control and optimize the furnace's operations, there should be a suitable temperature prediction model to predict the accurate temperatures for the slabs inside the furnace. Given the continuous development of artificial intelligence techniques, the demand for a suitable temperature prediction model is increasing [2]. Therefore, a suitable mathematical model which can predict the discharge temperatures of billets accurately and quickly should be proposed for the control and optimization of the reheating furnaces. In general, the prediction models can be divided into two categories [3]: the mechanism models based on first principles [4] and the empirical models based on the production data and black-box approaches [5]. The first kind of model needs to fully understand the physical and chemical processes inside the reheating furnace—e.g., [1,6–8]. The computational requirements of these models vary widely depending on the level of complexity [3]. Finally, the heat-transfer process is often summarized by partial differential equations (PDEs). Usually, mechanism models are complicated and nonlinear (such as those in [9–14]). Hong et al. [13] investigated the sequential function specification coupled with the Broyden combined method (BC-SFSM) to obtain the temperature field of a steel billet based on the inverse heat-conduction problem. The results

illustrate that the majority of relative errors during the whole reheating time are less than 5%. Chen et al. [14] presented a novel method to obtain these parameters by combining a "black box" test with a billet heat transfer model. The surface temperature and center temperature's relative error were 2.34% and 3.51%, respectively. The numerical computation of PDEs will require a lot of computational time, which will exceed a practical time criterion. Therefore, this kind of model cannot satisfy the requirements for an online system.

The empirical models are often determined by identification methods involving the genetic algorithm (GA), support vector machines (SVMs), neural networks (NNs), particle swarm optimization (PSO) and other intelligent techniques ([15–18]). For instance, Thanawat et al. [19] investigated a prediction model using the production data from Ratchasima Steel Products Company. The GA method was used to identify the model's unknown factors. Tang et al. [20] presented the SVM predictive model for the temperature control problem. The PSO was applied to determine proper parameters for the SVM model and finally obtained good performance. Wang et al. [21] constructed a prediction model of slab discharging temperature by combining GA with a BP neural network. The mean-square error of the network was 72.3477, and the error was lower than 20 °C. Yang et al. [22] used the relevance vector machine (RVM) method to predict the slab temperature. The maximum prediction error of slab temperature was 10.46 °C. In general, the empirical model is often simplified to a simple formula, so the calculation time is small enough to satisfy online production [23]. The production data and the performance of the intelligent algorithm used will determine the advantages and disadvantages of an empirical model. As the industrial software and database techniques continue developing, more production data are being obtained [24]. Thus, an intelligent algorithm with excellent performance is indispensable, and it behooves us to study the intelligent algorithms carefully.

The PSO algorithm has the characteristics of high solution accuracy and a fast approach to the optimal solution. However, the basic PSO varies in its ability to solve problems in different application contexts. It also easily falls into local optima. Researchers have studied various strategies for the improvement of PSO. For instance, Alsaidy et al. [25] proposed the longest job to fastest processor PSO (LJFP-PSO) algorithm and the minimum completion time PSO (MCT-PSO) algorithm for the task-scheduling problem. The effective performance of the two algorithms was proved by simulation results. Yue et al. [26] presented a novel multi-objective PSO that has ring topology for solving multimodal multi-objective optimization problems. The ring topology is used to form stable niches and locate multiple optima. Peng et al. [27] proposed a symbiotic PSO (SPSO) algorithm to control a water-bath-temperature system. A multiple swarm scheme was proposed for the SPSO algorithm. Three major components (create initial swarms, evaluating fitness values and updating each particle) are used to escape from a locally optimal solution.

Inspired by these algorithms, we propose an improved PSO (named XPSO) algorithm that uses the multiple swarm scheme in this paper. The scheme comprises four modified components: (1) improving the positional initialization of the particle swarms: one randomly generated and the other uniformly generated; (2) adding the mutation strategy for the particle swarm to increase its population diversity; (3) adjusting the inertia weight through a "stepped" adaptive model; (4) adding the strategy of escaping from the local minimized point.

This paper is presented as follows: the prediction model of the slab temperature is established in Section 2; the detailed strategies for improvement of XPSO are described in Section 3; the simulation and discussion are given in Section 4; Section 5 summarizes the conclusions.

2. The Prediction Model of the Slab Temperature

2.1. The Structure of a Reheating Furnace

The heat transfer processes in the furnace mainly consist of radiation heat transfer and convection heat exchange. The main function of reheating furnaces is to help the slabs reach the desired discharging temperatures for the next rolling process. The slab passes

through the preheating zone, multistage heating zone and soaking zone from the furnace's inlet to the outlet, as shown in Figure 1. The multi-stage heating zone can be divided into four subzones (upper zones 1 and 2; bottom zones 4 and 5), and the soaking zone is divided into two subzones (upper zone 3, bottom zone 6). The key components of a subzone are a series of regenerative burners, the corresponding furnace nozzle temperatures TN_j and the furnace zone temperature TP_k . Here, TN_j is easily obtained by the thermocouples nearby the location of burner's nozzle j and $TP_k = \frac{1}{n} \sum_{j=1}^n TN_j$, which stands for the average value of the nozzle temperatures TN_j in zone k .

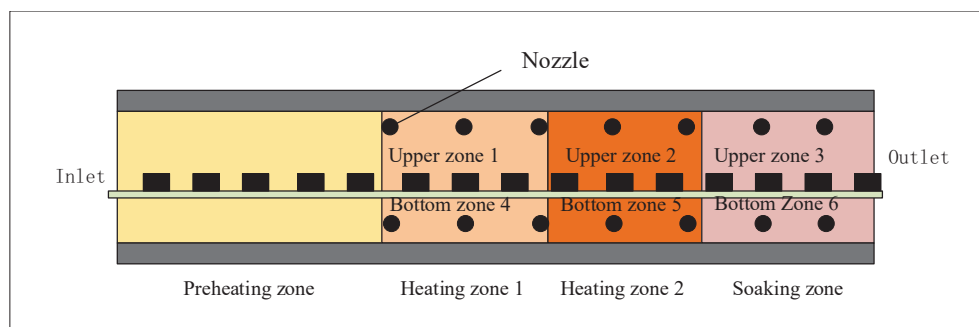


Figure 1. Schematic diagram of a heating furnace's structure.

2.2. The Prediction Model and Optimization Problem

The most important quality criterion of reheating furnace is the average outlet temperature of the steel slab. There are many factors affecting the slab's discharging temperature. By analyzing the field data and some related research ([22,23]), we can confirm some key factors: the initial temperature of the billet, T_0 ; the furnace nozzle temperature, T_j ; the mean temperature of each zone, T_p ; the reheating time of the billet in the furnace, θ ; the material of the slab, α ; the thickness of the slab, d . Thus, the inputs of the prediction model are $X = [X_1, X_2, X_3]^T$, which consist of the slab's physical parameters, $X_1 = [\alpha, d, \theta, T_0]^T$; the vector of the furnace nozzle temperatures, $X_2 = [TN_1, TN_2, \dots, TN_m]^T$; and the vector of furnace zone temperatures, $X_3 = [TP_1, TP_2, \dots, TP_6]^T$. Notice, m is the total number of burners in the reheating furnace. The outputs are the predicted temperature $Y = TE$, which is the vector of the predicted temperatures of the slabs when discharged out from the furnace. Finally, the formula of predicting model is constructed as:

$$Y = f(X, W) = w_0 d + w_1 \alpha + w_2 T_0^1 + w_3 T_0^2 + \sum_{i=1}^m TN_i w_{(i+3)} TN_i + \sum_{j=1}^6 w_{(j+m+3)} \cos(TP_j \theta) + \sum_{j=1}^6 w_{(j+m+9)} \sin(TP_j \theta) \quad (1)$$

where $W = [w_0, w_1, \dots, w_{m+15}]$ represents the vector of unknown weight parameters, which will be determined by the proposed XPSO algorithm. The formula f is composed of a polynomial and a Fourier function, which was designed by the author based on experience. To make the analytical response Y equal to the measured value Y^* , an optimization problem should be established with the objective of minimizing the error between the theoretically calculated values and the measured data. To alleviate overfitting and improve generalization performance, the strategy of regularization is employed for the optimization problem. Finally, the formula of the optimization problem is shown as follows.

$$\begin{aligned} \text{Minimize } J &= \|Y - Y^*\|^2 + \lambda_1 \|W\| + \lambda_2 \|W\|^2 \\ \text{st. } Y &= f(X, W) \end{aligned} \quad (2)$$

where Y^* represents the measured temperature of the slab, and λ_1, λ_2 are the regularization parameters.

3. Improved Particle-Swarm-Optimization Algorithm

3.1. The Basic PSO Algorithm

The PSO algorithm originates from a researcher observing the social behavior of a flock of birds or fish [28]. Each particle in the population is a potential solution to the objective function. The particle has two attributes: velocity $V_i = [v_{i1}, v_{i2}, \dots, v_{ij}, \dots, v_{ND}]$ and position $X_i = [x_{i1}, x_{i2}, \dots, x_{ij}, \dots, x_{ND}]$, where $i = 1, 2, \dots, N$ — N is the size of particle swarm; and $j = 1, 2, \dots, D$ — D is the dimension of the solution space.

In each iteration, the information of individual particle is filtered to find the information about the historically optimal position p of the individual and the historically optimal position g of the population. The known information is brought into the velocity updating equation, Equation (3), and the position updating equation, Equation (4), to adjust the search direction of the population, so that the particle swarm approaches the global optimal solution, which is the optimal position of the population.

$$v_{ij}(k+1) = wv_{ij}(k) + r_1c_1(p_i - x_{ij}(k)) + r_2c_2(g - x_{ij}(k)) \quad (3)$$

$$x_{ij}(k+1) = x_{ij}(k) + v_{ij}(k+1) \quad (4)$$

where w represents the inertia weight; $r_1, r_2 \in [0, 1]$ are two uniformly distributed random values; c_1, c_2 are the acceleration parameters, which are non-negative constants; k represents the current iteration; and $k = 1, 2, 3, \dots, G$, where G is the maximum number of iterations. The velocity updating of the particle is influenced by three factors: the current moment particle velocity $V_{ij}(k)$, the particle's self-experience ΔV_p and the experience of particle swarm ΔV_g . ΔV_p is the part of the particle that learns from its historical information, and ΔV_g represents the part of the particle that learns from the historical information of other particles within the population.

3.2. Improvement Strategies of the XPSO Algorithm

The basic PSO algorithm is a non-globally-convergent optimization algorithm [29]. To reduce the premature probability of falling into a local optimal solution and improve the convergence speed of the basic PSO, an improved PSO (named XPSO) algorithm is proposed based on the multi-strategy co-evolutionary approach. Four specific improvements are described as follows.

1. Improving the positional initialization of the particle swarm: one randomly generated and the other uniformly generated.

In a basic PSO algorithm, all of the particles are randomly initialized. The expression is given as follows:

$$X_{ND} = \begin{bmatrix} lx_{11} & x_{12} & \cdots & x_{1D} \\ x_{21} & x_{22} & \cdots & x_{2D} \\ \vdots & \vdots & \ddots & \vdots \\ x_{N1} & x_{N2} & \cdots & x_{ND} \end{bmatrix} \quad (5)$$

An increase in the positional diversity of particle swarms can facilitate the exploration of global range. However, increasing the diversity of particle swarms also makes it difficult to converge to the global optimum every time. Hence, an improved approach, based on the “double-edged sword” nature of particle swarm's diversity, is proposed to improve the algorithm's stability. During the initialization of the particle swarm, a dimension called X-Dim in the position matrix is randomly selected. The positional information of the particle in X-Dim is generated according to a uniform distribution, as shown in Equation (6).

$$x_{ij} = \frac{O_{\max} - O_{\min}}{N} * i \quad (6)$$

where j is the randomly selected dimension; and O_{\max} and O_{\min} are the upper and lower limits of the value range of independent variables in different dimensions, respectively.

2. The mutation strategy is introduced into the position updating of particle swarm to compensate for the decline in the overall diversity of particle swarm after improved initialization.

Unlike some other meta-heuristic algorithms, standard PSO has no evolution operators such as crossover or mutation. The mutation strategy will be implemented by screening the particles in each iteration. If the corresponding fitness function value of someone particle is lower than the average fitness function value, the mutation strategy is performed in the current iteration. The formula of positional mutation is:

$$x_{ij}^*(k) = x_{ij}(k) - wv_{ij}(k) - w(g - p_i) \quad (7)$$

where x^* denotes the position of the particle after mutation.

3. The adjustment of inertia weight is given to improve the flexibility of particle flight speed change, and the idea of “stepped” adaptive change is injected into the updating of inertia weight.

Inertia weight w is directly related to the convergence speed. Most researches use the subtraction function as its updating formula for inertia weight [30]. Some others use the “stepped” improvement method to update the inertia weight [31]. In our method, the inertia weight is adjusted by combining the strategy of decreasing function and the “stepped” improvement. The specific change is given as follows:

- A “three-step” strategy is proposed to switch the range $[w_s, w_e]$ of inertia weight by determining the fitness function value of the best position so far. The switching formula is given as follows:

$$[w_s, w_e] = \begin{cases} [w_{s1}, w_{e1}] & f(g) \gg \text{Fitness1} \\ [w_{s2}, w_{e2}] & \text{Fitness2} < f(g) < \text{Fitness1} \\ [w_{s3}, w_{e3}] & f(g) \ll \text{Fitness2} \end{cases} \quad (8)$$

where $[w_s, w_e]$ is the range of inertia weight; $f(g)$ is the fitness function value corresponding to the global optimal solution; *Fitness1* and *Fitness2* are the autonomous set values. The values of $([w_{s1}, w_{e1}], [w_{s2}, w_{e2}]$ and $[w_{s3}, w_{e3}])$ need to be adjusted according to the conditions of the objective function in different application contexts.

- After the ranges of the inertia weight $[w_s, w_e]$ have been determined, a decreasing function is introduced to adjust the w . The switching condition is related to the fitness function value of the best position so far. The update formula is given as follows:

$$w = \begin{cases} \frac{r \sin(w_s \pi)}{4}, & f(g) \gg \text{Fitness3} \\ w_s - (w_s - w_e) \sqrt{\frac{k}{G}}, & f(g) < \text{Fitness3} \end{cases} \quad (9)$$

where $r \in [0, 4)$ is a uniformly distributed random number; and w_s and w_e are the initial and final values of the range $[w_s, w_e]$ of the inertia weight, respectively. *Fitness3* is the autonomous set value, k is the current iteration and G is the maximum iterations.

4. The strategy of jumping out local optimum is proposed.

A slope parameter tr is given to judge whether the particle swarm has fallen in the local optimum. Here, tr is the count of the condition when *Slope* is less than the value ε in five iterations. The slope is calculated as follows:

$$\text{Slope} = \frac{(f_k(g) - f_{(k-5)}(g))}{5} \quad (10)$$

If the value of tr equals the value of s , which is an autonomous set value, the particle swarm is trapped in a local optimum. Then, the particle swarm will perform a

“jumping out local optimum” operation, which is done to change its position. The specific formula of a particle jumping out of a local optimum is given as follows:

$$x_{ij}(k) = x_{ij}(k) - r_1 c_1 (g - x_{ij}(k)) + r_2 c_2 (bad - x_{ij}(k)) \quad (11)$$

where *bad* represents the information of the global worst position. The core of this strategy is that the particle swarm should be nearest to the global worst position while staying away from the local optimum.

Finally, the pseudo-code of the XPSO algorithm is demonstrated in Algorithm 1.

Algorithm 1: The pseudo-code of the XPSO algorithm

```

1: Initialize the parameters: (N, G, D,  $O_{max}, O_{min}, V_{max}, V_{min}, t, s, \varepsilon$ )
2: Combine uniform and random distribution to initialize position matrix  $X_{N \times D}$ 
3: Generate the initial velocity  $V_i$  of each particle randomly
4: Evaluate the fitness value of each particle
5: Set  $p_i$  with a copy of  $X_i$ 
6: Initialize g and bad with the best and worst fitness value among population
7: While  $k < G$ 
8:   If  $k \geq 6$ 
9:     Update the slope of the fitness function curve
10:    Slope =  $(f(g)_k - f(g)_{k-5})/5$ 
11:    If Slope  $\leq \varepsilon$ 
12:       $t = t + 1$ 
13:    End If
14:  End If
15:  Update inertia weight  $\omega$  by Equations (8) and (9)
16:  For  $i = 1 : N$ 
17:    Update the velocity  $V_i$ 
18:     $v_{ij}(k+1) = \omega v_{ij}(k) + r_1 c_1 (p_i - x_{ij}(k)) + r_2 c_2 (g - x_{ij}(k))$ 
19:    Update the velocity  $X_i$ 
20:    If  $t = s$ 
21:      For  $m = 1 : 50$ 
22:         $x_{ij}(k) = x_{ij}(k) - r_1 c_1 (g - x_{ij}(k)) + r_2 c_2 (bad - x_{ij}(k))$ 
23:      End For
24:    Else
25:       $x_{ij}(k+1) = x_{ij}(k) + v_{ij}(k+1)$ 
26:    End If
27:    Calculate the fitness values of the new particle  $X_i$ 
28:    Execute position mutation
29:     $x_{ij}^*(k) = x_{ij}(k) - \omega v_{ij}(k) - \omega (g - p_i)$ 
30:    Calculate the fitness values of the new particle  $X^*$ 
31:    If  $X_i$  or  $X^*$  is better than  $p_i$ 
32:      Update  $p_i$ 
33:    End If
34:    If  $X_i$  or  $X^*$  is better than g
35:      Update g
36:    End If
37:    If  $X_i$  or  $X^*$  is worse than bad
38:      Update bad
39:    End If
40:  End For
41:   $k = k + 1$ 
42: End While

```

4. Simulations and Discussion

To verify the performance of the XPSO algorithm, some simulations are designed to involve both the performance and application of the algorithm. To obtain an unbiased CPU time comparison, all simulations were programmed by MATLAB R2017b and implemented on a computer with an Intel i5-11400F GPU, 2.60 GHz, 16 GB RAM.

4.1. Validation of XPSO by Benchmark Test Functions

The XPSO algorithm is compared with some popular variant PSO algorithms (PSO [32], IPSO [33], IPSO2 [30], HPSO [34], CPSO [35]) on a series of widely used optimization benchmark functions. A set of benchmark functions were selected from papers ([36,37]).

The benchmark set consisted of three main groups of benchmark functions: 4 unimodal (UM) functions, 2 multimodal (MM) functions and 3 composition (CM) functions. The UM functions (f1–f4) with a unique global best can expose the intensification capacities of different algorithms. The MM functions (f5–f6) can expose the diversification of algorithms. The CM functions (f7–f9) were selected from the IEEE CEC 2005 competition [37], which are also utilized in many papers to test the performances (balancing the exploration and exploitation inclinations and escaping from local optima) of algorithms.

The mathematical formulation and characteristics of UM and MM functions are shown in Table 1. Details of the CM functions are shown in Table 2. The parameters of both the PSO algorithms and the optimization problem (2) were as follows. The specific parameter combinations for the inertia weight were $[w_{s1}, w_{e1}] = [0.9, 0.4]$, $[w_{s2}, w_{e2}] = [0.65, 0]$ and $[w_{s3}, w_{e3}] = [0.55, 0.05]$. The maximum and minimum velocities of the particle were $V_{max} = 0.1$ and $V_{min} = -0.1$, respectively. In addition, the acceleration coefficients c_1 and c_2 were selected to be 2.5 and 1.5, respectively. The inertia weight of the HPSO varied randomly in the range (0, 1). The parameters related to jumping out of local optimal were $s = 270$ and $\varepsilon = 0.001$. The values of the regularization parameters in the optimization problem were $\lambda_1 = 1.2$, $\lambda_2 = 1.0$.

Table 1. Descriptions of unimodal and multimodal benchmark functions.

Function	Name	Function's Expressions	Search Range	Global opt. ¹
f1	Sphere	$f_1 = \sum_{i=1}^n x_i^2$	$[-100, 100]^n$	0
f2	Schwefel's 1.2	$f_2 = \sum_{i=1}^n \sum_{j=1}^i x_j^2$	$[-100, 100]^n$	0
f3	Schwefel's 2.21	$f_3 = \max\{ x_i , 1 \leq i \leq n\}$	$[-100, 100]^n$	0
f4	Quartic Noise	$f_4 = \sum_{i=1}^n ix_i^4 + \text{random}[0.1]$	$[-1.28, 1.28]^n$	0
f5	Generalized Rastrigin	$f_5 = \sum_{i=1}^n [x_i^2 - 10 \cos(2\pi x_i) + 10]$	$[-5.12, 5.12]^n$	0
f6	Generalized Penalized Function 2	$f_6 = 0.1 \sin^2(3\pi x_1) + 0.1 \sum_{i=1}^n (x_i - 1)^2 [1 + \sin^2(3\pi x_i + 1)] + 0.1(x_n - 1)^2 [1 + \sin^2(2\pi x_n)] + \sum_{i=1}^n u(x_i, 5, 100, 4)$	$[-50, 50]^n$	0

¹ Global opt.: global optimal solution.

The maximum number of iterations for all benchmark functions (f1–f9) was selected as 8000. The dimensions of these benchmark functions (f1–f9) were selected as 10, 30 and 50. Thus, the performances of the six variant PSO algorithms can be compared in different dimensions.

Each algorithm was run individually 10 times, and the average statistical error was calculated. The mean of objective values (Mean) and standard deviation of its solving error (S.D.) were chosen as the performance measures for each algorithm. The simulation results are shown in Table 3 and Figures 2–10. Table 3 shows best values in bold.

Table 2. Details of hybrid composition functions.

Function (CEC2005-ID)	Description	Properties	Range	Global opt.
f7(C16)	Rotated Hybrid Composition Function	MM ¹ , R ² , NS ³ , S ⁴	$[-5, 5]^n$	120
f8(C18)	Rotated Hybrid Composition Function	MM, R, NS, S	$[-5, 5]^n$	10
f9(C21)	Rotated Hybrid Composition Function	MM, R, NS, S	$[-5, 5]^n$	360

¹ MM: Multi-modal, ² R: Rotated, ³ NS: Non-Separable, ⁴ S: Scalable.**Table 3.** Results of benchmark functions (Dim = 10, 30, 50).

F ¹	D ²	XPSO		CPSO		IPSO		IPSO2		PSO		HPSO	
		Mean ³	S.D. ⁴	Mean	S.D.	Mean	S.D.	Mean	S.D.	Mean	S.D.	Mean	S.D.
f1	10	1.29×10^{-102}	2.89×10^{-102}	3.42×10^2	2.07×10^2	5.81×10^{-8}	2.39×10^{-8}	1.07×10^{-3}	2.38×10^{-4}	7.95×10^{-9}	1.63×10^{-8}	2.33×10^{-8}	6.15×10^{-8}
	30	6.41×10^{-57}	1.92×10^{-56}	4.40×10^2	2.25×10^2	4.15×10^{-6}	1.22×10^{-6}	0.31	0.41	7.51×10^{-6}	4.04×10^{-6}	4.22×10^{-7}	2.57×10^{-7}
	50	1.59×10^{-8}	3.89×10^{-8}	4.57×10^2	2.80×10^2	1.93×10^{-5}	5.87×10^{-6}	6.73	13.42	2.00×10^{-5}	1.30×10^{-5}	1.02×10^{-6}	3.08×10^{-7}
f2	10	1.06×10^{-77}	1.50×10^{-77}	1.06×10^3	8.87×10^2	5.93×10^{-7}	3.33×10^{-7}	2.95×10^2	3.70×10^2	4.08×10^{-7}	4.74×10^{-7}	1.35×10^{-8}	1.71×10^{-8}
	30	8.67×10^{-12}	1.23×10^{-11}	4.36×10^3	1.95×10^3	1.44×10^{-3}	4.36×10^{-4}	9.07×10^2	8.11×10^2	5.74×10^{-3}	2.33×10^{-3}	3.11×10^{-5}	1.98×10^{-5}
	50	1.36×10^{-5}	1.35×10^{-2}	7.74×10^3	6.45×10^3	1.88×10^{-2}	3.33×10^{-3}	1.25×10^3	2.74×10^3	2.49×10^{-2}	9.20×10^{-3}	1.91×10^{-4}	8.34×10^{-5}
f3	10	1.11×10^{-21}	1.91×10^{-21}	4.59	1.13	2.70×10^{-4}	1.47×10^{-4}	6.41×10^{-2}	7.51×10^{-2}	4.45×10^{-4}	2.61×10^{-4}	8.41×10^{-4}	7.47×10^{-4}
	30	1.03×10^{-19}	1.79×10^{-19}	6.15	1.65	9.01×10^{-3}	2.77×10^{-3}	0.71	0.16	3.03×10^{-2}	1.62×10^{-2}	1.96×10^{-2}	1.99×10^{-2}
	50	6.84×10^{-5}	1.37×10^{-4}	4.87	0.65	0.23	0.22	5.76	0.41	0.36	0.33	0.13	0.11
f4	10	0.24	0.16	0.43	0.26	0.44	0.26	0.46	0.32	0.61	0.24	0.5	0.29
	30	0.27	0.2	0.58	0.28	0.53	0.32	0.35	0.3	0.64	0.31	0.52	0.18
	50	0.35	0.24	0.65	0.3	0.54	0.31	0.38	0.23	0.53	0.23	0.58	0.3
f5	10	12.93	3.98	12.08	4.46	10.45	4.43	9.3	3.4	10.94	4.09	9.83	4.16
	30	18.05	4.16	48.43	17.81	26.96	6.91	24.81	6.5	27.16	9.67	28.56	6.13
	50	20.9	2.54	67.23	18.56	38.51	11.94	34.18	4.93	39.99	14.36	33.73	10.42
f6	10	1.45	0.94	9.41	4.09	2.13	1.37	2.62	2.47	2.81	3.26	1.48	1.46
	30	5.08	3.56	25.39	5.56	14.51	8.42	22.09	5.69	9.49	5.42	6.59	6.24
	50	9.83	6.98	37.21	7.54	24.36	9.83	31.42	8.14	14.71	8.78	9.29	8.89
f7	10	196.35	26.50	502.96	179.38	381.96	94.03	731.48	80.86	362.11	36.18	428.34	59.63
	30	542.93	46.56	867.86	204.51	584.27	122.68	1223.15	110.51	505.28	80.91	623.86	90.26
	50	563.92	97.82	937.18	241.44	593.34	132.26	1378.35	129.68	599.16	106.17	651.98	126.37
f8	10	1090.72	41.53	1364.68	23.43	1135.18	22.51	1492.86	39.30	1136.88	65.80	1098.15	59.30
	30	1147.03	123.61	1408.69	50.61	1182.64	70.86	1561.77	56.23	1194.76	120.68	1287.80	84.09
	50	1167.73	134.83	1486.24	56.47	1202.59	132.75	1620.53	70.99	1249.79	131.05	1464.34	151.77
f9	10	1066.48	28.84	1387.39	19.11	1120.63	38.33	1538.21	9.21	1286.09	23.52	1287.69	39.38
	30	1291.78	38.31	1440.31	31.75	1319.86	43.93	1604.27	41.32	1303.97	30.27	1309.14	52.25
	50	1316.15	54.37	1485.75	41.98	1338.22	68.71	1633.61	82.42	1326.48	43.43	1524.77	68.02

¹ F: Function, ² D: dimensional, ³ Mean: mean of objective values, ⁴ S.D.: standard deviation.

According to Table 3, the XPSO algorithm is superior to other PSO algorithms in terms of solution accuracy. Considering the UM benchmark functions, the results of (f1–f3) solved by XPSO are better than those of the other algorithms. For f4, the best value of Mean was obtained by the XPSO algorithm for the (10, 30, 50)-dimensional cases. The best values of S.D for the (10, 30, 50)-dimensional cases were obtained by XPSO, HPSO and IPSO2. Except f5 in the 10-dimensional case and f6 in the 50-dimensional case, the results for the MM benchmark functions by XPSO are superior to those of the other algorithms. Based on values of the Mean of hybrid CM functions (f7–f9) in Table 3, high-quality solutions can be obtained by the XPSO algorithm.

The convergence curves of the mean of best function were plotted in Figures 2–10 to enable clearer visualization of each algorithm's performance. In Figures 2–10, the XPSO algorithm does not show outstanding performance in the early stage of the solution, but its search capability is better in the late stage of the solution, and it can significantly improve the convergence speed in the late evolution. The reason is that the updating strategy of inertia weight includes the formula based on chaotic mapping; consequently, the global search has a high convergence speed for particles. In addition, the updating formula for inertia weight switched in local search, which resulted a slow flying speed of particles but improved the accuracy of the solution. Finally, it can be concluded that the XPSO algorithm has excellent performance in numerical optimization problems and can be used to solve problems in various application contexts.

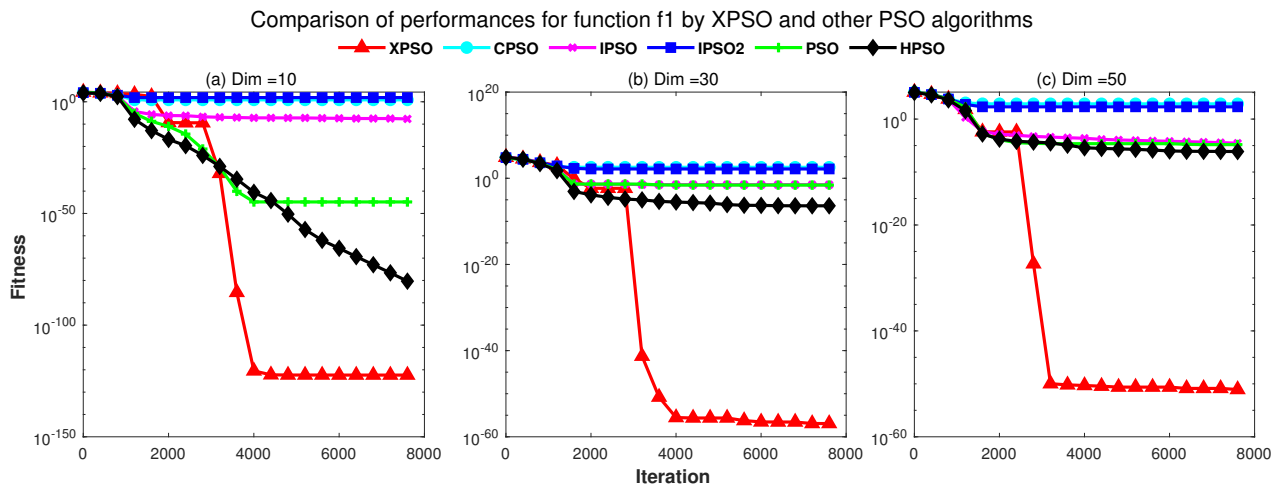


Figure 2. Comparison of performances on f1 by XPSO and other PSO algorithms.

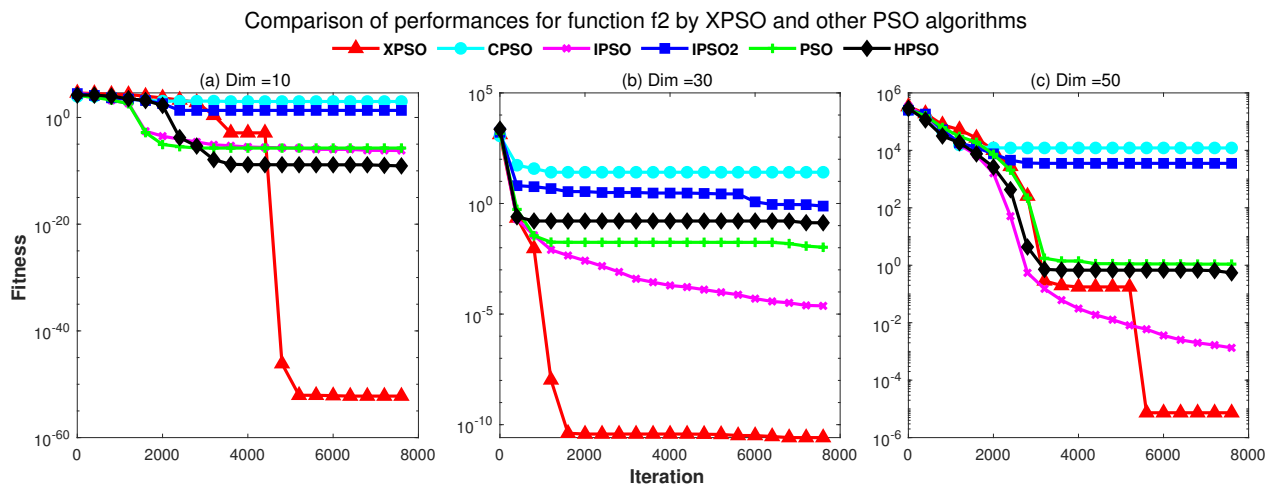


Figure 3. Comparison of performances on f2 by XPSO and other PSO algorithms.

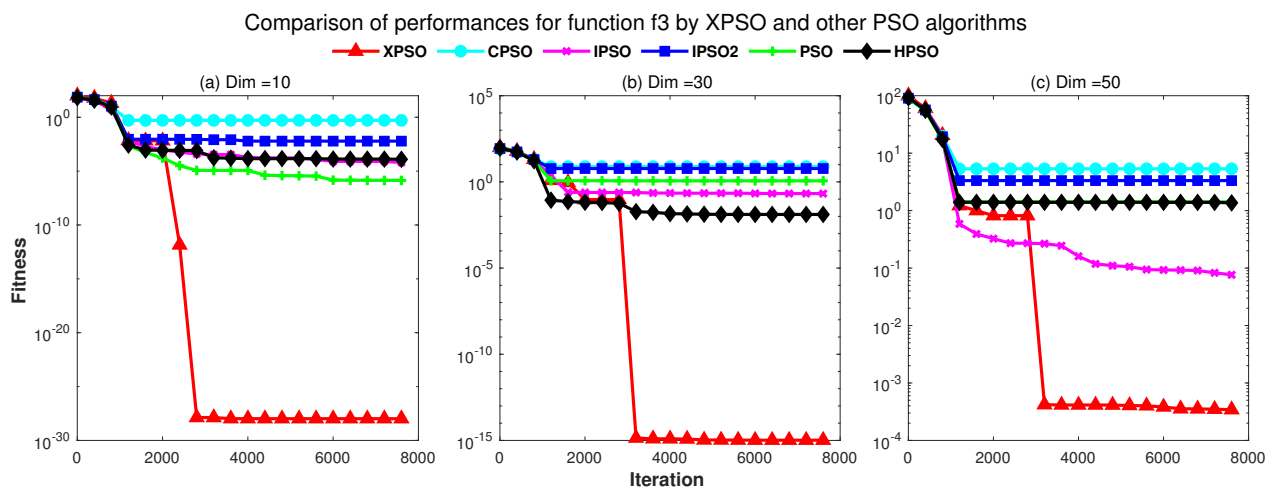


Figure 4. Comparison of performances on f3 by XPSO and other PSO algorithms.

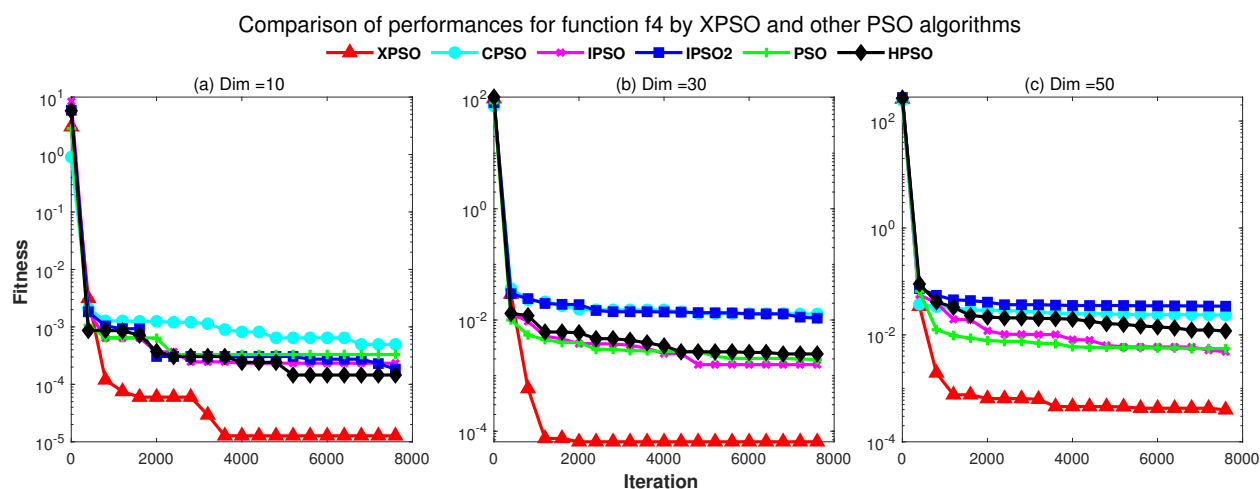


Figure 5. Comparison of performances on f4 by XPSO and other PSO algorithms.

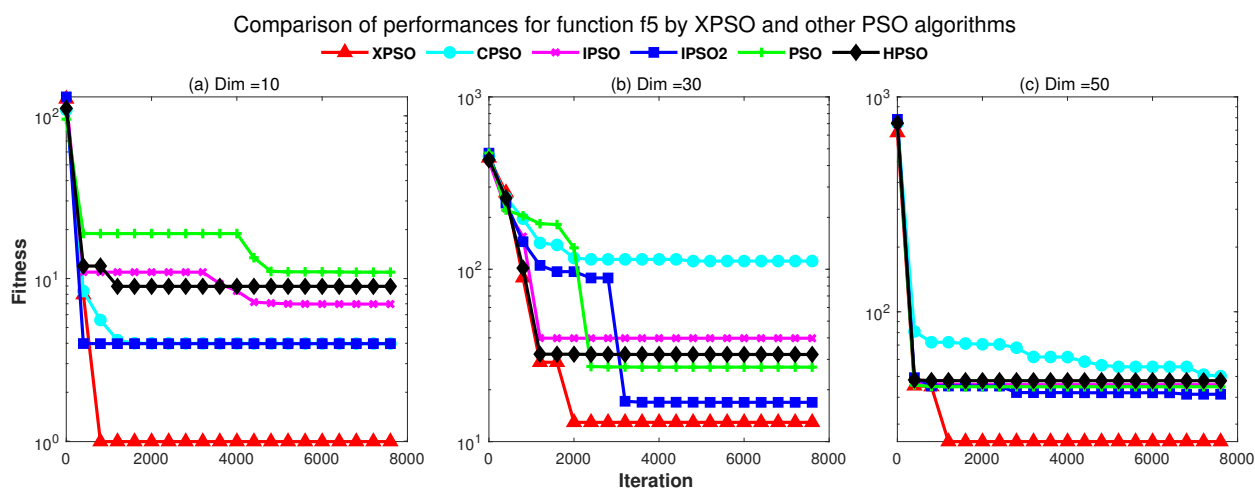


Figure 6. Comparison of performances on f5 by XPSO and other PSO algorithms.

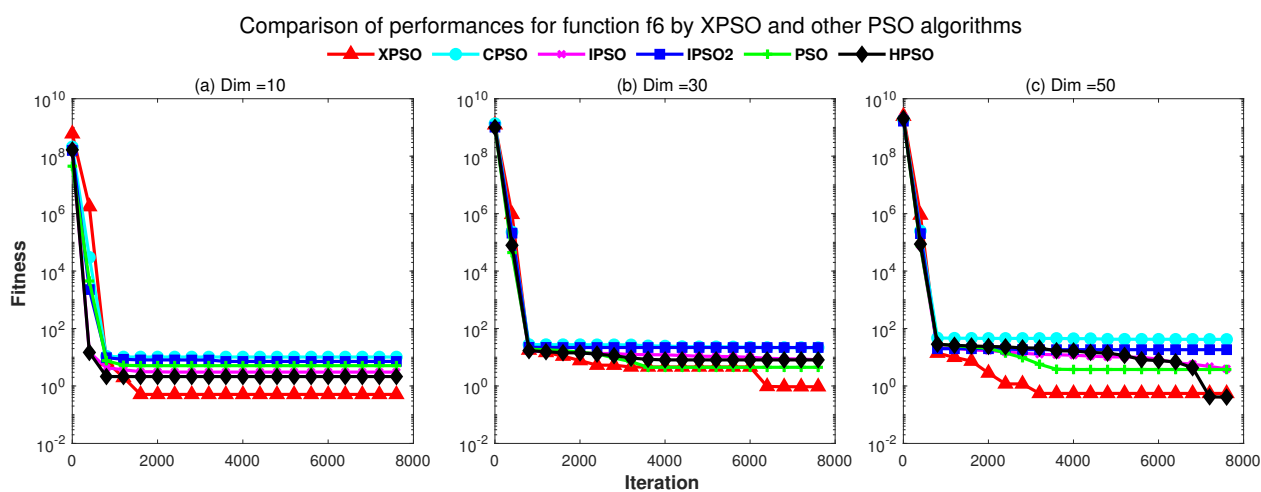


Figure 7. Comparison of performances on f6 by XPSO and other PSO algorithms.

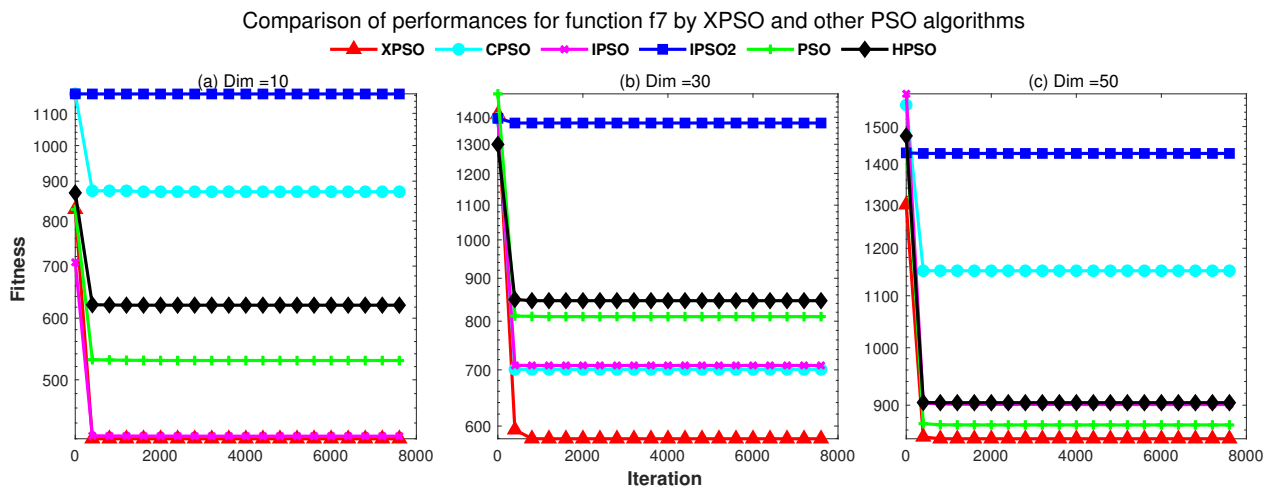


Figure 8. Comparison of performances on f7 by XPSO and other PSO algorithms.

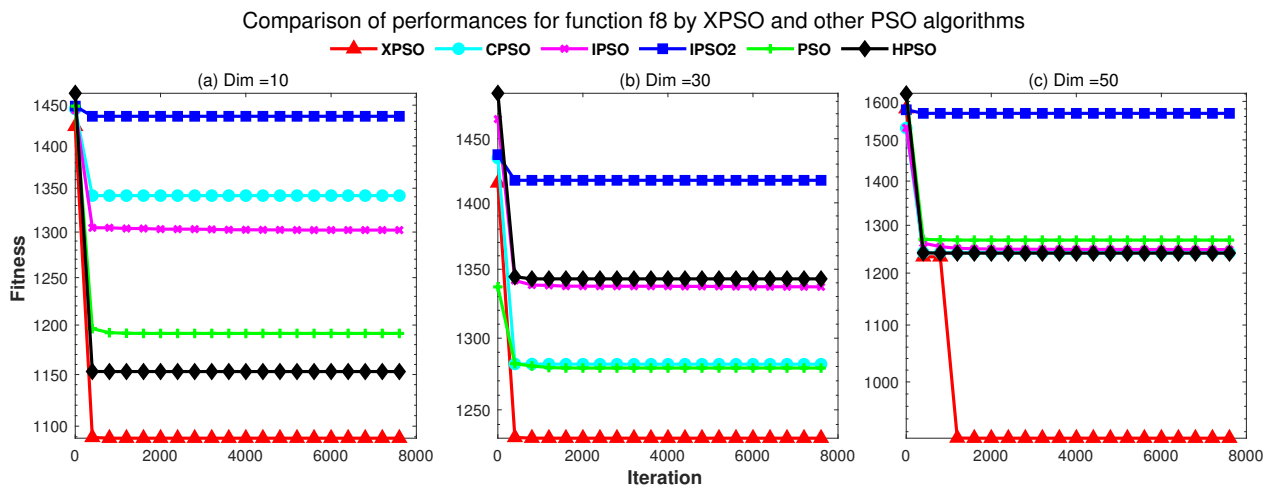


Figure 9. Comparison of performances on f8 by XPSO and other PSO algorithms.

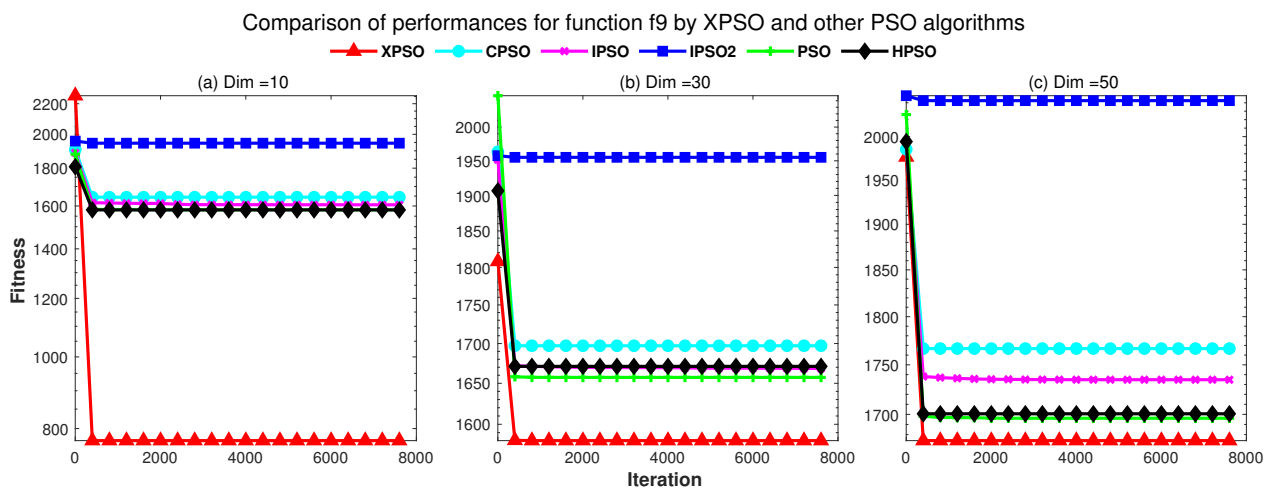


Figure 10. Comparison of performances on f9 by XPSO and other PSO algorithms.

4.2. Validation Of XPSO by Benchmark Test Functions

Firstly, 1280 simulation data sets were generated based on the existing mechanism model to verify the validity of the XPSO algorithm. In total, 1200 data sets were randomly selected as training sets and the remaining 80 as test sets. Here, the XPSO algorithm is compared with

not only other PSO algorithms (PSO [32], IPSO [33], IPSO2 [30], HPSO [34], CPSO [35]), but also the other optimization algorithms (WOA [38], IA [39], GWO [40], DE [41], ABC [42]). Secondly, the actual data sets were collected from a reheating furnace in Angang's building. Forty-three sets were randomly selected as the training sets. The remaining 10 sets were used as the test sets.

4.2.1. Comparison of XPSO and Other PSO Algorithms

Due to the random initialization of the PSO algorithms, each PSO algorithm independently ran 10 times. The relevant parameters for the PSO algorithms are shown in Table 4. Each algorithm was evaluated by the mean, maximum, median, variance and standard deviation of the errors. The simulation results are shown in Table 5 and Figures 11 and 12.

Table 4. Classical benchmark functions.

Symbol	Name	Size
N	Particle swarm size	125
D	Particle Swarm Dimension	35
G	Maximum number of iterations	8000
w_s	Initial value of inertia weights	0.8
w_e	Final value of inertia weights	0.05
c_1	Acceleration coefficient 1	2.5
c_2	Acceleration coefficient 2	1.5
V_{max}	Value of maximum particle's velocity	0.1
V_{min}	Value of minimum particle's velocity	−0.1

Table 5. Classical benchmark functions.

Algorithm	Mean	Maximum	Median	Variance	S.D.
XPSO	0.55	2.29	0.46	0.216	0.465
CPSO	3.9	13.99	3.41	8.098	2.846
IPSO	7	23.75	5.85	26.582	5.156
IPSO2	3.76	13.58	3	8.388	2.896
PSO	3.58	11.65	2.77	6.818	2.611
HPSO	0.78	2.94	0.61	0.446	0.668

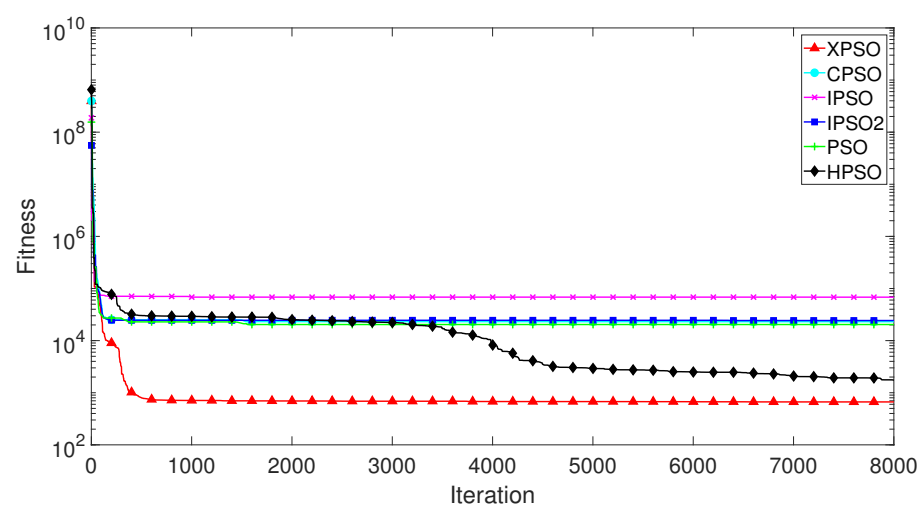


Figure 11. Comparison of fitness for XPSO and other PSO algorithms.

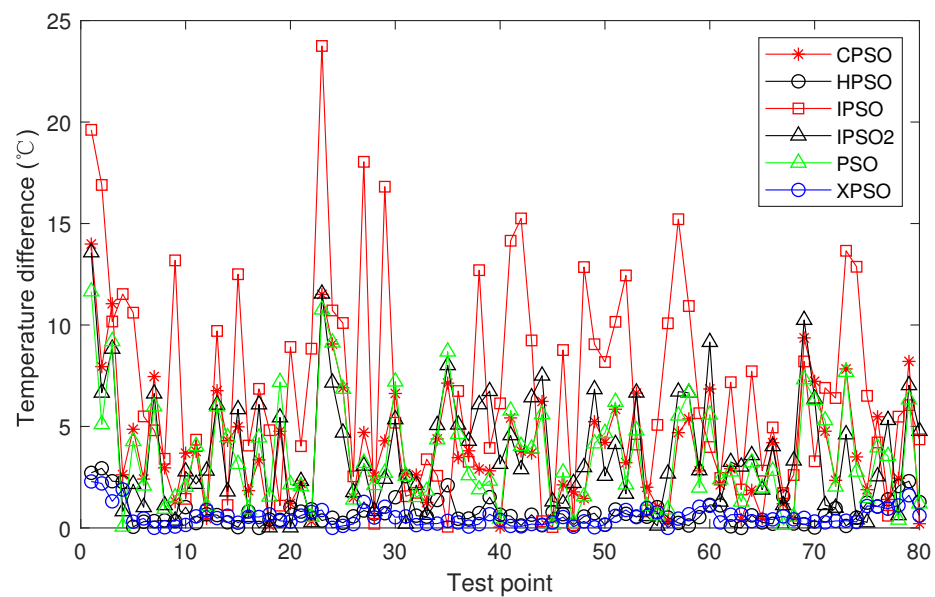


Figure 12. Prediction error of XPSO and other PSO algorithms.

In Figure 11, the XPSO algorithm clearly has a faster search speed than other algorithms in the early iterations and can quickly move to convergence. Table 5 shows that XPSO is also more accurate in terms of computational accuracy at the later stages of the iterations. Figure 12 ensures the accuracy of the proposed XPSO method for temperature prediction. The IPSO algorithm gave the worst results, for which the maximum error value was almost 24 °C. The mean and median prediction errors by the XPSO algorithm were 0.55 and 0.46 °C, and 99% of the prediction errors by the XPSO algorithm were within 2 °C.

4.2.2. Comparison of XPSO and Other Optimization Algorithms

In this section, the XPSO algorithm is compared with the other optimization algorithms (WOA [38], IA [39], GWO [40], DE [41], ABC [42]) that have been proposed in recent years. The parameters of these algorithms are listed in Table 6. Each algorithm was tested 10 times independently to reduce statistical errors. The mean, maximum, median, variance and standard difference of simulation results were recorded and are shown in Table 7. The best results are shown in bold type. The convergence graph of each algorithm is shown in Figure 13. The slab temperature prediction errors of the XPSO algorithm and other optimization algorithms are shown in Figure 14.

Table 6. Parameters of other optimization algorithms.

Algorithms	Population	Maximum Iteration	Dim	Other
WOA	125	8000	35	$r_1, r_2 \in [0, 1]$ are random numbers
IA	125	8000	35	$p_m = 0.7, \alpha = \beta = 1, \delta = 0.2, ncl = 10$
GWO	125	8000	35	$r_1, r_2 \in [0, 1]$ are random numbers
DE	125	8000	35	$F0 = 0.4, CR = 0.1$
ABC	125	8000	35	$\alpha = 1$

Table 7. Results of XPSO and other optimization algorithms.

Algorithm	Mean	Maximum	Median	Variance	S.D.
XPSO	0.55	2.29	0.46	0.216	0.465
WOA	4.53	28.27	3.45	18.94	4.3519
IA	6.92	27.52	6.43	28.0032	5.2918
GWO	2.28	13.39	1.2	6.6249	2.5739
DE	2.3	10.53	2.1	2.8971	1.7021
ABC	6.59	27.23	9.79	24.2055	4.9199

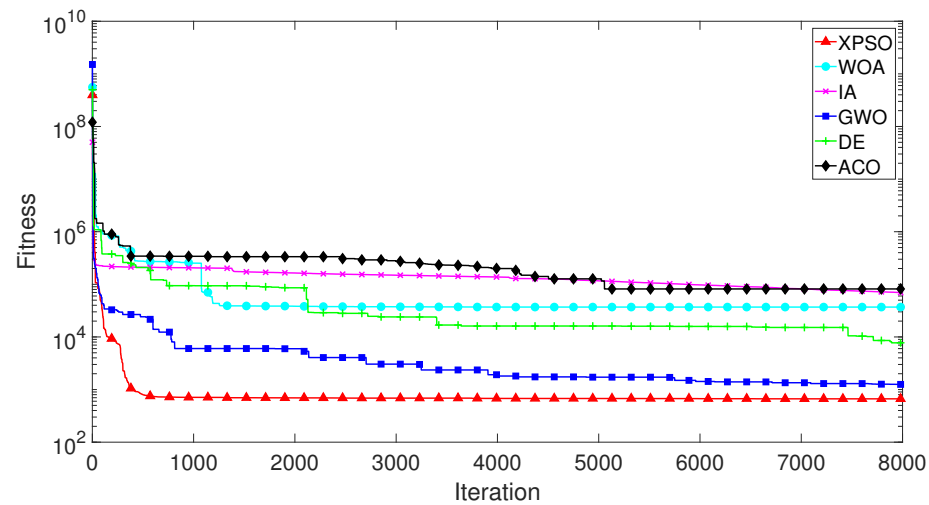


Figure 13. Comparison of XPSO with other optimization algorithms.

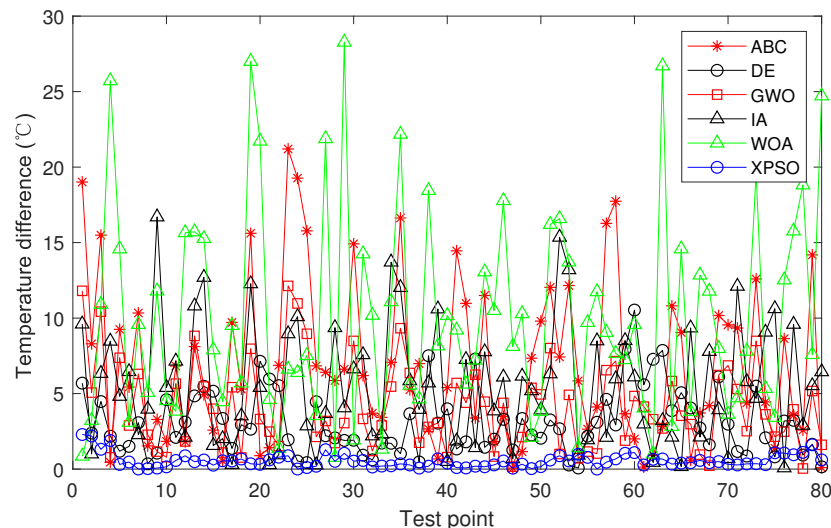


Figure 14. Prediction error of XPSO and other optimization algorithms.

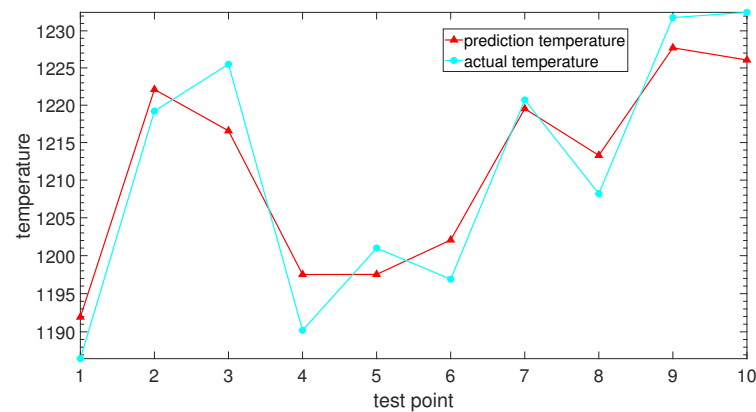
Table 7 proves that the solution of the XPSO algorithm gives the best value. In Figure 13, the XPSO algorithm is more successful than all of the other optimization approaches, and the algorithm determined the global optimal solution after approximately 500 generations. As shown in Figure 14, the temperature prediction errors by the XPSO algorithm were much lower than the errors by the other optimization algorithms. The WOA algorithm gave the worst results; its maximum error value was almost 29 °C. In summary, the proposed XPSO algorithm exhibited fast search performance and accuracy when predicting the billet temperature based on simulation data sets. The results and figures show that this prediction model of billet temperature is credible and reliable. Its accurate prediction is expected to satisfy the future control needs of industrial reheating furnace systems, which will let operators adjust production plans in time to ensure efficiency and reliability.

4.2.3. Validation of the Temperature Prediction Model With Measured Data

The proposed XPSO algorithm was applied to predict slabs' discharging temperatures based on actual data sets from Angang (company). The algorithm was independently run 20 times, and then the average prediction error was calculated. The predicted temperatures are compared with the actual temperatures in Figure 15. The errors between prediction results and measured data $|Y - Y^*|$ are shown in Table 8.

Table 8. Prediction errors between calculation results and measured data.

Points	1 (°C)	2 (°C)	3 (°C)	4 (°C)	5 (°C)	6 (°C)	7 (°C)	8 (°C)	9 (°C)	10 (°C)	Mean (°C)
XPSO	5.43	2.91	8.93	7.32	3.47	5.17	1.17	5.09	4.09	6.43	4.99

**Figure 15.** The slab temperature prediction by the XPSO algorithm.

From Figure 15 and Table 8, the minimum error of the XPSO algorithm can be seen to be 1.17 °C, and the average error was 4.99 °C. For this actual reheating furnace company, the error between the calculation results and measured data should be lower than 10 °C. Thus, the accuracy of the proposed method is high enough. As the actual discharging temperature was between 1150–1250 °C, the relative error was only 0.4%. Finally, the slab temperature prediction by the XPSO algorithm has achieved the desired effect.

5. Conclusions

In this paper, the XPSO algorithm was proposed to establish a prediction model of slab temperature in a reheating furnace. A novel weight-updating strategy that combines a decreasing function and the adaptive "stepped" strategy was introduced into the XPSO algorithm, so it can greatly improve the search capabilities at a later stage. The validity and feasibility of the XPSO were verified by nine classical benchmark functions, simulation data sets generated by the existing mechanism model and actual data sets from Angang. The following conclusions are given.

1. The benchmark results indicate that the XPSO algorithm has a superior performance to other PSO algorithms (PSO, IPSO, IPSO2, HPSO, CPSO).
2. The XPSO algorithm, which can accurately predict the billet temperature (99% of the prediction errors were less than 2 °C) while ensuring faster convergence, was more successful than all of the other optimization approaches (WOA, IA, GWO, DE, ABC).
3. The prediction model based on the XPSO algorithm can predict more accurate discharging temperatures for the operators. Consequently, the paper verifies the feasibility of the XPSO algorithm and the success of the establishment of the prediction model of slab temperature, and provides a theoretical basis for subsequent research.

Author Contributions: Conceptualization, M.L., P.Y. and Z.Y.; methodology, M.L.; software, M.L. and P.L.; validation, M.L. and J.Q.; formal analysis, J.Q.; investigation, P.L. and Z.Y.; resources, M.L. and P.L.; data curation, M.L.; writing—original draft preparation, M.L.; writing—review and editing, M.L. and Z.Y.; visualization, Z.Y.; supervision, P.Y. and Z.Y.; project administration, P.Y. and Z.Y.; funding acquisition, Z.Y. All authors have read and agreed to the published version of the manuscript.

Funding: This research was funded by the PhD research startup foundation of Qilu University of Technology, grant number (81110535), and the Industry-University-Research Collaborative Innovation Fund (grant number 2020-CXY46)—Development of an automated system for casting post-processing processes.

Institutional Review Board Statement: Not applicable.

Informed Consent Statement: Not applicable.

Data Availability Statement: Not applicable.

Conflicts of Interest: The authors declare no conflict of interest.

References

- Gu, M.; Chen, G.; Liu, X.; Wu, C.; Chu, H. Numerical simulation of slab heating process in a regenerative walking beam reheating furnace. *Int. J. Heat Mass Transf.* **2014**, *76*, 405–410. [CrossRef]
- Gao, Q.; Pang, Y.; Sun, Q.; Liu, D.; Zhang, Z. Modeling approach and numerical analysis of a roller-hearth reheating furnace with radiant tubes and heating process optimization. *Case Stud. Therm. Eng.* **2021**, *28*, 101618. [CrossRef]
- Hu, Y.; Tan, C.; Broughton, J.; Roach, P.A.; Varga, L. Model-based multi-objective optimisation of reheating furnace operations using genetic algorithm. *Energy Procedia* **2017**, *142*, 2143–2151. [CrossRef]
- Pantelides, C.C.; Renfro, J.G. The online use of first-principles models in process operations: Review, current status and future needs. *Comput. Chem. Eng.* **2013**, *51*, 136–148. [CrossRef]
- Staalman, D.F.; Kusters, A. On-line slab temperature calculation and control. *Manuf. Sci. Eng.* **1996**, *4*, 307–314.
- Ji, W.; Li, G.; Wei, L.; Yi, Z. Modeling and determination of total heat exchange factor of regenerative reheating furnace based on instrumented slab trials. *Case Stud. Therm. Eng.* **2021**, *24*, 100838. [CrossRef]
- Emadi, A.; Saboonchi, A.; Taheri, M.; Hassanpour, S. Heating characteristics of billet in a walking hearth type reheating furnace. *Appl. Therm. Eng.* **2014**, *63*, 396–405. [CrossRef]
- Tang, G.; Wu, B.; Bai, D.; Wang, Y.; Bodnar, R.; Zhou, C.Q. Modeling of the slab heating process in a walking beam reheating furnace for process optimization. *Int. J. Heat Mass Transf.* **2017**, *113*, 1142–1151. [CrossRef]
- Kim, M.Y. A heat transfer model for the analysis of transient heating of the slab in a direct-fired walking beam type reheating furnace. *Int. J. Heat Mass Transf.* **2007**, *50*, 3740–3748. [CrossRef]
- Singh, V.K.; Talukdar, P. Comparisons of different heat transfer models of a walking beam type reheat furnace. *Int. Commun. Heat Mass Transf.* **2013**, *47*, 20–26. [CrossRef]
- Morgado, T.; Coelho, P.J.; Talukdar, P. Assessment of uniform temperature assumption in zoning on the numerical simulation of a walking beam reheating furnace. *Appl. Therm. Eng.* **2015**, *76*, 496–508. [CrossRef]
- Casal, J.M.; Porteiro, J.; Míguez, J.L.; Vázquez, A. New methodology for CFD three-dimensional simulation of a walking beam type reheating furnace in steady state. *Appl. Therm. Eng.* **2015**, *86*, 69–80. [CrossRef]
- Hong, D.; Li, G.; Wei, L.; Yi, Z. An improved sequential function specification coupled with Broyden combined method for determination of transient temperature field of the steel billet. *Int. J. Heat Mass Transf.* **2022**, *186*, 122489. [CrossRef]
- Chen, D.; Xu, H.; Lu, B.; Chen, G.; Zhang, L. Solving the heat transfer boundary condition of billet in reheating furnace by combining “black box” test with mathematic model. *Case Stud. Therm. Eng.* **2022**, *40*, 102486. [CrossRef]
- Kim, Y.I.; Moon, K.C.; Kang, B.S.; Han, C.; Chang, K.S. Application of neural network to the supervisory control of a reheating furnace in the steel industry. *Control. Eng. Pract.* **1998**, *6*, 1009–1014. [CrossRef]
- Laurinen, P.; Rönning, J. An adaptive neural network model for predicting the post roughing mill temperature of steel slabs in the reheating furnace. *J. Mater. Process. Technol.* **2005**, *168*, 423–430. [CrossRef]
- Liao, Y.; Wu, M.; She, J.H. Modeling of reheating-furnace dynamics using neural network based on improved sequential-learning algorithm. In Proceedings of the 2006 IEEE Conference on Computer Aided Control System Design, 2006 IEEE International Conference on Control Applications, 2006 IEEE International Symposium on Intelligent Control, Munich, Germany, 4–6 October 2006; pp. 3175–3181.
- Tan, C.; Wilcox, S.; Ward, J. Use of artificial intelligence techniques for optimisation of co-combustion of coal with biomass. *J. Energy Inst.* **2006**, *79*, 19–25. [CrossRef]
- Pongam, T.; Khomphis, V.; Srisertpol, J. System modeling and temperature control of reheating furnace walking hearth type in the setting up process. *J. Mech. Sci. Technol.* **2014**, *28*, 3377–3385. [CrossRef]
- Tang, Z.; Yang, Y. Two-stage particle swarm optimization-based nonlinear model predictive control method for reheating furnace process. *ISIJ Int.* **2014**, *54*, 1836–1842. [CrossRef]
- Aoxiang, W.; Xiaohua, L.; Xiaolin, W. Temperature optimization setting model of the reheating furnace on 1700 line in tangsteel. In Proceedings of the 2018 Chinese Control Additionally, Decision Conference (CCDC), Shenyang, China, 9–11 June 2018; pp. 4099–4103.
- Yang, Y.; Liu, Y.; Liu, X.; Qin, S. Billet temperature soft sensor model of reheating furnace based on RVM method. In Proceedings of the 2011 Chinese Control and Decision Conference (CCDC), Mianyang, China, 23–25 May 2011; pp. 4003–4006.
- Yi, Z.; Su, Z.; Li, G.; Yang, Q.; Zhang, W. Development of a double model slab tracking control system for the continuous reheating furnace. *Int. J. Heat Mass Transf.* **2017**, *113*, 861–874. [CrossRef]
- Chen, Y.W.; Chai, T.Y. Modelling and prediction for steel billet temperature of heating furnace. *Int. J. Adv. Mechatron. Syst.* **2010**, *2*, 342–349. [CrossRef]

25. Alsaidy, S.A.; Abbood, A.D.; Sahib, M.A. Heuristic initialization of PSO task scheduling algorithm in cloud computing. *J. King Saud Univ.-Comput. Inf. Sci.* **2020**, *34*, 2370–2382. [CrossRef]
26. Yue, C.; Qu, B.; Liang, J. A multiobjective particle swarm optimizer using ring topology for solving multimodal multiobjective problems. *IEEE Trans. Evol. Comput.* **2017**, *22*, 805–817. [CrossRef]
27. Peng, C.C.; Chen, C.H. Compensatory neural fuzzy network with symbiotic particle swarm optimization for temperature control. *Appl. Math. Model.* **2015**, *39*, 383–395. [CrossRef]
28. Eberhart, R.; Kennedy, J. Particle swarm optimization. In Proceedings of the IEEE International Conference on Neural Networks, Perth, WA, Australia, 27 November–1 December 1995; Volume 4, pp. 1942–1948.
29. Kennedy, J. The particle swarm: Social adaptation of knowledge. In Proceedings of the 1997 IEEE International Conference on Evolutionary Computation (ICEC'97), Indianapolis, IN, USA, 13–16 April 1997; pp. 303–308.
30. Ravi, K.; Rajaram, M. Optimal location of FACTS devices using improved particle swarm optimization. *Int. J. Electr. Power Energy Syst.* **2013**, *49*, 333–338. [CrossRef]
31. Zhang, L.; Zhao, L. High-quality face image generation using particle swarm optimization-based generative adversarial networks. *Future Gener. Comput. Syst.* **2021**, *122*, 98–104. [CrossRef]
32. Ouyang, A.; Tang, Z.; Zhou, X.; Xu, Y.; Pan, G.; Li, K. Parallel hybrid pso with cuda for 1d heat conduction equation. *Comput. Fluids* **2015**, *110*, 198–210. [CrossRef]
33. Gao, Z.; Lu, H. Logistics Route Optimization Based on Improved Particle Swarm Optimization. In Proceedings of the Journal of Physics: Conference Series, Diwanayah, Iraq, 21–22 April 2021; Volume 1995, p. 012044.
34. Wu, J.; Long, J.; Liu, M. Evolving RBF neural networks for rainfall prediction using hybrid particle swarm optimization and genetic algorithm. *Neurocomputing* **2015**, *148*, 136–142. [CrossRef]
35. Liu, B.; Wang, L.; Jin, Y.H.; Tang, F.; Huang, D.X. Improved particle swarm optimization combined with chaos. *Chaos, Solitons Fractals* **2005**, *25*, 1261–1271. [CrossRef]
36. Yao, X.; Liu, Y.; Lin, G. Evolutionary programming made faster. *IEEE Trans. Evol. Comput.* **1999**, *3*, 82–102.
37. Suganthan, P.N.; Hansen, N.; Liang, J.J.; Deb, K.; Chen, Y.P.; Auger, A.; Tiwari, S. *Problem Definitions and Evaluation Criteria for the CEC 2005 Special Session on Real-Parameter Optimization*; KanGAL Report Number 2005005; Nanyang Technological University: Singapore, 2005.
38. Mirjalili, S.; Lewis, A. The whale optimization algorithm. *Adv. Eng. Softw.* **2016**, *95*, 51–67. [CrossRef]
39. Hong, G.; Zong-Yuan, M. Immune algorithm. In Proceedings of the 4th World Congress on Intelligent Control and Automation (Cat. No. 02EX527), Shanghai, China, 10–14 June 2002; Volume 3, pp. 1784–1788.
40. Mirjalili, S.; Mirjalili, S.M.; Lewis, A. Grey wolf optimizer. *Adv. Eng. Softw.* **2014**, *69*, 46–61. [CrossRef]
41. Arslan, M.; Çunkaş, M.; Sağ, T. Determination of induction motor parameters with differential evolution algorithm. *Neural Comput. Appl.* **2012**, *21*, 1995–2004. [CrossRef]
42. Karaboga, D.; Basturk, B. A powerful and efficient algorithm for numerical function optimization: Artificial bee colony (ABC) algorithm. *J. Glob. Optim.* **2007**, *39*, 459–471. [CrossRef]

Article

Structure of Randomly Distributed Nanochain Aggregates on Silicon Substrates: Modeling and Optical Absorption Characteristics

Tianze Zhao ^{1,2,3}, Yanze Gao ^{1,2,3,*}, Rui Shi ^{1,2,3}, Zhuo Li ^{1,2,3} and Qingfeng Shi ^{1,2,3}

- ¹ School of Optics and Photonics, Beijing Institute of Technology, Zhongguancun South Street 5, Beijing 100081, China; zhaotz12@163.com (T.Z.); bitsr@126.com (R.S.); lizhuo@bit.edu.cn (Z.L.); 81908027@bit.edu.cn (Q.S.)
- ² Beijing Key Laboratory for Precision Optoelectronic Measurement Instrument and Technology, Zhongguancun South Street 5, Beijing 100081, China
- ³ Analysis & Testing Center, Beijing Institute of Technology, Zhongguancun South Street 5, Beijing 100081, China
- * Correspondence: gao_yanze@bit.edu.cn

Abstract: Nanoparticle aggregate structures allow for efficient photon capture, and thus exhibit excellent optical absorption properties. In this study, a model of randomly distributed nanochain aggregates on silicon substrates is developed and analyzed. The Gaussian, uniform, and Cauchy spatial distribution functions are used to characterize the aggregate forms of the nanochains and their morphologies are realistically reconstructed. The relationships between the structural parameters (thickness and filling factor), equivalent physical parameters (density, heat capacity, and thermal conductivity), and visible absorptivity of the structures are established and analyzed. All the above-mentioned parameters exhibit extreme values, which maximize the visible-range absorption; these values are determined by the material properties and nanochain aggregate structure. Finally, Al nanochain aggregate samples are fabricated on Si substrates by reducing the kinetic energy of the metal vapor during deposition. The spectral reflection characteristics of the samples are studied experimentally. The Spearman correlation coefficients for the calculated spectral absorption curves and those measured experimentally are higher than 0.82, thus confirming that the model is accurate. The relative errors between the calculated visible-range absorptivities and the measured data are less than 0.3%, further confirming the accuracy of the model.

Keywords: optical absorber; nanoparticle clusters; morphological reconstruction; equivalent physical characteristics; visible-range absorption

Citation: Zhao, T.; Gao, Y.; Shi, R.; Li, Z.; Shi, Q. Structure of Randomly Distributed Nanochain Aggregates on Silicon Substrates: Modeling and Optical Absorption Characteristics. *Materials* **2022**, *15*, 4778. <https://doi.org/10.3390/ma15144778>

Academic Editors: Shuwen Wen, Yongle Sun and Xin Chen

Received: 30 May 2022

Accepted: 6 July 2022

Published: 7 July 2022

Publisher's Note: MDPI stays neutral with regard to jurisdictional claims in published maps and institutional affiliations.



Copyright: © 2022 by the authors. Licensee MDPI, Basel, Switzerland. This article is an open access article distributed under the terms and conditions of the Creative Commons Attribution (CC BY) license (<https://creativecommons.org/licenses/by/4.0/>).

1. Introduction

Nanostructures consisting of metal nanoparticle clusters can be described as aggregates of nanocells. These sparse and porous nanostructures can efficiently capture photons, and thus exhibit excellent optical properties [1–3]. Hence, optical absorbers based on nanoaggregate structures are widely used in microbolometers [4], photothermal converters [5,6], solar cells [7,8], and photocatalysis [9]. In addition, nanoaggregate structures show several desirable physical properties, such as low heat capacity, high specific surface area, and low density. As a result, these structures have shown significant potential in the fields of tunable excitation radiation and photothermoacoustics [10].

Several quasianalytical models have been developed for characterizing the nanoaggregate structures, including the effective medium model [11], cluster-cluster aggregation (CCA) model [12], and fractal lossy antennas (FLA) model [13]. The effective medium model simplifies complex nanoclusters into hypothetical ellipsoids. However, the permittivity elucidated by the effective medium model is based on statistical parameters, and the

model lacks a description of the nanostructures. The CCA model represents the aggregate morphology of spherical units and the growth process of clusters based on the theory of diffusion-limited aggregation [14–16]. The FLA model describes the nanoaggregate structure as a forest-like structure composed of chains. The length of the chains in the FLA model is the order of microns.

In this paper, a new model of randomly distributed nanochain aggregate structures is proposed to describe their micromorphology. The relationships between the structural parameters (thickness and filling factor), equivalent physical parameters (density, heat capacity, and thermal conductivity), and visible-range absorptivity of the model were established and analyzed. These relationships can serve as a theoretical reference for further research on areas such as the study of the photothermoacoustic effect of nanoaggregate structures. To evaluate the model, Al nanochain aggregate structures were fabricated on Si substrates, and the spectral reflection characteristics of the samples were determined experimentally. The experimental results showed that the model can realistically reconstruct the morphology of the structures and allows for accurate calculations of their spectral absorptivity.

2. Materials and Methods

2.1. Fabrication of Nanoaggregate Structures

To fabricate nanoaggregate samples, we chose two types of substrates, Si wafers and polyimide (PI) films. The Si wafers were cleaned using an oxygen plasma. The PI films were fabricated on Si wafers by spin coating. A 6 mL polyamic acid (PAA) solution was spin-coated on the Si wafers at a low speed (800 r min^{-1}) for 1 min and then at a high speed (7000 r min^{-1}) for 3 min. The PAA coating was then air-dried at 25°C for 1 h and cured in an oven filled with N_2 gas for 3 h at 300°C to chemically transform PAA into PI. The process for fabricating a layer of the nanoaggregate structure is shown in Figure 1. Metal Al was evaporated in a He atmosphere at a pressure of 980 Pa, and the Al metal vapor was made to pass through the He atmosphere to reduce its kinetic energy before it was deposited on the substrate.

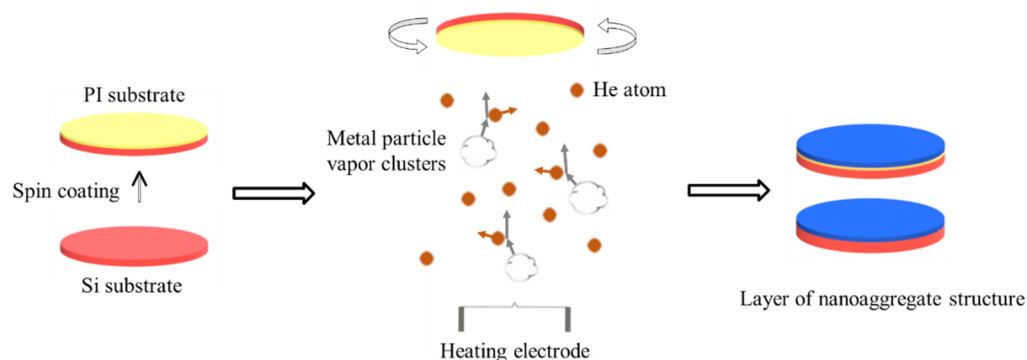


Figure 1. Process for fabricating layer of nanoaggregate structure.

2.2. Model of Nanochain Aggregates

2.2.1. Basic Structural Unit of Model

We obtained scanning electron microscopy (SEM, Supra55, Zeiss, Oberkochen, Germany) images of the fluffy, “smoke-like” metal deposition structure, as shown in Figure 2. The fluffy structure is porous, micron sized, and composed of a large number of clusters, which, in turn, consist of randomly distributed nanochains. These nanochains are composed of metal nanoparticles, which can be considered as nanospheres.

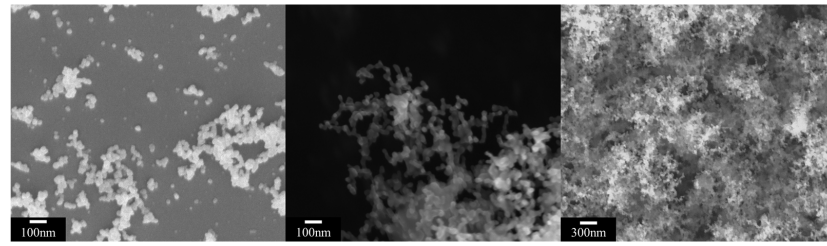


Figure 2. SEM images of nanoaggregate structure.

2.2.2. Spatial Distribution of Nanochains

A large number of nanochains were generated in a three-dimensional space to form clusters. The distribution of nanochains is disordered, but this disordered distribution shows statistical regularity. Therefore, we try to use classical probability distribution functions, Gaussian, uniform and Cauchy distributions, to characterize such statistical regularity. The spatial distribution function represents the aggregate form of the nanochains and reflects the probability density distribution of the nanochains in the clusters, as shown in Figure 3. In the spatial coordinate system with the cluster centroid as the origin, the probability density functions corresponding to the three spatial distributions are as follows:

$$G(r) = \frac{1}{\sqrt{2\pi}\sigma} \exp\left(-\frac{r^2}{2\sigma^2}\right), \quad (1)$$

$$U(r) = \frac{1}{2\sigma\sqrt{3}}, \quad (2)$$

$$C(r) = \frac{1}{\pi} \left(\frac{\sigma}{r^2 + \sigma^2} \right), \quad (3)$$

where $G(r)$, $U(r)$, and $C(r)$ represent the probability density functions of the Gaussian, uniform, and Cauchy distributions, respectively; r represents the distance between the nanochain and the cluster centroid; σ is the size parameter of the spatial distribution, which determines the radius of the cluster.

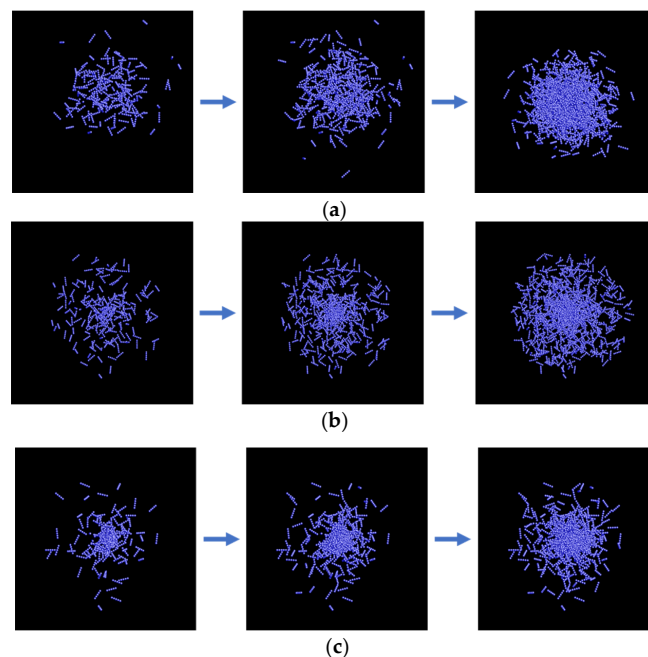


Figure 3. Nanochain cluster models generated using different distribution functions. (a) Clusters whose form is represented by Gaussian distribution. (b) Clusters whose form is represented by uniform distribution. (c) Clusters whose form is represented by Cauchy distribution.

As a structural parameter, the distribution function used affects the propagation path of photons within the structure. Thus, the selection of the appropriate distribution function is essential for accurately calculating the optical absorption. Given that the actual spatial distribution of nanochains is highly random, we add a weight to each distribution function to improve the accuracy of the model, demonstrated by the following equation:

$$W_G + W_U + W_C = 1, \quad (4)$$

where W_G is the weight of the nanochain clusters based on the Gaussian distribution function; W_U is the weight of the nanochain clusters based on the uniform distribution function, and W_C is the weight of the nanochain clusters based on the Cauchy distribution function. The weight of the distribution function reflects the number (percentage) of clusters aggregated by a specific distribution function to all clusters in the model.

2.2.3. Aggregation Model of Clusters

In addition to the spatial distribution of nanochains in a cluster, we use the uniform distribution function to describe the spatial distribution of the clusters in the aggregation model as well. Similar to the spatial distribution of nanochains, the spatial distribution of the clusters in the aggregation model can be described as $U(x, y, z) = \frac{1}{2\sigma\sqrt{3}}$. This completes the physical modeling of the nanochain aggregate structure, as shown in Figure 4.

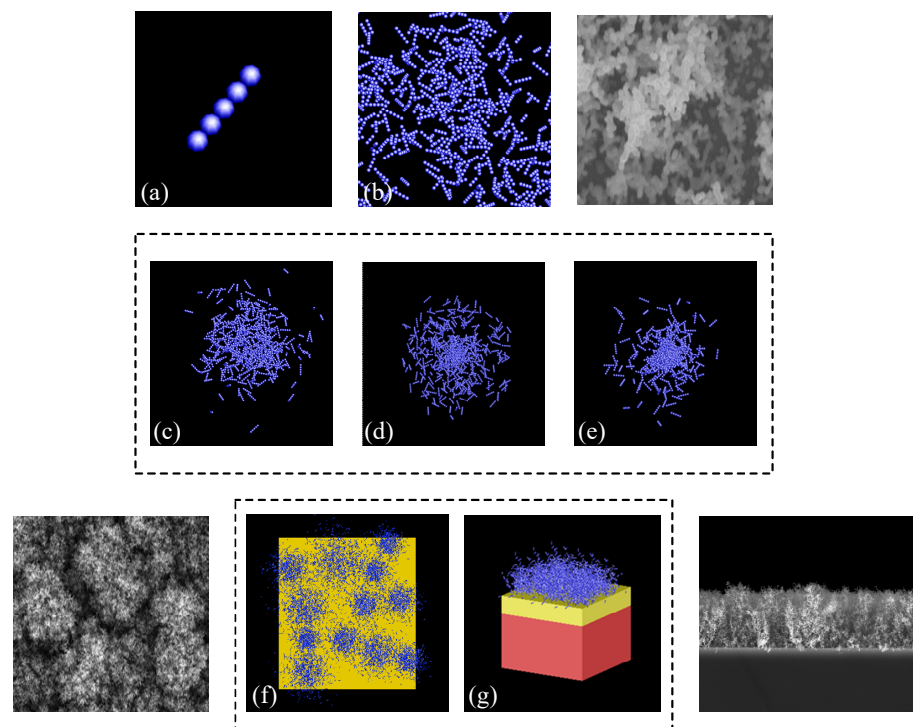


Figure 4. Modeling of nanochain aggregate structure. (a) Basic nanochain structure. (b) Nanochains with random three-dimensional orientations. (c) Cluster based on Gaussian distribution. (d) Cluster based on uniform distribution. (e) Cluster based on Cauchy distribution. (f) Top view of physical model. (g) Sectional view of physical model.

We define the dimension of the model in the direction perpendicular to the substrate as the model thickness, d . In addition to the thickness, we define a structural parameter, namely, the filling factor (γ), to describe the relative density of the nanochain aggregate structure. The filling factor was calculated as the ratio of the structural density to the material density. It also reflects the porosity of the nanochain aggregate structure. In the proposed model, the filling factor was varied by changing the number of nanospheres contained in each cluster.

2.2.4. Finite-Difference Time-Domain (FDTD) Method

The FDTD method was used to calculate the spectral absorptivity of the model [17–20]. The FDTD method discretized the time-domain Maxwell's equations by central difference approximation of the spatial and temporal partial derivatives. The finite difference equations with the following form were obtained:

$$E_x^{n+1}(i+1, j, k) = \frac{1 - \frac{\sigma(i+1/2, j, k)\Delta t}{2\epsilon(i+1/2, j, k)}}{1 + \frac{\sigma(i+1/2, j, k)\Delta t}{2\epsilon(i+1/2, j, k)}} \cdot E_x^n(i+1/2, j, k) + \frac{\Delta t}{\epsilon(i+1/2, j, k)} \cdot \left[\frac{1}{1 + \frac{\sigma(i+1/2, j, k)\Delta t}{2\epsilon(i+1/2, j, k)}} \cdot \left[\frac{H_z^{n+1/2}(i+1/2, j, k) - H_z^{n+1/2}(i+1/2, j-1/2, k)}{\Delta y} + \frac{H_y^{n+1/2}(i+1/2, j, k-1/2) - H_y^{n+1/2}(i+1/2, j, k+1/2)}{\Delta z} \right] \right] \quad (5)$$

where i , j , and k are the grid numbers in x , y , and z directions, respectively; n is the number of time domain iterations; Δt is the time step; σ is the conductivity; and ϵ is the dielectric constant. The dielectric constant and conductivity were wavelength-dependent parameters taken from the literature [21]. The reflectivity and transmittivity of the model were calculated using frequency domain power monitors with the following formula:

$$T(f) = \frac{\text{Re}(P(f)) \cdot d\vec{S}}{\text{Re}(P_{\text{source}}(f)) \cdot d\vec{S}} \quad (6)$$

where $T(f)$ is the normalized transmittivity of the monitor; $P(f)$ and $P_{\text{source}}(f)$ are the Poynting vectors on the surfaces of the monitor and light source, respectively; and $d\vec{S}$ is the differential element of normal direction. The incident light source was set as a plane wave with a wavelength step of 2 nm. To simplify the model and allow for faster computations, the periodic boundary condition was used for the FDTD calculations. The spectral reflectivity (R_λ) and transmittance (T_λ) of the model were obtained using power monitors. The spectral absorptivity (A_λ) of the model was calculated using Equation (7), and the visible absorptivity (A) of the model was calculated by integrating the spectral absorptivity.

$$A_\lambda = 1 - R_\lambda - T_\lambda, \quad (7)$$

We designed the Gaussian, uniform, and Cauchy models based on the spatial distribution of the nanochains. The spatial distribution of the clusters within the computational region was uniform for all three models, as described in the previous subsection.

3. Results and Discussion

3.1. Optical Absorption Properties of Model

3.1.1. Relationship between Filling Factor and Optical Absorption

We first analyzed the relationship between the filling factor and optical absorption. We set the nanochain materials as Al, Au, and Cr and used a model thickness of 1 μm and filling factor of 0.5–8%. The spectral absorption curves in the wavelength range of 400–800 nm, as well as the visible-range absorptivity of the model for different filling factors, are shown in Figure 4. The filling factor affects the motion path of the incident photons, and thus the efficiency of the model in capturing photons. An extremely sparse or dense distribution of nanochains leads to a reduction in the model absorptivity. For all three models, the filling factor and visible-range absorptivity exhibited a quadratic relationship. The extreme values of the filling factor, which enhanced the visible-range absorption, are listed in Table 1. We propose the following equation to describe the relationship between the filling factor and visible-range absorptivity:

$$A = c + c_1 \cdot \gamma + c_2 \cdot \gamma^2, \quad (8)$$

where c_1 , c_2 , and c are constant coefficients, whose values are determined from the FDTD results. The aggregate form of the nanochains has a significant effect on the visible-range absorptivity, as shown in Figure 5. The Gaussian model possesses the highest visible-range absorptivity, indicating that the nanostructure corresponding to this model is more efficient at capturing photons.

Table 1. Relationships between model parameters and visible-range absorptivity.

Parameter	Type of Relationship Curve	Material of the Models	Extreme Values for Gaussian, Uniform and Cauchy Models
Filling factor (%)	Quadratic	Al	$\gamma_G = 5.4$, $\gamma_U = 4.4$, $\gamma_C = 4.6$
		Au	$\gamma_G = 7.4$, $\gamma_U = 5.0$, $\gamma_C = 5.6$
		Cr	$\gamma_G = 6.0$, $\gamma_U = 4.4$, $\gamma_C = 5.2$
Thickness (μm)	Exponential	Al	$d_G = 21$, $d_U = 29$, $d_C = 36$
		Au	$d_G = 47$, $d_U = 49$, $d_C = 59$
		Cr	$d_G = 37$, $d_U = 42$, $d_C = 43$
Density ($\times 10^3 \text{ kg m}^{-3}$)	Quadratic	Al	$\rho_G = 0.146$, $\rho_U = 0.113$, $\rho_C = 0.124$
		Au	$\rho_G = 1.430$, $\rho_U = 0.996$, $\rho_C = 1.121$
		Cr	$\rho_G = 0.431$, $\rho_U = 0.316$, $\rho_C = 0.374$
Thermal conductivity ($\text{W m}^{-1} \text{ K}^{-1}$)	Cubic	Al	$k_G = 33.86$, $k_U = 28.64$, $k_C = 30.43$
		Au	$k_G = 55.87$, $k_U = 43.02$, $k_C = 47.50$
		Cr	$k_G = 14.36$, $k_U = 11.68$, $k_C = 13.05$
Volumetric heat capacity ($\times 10^3 \text{ J m}^{-3} \text{ K}^{-1}$)	Quadratic	Al	$s_G = 128.3$, $s_U = 99.79$, $s_C = 109.3$
		Au	$s_G = 183.15$, $s_U = 123.75$, $s_C = 143.55$
		Cr	$s_G = 194.13$, $s_U = 123.75$, $s_C = 143.55$

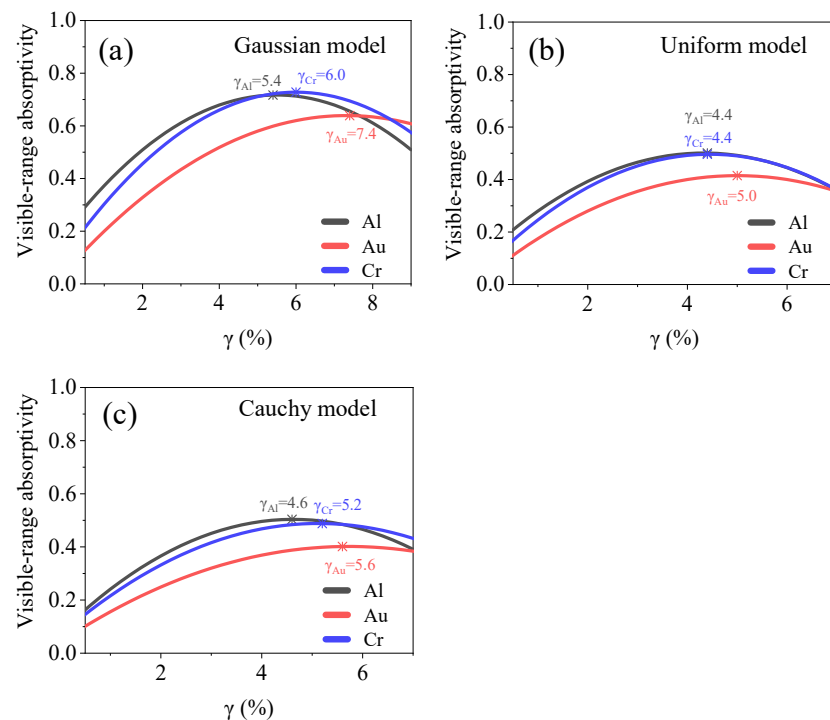


Figure 5. Relationship between optical absorption and filling factor for (a) Gaussian, (b) uniform, and (c) Cauchy models. Filling factor of each model and maximum absorptivity are shown in the figures.

3.1.2. Relationship between Thickness and Optical Absorption

The nanoaggregate structure demonstrates ultralow surface reflection in the visible band [1–3]. For nanochain aggregate structures with the same filling factor, a higher value of thickness would mean that the expected motion path of the incident photons would be longer. Once the thickness of the model exceeds a threshold value, the visible-range transmittance of the model decreases to zero. When the model thickness is more than this threshold value, it no longer affects the visible-range absorptivity of the model. Therefore, the relationship between the thickness and absorptivity takes the form of an exponential function, as shown in Figure 6. We set the nanochain material as Al, Au, and Cr and used the model filling factor of 0.6% and thickness of 1–60 μm . The extreme values of the thickness, which enhanced the visible-range absorption, are listed in Table 1. The critical thickness for the Gaussian model is much smaller than those for the uniform and Cauchy models because of the higher photon-capturing efficiency of the former. The maximum visible-range absorptivities of the three models are similar, indicating that the aggregate form of the nanochains has a negligible effect on the surface reflection of the model. Based on Equation (6), we obtained the following fitting equation:

$$A = c + C_1 \cdot (\gamma + C_2 \cdot \gamma^2) \cdot e^{-d / C_3}, \quad (9)$$

where C_1 , C_2 , and C_3 are constant coefficients, whose values can be obtained from the FDTD results. Equation (7) represents the relationship between the visible-range absorptivity, filling factor, and model thickness. It can be observed that $c_1 = C_1 \cdot e^{-d / C_3}$ and $c_2 = C_1 \cdot C_2 \cdot e^{-d / C_3}$.

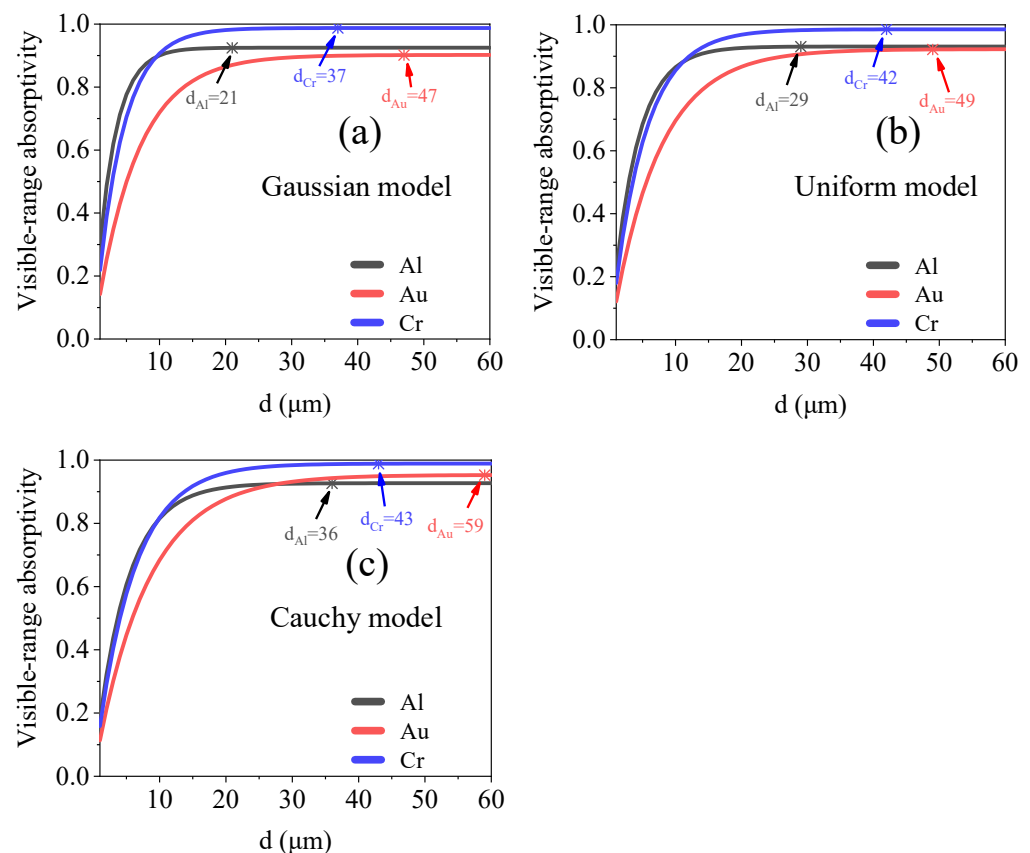


Figure 6. Relationship between optical absorption and thickness for (a) Gaussian, (b) uniform, and (c) Cauchy models. Critical thicknesses of models are shown in the figures.

3.1.3. Relationship between Equivalent Density and Optical Absorption

High optical absorption can be achieved by fabricating nanochain aggregate structures from various materials. Specific application scenarios would result in limitations in terms of the density of the optical absorber. Therefore, it is essential to study the relationship between the equivalent density and optical absorption of nanochain aggregate structures. Based on the above-stated definition of the filling factor, the relationship between the filling factor and equivalent density of the structure can be described as follows:

$$\rho_{eff} = \rho_0 \cdot \gamma + \rho_m \cdot (1 - \gamma), \quad (10)$$

where ρ_{eff} is the equivalent density of the structure; ρ_0 is the density of the material used, and ρ_m is the density of the medium. The structural equivalent densities are affected by the filling factor and material density, as shown in Figure 6a. For vacuum, $\rho_m = 0$. Therefore, the relationship between ρ_{eff} and A is as follows:

$$A = c + C_1 \cdot \left[\frac{\rho_{eff}}{\rho_0} + C_2 \cdot \left(\frac{\rho_{eff}}{\rho_0} \right)^2 \right] \cdot e^{-d / C_3}, \quad (11)$$

We set the model thickness as 1 μm and the filling factor as 0.6–8%. The nanochain materials included Al, Au, and Cr. The relationship between the equivalent density and visible-range absorptivity of the nanochain aggregate models is shown in Figure 7. The models use the same structural parameters. Thus, the material density of the model has a distinct effect on its equivalent density. The extreme values of the equivalent density, which enhanced the visible-range absorption, are listed in Table 1.

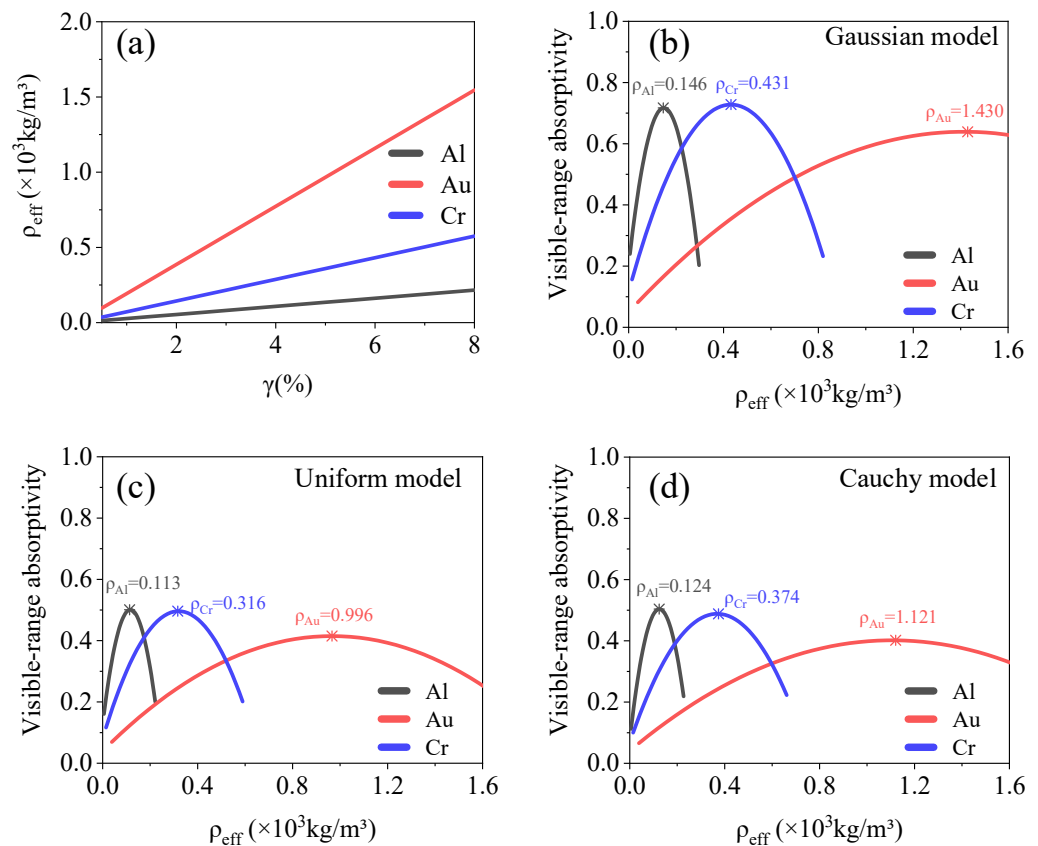


Figure 7. (a) Relationship between filling factor and equivalent density of model used. (b–d) Relationship between equivalent density and visible absorptivity for Gaussian, uniform, and Cauchy models. Equivalent density of model with maximum absorptivity is marked in the figures.

3.1.4. Relationship between Equivalent Thermal Conductivity and Optical Absorption

Thermal conductivity is an important physical parameter for optical absorbers, with respect to infrared scene generation and photoacoustic effects. Optical absorbers with high thermal conductivities exhibit fast heat dissipation and high-sensitivity time-domain temperature responses. Optical absorbers with low thermal conductivities can generate high-temperature radiation signals at relatively low incident laser powers. The relationship between the equivalent thermal conductivity of the model and its filling factor can be estimated from the classical cheese model [22], which is as follows:

$$k_{eff} = k_0 \cdot \varepsilon + k_m \cdot (1 - \varepsilon), \quad (12)$$

where k_{eff} is the equivalent thermal conductivity of the model; k_0 is the thermal conductivity of the material used; k_m is the thermal conductivity of the medium, and $\varepsilon = \gamma^{2/3}$ represents the two-dimensional (2D) porosity in the direction of heat conduction. After combining Equations (7) and (10), we obtain the following equation:

$$A = c + C_1 \cdot \left(\frac{k_{eff}}{k_0} \right)^{\frac{3}{2}} + C_2 \cdot \left(\frac{k_{eff}}{k_0} \right)^3 \cdot e^{-d/C_3}, \quad (13)$$

Figure 8 shows the relationship between the filling factor, equivalent thermal conductivity, and visible-range absorptivity for the Gaussian, uniform, and Cauchy models. The extreme values of the equivalent thermal conductivity, which enhanced the visible-range absorption, are listed in Table 1. Thus, Au nanoaggregate structures are more suitable as optical absorbers that must exhibit efficient absorption and fast heat dissipation. However, Cr nanoaggregate structures allow for efficient energy capture and accumulation.

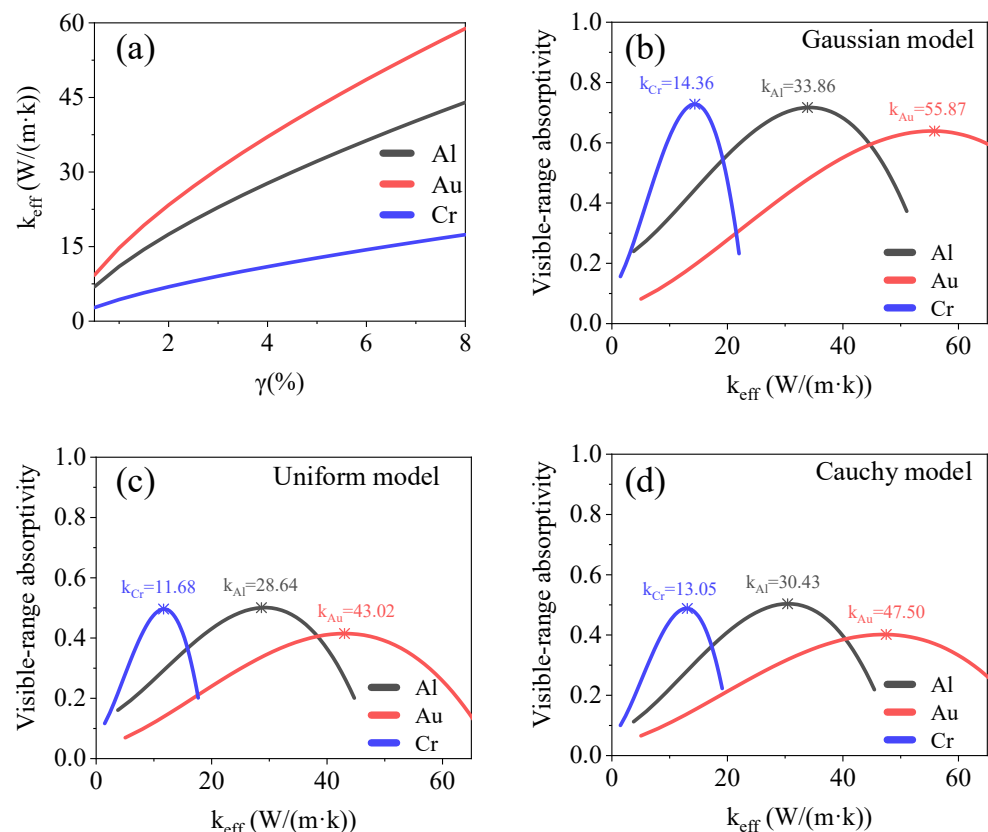


Figure 8. (a) Relationship between filling factor and equivalent thermal conductivity of model used. (b–d) Relationship between equivalent thermal conductivity and visible-range absorptivity for Gaussian, uniform, and Cauchy models. Equivalent thermal conductivity of model with maximum absorptivity is marked in the figures.

3.1.5. Relationship between Equivalent Volumetric Heat Capacity and Optical Absorption

The specific heat capacity affects the time-domain temperature response rate of optical absorbers. High optical absorption and low specific heat capacity are essential material properties for ensuring a strong photoacoustic effect [10,23]. Similar to the case for the equivalent density, the relationship between the filling factor and equivalent volume heat capacity of the model can be described as follows:

$$s_{eff} = s_0 \cdot \gamma + s_m \cdot (1 - \gamma), \quad (14)$$

$$A = c + C_1 \cdot \left[\frac{s_{eff}}{s_0} + C_2 \cdot \left(\frac{s_{eff}}{s_0} \right)^2 \right] \cdot e^{-d / C_3}, \quad (15)$$

where s_{eff} is the equivalent volumetric heat capacity of the model; s_0 is the volumetric heat capacity of the material used, and s_m is the volumetric heat capacity of the medium. The equivalent volumetric heat capacities of the Al and Au models were almost equal, while that of the Cr model was slightly higher, as shown in Figure 9. The extreme values of the equivalent volumetric heat capacity, which enhanced the visible-range absorption, are listed in Table 1. Because its absorptivity is higher, the Al nanoaggregate structure is more suitable as an optical absorber that shows a low volumetric heat capacity and high-sensitivity time-domain temperature response.

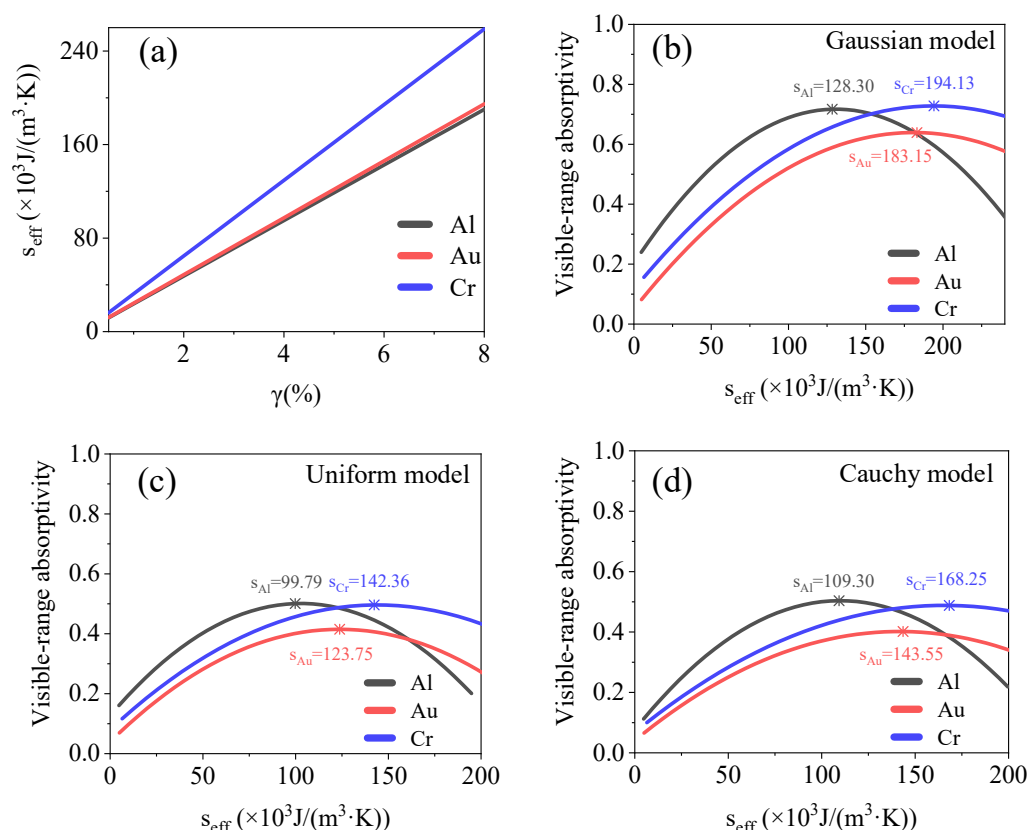


Figure 9. (a) Relationship between filling factor and equivalent volumetric heat capacity of model. (b–d) Relationship between equivalent volumetric heat capacity and visible-range absorptivity of Gaussian, uniform, and Cauchy models. Equivalent volumetric heat capacity of model with maximum absorptivity is marked in the figures.

3.2. Model Validation

3.2.1. Sample Characterization

We fabricated six different samples with nanoaggregate-structured layers. Photographs and SEM images of the samples are shown in Figure 10. The thickness and

2D porosity of the layers of the nanochain aggregates were measured. The filling factor of the samples was calculated using the expression $\varepsilon = \gamma^2 / 3$. The structural parameters of the samples are listed in Table 2.

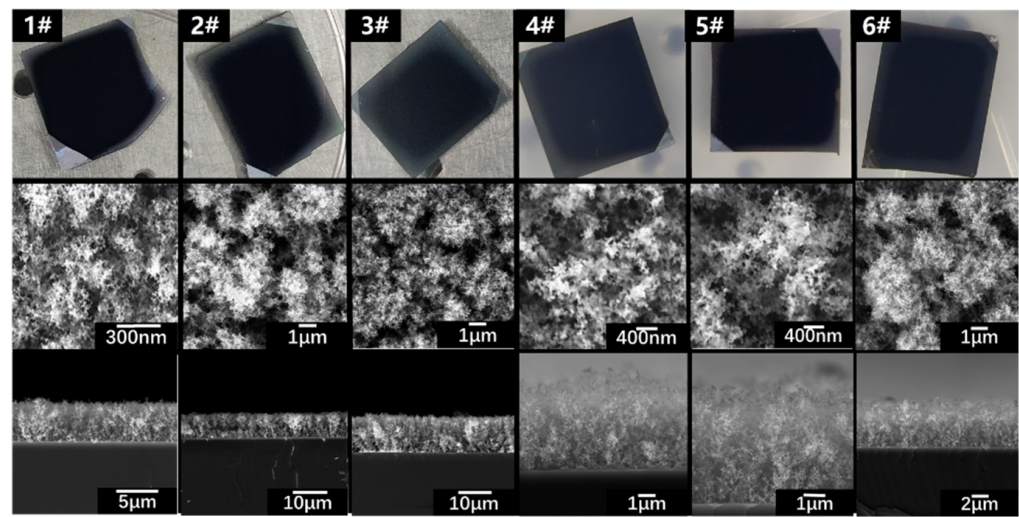


Figure 10. Photographs and SEM images of nanoaggregate samples. Samples #1–3 were formed on 500 µm Si substrates. Samples #4–6 were formed on 300 nm PI layer; PI layer was fabricated by spin-coating.

Table 2. Structural parameters of nanoaggregate samples.

Number	1#	2#	3#	4#	5#	6#
Thickness of the absorbed layer (µm)	4.78	7.34	8.37	4.83	5.07	5.56
Filling factor (%)	6.1	5.1	4.1	5.9	6.3	6.8
Substrate thickness and material	500 µm Si			300 nm PI + 500 µm Si		

Energy dispersive spectroscopy (EDS, Ultim Extreme, Oxford, UK) detection is performed on the sample and Si substrate to quantitatively analyze the oxide content in Al nano aggregates. Figure 11a shows the types (O, Al and Si) and the relative weight ratio (0.175:1:0.416) of the elements contained in the sample. According to the relative atomic mass of each element, the atomic ratio of O, Al and Si is calculated as 0.0109:0.037:0.0149. Since EDS detection is carried out in vacuum, the O element is derived from aluminum oxide and silicon oxide. The Al element is derived from aluminum and oxide in the nano aggregates, and the Si element is derived from silicon and oxide in the substrate. Figure 11b shows the types (O and Si) and the relative weight ratio (0.011:0.416) of the elements contained in the substrate. Results of the substrate are normalized based on the Si weight ratio in the sample (0.416). The atomic ratio of O and Si is calculated as 0.0007:0.0149. The O element in the substrate is derived only from silicon oxide. Therefore, it can be calculated that 93.6% of the O element in the sample is derived from aluminum oxide and 6.4% from silicon oxide. In addition, 81.5% of the Al element is derived from aluminum; 18.5% from aluminum oxide. The molecular ratio of aluminum to its oxide is calculated as 8.81:1.

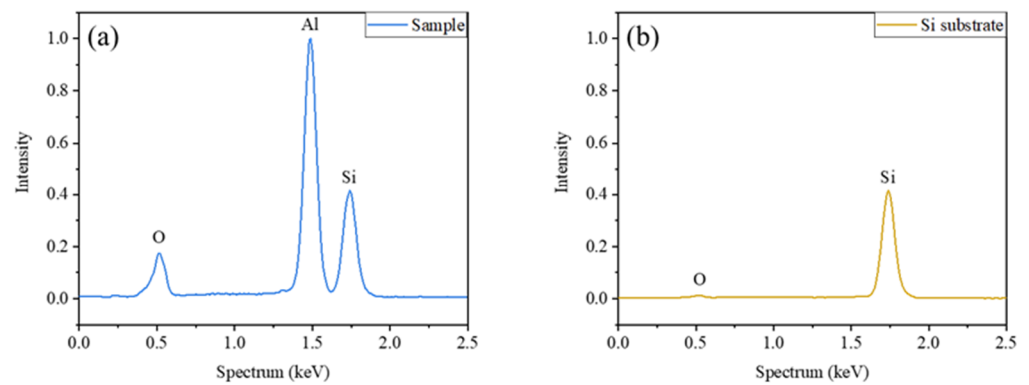


Figure 11. EDS results of the sample and Si substrate. (a) Results of the sample are normalized based on Al peak intensity, and the relative weight ratio of O, Al and Si is 0.175:1:0.416. (b) Results of Si substrate are normalized based on the Si weight ratio in the sample (0.416), and the relative weight ratio of O and Si is 0.011:0.416.

The spectral absorption curves of the samples in the 400–800 nm band were measured using a dual optical path ultraviolet–visible (UV–vis) spectrophotometer (TU-1901, Persee, Beijing, China). Two standard reflectance plates were used for correction. All the samples were supported by a 500 μm Si wafer, which was completely opaque in the visible range. The spectral absorptivities of the samples were calculated using Equation (7). The spectral absorption curves of the Si substrates, PI substrates, and samples are shown in Figure 12. The root mean square error (RMSE) between the measured and fitted curves was less than 0.7%, as shown in Table 3. The absorptivities of the samples were higher than 0.97 in the 400–800 nm band.

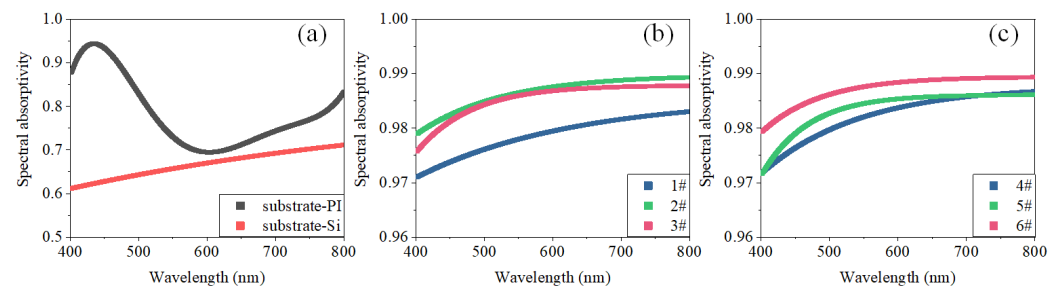


Figure 12. Measured spectral absorption curves of various substrates and nanoaggregate samples. (a) Measured spectral absorption curves of Si and PI substrates. (b) Measured spectral absorption curves of samples #1–3. (c) Measured spectral absorption curves of samples #4–6.

Table 3. Statistics of measured error.

Object	RMSE between Measured and Fitted Curves
Si	0.0044
1#	0.0008
2#	0.0001
3#	0.0007
PI	0.0071
4#	0.0002
5#	0.0007
6#	0.0001

3.2.2. Analysis of Calculation and Experimental Results

We constructed a physical model of the nanoaggregate samples based on the structural parameters listed in Table 2. The spectral reflectivity and absorptivity of the substrate used were included in the model as the boundary conditions. The weights of the three distribution functions in the aggregation model were adjusted to optimize the calculation results. The values of W_G , W_U , and W_C were set at 0.6, 0.2, and 0.2, respectively. A comparison of the calculation and experimental results is shown in Figure 13. The Spearman correlation coefficient was used to evaluate the correlation between the calculation and measurement curves; the values obtained are listed in Table 4.

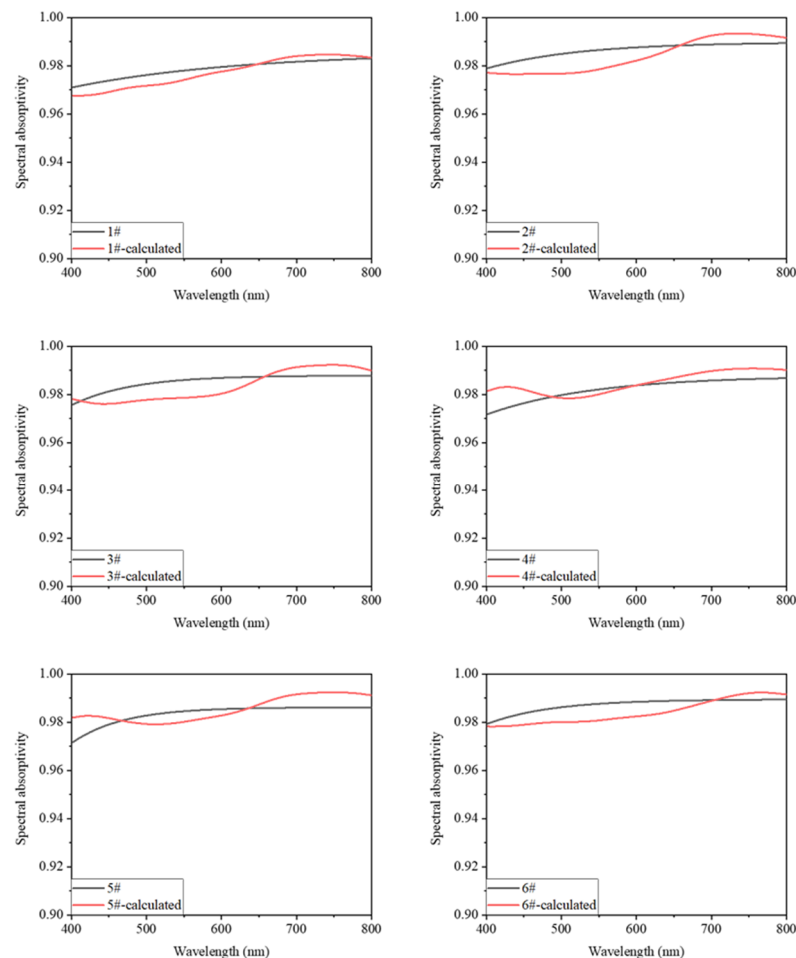


Figure 13. Spectral absorption curves determined based on weighted Gaussian, uniform, and Cauchy distribution models and those obtained experimentally.

Table 4. Comparison of calculation and measurement results.

Object	Spearman Correlation Coefficient of Spectral Absorption Curves	Relative Error of Visible Absorptivity
1#	0.976	0.0018
2#	0.954	0.0031
3#	0.962	0.0017
4#	0.846	0.0028
5#	0.822	0.0013
6#	0.996	0.0029

To evaluate the accuracy of the model described by Equation (9), we compared the calculated values of the visible-range absorptivity with the measured ones, as shown in Figure 14. The relative errors are presented in Table 4.

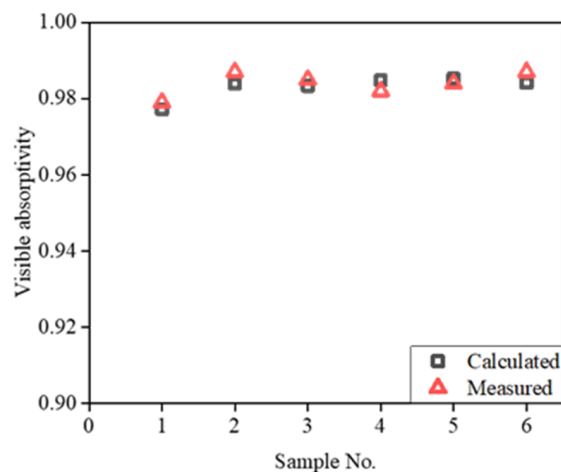


Figure 14. Calculated and measured values of visible-range absorptivity of various samples.

The calculated spectral absorption curves of the samples are in good agreement with the experimental curves, with the Spearman correlation coefficients being higher than 0.82. Within the range of values used for the structural parameters of the samples, the relative errors between the calculated visible-range absorptivities and those determined experimentally were less than 0.3%. This confirmed that the model was accurate.

3.3. Discussion

The model of nanoaggregate structure presented here is only a preliminary model, which is mainly established and verified for Al. Due to the limitation of the experimental conditions, the samples have a relatively small range of fill factor and thickness compared to the range of the presented model predictions. Therefore, the accuracy of the model is only verified in a relatively small range. We will study and improve the fabrication method to expand the range of sample thickness and filling factor in subsequent research. In addition, the model should be further improved to make it universal. The general form of nanoaggregate structure can be applied to metal absorbers obtained by various processes. This model is suitable for the study of surface absorption of various optical sensors, photothermal effect and photovoltaic, as well as terahertz generation and detection.

4. Conclusions

In this study, the structures of randomly distributed nanochain aggregates on silicon substrates were modeled, and the model was evaluated. The relationship between the structural parameters (thickness and filling factor), equivalent physical parameters (density, heat capacity, and thermal conductivity), and visible-range absorptivity of the model were established and analyzed. All the above-mentioned parameters exhibited extreme values, which enhanced the visible-range absorptivity. The accuracy of the model was verified experimentally. The following conclusions were drawn based on the results obtained.

- (1) The visible-range absorptivity of the structure was quadratically related to the filling factor. The filling factor affects the motion path of incident photons and, thus, the efficiency of capturing photons. An extremely sparse or dense distribution of nanochains leads to a reduction in the model absorptivity.
- (2) The visible-range absorptivity of the modeled structure is exponentially related to its thickness. The critical thickness of the Gaussian model is much smaller than those of the uniform and Cauchy models because of the higher photon-capturing efficiency of the former. The maximum visible-range absorptivities of the three models are similar,

indicating that the aggregate form of the nanochains has a negligible effect on the surface reflection of the model.

- (3) The visible-range absorptivity of the modeled structure is quadratically related to its equivalent density. The Al nanochain aggregate structure is more suitable as an optical absorber that exhibits a low density and high visible-range absorption.
- (4) The visible-range absorptivity of the modeled structure is also related to its equivalent thermal conductivity. The Au nanochain aggregate structure allows for efficient optical absorption and fast heat dissipation. Meanwhile, the Cr nanoaggregate structure allows for efficient energy capture and accumulation.
- (5) Finally, the visible-range absorptivity of the modeled structure is quadratically related to its equivalent volumetric heat capacity. The Al nanoaggregate structure is more suitable as an optical absorber with a low volumetric heat capacity and high-sensitivity time-domain temperature response.

Actual nanochain aggregate samples were fabricated by reducing the kinetic energy of the deposited Al nanoparticle clusters. The visible-range spectral absorption curves of the fabricated samples were measured using a Fourier spectrometer. The Spearman correlation coefficients for the calculated spectral absorption curves and those measured experimentally were higher than 0.82; this confirmed the accuracy of the model. In addition, the relative errors between the calculated visible-range absorptivities and the measured values were less than 0.3%; this confirmed that the model is suitable for calculating the absorptivity.

Author Contributions: Conceptualization, Z.L.; Funding acquisition, Y.G.; Investigation, T.Z. and Q.S.; Methodology, T.Z. and Y.G.; Project administration, Y.G. and R.S.; Resources, Y.G. and R.S.; Software, T.Z.; Validation, T.Z. and Q.S.; Writing—original draft, T.Z.; Writing—review and editing, Y.G. and Z.L. All authors have read and agreed to the published version of the manuscript.

Funding: This research was funded by China Postdoctoral Science Foundation, grant number 2020TQ0036.

Institutional Review Board Statement: Not applicable.

Informed Consent Statement: Not applicable.

Data Availability Statement: Not applicable.

Acknowledgments: The authors thank Yao Zhaozhao for her help with this study.

Conflicts of Interest: The authors declare no conflict of interest.

References

- More-Chevalier, J.; Yudin, P.V.; Cibert, C.; Bednyakov, P.; Lančok, J. Black aluminum-coated Pt/Pb (Zr_{0.56}Ti_{0.44}) O₃/Pt thin film structures for pyroelectric energy harvesting from a light source. *J. Appl. Phys.* **2019**, *126*, 214501. [CrossRef]
- Li, N.; Yang, D.J.; Shao, Y.; Liu, Y.; Tang, J.; Yang, L.; Sun, T.; Zhou, W.; Liu, H.; Xue, G. Nanostructured Black Aluminum Prepared by Laser Direct Writing as a High-Performance Plasmonic Absorber for Photothermal/ Electric Conversion. *ACS Appl. Mater. Interfaces* **2021**, *13*, 4305–4315. [CrossRef]
- Kwon, N.; Oh, H.; Kim, R.; Sinha, A.; Kim, J.; Shin, J.; Chon, J.W.M.; Lim, B. Direct Chemical Synthesis of Plasmonic Black Colloidal Gold Superparticles with Broadband Absorption Properties. *Nano. Lett.* **2018**, *18*, 5927–5932. [CrossRef] [PubMed]
- Georgieva, E.; Priestley, K.J.; Dunn, B.; Cageao, R.; Barki, A.; Osmundsen, J.; Turczynski, C.; Abedin, N. Radiation budget instrument (RBI) for JPSS-2. In Proceedings of the Conference on Characterization and Radiometric Calibration for Remote Sensing, Logan, UT, USA, 24 August 2015.
- Xu, C.; Liu, D.; Zhou, L.; Shi, Q.; Gao, Y.; Wang, X.; Li, Z. Thermodynamics characteristics of MEMS infrared thin film. *Opt. Express.* **2019**, *27*, 32779–32788. [CrossRef] [PubMed]
- Wang, X.; Li, D.F.; Li, Z.; Yang, S.H.; Zhang, J.Y.; Zhao, Q. Performance improvement of an infrared scene generation chip by in-plane microstructures. *Opt. Express.* **2020**, *28*, 26807–26822. [CrossRef] [PubMed]
- Arinze, E.; Qiu, B.; Nyirjesy, G.; Thon, S.M. Plasmonic Nanoparticle Enhancement of Solution-Processed Solar Cells: Practical Limits and Opportunities. *ACS. Photonics* **2016**, *3*, 158–173. [CrossRef]
- Liu, C.; Zhang, D.; Liu, Y.; Wu, D.; Chen, L.; Ma, R.; Yu, Z.; Yu, L.; Ye, H. Numerical Study of an Efficient Solar Absorber Consisting of Metal Nanoparticles. *Nanoscale. Res. Lett.* **2017**, *12*, 601. [CrossRef]
- Mascaretti, L.; Schirato, A.; Fornasiero, P.; Boltasseva, A.; Shalae, V.M.; Alabastri, A.; Naldoni, A. Challenges and prospects of plasmonic metasurfaces for photothermal catalysis. *Nanophotonics* **2022**, *11*, 3035–3056. [CrossRef]

10. Giorgianni, F.; Vicario, C.; Shalaby, M.; Tenuzzo, L.D.; Marcelli, A.; Zhang, T.; Zhao, K.; Chen, Y.; Hauri, C.; Lupi, S. High-Efficiency and Low Distortion Photoacoustic Effect in 3D Graphene Sponge. *Adv. Funct. Mater.* **2017**, *28*, 1702652. [CrossRef]
11. Morales-Luna, G.; Morales-Luna, M. Effective medium theory to the description of plasmonic resonances: Role of Au and Ti nanoparticles embedded in MoO₃ thin films. *Sci. Rep.* **2020**, *10*, 1–12. [CrossRef]
12. Schmitt, A.; Odrizola, G.; Moncho-Jordá, A.; Callejas-Fernández, J.; Martínez-García, R.; Hidalgo-Álvarez, R. Multiple contact kernel for diffusionlike aggregation. *Phys. Rev. E* **2000**, *62*, 8335–8343. [CrossRef]
13. Munir, N.B.; Mahan, J.R.; Priestley, K.J. First-principle model for the directional spectral absorptivity of gold-black in the near infrared. *J. Opt. Soc. Am. A* **2019**, *36*, 1675–1689. [CrossRef] [PubMed]
14. Witten, J.T.A.; Sander, L.M. Diffusion-Limited Aggregation, a Kinetic Critical Phenomenon. *Phys. Rev. Lett.* **1981**, *47*, 1400–1403. [CrossRef]
15. Jensen, P.; Barabási, A.L.; Larralde, H.; Havlin, S.; Stanley, H.E. Connectivity of diffusing particles continually deposited on a surface: Relation to LECBD experiments. *Physica A* **1994**, *207*, 219–277. [CrossRef]
16. Jensen, P.; Barabási, A.L.; Larralde, H.; Havlin, S.; Stanley, H.E. Controlling nanostructures. *Nature* **1994**, *368*, 22. [CrossRef]
17. Atteia, F.; Rouzo, J.; Denaix, L.; Duché, D.; Berginc, G.; Simon, J.J.; Escoubas, L. Morphologies and optical properties of black silicon by room temperature reactive ion etching. *Mater. Res. Bull.* **2020**, *131*, 110973. [CrossRef]
18. Chen, C.; Youngblood, N.; Peng, R.; Yoo, D.; Mohr, A.D.; Johnson, W.T.; Oh, S.H.; Li, M. Three-Dimensional Integration of Black Phosphorus Photodetector with Silicon Photonics and Nanoplasmonics. *Nano. Lett.* **2017**, *17*, 985–991. [CrossRef]
19. Ryu, Y.; Kim, C.; Ahn, J.; Urbas, A.M.; Park, W.; Kim, K. Material-Versatile Ultrabroadband Light Absorber with Self-Aggregated Multiscale Funnel Structures. *ACS. Appl. Mater. Interfaces* **2018**, *10*, 29884–29892. [CrossRef]
20. Deng, G.; Dereshgi, S.A.; Song, X.; Aydin, K. Polarization dependent, plasmon-enhanced infrared transmission through gold nanoslits on monolayer black phosphorus. *J. Opt. Soc. Am. B. Opt. Phys* **2019**, *36*, F109–F116. [CrossRef]
21. Palik, E.D. *Handbook of Optical Constants of Solids*; Academic Press: New York, NY, USA, 1998.
22. Boomsma, K.; Poulikakos, D. On the effective thermal conductivity of a three-dimensionally structured fluid-saturated metal foam. *Int. J. Heat. Mass. Transf.* **2001**, *44*, 827–836. [CrossRef]
23. Xin, G.Z.; Chen, D.Q.; Cai, Y.; Huang, Y.; Wang, L.; Bai, T.Z.; Wang, L.X. Direct observation of widely tunable mid-infrared emission of graphene foam induced by modulated laser diode light. *Carbon* **2021**, *179*, 486–492. [CrossRef]

Article

Effect of the Addition of Steel Fibers on the Bonding Interface and Tensile Properties of Explosion-Welded 2A12 Aluminum Alloy and SS-304 Steel

Yao Chen ¹, Yonghong Gao ^{1,*}, Chuanxiang Guo ¹, Yanping Guo ², Zhijun Guo ³, Yingbin Liu ¹ and Tiansheng Liu ¹

¹ School of Environment and Safety Engineering, North University of China, Taiyuan 030051, China

² Department of Environmental and Safety Engineering, Taiyuan Institute of Technology, Taiyuan 030008, China

³ Shanxi Fenxi Heavy Industry Co., Ltd., Taiyuan 030027, China

* Correspondence: gyh54gyh@163.com

Abstract: First of all, the explosion-welding method was adopted to prepare steel fiber-reinforced steel-aluminum composite plates. Secondly, the smooth particle hydrodynamic (SPH) method was used to investigate the effect of introducing steel fibers to a vortex region created at the bonding interface of the steel-aluminum composite plate. Thirdly, the following conclusions were drawn through an analysis of the vortex region with the assistance of scanning electron microscopy and energy-dispersive X-ray spectroscopy. A brittle intermetallic compound FeAl was produced in the vortex region in an environment characterized by high temperature, high pressure, and high strain rate, resulting in cracks, holes and pores. In addition, the hardness of the vortex area was less than the estimated value, which is mainly because the main element in the vortex area was 2A12 aluminum with low hardness, and there were cracks, holes, pores and other defects that caused hardness reduction. Although the addition of steel fibers caused defects at the bond interface, the addition of steel fibers was effective in improving the tensile resistance performance of steel-aluminum composite panels to a certain extent. In addition, the larger the fiber diameter, the more significant the increase in tensile resistance.

Keywords: steel fiber; explosive welding; numerical simulation; bonding interface

Citation: Chen, Y.; Gao, Y.; Guo, C.; Guo, Y.; Guo, Z.; Liu, Y.; Liu, T. Effect of the Addition of Steel Fibers on the Bonding Interface and Tensile Properties of Explosion-Welded 2A12 Aluminum Alloy and SS-304 Steel. *Materials* **2023**, *16*, 116. <https://doi.org/10.3390/ma16010116>

Academic Editor: Matthias Bönisch

Received: 12 November 2022

Revised: 14 December 2022

Accepted: 20 December 2022

Published: 22 December 2022



Copyright: © 2022 by the authors. Licensee MDPI, Basel, Switzerland. This article is an open access article distributed under the terms and conditions of the Creative Commons Attribution (CC BY) license (<https://creativecommons.org/licenses/by/4.0/>).

1. Introduction

With the rapid development of industry, more and more regions need to produce special equipment by machining high-quality metals into sheets with excellent anticorrosion, antioxidation, and mechanical properties. If all these devices are made of high-quality metals, their costs will be inevitably high, resulting in unnecessary waste. Therefore, replacing high-quality metals with bimetallic materials is the most ideal solution. SS-304 stainless steel is characterized by high strength, impact resistance, reliable performance, and good welding and riveting performance, but it has a lot of shortcomings, such as high maintenance cost, heaviness, and large production energy consumption. However, 2A12 aluminum material has a lot of advantages, including lightness, good electrical conductivity, ease of extension, corrosion resistance, and few toxic and side effects. Bimetallic materials have the advantages of two metal components, so the application of steel-aluminum composite plates can reduce the mass of SS-304 stainless steel and improve its corrosion resistance. Explosive welding is a solid-phase welding method, which can be used for the welding of double-layer or multilayer composite plates of the same or different metals [1–6]. Compared with traditional diffusion welding [7,8], light welding [9,10], magnetic pulse welding [11,12], and hot rolling welding [13,14], the explosive welding method still has very good welding quality in the case of large differences in the points or mechanical properties of the welded metal, so it is extensively used in metal welding. Because of its high tensile strength, low price, and outstanding corrosion resistance, steel fiber is widely

used to reinforce concrete and improve its protective performance. In this paper, explosive welding was used to produce a new fiber-reinforced steel aluminum composite plate by combining the advantages of SS-304 stainless steel, 2A12 aluminum, and steel fiber.

Extensive studies have been conducted on steel-aluminum composite plates, with outstanding achievements. In 1983, Kotov V A studied [15] unidirectional fiber-reinforced composites composed of steel wires based on Amr6 aluminum alloy, and the results revealed that under uniaxial or biaxial loads, the strength of the fiber-reinforced composites was mostly dependent on the bonding strength of the wire and the base plate, as well as the internal geometric installation, and when the load was along the wire, the effect was relatively obvious. Therefore, fiber-reinforced composites and tubular products prepared by explosive welding have sufficient strength under various loads. Zhou et al. [16] successfully prepared steel fiber-reinforced composite plates and used numerical simulation and experimental methods to study the impact of the addition of steel fiber on the antipenetration performance of the composite plate. It was concluded that the addition of the fiber-reinforced phase was improved the antipenetration performance of the composite target plate, and the reduced fiber distribution spacing and orthogonal arrangement distribution were helpful in improving the antipenetration performance of the target plate. Wang et al. [17] applied numerical simulation and experimental methods to study the impact of carbon fiber-reinforced polymer laminates under high-speed impact. The results showed that within a certain impact velocity range, carbon fiber composite laminates had the advantage of replacing metal plates to resist high-speed impact. Mahfuz et al. [18] comprehensively studied the antipenetration performance of multilayer ceramic–rubber–glass fiber composite target plates against high-velocity projectiles by numerical simulation and hydrogen gun experiments, and discussed the failure mode of the target plate at ballistic limit velocity. The addition of fiber can significantly increase the difficulty of explosive welding, so the experiment needed to calculate the dynamic parameters of explosive welding in advance to guarantee the rationality of the parameters.

The effects of steel fiber with different diameters on the interface and mechanical properties of steel-aluminum composite sheets were studied. In the early stage, the SPH method in Autodyn software was used to study the influence of high-temperature and high-pressure environments on steel fiber and composite interface to simulate the explosive welding experiment. Later, scanning electron microscopy and energy-dispersive spectroscopy were adopted to systematically study the changes in the bonding interface and the formation of intermetallic compounds after adding steel fibers. The effect of the addition of steel fiber on the hardness of the base plate was further studied by microhardness tests. Finally, a universal testing machine was used to verify the impact of the addition of steel fibers on the tensile properties of steel-aluminum composite plates.

2. Materials and Methods

Ansys/Autodyn software was used to carry out simulation experiments on SS-304 and 2A12 aluminum composite plates prepared by explosive welding. The SPH method can extensively simulate large deformation problems such as disintegration, fragmentation, solid spalling, and brittle fracture of continuum structures and avoid algorithm coupling, so it is very suitable for numerical simulation of explosive welding of multilayer metal plates [19,20]. Therefore, the SPH method can simulate the interaction of jet particles in the preparation of steel fiber-reinforced steel-aluminum composite plates by explosive welding and provide reasonable and effective experimental parameters for the following explosive welding experiment. As the contrast between the plate thickness and length width was large, a two-dimensional plane model was constructed. To save the calculation time of the model, the length of the base plate, aluminum composite plate, and explosive was all set to 40 mm. The particle size was set to 10 μm , and a total of 1.1815 million particles were generated to obtain accurate numerical results. The specific model is shown in Figure 1, where the density of the ANFO explosive is 0.6821 g/cm^3 , the explosive height is 20 mm, and the detonation velocity is 2430 m/s. The specific parameters of ANFO are shown in Table 1.

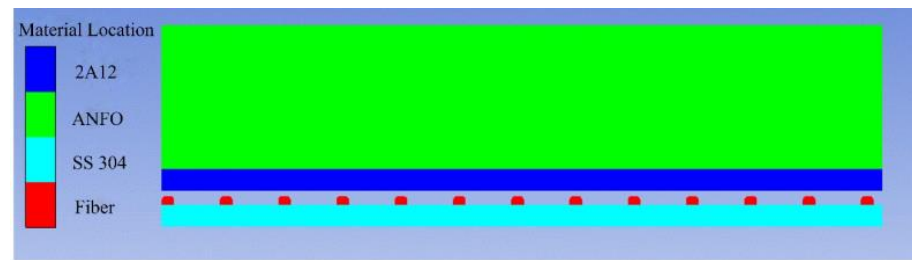


Figure 1. Explosive welding model.

Table 1. Performance parameters of ANFO.

Material	Density $\rho/(\text{g cm}^{-3})$	Detonation Velocity $D/(\text{m s}^{-1})$	Specific Internal Energy $E_0/(\text{kg cm}^{-3})$	Detonation Pressure /MPa	Heat Capacity Ratio
ANFO	0.681	2430	2.484	1160	2.5

Experimental Procedure

Explosive welding mainly includes: directly in the atmosphere, in water, and in rough vacuum. Compared with explosive welding experiments in low vacuum and water, explosive welding experiments in the air have a simpler assembly process, use lower detonation velocity of explosives, and are safer and more efficient. Therefore, in this paper, explosive welding experiments in the air [21–23] were selected. As shown in Figure 2, taking the SS-304 stainless steel with a size of $200 \text{ mm} \times 300 \text{ mm} \times 1 \text{ mm}$ as the base plate, and the 2A12 aluminum plate with a size of $200 \text{ mm} \times 300 \text{ mm} \times 1 \text{ mm}$ as the flyer plate, a steel fiber was evenly wound on the base plate every 5 mm to ensure that the length of the steel fiber was the same as that of the base plate, and the standoff distance between the base plate and cladding plate was 4 mm. Then, the base plate, flyer plate, and steel fiber were welded together by explosive welding. The performance parameters of steel and aluminum are shown in Table 2. S20910 is the material parameter of steel fiber and SS 304 is the material parameter of the base plate. In this experiment, the diameter of the steel fibers needs to be strictly controlled and the fibers are exposed to extrusion and extreme thermomechanical conditions in the welding process. The mechanical properties of the fibers therefore need to be good and the hot drawing process produces steel fibers of a more uniform size and high precision. Because the working temperature is above the recrystallization temperature, the resulting process hardening phenomenon is eliminated by recrystallization, the internal stress of the steel fibers is also eliminated, the toughness and plasticity will be better, so that the welded composite plate can better reflect the impact of the fibers on the composite plate. While cold rolled out of the steel plate as the base plate of the explosion welding, it ensures the strength and hardness of the base plate, in line with the experimental design. SS 304 steel as the base plate ensures the strength and hardness of the base plate, in line with the experimental design. The abovementioned metal materials were purchased by the teachers of the research group in Shenzhen Hongwang Mold Co., Ltd., Guangzhou, China.

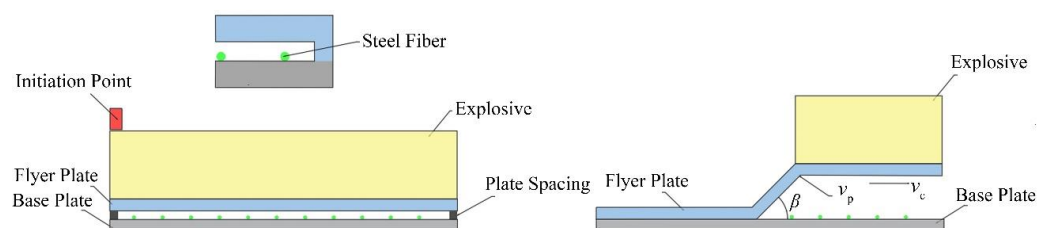


Figure 2. Welding diagram.

Table 2. Performance parameters of metal materials [24,25].

Material	Density $\rho/(\text{g}\cdot\text{cm}^{-3})$	Yield Strength σ_b/MPa	Vickers Hardness /Hv	Wave Velocity $C_0/(\text{m}\cdot\text{s}^{-1})$	Melting Point T/K	Specific Heat C_p / $(\text{J}\cdot\text{kg}^{-1}\cdot\text{K}^{-1})$	Thermal Conductivity $K/(\text{W}\cdot\text{m}^{-1}\cdot\text{K}^{-1})$
2A12 aluminum	2.79	354	110	5328	933	940	237
S20910 steel	7.88	380	201	4569	1450	476	14
SS-304 steel	7.93	515	200	5790	1400	500	21.5

Explosive welding aims to connect weldments by using the impact force generated by the explosion to cause the rapid collision of the weldments. The three most critical parameters are the impact velocity of the composite plate v_p , the collision angle β , and the moving speed of the collision point v_c . The moving speed of the collision point is equal to the detonation velocity of the explosive. Using 2# rock ammonium nitrate explosive, the parallel explosive welding experiment was used, satisfying the following relationship [26]:

$$R = \frac{\rho_e h_e}{\rho_f h_f} \quad (1)$$

$$R = \frac{C}{m} \quad (2)$$

$$M = C \cdot S_e \quad (3)$$

$$v_p = \sqrt{2E} \left[\frac{(1 + 2/R)^3 + 1}{6(1 + 1/R)} + \frac{1}{R} \right]^{-\frac{1}{2}} \quad (4)$$

$$\sqrt{2E} = \frac{v_d}{3.08} \quad (5)$$

$$v_p = 2v_d \sin \frac{\beta}{2} \quad (6)$$

where v_p is the impact velocity; $2E$ is the Gurney energy; m is the mass of the flyer plate; R is the explosion ratio; ρ_e is the density of the explosive; ρ_f is the density of the flyer plate; h_e is the height of the explosive; h_f is the thickness of the flyer plate; C is the explosive mass per unit area; S_e is the explosive area, which is the same as the surface area of the flyer plate; M is the explosive payload; $v_d = v_c$ equals the detonation velocity of the explosive. Therefore, the detonation velocity is 2400 m/s [27]. $v_p = 668$ m/s, $\beta = 17.5^\circ$.

3. Results and Discussion

3.1. Interface Evolution Mechanism

The bonding of explosive welding is divided into three categories: (1) direct bonding of metals; (2) forming a uniform and continuous melting layer; and (3) undulate bonding, which is the most common form. In undulate bonding, because the molten material at the bonding interface is retained in the vortex and is periodically and discontinuously separated, when there is an external load, the microcrack source generated by the interface defects in the melting tank is not easily propagated. Therefore, the most ideal method is tiny undulate bonding. Many experiments and studies have shown that to realize high-quality explosive welding, the following three requirements should be met: (1) undulate bonding can be obtained under certain collision conditions, that is, the impact velocity v_p and the impact angle β meet the explosive welding window; (2) there must be jet formation when welding, so that the interface can be self-cleaning, exposing the fresh surface; and (3) a fine and uniform corrugated interface or a flat interface with sufficient strength is formed. Finally, to better understand this problem, SPH simulation was introduced to study the detailed evolution process of the steel-aluminum interface.

Figure 3a–c shows the evolution mechanism of the influence of steel fibers on jet particles. As shown in Figure 3a, during the welding process, the incident jet consisted of two layers on the surface. These particles ejected from the flyer plate moved obliquely downwards and acted on the base plate surface, thereby compressing the base plate, causing it to form a depression, forming a corresponding bulge on the base plate surface, and generating a forward jet. The incident jet could also remove oxides and other impurities on the surface, and help to establish ideal welding conditions under the circumstance of original clean contact [28]. However, after the detonation of the explosive, the explosive product formed a high-voltage pulse load, which directly acted on the flyer plate. Then, the flyer plate accelerated and reached a speed of several hundred meters/second in a few microseconds, starting from the starting end, collided with the base plate in turn, and formed a certain angle. At this time, the fixed included angle formed between the flyer plate, the steel fiber, and the base plate prevented the jet from continuing to act on the surface of the base plate, so that a large number of particles converged on the side of the steel fiber, as shown in Figure 3b. As the steel fiber spacing was 5 mm, when the jet was blocked, the new jet continued to generate. According to Figure 3c, the process of the jet from being blocked to being regenerated was repeated. Figure 3d is a schematic diagram for simulating jet particles without steel fibers. By comparing with Figure 3a,c, both the number of jet particles and the distance of propagation in Figure 3d were much larger than those in Figure 3a,c. It should be emphasized that Yang et al. [29] studied the evolution mechanism of the Ag–Fe welding interface by SPH simulation. The results showed that the movement direction of these jet particles was the main reason for the formation of the undulating interface, which explained why the undulating structure formed at the interface of the steel–aluminum composite plate with a steel fiber diameter of 0.5 mm in Figure 4a was more uniform than that without steel fibers in Figure 4b, and the wavelength and wave height in Figure 4b were greater than those in Figure 4a.

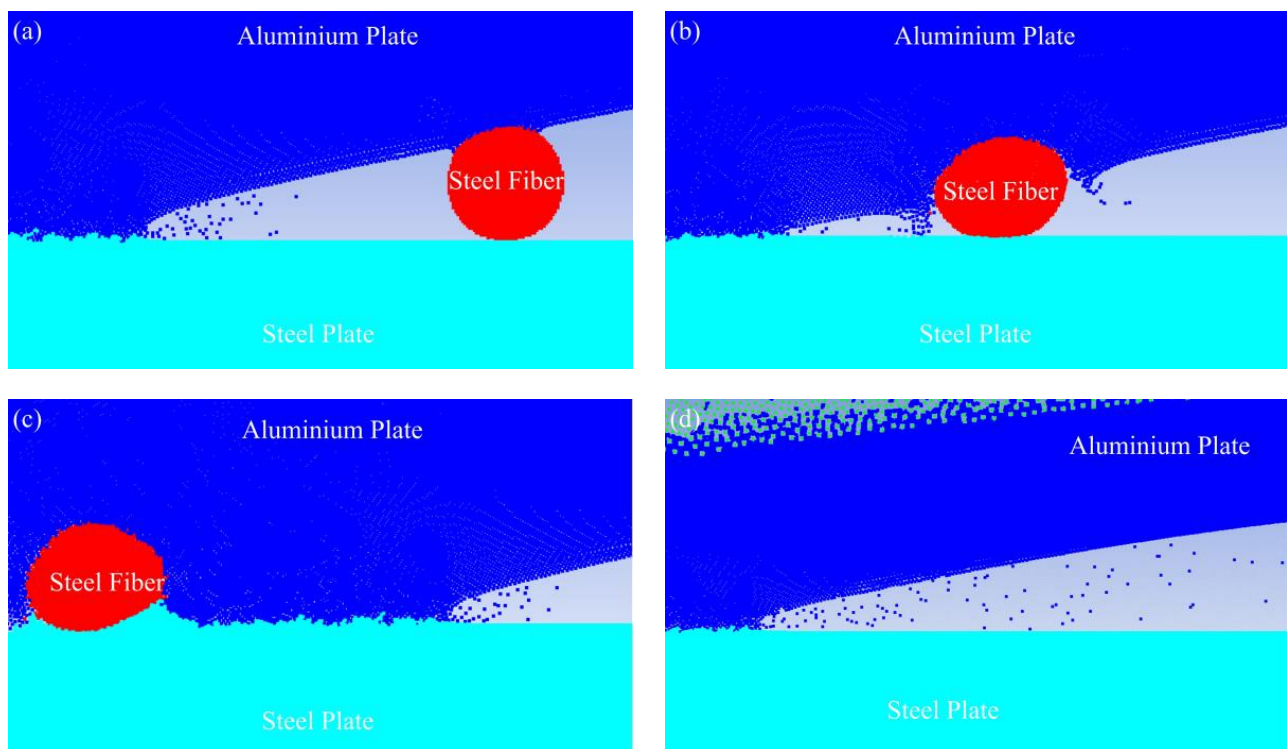


Figure 3. Evolution mechanism of welding interface: (a) time 3.5 μ s; (b) time 4.0 μ s; (c) time 4.5 μ s; (d) time 4.0 μ s.

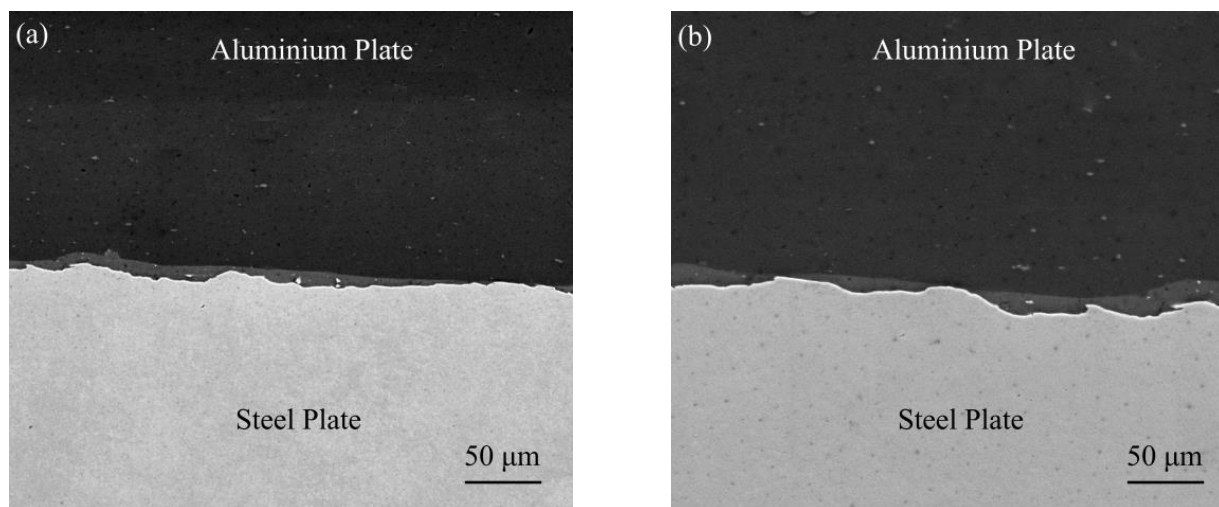


Figure 4. SEM images of explosion welded interfaces: (a) for steel fiber diameter 0.5 mm; (b) without steel fiber.

The thermodynamic state of the explosive welding process was simulated by the SPH method to better understand the interface evolution. Figure 5 shows the cross-sections of steel fibers with diameters of 0.5 mm, 0.35 mm, and 0.25 mm under an optical microscope. In the figure, three groups of steel fibers all showed a deformation to varying degrees, but all maintained a complete fiber structure. Among them, the addition of steel fibers with a diameter of 0.5 mm produced the most obvious vortex area and cracks, so it was taken as an example to analyze the impact of the addition of steel fibers on the bonding interface of the composite plate by combining with numerical simulation. Figure 6 is a schematic diagram of the thermodynamic state during the explosive welding process. As shown in Figure 6a, when the jet particles filled the unilateral side of the steel fiber, a high-temperature and high-pressure environment was formed, with a pressure of up to 10 GPa. For the three materials, the pressure was much greater than the yield strength of 235 MPa, so the steel fiber directly contacting the jet particles would behave as a fluid and undergo a strong plastic deformation. Figure 6b shows the temperature field. A high-temperature region was constituted by the molten jet particles on the steel fiber side, and combined with the uneven thin melt formed by the molten jet particles at the interface, a lot of heat accumulated in these two areas because time was not enough to spread heat. Figure 6c shows the maximum plastic deformation on one side of the steel fiber, where the maximum deformation occurred on the steel fiber side blocking the jet advance, with a maximum strain rate of 5. Figure 6d shows that the ultrahigh strain rate occurred at the steel fiber surface and the welding interface was up to 900/s. To sum up, the explosive welding process occurred in an extreme environment with high temperature, high pressure, large strain, and superhigh strain rate, and this extreme thermodynamic state was closely related to the bonding interface. These high-temperature molten particles driven by the kinetic energy of the composite plate were correlated with the combined effects of the two materials, including plastic deformation, friction, shear, and stirring [30,31]. Since the time was not enough to reduce the large-scale heat, these molten particles could not be rapidly solidified. Then, the residual velocity forced the molten particles on one side of the steel fiber to stir and mix strongly, and finally a vortex region with cracks was formed, as shown in the yellow region in Figure 7b. Yang, Zhang, Bazarnik et al. [32–34] proved that the formation of the vortex structure might be due to the good ductility and high density of steel. Figure 7a shows the cross-section of the steel fiber-reinforced steel-aluminum composite plate with a steel fiber diameter of 0.5 mm. For the shape and cracks in the vortex region in the figure, by comparing it to Figure 7b, it was found that the numerical simulation results were in good agreement with the experimental observations.

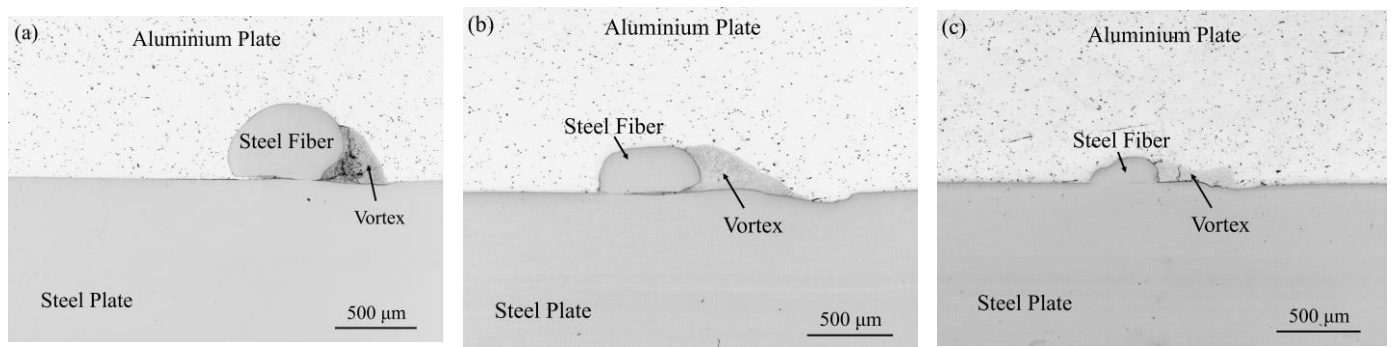


Figure 5. Schematic cross-section of steel fibers with different diameters: (a) steel fiber diameter: 0.5 mm; (b) steel fiber diameter: 0.35 mm; (c) steel fiber diameter: 0.25 mm.

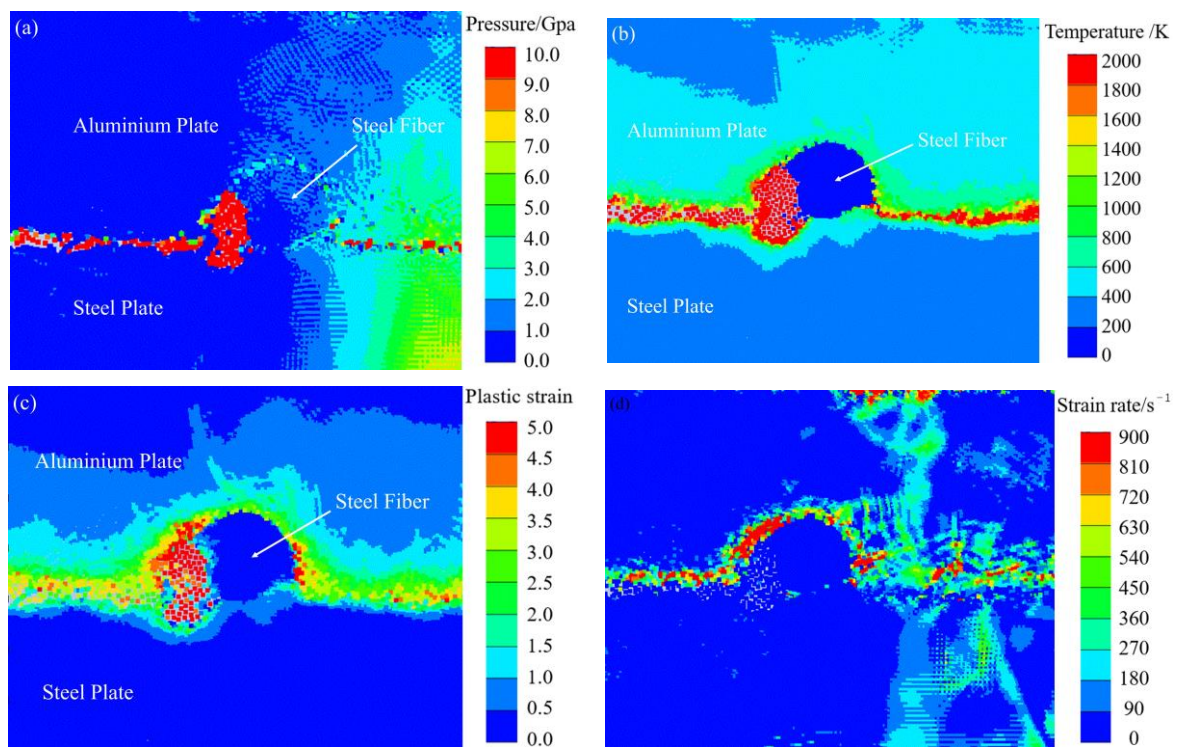


Figure 6. Thermodynamic state of bonding interface during explosive welding: (a) pressure; (b) temperature; (c) plastic strain; (d) strain rate.

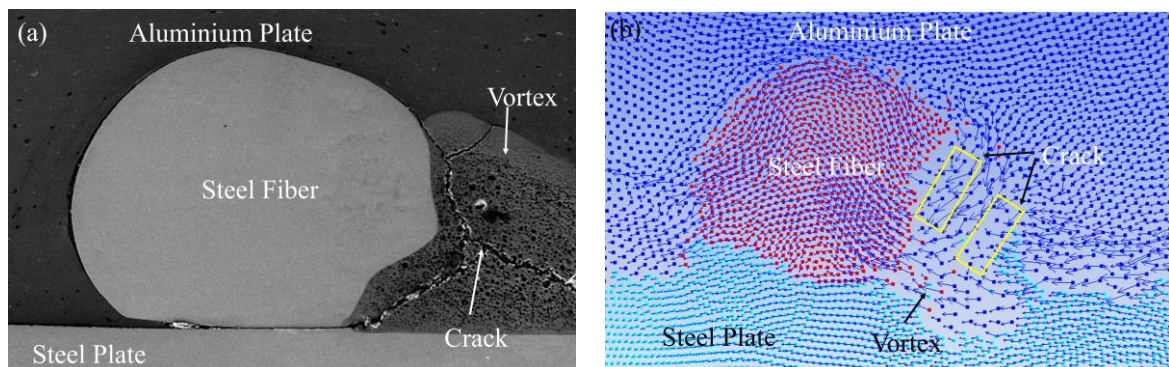


Figure 7. SEM and simulation results of vortex region: (a) SEM of steel fiber with a diameter of 0.5 mm; (b) numerical simulation of steel fiber diameter of 0.5 mm.

3.2. Energy Spectrum Analysis

To further analyze the distribution of elements in the unilateral vortex area of steel fiber, 8 points were selected for EDS point scanning in this area, as shown in Figure 8. The percentage of iron and aluminum is shown in Table 3. The first point and the second points were in the iron base plate, and the main components were 66.2% iron and 64.8% iron. The seventh and eighth points were in the aluminum base plate, and the main components were 88.6% aluminum, 1.3% iron, 86.9% aluminum, and 0.9% iron, respectively. There was element diffusion of the iron element in the aluminum base plate, but the diffusion of the aluminum element in the iron base plate near the interface was not obvious. The elements measured near the iron base plate were 55% aluminum, 14.4% iron, 32.3% aluminum, and 10% iron, while the elements near points 5 and 6 were 71.8% aluminum, 9.7% iron, 73.9% aluminum, and 9.3% iron. The results revealed that the elements in the vortex region were mainly aluminum and iron, and the closer to the middle region of the vortex, the higher the iron content. The main reason is that under the circumstance of high temperature and high pressure, the molten iron and molten aluminum would occur in a mutual melting phenomenon to form an iron aluminum alloy, and with the gradual decrease in temperature and pressure, the proportion of iron and aluminum in the alloy gradually changed until the aluminum and iron separated. However, because the cooling rate was too fast, the iron element in the middle of the molten region had been solidified before it was separated, so the content of iron element near the bonding interface was less than that in the middle of the vortex, which also indirectly confirmed the research results obtained by Zeng [35] and Zhang et al. [36]: intermetallic compounds were mainly formed in the vortex region on the base plate side and rarely formed on other sides of the interface. Wu Tong et al. [37,38] found that a large number of brittle intermetallic compounds produced during explosive welding were the main causes of cracking at the bonding interface. These intermetallic compounds formed cracks, pores, and voids in the vortex region, resulting in a decrease in the mechanical properties of metal composites [39–41]. To explore the types of metal compounds in the vortex region, EDS scanning was performed on cracks, holes, and air pores in the vortex region, and the results are shown in Figure 9. The four groups of dotted lines in Figure 9 are the line scanning results corresponding to the SEM images of pores and air holes in the vortex region. By comparing the SEM and EDS results in the figure, it was found that the content of iron and aluminum in the EDS scanning results corresponding to cracks, holes, and air pores decreased at the same time, while other elements increased. Therefore, the metal compound formed in the vortex region might be FeAl.

To further explore the impact of the addition of steel fibers on the interface of the steel-aluminum composite plate prepared by explosive welding, EDS scanning was carried out on the interface of the steel-aluminum composite plate without steel fibers and the steel-aluminum composite plate with a steel fiber diameter of 0.5 mm, and the results are shown in Figure 10a,d, respectively, forming an obvious contrast. There was a gradual element change in Figure 10a, transiting from iron element to aluminum element. The mixing amount of elements in the transition zone reached about 500, and the content of aluminum and iron elements was 41.6% and 34.3%, respectively, as shown in Figure 10c. In Figure 10d, the transition from iron to aluminum was very fast. The mixing amount of elements in the transition zone was about 300, and the aluminum and iron contents were 64.2% and 17.5%, respectively, as shown in Figure 10f. The element transition in the group without steel fibers was more obvious and the mixing amount of the two elements in the transition zone was larger than in the steel fiber group. Studies have shown that the formation of the transition zone of chemical elements was caused by the strong stirring of jet particles, and the diffusion rate increased significantly with the increase in the defect density caused by plastic deformation [42–44]. Therefore, the simulation results and experimental results also simultaneously verified that the addition of steel fiber blocked the continuous action of jet particles on the base plate surface and affected the element transition at the bonding interface of the composite plate.

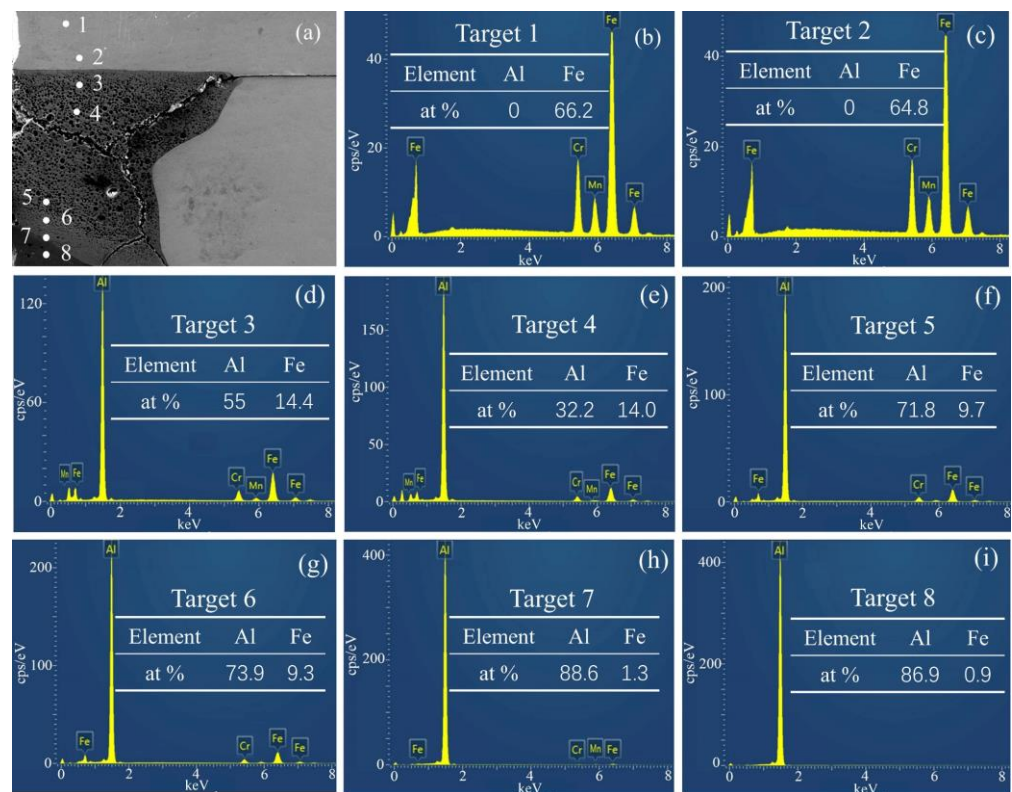


Figure 8. Position points and numerical results of welding interface analyzed by EDS in SEM image: (a) Schematic diagram of SEM positions of 8 points; (b) Scan result of point 1; (c) Scan result of point 2; (d) Scan result of point 3; (e) Scan result of point 4; (f) Scan result of point 5; (g) Scan result of point 6; (h) Scan result of point 7; (i) Scan result of point 8.

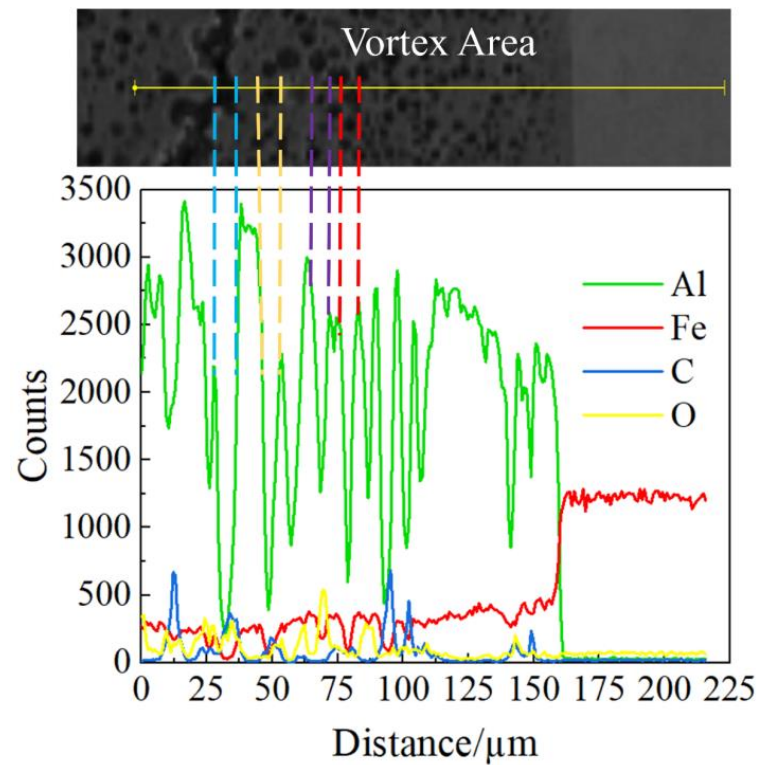


Figure 9. SEM scanning and EDS analysis of vortex, crack and hole.

Table 3. Iron and aluminum contents at 8 EDS points.

Element	1	2	3	4	5	6	7	8
iron	66.2%	64.8%	14.4%	10%	9.7%	9.3%	1.3%	0.9%
aluminum	0	0	55%	32.2%	71.8%	73.9%	88.6%	86.9%

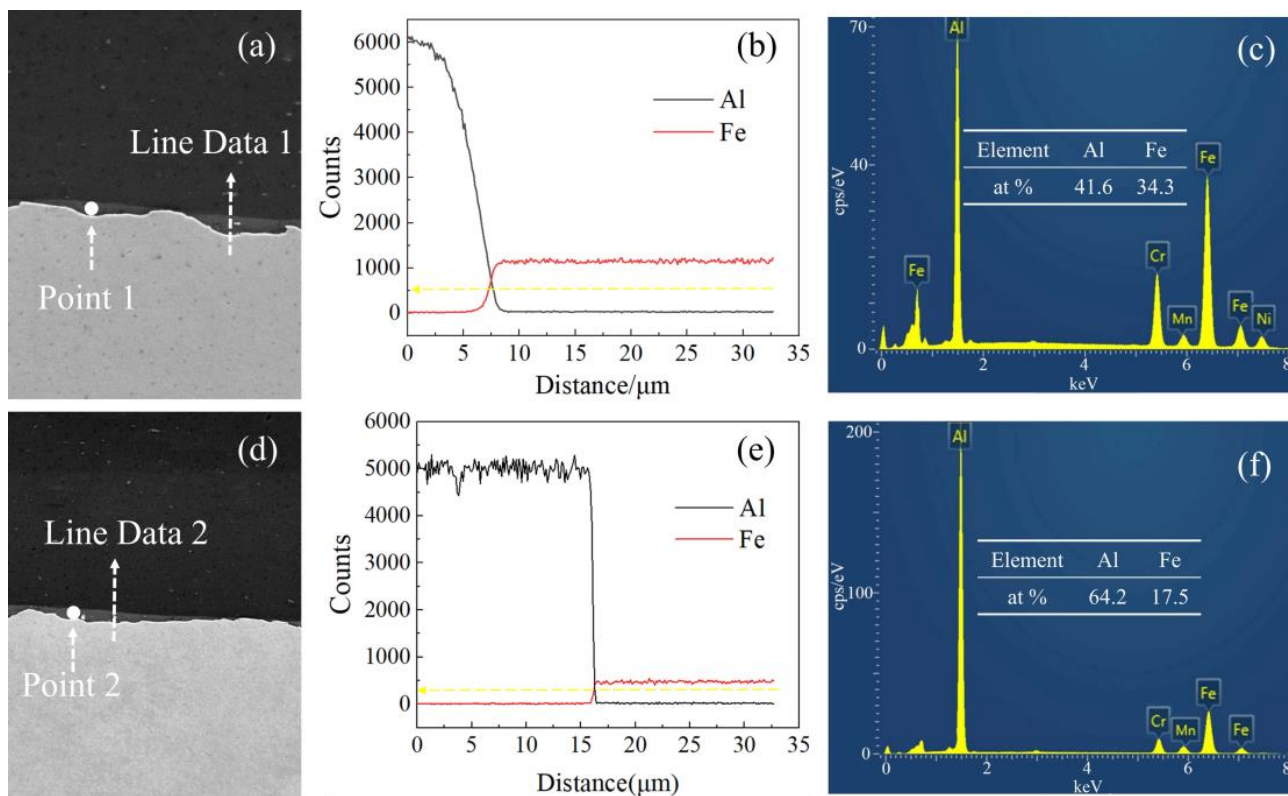


Figure 10. SEM and EDS results of the bonding interface of steel-aluminum composite plate: (a) no bonding interface of steel fiber; (b) figure a line scan results; (c) figure a point scan results; (d) bonding interface with steel fiber diameter of 0.5 mm; (e) figure d line scan results; (f) figure d point scan results.

3.3. Microhardness Analysis

To explore the micromechanical properties of the steel fiber-reinforced steel-aluminum composite plate, a microhardness test of the cross-section of the steel-aluminum composite plate with a steel fiber diameter of 0.5 mm was carried out. The corresponding test area was divided into five parts, as shown in Figure 11a. Among them, Zone 1 is the microhardness test area of the cross-section of the 2A12 aluminum, Zone 2 is the microhardness test area of the interface between the vortex region and 2A12 aluminum, Zone 3 is the microhardness test area of the vortex region, Zone 4 is the microhardness test area of the interface between vortex region and SS-304 stainless steel, and Zone 5 is the microhardness test area of SS-304 stainless steel. Figure 11b shows the numerical results of the microhardness values of the five zones in Figure 11a. The highest hardness was 419 Hv for the SS-304 stainless steel base plate, the lowest hardness was 126 Hv for 2A12 aluminum, the interface between the vortex region and 2A12 aluminum was 190 Hv, the interface between the vortex region and SS-304 stainless steel was 381 Hv, and the vortex region was 276 Hv. According to previous studies, the highest hardness of the composite plate prepared by explosive welding should be in the intermetallic compound layer [45,46], that is, the vortex region. However, the experimental data obtained in this paper deviated from the previous conclusions, and there might be two reasons for the decrease in the hardness in the vortex region. First of all, during the experimental process of explosive welding, a large number of high-temperature

molten jet particles were strongly stirred and mixed on one side of the steel fiber to form the intermetallic compound FeAl. As the time was not enough to reduce the large-scale heat, these molten particles could not rapidly solidify, and the continuous stirring and mixing led to a large number of cracks, holes, and air pores in the vortex region, as shown in Figure 8, so the hardness of the vortex region decreased. Secondly, it can be seen from the EDS point scanning results of points 3 and 7 in Figure 8 that the interface between the vortex zone and the SS-304 stainless steel was composed of 14.4% SS-304 stainless steel and 55% aluminum, and the interface between the vortex zone and the 2A12 aluminum was composed of 1.3% SS-304 stainless steel and 88.6% 2A12 aluminum. According to the point scanning results of points 5 and 6, it can be seen that the vortex region was mainly composed of about 32% 2A12 aluminum and about 10% SS-304 stainless steel, while the microhardness of 2A12 aluminum was 126 Hv, so the microhardness of the vortex region decreased. The microhardness of SS-304 stainless steel in this test reached 419 Hv. The main reason for the significant increase in the microhardness of SS-304 stainless steel was that austenitic steel is one of the most obvious metal materials subjected to explosive strengthening. Therefore, explosive strengthening was more widely used in the strengthening process of austenitic steel than mechanical forging.

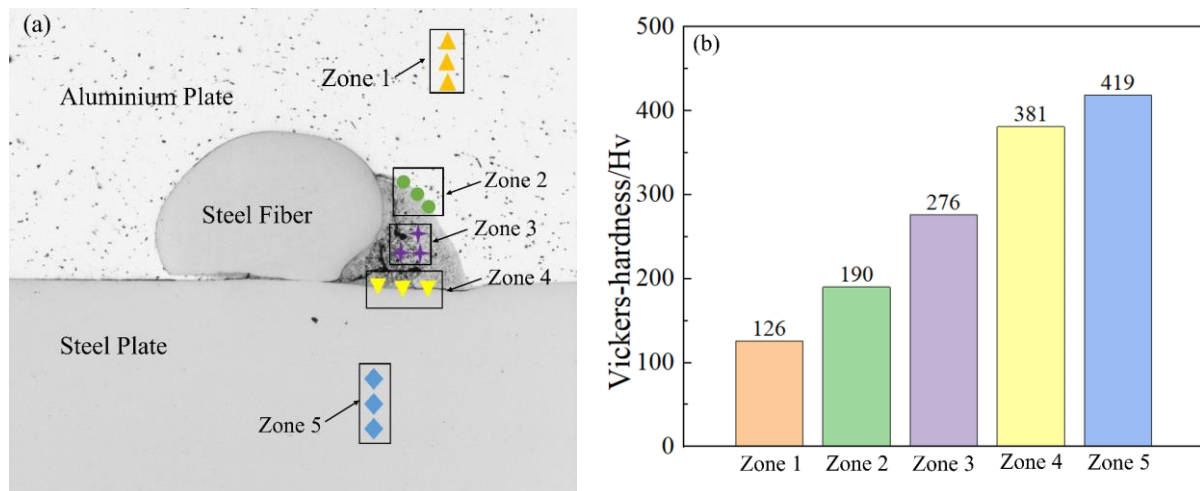


Figure 11. Microhardness at the interface of steel fiber-reinforced steel-aluminum composite plate: (a) microhardness test area; (b) microhardness test value.

3.4. Mechanical Property Testing

A 0.5 mm notch was opened on one side of the sample to measure the tensile strength of the sample, then the impact of the addition of steel fibers on the tensile properties of steel-aluminum composite plates prepared by explosive welding was explored. Three specimens were taken in the steel fiber parallel to the tensile load direction and the steel fiber perpendicular to the tensile load direction. The specific location and size parameters of the sample are shown in Figure 12. Then, the tensile test of the specimen was performed at room temperature by the UTM5000 series microcomputer-controlled electronic multipurpose testing machine at a loading rate of 2 mm/min. The accuracy of this series of equipment is class 0.5, and the error of test force indication of load parameters is within $\pm 0.5\%$ of the indicated value. Finally, the tensile strength of the specimen was calculated by the following formula [47].

$$\sigma = \frac{F}{S} \quad (7)$$

where σ is the tensile strength, F is the loading load, and S is the stressed area of the sample.

The samples in each group were from the same position in the center of four steel-aluminum composite plates prepared by explosive welding, aiming to avoid the influence of boundary effect on tensile samples. In Figure 13 there were no steel fibers in 1⁻ and 5⁺

samples, and the fiber diameters in 2[−] and 6⁺, 3[−] and 7⁺, 4[−] and 8⁺ samples were 0.25 mm, 0.35 mm, and 0.5 mm, respectively. To ensure the accuracy of the experimental data, each sample of the steel fiber parallel to the tensile load direction contained four steel fibers.

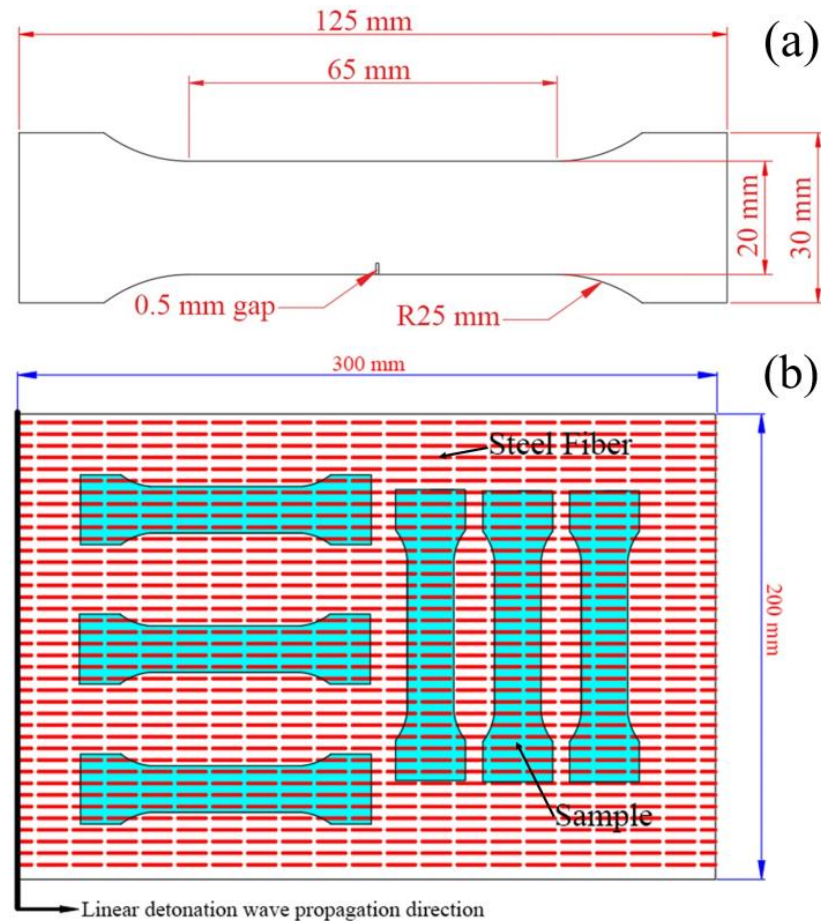


Figure 12. Tensile specimen parameters: (a) dimensional drawing of tensile specimen; (b) composite plate size, sampling position and linear detonation wave propagation direction diagram.

Table 4 shows the specific parameters of the tensile resistance of the steel fiber-reinforced steel-aluminum composite plate. “−” and “+” indicate that the steel fiber is parallel and perpendicular to the tensile load direction, respectively. In the direction of the steel fiber parallel to the tensile load, the average tensile strength of sample 1[−] was 420.53 MPa. The average tensile strength of sample 2[−] increased by 8.5% compared with sample 1[−], with the highest increase of 9.8% and the lowest increase of 7.0%; the average tensile strength of sample 3[−] increased by 15.4% compared with sample 1[−], with the highest increase of 18.3% and the lowest increase of 13.8%. The average tensile strength of sample 4[−] increased by 33.7% compared with sample 1[−], with the highest increase of 38.6% and the lowest increase of 29.9%. In the direction of the steel fiber perpendicular to the tensile load, the average tensile resistance of sample 5⁺ was 435.48 MPa, and the average tensile resistance strength of sample 6⁺ was 2.9% higher than that of sample 5⁺, with the highest increase of 3.5% and the lowest increase of 2.2%. Compared with sample 5⁺, the average tensile resistance strength of sample 7⁺ increased by 6.5%, with the highest increase of 8.9% and the lowest increase of 2.2%. Compared with sample 5⁺, the average tensile resistance strength of sample 8⁺ increased by 11.2%, with the highest increase of 14.8% and the lowest increase of 8.4%. The main difference between samples 1[−], 2[−], 3[−], 4[−] and samples 5⁺, 6⁺, 7⁺, 8⁺ was that the first four groups of samples were parallel to the direction of the tensile load and along the direction of the detonation wave propagation, while the last four groups were perpendicular to the direction of the tensile load and the

detonation wave propagation. Among them, the sample groups 1[−] and 5⁺ were from the steel-aluminum composite plates without steel fibers. When the highest and lowest tensile resistance properties were removed from the two groups of data, they were 435.35 MPa and 438.93 MPa, respectively. The difference in the tensile resistance between the two groups could be neglected, so the influence of the propagation direction of the detonation wave on the tensile resistance was excluded. In summary, the addition of steel fibers could improve the tensile resistance of steel-aluminum composite plates prepared by explosive welding. With the increase in steel fiber diameter, the tensile resistance strength increased gradually. Agraw Ryuichi [15] used explosive welding to produce a fiber composite consisting of a high-strength plastic steel wire and a pure aluminum or titanium matrix, and then verified the strength of the composite by tensile tests. The results revealed that the optimum tensile resistance load was determined by the volume of the fiber part, that is, the larger the volume of fibers added, the stronger the tensile resistance. Taking AMr6 aluminum alloy as the base plate and unidirectional fiber composited by steel wire as the reinforced composite material, Kotov V A [15] pointed out that the strength of this material depended on the internal geometric installation under uniaxial and biaxial loads in many cases. When the load was parallel to the fiber, the fiber had a particularly large effect on the composite. The results revealed that the fiber-reinforced composites and tubular products prepared by explosive welding had high enough strength under various loads. Explosion strengthening is using the force generated by explosives to replace mechanical forging so that the strength of steel is improved to a certain extent, and the effect of austenitic steel is more obvious when subjected to explosion strengthening process. Therefore, steel fiber was selected as the steel fiber-reinforced phase. The strengthening of metal composite materials prepared by explosive welding mainly includes two aspects: (1) after explosive welding, the base plate, composite plate, and steel fiber were all subjected to explosion strengthening, so their tensile strength was improved; (2) the overall tensile resistance strength of the composite material after explosive welding was better than that of the base plate metal [48]. With the addition of steel fibers, the tensile resistance of steel-aluminum composite plates was greatly increased. The tensile resistance of the steel fiber parallel to the tensile load direction was much larger than that perpendicular to the tensile load direction. Therefore, the tensile resistance of steel fiber-reinforced steel-aluminum composite plates was greatly improved. The main reasons are as follows. (1) During the explosive welding process, the tensile resistance of the steel fiber was improved due to the explosion strengthening. (2) The addition of steel fiber improved the overall tensile resistance of steel fiber-reinforced steel-aluminum composite plates.

Table 4. Tensile performance parameters of steel-aluminum composite plates.

Serial No.	First Group of Data/MPa	Second Group of Data/MPa	Third Group of Data/MPa	Mean Value/MPa
1 [−]	449.53	435.35	406.72	420.53
2 [−]	462.11	456.41	450.11	456.21
3 [−]	497.36	479.85	478.65	485.29
4 [−]	582.79	557.06	546.59	562.15
5 ⁺	442.36	438.93	425.15	435.48
6 ⁺	450.77	448.27	444.95	447.99
7 ⁺	474.48	468.88	448.09	463.80
8 ⁺	500.05	480.38	472.14	484.19

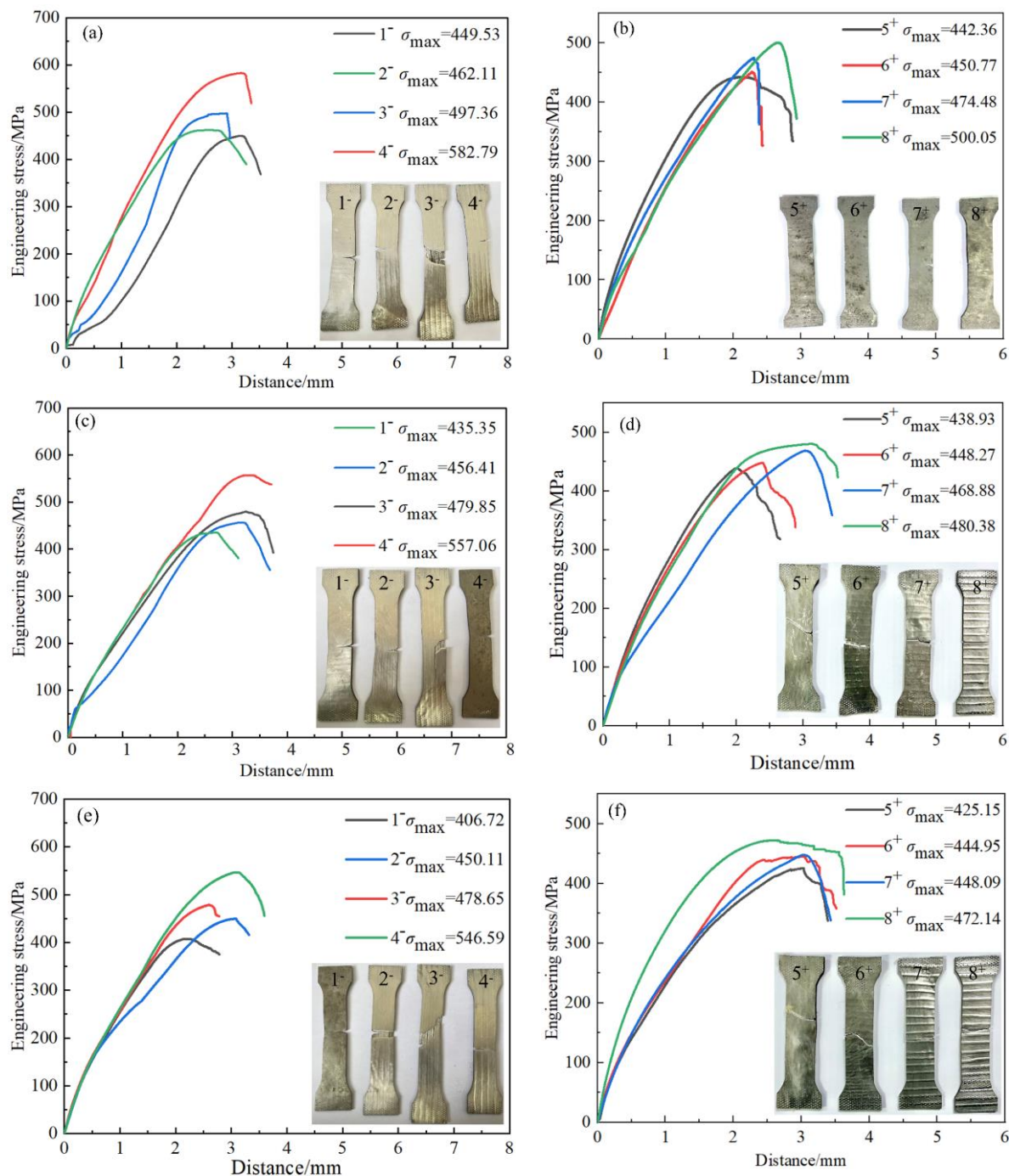


Figure 13. Tensile test and results: (a) the first group of tensile test samples and tensile data parallel to the fiber direction; (b) the first group of tensile test samples and tensile data orthogonal to the fiber direction; (c) the second group of tensile test samples and tensile data parallel to the fiber direction; (d) the second group of tensile test samples and tensile data orthogonal to the fiber direction; (e) the third group of tensile test samples and tensile data parallel to the fiber direction; (f) the third group of tensile test samples and tensile data orthogonal to the fiber direction.

3.5. Fracture Appearance Analysis

SEM was used to analyze the fracture of the tensile specimen and study the failure mechanism of steel fiber-reinforced steel-aluminum composite plates. Figure 14a shows the overall morphology of the fracture of the tensile specimen. From top to bottom, the layers are 2A12 aluminum, S20910 steel fibers and SS 304 stainless steel. The overall fracture morphology is relatively flat, but small tough nests and quasi-dissociative fracture

openings can still be observed, which proves that different fractures have occurred in the different materials. Meanwhile, it can be observed that the steel fibers have separated from the aluminum layer and remain bonded to the steel layer. Figure 14b shows the fracture morphology of the 2A12 aluminum layer, from which it can be observed that the fracture surface is hole-like, the hole is shallow and the edge of the hole is parabolic, showing an obvious dimple shape. Therefore, the fracture of the 2A12 aluminum layer is a ductile fracture, so it is worth noting that near the edge of the welding line, the dimple morphology of the 2A12 aluminum layer gradually changed, and the depth of the hole gradually became shallow. The main reason is that the composite plate was subjected to explosion strengthening during the explosive welding process, and as the deformation increased, the strength of the explosive strengthening also gradually increased, which also verified that the maximum deformation in the numerical simulation results occurred at the bonding interface, as shown in Figure 6c. The microhardness at the bonding interface between the 2A12 aluminum and steel fiber was also greater than that of the 2A12 aluminum, which further confirmed that the bonding interface was subjected to explosion strengthening, as shown in Figure 11. Figure 14c shows the fracture morphology of the steel layer under high multiples. Obvious tearing edges and holes can be observed, and there is no flat cleavage section, so the steel layer has a quasi-cleavage fracture. The fracture morphology of the steel fiber is shown in Figure 14d, from which it can be seen that the fracture of steel fiber is relatively flat, and there are small dimples and obvious tearing edges on the surface, so the steel fiber also has a quasi-cleavage fracture. Meanwhile, it can also be observed that not all the steel fiber is extracted, and the local section is reduced while maintaining the connection with the base plate and the composite plate, and it was judged that the steel fiber had a necking phenomenon. This is because the steel fiber has not completely broken after the fracture behavior of the plate during the stretching process, and the necking phenomenon was finally broken by stretching.

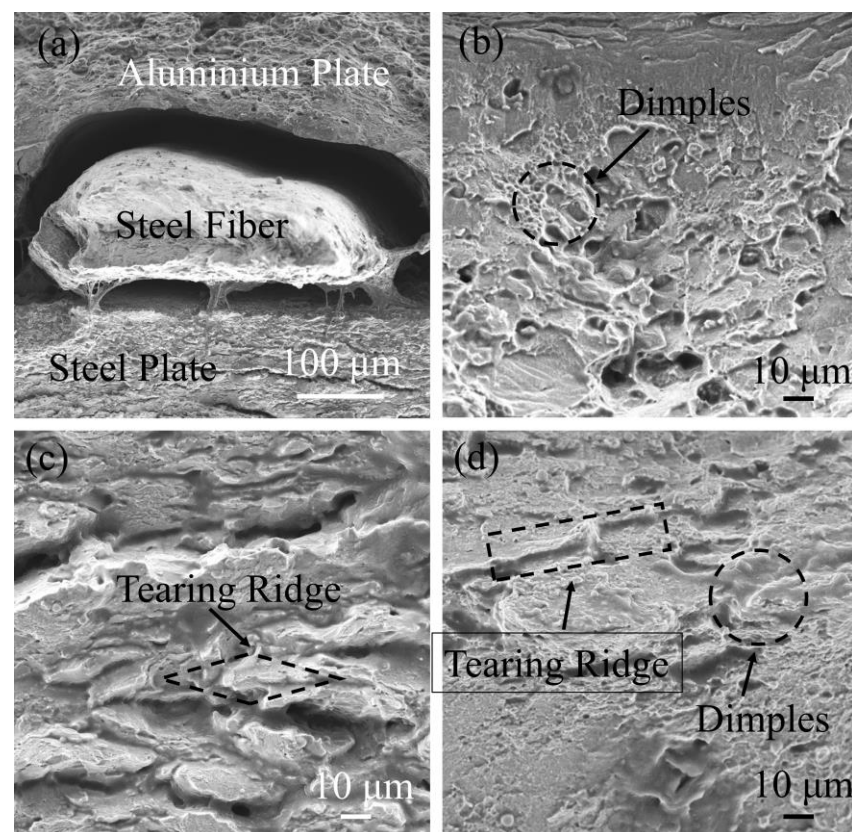


Figure 14. Fracture SEM of fiber-reinforced composite plate: (a) fracture SEM; (b) 2A12 aluminum fracture SEM; (c) SS-304 stainless steel fracture SEM; (d) fiber fracture SEM.

4. Conclusions

The steel fiber-reinforced steel-aluminum composite plate was successfully prepared by explosive welding, and the interface evolution mechanism of the steel-aluminum composite interface after adding steel fiber was simulated by the SPH method. Then, steel fiber-reinforced steel-aluminum composite plates were further studied using SEM, EDS, and tensile tests, and the following conclusions were drawn.

- (1) The SPH simulation method proved that there was a certain angle formed by the steel fiber, the base plate, and the composite plate, which blocked the direction of the jet so that the jet accumulated on one side of the steel fiber to form an environment with high temperature, high pressure, and high strain rate, thereby forming a vortex area. The residual stress of the jet particles in the vortex region forced them to undergo strong stirring, producing cracks, holes, and air pores in the vortex region.
- (2) SEM and EDS analysis proved the following two points. 1. The main reason for cracks, holes, and air pores in the vortex area was the formation of a large number of brittle intermetallic compounds, and the brittle intermetallic compound was mainly FeAl. 2. due to the blocking effect of steel fiber on the jet, the transition of elements at the interface of the composite plate with steel fiber was relatively fast.
- (3) Microhardness test results revealed that the cracks, holes, and air pores in the vortex region influenced the microhardness of the bonding interface to a certain extent. As the microhardness of 2A12 aluminum was relatively small, the microhardness increased with the decrease in 2A12 aluminum content in the vortex region.
- (4) The tensile test on the universal specimen machine proved that adding steel fibers could improve the antitensile properties of the steel-aluminum composite plates. The larger the diameter of steel fiber, the more obvious the tensile properties are. The main reason is that the steel fiber material is S20910 stainless steel, which was significantly strengthened during the explosion process.
- (5) Fracture morphology analysis indicated that 2A12 aluminum had a typical ductile fracture. The ductile fracture far from the bonding interface was more obvious because of explosion strengthening. The SS-304 stainless steel layer and steel fiber were quasi-cleavage fractures, and the steel fibers showed a necking phenomenon during fracture.

Author Contributions: Conceptualization, Y.G. (Yonghong Gao) and Y.C.; methodology, Y.G. (Yonghong Gao), Y.C. and C.G.; software, Y.C. and C.G.; validation, Y.G. (Yonghong Gao), Y.C., C.G. and Y.G. (Yanping Guo); formal analysis, Y.C., C.G. and Z.G.; investigation, Y.G. (Yonghong Gao), Y.C. and C.G.; resources, Y.G. (Yonghong Gao); data curation, Y.C., C.G. and Y.L.; writing—original draft preparation, Y.C.; writing—review and editing, Y.G. (Yonghong Gao), Y.C. and C.G.; visualization, T.L.; supervision, Y.G. (Yonghong Gao), Y.C., C.G. and T.L.; project administration, Y.G. (Yonghong Gao), Y.C. and C.G.; funding acquisition, Y.G. (Yonghong Gao). All authors have read and agreed to the published version of the manuscript.

Funding: This research received no external funding.

Data Availability Statement: Data are contained within this article.

Acknowledgments: The authors thank the North University of China for fabrication and characterizations, and specially Chuanxiang Guo for the co-supervision of Yao Chen.

Conflicts of Interest: The authors declare no conflict of interest.

References

1. Zeng, X.Y.; Li, X.J.; Chen, X.; Wang, X.-H.; Yan, H.-H. Numerical and experimental studies on the explosive welding of plates with different initial strength. *Weld. World* **2019**, *63*, 967–974. [CrossRef]
2. Wu, X.; Shi, C.; Fang, Z.; Lin, S.; Sun, Z. Comparative study on welding energy and Interface characteristics of titanium-aluminium explosive composites with and without interlayer. *Mater. Des.* **2021**, *197*, 109279. [CrossRef]
3. Zhang, Z.L.; Liu, M.B. Numerical studies on explosive welding with ANFO by using a density adaptive SPH method. *J. Manuf. Process.* **2019**, *41*, 208–220. [CrossRef]

4. Zhang, H.; Jiao, K.X.; Zhang, J.L.; Liu, J. Microstructure and mechanical properties investigations of copper-steel composite fabricated by explosive welding. *Mater. Sci. Eng. A* **2018**, *731*, 278–287. [CrossRef]
5. Gulenc, B. Investigation of interface properties and weldability of aluminum and copper plates by explosive welding method. *Mater. Des.* **2008**, *29*, 275–278. [CrossRef]
6. Chu, Q.; Tong, X.; Xu, S.; Zhang, M.; Li, J.; Yan, F.; Yan, C. Interfacial investigation of explosion-welded titanium/steel bimetallic plates. *J. Mater. Eng. Perform.* **2020**, *29*, 78–86. [CrossRef]
7. Kundu, S.; Ghosh, M.; Laik, A.; Bhanumurthy, K.; Kale, G.; Chatterjee, S. Diffusion bonding of commercially pure titanium to 304 stainless steel using copper interlayer. *Mater. Sci. Eng. A* **2005**, *407*, 154–160. [CrossRef]
8. Ghosh, M.; Bhanumurthy, M.; Kale, G.B.; Krishnan, J.; Chatterjee, S. Diffusion bonding of titanium to 304 stainless steel. *J. Nucl. Mater.* **2003**, *322*, 235–241. [CrossRef]
9. Gao, X.L.; Zhang, L.J.; Liu, J.; Zhang, J.-X. Porosity and microstructure in pulsed Nd:YAG laser welded Ti6Al4V sheet. *J. Mater. Process. Technol.* **2014**, *214*, 1316–1325. [CrossRef]
10. Akbari, M.; Saedodin, S.; Toghraie, D.; Shoja-Razavi, R.; Kowsari, F. Experimental and numerical investigation of temperature distribution and melt pool geometry during pulsed laser welding of Ti6Al4V alloy. *Opt. Laser Technol.* **2014**, *59*, 52–59. [CrossRef]
11. Yu, H.P.; Xu, Z.D.; Fan, Z.S.; Zhao, Z.; Li, C. Mechanical property and microstructure of aluminum alloy-steel tubes joint by magnetic pulse welding. *Mater. Sci. Eng. A* **2013**, *561*, 259–265. [CrossRef]
12. Geng, H.; Mao, J.; Zhang, X.; Li, G.; Cui, J. Strain rate sensitivity of Al-Fe magnetic pulse welds. *J. Mater. Process. Technol.* **2018**, *262*, 1–10. [CrossRef]
13. Liu, J.G.; Cai, W.C.; Liu, L.; Han, J. Investigation of interfacial structure and mechanical properties of titanium clad steel sheets prepared by a brazing-rolling process. *Mater. Sci. Eng. A* **2017**, *703*, 386–398. [CrossRef]
14. Xie, G.M.; Yang, D.H.; Luo, Z.A.; Li, M.; Wang, M.-K.; Misra, R.D.K. The determining role of Nb interlayer on interfacial microstructure and mechanical properties of Ti/steel clad plate by vacuum rolling cladding. *Materials* **2018**, *11*, 1983. [CrossRef]
15. Zheng, Y.M. *Explosive Welding and Explosive Composite Material*; National Defense Industry Press: Beijing, China, 2017.
16. Zhou, N. Study on Penetration Resistance and Damage Mechanism of Explosive Composite Functional Gradient Target. Ph.D. Thesis, Nanjing University of Science and Technology, Nanjing, China, 2014.
17. Wang, B.; Xiong, J.; Wang, X.J.; Ma, L.; Zhang, G.-Q.; Wu, L.-Z.; Feng, J.-C. Energy absorption efficiency of carbon fiber reinforced polymer laminates under high velocity impact. *Mater. Des.* **2013**, *50*, 140–148. [CrossRef]
18. Mahfuz, H.; Zhu, Y.; Haque, A.; Abutalib, A.; Vaidya, U.; Jeelani, S.; Gama, B.; Gillespie, J.; Fink, B. Investigation of high-velocity impact on integral armor using finite element method. *Int. J. Impact Eng.* **2000**, *24*, 203–217. [CrossRef]
19. Yang, M.; Xu, J.F.; Chen, D.G.; Ma, H.; Shen, Z.; Zhang, B.; Tian, J. Understanding interface evolution during explosive welding of silver foil and Q235 substrate through experimental observation coupled with simulation. *Appl. Surf. Sci.* **2021**, *566*, 150703.1–150703.10. [CrossRef]
20. Sun, Z.R.; Shi, C.G.; Shi, H.; Li, F.; Gao, L.; Wang, G. Comparative study of energy distribution and interface morphology in parallel and double vertical explosive welding by numerical simulations and experiments. *Mater. Des.* **2020**, *195*, 109027. [CrossRef]
21. Sun, W.; Li, X.J.; Yan, H.H.; Hokamoto, K. Effect of Initial Hardness on Interfacial Features in Underwater Explosive Welding of Tool Steel SKS3. *J. Mater. Eng. Perform.* **2014**, *23*, 421–428. [CrossRef]
22. Chen, X.Q.; Zhang, K.Y.; Zhan, F.M. Experiment and analysis of underwater explosive welding repair. *Blasting* **2004**, *21*, 3.
23. Liang, H.; Luo, N.; Li, X.J.; Sun, X.; Shen, T.; Ma, Z. Joining of Zr 60 Ti 17 Cu 12 Ni 11 bulk metallic glass and aluminium 1060 by underwater explosive welding method. *J. Manuf. Process.* **2019**, *45*, 115–122.
24. Zhang, Z.H.; Xue, J.X. Influence of droplet impact direction on weld quality. *J. South China Univ. Technol.* **2019**, *47*, 138–144.
25. Wu, Y.K.; Wu, R.; Zhang, M.Y.; Tan, S.; Lu, J.; Jiang, F. Enhancing explosive weldability of thick precipitate-hardened alloys. *J. Manuf. Process.* **2022**, *77*, 339–347. [CrossRef]
26. Zhou, Q.; Liu, R.; Chen, P.W.; Zhu, L. Microstructure characterization and tensile shear failure mechanism of the bonding interface of explosively welded titanium-steel composite. *Mater. Sci. Eng. A* **2021**, *820*, 141559. [CrossRef]
27. Zheng, Z.M.; Yang, Z.S. *Explosive Processing*; National Defense Industry Press: Beijing, China, 1981.
28. Zhou, Q.; Liu, R.; Zhou, Q.; Ran, C.; Fan, K.S.; Xie, J.; Chen, P.W. Effect of microstructure on mechanical properties of titanium-steel explosive welding interface. *Mater. Sci. Eng. A* **2022**, *830*, 142260. [CrossRef]
29. Yang, M.; Ma, H.; Shen, Z.; Chen, D.-G.; Deng, Y.-X. Microstructure and mechanical properties of Al-Fe meshing bonding interfaces manufactured by explosive welding. *Trans. Nonferrous Met. Soc. China* **2019**, *29*, 680–691. [CrossRef]
30. Chu, Q.; Zhang, M.; Li, J.; Yan, C. Experimental and numerical investigation of microstructure and mechanical behavior of titanium/steel interfaces prepared by explosive welding. *Mater. Sci. Eng. A* **2017**, *689*, 323–331. [CrossRef]
31. Gloc, M.; Wachowski, M.; Plocinski, T.; Kurzydowski, K.J. Microstructural and microanalysis investigations of bond titanium grade1/low alloy steel st52-3N obtained by explosive welding. *J. Alloys Compd.* **2016**, *671*, 446–451. [CrossRef]
32. Yang, M.; Ma, H.; Shen, Z.; Huang, Z.; Tian, Q.; Tian, J. Dissimilar material welding of tantalum foil and Q235 steel plate using improved explosive welding technique. *Mater. Des.* **2020**, *186*, 108348. [CrossRef]
33. Zhang, H.; Jiao, K.X.; Zhang, J.L.; Liu, J. Experimental and numerical investigations of interface characteristics of copper/steel composite prepared by explosive welding. *Mater. Des.* **2018**, *154*, 140–152. [CrossRef]

34. Bazarnik, P.; Adamczyk, C.B.; Gałka, A.; Płonka, B.; Sniezek, L.; Cantoni, M.; Lewandowska, M. Mechanical and microstructural characteristics of Ti6Al4V/AA2519 and Ti6Al4V/AA1050/AA2519 laminates manufactured by explosive welding. *Mater. Des.* **2016**, *111*, 146–157. [CrossRef]
35. Zeng, X.; Wang, Y.; Li, X.; Li, X.-J.; Zhao, T.-J. Effects of gaseous media on interfacial microstructure and mechanical properties of titanium/steel explosive welded composite plate. *Fusion Eng. Des.* **2019**, *148*, 111292.1–111292.9. [CrossRef]
36. Ning, J.; Zhang, L.J.; Xie, M.X.; Yang, H.-X.; Yin, X.-Q.; Zhang, J.-X. Microstructure and property inhomogeneity investigations of bonded Zr/Ti/steel trimetallic sheet fabricated by explosive welding. *J. Alloys Compd.* **2017**, *698*, 835–851. [CrossRef]
37. Wu, T.; Yang, C.L. Influence of pulse TIG welding thermal cycling on the microstructure and mechanical properties of explosively weld titanium/steel joint. *Vacuum* **2022**, *197*, 110817. [CrossRef]
38. Hoseini, M.M.; Tolaminejad, B. Weldability window and the effect of interface morphology on the properties of Al/Cu/Al laminated composites fabricated by explosive welding. *Mater. Des.* **2015**, *86*, 516–525. [CrossRef]
39. Jiang, S.; Shen, J.; Nagasaka, T.; Muroga, T.; Sagara, A.; Ohnuki, S.; Hokamoto, K.; Tanaka, S.; Inao, D.; Morizono, Y.; et al. Interfacial characterization of dissimilar-metals bonding between vanadium alloy and Hastelloy X alloy by explosive welding. *J. Nucl. Mater.* **2020**, *539*, 152322. [CrossRef]
40. Akbari, M.S.A.A.; Farhadi, S.P. Experimental investigation of explosive welding of cp-titanium/AISI 304 stainless steel. *Mater. Des.* **2009**, *30*, 459–468. [CrossRef]
41. Aceves, S.M.; Espinosa, L.F.; Elmer, J.W.; Huber, R. Comparison of Cu, Ti and Ta interlayer explosively fabricated aluminum to stainless steel transition joints for cryogenic pressurized hydrogen storage. *Int. J. Hydrogen Energy* **2015**, *40*, 1490–1503. [CrossRef]
42. Zhang, Z.L.; Feng, D.; Liu, M.B. Investigation of explosive welding through whole process modeling using a density adaptive SPH method. *J. Manuf. Process.* **2018**, *35*, 169–189. [CrossRef]
43. Nassiri, A.; Abke, T.; Daehn, G. Investigation of melting phenomena in solid-state welding processes. *Scr. Mater.* **2019**, *168*, 61–66. [CrossRef]
44. Song, J.; Kostka, A.; Veehmayer, M.; Raabe, D. Hierarchical microstructure of explosive joints: Example of titanium to steel cladding. *Mater. Sci. Eng. A* **2011**, *528*, 2641–2647. [CrossRef]
45. Carvalho, G.; Galvo, I.; Mendes, R.; Leal, R.; Loureiro, A. Explosive welding of aluminium to stainless steel using carbon steel and niobium interlayers. *J. Mater. Process. Technol.* **2020**, *283*, 116707. [CrossRef]
46. Venkateswaran, P.; Xu, Z.H.; Li, X.; Reynolds, A.P. Determination of mechanical properties of Al–Mg alloys dissimilar friction stir welded interface by indentation methods. *J. Mater. Sci.* **2009**, *44*, 4140–4147. [CrossRef]
47. Wang, Y.X.; Beom, H.G.; Sun, M.; Lin, S. Numerical simulation of explosive welding using the material point method. *Int. J. Impact Eng.* **2011**, *38*, 51–60. [CrossRef]
48. Zheng, Y.M.; Huang, G.R.; Chen, S.H. Strengthening of metals in explosive composites. *Eng. Blasting* **2000**, *6*, 7–25.

Disclaimer/Publisher’s Note: The statements, opinions and data contained in all publications are solely those of the individual author(s) and contributor(s) and not of MDPI and/or the editor(s). MDPI and/or the editor(s) disclaim responsibility for any injury to people or property resulting from any ideas, methods, instructions or products referred to in the content.

MDPI AG
Grosspeteranlage 5
4052 Basel
Switzerland
Tel.: +41 61 683 77 34

MDPI Books Editorial Office
E-mail: books@mdpi.com
www.mdpi.com/books



Disclaimer/Publisher's Note: The title and front matter of this reprint are at the discretion of the Topic Editors. The publisher is not responsible for their content or any associated concerns. The statements, opinions and data contained in all individual articles are solely those of the individual Editors and contributors and not of MDPI. MDPI disclaims responsibility for any injury to people or property resulting from any ideas, methods, instructions or products referred to in the content.



Academic Open
Access Publishing

mdpi.com

ISBN 978-3-7258-3882-0